



HAL
open science

Modeling flow boiling in nuclear reactor conditions using computational fluid dynamics: application to critical heat flux prediction

Corentin Reiss

► **To cite this version:**

Corentin Reiss. Modeling flow boiling in nuclear reactor conditions using computational fluid dynamics: application to critical heat flux prediction. Fluid Dynamics [physics.flu-dyn]. Université de Toulouse, 2024. English. NNT : 2024TLSEP080 . tel-04804622

HAL Id: tel-04804622

<https://theses.hal.science/tel-04804622v1>

Submitted on 26 Nov 2024

HAL is a multi-disciplinary open access archive for the deposit and dissemination of scientific research documents, whether they are published or not. The documents may come from teaching and research institutions in France or abroad, or from public or private research centers.

L'archive ouverte pluridisciplinaire **HAL**, est destinée au dépôt et à la diffusion de documents scientifiques de niveau recherche, publiés ou non, émanant des établissements d'enseignement et de recherche français ou étrangers, des laboratoires publics ou privés.

Doctorat de l'Université de Toulouse

préparé à Toulouse INP

Modélisation des écoulements bouillants en réacteur nucléaire
par CFD : application à la prédiction du flux critique

Thèse présentée et soutenue, le 15 octobre 2024 par

Corentin REISS

École doctorale

MEGEP - Mécanique, Energétique, Génie civil, Procédés

Spécialité

Dynamique des fluides

Unité de recherche

IMFT - Institut de Mécanique des Fluides de Toulouse

Thèse dirigée par

Catherine COLIN et Antoine GERSCHENFELD

Composition du jury

M. Olivier SIMONIN, Président, Toulouse INP

M. Yohei SATO, Rapporteur, Paul Scherrer Institut

M. Dirk LUCAS, Rapporteur, Helmholtz-Zentrum Dresden-Rossendorf

M. Pierre RUYER, Examineur, IRSN

Mme Catherine COLIN, Directrice de thèse, Toulouse INP

M. Antoine GERSCHENFELD, Co-directeur de thèse, CEA Paris-Saclay

Membres invités

M. Nicolas Goreaud, Framatome

**Modeling flow boiling
in nuclear reactor conditions
using computational fluid dynamics:
application to critical heat flux prediction**

All models are wrong. Some are useful.
George Box

*Quand on veut être sûr de son coup, mon petit bonhomme,
on plante des carottes, on ne fait pas de la CFD diphasique !*
Adapté de Anne de Tintagel, Kaamelott

Remerciements

C'est ici que s'achève cette aventure, qui, comme toute thèse, a pris un chemin bien différent de celui initialement prévu: à l'instar de nombreux doctorants en "physique" au STMF, j'ai dû commencer par deux années de code. Obtenir des résultats moyens avec les fermetures historiques m'a néanmoins permis de faire ce que je préfère, de la modélisation, au cœur de ma dernière année de thèse. Mine de rien, je n'ai pas fini si loin de l'objectif initial. J'ai même versé une petite larme en voyant les points s'aligner sur la figure 10.11.

Si mon nom figure en grand sur la couverture de ce document, la recherche scientifique, elle, se construit toujours en équipe.

En premier lieu, ce sont mes encadrants qui m'ont permis d'aborder autant de facettes différentes du diphasique. Leur expertise, leur ambition et leur disponibilité ont été cruciaux. Ils ont même accepté de ma faire confiance quand j'ai dit "je vais à la cave chercher des papiers soviétiques sur microfilm" ou "je vais enlever le diamètre de bulles de mes simulations".

Merci Antoine. Tu as construit le sujet pour moi et a su m'accompagner dans tous les aspects de ma thèse. J'ai choisi de partir avec toi pour deux raisons: tu avais l'air cool (même si tu doutes que ce soit possible) et assez brillant pour continuer à m'apprendre des choses même après 3 ans de thèse. Je ne me suis pas trompé: tu as été un encadrant utile et agréable. Tu as pris beaucoup de temps pour me former et tu étais toujours disponible pour discuter autour d'un café. C'était très confortable de travailler avec quelqu'un qui comprenait immédiatement là où je voulais en venir sur tous les sujets, même quand ce n'était pas clair pour moi.

Merci Catherine. Tu commences à avoir l'habitude d'encadrer des thèses sensées être sur la prédiction du flux critique par CFD diphasique et qui se terminent par la construction d'une partition de flux pariétale. Bien qu'à distance, et bien que tu n'aies choisi ni le sujet ni le candidat, tu as été très présente au cours de la thèse. Ta gentillesse est sans limites, ta maîtrise de la littérature encyclopédique, et tes remarques m'ont permis de beaucoup améliorer la clarté de mon travail. Merci en particulier dans la rédaction du manuscrit et pour la préparation de la soutenance, et désolé d'avoir un peu laissé tomber le drift-flux.

Many thanks to Dirk Lucas and Yohei Sato for reviewing the manuscript and coming to Saclay for my defense. Merci à Olivier Simonin d'avoir assuré la présidence de mon jury. Merci à Pierre Ruyer pour avoir fait partie de mon jury et de mon CSI.

L'origine lointaine de cette thèse se trouve chez les enseignants qui m'ont transmis leur vision de la science. Merci à Jérôme Coup, qui m'a appris que la belle physique se fait avec le moins d'équations possible. Merci aussi à Christophe Clanet de m'avoir inculqué son approche de simplification de phénomènes complexes: si un rugbyman est une poutre, un cycliste une boule et un muscle une seringue, alors peut-être qu'un écoulement bouillant est moins compliqué qu'il n'y paraît. Thanks to Peko Hosoi, for who every aspect of scientific research can be fun, including

creating beautiful graphs.

Merci à Catherine Lagneau, Clément Le Gouellec, Yannick D'Escatha, Gilles Perrin et Yves Bréchet d'avoir contribué à la construction de ma thèse, et à la direction scientifique du CEA de l'avoir financée.

Pour avoir toujours sù répondre à mes questions sur TRUST et intégré mes développements au fur et à mesure, un immense merci à Élie Saikali et Yannick Gorsse, qui formaient avec Antoine les trois mousquetaires de Pb_Multiphase. Merci au reste de l'équipe TRUST pour leur aide: Adrien, Pierre, Anida et Luc. Je garde un super souvenir des cafés TRUST, des verres au golf, des barbecues et des soirées crêperie.

Merci à mes chefs de labo, d'abord Didier (le soldat Schneider de base!) puis Sandrine. Toujours à l'écoute, vous avez tout fait pour me simplifier la vie tout au long de ma thèse.

Merci à la team CFD diphasique du LMSF pour de nombreuses discussions et débats passionnants (les mailles peuvent-elles être plus petites que les bulles ?) : Alan et son cliquage, Guillaume, Étienne, Antoine et Clément. Merci à Moncef et Mathilde, les merveilleux stagiaires coencadrés avec Alan, qui m'ont permis d'échapper un peu à la haute pression et avec qui on a fait des choses sympas.

Pour l'inspiration et les déclics qui m'ont fait avancer : merci à messieurs Saha et Zuber, auteurs d'un rare modèle diphasique simple qui marche bien sur une base de données large, Michel Klédy pour la figure 7.9 de sa thèse, Artyom Kossolapov pour la figure 5.2 de la sienne et Raskmy Nop pour son modèle de manteau homogène.

Sans eux, notre travail de numériciens n'aurait aucun sens : merci aux expérimentateurs qui nous fournissent des données à exploiter pour comprendre la physique. Merci Fabrice et Paul pour nos nombreux partages. Bien que je ne les ai jamais rencontrés, merci à G. Cubizolles, R. Martin, F.W. Staub, C.C. St. Pierre, G.G. Bartolomei et tous les autres.

Les échanges avec des spécialistes de Framatome tout au long de ma thèse, sur le RIA ou les GV, ont été très précieux. Merci à Nicolas Goreaud, Ferdinand Louis, Hamza Ahfidi, Florian Vinauger et Benjamin Farges.

Pour compléter l'équipe de France du nucléaire, merci à l'équipe NEPTUNE_CFD d'EDF R&D d'avoir toujours gardé la porte ouverte pour parler de physique malgré les dissensions stratégiques sur le code utilisé : Luc Favre, Stéphane Mimouni, Nicolas Méricoux, Chai Koren et Jérôme Laviéville.

Merci au groupe interfaces de l'IMFT de m'avoir toujours réservé un bon accueil quand je venais passer du temps dans ce bureau avec vue sur la Garonne: Pierre, Johann, Paul, Modou, Julien, Frédéric, Rémi et Thierry.

Merci aux doctorants du STMF pour les bons moments passés ensemble au CEA, au Deer 'n' Beer ou en conférence: Tanguy, Mathis, Gabriel, Ayoub, Matthieu, Antonin, Élie, Alexis, Antony, Pierre-Louis, Héloïse, Nathalie, Nicolas, Grégoire, François... Merci à Clément d'avoir géré le séminaire avec moi et Noa et Capucine de l'avoir repris.

Pour les fous rires à la salle café et à la cantine, les verres à l'Indiana, les discussions absurdes pouvant être plus ou moins cringe portant sur la timidité, le port de la moustache, la Belgique, le tofu, les spectres, la masculinité, les couques

ou le 1-2-1, merci aux jeunes du LMEC. Les meubles: Esteban (sans accent), co-bureau pendant la plupart de ma thèse, Théotime, Damien et Pierre-Loïc. Les nouveaux arrivés: Quentin, Matthieu, Thomas et Lidija. Les stagiaires partis trop tôt: Pierre, Lucas, Pierre-Louis. Vous allez me manquer. Maintenant qu'on n'est plus collègues, on peut se dire amis ;) Glouglou !

Je ne peux citer tous les membres du LMEC, STMF et SGLS avec qui j'ai passé de bons moments. Merci à Marc, Florian, Thomas, Michaël, Simon, Martin, Clément, Raphaël, Jean Marc, Alexis, Sofia, Erwan, Cassiano, Nicolas, Thibaut et tous les autres.

J'ai eu la chance de compter sur des amis ayant connu une expérience similaire pendant ma thèse: Félix, Flavien, Clémence, Robin et Lucien. En plus des éclats de rire, le partage d'expérience et votre recul m'ont beaucoup aidé. Merci aussi à Théo, Roché et Mimou que j'ai souvent retrouvé à la montagne et sur les quais.

Merci à ma famille pour leur amour et leur soutien. Merci à mes parents d'avoir toujours encouragé ma curiosité, de m'avoir fait manger des cahiers de maths dès le CP et de m'avoir inculqué le goût de l'effort. Merci à Guilhem, qui aura réussi à commencer à bosser avant moi. Merci à mes grand-parents, à Thierry et à Marion, à Christine et Didier.

Et merci à Jasmine. Vivre avec toi suffit à mon bonheur.

Abstract

Under incidental conditions in pressurized water reactors, the water used to cool the nuclear fuel can start to boil. It is essential to predict the dynamics of such multi-phase flows to guarantee reactor safety. The methods currently used in the industry today are focused on the large-scale characteristics of the flows and require specific experiments for every geometry and flow configuration. The aim of the present work is to build a numerical tool and a set of physical models to predict the characteristics of boiling flows in nuclear reactor conditions at a local scale, in a framework called computational fluid dynamics (CFD). In the future, this will enable us to simulate configurations where no experiment is available. We develop a multiphase module in CEA's TrioCFD open-source CFD code. A Reynolds averaged Navier-Stokes two-fluid framework that can solve a mass, momentum and energy equation for an arbitrary number of phases is implemented in two different numerical schemes: one that enables good performance on Cartesian and axisymmetric grids and one that can handle arbitrary polynomial meshes. For multiphase flows, standard drag, lift, turbulent dispersion and wall repulsion forces are coded. The software is validated on standard atmospheric-pressure adiabatic databases where the simulations agree with experimental data. A condensation term and a heat flux partition are added to this set of closures to simulate boiling flows. We first use the DEBORA database, a Freon-filled tube, to evaluate the performance of our set of closures. The experimental bubble diameter is enforced in the code along the whole length of the test section, enabling simulations without the uncertainty of interfacial area transport equations. The predicted void fraction profiles are far from the experimental results, often too high in the near-wall region. This prompts us to investigate the onset of significant void (OSV) in CFD codes. Using experimental data from a dozen different sources, we construct an OSV database. Combining this database with experimental liquid temperature measurements in boiling flows, we show that the OSV in a stationary developed flow occurs when the turbulent boundary layer reaches saturation temperature. This criterion is used to develop a simple heat flux partition that improves results on the DEBORA database compared with the closures from the literature. We then work on improving the bulk closure terms adapted to high-pressure, heat flux, mass flux and void fraction conditions of nuclear reactors. We show that in this situation, bubbles are deformable, i.e. non-spherical. We use this to construct our own lift coefficient and condensation term, and combine them with references from the literature for drag and turbulent dispersion. Innovatively, no interfacial area equation or population balance is required. This set of closures provides good agreement with the DEBORA experiment. To extend the validation, we built a database that includes recent and ancient high-pressure (>40 bar) local void fraction measures in pipes, annulus and channels. The results obtained in 114 test conditions are close to experimental data. We then simulate critical heat flux (CHF) experiments to obtain physical quantities in the near-wall region at the boiling crisis. By analyzing these results, we build an empirical CHF criterion for stationary flows where the liquid remains subcooled in the near-wall region. It predicts the CHF with $\sim 10\%$ precision.

Résumé

Sous des conditions incidentelles dans les réacteurs à eau pressurisée, l'eau utilisée pour refroidir le combustible nucléaire peut entrer en ébullition. Pour garantir la sûreté des réacteurs, il est indispensable de prédire la dynamique de ces écoulements multiphasiques. Les méthodes actuellement utilisées dans l'industrie s'intéressent aux caractéristiques à grande échelle des écoulements et nécessitent des expériences spécifiques pour chaque géométrie et configuration. L'objectif de cette thèse est de construire un outil numérique et un ensemble de modèles physiques pour prédire les caractéristiques des écoulements en ébullition dans des conditions de réacteur nucléaire à une échelle locale, dans le cadre des outils de CFD (computational fluid dynamics). Cela nous permettra à l'avenir de simuler des configurations pour lesquelles aucune expérience n'est disponible. Nous avons développé un module multiphasique dans le code TrioCFD du CEA. Il utilise un modèle RANS (Reynolds averaged Navier-Stokes) bi-fluide avec une équation de conservation de la masse, de la quantité de mouvement et de l'énergie pour un nombre de fluides quelconques, ou un modèle de dérive. Deux schémas numériques peuvent être utilisés pour résoudre ces équations : un qui permet des calculs rapides sur maillages cartésiens et axisymétriques et un qui permet des simulations sur maillages polyédriques quelconques. Des fermetures standards de forces de trainée, portance, dispersion turbulente et répulsion en paroi sont intégrées. L'outil de calcul est ensuite validé sur des écoulements à bulles eau-air à pression atmosphérique. Pour modéliser des écoulements bouillants, un terme de condensation et une partition de flux pariétale sont implémentés. La base de données DEBORA, un tube rempli de réfrigérant dans des conditions de similitude vis-à-vis des réacteurs nucléaires, est utilisée comme référence. Le diamètre expérimental est imposé dans le code pour simuler les expériences, ce qui nous permet de lancer des simulations sans les incertitudes liées à l'utilisation d'équations de transport d'aire interfaciale. Les taux de vide prédits par le code sont loin des résultats expérimentaux, et sont trop grands dans la zone en proche paroi. Ceci nous a poussé à regarder de près l'OSV (onset of significant void) dans les codes de CFD. Nous avons construit une base de données sur ce phénomène. En utilisant la structure de la température du liquide dans les écoulements bouillants, nous montrons que l'OSV en écoulement stationnaire développé a lieu lorsque la couche limite turbulente atteint la température de saturation. Ce critère est utilisé pour construire une partition de flux pariétale. Nous avons ensuite cherché à améliorer les fermetures dans le cœur de l'écoulement en réacteur nucléaire, soit dans des conditions de haute pression, flux thermique, débit massique et taux de vide. Nous montrons que dans cette situation les bulles de vapeur sont toujours déformées, i.e. non sphériques. Ceci nous permet de construire des fermetures de portance et de condensation, que nous combinons avec des formulations de trainée et de dispersion turbulente de la littérature. Ce jeu de fermetures est indépendant du diamètre de bulle. Les comparaisons avec l'expérience DEBORA donnent des bons résultats. Pour étendre la validation, nous avons construit une base de données haute pression (>40 bar) en eau ou en similitude basée sur des expériences de la littérature qui incluent des sections annulaires, circulaires et rectangulaires. Les résultats obtenus sur les 114 conditions d'essai et 7 campagnes expérimentales sont satisfaisants. Pour finir, nous avons simulé des expériences de flux critique pour obtenir les conditions en proche paroi lors de la crise d'ébullition. L'analyse de ces résultats nous permet de construire un critère simple de flux critique en écoulement stationnaire où le liquide est sous-refroidi en proche paroi.

Contributions

Journal papers:

- **Corentin Reiss**, Antoine Gerschenfeld, and Catherine Colin. "Boiling-flow multiphase CFD simulations for nuclear reactor conditions without interfacial area transport equation." *Nuclear Engineering and Design*. 2024. Vol 428. DOI: [10.1016/j.nucengdes.2024.113453](https://doi.org/10.1016/j.nucengdes.2024.113453).
- **Corentin Reiss**, Antoine Gerschenfeld, and Catherine Colin. "Heat flux partition based on onset of significant void." *International Journal of Multiphase Flow*. 2024. Vol 181. DOI: [10.1016/j.ijmultiphaseflow.2024.104972](https://doi.org/10.1016/j.ijmultiphaseflow.2024.104972).

Conference papers:

- **Corentin Reiss**, Antoine Gerschenfeld, and Catherine Colin. "Building a boiling-flow multiphase CFD framework for interfacial area and heat transfer modeling." *NURETH20-20th International Topical Meeting on Nuclear Reactor Thermal Hydraulics*. 2023. url: <https://cea.hal.science/cea-04190863>.
- **Corentin Reiss**, Antoine Gerschenfeld, Elie Saikali, Yannick Gorsse and Alan Burlot. "Presenting the multi-phase solver implemented in the open source TrioCFD code based on the TRUST HPC platform." *EPJ Web Conf*. Vol. 302. No. 03001. *Joint International Conference on Supercomputing in Nuclear Applications + Monte Carlo (SNA + MC 2024)*. DOI: [10.1051/epj-conf/202430203001](https://doi.org/10.1051/epj-conf/202430203001).

CEA technical reports:

- Cassiano Tecchio, Raksmy Nop, Alberto Ghione, Jean-Marc Labit, **Corentin Reiss**. "Spécifications techniques des besoins expérimentaux pour la validation des modèles d'ébullition en convection forcée". "Technical specifications for experimental needs for forced convection boiling model validation". 2023.
- Alan Burlot, Clément Bazin, Guillaume Jomée, François Pecquery, Andrew Peitavy, **Corentin Reiss**. "Multiphase TRUST/TrioCFD module documentation". 2024.

Part of the data and associated data analysis is available on my GitHub page (<https://github.com/CoReiss>).

If you wish to discuss my work or multiphase flows in general, notice any mistake in the document, would like to obtain data, Python programs or results, please contact me at my permanent e-mail address:

`corentin.reiss@gmail.com`

Contents

Abstract	vii
Résumé	viii
Contents	x
1 Introduction	1
1.1 Pressurized water reactors	3
1.2 Fluid dynamics in the nuclear industry	5
1.3 Reactivity-Initiated Boiling Crisis	7
1.4 Multiphase computational fluid dynamics	11
1.5 Contribution	17
1.6 Outline of this thesis	20
Baseline simulation	23
2 Presentation of the TrioCFD multiphase module	23
2.1 TrioCFD N -fluid multiphase solver	25
2.2 Physical closure models	30
2.3 The drift-flux model	38
3 Verification and validation	45
3.1 Code verification	47
3.2 Framework validation	53
3.3 Comparing the two-fluid model with the drift-flux model	59
3.4 Conclusion	60
4 Analysis of the DEBORA experimental database	61
4.1 Similarity for nuclear reactor conditions	63
4.2 The DEBORA loop	64
4.3 The liquid temperature log-law	70
4.4 The test tube hypothesis	74
4.5 Determining vapor radial velocities	79
4.6 Coalescence and breakup for interfacial area modeling	79

5	Fixed-diameter simulations	81
5.1	Detailed analysis of selected runs	83
5.2	Results on a larger part of the DEBORA database	87
5.3	Main issues with the baseline set of closures	88
	Model improvement	91
6	Heat flux partition based on onset of significant void	91
6.1	Introduction	93
6.2	Construction and analysis of an OSV database	96
6.3	CFD-scale approach	102
6.4	Use for Heat Flux Partitioning	108
6.5	Conclusion	118
7	Improving bulk flow closures	119
7.1	Relative velocity inversion	121
7.2	Deformed bubble hypothesis	121
7.3	Drag force	124
7.4	Lift force	125
7.5	Turbulent dispersion force	126
7.6	Condensation	129
7.7	Complete model	143
8	Simulations on the extended local database	147
8.1	Building a large local high-pressure database	149
8.2	DEBORA	152
8.3	Saint-Pierre	156
8.4	Staub et al.	159
8.5	Martin	164
8.6	Chu et al.	170
8.7	Strengths and limits of the proposed set of closures	174
8.8	Other databases that can be used for multi-phase CFD validation	175
	Towards CHF	179
9	A critical heat flux criterion for R12 subcooled flow	179
9.1	CHF prediction approaches from the literature	181
9.2	DEBORA critical heat flux measuring campaigns	187
9.3	CFD Simulations of conditions at CHF in the DEBORA database	187
9.4	A simple CHF correlation for subcooled high-pressure freon-R12	191
9.5	Limits of the proposed correlation	197
10	Subcooled CHF in the Groeneveld database	199
10.1	The Groeneveld database	201

10.2	Simulation setup	206
10.3	The CHF in subcooled high-pressure developed water flow	207
10.4	Towards a single criterion for two different fluids	210
10.5	Simulations of PATRICIA transient flows	215
10.6	Perspectives	221
11	Conclusion	223
11.1	Main results	224
11.2	Perspectives	228
11.3	What I learned	230
	References	232
	 Appendix	 261
A	Horizontal flow lift force differs from vertical flow lift force	261
A.1	Introduction	262
A.2	Simulation setup	263
A.3	Results and discussion	265
A.4	Conclusion	267
B	Reconstruction of velocity and temperature profiles in DEBORA	269
B.1	Experimental data interpolation on a test tube	270
B.2	Axial velocity approximation	271
B.3	Radial mixture integration	273
B.4	Liquid temperature determination	274
B.5	Vapor and liquid radial velocity determination	275
C	Analysis of bubble coalescence and breakup in DEBORA	279
C.1	Different frameworks to determine bubble diameter distributions	280
C.2	Coalescence-breakup term determination	281
C.3	Coalescence and breakup formulations from the literature	282
C.4	A simple return-to-equilibrium proposal	286
D	Burns turbulent dispersion considers the dispersed phase as a passive scalar	289
D.1	Introduction	291
D.2	Analytical analysis	294
D.3	Simulation	296
D.4	Conclusion	297
E	Onset of significant void database	299
F	All local flow boiling simulation results	303

Nomenclature

Acronyms

Symbol	Description	Units
BC	Boiling Crisis	
BIT	Bubble-Induced Turbulence	
BWR	Boiling Water Reactor	
CFD	Computational Fluid Dynamics	
CHF	Critical Heat Flux	
DNB	Departure from Nucleate Boiling	
DO	Dry-Out	
HFP	Heat Flux Partition	
LSD	Liquid Sublayer Dryout	
LUT	Look-Up Table	
MAE	Mean Average Error	
MSE	Mean Square Error	
MVG	Mixing Vane Grid	
NMSE	Normalized Mean Square Error	
ONB	Onset of Nucleate Boiling	
OSV	Onset of Significant Void	
PWR	Pressurized Water Reactor	
REA	Rod Ejection Accident	
RIA	Reactivity-Induced Accident	
SZ	Saha and Zuber 1974 OSV correlation	

Dimensionless Numbers

Symbol	Description	Units
$\Phi_{loc} = \frac{q_w}{\rho_l u_\tau h_{lv}}$	Local boiling number	1
$Bo = \frac{q_w}{G h_{lv}}$	Boiling number	1
$EO = \frac{(\rho_l - \rho_g) g d_b^2}{\sigma}$	Eötvös number	1
Nu_b	Bubble Nusselt number	1
$Nu_h = \frac{q_w D_h}{\lambda_l (T_s - T_{bulk})}$	Nusselt number	1
$Pe_h = \frac{D_h u_{bulk} \rho_l C_p}{\lambda_l}$	Bulk Peclet number (uses hydraulic diameter)	1
$Pr = \frac{\nu_l \rho C_{pl}}{\lambda_l}$	Liquid Prandtl number	1
$Re_h = \frac{D_h u_{bulk}}{\nu_l}$	Bulk Reynolds number (uses hydraulic diameter)	1
$St = \frac{q_w}{G C_p (T_s - T_{bulk})}$	Stanton number	1
$We_h = \frac{G^2 D_h}{\sigma \rho_l}$	Channel Weber number	1
$We_\epsilon = \frac{\rho_l d_b (\epsilon d_b)^{2/3}}{\sigma}$	Turbulent Weber number	1

Greek Symbols

Symbol	Description	Units
$\langle \alpha \rangle$	Average vapor fraction on the test section	1
α_k	Volume fraction of phase k	1
$\alpha_{CHF,1}$	Vapor volume fraction in the near-wall cell at CHF	1
$\alpha_{v,1}$	Vapor volume fraction in the near-wall cell	1
β	Additive constant in the liquid temperature log-law	1
$\beta_{CHF,1}$	Value of β at the boiling crisis calculated using the liquid temperature in the near-wall cell	1
β_{CHF}	Value of β at the boiling crisis	1
β_{OSV}	Value of β at the point of onset of significant void	1

$\Delta T_{\text{bulk}} = T_s - T_{\text{bulk}}$	Liquid bulk subcooling	K
Γ_{km}	Bulk interfacial mass transfer towards phase k from phase m	$\text{m}^{-3}\text{s}^{-1}$
$\Gamma_{w,km}$	Wall interfacial mass transfer towards phase k from phase m	$\text{m}^{-2}\text{s}^{-1}$
λ_k	Thermal conductivity of phase k	$\text{Wm}^{-1}\text{K}^{-1}$
μ_k	Dynamic viscosity of phase k	$\text{Pa}\cdot\text{s}$
ν_k	Kinematic viscosity of phase k	m^2s^{-1}
ν_t	Turbulent kinetic viscosity of liquid	m^2s^{-1}
ω	Specific turbulent dissipation rate of liquid	s^{-1}
$\omega_+ = \frac{\omega u_\tau}{\nu}$	Non-dimensional specific turbulent dissipation rate	1
ρ_k	Volume mass of phase k	kgm^{-3}
σ	Surface tension	Nm^{-1}
τ_{wf}	Shear stress at the wall	Nm^{-2}
$\Theta_+^s = \frac{T_l - T_s}{T_*}$	Normalized liquid temperature with respect to saturation temperature	1
$\Theta_+^w(y_+) = \frac{T_w - T_l}{T_*}$	Normalized liquid temperature with respect to wall temperature	1

Roman Symbols

Symbol	Description	Units
\mathcal{A}	Area of the test section	m^2
\mathcal{P}	Perimeter of the test section	m
\mathcal{P}_h	Heated perimeter of the test section	m
\vec{F}_{ki}	Interfacial momentum transfer to phase k	Nm^{-3}
\vec{g}	Gravity	ms^{-2}
\vec{u}_k	Velocity of phase k	ms^{-1}
A_b	Surface fraction of the wall occupied by bubbles	1
$a_i = \frac{6\alpha_g}{d_b}$	Interfacial area	m^{-1}

C_D	Drag coefficient	1
C_L	Lift coefficient	1
$C_{p,k}$	Heat capacity of phase k	$\text{Jkg}^{-1}\text{K}^{-1}$
C_{TD}	Turbulent dispersion coefficient	1
C_{VM}	Virtual mass coefficient	1
d_b	Bubble diameter, taken as Sauter mean diameter	m
$D_h = 4\mathcal{A}/\mathcal{P}$	hydraulic diameter of the test section	m
d_S	Sauter mean diameter	m
$d_{\text{departure}}$	Detachment bubble diameter	m
d_{dist}	Distance between two bubbles	m
$D_{he} = 4\mathcal{A}/\mathcal{P}_h$	Heated diameter of the test section	m
e_k	Internal energy of phase k	Jkg^{-1}
f_{dep}	Bubble departure frequency	s^{-1}
G	Flow mass flux	$\text{kgm}^{-2}\text{s}^{-1}$
h	Enthalpy of the mixture	Jkg^{-1}
h_{OSV}	Bulk liquid enthalpy at onset of significant void	Jkg^{-1}
h_k	Enthalpy of phase k	Jkg^{-1}
$h_{k,\text{bulk}}$	Bulk enthalpy of phase k	Jkg^{-1}
h_{ks}	Enthalpy of phase k at saturation	Jkg^{-1}
$H_{l,\text{OSV}}(y_+)$	CFD-scale heat transfer coefficient towards the liquid phase at onset of significant void, enhanced by bubble agitation	$\text{Wm}^{-2}\text{K}^{-1}$
$H_{l,\text{SP}}(y_+)$	CFD-scale single-phase heat transfer coefficient	$\text{Wm}^{-2}\text{K}^{-1}$
h_{lv}	Evaporation latent heat	Jkg^{-1}
H_l	Heat transfer coefficient towards the liquid phase	$\text{Wm}^{-2}\text{K}^{-1}$
J_k	Superficial velocity of phase k	ms^{-1}

k	Turbulent kinetic energy of liquid	m^2s^{-2}
$k_+ = k/u_\tau^2$	Non-dimensional turbulent kinetic energy	1
L	Length of the test section	m
$L_c = \sqrt{\frac{\sigma}{g(\rho_l - \rho_v)}}$	Capillary length	m
N_{sites}	Nucleation site density	m^{-2}
P	Pressure	Pa
P_{out}	Pressure at the outlet pressure of a test tube	Pa
q_{km}^i	Interfacial heat flux from phase k to the (k, m) interface	Wm^{-3}
q_{Boil}	Boiling flow total heat flux	Wm^{-2}
q_{SP}	Single-phase flow total heat flux	Wm^{-2}
q_w	Total wall heat flux	Wm^{-2}
q_{CHF}	Wall heat flux at the boiling crisis	Wm^{-2}
q_{ki}	Total interfacial heat flux towards phase k	Wm^{-3}
q_{kw}	Wall heat flux towards phase k	Wm^{-2}
$q_{l,\text{OSV}}$	Heat flux to liquid at onset of significant void	Wm^{-2}
$q_{w,l \rightarrow v}$	Evaporation wall heat flux	Wm^{-2}
$r_+ = \frac{r}{R_{\text{pipe}}}$	Dimensionless radial position ($r_+ = 0$ at the center of a tube and $r_+ = 1$ at the wall)	1
$T_* = \frac{q_w}{\rho_l C_{p,l} u_\tau}$	Liquid temperature turbulent scale	K
$T_{\text{bulk}} = \frac{\langle u T_l \rangle}{\langle u \rangle}$	Bulk liquid temperature	$^\circ\text{C}$
T_{in}	Inlet temperature	$^\circ\text{C}$
T_k	Temperature of phase k	$^\circ\text{C}$
T_s	Saturation temperature	$^\circ\text{C}$
T_w	Wall temperature	$^\circ\text{C}$
u_τ	Friction velocity at the wall	ms^{-1}
u_{bulk}	Bulk fluid velocity	ms^{-1}

u'_{SP}	Turbulent fluctuations of a single-phase flow with the same mass flux as the studied flow	ms^{-1}
$X = \frac{h-h_{ls}}{h_{gs}-h_{ls}}$	Thermodynamic quality of the flow	1
X_{in}	Inlet thermodynamic quality	1
X_j	Outlet thermodynamic quality of run j	1
X_{OSV}	Thermodynamic quality at critical heat flux	1
X_{OSV}	Thermodynamic quality at onset of significant void	1
y	Distance to the nearest wall	m
$y_+ = \frac{yu_\tau}{\nu_l}$	Dimensionless distance to wall	1
y_1	Size of the near-wall mesh element	m
$y_{+,1} = \frac{y_1u_\tau}{\nu_l}$	Normalized size of the near-wall mesh element	1
$y_{+,c}$	Critical thickness of the saturated liquid layer at which OSV is observed	1
$y_{+,s}$	Thickness of the liquid layer that is at T_s	1
z	Axial position along the test tube	m

Subscripts

Symbol	Description	Units
b	Bubble	
g	Gas phase	
h	Hydraulic	
i	Interfacial	
j	Number of a run in a test tube	
k	Any phase	
l	Liquid phase	
r	Radial	
s	Saturation	
v	Vapor phase	

w	Wall
z	Axial

CHAPTER 1



Framatome GAIA EATF fuel assembly, from Framatome website (<https://www.framatome.com/medias/le-combustible-gaia-eatf-de-framatome-acheve-son-premier-cycle-en-reacteur/>).

Introduction

Chicago Pile-1, the world's first artificial nuclear reactor, sustained its first chain reaction in 1942. Colossus, largely regarded as the world's first programmable computer, first functioned in 1943. Shippingport Atomic Power Station, the first pressurized water reactor (PWR) devoted to peacetime uses, reached criticality in 1957. Turkey Point reactor 1, the first 3-loop Westinghouse PWR, was completed in 1972. Variants of this model make up 32 of the 56 reactors in France, where they are called REP 900. The IBM 360, the first computer to cover a broad range of applications, was delivered in 1965 and the first commercially successful personal computers in 1977.

In the early days of the nuclear industry, during the design phase of most reactors that are currently in operation, very little computing power was available. Today however complex simulations are a key part of nuclear safety demonstrations for modern reactors. They are also used to support extending the lifetime of reactors that were designed at a time where the fastest computer had less computing power than a modern wristwatch. Each generation of codes used for safety analysis contains more precise modeling and uses more computing power. Some consider multiphase computational fluid dynamics (CFD), which is the focus of this thesis, to be the next step in this evolution.

In this introduction, I will briefly present the operating principles of pressurized water reactors (PWR), that make up all of the French nuclear power plant fleet (section 1.1). I will then outline the key role of thermohydraulic modeling in safety analysis (section 1.2.1), before describing current system-scale and component-scale codes used in the nuclear industry (section 1.2.2). One of the shortcomings of these codes is the prediction of the critical heat flux in reactivity-initiated accident (RIA) conditions (section 1.3). Reynolds-averaged Navier-Stokes Multiphase computational fluid dynamics (RANS CFD) codes could participate in solving this issue (section 1.4). I present my contribution to building a boiling-flow multi-phase CFD framework for nuclear reactor conditions (section 1.5) and finish with the outline of this thesis (section 1.6).

Contents

1.1	Pressurized water reactors	3
1.1.1	Operating principle	3
1.1.2	Design of the core	4
1.2	Fluid dynamics in the nuclear industry	5
1.2.1	Importance of thermohydraulics for safety analysis . .	5
1.2.2	System and component codes	6
1.3	Reactivity-Initiated Boiling Crisis	7
1.3.1	Ascending flow boiling regimes	7
1.3.2	The Boiling Crisis	7
1.3.3	Reactivity-Initiated Accidents	8
1.4	Multiphase computational fluid dynamics	11
1.4.1	Sharp-interface multiphase CFD	12
1.4.2	Dispersed-interface multiphase CFD	12
1.4.3	All-regime approaches	15
1.4.4	Specificities of PWR flows	15
1.4.5	What is relevant in the context of a PWR RIA	16
1.5	Contribution	17
1.6	Outline of this thesis	20

1.1 Pressurized water reactors

1.1.1 Operating principle

Figure 1.1 presents a diagram of a pressurized water reactor (PWR). Delhaye 2008 and Todreas and Kazimi 2021 give detailed descriptions of this type of reactor and its operating conditions. They also describe boiling water reactors (BWR), in which the turbine is integrated to the primary circuit itself.

In a PWR design, the nuclear fuel that produces energy is located in the reactor pressure vessel (1 in figure 1.1). This vessel is filled with water that typically moves at a mass flow rate of 3000-5000 kg/(m²s). It is at 155 bar in operating conditions. At this high pressure the saturation temperature of water is around 345 °C. This enables the coolant temperature to reach 320 °C at the outlet without boiling. The thermodynamic efficiency of such reactors can therefore reach 37% for the European pressurized reactor (EPR), which is much higher than if they operated at lower pressure.

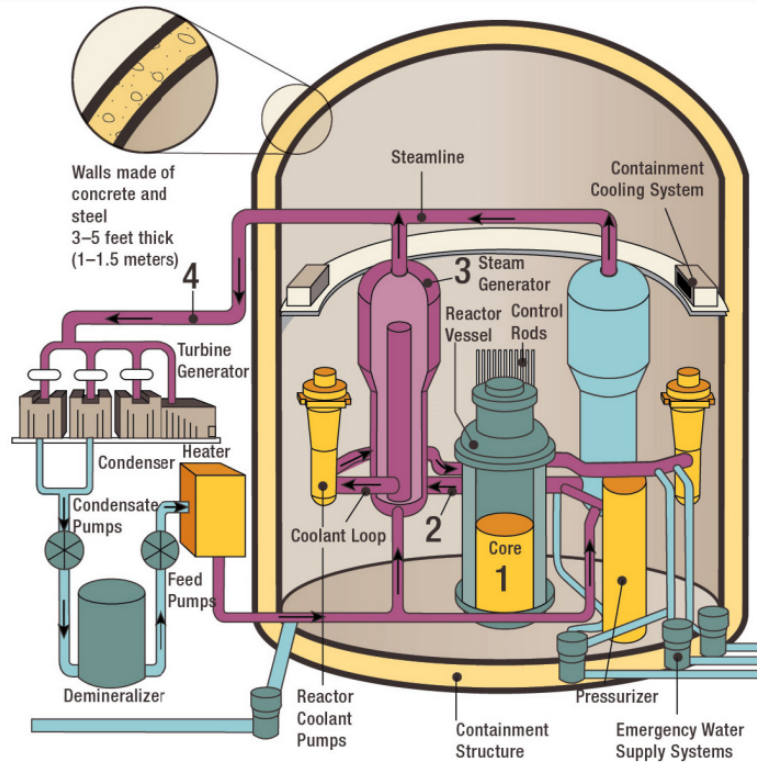


Figure 1.1: Diagram of the main components of a pressurized water reactor. Image from NRC [n.d.](#)

The reactor vessel is part of the primary loop, that transfers the heat produced by the core through the hot legs to the steam generators before coming back to the reactor vessel (2 in figure 1.1). Inside the steam generator the heat is transferred to the secondary circuit (3 in figure 1.1), which is around 70 bar in a PWR. It then leaves the containment structure to go through the turbine generator to produce electricity (4 in figure 1.1). Afterwards it enters a condenser cooled by the tertiary circuit and goes back to the steam generators.

1.1.2 Design of the core

In the core, nuclear fuel is located inside *fuel rods* (see figure 1.2). These rods are put together in square *assemblies*, which usually contain 17 by 17 rods. These assemblies are held together at each end by nozzles and along their lengths by grids. Some of the grids include mixing vanes that enhance heat transfers from the fuel to the water. These are called *mixing vane grids* (MVG). The assemblies include guide-tubes, that enable control rods to be lowered in the assemblies. Control rods are used by the reactor operators to regulate the chain reaction. When they are lowered, the reactor power decreases.

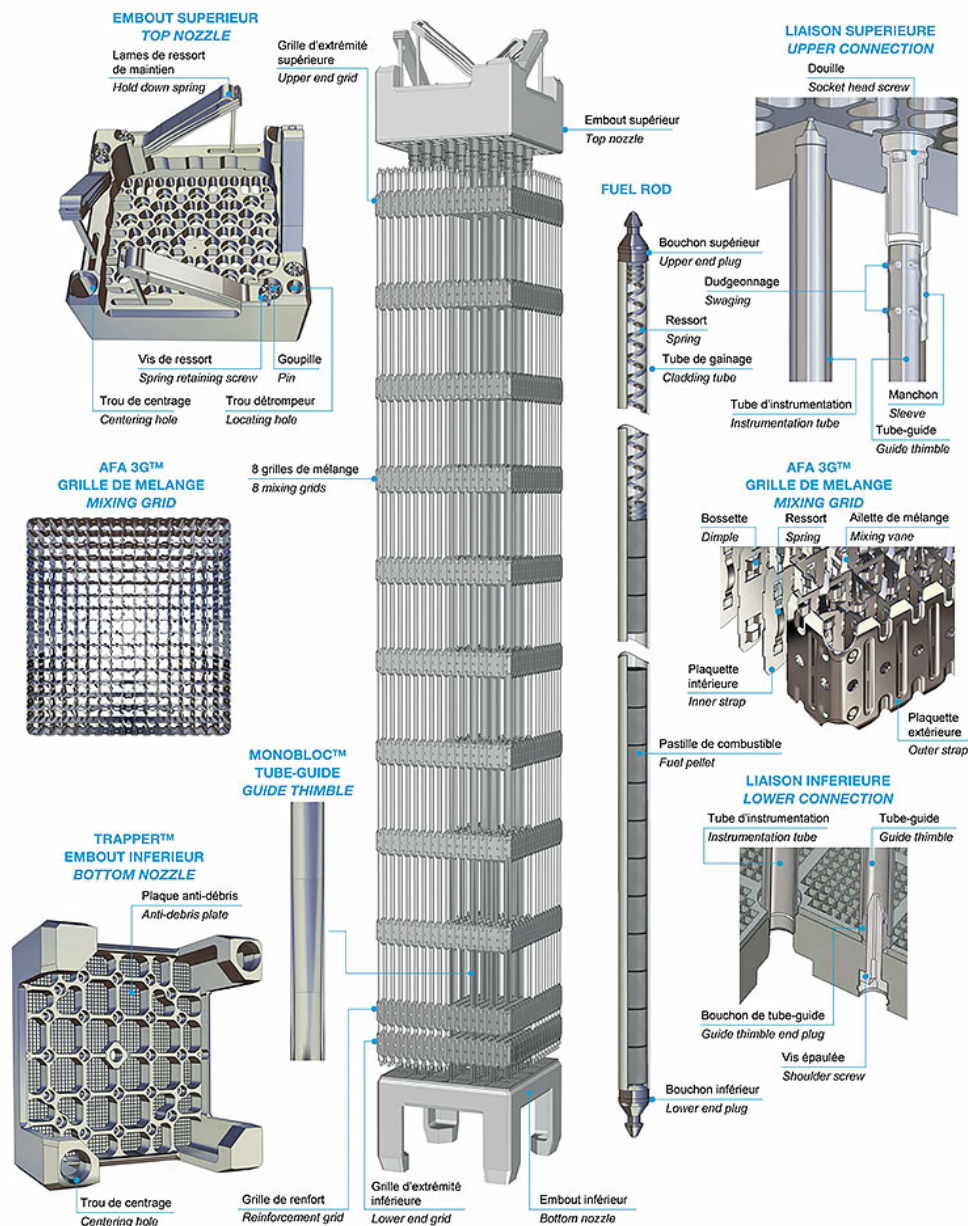


Figure 1.2: Diagram of the main components of a pressurized water reactor. Image from EDF website (<https://ignsr.com/en/7-nuclear-fuel-and-reactivity-control-the-heart-of-nuclear-safety/>).

1.2 Fluid dynamics in the nuclear industry

1.2.1 Importance of thermohydraulics for safety analysis

Water reactor thermohydraulics are the study of the heat transfer from the fuel rods to the external cold source. It includes the optimization of nominal operating conditions to maximize reactor power. French REP 900 reactors have thus gained ~10% in operating power since their construction. Most of the work in the domain

consists in studying incidental and accidental conditions. The goal is to ensure that the various safety systems in the reactor can prevent accidents when deviations from normal operation or subsystem failures occur. This includes specifically preventing the discharge of fission products into the environment or core melting.

To this aim, one of the key quantities to monitor is the temperature of the fuel rods. If they become too hot, they can break, releasing fission products in the primary circuit, and even melt (NEA 2022). System pressures, mass inventories, reactor power and reactivity are also important to evaluate. In incidental conditions, water can start boiling due to depressurization, a reduction in flow velocity or an increase in reactor power: understanding multi-phase dynamics is key even for nominally single-phase PWR's.

One of the most studied accidents in the industry is the loss-of-coolant accident (LOCA), which happens when there is a breach in the primary loop (Martin and O'Dell 2005). The risk is for the level of water to drop in the reactor vessel, uncovering the core. This happened in 1979 at the Three Mile Island nuclear generating station (Broughton et al. 1989).

1.2.2 System and component codes

To simulate such incidents, system codes aim to model nuclear reactors as a whole. The first such code, FLASH-1, dates back to the 1960s (Mesina 2016). It enabled explicit simulation of time advancement in three cells: one for the reactor vessel, one for the primary side of the steam generator, and one for the pressurizer. RELAP-1 was created in 1966 with, among other improvements, pressure-dependent steam tables and pumps. RELAP-4, in 1973, was the first version to include one-dimensional flow, a slip velocity between phases and a representation of the secondary loop. At that time, the Turkey Point 900 MW Westinghouse reactor had already started operation. RELAP-5 began development in 1979. It was based on the two-fluid model, that was elaborated in the 1970s (Lyczkowski 2010). It later gained a 3D-dimensional model of the reactor vessel. RELAP-7 is the most recent version (Berry et al. 2018). Other codes include TRACE (NRC 2010) and Cathare (Emonot et al. 2011).

Component scale codes, on the other hand, aim to simulate the 3D flow in the reactor vessel. To this end, the FLICA program was launched in the 1960's in France (Fajeau 1969). They provide a more precise, and local, view of the thermohydraulic conditions in the core. The size of one mesh element is set by that of a subchannel or of an assembly. Other such codes include THYC (Tinc et al. 1994) and CTF (Salko Jr et al. 2023).

Both of these types of codes are extensively used in current safety methodologies. They must predict flow conditions in complex boiling and multi-phase situations. They are based on a set of conservation equations for mass, momentum and energy. Physical models that quantify exchanges between liquid water and vapor and between different parts of the circuit are needed to close the system of equations. These models are derived from experiments conducted in geometries and operating conditions close to those of nuclear reactors. Channel or subchan-

nel quantities are measured: wall temperatures, average flow rates, average void fractions... Separate effect tests (SET) focus on a subsystem or a single physical mechanism (Emonot et al. 2011). Integral effect tests (IET) aim to evaluate code performance and model validity on a system representative of the complete reactor (Bazin et al. 1990). When investigating new geometries or operating conditions, expensive experimental programs must be conducted to calibrate these models.

1.3 Reactivity-Initiated Boiling Crisis

1.3.1 Ascending flow boiling regimes

An ascending heated flow will pass through different flow regimes as the fluid rises (figure 1.3). It starts in single-phase, with the wall temperature smaller than the saturation temperature. As the wall heats up, it will exceed saturation temperature. At this point, called onset of nucleate boiling (ONB) bubbles will start to form on the wall. The wall temperature will become almost constant above this point. A little higher up the channel, bubbles will detach. When the volume fraction of vapor becomes non-negligible, the onset of significant void (OSV) threshold has been passed. The flow is in bubbly subcooled boiling. As the liquid heats up, the flow will become saturated. As more vapor is formed, it will accelerate by mass conservation and become annular. In this regime, vapor is located in the center of the channel and is surrounded by a liquid film on the walls.

1.3.2 The Boiling Crisis

The liquid film enhances the heat transfer from the wall to the channel. At some point, it will completely evaporate. This is called the *dryout* (DO). In a power-imposed situation, as in nuclear reactors where the heat flux is determined by neutron physics, the wall temperature will then increase significantly (see figure 1.3). This decrease in heat transfer coefficient is called the *boiling crisis*. For a given channel, pressure, flow rate and inlet temperature, the wall heat flux at which this occurs is called the *critical heat flux* (CHF).

Dryout is the key boiling crisis mechanism in boiling water reactors. However, in pressurized water reactors, during the subcooled boiling phase the vapor production can become so large at the wall that a vapor blanket is formed between the wall and the liquid at the center of the channel. This is called *departure from nucleate boiling* (DNB). The flow then enters a so-called inverted annular regime.

This mechanism is often described using the Nukiyama curve (figure 1.4). For low heat fluxes, the flow is single-phase. As the heat flux increases, the point of ONB is passed and the heat transfer efficiency increases. The wall temperature remains low. However, when the CHF is exceeded, the heat transfer efficiency decreases dramatically. This is due to liquid being denser, and therefore a better heat-carrying fluid, than vapor. The wall temperature suddenly jumps.

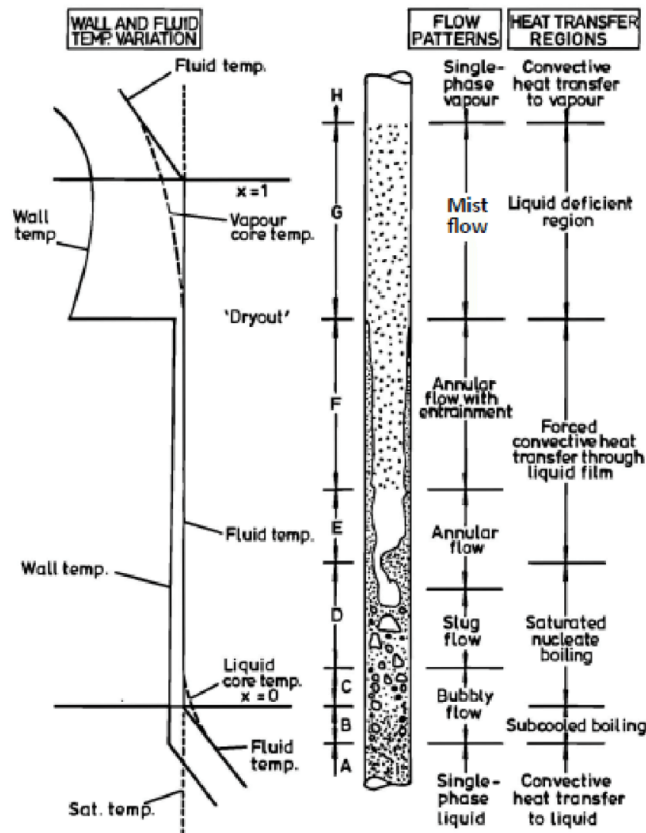


Figure 1.3: Diagram of the typical evolution of the main stages of a moderate-heat flux developing flow. Reproduced from Collier and Thome 1994.

Recent experimental and modeling efforts focus either on DO (Morse et al. 2024) or DNB (Zhang et al. 2022). The DNB is often recognized as a local, near-wall phenomenon (Zhang et al. 2022; Alvarez and Bucci 2024; Nop et al. 2021). A clear understanding of the mechanisms adapted to PWR pressure and flow rate is still lacking.

A more detailed review on the CHF and different CHF mechanisms is given in section 9.1.

1.3.3 Reactivity-Initiated Accidents

In nuclear reactors, during *Reactivity-Initiated Accidents* (RIA), a sudden increase in neutronic reactivity can lead to a sharp increase in the heating power (NEA 2022). This happens when neutron absorbers, i.e. control rods for commercial plants, are ejected quickly. In PWR's, this is called a *rod ejection accident* (REA). It can happen in particular if the rod control mechanism breaks off from the cover of the reactor vessel lid. This happening was one of the main concerns when cracks were discovered in the welds that link the two together in the French nuclear fleet, leading to the replacement of most lids (Meunier 2001).

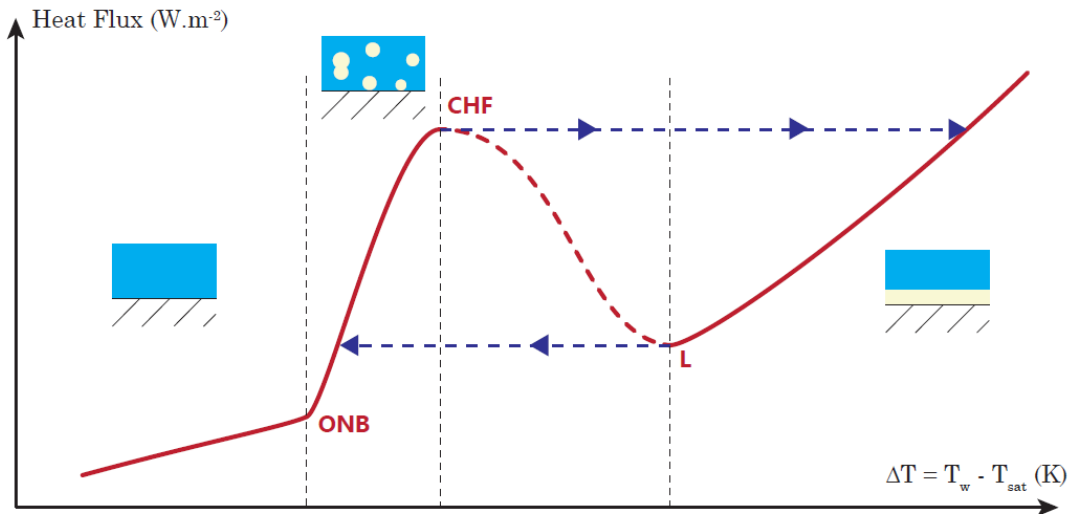


Figure 1.4: Nukiyama curve: heat flux as a function of subcooling for different flow regimes (Nukiyama 1966). Reproduced from Nop 2020.

Due to their fuel composition, if research reactors undergo a RIA, called BO-RAX for these reactors (Nop 2020), the fission reaction can get out of control. This happened on the SL-1 reactor in 1961 (Board 1961).

However, in commercial plants, when the fuel has heated sufficiently because of the increase in reactor power, the reactivity diminishes thanks to the doppler effect (Coste-Delclaux et al. 2013), which leads to a power decrease and stabilization. Figure 1.5 presents two examples of such power excursions. The first is a simulation in PWR conditions. The second contains experimental measurements of the power in the CABRI experimental reactor. This is representative of a PWR RIA. The control rod ejection is emulated by the depressurization of helium tanks that are located in the reactor pool (helium is a neutron absorber).

The primary risk in PWRs and BWRs during a RIA is that exceeding the critical heat flux can cause severe damage to the coolant cladding. Figure 1.6 presents a fuel rod that was damaged during trials on the NSRR experiments (Tomiyasu et al. 2007). Being able to predict the occurrence of a boiling crisis during a RIA transient, or at least guarantee that it cannot occur, is therefore of utmost importance to the nuclear industry.

The configuration of a PWR core during a RIA has two fundamental differences with the situation shown in figure 1.3: a complex geometry and a transient behavior.

First of all, an assembly is different from a pipe (figure 1.2). This modifies the structure of the flow in single-phase and in multi-phase flow. Mixing vane grids are built to enhance turbulent mixing, which cools the fuel rods more efficiently and increases condensation in the bulk.

Secondly, an RIA is a transient phenomenon. Depending on the initial conditions, the excursion duration is between 50 and 300 ms. However, in a PWR,

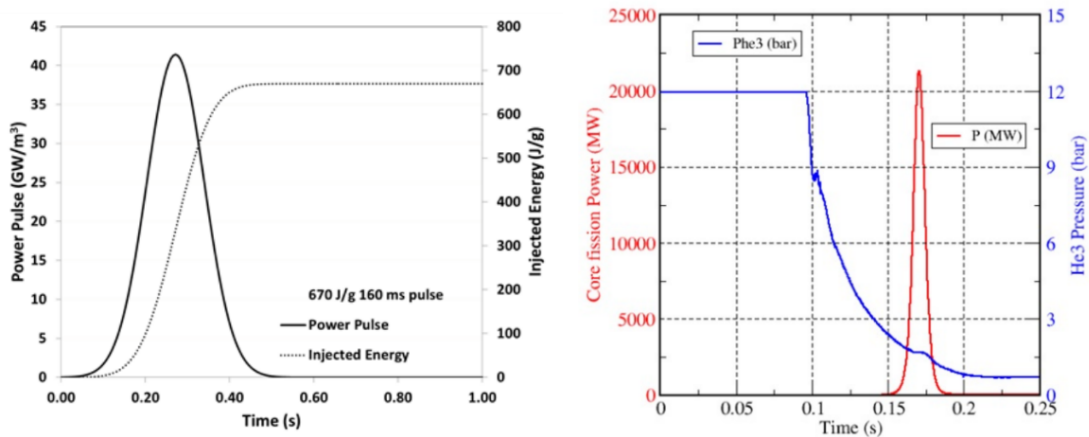


Figure 1.5: Left: simulation of the power in a PWR RIA power excursion with water at 300 °C and 158 bar (Folsom et al. 2016). Right: experimental power excursion in the CABRI experimental reactor, which is representative of PWR conditions (Labit et al. 2021a).

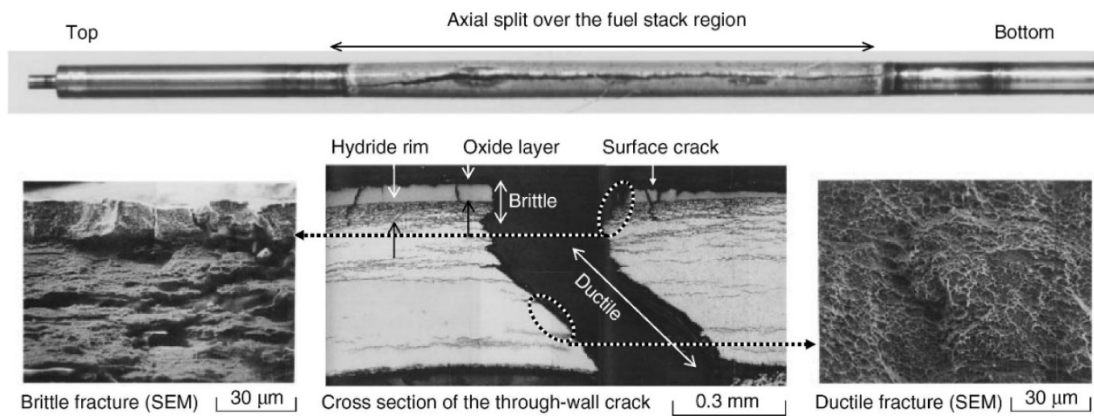


Figure 1.6: Picture of a fuel rod that was purposefully damaged during the NSRR experiments (Tomiyasu et al. 2007).

water flows at approximately 5 m/s and the assemblies are 4.2 m high. ~ 800 ms are needed to convect the fluid from top to bottom, and ~ 100 ms to go from one mixing vane grid to another.

In an ideal situation, RIA conditions would be applied to model assemblies in which electrically-heated rods would replace fuel rods to measure the transient CHF.

For safety demonstrations, the stationary CHF is measured for each possible assembly geometry, i.e. the shape of mixing vanes and axial location of mixing grids. Experiments are carried out in various flow conditions in complex testing facilities that are expensive to operate (Herer et al. 2005). The KATHY loop, currently used by Framatome, can operate with powers up to 20 MW. However, running 100 ms-transients on this setup is not experimentally feasible.

Experimental programs on tubes, channels or annulus have tended to show that

the critical heat flux is larger in transient conditions than in stationary conditions (Bessiron 2007; Kossolapov et al. 2020). The work of Sakurai 2000 is a notable exception. He finds that with escalating heat inputs, the heat transfer can be less efficient just before nucleate boiling begins, which can lead to lower CHF in transient than in stationary conditions. In safety demonstrations it is therefore generally accepted that the stationary CHF is larger than transient CHF, as this is found by a majority of studies. The steady-state CHF is then used as a conservative value. This begs the following questions:

1. Are stationary flow CHF correlations conservative for RIA conditions?
2. If so, can the difference between transient and stationary CHF be quantified?
3. Assembly geometries are optimized for stationary conditions, should they be different to maximize RIA CHF?

This thesis aims to contribute to building a tool able to predict near-wall conditions in stationary and transient boiling PWR assemblies (see table 1.1). The second long-term objective is to determine a CHF criterion depending on near-wall conditions. The simulation tool and CHF criterion used together would make it possible to answer the prior safety-related questions.

	Stationary	Transient
Tube	Groeneveld et al. 2007	PATRICIA (Bessiron 2007)
Assembly	KATHY (Herer et al. 2005)	Long-term objective of this work

Table 1.1: Long-term objective of this work: build a tool to explore transient CHF in assemblies.

1.4 Multiphase computational fluid dynamics

To determine near-wall conditions in boiling-flow, which is the key to predict DNB, the obvious tool is multiphase computational fluid dynamics. Like system and component codes, multiphase CFD codes solve mass momentum and energy conservation equations. However, the fluid domain is modeled with smaller cells. Most importantly, the closure laws are independent of the flow geometry. Scientists have been working on this approach since the 1970s (Lyczkowski 2010). It is often based on elements from single-phase CFD.

The latter has a solid track record and is widely used in multiple applications (Cebeci 2013). In the nuclear industry, it is used for design purposes (Bellet et al. 2005). It is now possible to run fine simulations at an assembly level (Bieder et al. 2014; Kraus et al. 2021) and rough simulations of complete reactor cores (Martinez and Galpin 2014; Fang et al. 2021).

Multi-phase CFD however is much less mature and still faces many challenges (Tomiyaama 1998; Bestion et al. 2009; Lahey et al. 2021) It broadly encompasses two kinds of models: either with sharp or with dispersed interfaces.

1.4.1 Sharp-interface multiphase CFD

In sharp-interface multiphase CFD, most computational cells contain only one phase. The equations solved locally are therefore the same as in single-phase CFD. Tracking methods are used to locate the interface. The tracking technique, and the way it is used to calculate surface tension forces at the interface, is one of the major differentiating factors between codes. The most famous of these methods is called *volume of fluid* (Hirt and Nichols 1981). Others include tracking the interface between phases with surface markers (Tryggvason et al. 2001) or based on a level set function (Sussman et al. 1994).

The modeling of each separate phase can also vary between codes. Some use no additional models, i.e. direct numerical simulation (DNS) methods. Other implement large-eddy simulation (LES) or unsteady-Reynolds-averaged Navier-Stokes (URANS) to reduce computational cost.

These codes are for example successfully used to model jet atomization (Lebas et al. 2009), wave breakup (Deike et al. 2015) or bubble-induced turbulence (Cluzeau 2019). In the case of bubble simulations, mesh convergence can be obtained from ~ 20 cells across the bubble diameter (Cluzeau 2019).

1.4.2 Dispersed-interface multiphase CFD

In dispersed-interface multiphase CFD, each phase can be simultaneously present in every cell. Through *ensemble averaging*, the average velocity, energy and *volume fraction* of each phase are the unknowns of the code in every cell of the simulation. A diagram of this process is presented in figure 1.7. Much larger mesh cells can be used for flows that have small bubbles than with sharp interface codes. Reynolds-averaged Navier-Stokes (RANS) turbulence models are systematically used. The set of equations solved locally is different from single-phase flow.

In the literature the models used are based on a set of mass, momentum and energy conservation equations. The two most common sets are the Euler-Euler model and the drift-flux model (Ishii and Hibiki 2006). These will be described at length in chapter 2. Dispersed phase CFD codes include NEPTUNE_CFD (Guelfi et al. 2007), Ansys fluent (*Ansys Fluent Theory Guide* 2022), OpenFOAM (Jasak 2009) and CUPID (Jeong et al. 2010).

In the same way as for system and component codes, the systems of equations derived must be closed by physical modeling. In the Euler-Euler framework, this means determining interfacial forces. In the drift-flux framework, it means working on the drift velocity. In both, interfacial heat transfers and wall boiling must be quantified as well.

However, it is extremely difficult to carry out experiments in PWR conditions. To the best of my knowledge, no boiling flow at 155 bar and 300 °C has ever been

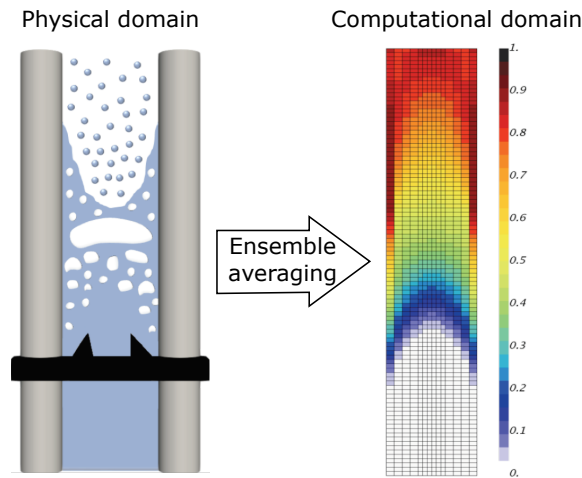


Figure 1.7: Diagram of the ensemble averaging procedure. Image from Sugrue 2017.

caught on high-speed camera. Bubbles are very small in these conditions, around 0.1 mm at the wall, and thermal distortions significant (Kossolapov 2021). Optical fibers inside the flow can be damaged. The electrical power required for heating and the flow rates are large, easily up to 1 MW and 4000 kg/(m²s). For system and component code calibration, these difficulties are much less important as only measurements at the scale of the channel, not local quantities, are required.

Five broad strategies have been employed by the community to close these systems of equations:

- **Channel-scale measurements:** in many cases experimental data can be obtained at the scale of the channel. For example, this can happen when void fractions are measured through radiography. The Zeitoun et al. 1995 condensation correlation was built with this methodology. Though a few such terms can be used in a CFD code, using mostly system and component scale correlations is not possible.
- **Experimental dynamics of single bubbles:** multiple experiments have been carried out throughout the years to understand the precise dynamics of single bubbles. The Tomiyama et al. 1998 drag coefficient, Tomiyama et al. 2002 lift coefficient and Chen and Mayinger 1992 condensation correlation originate from this approach. These correlations have relatively narrow ranges of validity, as the systems studied are mostly atmospheric-pressure single-bubbles in still tanks. The ranges are not systematically verified by the users when running simulations. With the continued improvement of experimental methods, researchers are beginning to analyze single bubbles in complex turbulent flow (Salibindla et al. 2020, Qi et al. 2022).
- **Upscaling:** this consists in exploiting simulation results at a smaller, well-resolved scale, usually sharp interface DNS or LES, to feed dispersed-interface

RANS models. Formulations for lift (Legendre and Magnaudet 1998) or condensation (Legendre et al. 1998) on single bubbles and bubble-induced turbulence in swarms (Cluzeau et al. 2022) have been derived in this way. However, due to large computational cost the flow in these simulations is slower, less turbulent and with lower void fractions than in incidental nuclear reactor conditions.

- **Theoretical analysis:** when the flow conditions are adequate or no experimental data is available, authors can resort to analytical calculations in simplified situations. In particular, the Zuber 1964 virtual mass force, the turbulent dispersion forces proposed by Burns et al. 2004 and Laviéville et al. 2017, the Lubchenko et al. 2018 wall repulsion and the Liao et al. 2019 interfacial heat transfer are derived in this way. These correlations are then validated on experimental data by the authors.
- **Fit on local flow quantities:** this can be done when local CFD-scale data is available and most terms are already set. A small number of terms can then be adjusted to optimize the fit of the local data. This was done by Sugrue 2017, who adjusted a novel lift coefficient in this way. Leoni et al. 2024 proposed a method to simultaneously calibrate multiple coefficients.

In practice, most of the time combinations of these methods are used. For example, the Kurul and Podowski 1990 heat flux partition couples theoretical analysis on near-wall boiling dynamics and the quenching heat flux with measurements of various parameters like nucleation site density. The structure of Hibiki and Ishii 2000a coalescence and breakup terms comes from theoretical analysis but some coefficients were adjusted so the model fits experimental data. The limit of the Ranz and Marshall 1952 interfacial heat transfer for low Reynolds numbers comes from a theoretical analysis.

Most of these coefficients are designed separately. In total, including the formulations of every model CFD codes typically have around two dozen closure coefficients. The choice of a set of closures is often made by comparing the outputs of various combinations of closures on a small number of experimental cases (Pham et al. 2023; Vlček and Sato 2023). This leads to many closure terms being widely used outside of their validity domain in the literature. This is different from system and component scale codes, where looking at a larger scale increases the amount of relevant experimental data and smaller calculation times ease model calibration. All of these closure terms are interdependent. For example, changing the drag coefficient will affect the relative velocity between phases, then condensation, bubble diameters and the drag coefficient again. This can lead to significant error compensation in CFD codes (Leoni 2022). This error compensation can in turn result in major difficulties in improving sets of closures on a model-by-model basis (Lucas et al. 2016).

Error compensation is also made easier by the small number of experimental conditions where different quantities are measured at the same points. It is therefore possible to have a correct void fraction profile for example with an incorrect

velocity field. In recent years however considerable efforts have been made to measure various quantities at the same location (Lucas et al. 2013; Chu et al. 2017; Kledy 2018).

Finally, the lack of separate effect tests complicates the independent calibration of various closure terms. For example, the lift, turbulent dispersion and drag forces in ascending flow are always present together and will affect the radial void fraction distribution.

Bois et al. 2024 recently carried out a code benchmark on the DEBORA database (Cubizolles 1996), that is representative of PWR conditions. It included 30 conditions and 12 participants. Though boiling-flow dispersed-phase CFD has existed for 30 years (Tomiyama 1998), their conclusions are that though very different closures were used by the participants, no model is able to consistently capture the experimental behavior of the flow. In particular, interactions between mechanisms and their hierarchy were difficult to understand. A novel modeling approach is necessary to tackle these issues.

1.4.3 All-regime approaches

As seen in figure 1.3, a heated ascending flow can transition from a subcooled boiling regime with small bubbles, that can be efficiently modeled with dispersed-interface approaches, to an annular regime that could require a sharp interface modeling. Various methods have been developed to bridge the two regimes. Solvers include NEPTUNE_CFD (Bazin 2023), NEK2P (Tentner et al. 2018) and OpenFOAM (Colombo et al. 2023; Krull et al. 2024).

Having an all-regime model valid for arbitrary pressures and flow conditions would enable us to simulate steam generator tubes, depressurization during loss-of-coolant accidents or thermosiphons for example. Building such a model is, in my opinion, the long-term goal for the community.

1.4.4 Specificities of PWR flows

Hosler 1967 and François et al. 2011 have shown that at PWR pressures and in PWR-similarity conditions using a refrigerant fluid, the flow pattern remains bubbly, like an emulsion, at high thermodynamic qualities ($X = 0.3$) and average vapor volume fractions ($\langle \alpha_v \rangle = 0.7$). According to Kossolapov 2021, characteristic bubble sizes at the wall at high pressure is 0.1 mm.

In PWR's, the pressure is 155 bar. This is close to the critical pressure of water (220 bar). The ratio of the liquid density to the vapor density is much smaller than at atmospheric pressure: ~ 5 rather than ~ 1000 . This has many indirect consequences. Vapor bubbles have non-negligible inertia in these conditions compared with the liquid. They also have much more thermal inertia when condensing. The collapsing speed therefore changes significantly, which will affect condensation dynamics (Legendre et al. 1998). When heating a channel, if one evaporates 1% of the mass of liquid at 1 bar, the resulting flow is 90% vapor in volume. At PWR pressure, this number is 5%. The high pressure influences the surface tension,

which is $\sim 0.01 \text{ Nm}^{-1}$, 5-10 times smaller than at atmospheric pressure. This will influence bubble coalescence and breakup, as well as drag and lift forces.

As the characteristic flow velocity is 5 m/s and the kinematic viscosity $\sim 10^{-7} \text{ m}^2\text{s}^{-1}$, the flow is very turbulent and the Reynolds around 200,000. The Kolmogorov length scale is of the order of 10^{-5} m (Fang et al. 2017).

1.4.5 What is relevant in the context of a PWR RIA

For a resolved DNS or LES approach to be possible in a PWR subchannel with around 10 elements along a bubble diameter, a 10^{-5} m mesh size would be required. This would result in an unstructured mesh of $\sim 10^{13}$ elements able to handle multiphase flows with heat transfer. Unstructured meshes can currently run single-phase simulations of $\sim 10^{10}$ degrees of freedom (Fang et al. 2021), which is still far from the mark.

Dispersed multiphase CFD simulations use larger mesh cells and require a smaller number of them. They have been carried out on simplified spacer geometries for the past 30 years (Anglart and Nylund 1996; Anglart et al. 1997; Favre et al. 2022). With the improvement of code performance and computing power, multiple studies present simulations on assemblies. The review of Taş 2024 can be referred to for a list of examples.

Simulating the critical heat flux in transient conditions was one of the three main initial objectives of the NEPTUNE project (Guelfi et al. 2007), along with the loss-of-cooling accident and the pressurized thermal shock. Multiple authors have sought to predict the critical heat flux in PWR conditions through dispersed-interface CFD (Montout 2009; Zhang et al. 2015; Mimouni et al. 2016a; Pothukuchi et al. 2019; Favre 2023). However, the results from the DEBORA benchmark (Bois et al. 2024) question the current ability of CFD codes to predict precise near-wall quantities, and therefore the robustness of CHF predictions based on these codes.

As discussed in section 1.4.2, there is still debate in the community on the choice of the adequate sets of closures and on their formulations in dispersed interface models. Work still needs to be done to improve these models so that they can be used at an industrial scale: dispersed interface CFD has never been used in a safety demonstration in France.

As the flow remains bubbly even at high qualities at PWR pressures, a RANS dispersed-interface model with the right closures should be able to capture the flow adequately to predict DNB conditions. In this thesis, I propose a different approach than the traditional assembly of independently derived closures. It is inspired from the work of Sugrue 2017. My aim was to build a minimalistic set of closures for PWR flows in the two-fluid framework, i.e. with the simplest possible formulation and the minimal number of fitted parameters to correctly describe experimental data, without modeling all micro-mechanisms encountered in the flow.

1.5 Contribution

The objective of my thesis was therefore to contribute to the development of a dispersed interface multiphase CFD tool for the prediction of the critical heat flux in PWR conditions, to answer the safety-related questions asked in section 1.3.3. Figure 1.8 presents the different steps that are required to go from the numerical scheme to the industrial simulation. It is a multidisciplinary endeavor.

At the beginning of my thesis, there were already numerical blocks in place in the open-source TRUST platform developed at CEA (Saikali et al. 2021). In particular, mass, momentum and energy conservation equations were coded by Gerschenfeld and Gorsse 2022 in an Euler-Euler framework that can handle any number of phases. It was based on the PolyMAC numerical scheme, that can handle arbitrary polyhedral meshes.

A timeline of my thesis can be found in figure 1.9. I started out by selecting, implementing and validating in simple conditions a set of closure terms based on reference formulations from the literature. However, extending it to PWR conditions proved difficult. The second year-and-a half of my thesis was devoted to building a minimalistic set of closures that is valid in nuclear reactor conditions. I then used this set of closures to build a CHF criterion for subcooled flow. In the end, I did not have enough time to run simulations in assembly geometries. I leave this for future generations of PhD students.

During this time, I worked on a few projects that are not directly linked with the main objective of understanding PWR-condition flows. These included overseeing the internships of Moncef El Moatamid, who worked on Euler-Euler modeling of bubble-induced turbulence, and Mathilde Lemoine, who simulated boiling atmospheric-pressure flows. I also wrote appendix A, that contains an analysis of the lift force in horizontal channels.

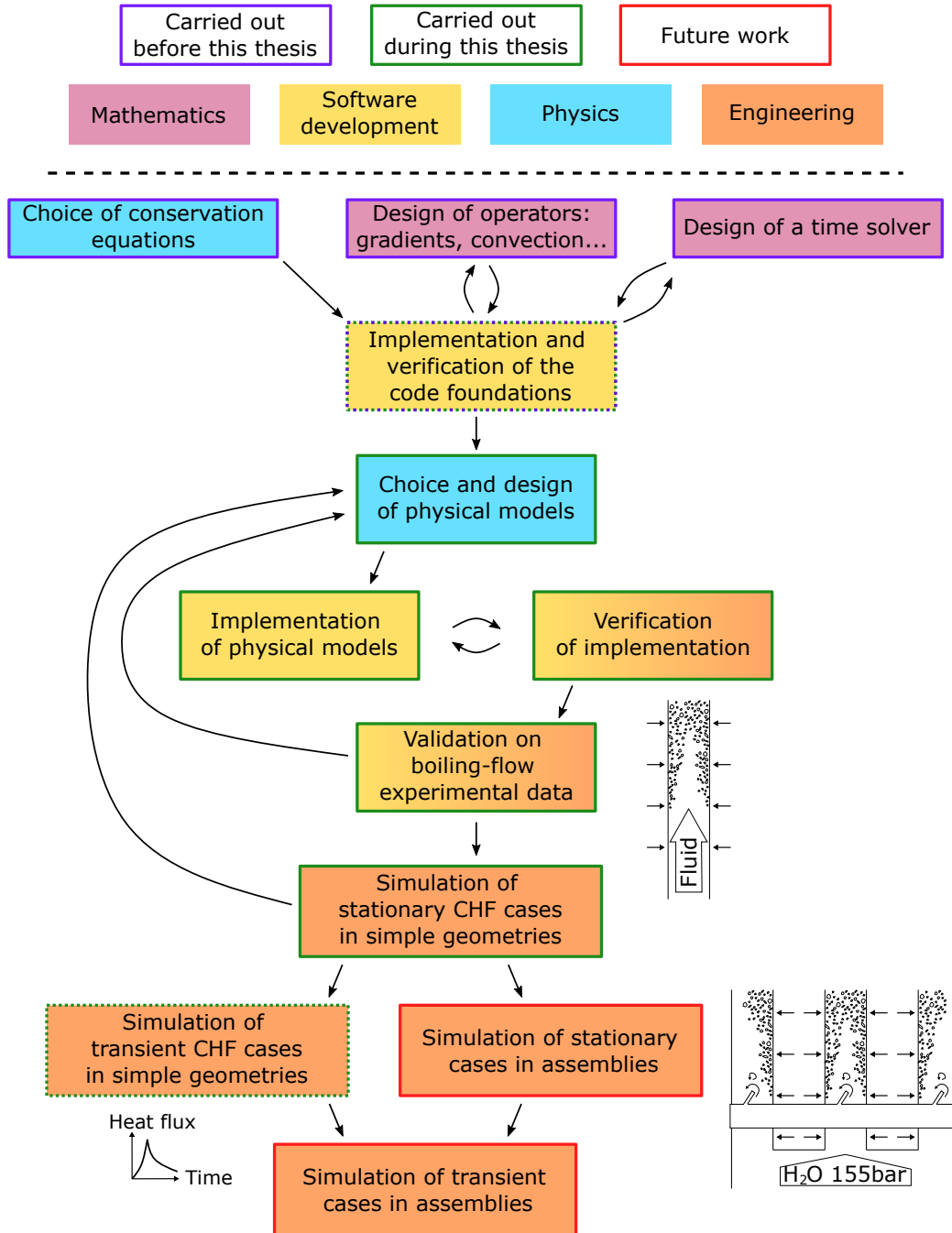


Figure 1.8: Diagram of the different steps required to carry out CFD-scale transient boiling-flow simulations in a PWR assembly. Some of these steps were carried out before this thesis. Simulating complete assemblies will be done in the future.

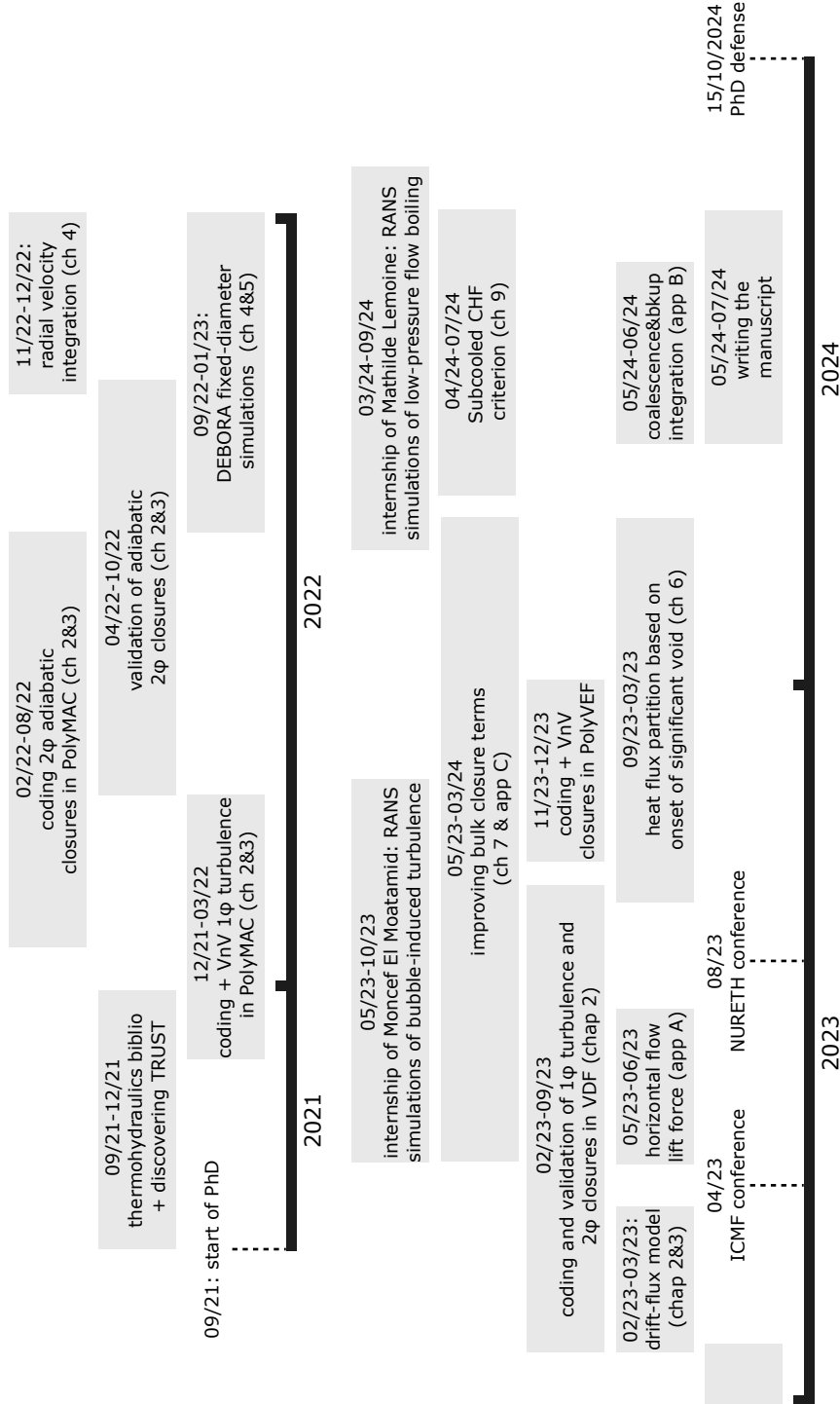


Figure 1.9: Timeline of the work done during this thesis.

1.6 Outline of this thesis

This thesis seeks to answer the following questions:

1. Are physical models that are valid in atmospheric-pressure adiabatic flows still functional in nuclear reactor conditions?
2. Can a simple set of closures be developed to model high-pressure boiling flows?
3. Can the critical heat flux be predicted at a local scale in stationary and transient conditions?

The first part of this thesis presents the journey towards the first high-pressure boiling-flow CFD simulations using TrioCFD. I review the conservation equations, the numerical methods that are used for space discretization and the resolution algorithms that are used (chapter 2). I then describe the baseline set of closures, which comes from state-of-the art literature. The code is verified and validated on single-phase turbulent flow and adiabatic bubbly flow (chapter 3). I present DEBORA, a nuclear reactor similarity experiment conducted at CEA (chapter 4). The experimental data is used to extract information on the liquid temperature fields and radial velocities (appendix B) and on coalescence and breakup mechanisms (appendix C). I then show that the baseline set of closures, where the experimental bubble diameter is enforced, is unable to reproduce results from DEBORA (chapter 5).

In the second part, I aim to improve the physical modeling of high-pressure ascending boiling flows using a minimalistic approach. I begin by showing that the onset of significant void occurs when the turbulent boundary layer reaches saturation temperature (chapter 6). This is validated across multiple geometries and flow conditions. It is used to build a heat flux partition that takes a much simpler form and improves void fraction and liquid temperature predictions compared with traditional approaches. I then work on improving models in the bulk of the flow (chapter 7). Bubbles are shown to be deformed, i.e. non-spherical, in nuclear reactor conditions due to the combined effect of turbulence and crowding. Drag, lift, turbulent dispersion and condensation formulations that account for this deformation and packing are proposed. All closures selected are independent from the bubble diameter. The complete set of closures therefore does not require an interfacial area transport equation or an equivalent approach. It is compared to an extended high-pressure boiling flow database that I assembled (chapter 8).

The third part presents simulations in boiling crisis conditions with TrioCFD and the minimalistic set of closures. I simulate the conditions at the outlet of DEBORA tubes where the critical heat flux is exceeded (chapter 9). By conducting a physical analysis of the simulation results, I propose a critical heat flux criterion valid for flows that remain subcooled in the near-wall region. This criterion is extended to the Groeneveld database (chapter 10). To evaluate the applicability of this steady-state criterion to transient flows, I then simulate the transient PATRICIA CHF experiment.

Baseline simulation

2

Presentation of the TrioCFD multiphase module

This chapter describes the multiphase solver that CEA is developing in its fluid dynamics code TrioCFD using the TRUST HPC Platform. Section 2.1 describes the structure of the code, the systems of equations that are solved, the numerical methods and the resolution algorithms. These were mainly implemented by Gerschenfeld and Gorsse 2022 before the beginning of my thesis, though I marginally adapted them for my needs. Section 2.2 describes the physical models that I implemented to solve single-phase turbulence and bubbly flows. Various models that can be selected by the user are presented. Some are employed to verify the implementation of the code, some are part of the baseline set of closures selected for the first multiphase simulations (those proposed by Sugrue 2017), and a few are not exploited in this work. Table 2.1 summarizes the choices made for the baseline simulations. Section 2.3 describes the drift-flux solver that was incorporated in TrioCFD. Development of the drift-flux solver was a collaboration between Antoine Gerschenfeld, Yannick Gorsse, Elie Saikali and me. Chapter 3 contains the verification and the validation of the terms presented here.

Parts of this chapter were adapted from Reiss et al. 2024a and from Reiss et al. 2024c.

Contents

2.1	TrioCFD N -fluid multiphase solver	25
2.1.1	Inheritance from the open source HPC TRUST platform	25
2.1.2	Numerical methods	25
2.1.3	The generic multi-phase problem for an N -fluid system	26
2.1.4	The solution algorithm	28
2.1.5	Treatment of vanishing phases	30
2.2	Physical closure models	30
2.2.1	Turbulence modeling	30
2.2.2	Bubble diameter modeling	32

2.2.3	Interfacial momentum exchanges modeling	33
2.2.4	Interfacial heat transfer	35
2.2.5	Heat Flux Partitioning: Original Kurul and Podowski	35
2.2.6	Summary of the baseline set of closures	37
2.3	The drift-flux model	38
2.3.1	Building a drift-flux model base on a two-fluid system	38
2.3.2	Modeling the drift velocity in bubbly flow	42

2.1 TrioCFD *N*-fluid multiphase solver

2.1.1 Inheritance from the open source HPC TRUST platform

The multi-phase solver is developed in the TrioCFD code (Angeli et al. 2015) based on the HPC platform TRUST (Saikali et al. 2021, github.com/cea-trust-platform). Both the code and the platform are open-source (BSD license) and developed at the Energy Division (DES) of the French Atomic and Alternative Energy Commission (CEA). They are based on an object-oriented intrinsically parallel approach and written in the C++ language.

The METIS library is used to perform HPC simulations where the computational domain is splitted into several overlapping sub-domains. METIS always insures a small load imbalance of the domain partition (defined by the product of the maximum cells among sub-domains and the number of sub-domains divided by the total number of cells). As a result, all sub-domains are normally distributed quite equally among different processor cores, which, by using message passing interface libraries (MPI), communicate only with required neighbor processors when data transfer is needed.

All I/O processes are parallelized with the possibility to read and write from a single HDF5 file or from distributed files. When a calculation domain comprises more than $2^{31}/8$ cells (~ 268.5 M cells), the integers need to be represented on 64 bits. This feature is included as a compiler option. The largest simulation ever run on a TRUST architecture contained 2 billion cells (Saikali et al. 2021).

In what follows, a detailed description of the TrioCFD multiphase solver will be presented.

2.1.2 Numerical methods

The TrioCFD multiphase solver inherits directly from the generic classes of the TRUST platform that define the kernel of this code: numerical methods, spatial and time discretizations, linear systems, equations, boundary conditions, pre/post-processing, etc. The PETSc library is used to solve linear systems.

The multiphase software can handle arbitrary meshed geometries where two spatial discretizations can be used.

The first is a finite difference volume (VDF) method for conformal cartesian unstructured-hexahedral type meshes (Saikali et al. 2019). It is implemented on a staggered grid of type Marker and Cell (MAC, Harlow and Welch 1965). This scheme can also handle axisymmetric pipe flows. It enables very fast and stable simulations on cartesian meshes.

The second, called PolyMAC, is a method for an arbitrary polyhedral conform/non-conform mesh (Gerschenfeld and Gorsse 2022; Bacq et al. 2023). Figure 2.1 illustrates mesh types that can be used by multiphase TrioCFD with PolyMAC.

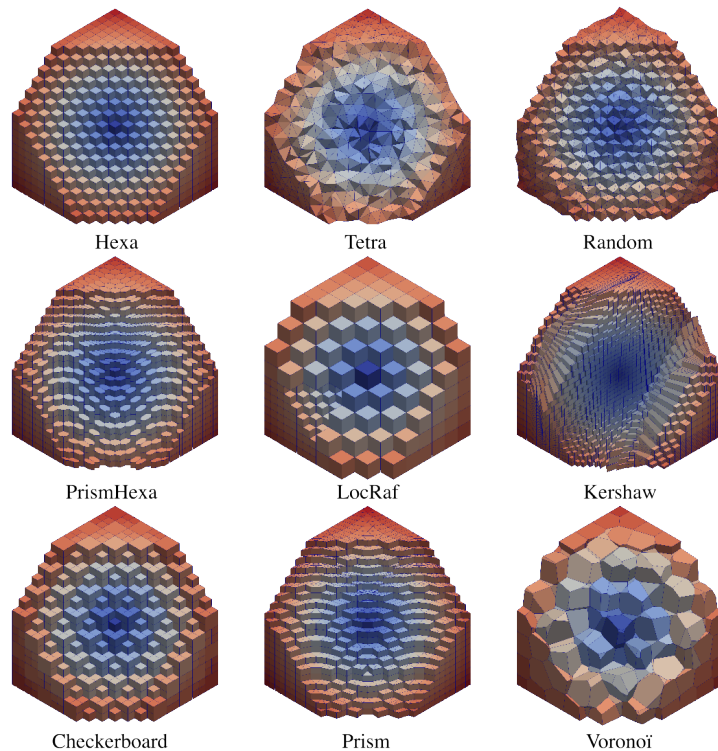


Figure 2.1: Meshes from the FVCA benchmark that can be used by the multiphase TrioCFD solver with PolyMAC (Bacq et al. 2023). Image courtesy of Antoine Gerschenfeld.

2.1.3 The generic multi-phase problem for an N -fluid system

The historic single-phase TrioCFD code offers a flexible architecture where the user can specify one or more *problems* consisting each in one or more *equations*. For instance, one can solve a single-phase incompressible fluid through an *equation* for the velocity/pressure (p, \vec{v}) and another for the temperature T in a single-phase thermal hydraulic *problem*. Default classes implement heat conduction problems as well as incompressible and quasi-compressible (thermal-)hydraulics problems. For

turbulent simulations, the user can simply define a turbulent problem by associating an appropriate turbulence and boundary layer model to each equation. Both RANS and LES models are available.

Aside from its equations, each problem is associated with a *medium* class (describing its medium properties), a *discretization* class (describing how the equations should be discretized in space), and a *time scheme* class (describing the solution algorithm to be performed at each time step).

In order to describe multi-phase flows, Gerschenfeld and Gorse 2022 recently implemented a multiphase problem. It describes an N -fluid system in which mass, momentum and energy balances are considered. The following equations for the k -th phase ($1 \leq k \leq N$) are solved (Ishii and Hibiki 2006):

$$\left\{ \begin{array}{l} \frac{\partial \alpha_k \rho_k}{\partial t} + \nabla \cdot (\alpha_k \rho_k \vec{u}_k) = \sum_{m \neq k} \Gamma_{km} \quad (\mathcal{M}_k) \\ \alpha_k \rho_k \frac{\partial \vec{u}_k}{\partial t} + \nabla \cdot (\alpha_k \rho_k \vec{u}_k \otimes \vec{u}_k) - \vec{u}_k \nabla \cdot (\alpha_k \rho_k \vec{u}_k) = \\ \quad - \alpha_k \nabla P + \nabla \cdot (\alpha_k \mu_k (\nabla \vec{u}_k) - \alpha_k \rho_k \overline{u'_i u'_j}) + \alpha_k \rho_k \vec{g} + \sum_{m \neq k} \vec{F}_{km}^i \quad (\mathcal{Q}_k) \\ \frac{\partial \alpha_k \rho_k e_k}{\partial t} + \nabla \cdot (\alpha_k \rho_k e_k \vec{u}_k) = -P \left(\frac{\partial \alpha_k}{\partial t} + \nabla \cdot (\alpha_k \vec{u}_k) \right) \\ \quad + \nabla \cdot (\alpha_k \lambda_k \nabla T_k - \alpha_k \rho_k \overline{u'_i e'_k}) + \sum_{m \neq k} (q_{km}^i + \Gamma_{km} h_{km}) \quad (\mathcal{E}_k) \end{array} \right. \quad (2.1)$$

The primary unknowns of this system are the volumetric fractions α_k , the phase velocities \vec{u}_k , the phase temperatures T_k and the common pressure P . \vec{g} is the gravity vector. The associated medium specifies the physical and transport properties for each phase (density ρ_k , internal energy e_k , dynamic viscosity μ_k , thermal conductivity λ_k , saturation enthalpy h_{ks} , phase change enthalpy $h_{km} = |h_{ks} - h_{ms}|$) are calculated as a function of (P, T_k) . Though the thermal unknown is internal energy, the phase change enthalpy must be used to calculate the heat transfer associated with condensation and evaporation (Ishii and Hibiki 2006). TRUST offers a Thermo-Physical Properties Interface (TPPI) that calls external libraries such as EOS, the Neptune project library (Guelfi et al. 2007), CoolProp (Bell et al. 2014), or others.

In equation 2.1, the turbulent terms $\overline{u'_i u'_j}$ and $\overline{u'_i e'_k}$ require closure laws. Physical models prescribe the mass and heat transfer terms from the (k, m) interface to phase k Γ_{km} and q_{km}^i . They also determine the interfacial forces accounting for momentum transfers between phases per unit of volume and time term \vec{F}_{km}^i .

In the case where phase change is present, interface jump conditions prescribe $\Gamma_{km} = -\Gamma_{mk} = (q_{km}^i + q_{mk}^i)/(h_{ks} - h_{ms})$. $\vec{F}_{mk}^i = -\vec{F}_{km}^i$ is also always verified.

The wall heat transfer to phase k , q_{kw} , which is a boundary condition of the energy equation, also requires modeling. It can be linked to the phase change at the wall $\Gamma_{w,km}$.

The system is finally closed by the condition:

$$\sum \alpha_k = 1 \quad (2.2)$$

In this thesis, I work with two fluids: a continuous liquid phase l and a dispersed phase, written g for gas phase in adiabatic flow and v for vapor phase in boiling flow.

2.1.4 The solution algorithm

Among the many possible forms for these equations, the above system uses a semi-conservative form for \mathcal{Q} (Park et al. 2009) and the internal energy form of \mathcal{E} , which facilitate the implementation of the semi-implicit scheme ICE (Harlow and Amsden 1968).

The system $(\mathcal{M}, \mathcal{Q}, \mathcal{E})$ is in most cases nonlinear and tightly coupled by its source terms Γ_{km} , \vec{F}_{km}^i and q_{km}^i : ICE offers a way to integrate these terms implicitly while avoiding the solution of a full linear system in (α, \vec{v}, T, p) . It consists in the following choice of implicit terms (in red):

$$\left\{ \begin{array}{l} \frac{\partial \alpha_k \rho_k}{\partial t} + \nabla \cdot (\alpha_k \rho_k \vec{u}_k) = \sum_{m \neq k} \Gamma_{km} \quad (\mathcal{M}_k) \\ \alpha_k \rho_k \frac{\partial \vec{u}_k}{\partial t} + \nabla \cdot (\alpha_k \rho_k \vec{u}_k \otimes \vec{u}_k) - \vec{u}_k \nabla \cdot (\alpha_k \rho_k \vec{u}_k) = \\ \quad - \alpha_k \nabla P + \nabla \cdot (\alpha_k \mu_k (\nabla \vec{u}_k) - \alpha_k \rho_k \overline{u'_i u'_j}) + \sum_{m \neq k} \vec{F}_{km}^i + \alpha_k \rho_k \vec{g} \quad (\mathcal{Q}_k) \\ \frac{\partial \alpha_k \rho_k e_k}{\partial t} + \nabla \cdot (\alpha_k \rho_k e_k \vec{u}_k) = -P \left(\frac{\partial \alpha_k}{\partial t} + \nabla \cdot (\alpha_k \vec{u}_k) \right) \\ \quad + \nabla \cdot (\alpha_k \lambda_k \nabla T_k - \alpha_k \rho_k \overline{u'_i e'_k}) + \sum_{m \neq k} (q_{km}^i + \Gamma_{km} h_{km}) \quad (\mathcal{E}_k) \end{array} \right. \quad (2.3)$$

The boundary conditions q_{kw} and $\Gamma_{w,km}$ are also implicit.

Under this form, linearizing each equation E for a given increment $(\delta\alpha, \delta\vec{v}, \delta T, \delta P)$ of the primary variables as $\delta E = \frac{\partial E}{\partial \alpha} \cdot \delta\alpha + \frac{\partial E}{\partial \vec{v}} \cdot \delta\vec{v} + \frac{\partial E}{\partial T} \cdot \delta T + \frac{\partial E}{\partial p} \cdot \delta P$ leads to the following linear system:

$$\begin{pmatrix} \frac{\partial \mathcal{M}}{\partial \alpha} & \frac{\partial \mathcal{M}}{\partial T} & \frac{\partial \mathcal{M}}{\partial \vec{u}} & \frac{\partial \mathcal{M}}{\partial P} \\ \frac{\partial \mathcal{E}}{\partial \alpha} & \frac{\partial \mathcal{E}}{\partial T} & \frac{\partial \mathcal{E}}{\partial \vec{u}} & \frac{\partial \mathcal{E}}{\partial P} \\ 0 & 0 & \frac{\partial \mathcal{Q}}{\partial \vec{u}} & \frac{\partial \mathcal{Q}}{\partial P} \end{pmatrix} \cdot \begin{pmatrix} \delta\alpha \\ \delta T \\ \delta \vec{u} \\ \delta P \end{pmatrix} = \begin{pmatrix} \delta \mathcal{M} \\ \delta \mathcal{E} \\ \delta \mathcal{Q} \end{pmatrix} \quad (2.4)$$

Where the blue and green blocks are purely *local*: when the equations are discretized, these blocks only contain non-zero terms for lines and columns belonging to the same mesh location. This system can be re-written:

$$\begin{pmatrix} \frac{\partial \mathcal{M}}{\partial \alpha} & \frac{\partial \mathcal{M}}{\partial T} & \frac{\partial \mathcal{M}}{\partial \vec{u}} \\ \frac{\partial \mathcal{E}}{\partial \alpha} & \frac{\partial \mathcal{E}}{\partial T} & \frac{\partial \mathcal{E}}{\partial \vec{u}} \\ 0 & 0 & \frac{\partial \mathcal{Q}}{\partial \vec{u}} \end{pmatrix} \cdot \begin{pmatrix} \delta\alpha \\ \delta T \\ \delta \vec{u} \end{pmatrix} = \begin{pmatrix} \delta \mathcal{M} \\ \delta \mathcal{E} \\ \delta \mathcal{Q} \end{pmatrix} - \begin{pmatrix} \frac{\partial \mathcal{M}}{\partial p} \\ \frac{\partial \mathcal{E}}{\partial p} \\ \frac{\partial \mathcal{Q}}{\partial p} \end{pmatrix} \cdot \delta P \quad (2.5)$$

Using the local character of the blue and green blocs, it is possible to express all increments as a function of the pressure increment δP . First the velocity increment $\delta \vec{u} = \delta \vec{u}^0 + M_{\vec{u}} \delta P$, then $\delta \alpha = \delta \alpha^0 + M_{\alpha} \delta P$ and $\delta T = \delta T^0 + M_T \delta P$. The matrices M_{α} , $M_{\vec{u}}$ and M_T are sparse. Inserting the first relationship into the continuity constraint $\sum \alpha_k = 1$ leads to a system involving only the pressure increments δP . This system can be solved using an iterative solver at each step of a Newton algorithm. Once the pressure increments are known, the other increments are calculated using δP .

Compared to a full system over the increments (α, \vec{u}, T, P) , this reduced system offers several advantages:

- it is vastly smaller (by a factor of $\sim 8N + 1$ in 3D) and does not increase in size with N ;
- its structure is in most cases elliptic (it can be shown to be the sum of a Poisson matrix and a diagonal matrix), and can thus be solved efficiently at large scale and/or in parallel by multigrid methods.

On the other hand, the explicit discretization of convected quantities in (2.4) means that timesteps are limited by a CFL condition. In order to overcome this limit, additional predictor steps can be implemented to provide initial estimates for convected quantities: this scheme, known as the prediction-correction scheme SETS (Mahaffy 1982), was implemented as well.

In order to implement the ICE scheme, the underlying architecture must be capable of providing the sparse matrices corresponding to each block of the Jacobian (2.4). In TRUST, this computation is spread between the space discretization, equation and medium classes in order to maximize code reuse. For instance, the derivative of the convective term of the mass equation \mathcal{M}_k w.r.t. the phase temperature T_k is computed as:

$$\frac{\partial \nabla \cdot (\alpha_k \rho_k \vec{u}_k)}{\partial T_k} = \frac{\partial \nabla \cdot (\alpha_k \rho_k \vec{u}_k)}{\partial \alpha_k \rho_k} \cdot \frac{\partial \alpha_k \rho_k}{\partial \rho_k} \cdot \frac{\partial \rho_k}{\partial T_k} \quad (2.6)$$

Where:

- the red term is computed by the convection operator of the underlying space discretization, such as PolyMAC or VDF. This operator implements a term of the form $\nabla \cdot (F \vec{u})$ for a convected field F : the instance of this term associated with \mathcal{M}_k operates with $F = \alpha_k \rho_k$, while another instance associated to \mathcal{E}_k operates with $F = \alpha_k \rho_k e_k$. Both equations rely on the same code to compute the matrix $\partial \nabla \cdot (F \vec{u}) / \partial F$;
- the green term $\partial \alpha_k \rho_k / \partial \rho_k$ is local, and computed by the equation \mathcal{M}_k where the convected field $F = \alpha_k \rho_k$ is defined. This field relies on the fields α_k (a primary unknown) and ρ_k (the density, provided by the medium);
- finally, the blue term is computed by the medium class, which defines the density field $\rho_k(p, T_k)$.

This architecture has been designed to maximize code reuse, in particular at the numerical scheme level. It has been found to be flexible and efficient.

2.1.5 Treatment of vanishing phases

The $3N$ -equation system $(\mathcal{M}, \mathcal{Q}, \mathcal{E})$ presents particular difficulties in the case of a vanishing phase ($\alpha_k \rightarrow 0$). In `Pb_Multiphase`, a limiter is placed on the total phase change $\Gamma_k = \sum_l \Gamma_{km}$ to deal with this issue. For a time step Δt , the time-discretized form of the mass equation \mathcal{M}_k reads

$$\frac{\alpha_k^+ \rho_k^+ - \alpha_k^- \rho_k^-}{\Delta t} + \nabla \cdot (\alpha_k \rho_k \vec{u}_k) = \Gamma_k \quad (2.7)$$

with the $-/+$ superscripts denoting values at times t and $t+\Delta t$: hence, the condition $\alpha_k^+ \geq 0$ leads to

$$\Gamma_k \geq \Gamma_k^{lim} = \nabla \cdot (\alpha_k \rho_k \vec{u}_k) - \frac{\alpha_k^- \rho_k^-}{\Delta t}. \quad (2.8)$$

At a given iteration, if $\Gamma_k < \Gamma_k^{lim}$, the mass flux Γ_{km} to the phase m with the highest α_m (the *dominant* phase) is modified so that $\Gamma_k = \Gamma_k^{lim}$: then, the heat flux q_{mk}^i is modified in order to preserve the jump condition $\Gamma_{km} = (q_{km}^i + q_{mk}^i)/(h_l - h_k)$. This process ensures that the converged solution of the Newton algorithm will satisfy $\alpha_k \geq 0$ while maintaining consistent mass, energy and momentum balances between the phases. At the end of each Newton iteration, the field α_k must be post-processed to ensure $\alpha_k = 0$ while preserving $\sum \alpha_k = 1$. Final convergence is only declared once the algorithm converges to a solution satisfying $\alpha_k \geq 0$.

Additionally, for stability reasons the momentum and energy equations guarantee that $\vec{u}_k \rightarrow \vec{u}_m$ and $T_k \rightarrow T_{sat}$ when $\alpha_k \rightarrow 0$. In `Pb_Multiphase`, this is obtained by ensuring that the interfacial exchange terms \vec{F}_{km}^i and q_{km}^i do not cancel out as $\alpha_k \rightarrow 0$. For cases where α_k becomes close to zero ($\approx 10^{-6}$), a vanishing operator is used to manage the situation (Gerschenfeld and Gorsse 2022). This operator forces the velocity of the vanishing phase to be the same as that of the majority phase. It also adds the momentum of the vanishing phase to that of the majority phase so the total momentum balance is respected.

2.2 Physical closure models

2.2.1 Turbulence modeling

Shear-induced turbulence In rod bundles, two-equations turbulence models yield similar results as Reynolds stress models with faster calculation times (Franck et al. 2012). I therefore selected the Kok 1999 $k - \omega$ turbulence model as it has similar properties to the more commonly used Menter 1993 $k - \omega$ model, i.e., a cross-diffusion term that is suppressed in the near-wall region, but is easier to

implement. This yields:

$$\begin{aligned}
\nu_t &= \frac{k}{\omega} & \overline{u'_i u'_j} &= -\nu_t \nabla \vec{u}_i & \overline{u'_i e'_l} &= -\frac{1}{Pr_t} \nu_t C_{pl} \nabla T_l \\
\partial_t k + \nabla \cdot (k \vec{u}_i) &= \nu_t (\nabla \vec{u}_i + {}^t \vec{u}_i) \cdot \nabla \vec{u}_i - \beta_k k \omega + \nabla \cdot (\alpha_l (\nu_l + \sigma_k \nu_t) \nabla k) \\
\partial_t \omega + \nabla \cdot (\omega \vec{u}_i) &= \alpha_\omega (\nabla \vec{u}_i + {}^t \nabla \vec{u}_i) \cdot \nabla \vec{u}_i - \beta_\omega \omega^2 \\
&+ \nabla \cdot (\alpha_l (\nu_l + \sigma_\omega \nu_t) \nabla \omega) + \sigma_d \frac{1}{\omega} \max \{ \nabla k \cdot \nabla \omega, 0 \}
\end{aligned} \tag{2.9}$$

Where k is the turbulent kinetic energy of the liquid, ω it's specific turbulent dissipation rate, ν_t it's turbulent viscosity, ν_l it's kinematic viscosity and Pr_t the turbulent Prandtl number. The values of the constants are $Pr_t = 0.9$, $\alpha_\omega = 0.5$, $\beta_k = 0.09$, $\beta_\omega = 0.075$, $\sigma_k = 2/3$, $\sigma_\omega = 0.5$ and $\sigma_d = 0.5$.

The Kok and Spekreijse 2000 $k - \tau$ turbulence model was also implemented and tested. It is derived from the $k - \omega$ model, where $\tau = 1/\omega$, and is used in the NEK-5000 code (Shaver et al. 2020). It proved much harder to stabilize in multi-phase flows than the $k - \omega$, so all multi-phase simulations in this thesis are carried out with the $k - \omega$ model.

$$\begin{aligned}
\tau &= \frac{1}{\omega} & \overline{u'_i u'_j} &= -\nu_t \nabla \vec{u}_i \\
\nu_t &= k\tau & \overline{u'_i e'_l} &= -\frac{1}{Pr_t} \nu_t C_{pl} \nabla T_l \\
\partial_t k + \nabla \cdot (k \vec{u}_i) &= \nu_t (\nabla \vec{u}_i + {}^t \vec{u}_i) \cdot \nabla \vec{u}_i - \beta_k \frac{k}{\tau} + \nabla \cdot (\alpha_l (\nu_l + \sigma_k \nu_t) \nabla k) \\
\partial_t \tau + \nabla \cdot (\tau \vec{u}_i) &= -\alpha_\omega \tau^2 (\nabla \vec{u}_i + {}^t \nabla \vec{u}_i) \cdot \nabla \vec{u}_i + \beta_\omega + \nabla \cdot ((\nu_l + \sigma_\omega \nu_t) \nabla \tau) \\
&+ \sigma_d \tau \min \{ \nabla k \cdot \nabla \tau, 0 \} - 8(\nu_l + \sigma_\omega \nu_t) \|\nabla \sqrt{\tau}\|^2
\end{aligned} \tag{2.10}$$

The values of the constants are the same as for the $k - \omega$ equation.

Turbulent boundary conditions I implemented an adaptive wall-law algorithm that begins by determining the friction velocity u_τ in the same way as in Carlson et al. 2015. The shear stress at the boundary is then computed and is used as a Navier boundary condition for the momentum equation: $\tau_{wf} = \alpha_l \rho_l u_\tau^2$.

The boundary condition on k is $k = 0$ at the wall for $y_+ < 5$, where $y_+ = y u_\tau / \nu_l$ and y is the distance between the wall and the first element center. For larger wall elements, it is a zero-flux condition. The transition is smoothed by a transition factor $\tanh((y_+/10)^2)$.

For ω , Knopp et al. 2006 give an analytical value in the near-wall region. A simple solution would be to enforce this value in the first element. However, it was already used in TrioCFD and creates numerical issues for tetrahedron meshes. Instead, the analytical solution at a distance $y/2$ from the wall is calculated. A fixed boundary condition at the wall is then enforced: $\omega_{\text{wall}} = 2 \cdot \omega(y/2)$. This amounts to creating a virtual element between the first element and the wall in which the value of ω is known.

For τ , $\tau = 0$ at the wall is enforced.

Kader single-phase heat transfer The single-phase boundary condition implemented is the one proposed by Kader 1981. The wall heat flux towards phase k at a distance y from the wall is:

$$q_{wk} = (T_w - T_k(y)) \frac{\rho_l C_{p,k} u_\tau}{\Theta_+^w(y_+)} \quad (2.11)$$

Where $\Theta_+^w(y_+)$ is the dimensionless fluid temperature in the near-wall region and u_τ is calculated using the adaptive wall law. In the near-wall region it is proportional to y_+ and in the turbulent region is proportional to $\log(y_+)$. It is calculated using:

$$\beta_{\text{SP}} = (3.85(Pr^{1/3}) - 1.3)^2 + 2.12 \log(Pr) \quad (2.12)$$

And the transition coefficient:

$$\gamma = \frac{0.01(Pr y_+)^4}{1 + 5Pr^3 y_+} \quad (2.13)$$

Then:

$$\Theta_+^w(y_+) = Pr y_+ \exp(-\gamma) + (2.12 \cdot \log(1 + y_+) + \beta_{\text{SP}}) \exp\left(-\frac{1}{\gamma}\right) \quad (2.14)$$

Here T_w is the wall temperature, $C_{p,k}$ is the heat capacity of phase k and $Pr = \frac{\nu_l \rho_l C_{pl}}{\lambda_l}$ the Prandtl number. This expression is based on experimental measurements for y_+ ranging from 0 to 300. The Kader expression is used to estimate the convective heat transfer contribution in the wall heat flux partition model (see section 2.2.5).

Bubble-induced turbulence Bubble-induced turbulence models proposed by Sato et al. 1981, Rzehak and Krepper 2013 and Cluzeau 2019 are included in TrioCFD.

However, according to Almeras et al. 2017, liquid velocity fluctuations induced by bubble movements are small compared to those from shear if the bubble parameter $b = \frac{\alpha_g \|\vec{u}_g - \vec{u}_l\|^2}{u_{\text{SP}}'^2} < 0.5$, where u_{SP}' are the turbulent fluctuations for a single-phase flow with the same mass flux. At PWR pressures, the bubble diameter $d_b < 1$ mm, which yields $\|\vec{u}_g - \vec{u}_l\| < 0.1$ m/s, and $\alpha_g < 0.5$. Using the Reichardt 1951 correlation for a bulk Reynolds number $Re = 10^5$, bubble-induced turbulence can be neglected in PWR's (i.e. $b < 0.5$) for bulk velocities $u_{\text{bulk}} > 1.5$ m/s. This is a low value as $u_{\text{bulk}} \sim 4$ m/s in operation (Delhay 2008), and $b \sim 0.1$. Therefore, I do not use bubble-induced turbulence in this thesis.

2.2.2 Bubble diameter modeling

Virtually all multi-phase closure terms require a bubble diameter. In multiphase TrioCFD, one can impose a constant diameter or a 3D time-dependent field. These

solutions are used respectively in the code verification (section 3.1) and in the validation and preliminary calculations (section 3.2 and chapter 5).

The Yao and Morel 2004 interfacial area transport equation and a MUSIG population balance model (Krepper et al. 2008) are included in TrioCFD. However, as the modified set of closures that I propose does not require the modeling of the bubble diameter (chapter 7), I do not discuss them further in this thesis in relation with the code.

2.2.3 Interfacial momentum exchanges modeling

The interfacial force exerted by the liquid on the gas is $\vec{F}_{gi} = -\vec{F}_{li}$. In this subsection, all forces written apply to the gas phase and are written in their volumetric form. I separate the interfacial momentum transfer term in five different contributions: the drag, virtual mass, lift and turbulent dispersion forces, and the wall correction.

$$\vec{F}_{lg}^i = \vec{F}_{\text{drag}} + \vec{F}_{\text{VM}} + \vec{F}_{\text{lift}} + \vec{F}_{\text{TD}} + \vec{F}_{\text{wall}} \quad (2.15)$$

Apart from a modification to the virtual mass force, the set of momentum closures that I selected was proposed by Sugrue 2017. I do not review the derivations of these momentum transfer terms or compare different formulations here. Recent reviews can be found in the works of Sugrue 2017 or Chuang and Hibiki 2017 for example.

Drag force The contaminated drag force of Tomiyama et al. 1998 is implemented:

$$\begin{aligned} \vec{F}_{\text{drag}} &= -a_i \frac{1}{2} C_D \rho_l \|\vec{u}_g - \vec{u}_l\| (\vec{u}_g - \vec{u}_l) \\ &= -\frac{3}{4} C_D \frac{\alpha_g \rho_l}{d_b} \|\vec{u}_g - \vec{u}_l\| (\vec{u}_g - \vec{u}_l) \\ C_D &= \max\left(\frac{24}{Re_b} (1 + 0.15 Re_b^{0.687}), \frac{8Eo}{3Eo+12}\right) \end{aligned} \quad (2.16)$$

Where C_D is the drag coefficient, $a_i = \frac{6\alpha_g}{d_b}$ is the interfacial area of the gas phase, $Eo = \frac{(\rho_l - \rho_g) g d_b^2}{\sigma}$ the Eötvös number and $Re_b = \frac{d_b \|\vec{u}_g - \vec{u}_l\|}{\nu_l}$ the bubble Reynolds number.

Virtual mass force The virtual mass reads:

$$\vec{F}_{\text{VM}} = -C_{\text{VM}} \rho_l (\partial_t \vec{u}_g - \partial_t \vec{u}_l + \vec{u}_g \nabla \vec{u}_g - \vec{u}_l \nabla \vec{u}_l) \quad (2.17)$$

Where C_{VM} is the virtual mass coefficient. It can be interpreted as the volume of liquid entrained by the accelerating or decelerating bubbles.

The most commonly used formulations are the constant coefficient $C_{\text{VM}} = \frac{1}{2} \alpha_g$ and the $C_{\text{VM}} = \frac{1}{2} \frac{1+2\alpha_g}{1-\alpha_g} \alpha_g$ (Zuber 1964), that were both derived theoretically. Recently, Béguin et al. 2016 performed potential flow simulations with random bubble positions and found $C_{\text{VM}} = \alpha_g \left(\frac{1}{2} + 0.34 \alpha_g^2\right) \sim \frac{1}{2} \alpha_g$. Furthermore, in some DEBORA experimental runs (Garnier et al. 2002), the local void fraction can reach 0.7. If I used the standard constant coefficient $C_{\text{VM}} = \frac{1}{2} \alpha_g$, the liquid volume

fraction entrained by the gas phase would be $0.7 \cdot 1/2 = 0.35$. The total liquid fraction, which is $\alpha_l = 1 - \alpha_g = 0.3$, would be less than the entrained liquid fraction. This is non-physical and leads to numerical stability issues. I therefore assume that at most 1/2 of the remaining liquid can be entrained by the gas, the value 1/2 being arbitrary. This leads to:

$$C_{VM} = \min\left(\frac{1}{2}\alpha_g, \frac{1}{2}\alpha_l\right) \quad (2.18)$$

This modification affects C_{VM} for $\alpha_g > 0.5$.

Lift force The general formulation for the lift force is:

$$\vec{F}_{\text{lift}} = -C_L \rho_l \alpha_g (\vec{u}_g - \vec{u}_l) \wedge (\nabla \wedge \vec{u}_l) \quad (2.19)$$

The difference between lift force models is the lift coefficient C_L . A constant coefficient can be chosen by the user. The Sugrue 2017 formulation was also implemented, as it was designed to operate on high-void fraction ascending flows and not only single bubbles, contrarily to the Tomiyama et al. 2002 formulation. The Sugrue 2017 lift coefficient requires a so-called Wobble number Wo and reads:

$$C_L = f(Wo) \cdot g(\alpha) \quad , \quad g(\alpha) = \max(0, 1.0155 - 0.0154 \exp(8.0506\alpha)) \\ Wo = Eo \frac{k}{\|\vec{u}_g - \vec{u}_l\|^2} \quad , \quad f(Wo) = \min(0.03, 5.0404 - 5.0781 Wo^{0.0108}) \quad (2.20)$$

Turbulent dispersion force The Burns et al. 2004 force is selected:

$$\vec{F}_{TD} = -C_{TD} \rho_l k \nabla \alpha_g \quad , \quad C_{TD} = \frac{3}{4} \frac{C_D}{d_b} |\vec{u}_g - \vec{u}_l| \frac{1}{\omega} \left(1 + \frac{\alpha_g}{\alpha_l}\right) \quad (2.21)$$

Where C_{TD} is the turbulent dispersion coefficient.

Wall correction The main wall correction term implemented is the one proposed by Lubchenko et al. 2018. It is based on geometrical arguments. It suppresses lift and turbulent dispersion when the bubble touches the the wall. The lift coefficient becomes:

$$C_L \rightarrow \begin{cases} 0 & \text{if } y/d_b < 1/2 \\ C_L \left(3 \left(\frac{2y}{d_b} - 1\right)^2 - 2 \left(\frac{2y}{d_b} - 1\right)^3\right) & \text{if } 1/2 \leq y/d_b < 1 \\ C_L & \text{if } y/d_b \geq 1 \end{cases} \quad (2.22)$$

If \vec{n} is the unit vector normal to the wall, the turbulent dispersion wall correction reads:

$$\vec{F}_{\text{wall}} = \begin{cases} C_{TD} \rho_l k \cdot \alpha_g \frac{1}{y} \frac{d_b - 2y}{d_b - y} \vec{n} & \text{if } y/d_b < 1/2 \\ 0 & \text{if } y/d_b \geq 1/2 \end{cases} \quad (2.23)$$

2.2.4 Interfacial heat transfer

As I study bubbly flows, I select interfacial heat transfer formulations from the liquid to the interface based on the calculation of the Nusselt number Nu_b . If the liquid is colder than T_s :

$$q_{lv}^i = a_i \frac{\lambda_l}{d_b} (T_s - T_l) Nu_b = \frac{6\alpha_v}{d_b} \frac{\lambda_l}{d_b} (T_s - T_l) Nu_b \quad (2.24)$$

The Ranz and Marshall 1952 model is implemented to determine the Nusselt number. It is used by many authors (Kommajosyula 2020; Favre 2023).

$$Nu_{\text{Ranz\&Marshall}} = 2 + 0.6Re_b^{1/2} Pr^{1/3} \quad (2.25)$$

To the best of my knowledge, no liquid temperature was ever measured above the saturation temperature in flow boiling experiments (Roy et al. 2002; Garnier et al. 2001; François et al. 2021). Therefore, I do not allow the liquid to overcome the saturation temperature by enforcing an extremely high heat transfer coefficient if $T_l > T_s$, set at $10^8 \text{Wm}^{-3}\text{K}^{-1}$. For the same, I do not allow the vapor phase to achieve a higher temperature than T_s . This yields:

$$q_{vl}^i = 10^8 (T_s - T_v)$$

$$q_{lv}^i = \begin{cases} \frac{6\alpha_v}{d_b} \frac{\lambda_l}{d_b} (T_s - T_l) Nu_{\text{Ranz\&Marshall}} & \text{if } T_l \leq T_s \\ 10^8 (T_s - T_l) & \text{if } T_l > T_s \end{cases} \quad (2.26)$$

The mass transfer between phases is entirely then determined using the interfacial heat transfers.

2.2.5 Heat Flux Partitioning: Original Kurul and Podowski

This model is considered the first heat flux partition. It was originally proposed by Kurul and Podowski 1990. Though more recent and complex formulations have been proposed (Basu et al. 2005; Kommajosyula 2020; Favre 2023), it is used as the reference in the literature and I select it for the baseline set of closures. A recent review can be found in the work of Favre 2023.

The departure diameter is a linear interpolation between those of Ünal 1976 and Thomas 1981:

$$d_{\text{departure}} = 10^{-4}(T_w - T_s) + 0.0014 \quad (2.27)$$

The nucleation site density is from Del Valle and Kenning 1985:

$$N_{\text{sites}} = (210(T_w - T_s))^{1.8} \quad (2.28)$$

The area influenced by the presence of bubbles is:

$$A_{\text{bubbles}} = \min \left(1, \frac{\pi}{4} N_{\text{sites}} d_{\text{departure}}^2 \right) \quad (2.29)$$

The bubble departure frequency is given by Cole 1960:

$$f_{\text{departure}} = \sqrt{\frac{4 \cdot 9.81(\rho_l - \rho_v)}{3\rho_l d_{\text{departure}}}} \quad (2.30)$$

The quenching heat flux is also from Del Valle and Kenning 1985, where the waiting period used is $t_{\text{wait}} = 1/f_{\text{departure}}$:

$$q_{\text{quench}} = 2A_{\text{bubbles}}(T_w - T_l(y))f_{\text{departure}}\sqrt{\frac{t_{\text{wait}}\lambda_l\rho_l C_p}{\pi}} \quad (2.31)$$

Placing ourselves at a distance y from the wall and using the Kader 1981 single-phase heat transfer, this yields the following transfer towards the liquid phase:

$$q_{wl} = (1 - A_{\text{bubbles}})q_{\text{SP}}(y) + q_{\text{quench}}(y) \quad (2.32)$$

And the evaporation heat flux is:

$$q_{l \rightarrow v} = \frac{\pi}{6}f_{\text{departure}}d_{\text{departure}}^3\rho_v(h_{vs} - h_{ls})N_{\text{sites}} \quad (2.33)$$

Where h_{vs} (h_{ls}) is the vapor (liquid) saturation enthalpy. It can be noted that the evaporation heat flux in this formulation is independent of the local liquid temperature, while the quenching and single-phase heat fluxes are not.

The total heat flux is:

$$q_w = (1 - A_{\text{bubbles}})q_{\text{SP}}(y) + q_{\text{quench}}(y) + q_{l \rightarrow v} \quad (2.34)$$

2.2.6 Summary of the baseline set of closures

Table 2.1 contains a all of the elements that are part of the baseline set of closures.

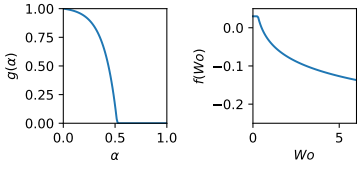
Term	Baseline closure
Drag	Tomiyama et al. 1998 $C_D = \max\left(\frac{24}{Re_b}(1 + 0.15Re_b^{0.687}), \frac{8Eo}{3Eo+12}\right)$
Lift	Sugrue 2017 $C_L = f(Wo) \cdot g(\alpha_v)$ 
TD	Burns et al. 2004 $C_{TD} = \frac{3}{4} \frac{C_D}{d_b} \vec{u}_g - \vec{u}_l \frac{1}{\omega} \left(1 + \frac{\alpha_v}{\alpha_l}\right)$
VM	Zuber 1964 adapted in current work $C_{VM} = \min\left(\frac{1}{2}\alpha_g, \frac{1}{2}\alpha_l\right)$
HFP	Kurul and Podowski 1990 $q_{SP} = (T_w - T_l(y)) \frac{\rho_l C_{pl} u_\tau}{\Theta_+^w(y_+)}$ $N_s = (210(T_w - T_s))^{1.8}$ $d_{b, \det} = 10^{-4} \cdot (T_w - T_s) + 0.0014$ $f_{\text{dep}} = \sqrt{\frac{4}{3} \frac{g(\rho_l - \rho_g)}{\rho_l d_{b, \det}}}$ $A_b = \min(1, \pi/4 \cdot N_s d_{b, \det}^2)$ $q_c = (1 - A_b) q_{SP}$ $q_q = 2A_b \lambda_l (T_w - T_l) \sqrt{\frac{f_{\text{dep}} \rho_l C_{pl}}{\pi \lambda_l}}$ $q_{wl} = q_c + q_q$ $q_{w, l \rightarrow v} = \frac{\pi}{6} f_{\text{dep}} d_{b, \det}^3 \rho_g h_{lg} N_s$ $q_w = q_c + q_q + q_{w, l \rightarrow v}$
Cond	Ranz and Marshall 1952 $q_{ki} = \frac{6\alpha_v \lambda_l (T_g - T_l)}{d_b^2} \left(2 + 0.6Re_b^{1/2} Pr^{1/3}\right)$

Table 2.1: Baseline set of models selected in this thesis. *TD*: turbulent dispersion. *VM*: virtual mass. *HFP*: heat flux partition. *Cond*: condensation.

2.3 The drift-flux model

I present a drift-flux framework that is included in TrioCFD in order to analyze the differences between it and the two-fluid framework that is mainly used in this thesis. In section 2.3.1, the equations that are solved and the numerical implementation are presented. In section 2.3.2, a method to obtain a 3-dimensional closure for the relative velocity using a force balance on the vapor phase is proposed. A comparison of simulation results between the drift-flux model and the two-fluid framework is shown in section 3.3.

2.3.1 Building a drift-flux model base on a two-fluid system

Momentum equation: using the vanishing operator The vanishing operator presented in section 2.1.5 can be hijacked in TrioCFD to couple the momentum equations of both phases.

Here, a phase k is described as vanishing for $\alpha_k < 0.5$. If \tilde{k} is the majority phase, the two velocities \vec{u}_k and $\vec{u}_{\tilde{k}}$ will be forced to be equal: $\vec{u}_k = \vec{u}_{\tilde{k}} = \vec{u}_m$ where \vec{u}_m is the mixture velocity.

Defining the mixture mass $\rho_m = \alpha_k \rho_k + \alpha_l \rho_l$, the mass equation solved by the system will then be:

$$\begin{aligned} \rho_m \frac{\partial \vec{u}_m}{\partial t} + \nabla \cdot (\rho_m \vec{u}_m \otimes \vec{u}_m) - \vec{u}_m \nabla \cdot (\rho_m \vec{u}_m) = \\ - \nabla P + \nabla \cdot ((\alpha_k \mu_k + \alpha_{\tilde{k}} \mu_{\tilde{k}})(\nabla \vec{u}_m) - \rho_m \overline{u'_i u'_j}) + \rho_m \vec{g} \end{aligned} \quad (2.35)$$

I now consider a gas-liquid mixture. Furthermore, instead of enforcing a zero-velocity difference between the liquid and the vapor phase, a drift velocity is enforced:

$$\vec{u}_r = \vec{u}_g - \vec{u}_l \quad (2.36)$$

The mixture velocity is defined as:

$$\vec{u}_m = \frac{\alpha_g \rho_g \vec{u}_g + \alpha_l \rho_l \vec{u}_l}{\rho_m} = \vec{u}_l + \frac{\alpha_g \rho_g \vec{u}_r}{\rho_m} = \vec{u}_g - \frac{\alpha_l \rho_l \vec{u}_r}{\rho_m} \quad (2.37)$$

Writing \vec{u}_l and \vec{u}_g as a function of \vec{u}_m and \vec{u}_r , the mixture momentum equation solved by TrioCFD is therefore:

$$\begin{aligned}
\rho_m \frac{\partial \vec{u}_m}{\partial t} + \nabla \cdot (\rho_m \vec{u}_m \otimes \vec{u}_m) - \vec{u}_m \nabla \cdot (\rho_m \vec{u}_m) \\
= -\nabla P + \nabla \cdot ((\alpha_l \mu_l + \alpha_g \mu_g)(\nabla \vec{u}_m) - \rho_m \overline{u'_i u'_j}) + \rho_m \vec{g} \\
+ \nabla \cdot \left(-\alpha_l \mu_l \nabla \left(\frac{\alpha_v \rho_v \vec{u}_r}{\rho_m} \right) + \alpha_v \mu_v \nabla \left(\frac{\alpha_l \rho_l \vec{u}_r}{\rho_m} \right) \right) \\
- \nabla \cdot \left(\frac{\alpha_g \rho_g \alpha_l \rho_l}{\rho_m} \vec{u}_r \otimes \vec{u}_r \right) + \vec{u}_r \nabla \cdot \left(\frac{\alpha_g \rho_g \alpha_l \rho_l}{\rho_m} \vec{u}_r \right) \\
+ \frac{\alpha_l \rho_l \vec{u}_r}{\rho_m} \nabla \cdot (\alpha_g \rho_g \vec{u}_m) - \frac{\alpha_g \rho_g \vec{u}_r}{\rho_m} \nabla \cdot (\alpha_l \rho_l \vec{u}_m)
\end{aligned} \tag{2.38}$$

This is a modified version of the drift-flux balance equation proposed by Ishii and Hibiki 2006. The difference is due to the use of the semi-conservative form of the momentum convection in TrioCFD (Park et al. 2009). The bottom two lines in equation 2.38 are often neglected when implementing the model in industrial codes.

Energy equation: an extremely large heat transfer from the vapor phase to the interface As discussed in section 2.2.4, an extremely large heat transfer coefficient from the vapor phase to the interface is enforced because no vapor superheat has ever been measured experimentally. The vapor phase is then always at saturation temperature, and the vapor energy and vapor mass balance equations are redundant.

Complete system of equations The complete system of equations that is solved in the TrioCFD drift-flux model is therefore:

$$\left\{ \begin{array}{l}
 \vec{u}_v = \vec{u}_m + \frac{\alpha_l \rho_l \vec{u}_r}{\rho_m} \\
 \vec{u}_l = \vec{u}_m - \frac{\alpha_v \rho_v \vec{u}_r}{\rho_m} \\
 \frac{\partial \alpha_v \rho_v}{\partial t} + \nabla \cdot (\alpha_v \rho_v \vec{u}_v) = \Gamma_{vl} \quad (\mathcal{M}_v) \\
 \frac{\partial \alpha_l \rho_l}{\partial t} + \nabla \cdot (\alpha_l \rho_l \vec{u}_l) = \Gamma_{lv} \quad (\mathcal{M}_l) \\
 \rho_m \frac{\partial \vec{u}_m}{\partial t} + \nabla \cdot (\rho_m \vec{u}_m \otimes \vec{u}_m) - \vec{u}_m \nabla \cdot (\rho_m \vec{u}_m) = \\
 \quad - \nabla P + \nabla \cdot ((\alpha_l \mu_l + \alpha_v \mu_v)(\nabla \vec{u}_m) - \rho_m \overline{u'_i u'_j}) + \rho_m \vec{g} \quad (2.39) \\
 \quad + \nabla \cdot \left(-\alpha_l \mu_l \nabla \left(\frac{\alpha_v \rho_v \vec{u}_r}{\rho_m} \right) + \alpha_v \mu_v \nabla \left(\frac{\alpha_l \rho_l \vec{u}_r}{\rho_m} \right) \right) \quad (\mathcal{Q}_m) \\
 \quad - \nabla \cdot \left(\frac{\alpha_v \rho_v \alpha_l \rho_l}{\rho_m} \vec{u}_r \otimes \vec{u}_r \right) + \vec{u}_r \nabla \cdot \left(\frac{\alpha_v \rho_v \alpha_l \rho_l}{\rho_m} \vec{u}_r \right) \\
 \quad + \frac{\alpha_l \rho_l \vec{u}_r}{\rho_m} \nabla \cdot (\alpha_v \rho_v \vec{u}_m) - \frac{\alpha_v \rho_v \vec{u}_r}{\rho_m} \nabla \cdot (\alpha_l \rho_l \vec{u}_m) \\
 \frac{\partial \alpha_l \rho_l e_l}{\partial t} + \nabla \cdot (\alpha_l \rho_l e_l \vec{u}_l) = -P \left(\frac{\partial \alpha_l}{\partial t} + \nabla \cdot (\alpha_l \vec{u}_l) \right) \\
 \quad + \nabla \cdot (\alpha_l \lambda_l \nabla T_l - \alpha_l \rho_l \overline{u'_i e'_l}) + (q_{lv}^i + \Gamma_{lv} h_{vl}) \quad (\mathcal{E}_l)
 \end{array} \right.$$

This system can be compared with the drift-flux model proposed by Ishii and Hibiki 2006, where the work of viscosity is neglected and it is assumed that the sum of momentum transfers between phases is zero:

$$\left\{ \begin{array}{l}
 \frac{\partial \rho_m}{\partial t} + \nabla \cdot (\rho_m \vec{u}_m) = 0 \quad (\mathcal{M}_m) \\
 \frac{\partial \alpha_v \rho_v}{\partial t} + \nabla \cdot (\alpha_v \rho_v \vec{u}_m) = \Gamma_{vl} - \nabla \cdot \left(\frac{\alpha_v \rho_v \alpha_l \rho_l}{\rho_m} \vec{u}_r \right) \quad (\mathcal{M}_v) \\
 \frac{\partial \rho_m \vec{u}_m}{\partial t} + \nabla \cdot (\rho_m \vec{u}_m \otimes \vec{u}_m) = \\
 \quad - \nabla P + \nabla \cdot ((\alpha_l \mu_l + \alpha_v \mu_v)(\nabla \vec{u}_m) - \rho_m \overline{u'_i u'_j}) + \rho_m \vec{g} \quad (\mathcal{Q}_m) \\
 \quad - \nabla \cdot \left(\frac{\alpha_l \rho_l \alpha_v \rho_v}{\rho_m} \vec{u}_r \otimes \vec{u}_r \right) \\
 \frac{\partial \rho_m h_m}{\partial t} + \nabla \cdot (\rho_m h_m \vec{u}_m) = -\frac{DP}{Dt} \\
 \quad + \nabla \cdot (\alpha_l \lambda_l \nabla T_l + \alpha_v \lambda_v \nabla T_v - \alpha_l \rho_l \overline{u'_i e'_l}) \quad (\mathcal{E}_m) \\
 \quad - \nabla \cdot \left(\frac{\alpha_v \rho_v \alpha_l \rho_l}{\rho_m} (h_{vs} - h_l) \vec{u}_r \right)
 \end{array} \right. \quad (2.40)$$

The first difference between these systems is that TrioCFD solves a vapor and liquid mass balance while Ishii and Hibiki 2006 solve a mixture and vapor mass balance. The second is that TrioCFD solves a liquid internal energy balance while Ishii and Hibiki 2006 solve a mixture enthalpy balance. These approaches are equivalent. The final difference is the form of the mixture momentum equation, that is due to the choice of the Park et al. 2009 semi-conservative momentum formulation in TrioCFD rather than the conservative one chose by Ishii and Hibiki 2006. Table 2.2 compares the system of equations solved by the drift-flux module of TrioCFD with the drift-flux model proposed by Ishii and Hibiki 2006.

TrioCFD drift-flux model Equation 2.39	Ishii and Hibiki 2006 drift-flux model Equation 2.40
Mixture momentum balance (\mathcal{Q}_m)	Mixture momentum balance (\mathcal{Q}_m)
Vapor mass balance (\mathcal{M}_v)	Vapor mass balance (\mathcal{M}_v)
Liquid mass balance (\mathcal{M}_l) + $\sum \alpha_k = 1$ (2.2) + Vapor mass balance (\mathcal{M}_v)	Mixture mass balance (\mathcal{M}_m)
Liquid energy balance (\mathcal{E}_l) + Vapor energy balance (eq 2.1)	Mixture enthalpy balance (\mathcal{E}_m)

Table 2.2: Comparison between the system of equations solved by the TrioCFD drift-flux model, i.e. based on a two-fluid model architecture, and the Ishii and Hibiki 2006 drift-flux model. TrioCFD solves redundant equations but the conservation equations are equivalent in both cases. Equations in italics in the left column are required for the equivalence but have already been cited in the table.

As it is based on a two-fluid numerical architecture, this implementation of the drift-flux model requires the same calculation time. However, it makes experimenting with various drift-flux closures possible.

2.3.2 Modeling the drift velocity in bubbly flow

Now that a drift-flux system of equations can be solved, a closure for the relative velocity must be determined. Multiple formulations exist for one-dimensional flows (Zuber and Findlay 1965; Ishii and Zuber 1979; Hibiki and Ishii 2003). However, such models are far less common for 3D CFD-scale simulations.

The approach of Manninen et al. 1996 is based on a force balance on individual bubbles. They take into account gravity, centrifugal acceleration, the drag force and bubble inertia.

I propose a different force balance-based approach where the specificities of ascending narrow flows are exploited. The order of magnitude of the difference in length scale between the vertical axis z and the orthogonal axes is 100 in the geometries of interest in this thesis. This means that the vorticity and volume fraction gradients will be almost orthogonal to the z -axis, and that the vertical velocities are large before the horizontal velocities. Finally, I assume like Zuber 1964 that the vertical relative velocity is set by a force balance between buoyancy and drag.

To compute the relative velocity, the following steps are carried out:

1. Compute $\|\vec{u}_g - \vec{u}_l\|$ using a Newton algorithm:

$$\|\vec{F}_{\text{drag}}\| = \frac{3}{4} C_D \frac{\alpha_g \rho_l}{d_b} \|\vec{u}_g - \vec{u}_l\|^2 \quad (2.41)$$

2. Compute the drift velocity along gravity in any coordinate system:

$$\vec{u}_g - \vec{u}_l = -\|\vec{u}_g - \vec{u}_l\| \frac{\vec{g}}{\|\vec{g}\|} \quad (2.42)$$

3. Compute the turbulent dispersion and lift forces (equations 2.19 and 2.21), using $\|\vec{u}_g - \vec{u}_l\|$ and $u_g - u_l$ as inputs for these forces
4. Determine the relative velocity orthogonal to gravity, written:

$$\vec{u}_\perp = \vec{u}_g - \vec{u}_l - \left((\vec{u}_g - \vec{u}_l) \cdot \frac{\vec{g}}{\|\vec{g}\|} \right) \frac{\vec{g}}{\|\vec{g}\|} \quad (2.43)$$

Through the following force balance on the direction orthogonal to gravity, that uses the fact that $\|\vec{u}_\perp\| \ll \|\vec{u}_g - \vec{u}_l\|$:

$$\frac{3}{4} C_D \frac{\alpha_g \rho_l}{d_b} \|\vec{u}_g - \vec{u}_l\| \|\vec{u}_\perp\| = \vec{F}_{\text{lift}} + \vec{F}_{\text{disp}} - \left((\vec{F}_{\text{lift}} + \vec{F}_{\text{disp}}) \cdot \frac{\vec{g}}{\|\vec{g}\|} \right) \frac{\vec{g}}{\|\vec{g}\|} \quad (2.44)$$

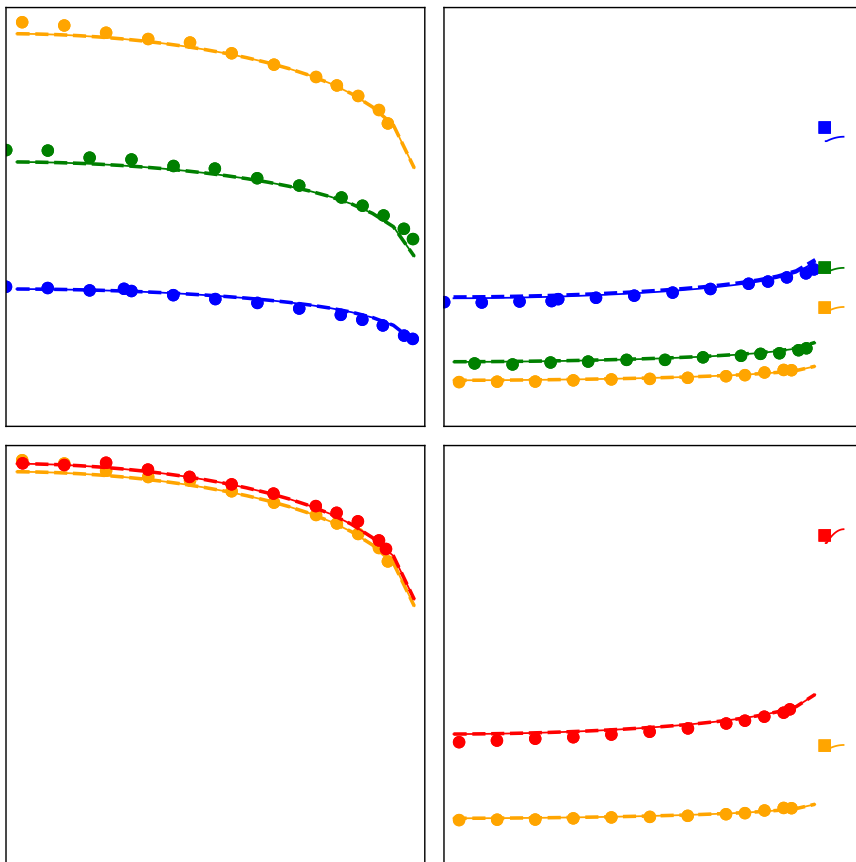
5. The relative velocity enforced is then:

$$\vec{u}_r = -\|\vec{u}_g - \vec{u}_l\| \frac{\vec{g}}{\|\vec{g}\|} + \vec{u}_\perp \quad (2.45)$$

This algorithm is compatible with any formulation of the lift and turbulent dispersion forces. The output of this algorithm will be compared with the two-fluid model in section 3.3 in ascending pipes. It's main limitation is that the $\|\vec{u}_\perp\| \ll \|\vec{u}_g - \vec{u}_l\|$ hypothesis may no longer be valid behind mixing vanes.

The drift-flux module will also be used in section 7.5 to analyze turbulent dispersion forces.

CHAPTER 3



Only single-phase simulations can work this well...

Verification and validation

This chapter begins with the verification methodology of the multiphase version of TrioCFD (section 3.1). The aim is to verify the implementation of the different multiphase terms independently of the physics and the models used, i.e. without validation on experimental data. This is done in two steps: post-treating single-term outputs to make sure that they are coherent with the desired implementation, and running simulations with arbitrary closure laws to verify the behavior of the complete system of equations.

In section 3.2, the baseline set of closure terms presented in section 2.2 is validated on single-phase and adiabatic atmospheric-pressure flow experimental data. Boiling flow results are presented in chapter 5.

The results from drift-flux and two-fluid approaches are compared in section 3.3.

Parts of this chapter were adapted from Reiss et al. 2024a and from Reiss et al. 2024c.

Contents

3.1	Code verification	47
3.1.1	Term-by-term output	47
3.1.2	Single-phase turbulence	47
3.1.3	Adiabatic multi-phase flow	47
3.1.4	Mesh refinement	49
3.1.5	Boiling multi-phase flow	50
3.2	Framework validation	53
3.2.1	Adiabatic single-phase flow	53
3.2.2	Heated single-phase flow	55
3.2.3	Two-phase adiabatic vertical tube	56
3.3	Comparing the two-fluid model with the drift-flux model	59
3.4	Conclusion	60

3.1 Code verification

3.1.1 Term-by-term output

The first step in the verification methodology is to check that the individual terms are coded correctly. This is done using modules of the TRUST architecture that enable the post-treatment of each term. Zero-time step simulations of analytical cases are run and the outputs are verified. These simulations are integrated to a set of case tests that are run automatically each time new developments of any kind are added to the code. These tests are implemented for turbulent wall laws, interfacial forces, turbulent source terms and interfacial heat flux for both numerical schemes used in this thesis (VDF and PolyMAC).

3.1.2 Single-phase turbulence

Flow simulations are run in the same 2D channel at $Re = 20,000$ with cartesian grids of varying refinements: y_+ in the first element ranges from 3 to 229 with both numerical schemes (PolyMAC results are shown in figure 3.1). The results are independent of y_+ in the first element and consistent with literature and refined solutions, except for k_+ in the near-wall region which is expected as the flow is transitioning from a wall-resolved to a wall-modeled solution. The implementation of the turbulence models and the adaptive wall laws are verified.

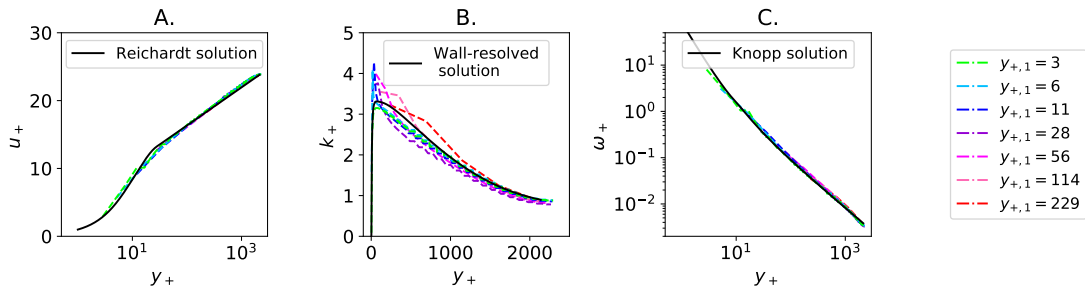


Figure 3.1: $k - \omega$ results for a turbulent 2D channel with $Re = 20,000$ with the PolyMAC numerical scheme. Results with VDF are identical. The size of the first element at the wall, and therefore y_+ , varies in each simulation. A. Non-dimensional velocity $u_+ = u/u_\tau$ as a function of y_+ . Black line: Reichardt 1951 solution. B. Non-dimensional turbulent kinetic energy $k_+ = k/u_\tau^2$ as a function of y_+ . Black line: refined solution for $y_{+,1} = 1$. C. Non-dimensional dissipation rate $\omega_+ = \omega u_\tau / \nu$ as a function of y_+ . Black line: Knopp et al. 2006 solution.

3.1.3 Adiabatic multi-phase flow

To verify the implementation of the multi-phase force terms, the analytic solution found by Marfaing et al. 2016 for a simplified set of closures is used. The authors

choose constant coefficient drag and lift forces. A variant of the Antal et al. 1991 wall correction is also considered:

$$\vec{F}_{\text{Antal}} = \frac{2\alpha_g \rho_l \|\vec{u}_g - \vec{u}_l\|^2}{d_b} \max \left[0, C_{W1} + C_{W2} \frac{d_b}{2y} \right] \quad (3.1)$$

They also use the following formulation of the turbulent dispersion:

$$\vec{F}_{\text{TD}} = -\rho_l \|\vec{u}_g - \vec{u}_l\|^2 D_{TD} \nabla \alpha_g \quad (3.2)$$

Where D_{TD} is a constant.

They find that, using this set of closures, the radial void fraction in a developed pipe and channel can be expressed analytically. If R is the tube radius and r the distance from the center of the pipe, they define the following dimensionless lengths:

$$y = R - r \quad , \quad y^* = \frac{2y}{d_b} \quad , \quad r^* = \frac{2r}{d_b} \quad , \quad R^* = \frac{2R}{d_b} \quad , \quad Y^* = \min \left(-\frac{C_{W2}}{C_{W1}}, y^* \right) \quad (3.3)$$

As well as a dimensionless liquid velocity and pressure:

$$u_l^* = \frac{u_{lz}}{\|\vec{u}_g - \vec{u}_l\|} \quad , \quad P^* = \frac{P}{\rho_l \|\vec{u}_g - \vec{u}_l\|^2} \quad (3.4)$$

The void fraction profile the takes the following form:

$$\alpha_g(r) = B \times (Y^*)^{C_{W2}/D_{TD}} \times \exp \left(\frac{C_{W1} Y^*}{D_{TD}} \right) \times \exp \left(-\frac{C_L}{D_{TD}} u_l^*(r) \right) \exp \left(-\frac{P^*(r) - P^*(r=R)}{D_{TD}} \right) \quad (3.5)$$

Where B is a constant that depends on the average void fraction in the channel. The void fraction profile is determined using the simulated values of the local liquid velocity and pressure.

Simulations are run in 3 different geometrical configurations for both schemes using the SETS solver and meshes with 40 radial and 200 axial elements. In all configurations, a gas-liquid mixture enters at 0.53 m/s and 4.2% void fraction at the bottom of the domain and the same coefficients as Marfaing et al. 2016 are used. $C_D = 0.1$, $C_L = 0.03$ and $D_{TD} = 0.003$. The liquid (gas) density is 1000 kg/m³ (1 kg/m³). The liquid (gas) viscosity is 10⁻³ Pa·s (10⁻⁵ Pa·s). The bubble diameter is 2.5 mm. A mixing-length turbulence model is used for this configuration Pope 2000. The domain is 1.5 m-long and 0.019 m-wide. A fixed-pressure boundary condition is enforced at the top. The first configuration is a 2D channel. The second is a 3D channel, with symmetry boundary conditions in the additional direction. This should behave exactly like a 2D channel. The third is a round pipe. It is simulated in VDF using the axisymmetric module, and with PolyMAC with a 1-cell wide slice with symmetry boundary conditions in the core (see figure 3.2 top left).

The results are shown in figure 3.3. Both schemes agree with the analytical solution in a channel and in a pipe, which validates the implementation of interfacial forces.

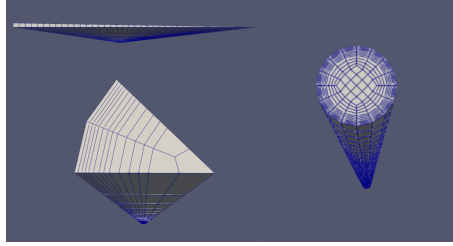


Figure 3.2: Different meshes used in this thesis. Top left: 2° slice with 20 radial elements of the same size. This mesh is equivalent to a 2D-axisymmetric configuration. Bottom left: 45° slice with 14 radial elements and mesh grading. Right: 360° tube with 14 radial elements and mesh grading.

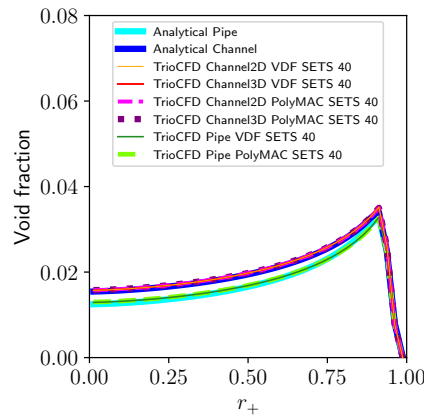


Figure 3.3: Simulation results for a simplified set of closures in an adiabatic flow vs analytical solution. All numerical schemes behave in the expected way.

3.1.4 Mesh refinement

To evaluate the mesh sensitivity of TrioCFD, I arbitrarily choose test case U1 from Colin et al. 2012. Using SALOME software (Bergeaud and Lefebvre 2010), a disk with quadrilaterals is meshed and extruded to obtain a hexahedral pipe mesh. Simulations are run on a full cylinder, a quarter of a cylinder and an eighth of a cylinder with symmetry boundary conditions on vertical planes, and on a 2° slice only one element wide. These meshes are shown in figure 3.2. The 2° slices have 20 or 40 radial elements of the same size. The others can have 7, 14 or 28 radial elements. They have 40, 80 or 160 vertical elements. There is a significant difference between 7 and 14 radial element results, but virtually none between 14 and 28. Calculations that run on a cylinder or a slice give identical results. The details of the configuration used for the mesh refinement are given in figure 3.4 that contains the mesh refinement results.

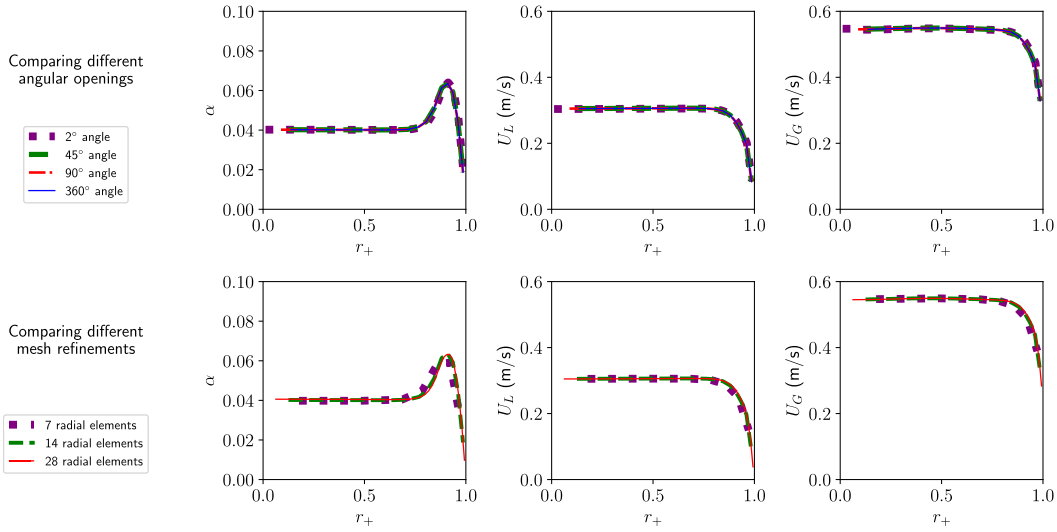


Figure 3.4: Mesh refinement verification for the TrioCFD multiphase module. The case simulated is a 3.08 m-long 4 cm-diameter adiabatic pipe (Colin et al. 2012). The liquid and gas superficial velocities are respectively 0.27 m/s and 0.023 m/s. Top row: verification of the equivalence of meshing different angular openings. These meshes are presented in figure 3.2. The 45°, 90° and 360° meshes have 14 radial elements with mesh grading. The 2° mesh has 40 radial elements and the same near-wall cell size. Bottom row: Mesh refinement tests on the 90° slice. The difference between 14 and 28 radial elements is negligible.

3.1.5 Boiling multi-phase flow

To the best of my knowledge, no steady-state analytic solution exists in the literature for boiling flow. To verify the implementation, as source terms are coded separately, one can compare simulations that use VDF and PolyMAC.

2 physical configurations with the ICE solver, both schemes, and meshes with 20 radial and 200 axial elements are simulated. The test case represents conditions from the DEBORA database, presented in chapter 4, but no experimental data is shown here.

The domain is 0.0096 m-wide and 5 m-long with a boiling length of 3.5 m. Physical quantities are extracted near the outlet. The fluid used is freon-R134A, with 14.6 bar outlet pressure, 2723 kg/(m²s) mass velocity and 44.5 °C inlet temperature. The contaminated Tomiyama et al. 1998 drag, Burns et al. 2004 turbulent dispersion, and constant coefficient $C_l = -0.05$ lift forces are used. The heat flux partition is from Kurul and Podowski 1990, and the condensation heat transfer from Ranz and Marshall 1952. The first configuration is a pipe, simulated with the axisymmetric module in VDF and with a 2° in PolyMAC (see figure 3.2 top left), where the imposed flux is 81.4 kW/m². The second is a 2D channel, where the imposed flux is 120.0 kW/m².

The results are shown in figures 3.5 and 3.6. Both schemes behave in the same way in channels and in pipes. This validates the implementation of boiling-specific

terms: heat flux partition, condensation heat transfer and their interplay with interfacial forces.

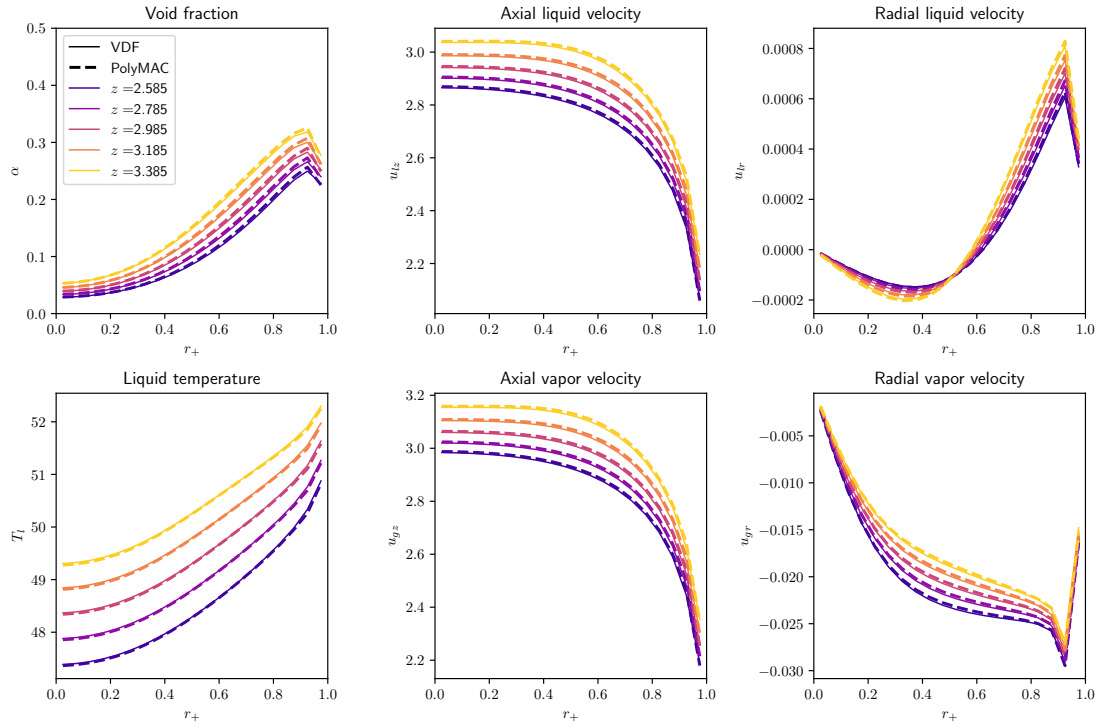


Figure 3.5: Comparison of VDF and PolyMAC simulation results for boiling multi-phase flow in a 2D channel.

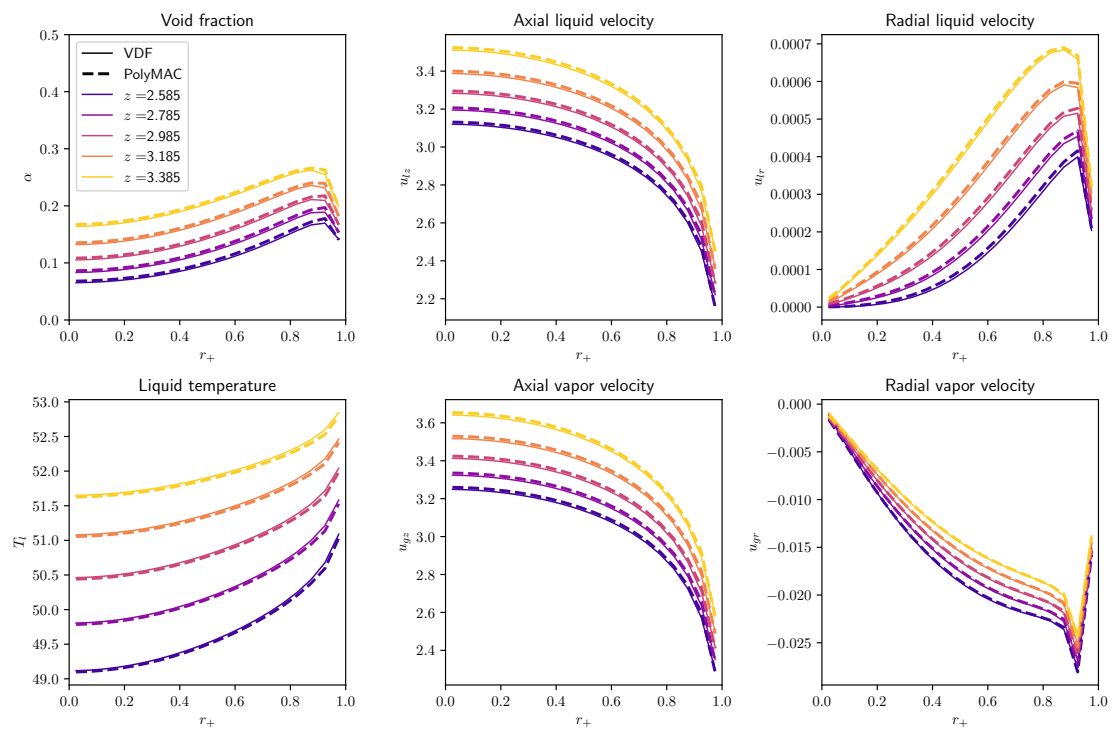


Figure 3.6: Comparison of VDF and PolyMAC simulation results for boiling multi-phase flow in a circular pipe.

3.2 Framework validation

3.2.1 Adiabatic single-phase flow

In addition to the verification in 2D channels presented in section 3.1.2, single-phase turbulence has been validated on two canonical geometries: a circular pipe and a backward facing step. For the latter, the database provided by the Turbulence Modeling Group was used Rumsey et al. 2010. The validation protocol was design to compare every model available in TrioCFD with every compatible discretization: the turbulence models in the multi-phase framework are compared with the validated historical turbulence in the single-phase framework. These are summarized in Table 3.1. After this validation process, due to a worse performance on the backward-facing step, the $k - \tau$ model was abandoned to concentrate the effort on the $k - \omega$ model.

Discretization	$k - \varepsilon$	$k - \omega$	$k - \tau$
Historic VEF	✓		
Historic VDF	✓		
Multiphase TrioCFD VDF		✓	✓
Multiphase TrioCFD PolyMAC		✓	✓

Table 3.1: Tested models and their associated discretizations for single-phase turbulence validation.

Circular pipe flow Figure 3.7 presents the predicted axial velocity and velocity fluctuations in single-phase adiabatic 40 mm-diameter circular pipe flows against experimental data from Colin et al. 2012. The predicted velocities are coherent with the experimental results.

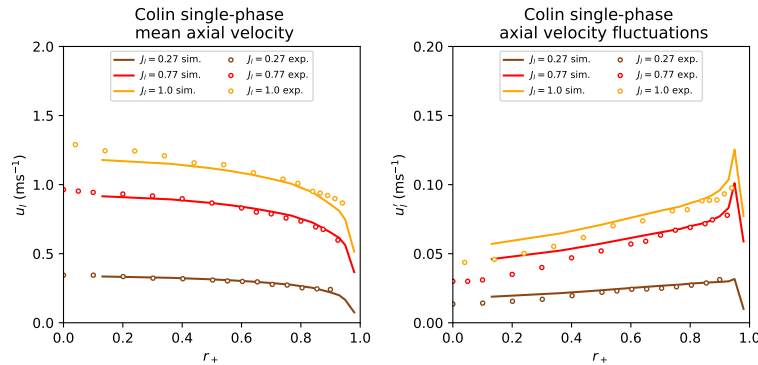


Figure 3.7: Adiabatic single-phase atmospheric-pressure water pipe flow validation of the multiphase module of TrioCFD on data from Colin et al. 2012. The velocities for each case are given in the legend of the figure. A. single-phase axial velocity in a 4cm-diameter pipe. B. Colin et al. 2012 single-phase axial velocity fluctuations in a 4cm-diameter pipe.

François et al. 2021 conducted velocity and velocity fluctuation measurements in single-phase R134A flow in nuclear reactor similarity conditions on the DEBORA experiment, a 19.2 mm-diameter round pipe. This setup is described in detail in chapter 4. Figure 3.8 presents a comparison between the code and the experiments. This validates the prediction of single-phase adiabatic flows in pipe geometries with complex fluids.

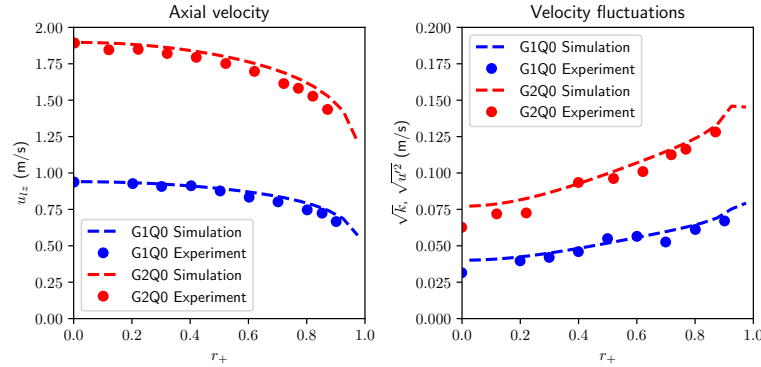


Figure 3.8: Adiabatic single-phase PWR similarity-pressure R134A pipe flow validation of the multiphase module of TrioCFD on data from François et al. 2021. Left: mean axial velocity. Right: axial velocity fluctuations. G1Q0: $P = 26$ bar, $G = 1000$ kg/(m²s), $T_l = 19.9$ °C. G2Q0: $P = 26$ bar, $G = 2040$ kg/(m²s), $T_l = 19.9$ °C.

Backward-facing step This test case is described by Driver and Seegmiller 1985. The domain length is divided in two sections. The first one is 1.1133 m long and 8 m high. The second section has an abrupt increase of height of $h = 0.0127$ m and is 0.5 m long. The inlet velocity is 44.2 m/s, the fluid density is 1 kg/m³ and its dynamic viscosity is $1.469 \cdot 10^{-5}$ Pa·s. A diagram of the setup and a close-up view of the mesh used around the step are presented in figure 3.9.

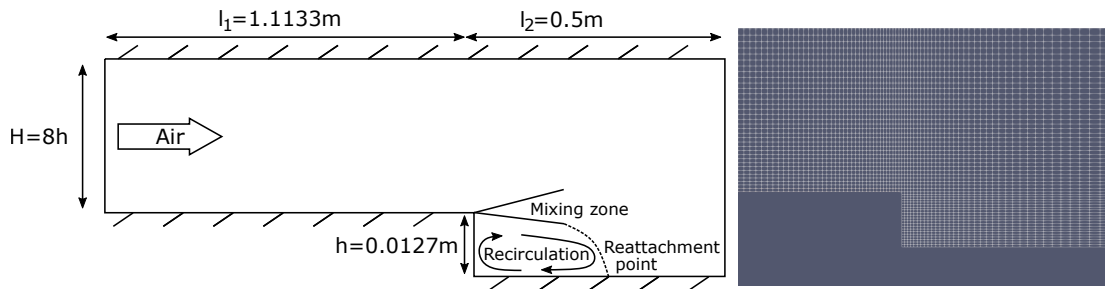


Figure 3.9: Left: diagram of the backwards step simulated here. Right: zoom-in on the mesh used around the step region.

In the chosen coordinate system, $x = 0$ at the level of the step. The velocity profile is plotted against the normalized height y/h at an axial distance $x = h$ in figure 3.10. Results are in a very good agreement with the experimental reference values (red crosses) and the numerical reference from Wilcox.

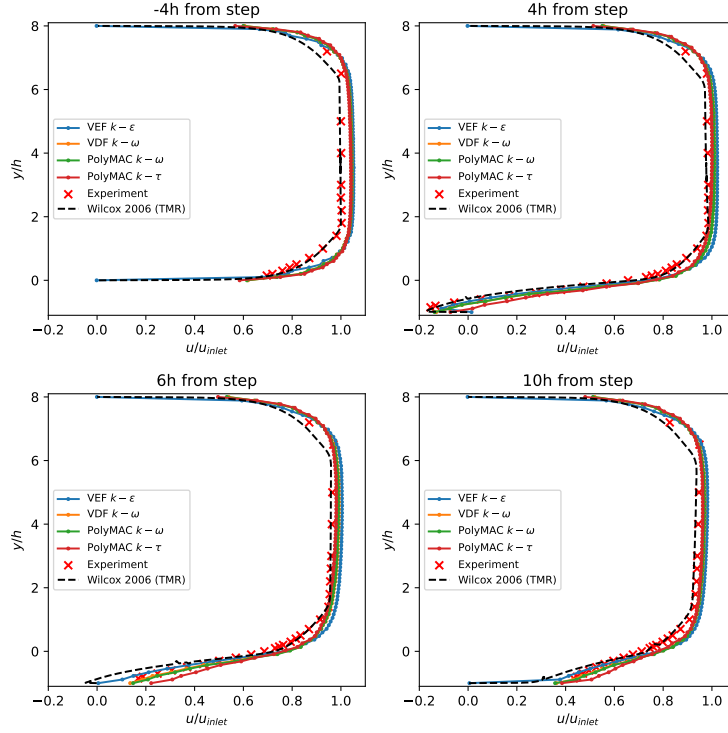


Figure 3.10: Velocity profile (abscissa) in normalized vertical unit y/h at an axial distance h from the backward step. Courtesy of Moncef El Moatamid.

Discretization	Recirculation length (x/h)	Error
Historic VEF $k - \varepsilon$	5.48	-10%
Multiphase TrioCFD VDF $k - \omega$	5.01	-17%
Multiphase TrioCFD PolyMAC $k - \omega$	5.04	-17%
Multiphase TrioCFD PolyMAC $k - \tau$	4.42	-26%
Driver's experiment	6.09	

Table 3.2: Recirculation lengths on a backwards-facing step predicted by different simulation configurations.

One of the criteria of validation is the capture of the recirculation length after the step. The relative gap with the experiment value is lower than 20 % for the different models and discretizations. This value is in compliance with other CFD codes for this level of discretizations.

I have therefore validated the choice and implementation of the adiabatic turbulence and wall laws.

3.2.2 Heated single-phase flow

I now present single-phase results for heated flows from François et al. 2021. These are part of the DEBORA experimental database, that is presented in detail in

chapter 4. The test section consists of a 19.2 mm-diameter round 3.5 m-long heated R-134A-filled pipe where the liquid temperature is measured along the width of the pipe at it's outlet. Two configurations are simulated: one with an imposed heat flux boundary condition at the wall and one where the thermal equation in the pipe, in which heat is injected, is solved. Figure 3.11 presents a comparison between the code and the experiments. These simulations enable me to validate the single-phase heat transfer in the bulk of the flow, the implementation of the thermal wall laws, the resolution of the thermal equation in the pipe and the call to physical properties libraries.

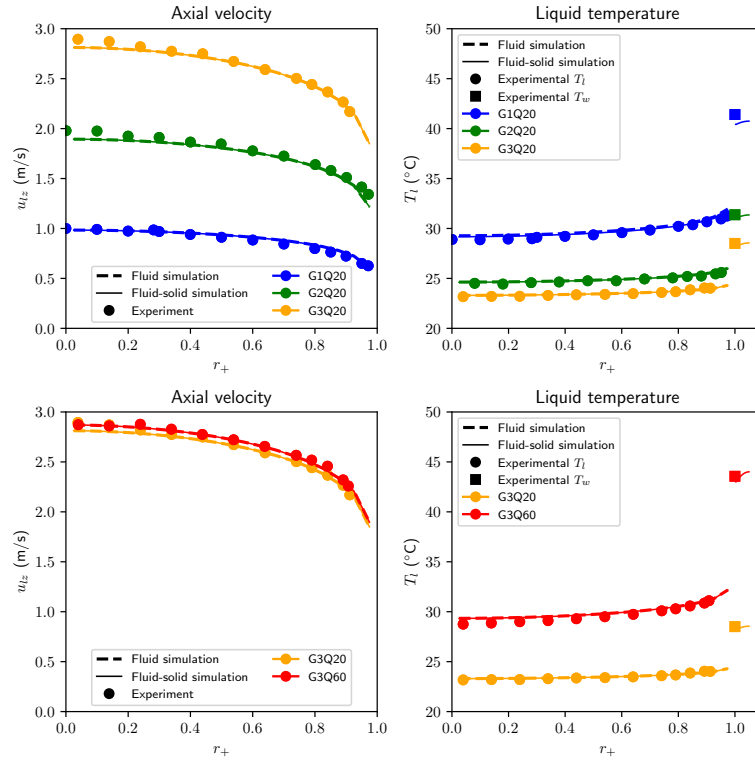


Figure 3.11: Heated single-phase PWR similarity-pressure R134A pipe flow validation of the multiphase module of TrioCFD on data from François et al. 2021. Left: mean axial velocity. Right: axial velocity fluctuations. Top row: changing mass flux. Bottom row: changing heat flux. For all cases, $P = 13.9$ bar and $T_{in} = 20$ °C. G1Q20: $G = 1011$ kg/(m²s), $q_w = 19.7$ kW/m². G2Q20: $G = 1998$ kg/(m²s), $q_w = 19.6$ kW/m². G3Q20: $G = 2998$ kg/(m²s), $q_w = 21$ kW/m². G3Q60: $G = 2999$ kg/(m²s), $q_w = 59.9$ kW/m².

3.2.3 Two-phase adiabatic vertical tube

Multiple experimental databases are available to study two-phase pipe flow. To validate the multiphase module, the Hibiki et al. 2001 database for upwards flow was selected, as it covers a broad range of liquid and gas injection fluxes. The geometry used is a 3.06 m-long 5.08 cm-diameter pipe. The Colin et al. 2012 experiments

for downwards and microgravity flow in a 3.08 m-long 4 cm-diameter pipe were also selected. Different test cases using the interfacial force models described in section 2.2.6 are run. To avoid modeling the interfacial area, the radially-dependent steady-state experimental diameter is enforced in the simulations. The diameter profiles of the presented simulations can be found in figure 3.12. The mesh used is a 45° slice with 14 radial elements, 80 axial elements and mesh grading (bottom left in figure 3.2). Air and water are injected at the bottom of the pipe at the mixture bulk velocity, with the void fraction set to respect experimental superficial velocities.

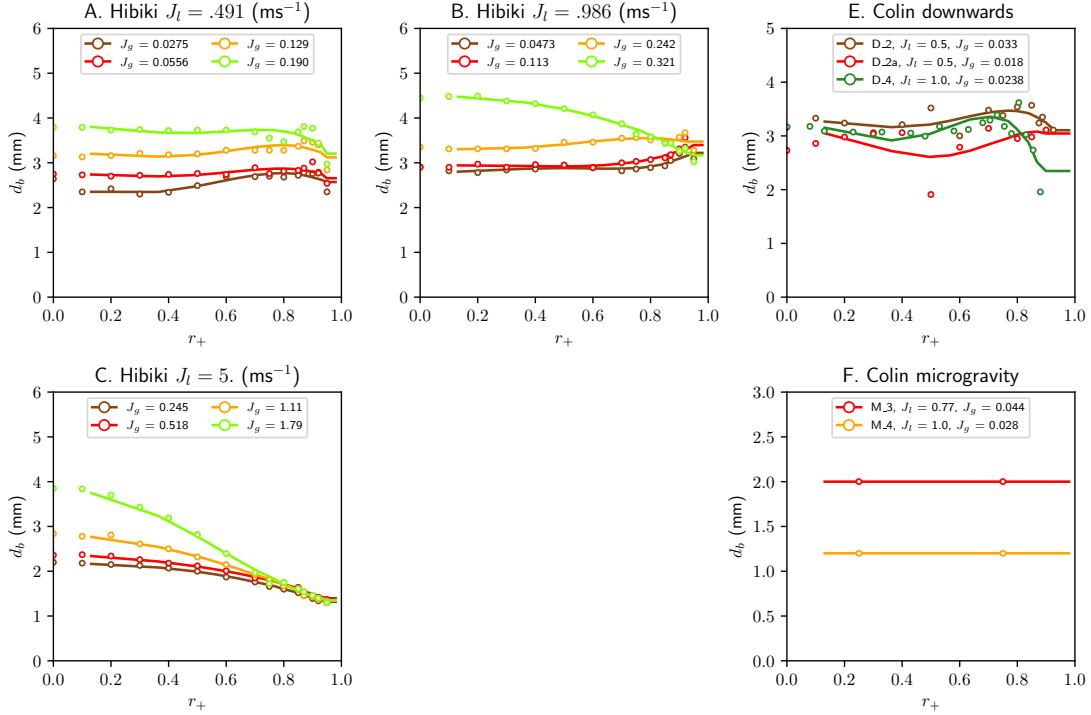


Figure 3.12: Two-phase adiabatic experimental and interpolated bubble diameter distributions in a pipe. Each subfigure matches a subfigure in figure 3.13. J_l : superficial liquid velocity. J_g : superficial gas velocity. Circles: experimental results. Lines: interpolation. A-C. Void fraction results in Hibiki et al. 2001 upwards flow experiments. E. Void fraction results in Colin et al. 2012 downwards flow experiments. F. Void fraction results in Colin et al. 2012 microgravity experiments. In this case, no experimental diameter profile was measured, only an average bubble diameter for each run.

Simulation results are shown in figure 3.13. The complete model is able to predict correctly void fraction profiles for low (figure 3.13-A) and high (figure 3.13-C) liquid fluxes, in wall-peaked and core-peaked situations respectively. This is not surprising, as the Sugrue 2017 lift force was tuned to data from Hibiki et al. 2001. The prediction of the transition between both regimes can still be improved, as can be seen in figure 3.13-B. Furthermore, in figure 3.13-D the gas velocities are well predicted by the model. The downwards and micro-gravity profiles are also well predicted (figure 3.13-E and F).

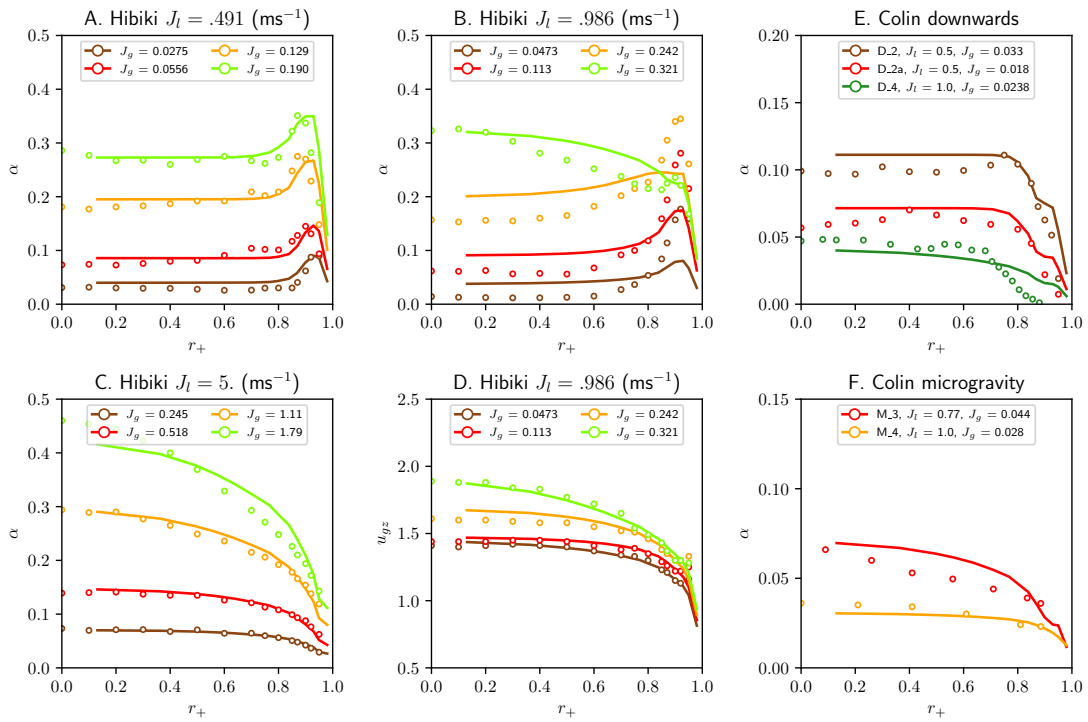


Figure 3.13: Two-phase adiabatic simulated and experimental void fraction distributions in a pipe. The interfacial force models described in section 2.2 are used. J_l : superficial liquid velocity. J_g : superficial gas velocity. Lines: simulations. Circles: experimental results. A-C. Void fraction results in Hibiki et al. 2001 upwards flow experiments. D. Axial gas velocity results in Hibiki et al. 2001 upwards flow experiments. E. Void fraction results in Colin et al. 2012 downwards flow experiments. F. Void fraction results in Colin et al. 2012 microgravity experiments.

3.3 Comparing the two-fluid model with the drift-flux model

Figure 3.14 compares flow boiling simulation results of the drift-flux model with the relative velocity calculated with the algorithm presented in section 2.3 and the two-fluid model presented in section 2.1.3. The test case represents conditions from the DEBORA database, presented in chapter 4, but no experimental data is shown here. The geometry simulated is a 19.2 mm-diameter 4 m-long pipe, with a 1 m entrance section, 2.5 m heated section and 0.5 m outlet section. The working fluid is R134A, the outlet pressure 14.6 bar, the mass flux $2723 \text{ kgm}^{-2}\text{s}^{-1}$, the heat flux 81.4 kWm^{-2} and the inlet temperature $44.5 \text{ }^\circ\text{C}$. The mesh is a 1° slice with 400 axial elements and 20 radial elements. The contaminated Tomiyama et al. 1998 drag, Burns et al. 2004 turbulent dispersion, and constant coefficient $C_l = -0.05$ lift forces are used. The heat flux partition is from Kurul and Podowski 1990, and the condensation heat transfer from Ranz and Marshall 1952. Simulation results are presented in figure 3.14.

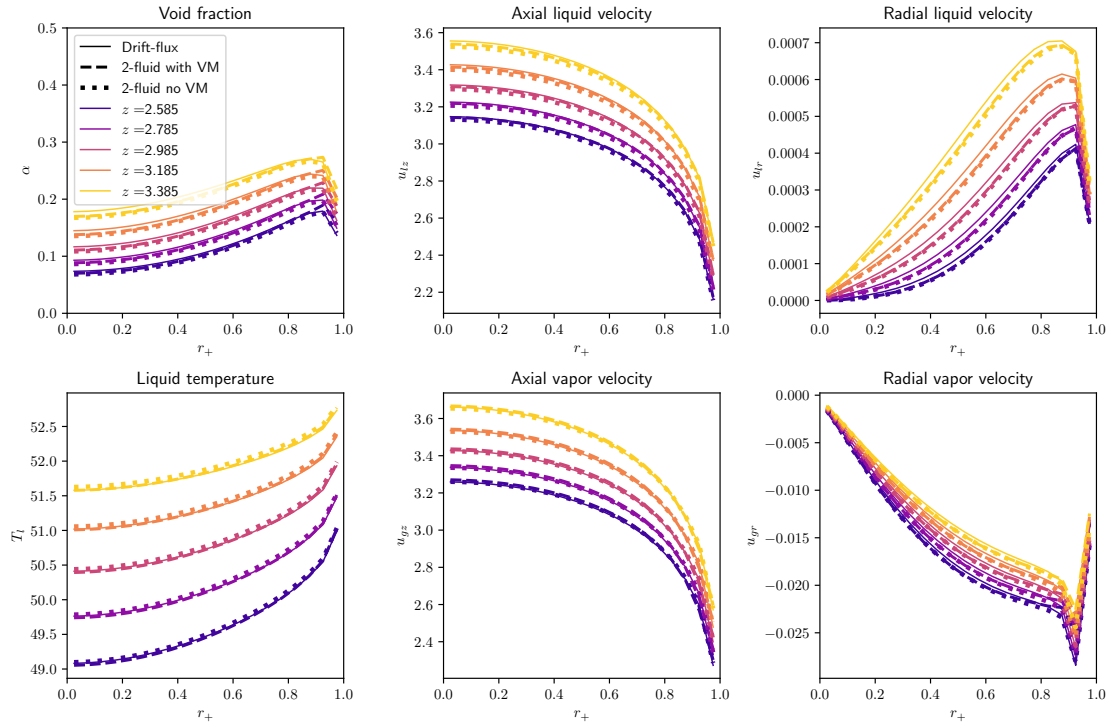


Figure 3.14: Comparison of the force balance-based drift-flux model (see section 2.3) with the two-fluid model (see section 2.1.3). The geometry simulated is a 19.2 mm-diameter 4 m-long pipe, with a 1 m entrance section, 2.5 m heated section and 0.5 m outlet section. The working fluid is R134A, the $P = 14.6 \text{ bar}$, $G = 2723 \text{ kgm}^{-2}\text{s}^{-1}$, $q_w = 81.4 \text{ kWm}^{-2}$ and $T_{\text{in}} = 44.5 \text{ }^\circ\text{C}$.

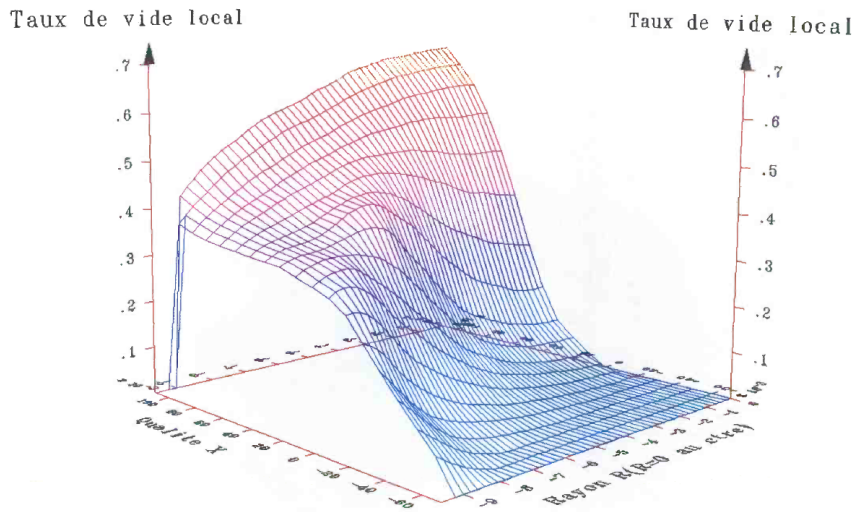
Despite the approximations in the drift-flux modeling presented in section 2.3, the difference with the two-fluid model without an added mass force is smaller

than the experimental error on the void fraction measurements ($\sim \pm 3\%$, see section 4.2.3). However, the difference between the two-fluid model with the added mass force and the others is non-negligible in the near-wall region: at $r_+ = 0.95$, for a given altitude the rectangle-dashed lines have α_v larger by ~ 0.05 than the full and square-dashed lines (figure 3.14 top left). This will be discussed in more detail in section 7.1. To conclude this section, in fast-flowing ascending boiling pipes the drift-flux model and the two-fluid model are interchangeable for a given set of closure coefficients if no virtual mass is used.

3.4 Conclusion

The numerical implementation of the 2-fluid framework and the different closure terms that are used in TrioCFD in this thesis were successfully verified. The code was validated on adiabatic and heated single-phase flow and on on adiabatic bubbly flow. All of the ingredients are in place to evaluate the baseline set of closures in nuclear reactor-condition boiling flow. This is done in chapter 5, after presenting the DEBORA database, used as a reference, in chapter 4.

CHAPTER 4



Experimental void fraction from G2P14W16 run in Cubizolles 1996.

Analysis of the DEBORA experimental database

This chapter presents the DEBORA experiment that is extensively used in this thesis. I begin by explaining the importance of similarity in thermalhydraulics and its use in DEBORA (section 4.1). I then present the experimental setup and the different measurements that were conducted (section 4.2). Data from the experiment is then exploited to show that the thermal log-law holds in boiling flow (section 4.3).

In section 4.4, I demonstrate that changing the entrance temperature for a same (Mass flux, Pressure, Power) triplet is akin to changing the point of measure. I call this the *test tube hypothesis*. It makes it possible to reconstruct radial gas and liquid velocities on much of the database (section 4.5 and appendix B) and extract information on coalescence and breakup terms (section 4.6 and appendix C).

Contents

4.1	Similarity for nuclear reactor conditions	63
4.2	The DEBORA loop	64
4.2.1	Past work on DEBORA data	64
4.2.2	Description of the test section	65
4.2.3	Instrumentation	66
4.2.4	Test matrix	68
4.2.5	Consistency tests	69
4.3	The liquid temperature log-law	70
4.3.1	Literature review on the liquid temperature profile in boiling flow	70
4.3.2	Analysis of the temperature profiles in the DEBORA experiment	71
4.4	The test tube hypothesis	74
4.4.1	Practical use : measuring along a developing flow . . .	74

4.4.2	A priori analysis: single-phase turbulent boundary layers and saturation temperature	75
4.4.3	A posteriori analysis: numerical verification	77
4.5	Determining vapor radial velocities	79
4.6	Coalescence and breakup for interfacial area modeling	79

4.1 Similarity for nuclear reactor conditions

It is difficult to reproduce the thermohydraulics of a pressurized-water reactor core in a laboratory: typical pressures, temperatures, heat fluxes and mass fluxes are 155 bar, 330 °C, 1 MW/m² and 4000 kg/(m²s). Many experimental loops nevertheless have ran and still run in these conditions, often measuring quantities outside of the flow: wall temperatures and void fractions through radiography (St.-Pierre 1965; Martin 1969; Bartolomei and Chanturiya 1967; Staub et al. 1969).

Carrying out measurements inside a test section is even more difficult. Some liquid temperature measurements are available (Bartolomei and Chanturiya 1967) but these are rare. Practical difficulties include building probes that can resist to the heat and pressure conditions, positioning the probes and moving them in the cross-section with small tolerances or running cables through the test section boundary so it remains watertight.

Simulant fluids are extensively used in the fluid mechanics community to mimic fluids that are difficult to work with for various conditions. For example, glucose syrup can emulate lava flows in volcanic eruptions (Stasiuk et al. 1993). Silicon oil has been used to study the absorption of flower nectar by bats (Nasto et al. 2018) and the extension of muscle sarcomeres (Cohen et al. 2015).

For PWR flows, refrigerant fluids have been used in the past 50 years to study the physics of pressurized-water reactors while having lower pressures, temperatures and heat fluxes. Staub et al. 1969 used R22 at General Electric, Hasan 1991 and Roy et al. 2002 used R113 at Arizona State University, Estrada-Perez and Hassan 2010 HFE-301 at Texas A&M University and Chu et al. 2017 R134A at the Korean Atomic Energy Research Institute. In France, the DEBORA loop initially used R12 (Garnier et al. 2001) and was later converted to R134A (Kledy 2018).

For the similarity to be valid between the experimental setup and the intended application, chosen dimensionless numbers must be identical in both configurations. However, all dimensionless numbers cannot be respected. The choice of the dimensionless numbers to prioritize and the design of experiments to respect this choice is a subdomain of thermohydraulics in itself called *scaling* (D’Auria and Galassi 2010). The DEBORA test section geometry was chosen to be close to that of a PWR subchannel. The dimensionless number that were prioritized when the DEBORA experiment was designed are (Garnier et al. 2001):

- Density ratio $\frac{\rho_l}{\rho_v}$. It is usually taken at saturation temperature. For a given simulant fluid run, this sets the equivalent pressure. This parameter is ex-

tremely important for similarity because it determines the volume of vapor produced for a given mass of evaporating fluid. For example, if 1% of the liquid evaporates with a density ratio of 10%, the volume fraction of vapor is $\sim 10\%$. But if 1% of the liquid evaporates with a density ratio of 1000%, the volume fraction of vapor is $\sim 90\%$.

- Channel Weber number $We_h = \frac{G^2 D_h}{\sigma \rho_l}$. As σ and ρ_l depend on the pressure that is already fixed, this number sets the mass flux G . The Weber number was chosen over the Reynolds number because of the importance of interfacial phenomena in flow boiling.
- Boiling number $Bo = \frac{q_w}{G h_{lv}}$. This sets the wall heat flux q_w . It enables the thermodynamic quality of the flow to evolve at the same rate for both fluids along the heated channel.
- Inlet quality $X_{in} = \frac{h_{l,in} - h_{ls}}{h_{vs} - h_{ls}}$, where $h_{l,in}$ is the liquid inlet enthalpy and h_{ls} (h_{vs}) the liquid (vapor) enthalpy at saturation. This sets the inlet temperature. As the boiling numbers of both fluids are the same, then the quality of the flow is the same for both fluids at any place along the heated length.

Other choices of dimensionless numbers can be made to compensate various dimensionless number distortions when changing fluids. These include the work of Francois and Berthoud 2003 and Ahmad 1973 for critical heat flux conditions in specific geometries for example.

4.2 The DEBORA loop

4.2.1 Past work on DEBORA data

The reference paper on the DEBORA experiment is Garnier et al. 2001. The authors present the experimental setup and the post-processing and raw results for a small number of test conditions. The thesis of Cubizolles 1996, who directly worked on the experiment, is much more complete. The appendix contains experimental results with Freon-R12 with around 10 times more datapoints than in Garnier et al. 2001. Kledy 2018 and François et al. 2021 later designed a single probe that can be used to measure the void fraction, liquid velocity and liquid temperature using thermal-anemometry. They carried out measurements in a few novel experimental conditions.

The collected data have been extensively used for physical analysis. Manon 2000 conducted one-dimensional analysis and compared system-scale void fraction models in his thesis. Some of his work is included in Garnier et al. 2001. Gueguen 2013 later developed a simplified axisymmetric model to analyze the developing flow without the need for a "black box" CFD code. This work was followed by those of Kledy 2018 and Kledy et al. 2021.

DEBORA also serves as a validation tool for CFD codes. Montout 2009, Končar et al. 2011 and Favre 2023 used Neptune_CFD with different closure laws. Recently, Vlček and Sato 2023 and Pham et al. 2023 conducted sensitivity analyses for different closures on DEBORA data. Results from Cubizolles 1996 were used for the DEBORA CFD benchmark conducted by Bois et al. 2024.

4.2.2 Description of the test section

The setup described in Cubizolles 1996 and Garnier et al. 2001 is presented in figure 4.1. R12 flows in a closed loop. It enters the heated section, a 19.2 mm-diameter 3.5 m-long tube, as a liquid with a controlled temperature. The measuring plane is 15 mm before the end of the heated length and the probes can be moved along the width of the pipe. As the fluid can boil at the end of the test section, a condenser is located after the outlet.

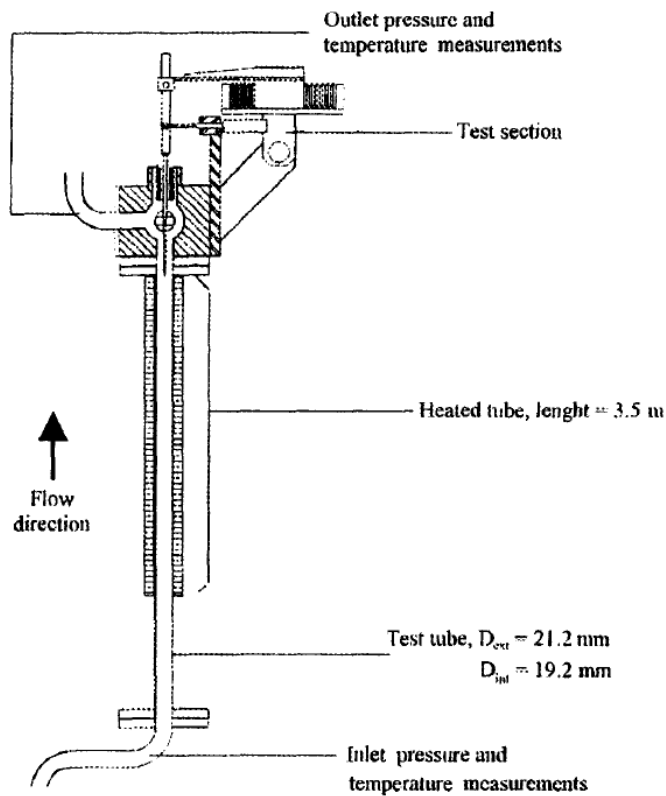


Figure 4.1: Test section of the original DEBORA measuring campaigns. Image from Garnier et al. 2001.

During experimental runs the control parameters measured are the outlet pressure, entrance temperature, heating power and liquid flow rate at the entrance.

For the experiments by Kledy 2018, carried out two decades later, the heated section was slightly shortened to 2.5 m and the working fluids switched to R134A.

4.2.3 Instrumentation

The instruments located in the flow are moved along the width of the channel to obtain data at multiple radial positions for each flow condition.

Optical probes These probes are made of an optical fiber in which light is emitted. The reflection and refraction at its tip depends on the refractive index of the medium in which it is immersed (see figure 4.2). As it is different for liquid and vapor, this enables the instantaneous detection of the phase at the tip of the probe. A time series called the *phase indicator function* is obtained. This function's average is the void fraction.

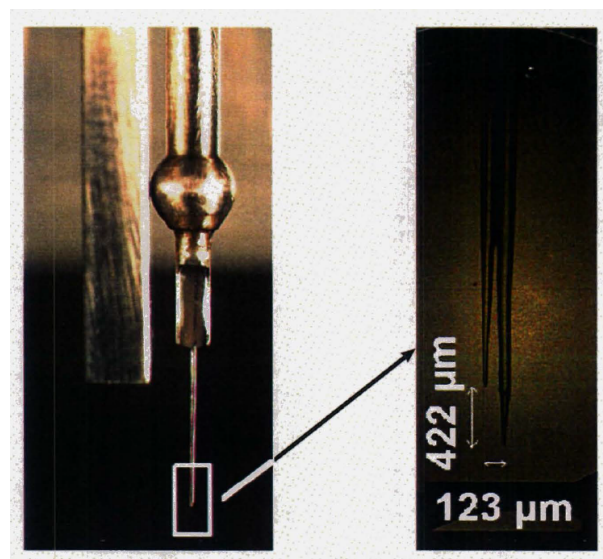


Figure 4.2: Left: double optical probe holder. Right: zoom on the double optical probe. Image from Manon 2000.

If the flow is bubbly, one can extract from the phase indicator function the time between the entrance and the exit of the probe tip in a bubble, called the *dwelt time*. If the velocity of the vapor phase is known, the distance between the entrance and exit points of the probe tip, called the *chord length*, can be obtained for each bubble passage. This yields a chord length distribution function.

To obtain the vapor velocity, different techniques were employed for the single probe and double probe setups. For the double probe, the phase indicator function of each probe are correlated and the time difference between the piercing of a bubble by each probe is evaluated. Knowing the axial distance between both probes the interface velocity is obtained. It is supposed equal to the vapor velocity. However with a single probe, no direct measurement of the velocity is possible. Cubizolles 1996 assumes that the liquid and vapor phases move at the same speed and uses the average void fraction in the flow to determine the average mixture velocity through mass conservation. He then uses a $1/7$ velocity power law function (Wilcox 2006), which is already an approximation in single-phase flow, to obtain the local

vapor velocity used to calculate the chord lengths. The chord length distribution itself in the single probe setup already has significant uncertainty.

To extract the bubble diameter distribution, additional hypothesis must be made. Authors often assume that the bubbles are either spherical or ellipsoidal, so their shape depends on one or two parameters. Garnier et al. 2001 make the hypothesis that they are spherical. The chord length histogram is then directly integrated to obtain the interfacial area (Gundersen and Jensen 1983). The latter is related to the Sauter mean diameter by the following formula:

$$d_S = \frac{6\alpha_g}{a_i} \quad (4.1)$$

In the remainder of the thesis, the Sauter mean diameter will be used as the bubble diameter in all correlations.

Sadly, the original phase indicator function signals of the DEBORA database were lost, as well as the dwell times and chord lengths. The treatments described above therefore cannot be re-applied to the raw data. It is also impossible to apply more complex treatments for ellipsoidal bubbles or polydisperse bubble sizes, or to compare the chord length distribution to those of polydisperse interfacial area models (Krepper et al. 2008; Yuan et al. 2012).

Thermocouples Temperature measurement campaigns were carried out using thermocouples. These could be placed at the outer wall of the pipe, and a treatment was applied to obtain the temperature at the inner wall. Some have also been placed in the flow itself and gave data on the liquid temperature. However, there are no simultaneous thermocouple and optical probe measurements.

Thermal-anemometry Kledy 2018 and François et al. 2021 designed a single hot wire probe that can be used to measure the void fraction, liquid velocity and liquid temperature thanks to a specific anemometer developed for constant current measurements. This makes measuring different quantities possible without needing to open the loop and changing its instrumentation, which makes operation easier and guarantees identical flow conditions.

A short and thin wire through which an electric current is passed makes up the tip of the probe. The resistance of the probe depends on its temperature. In single-phase liquid flow, when the current intensity is small, it behaves as a thermocouple and the liquid temperature can be calculated. When the current intensity is increased it behaves like a hot-wire probe, giving the liquid velocity. When a vapor bubble passes through the probe, the heat transfer from the wire to the fluid is reduced and a temperature spike is observed.

This remarkable setup was used only in a small number of flow conditions.

Uncertainty The uncertainties on the values measured by the probes given by Cubizolles 1996 are shown in table 4.1.

Quantity	Notation	Uncertainty
Mass flux	G	$\pm 1\%$ (relative)
Outlet pressure	P_{out}	5000 Pa (absolute)
Inlet temperature	T_{in}	± 0.2 °C (absolute)
Heat flux	q_w	$\pm 4\%$ (relative)
Void fraction	α_v	$\pm 2\%$ (absolute)
Bubble diameter	d_b	$\pm 12\%$ (relative)
Vapor velocity	u_{vz}	$\pm 10\%$ (relative)
Wall & liquid temperature	T_w & T_l	± 0.2 °C (absolute)

Table 4.1: Measurement uncertainties in the DEBORA experiment (from Cubizolles 1996)

Another way to evaluate the uncertainties on the measured parameters is to look at the difference between measurements that should be identical. The liquid temperature for example was measured along the whole width of the pipe. There are therefore two temperature measurements for each radial position. The mean square difference between temperatures at the same radial position is 0.2 °C, therefore the uncertainty is 0.4 °C with the 95% criterion.

Void fraction measurements on the DEBORA experiment that have not been published in the literature enable a similar analysis between the void fraction data measured on each side of the channel by the two points of a double optical probe. There are therefore 4 series of data to compare. A similar analysis as for liquid temperatures yields a 1.5% mean square difference between these series, i.e. a 3% uncertainty with the 95% criterion.

These uncertainty levels are larger than those for the single probes, because they include the impact of errors on the experimental conditions and the probe placement on the measurements.

4.2.4 Test matrix

In the following, I will call a *test tube* a series of runs that have identical outlet pressure, mass flux and heating power. Each test tube consists of different runs in which the inlet temperature is varied. In the DEBORA database, they are labeled G[ng]P[np]W[nw], where ng is the average mass flux (10^3 kg/(m²s)), np the average pressure (bar) and nw the average heating power in the experiment (kW). I call *run* a set of radial measurements for a given inlet temperature. Table 4.2 contains all of the conditions of the test tubes of the Cubizolles 1996 database. It also lists the number of runs for each test tube and probe type. In total there are 238 single-probe void fraction and Sauter mean diameter radial profiles, 37 double-probe void fraction, Sauter mean diameter and vapor velocity profiles and 56 temperature profiles. All of these tests are used in appendix F. The last column lists the sections of this PhD in which each test tubes are used.

Table 4.3 contains the conditions of the test tubes of the Kledy 2018 database. This data is used in chapter 8 and in appendix F. Only test tube G3P14Q110 was

Number	P_{out} bar	P_{out,H_2O} bar	G kg/(m ² s)	G_{H_2O} kg/(m ² s)	q_w kW/(m ²)	q_{w,H_2O} kW/(m ²)	X_{max}	Probes	Used in
G1P30W12	30	(173)	1000	(1250)	58.26	(807.2)	0.178	S24	5, 8, C, F F F
G1P30W14					66.79	(925.6)	0.117	S19	
G1P30W16					75.79	(1050)	0.107	S10	
G2P26W16	26.2	(154)	2012	(2520)	73.9	(1046)	0.062	S7, D7, T12	4.3, 4.5, 5, 6, 7, 8, C, F 4.5, 5, 7, 8, C, F
G3P26W23					109.3	(1548)	0.078	S11, D4	
G3P26W25			119.2	(1688)	0.081	S14	C, F		
G3P26W27			128.8	(1824)	0.06	S13, D6	F		
G3P26W29			138.8	(1965)	0.023	S9	F		
G3P26W31			148.3	(2100)	0.015	S8, D5	5, 8, F		
G3P26W33			158.2	(2240)	-0.007	S6	F		
G3P26W36			168.9	(2391)	-0.024	S6, DO2	F		
G3P26W38			179.4	(2540)	-0.029	S6	F		
G3P26W39			185.7	(2629)	-0.047	S5	F		
G3P26W40			188.1	(2663)	-0.054	S5, D3	7, 6, 8, F		
G3P26W42			198	(2804)	-0.064	S4	F		
G3P26W44			207.4	(2937)	-0.076	S2, D2	F		
G5P26W16			5100	(6400)	73.9	(1046)	0.024	T12	6
G5P26W24					113.2	(1602)	0.038	T11	
G2P14W16	14.6	(92.6)	2016	(2594)	76.26	(1151.3)	0.096	S17, D8, T11	4.3, 4.5, 5, 6, 7, 8, C, F 6 5, 8, C, F F F 5, 7, 8, F F F 5, 8, F F
G4P14W24			4009	(5156)	92.7	(1716)	0.055	T10	
G5P14W29			135	(2038)	0.054	S17			
G5P14W30			144.2	(2177)	0.040	S15			
G5P14W33			152.5	(2302)	0.028	S7			
G5P14W34			161.8	(2441)	0.023	S10			
G5P14W36			170.1	(2567)	0.016	S9			
G5P14W38			180	(2717)	0.010	S7			
G5P14W40			187.6	(2832)	-0.001	S5			
G5P14W42			197.1	(2975)	-0.015	S2			

Table 4.2: List of test tubes in the DEBORA database. Each (Pressure, Mass flux, Heating power) triplet is given for the experimental R12 configuration and the Water equivalent using the scaling criterion presented in section 4.1. The Probe column gives the probe type. S stands for single optical probe, D for double optical probe and T for thermocouple. The number behind the probe type gives the number of different inlet temperatures there are in the database for this probe and test tube. The final column lists the chapters and sections in which each test tube is used.

tested with multiple inlet temperatures.

4.2.5 Consistency tests

Gueguen 2013 compared the heating power with the inlet-outlet enthalpy flux difference calculated using liquid temperature measurements at the outlet for single-phase runs. Favre 2023 later did a similar analysis on two runs where the void fractions, gas velocities and liquid temperatures were measured for the same run, i.e. for the same test tube with the same inlet temperature. They both conclude that 5% of the total power is not transmitted to the liquid. In the remainder of this thesis, I will systematically reduce the injected power in DEBORA analysis and simulations by 5%.

Number	P_{out} bar	P_{out,H_2O} bar	G kg/(m ² s)	G_{H_2O} kg/(m ² s)	q_w kW/(m ²)	q_{w,H_2O} kW/(m ²)	X_{max}
G3P14Q200					203	(2704)	0.001
G3P14Q140					141	(1885)	0.005
G3P14Q110	14.6	(89.5)	2750	(3900)	112	(1490)	0.0577
G3P14Q81					81	(1085)	0.004
G3P14Q48					48	(641)	0

Table 4.3: List of test tubes in the Kledy 2018 boiling-flow database. Each (Pressure, Mass flux, Heating power) triplet is given for the experimental R134A configuration and the Water equivalent using the scaling criterion presented in section 4.1. The final column lists the chapters in which each test tube is used.

4.3 The liquid temperature log-law

4.3.1 Literature review on the liquid temperature profile in boiling flow

Kader and Yaglom 1972 showed that in the turbulent boundary layer of a heated wall in single-phase flow, the dimensionless temperature profile reads:

$$\Theta_+^w(y_+) = 2.12 \log(y_+) + \beta \quad (4.2)$$

Where $y_+ = yu_\tau/\nu_l$, y is the distance to the nearest wall, u_τ the friction velocity, ν_l the liquid kinematic viscosity, $\Theta_+^w(y_+) = (T_w - T_l(y))/T_*$ the dimensionless temperature, $T_l(y)$ the local liquid temperature, $T_* = q_w/(\rho_l C_p u_\tau)$, and β is a function of the Prandtl number. In particular, for low Prandtl numbers, β can be negative.

In boiling flow, this log-law holds, as seen on various experiments. Roy et al. 2002 studied R113 in an annular channel, and found that on their data, where the local void fraction at the wall went up to 35% and bubbles had reached 40% of annulus width, $\Theta_+^w(y_+) = 1.95 \log(y_+) + 6.5$ (see figure 4.3). Kledy 2018 performed measurements on R112 in a tube and for the 3 runs studied he finds $\Theta_+^w(y_+) = 2 \log(y_+) + 2.4$, $\Theta_+^w(y_+) = 1.9 \log(y_+) - 1.75$ and $\Theta_+^w(y_+) = 2.2 \log(y_+) - 8.05$ (see figure 4.4). In these configurations, the void fraction was up to 40% at the wall and bubbles reached the center of the pipe. The ~ 2 prefactor of the log-law stayed valid for the temperature boundary layer, even though for the velocity field it changed dramatically, going from 2.5 to 7 between these 3 runs. This indicates that a log law of the form $\Theta_+^w(y_+) = 2.12 \log(y_+) + \beta$ remains valid for fully developed boiling flows, with β depending on the flow regime, even though the velocity boundary layer changes form. I choose to keep the 2.12 pre-factor for consistency with the single-phase formulation.

In flow boiling databases, there are no systematic measurements of T_w to define $\Theta_+^w(y_+)$. Furthermore, the saturation temperature is a clear reference temperature. Therefore, I chose to work in the remainder of this thesis with:

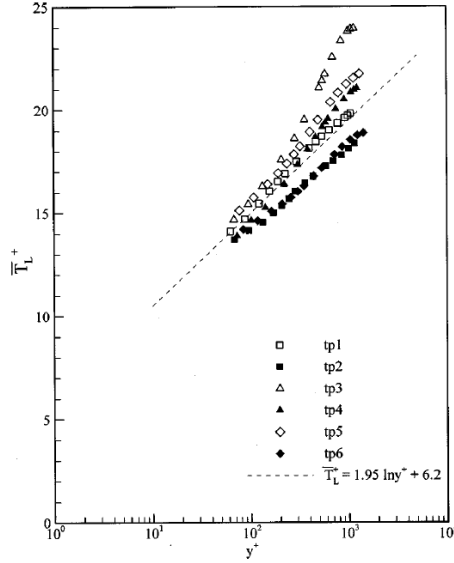


Figure 4.3: Dimensionless liquid temperature $\Theta_+^w(y_+)$ for an annular boiling R113 channel 2.75 m long with 15.78 mm inner diameter and 38.02 mm outer diameter. The outlet pressure is 2.69 bar, the inlet velocity is between 0.374 and 0.522 m/s, the wall heat flux between 95 and 116 kW/m² and the void fraction in the near-wall region from 10% to 40%. Reproduced from Roy et al. 2002.

$$\Theta_+^s(y_+) = (T_s - T_l(y))/T_* \quad (4.3)$$

This consists of shifting the log-law by a constant, i.e. changing β . The logarithmic profile should still be valid:

$$\Theta_+^s(y_+) = 2.12 \log(y_+) + \beta \quad (4.4)$$

4.3.2 Analysis of the temperature profiles in the DEBORA experiment

To verify equation 4.4, I use liquid temperature profiles from DEBORA tests G2P26W16 and G2P14W16. The dimensionless temperature profiles are plotted as a function of the dimensionless distance to the wall in figure 4.5. u_τ is calculated using the McAdams et al. 1942 correlation:

$$u_\tau = u_{\text{bulk}}(0.184 Re_h^{-0.2}/8)^{1/2} \quad (4.5)$$

The first plots discussed are the five coolest runs of the G2P24W16 test (top row in figure 4.5). In these runs, $T_{in} = 19.8, 24.5, 29.4, 31.4$ and 35.3 °C (see legend, to the left of figure 4.5). $\Theta_+^s(y_+) \geq \Theta_+^w(y_+)$ as the wall temperature is lower than the saturation temperature. The onset of nucleate boiling has not yet been reached, and the corresponding plots of $\Theta_+^w(y_+)$ superimpose on the Kader and Yaglom 1972 single-phase profile (top left box in figure 4.5).

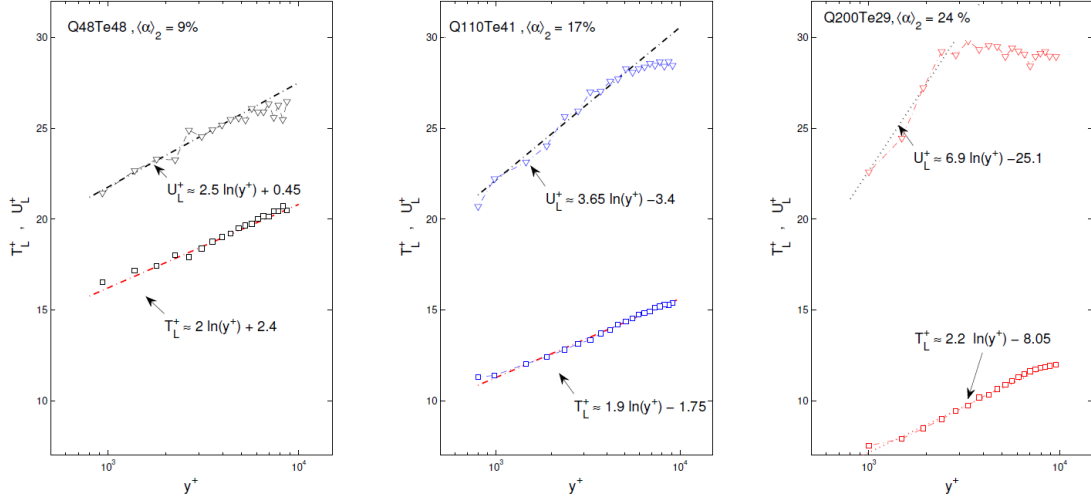


Figure 4.4: Dimensionless liquid temperature $\Theta_+^w(y_+)$ and velocity $u_+(y_+)$ for a boiling R134A pipe 3.5 m-long and 19.2 mm in diameter. The outlet pressure is 14.6 bar and the inlet mass flux is 2750 kg/(m²s). The wall heat flux (in kW/m²), inlet temperature (in °C) and average void fraction are given on each subfigure. Reproduced from Kledy 2018.

The onset of nucleate boiling (ONB) is reached when $T_{in} \geq 35.3$ °C. Θ_+^w and Θ_+^s shift together towards lower values. β decreases down to -15, becoming negative, until all of the liquid is at saturation temperature. The difference between the lower bound of Θ_+^w and Θ_+^s corresponds to the difference between wall and saturation temperatures.

The G2P14W16 test (bottom row in figure 4.5) behaves in a similar way, though there are no single-phase data points before ONB so no group of superimposed profiles of Θ_+^w is observed. For all of the plots in the figure, the log-law in equation 4.4 fitted for data points where $\Theta_+^s > 2$ remains valid, though Θ_+^s departs from the log-law when the flow is saturated.

Even for the high quality plots, $\Theta_+^s > 0$ is always verified. This is coherent with the fact that, to the best of my knowledge, no liquid temperature in boiling flow was ever measured above saturation temperature (Roy et al. 2002; François et al. 2021). The precise location of the OSV is not known here, but equation 4.4 remains valid for $X_{out} \sim 0$ in boiling flow. Therefore, the log-law is valid before ONB, between ONB and OSV and after OSV. The following equation is therefore a satisfying approximation for the dimensionless temperature on the complete data:

$$\Theta_+^s(y_+) = \max(0, 2.12 \log(y_+) + \beta) \quad (4.6)$$

Equation 4.6 will be extensively used in section 4.5 and in chapter 6.

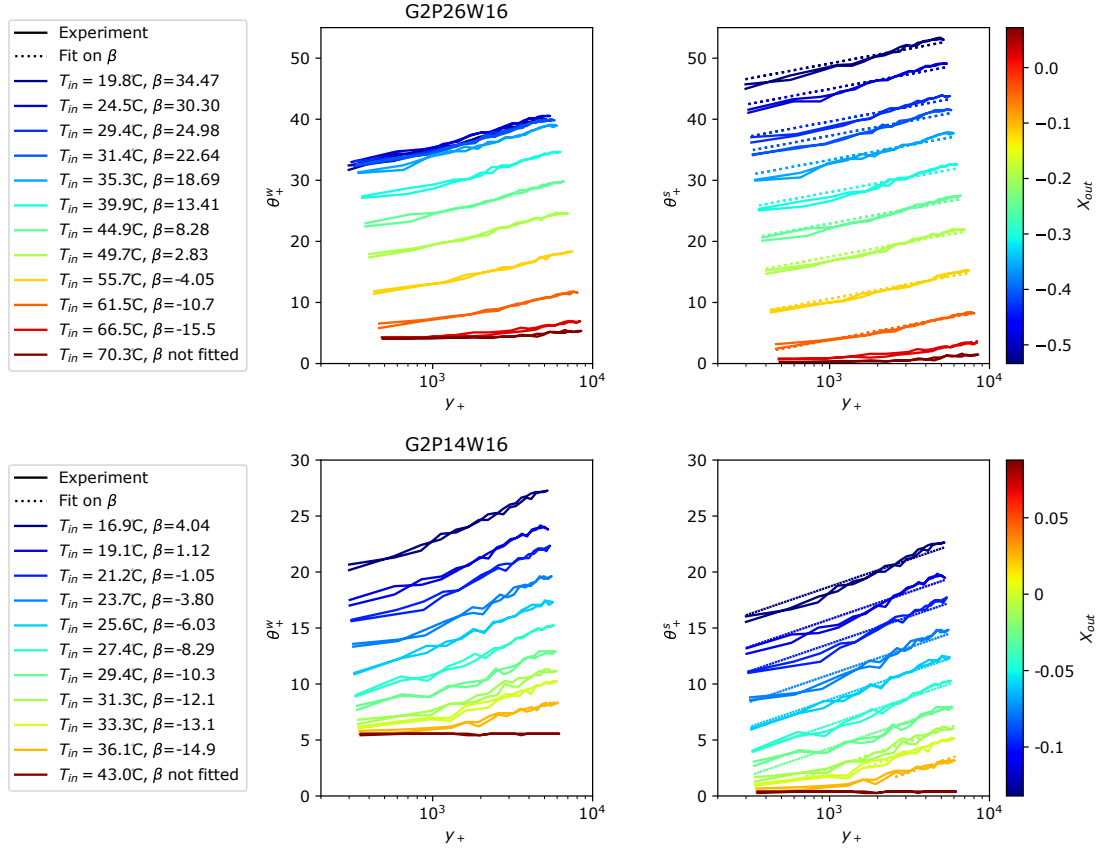


Figure 4.5: Dimensionless temperature profiles measured in the DEBORA experiment (Garnier et al. 2001; Cubizolles 1996). **On the left:** Entrance temperature in the test section, and β fitted on Θ_+^s on the corresponding run using equation 4.4. **Left column:** Dimensionless temperature difference between the liquid and the wall Θ_+^w . There are two lines for each condition: one for each side of the pipe. The difference between both lines is an indicator of experimental error. **Right column:** Dimensionless temperature difference between the liquid and saturation temperature Θ_+^s (full line) and fit on β using equation 4.4 (dashed line). **Color scale:** thermodynamic quality at the measuring point. **Top:** results for test number G2P26W16, conducted at $G = 2 \cdot 10^3 \text{ kg}/(\text{m}^2\text{s})$, $P_{out}=26.2 \text{ bar}$, $q_w = 73.9 \text{ kW}/\text{m}^2$ for various inlet temperatures. **Bottom:** results for test number G2P14W16, conducted at $G = 2 \cdot 10^3 \text{ kg}/(\text{m}^2\text{s})$, $P_{out}=14.6 \text{ bar}$, $q_w = 73.9 \text{ kW}/\text{m}^2$ for various inlet temperatures.

4.4 The test tube hypothesis

4.4.1 Practical use : measuring along a developing flow

Thermohydraulics codes aim to predict the space and time evolution of a flow in an industrial context. It is therefore key to have measurements of the characteristic physical quantities at multiple locations along the flow.

The most intuitive way of doing this is to have multiple measuring probes (Krepper et al. 2011), but this can be costly and difficult in cramped experiments.

A second method is to move the instrumentation along the direction of the flow. However, this is extremely challenging for measuring instruments that are located inside the flow as moving them along the flow often requires to open and close the circuits. This is time-consuming and can lead to differences in experimental conditions between measurements supposed to represent the same flow (this has already been observed in experiments at CEA). It is easier in cases where the measuring instrument is outside of the flow, which explains why it was extensively used in the early days of the nuclear industry with radiography measurements of void fraction (Egen et al. 1957, Maurer 1960, Foglia et al. 1961 or Staub et al. 1969). However, in the Staub et al. 1969 experiments for example, the measuring tool moves by 1 m per experimental condition and needs a $\sim 20 \mu\text{m}$ precision on the position of the beam. This makes precise calibration of the experiment difficult.

In the case of the aforementioned papers, the plots analyzed were often of the void fraction as a function of the thermodynamic quality of the flow for a given (Pressure, Heat Flux, Flow rate, Geometry) quartet. A methodology more practical and widespread today to obtain these is to vary the inlet subcooling and keep the instrumentation in the same place. An illustration of this procedure is presented in figure 4.6. This has been used extensively for external measurements since the 1960's (Bartolomei and Chanturiya 1967; Bartolomei et al. 1982; Martin 1972). It has also been used in the Debora experiments conducted at CEA (Garnier et al. 2001; Cubizolles 1996), with temperature and void fraction probes located inside the flow.

I call *test tube hypothesis* the assumption that reducing the inlet temperature is equivalent to measuring physical quantities at a lower location in the test section. This assumption has been used to simulate the DEBORA database in the past (Pham et al. 2023), but to the best of my knowledge its validity range has not been evaluated. In this section, I show that this hypothesis is accurate for the DEBORA database and for PWR conditions.

I consider a test section that has an area \mathcal{A} , a mass flux G , a heated perimeter \mathcal{P} , a length L and a heat flux q_w . z is the position along the test tube, and the instrumentation is located at the outlet at $z = L$. I consider two test runs, with inlet thermodynamic qualities X_1 and X_2 (see figure 4.6). Latent heat is h_{lg} . Then, through a simple heat balance:

$$X(z) = X_{in} + \frac{\mathcal{P}q_w}{GAh_{lg}}z \quad (4.7)$$

And the *equivalent altitude* of run 1 for the conditions of run 2 is:

$$z_{1,\text{equivalent}} = L - \frac{GAh_{lg}}{\mathcal{P}q_w}(X_1 - X_2) \quad (4.8)$$

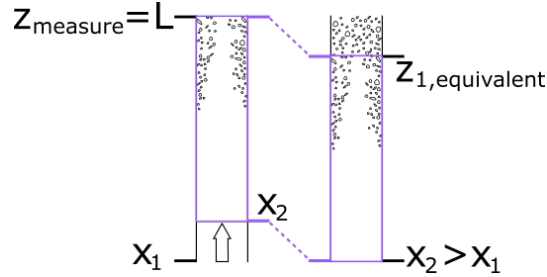


Figure 4.6: Diagram of the transition from thermodynamic quality to equivalent altitude. In run 1, fluid enters at quality X_1 , and measurements are performed at an altitude L . This is akin to measuring at an altitude $z_{1,\text{equivalent}} < L$ when the entrance quality is $X_2 > X_1$.

To assess the validity of the test tube hypothesis, I carry out two steps:

- *A priori* analysis: the impact of two physical mechanisms that can have an impact on the validity of the hypothesis are evaluated: the effect of hydrostatic pressure on saturation temperature, and the formation of the turbulent thermal boundary layer (section 4.4.2).
- *A posteriori* analysis: CFD simulations of different DEBORA test tubes and of a single tube with measurements at equivalent altitude are run (section 4.4.3).

4.4.2 A priori analysis: single-phase turbulent boundary layers and saturation temperature

Single-phase turbulent boundary layers In this paragraph, I analyze results from the DEBORA experiments (Cubizolles 1996; Garnier et al. 2001). An equivalent altitude for each test of the database is calculated using as a reference the runs with the highest inlet temperatures. For the boiling dynamics in the core of the flow to be similar at the outlet and at the equivalent altitude, the velocity and temperature fields must be the same at the point where vapor production substantially affects the flow, which is at the onset of significant void (OSV) (Saha and Zuber 1974). The equivalent altitude methodology guarantees identical average enthalpies on the cross-section. However, it does not guarantee identical velocity and temperature profiles. For profiles to be the same, single-phase temperature and velocity profiles before the OSV must be developed.

Labunstov et al. 1974 conducted average void fraction measurements in flow boiling after heated section of varying lengths and found no difference for identical thermodynamic qualities when $z/D > 20$. In single-phase adiabatic flows, velocity

profiles are developed after $z/D_h=40$ (Doherty et al. 2007). As there is a non-heated section where the flow can develop before the heated section this criterion is always met. When the velocity profile is already developed, Abbrecht and Churchill 1960 show that the difference between the thermal boundary layer and the developed boundary layer is small when $z/D_h=10$. Using the Al-Arabi 1982 correlation, the difference between the developed and developing Nusselt number is smaller than 3% at $z/D_h=30$. $z/D_h=30$ is therefore taken as an upper boundary of the reference length for the development of the thermal boundary layer in a turbulent flow. The vertical black lines are placed at that location in figure 4.7. The void fraction as a function of the equivalent altitude for each test tube is also plotted. Clearly, in the DEBORA database OSV occurs for $z/D_h>30$ and the developed turbulence at OSV criterion is verified. This may not be the case in other databases, in particular when the heated section is much shorter.

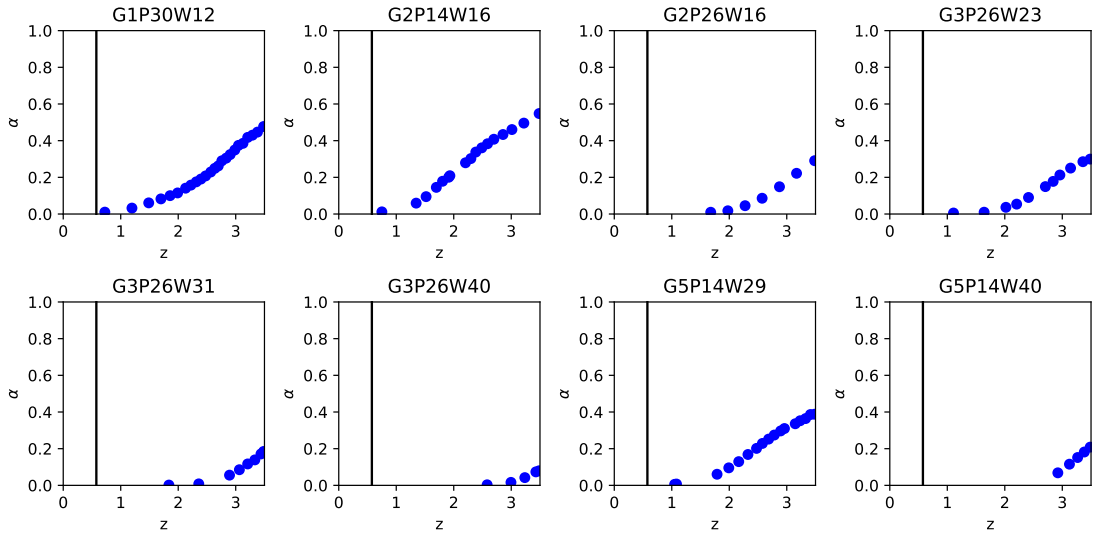


Figure 4.7: Void fraction as a function of equivalent altitude in the DEBORA 29 campaign. Each subplot represents a test tube. Vertical black lines represents $z/D_h=30$.

Saturation temperature In figure 4.7, it can be seen that the equivalent altitude of some DEBORA cases is 3 m lower than the measuring plane. The hydrostatic pressure variation between the measuring plane in the experiment and the equivalent altitude plane in the simulation at these points is 0.4 bar. This changes the saturation temperature of R12-freon by ~ 1 K (Bell et al. 2014). This is much smaller than the typical 20 K inlet subcoolings (Garnier et al. 2001), and the difference in saturation temperature due to pressure variations should not affect the simulation.

However, if the experimental outlet pressure had been 1 bar, the saturation temperature difference between both pressures would have been 10 K, which would have significantly affected the flow. For the equivalent altitude hypothesis to be valid, the pressure difference between the different equivalent altitudes must be

small enough for the saturation temperature variation to remain small with respect to typical subcoolings.

Use for experiment design To guarantee that the test tube hypothesis can be used in simulations, I recommend the following for future experiments:

- For a given test tube, reduce the hydrostatic pressure difference between the experimental outlet pressure and the one at the equivalent altitude. This can be done by increasing the outlet pressure by the hydrostatic pressure difference when the inlet temperature is reduced. This is key in low-pressure experiments ($P < 10$ bar).
- Have a sufficiently long heated section to guarantee developed single-phase flows before the onset of significant void

4.4.3 A posteriori analysis: numerical verification

In order to verify that the equivalent altitude hypothesis does not affect calculation results in the DEBORA experiment, I run two sets of simulations for a single test tube. As the aim of this subsection is not to compare simulations with experimental results the latter are not discussed here. The models presented in section 2.2 are selected, with a 1 mm constant Sauter mean diameter chosen arbitrarily. The mesh is a 1°-wide slice, with 20 radial and 500 axial cells. The contaminated Tomiyama et al. 1998 drag, Burns et al. 2004 turbulent dispersion, and constant coefficient $C_l = -0.05$ lift forces are used. The heat flux partition is from Kurul and Podowski 1990, and the condensation heat transfer from Ranz and Marshall 1952.

In the first set of simulations, the entrance temperature is the experimental temperature of a run. Physical quantities are extracted from the simulation at the outlet. This mimics the experimental conditions.

In the second set, the entrance temperature is the hottest experimental temperature in the test tube. Physical quantities are extracted from the equivalent altitudes for the experimental runs with lower entrance temperature.

I select the G2P14W16 series shown in figure 4.7, as it could be affected by both issues mentioned in the previous section. This series has among the earliest void production in the database. Furthermore, the outlet pressure is 14 bar, which should make it more sensitive to the saturation temperature variation evoked earlier than other series. 5 inlet temperatures are selected for the simulation: 23.9, 29.8, 34.9, 39.7 and 44.2 °C. These amount to an equivalent altitude compared to the inlet of the test section for the hottest run of respectively 0.75, 1.52, 2.20, 2.86 and 3.485 m, the test section being 3.5 m long. Simulation results are presented in figure 4.8.

The two quantities simulated that are measured in the experiment are void fraction and liquid temperature. One can see that the difference between simulations the local void fraction is around 0.01, and the difference on liquid temperature under 1 °C. However, looking at the difference between the liquid temperature and

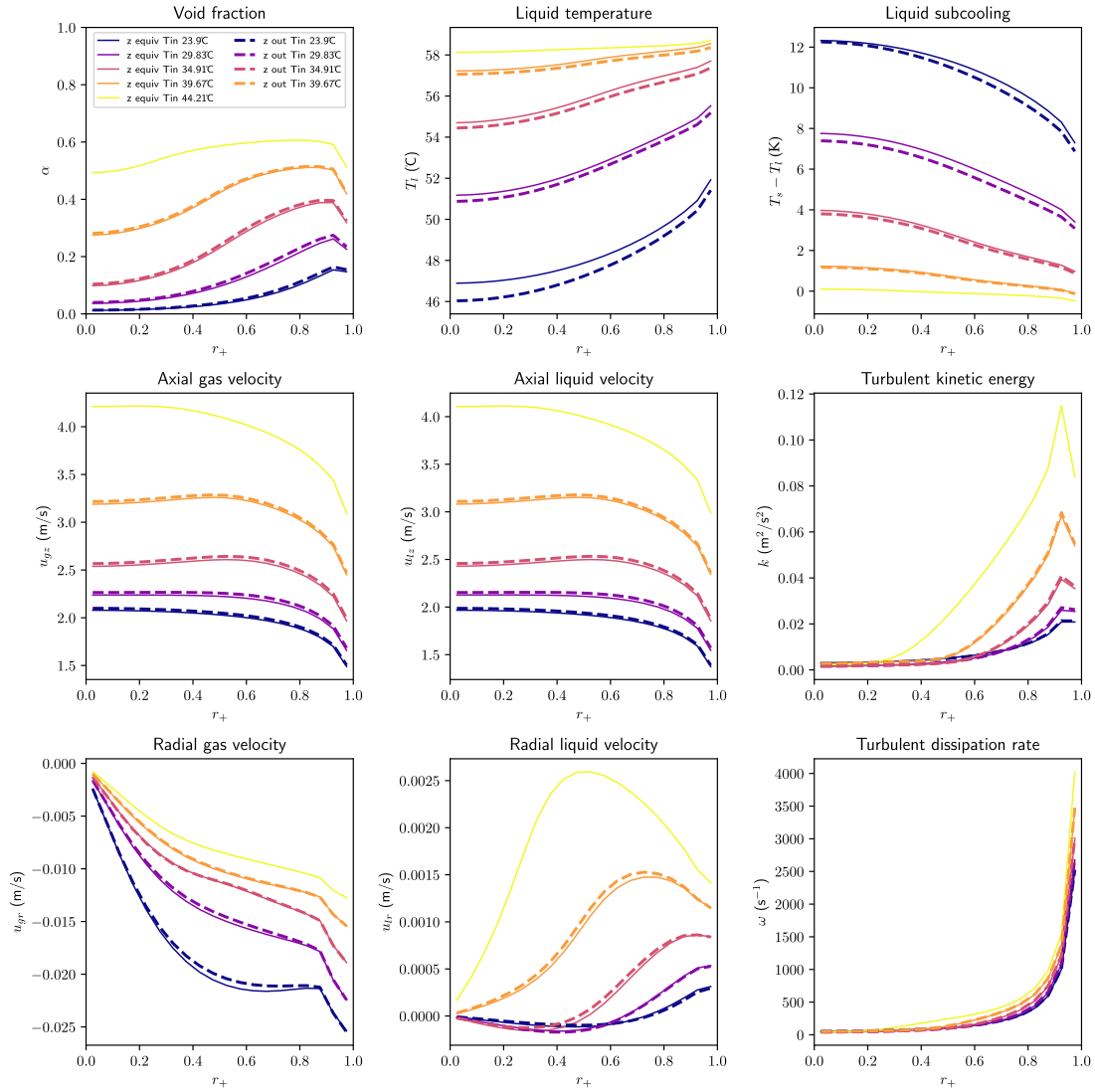


Figure 4.8: Comparison between simulations performed in experimental configuration and using the equivalent altitude. No experimental data is pictured here. Full lines correspond to physical quantities at the equivalent altitude for the highest inlet temperature of the run, and dashed lines to the value at the outlet for the experimental conditions.

the saturation temperature to take into account the effect of pressure on saturation temperature, the difference is reduced to at most 0.3 K. These are all well underneath the experimental uncertainty, which justifies the use of the equivalent altitude in the test tube of the DEBORA database where it had the most reasons not to be valid. Therefore, the use of the equivalent altitude is validated for the whole DEBORA experimental database.

4.5 Determining vapor radial velocities

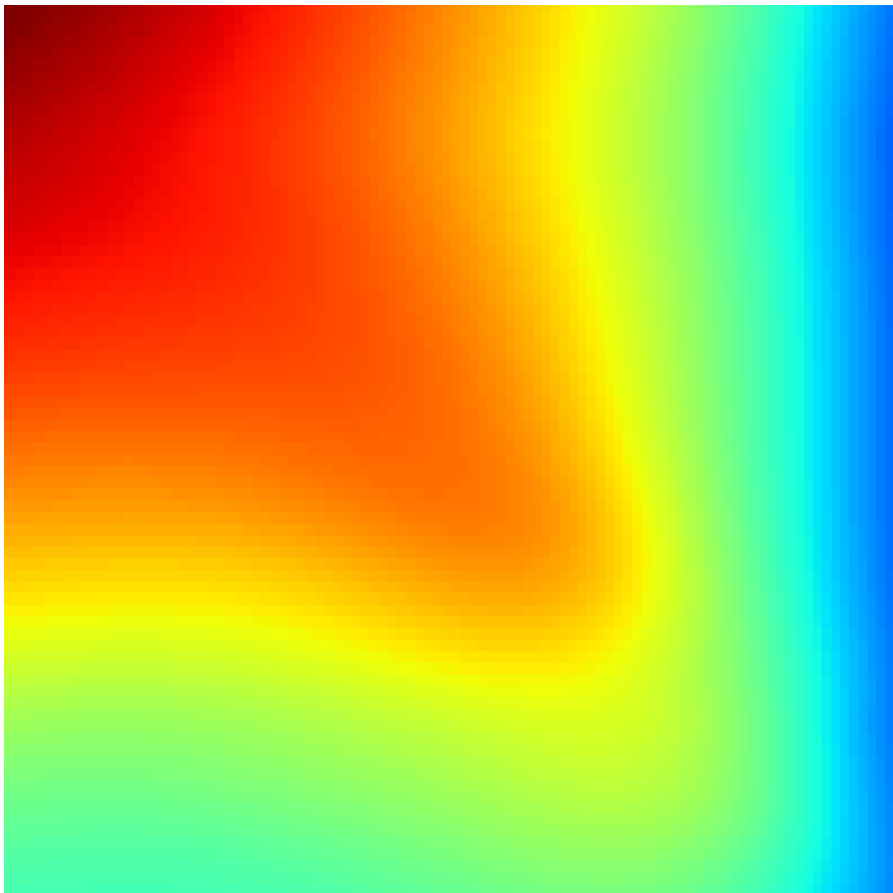
The instrumentation on the DEBORA database presented in section 4.2 makes it possible to obtain experimental void fractions, liquid temperatures, gas velocities and bubble Sauter mean diameters for multiple inlet conditions, i.e. at multiple equivalent altitudes. In appendix B, I seek to extract information on more physical quantities. Inspired by Kledy et al. 2021, I reconstruct the experimental 2D maps of void fraction and Sauter mean diameter. These are used to give an approached mixture axial and radial velocity on the whole test tube. Using an enthalpy balance, the liquid temperature fields are approached. By focusing on saturated region, the radial liquid and vapor velocities are calculated. These velocities are used in comparisons with two-fluid simulations in chapters 5 and 8.

4.6 Coalescence and breakup for interfacial area modeling

I continue integrating unknowns and source terms from experimental measurements and conservation equations in appendix C, where I take a close look at a monodisperse interfacial area transport equation (IATE, Yao and Morel 2004; Hibiki and Ishii 2000a). By focusing on the saturated region, it is possible to determine the sum of the coalescence and breakup term in such an IATE. I compare these results with coalescence-breakup pairs from the literature: those of Yao and Morel 2004, Hibiki and Ishii 2000a, Ruyer and Seiler 2009 and Wu et al. 1998, as well as the combination of the Prince and Blanch 1990 coalescence and the Luo and Svendsen 1996 breakup. These models are far from our integration results: they can predict breakup instead of coalescence and be two orders of magnitude away.

I then propose a simple return-to-equilibrium model with three fitted coefficients. Though my proposed model improves predictions compared to various formulations from the literature, it is still quite far from the inferred coalescence-breakup term, with an average $\sim 50\%$ difference. Given the large dispersion of the data and the sensitivity of many models to the predicted diameters, I decided to avoid working with interfacial area modeling in this thesis. In chapter 5, this means using the bubble diameter distribution from the DEBORA database to simulate the flow. In chapter 7, I propose a set of high-pressure flow closures that are independent of the bubble diameter. This set of closures is then used in chapters 8, 9 and 10.

CHAPTER 5



2D diameter interpolation used in this chapter's simulations.

Fixed-diameter simulations

In this chapter, I take advantage of the validity of the test tube hypothesis on the DEBORA database. I transform sets of experimental measurements of the Sauter mean diameter for different inlet temperatures into measurements at different altitudes. This makes it possible to run simulations with a 3D map of the experimental diameter. The physical quantities at each equivalent altitude are compared with quantities measured at the outlet for different inlet temperatures. This makes it possible to picture the evolution of the flow along the whole boiling length, and not only take snapshot at the outlet for a given inlet temperature.

In section 5.1 I discuss in detail three chosen test tubes from Garnier et al. 2001. More DEBORA test tubes are investigated in section 5.2.

Most of the text of this chapter was adapted from Reiss et al. 2024a.

Contents

5.1	Detailed analysis of selected runs	83
5.1.1	Simulation setup	83
5.1.2	Lift force	86
5.1.3	Turbulent dispersion force	86
5.1.4	Heat transfer and temperature profile	86
5.1.5	Gas velocities	87
5.1.6	Momentum balance	87
5.2	Results on a larger part of the DEBORA database	87
5.3	Main issues with the baseline set of closures	88

5.1 Detailed analysis of selected runs

5.1.1 Simulation setup

I call j a run number in a test tube and X_j the outlet thermodynamic quality of run j . j_{\max} is the run of a given test tube at the highest inlet temperature $T_{\text{in},j_{\max}}$. Using the test tube hypothesis described in section 4.4, calculations are launched for each test tube with $T_{\text{in}} = T_{\text{in},j_{\max}}$ and the physical parameters at the different z_j are extracted so that:

$$X_{T_{\text{in}}=T_{\text{in},j_{\max}}}(z_j) = X_j \quad (5.1)$$

The conditions of the runs selected are presented in table 5.1. These runs all come from Garnier et al. 2001. The Sauter mean diameter is measured along the radius of the channel for each $T_{\text{in},j}$. The experimental value at any z_j is then known. The experimental Sauter mean diameter at any (r,z) point in the test section is interpolated and enforced in the simulations. The are run without having to predict the mean Sauter diameter in the flow.

Test tube	Mass flux kg/(m ² s)	Press. MPa	Heat flux kW/m ²	$T_{\text{in},j_{\max}}$ °C	z_j m	$X(z_j)$
I G1P30W12	1007	3.01	58.2	73.7	0.72	-0.2165
					1.48	-0.0973
					2.48	0.0585
					2.98	0.1343
					3.485	0.2173
II G2P14W16	2016	1.458	76.26	44.21	0.75	-0.0677
					1.52	-0.0185
					1.81	0.0014
					2.20	0.0261
					2.49	0.046
					2.86	0.0687
3.485	0.1091					
III G3P26W23	2994	2.618	109.3	72.49	1.64	-0.0519
					2.02	-0.0177
					2.41	0.0164
					2.84	0.0479
					3.14	0.077
3.485	0.1005					

Table 5.1: Flow conditions of the DEBORA cases studied here. The DEBORA nomenclature for the test tube is given in the first column. z_j is taken at the beginning of the heated length. Each z_j matches a run in Garnier et al. 2001 in which $X_{\text{outlet}} = X(z_j)$.

The test tubes shown in table 5.1 are simulated using the baseline closure laws. The VDF numerical scheme is used, on axisymmetric meshes that contain 20

radial elements and 500 axial elements. The void fraction profiles are presented in figure 5.1, along with the experimental Sauter mean diameters that were enforced in the simulation. The wall-peaked profiles are relatively well predicted for test tubes I and III. However, the experimental void fraction in test tube II is core-peaked and the simulation is far off.

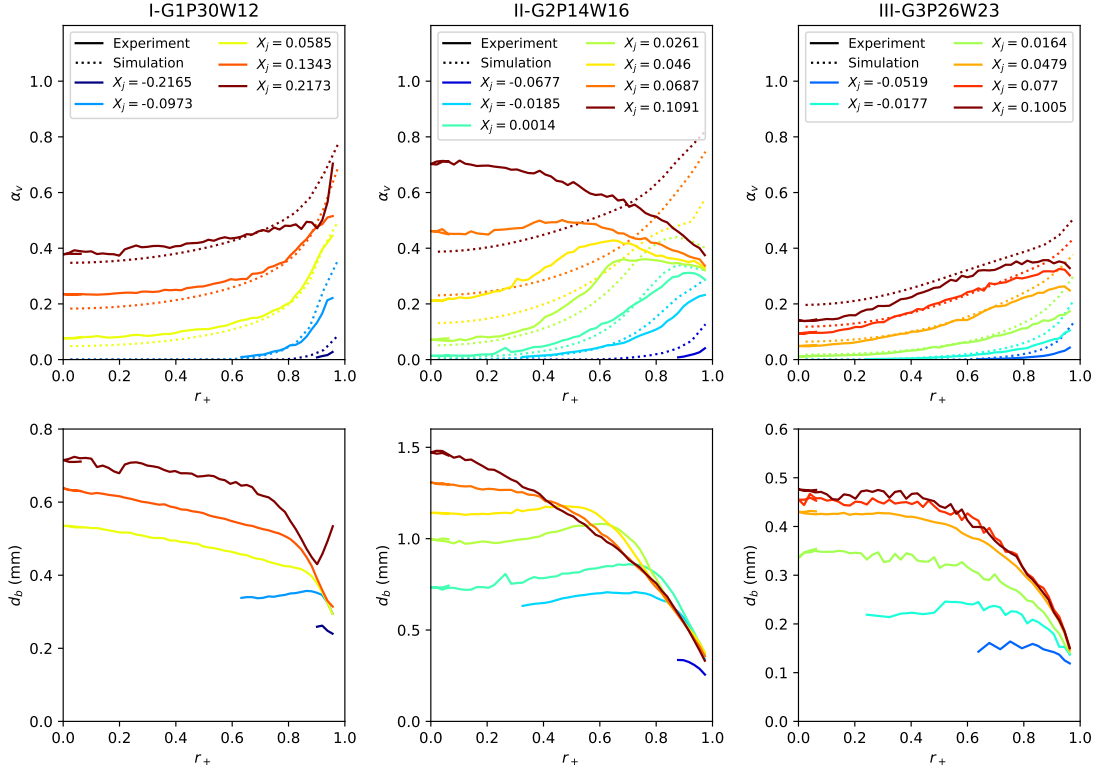


Figure 5.1: Void fraction results of simulations on the DEBORA setup using the baseline literature closure laws, and experimental Sauter mean diameters enforced in the simulation. The simulation configurations can be found in table 5.1.

More detailed simulation results, i.e. liquid temperatures, gas velocities and force balances, are presented in figure 5.2 for test tube II-G2P14W16. This test tube was selected as it is the only one in which all different measurements possible in the DEBORA setup were conducted.

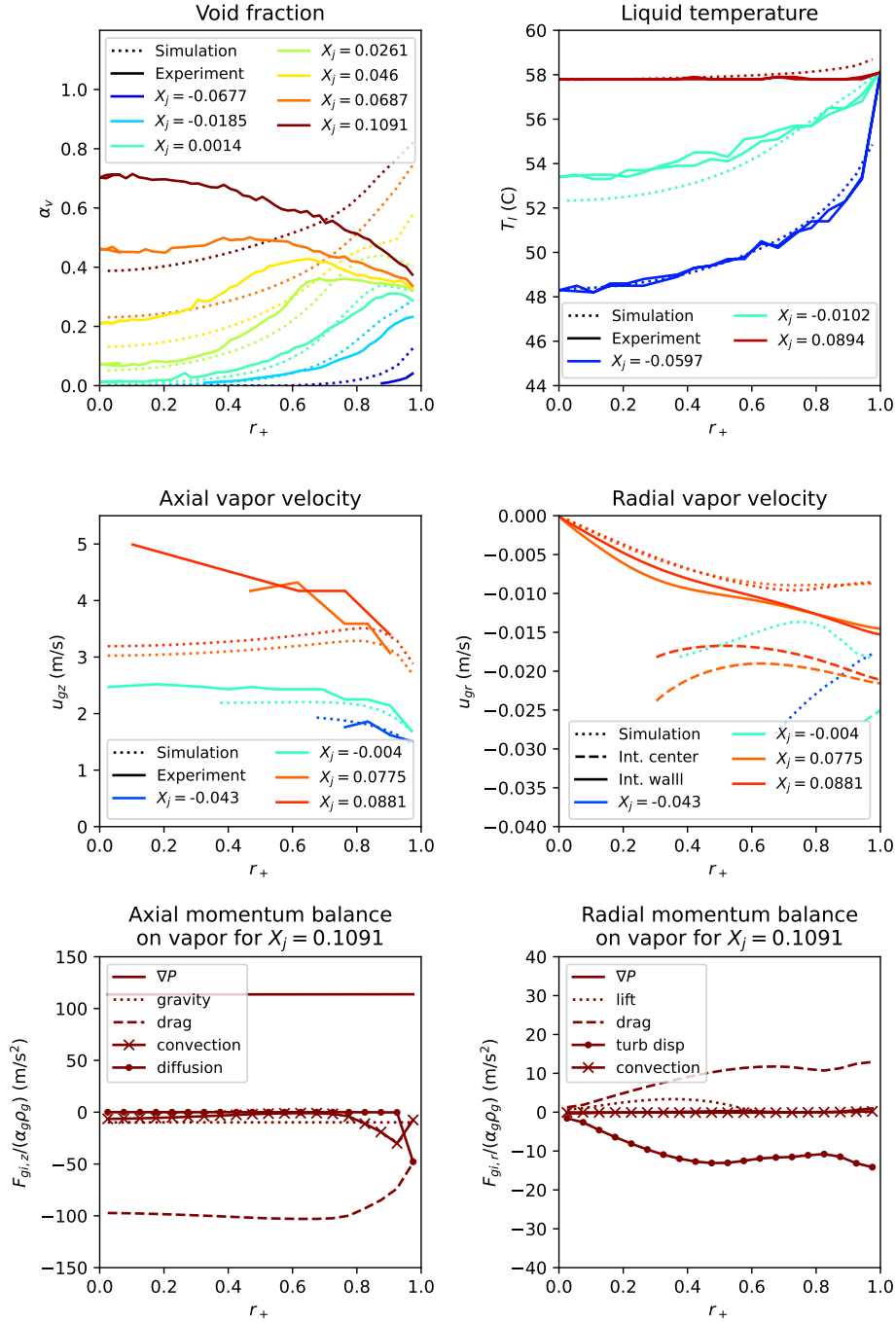


Figure 5.2: Detailed results of simulations on test tube II-G2P14W16 of the DEBORA setup using the baseline set of closures. Simulated radial and axial vapor velocities were only plotted when $\alpha_v > 0.02$. The force balances shown are divided by $\alpha_v \rho_v$ so that regions with different void fractions can be compared with ease.

5.1.2 Lift force

The experimental void fraction in test tube II is core-peaked. Furthermore, for $X_j = 0.1343$ in test tube I and $X_j \geq 0.0479$ in test tube III, the experimental void fraction peak moves away from the wall (this is very slight for test tube I). The only closure law in the 2-fluid framework that can create a center-peaked void fraction profile is the lift force with a negative lift coefficient. This means that in order to simulate the three test tubes studied, a lift force with a negative lift coefficient must be used in the near-wall region.

In all three test tubes, the $f(Wo)$ contribution to the Sugrue 2017 lift coefficient is negative at high outlet qualities (see equation 2.20). This strengthens the case of the use of a negative lift coefficient. However, the total lift coefficient is damped by the $g(\alpha)$ term and the resulting lift coefficient is near-zero, resulting in wall-peaked simulated profiles in all test tubes (see figure 5.2).

5.1.3 Turbulent dispersion force

The turbulent dispersion force pilots the void fraction gradient in the simulations, i.e. the slope of the void fraction profiles. For $\alpha_v < 0.2$, the slopes of the simulated profiles are coherent with those of the experiments. However, this is no longer the case for $X_j = 0.1343$ in test tube I: the void peak at the wall is much larger and the overall slope is much steeper than in the experiment. This suggests that the turbulent dispersion could be higher than that of Burns at high void fractions. The $X_j = 0.2173$ profile in test tube I is difficult to interpret as the void fraction peak at the wall is reminiscent of the beginning of a boiling crisis. The simulated void fraction profiles in test tube II are too different from the experimental ones due to the issues with the lift force to infer anything on turbulent dispersion.

5.1.4 Heat transfer and temperature profile

The wall-peaked void fraction profiles are too large for the smallest outlet qualities in all test tubes ($X_j \lesssim 0.03$). This suggests either too much vapor production in the heat flux partition, or insufficient vapor removal that could come from condensation or the momentum balance. The decrease of α_v is relatively well predicted as vapor approaches the core for test tubes I and III, when $r_+ \lesssim 0.8$. The flow is still subcooled in the simulation, and condensation takes place. This indicates that the interfacial heat transfer and momentum balances are probably satisfying in these regions, though temperature measurements lack to be sure of this. Efforts should therefore be made on the heat flux partition to improve predictions near the wall.

The temperature predictions for test tube II (see figure 5.2 top right) are lower than the experiment for $X_j = -0.0102$. This is coherent with an overestimation of the void fraction for $X_j = -0.0185$.

5.1.5 Gas velocities

In test tube II, the axial vapor velocities are not core-peaked like the experiment because the vapor profile is wall-peaked, leading to a buoyancy effect at the wall (figure 5.2 center left). Axial gas velocities are significantly underestimated, especially at high void fraction for $X_j \geq 0.0775$. At these qualities, the liquid is at saturation temperature. As the total mass flow rate is a conserved quantity, the fluid as a whole cannot accelerate. Therefore the discrepancy can only be explained by a too small relative velocity, i.e. a too large drag coefficient in the simulation.

Vapor radial velocities are negative (figure 5.2 center right), indicating that vapor is produced at the wall and migrates towards the center of the pipe. The predictions are slower than the integrated velocities (see appendix B for details on this methodology).

5.1.6 Momentum balance

The momentum balances are at equilibrium because the flow is stationary. The axial one on the vapor phase (bottom left plot in figure 5.2) shows that the pressure gradient is mainly compensated by the drag force, as expected. Two other terms play a role in the near-wall region. Wall friction at low void fraction is only applied to the liquid phase, and is calculated through the diffusion term in the code. However, when the near-wall void fraction in a cell exceeds 0.5, as is the case here, wall friction is also applied to the vapor for numerical stability which is why it is non-negligible. Convection plays a role as vapor is accelerated as it moves from the near-wall to the core region. This is discussed in detail in section 7.1. In TrioCFD, the convection and virtual mass terms are coded together, so the numerical contributions cannot be separated.

The radial force balance (bottom right plot in figure 5.2) shows that the drag force is compensated by the turbulent dispersion. The lift force is non-zero only where the void fraction is small enough for the α_v -dependent term in the Sugrue 2017 lift to be non-zero (see equation 2.20). This force balance is very different from a developed adiabatic flow, where there is no radial gas velocity. The turbulent dispersion force is then at equilibrium with the lift force, and the wall correction when it is included in the momentum balance (Marfaing et al. 2016).

5.2 Results on a larger part of the DEBORA database

Additional DEBORA database test tubes are presented in figure 5.3. Apart from case G2P26W16, all other test tubes present a too high void fraction at the wall, suggesting that the lift force is of the wrong sign. There is too much void fraction for low thermodynamic qualities, i.e. too much vapor production or insufficient condensation. The average void fraction in saturated conditions is similar in the

experiment and simulations. These results are in line with those presented in the previous section.

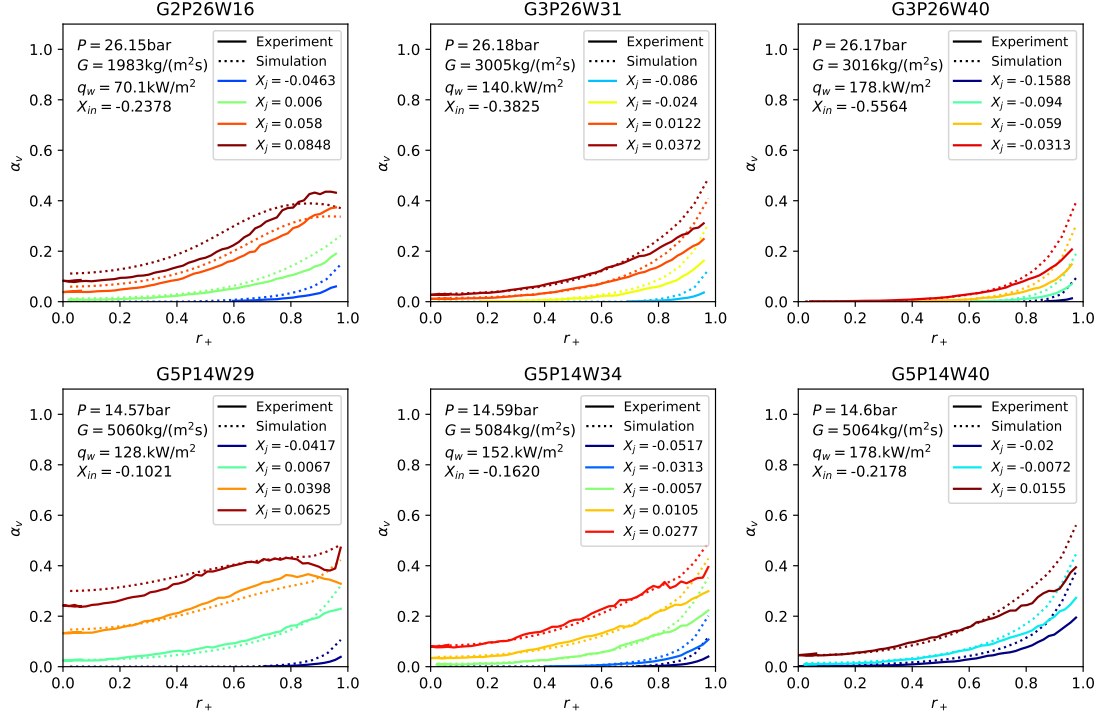


Figure 5.3: Simulated and experimental void fraction profiles for DEBORA test tubes with the baseline set of closures and enforced experimental bubble diameters. The test conditions for each series can be found in table 4.2.

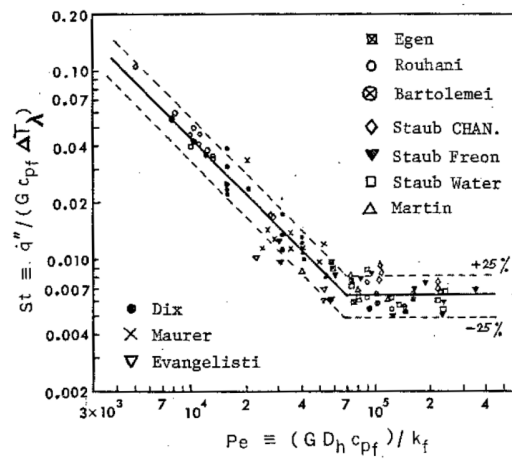
5.3 Main issues with the baseline set of closures

The first main issue on the database is a too high void fraction in the near-wall region at low subcoolings. This happens for every test tube in the DEBORA database. I address this in chapter 6, where I propose a new heat flux partitioning that reduces the amount of vapor injected in the flow at low qualities.

The second main issue is the shape of the void fraction profiles in the near-wall region. In experimental data for $X_j \gtrsim 0.05$ they do not peak on the wall. However, test tube G2P26W16 is the only simulation where the peak is shifted (see figure 5.3). The modifications of the lift force proposed in chapter 7 deals with this concern.

Model improvement

CHAPTER 6



Onset of significant void model from Saha and Zuber 1974.

Heat flux partition based on onset of significant void

This chapter presents a heat flux partition (HFP) based on a near-wall onset of significant void (OSV) criterion. The fact that the thermal log-law remains valid in flow boiling with a value of the additive constant that evolves as the flow develops is leveraged. Using a multiphase flow cross-literature database (section 6.2), this constant is shown to be $\beta_{OSV} = -7$ at the point of onset of significant void (section 6.3). The OSV predictions using this model have a similar mean average error as the Saha and Zuber 1974 correlation. This β_{OSV} -based model is used to build a heat flux partition inspired from Lahey 1978 (6.4). It predicts the distribution of the heat flux between the liquid phase and the evaporation term when the total heat flux is known. It does not give information on the total heat flux as a function of wall temperature and cannot be used to draw a boiling curve. In imposed flux conditions, this partition provides more coherent flux distribution between the evaporation and liquid terms than Kurul and Podowski 1990-based approaches (6.4.4). When the wall temperature is imposed, it must be coupled with an empirical boiling total heat flux correlation to replace a traditional HFP. The prediction of the total heat flux is then as good as that of the correlation.

Most of the text was adapted from Reiss et al. 2024b. The OSV database is located in appendix E. The code used to generate the figures using it can also be found at https://github.com/CoReiss/CFD_OSV.

Contents

6.1	Introduction	93
6.2	Construction and analysis of an OSV database	96
6.2.1	Current approaches to OSV prediction	96
6.2.2	Building an OSV database	97
6.2.3	Comparing the data points to other references	100
6.2.4	System-scale analysis	100
6.3	CFD-scale approach	102
6.3.1	Transforming average-scale data to CFD-scale data	102

6.3.2	A simple CFD-scale correlation	104
6.3.3	Comparing the β_{OSV} -based correlation to the literature	106
6.4	Use for Heat Flux Partitioning	108
6.4.1	Heat flux partitions used for comparisons with the literature	108
6.4.2	Physical interpretation of a stationary developing boiling flow	109
6.4.3	OSV-based heat flux partition	110
6.4.4	Comparing the OSV-based HFP with some from the literature	114
6.4.5	Bubble departure diameter calculation	118
6.5	Conclusion	118

6.1 Introduction

Heat flux partition (HFP) models are used to determine the total heat flux and its distribution between the phases. They require the wall, liquid, vapor and saturation temperatures and physical characteristics of the phases as inputs. They determine the heat flux that goes into each phase q_{lw} and q_v , and the evaporation heat flux $q_{w,l\rightarrow v}$ (Kurul and Podowski 1990). The heat flux that enters the vapor phase q_v is important only close to the critical heat flux (CHF) (Baglietto et al. 2019; Mimouni et al. 2016a). It will not be considered in this chapter. Furthermore, when the liquid is at saturation temperature in the near-wall region, virtually all of the heat flux is evaporation: to the best of my knowledge, no liquid superheat has ever been measured in flow boiling (Garnier et al. 2001; Roy et al. 2002; François et al. 2021).

In practice, simulations are most often run with an imposed total heat flux q_w at the wall (Favre 2023). A Newton algorithm is then used to find the wall temperature so that $q_{lw}(T_w) + q_{w,l\rightarrow v}(T_w) = q_w$. The HFP is therefore mainly used to determine the heat flux *distribution*, and not the heat flux itself. Simulations can also be run with an imposed wall temperature, in which case the HFP predicts q_w .

Heat flux partitioning in subcooled flow boiling The reference HFP for CFD codes was proposed by Kurul and Podowski 1990. It is a mechanistic model that includes three heat transfer mechanisms: one to the liquid phase that is based on single-phase flow, enabling a smooth transition as boiling picks off; one to the liquid phase that comes from the rewetting of the wall after bubble departure, called quenching; one evaporation term. The details of this model are given in section 2.2.5. In order to calculate these terms, many intermediate quantities are used like the nucleation site density, a bubble growth time scale and a bubble detachment diameter. Few measurements of these terms exist in the literature,

particularly at high pressures and mass fluxes. Furthermore, the authors make the hypothesis that all bubbles depart at the same size, that all nucleation points behave in the same way and do not interact with each other and that they do not affect single-phase convection in locations where there is not bubble nucleation. Finally, no direct measurements exist of the quenching heat flux, which is in this model a theoretical form based on conduction in the liquid phase, with no turbulent contribution. Again, the practical use of all of this modeling is mainly to determine which proportion of the heat flux enters the liquid phase through quenching and convection, and which proportion leads to evaporation.

More recent approaches, like those of Basu et al. 2005, Kommajosyula 2020 and Favre 2023, are also mechanistic. As time passes, the refinement of these models tends to increase by including more small-scale mechanisms, like bubble coalescence at the wall, interactions between nucleation sites, or the contribution of bubble sliding on the wall to the transfer to the liquid phase. This complexity makes the models very difficult to read and interpret without plotting the output heat fluxes as a function of the wall temperature or liquid temperature. It also makes code-to-code comparisons difficult and leads to long HFP calculation times. Though the number of closure terms increases significantly, some key mechanisms are missing, like the interaction between the bubble layer and detached bubbles which should influence the quenching flux.

To feed these models, experiments that allow a fine tracking of the bubble nucleation are being developed (Richenderfer et al. 2018; Tecchio 2022). However, it is difficult to obtain high-pressure data. As far as I know, precise measurements were done at a maximum of 40 bar (Kossolapov 2021), much lower than the 155 bar found in nuclear power plants (Todreas and Kazimi 2021). An interesting takeaway from the work of Kossolapov 2021 is the huge variability of nucleation frequency between sites : for similar conditions, some are 1000 times greater than others. Bubble growth time and departure diameter also present big variations. This means that a rigorous mechanistic approach should also take into account distributions. To the best of my knowledge such a model has not been proposed for now.

Heat flux partition in system and component scale codes These codes are used in the nuclear industry to simulate reactor cores, steam generators and primary and secondary circuits during steady-state operations and transients. Some aspects of these codes were described in section 1.2.2. In CTF and TRACE, the methodology from Lahey 1978 described hereafter can be selected by the user to determine the HFP in subcooled boiling. The first step consists in determining the total heat flux q_w from the wall: either it is imposed, or it is calculated using a correlation that requires the wall and bulk liquid temperatures like that of Thom et al. 1965.

The bulk liquid enthalpy at the point of onset of significant void (OSV) h_{OSV} is calculated in the second step. The OSV is defined as the point in a given flow where a noticeable increase in the void fraction of a flow takes place. h_{OSV} is most often calculated with the Saha and Zuber 1974 correlation. More details on the

definition of OSV and different approaches used in the literature can be found in section 6.2.1.

In the Lahey 1978 methodology, the heat fluxes directed towards the liquid phase and the evaporation are then:

$$\left\{ \begin{array}{l} \text{If } h_{l,\text{bulk}} < h_{\text{OSV}} \\ \text{If } h_{l,\text{bulk}} > h_{\text{OSV}} \end{array} \right. \left\{ \begin{array}{l} q_{lw} = q_w \\ q_{w,l \rightarrow v} = 0 \\ q_{lw} = q_w \frac{h_{ls} - h_{l,\text{bulk}}}{h_{ls} - h_{\text{OSV}}} \\ q_{w,l \rightarrow v} = q_w - q_{lw} \end{array} \right. \quad (6.1)$$

Where h_{ls} is the saturation enthalpy of the liquid phase.

Before OSV, all of the heat flux goes into the liquid. If the fluid is at saturation temperature, all of the energy is used for evaporation. There is a linear interpolation in between the two: as the fluid approaches saturation temperature, a larger part of the heat flux creates vapor.

This approach has a few advantages compared with mechanistic approaches. It reduces the uncertainty on the total heat flux as a correlation adapted to the situation can be used. The known heat flux distributions before the OSV (single-phase only) and after the liquid is saturated (evaporation only) are respected, which cannot be guaranteed using a HFP. The behavior of the correlation is predictable: there are no hidden variables to calibrate and they are linked with a small number of simple equations. From a numerical point of view, no Newton algorithm is required to obtain the partition for imposed-heat flux conditions. This makes the calculation fast and the coding easy.

Aims of this chapter The 2-step system-scale HFP approach described previously is applied to CFD codes to benefit from their advantages on physics and numerical standpoints. Numerous total heat flux correlations are already available in the literature (Jens and Lottes 1951; Thom et al. 1965; Frost and Dzakowic 1967), but they do not give the heat flux partition. Therefore, I strive to create a CFD-scale OSV criterion valid at high-Reynolds number to determine the heat flux distribution between the liquid phase and evaporation. The following steps are carried out:

- Review OSV prediction approaches from the literature (section 6.2.1);
- Create a database of thermodynamic quality at OSV for different geometries and flow conditions (section 6.2.2) and discuss preliminary results (section 6.2.4);
- Using the structure of the temperature distribution in a boiling flow (section 4.3), transform this system-scale data to local, CFD-scale data (section 6.3.1);
- Create a local correlation for OSV (section 6.3.2);

- Compare results from the proposed OSV to the Saha and Zuber 1974 correlation, chosen as reference (section 6.3.3);
- Use the local OSV correlation to build a heat flux partition (section 6.4);
- Compare the fraction of heat flux going to each phase for the OSV-based HFP and Kurul and Podowski 1990-based models (section 6.4.4).

6.2 Construction and analysis of an OSV database

6.2.1 Current approaches to OSV prediction

The onset of significant void (OSV), also called net vapor generation (NVG), is defined as the point where a noticeable increase in the void fraction in a boiling flow takes place. On a developing axial flow, this is a physical location. However, in general it is defined using the thermodynamic quality at this point, X_{OSV} . Cai et al. 2021 recently performed a literature review on the subject and compared different OSV correlations to data from the literature. Lee and Bankoff 1998 had previously done a similar exercise.

The methods most commonly used today to predict the point of OSV are global empirical approaches based on dimensionless numbers that do not go into the details of the physical mechanisms at play. Different mechanistic models have also been proposed, investigating bubble dynamics in the near-wall region.

Empirical approaches The most commonly used OSV correlation is from Saha and Zuber 1974. It is a full-channel, empirical formula. Two regions are defined using the bulk Peclet number $Pe_h = \frac{D_h u_{\text{bulk}} \rho_l C_{p,l}}{\lambda_l}$. For $Pe_h < 7 \cdot 10^4$, they propose that at the OSV vapor condensation and evaporation at the wall are at equilibrium. Evaporation is proportional to the heat flux q_w , and condensation to the local sub-cooling and conductivity $\lambda_l(T_s - T_{\text{bulk}})$, where T_{bulk} is the bulk liquid temperature. This leads to a constant Nusselt number $Nu = \frac{q_w D_h}{\lambda_l(T_s - T_{\text{bulk}})}$. For high- Pe_h , they propose that bubble detachment is hydro-dynamically controlled. They propose that the Stanton number $St = \frac{q_w}{GC_{p,l} \Delta T_{\text{bulk}}}$ is constant at the OSV. Fitting this law on data from 8 different experimental sources, they obtain that the flow is over the point of OSV if:

$$\begin{cases} Nu = \frac{q_w D_h}{\lambda_l(T_s - T_{\text{bulk}})} \geq 455 & \text{if } Pe_h \leq 7 \cdot 10^4 \\ St = \frac{q_w}{GC_{p,l} \Delta T_{\text{bulk}}} \geq 0.0065 & \text{if } Pe_h > 7 \cdot 10^4 \end{cases} \quad (6.2)$$

In recent years, several refinements of this correlation have been proposed (Ha et al. 2020; Lee and Jeong 2022). The formula and the results obtained are close to those of the original correlation. Both Cai et al. 2021 and Lee and Bankoff 1998 find that the Saha and Zuber expression and the ones that are similar outperform

the others encountered in the literature. On their database, Cai et al. find a mean average error of $\sim 20\%$, vs $\sim 35\%$ for the Levy 1967 correlation. The Saha and Zuber 1974 correlation, noted SZ in the rest of this thesis, will be considered the reference formulation.

Mechanistic approaches The Levy 1967 criterion is the first mechanistic approach on record. He determines a detachment radius for a bubble using an axial force balance between buoyancy, drag and the surface tension force holding back the bubble. He then assumes the point of OSV is reached when the thickness of the liquid layer that is at T_s is greater than the detachment radius. The obtained correlation is local, and contains two fitted parameters on a database containing data from 5 experimental sources. The temperature and velocity of the liquid layer used in the calculation follow single-phase developed distributions, not accounting for bubble presence. Furthermore, in high-pressure flows bubbles slide along the wall as soon as they nucleate before they are pulled in flow (Kossolapov 2021). Therefore the surface tension force holding back bubbles cannot be the key mechanism to determine the point of OSV.

Dix 1971 proposed a model based on radial, not axial, bubble movement. His experiments lead him to believe that the bubble ejection is hydro-dynamically controlled. He assumes the bubble radius at the wall is proportional to the heat transfer coefficient, and that at a critical bubble diameter depending on the Reynolds number can be defined. A single fitting parameter is used, but only on one experimental data set. This limits the validity of the correlation to a 9.6 mm inner diameter, 18.6 mm outer diameter annular tube, with $1 \cdot 10^4 \lesssim Pe_h \lesssim 2 \cdot 10^4$.

Anne and Beattie 1996 argue that the OSV occurs when bubbles can survive in the center of the tube. They determine the amplitude of turbulent fluctuations as a function of the total heat flux. They consider that the OSV is reached when turbulent fluctuations enable bubbles to reach a large part of the tube in a liquid pocket that is at saturation temperature, i.e. when these fluctuations become larger than the bulk subcooling. This yields that at the OSV, $St = 0.088Pe^{-1/2}$, without the use of any fitting coefficient. This expression is close to the SZ correlation for $Pe_h \sim 3 \cdot 10^5$, but does not match the data for lower Pe_h .

Recently, Nguyen and Okawa 2024 observed OSV occurs when an important bubble coalescence takes place at the wall. They do not propose a quantitative model, but they believe that coalescence in the bubble layer is the key mechanism for OSV.

6.2.2 Building an OSV database

The OSV is dependent on the structure of the flow. In particular, it will be different if the single-phase thermal boundary layer before OSV is developed or not. In the experiments selected here determine the OSV, sources are restricted to the cases where the heater is long enough for the single-phase thermal boundary layer to be developed.

One of the main difficulties in building an OSV database is the precise definition of the OSV. Most authors use plots of the void fraction α as a function of the thermodynamic quality X . The shape of the curve is often similar to a hyperbolic tangent (see figure 6.1). Depending on the authors, the OSV can be defined as the moment where the curve starts to take off, or after the void is already significant, leading to smaller subcooling at OSV. Many also extrapolated tanh-like functions from a small number of points and used the extrapolated plots to determine the point of OSV.

To harmonize the definition of the OSV, I selected myself the point of OSV from $(X, \langle \alpha \rangle)$ plots found in different sources. X is the thermodynamic quality of the flow and $\langle \alpha \rangle$ the average void fraction in the test section. Only runs where no curve fitting and extrapolation is necessary to see the inflection were used, so there must be measurements with $\langle \alpha \rangle$ close to 0. For a point to be considered, the inflection in void fraction must occur for $\langle \alpha \rangle < 5\%$, and the uncertainty on the OSV must be smaller than 10%. As the OSV determination is done by hand and the OSV definition is not extremely precise, I believe it is difficult to increase this accuracy. An example of the point of OSV determined here can be found in the red point in figure 6.1. Some plots that were eliminated can be found there as well. The only exception is the data from Edelman and Elias 1981, that I choose to include even without access to the original $(X, \langle \alpha \rangle)$ plots as I found no other database in the literature at so low Pe_h numbers ($2 \cdot 10^3 \lesssim Pe_h \lesssim 4 \cdot 10^3$).

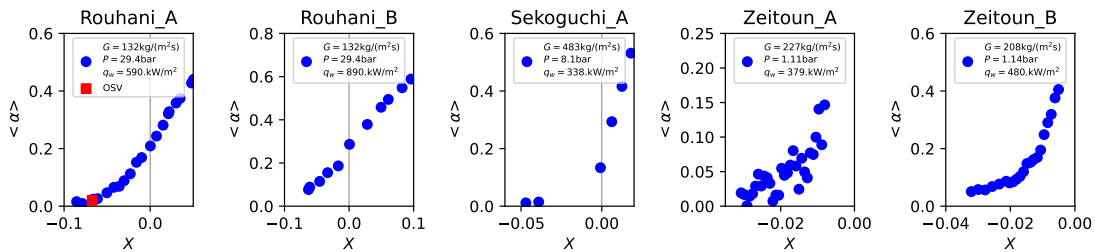


Figure 6.1: Examples of $(X, \langle \alpha \rangle)$ plots found in the literature that are used to determine the point of OSV. The red marker in the first plot represents the identified point of OSV. Series without markers are disqualified for different reasons. Each run condition is given in the legend of the figure. Water is used in every one. **Rouhani_A&B:** Data from Rouhani 1966b. Rouhani_B is disqualified as there are not enough points at low void fraction to see the inflection in $(X, \langle \alpha \rangle)$. **Sekoguchi_A:** Data from Sekoguchi et al. 1980. This run is not considered as it does not have enough datapoints. **Zeitoun_A&B:** Data from Zeitoun 1994. Data in run Zeitoun_A is too irregular. In Zeitoun_B $\langle \alpha \rangle \sim 10\%$ at the inflection, proposed at $X = -0.022$ by the author. This is too high for an OSV criterion.

In the end, the database contains 155 OSV data points in a wide range of geometries, pressures and Peclet numbers. This data can be written in the form $X_{OSV}(\text{Test section}, P, G, q_w)$. Table 6.1 contains the list of all of the sources used.

Label	Reference	Geometry	Press (bar)	Peclet	Nb Pts	Used in
Egen	Egen et al. 1957	2.6 mm 2W Channel	138	$3 \cdot 10^4 - 6 \cdot 10^4$	7	L, SZ, LJ
Ferrell	Ferrell 1964	11.6 mm Tube	4-16	$4 \cdot 10^4 - 8 \cdot 10^4$	11	L, LB, C, LJ
Rouhani	Rouhani 1966a; Rouhani 1966b	12 mm ID 25 mm OD Annulus	10-40	$1 \cdot 10^4 - 10 \cdot 10^4$	6	L, SZ LB, LJ
Bartolomei_1	Bartolomei and Chanturiya 1967	15.4 & 24 mm Tube	15-45	$9 \cdot 10^4 - 15 \cdot 10^4$	10	SZ, C, LJ
Bartolomei_2	Bartolomei et al. 1982	12 mm Tube	30-147	$9 \cdot 10^4 - 30 \cdot 10^4$	16	C, LJ
Staub_Ch	Staub et al. 1969	6.3 mm 1W Channel	1.3-3	$2 \cdot 10^4 - 20 \cdot 10^4$	17	SZ, LB
Staub_TuF	Staub et al. 1969	10.2 mm Tube	11-68	$3 \cdot 10^4 - 35 \cdot 10^4$	6	SZ, LB, LJ
Staub_TuW	Staub et al. 1969	10.2 mm Tube	11-68	$7 \cdot 10^4 - 11 \cdot 10^4$	2	SZ, LB, LJ
Martin	Martin 1969; Martin 1972	2 & 2.8 mm 2W Channel	78-138	$2 \cdot 10^4 - 16 \cdot 10^4$	22	SZ
Sabotinov	Sabotinov 1974 ¹	11.7 mm Tube	68-108	$8 \cdot 10^4 - 20 \cdot 10^4$	8	
Sekoguchi	Sekoguchi et al. 1980	11, 13.6 & 15.8 mm Tube	1.3-16	$3 \cdot 10^4 - 16 \cdot 10^4$	16	LB, LJ
Edelman	Edelman and Elias 1981	11.3 mm Tube	1	$2 \cdot 10^3 - 13 \cdot 10^3$	16	LB, C, LJ
Labuntsov	Labuntsov et al. 1984	12.1 & 34 mm Tube	5-70	$8 \cdot 10^4 - 40 \cdot 10^4$	4	C
Zeitoun	Zeitoun 1994	12.7 mm ID 25.4 mm OD Annulus	1.1-1.7	$1 \cdot 10^4 - 4 \cdot 10^4$	14	LJ

¹ From Kolev 1985.

Table 6.1: Bibliographic sources used to calibrate the proposed model. All runs are water, except the Staub_TuF runs which are R22 freon. *Label* column is used in subsequent figures. *Geometry* column gives the geometry of the test section (Pipe: circular cross-section pipe; Channel : rectangular cross-section, of which the short length is given; 1W (2W) means only 1 (2) wall(s) is (are) heated; Annulus : Annular cross-section, of which the inner diameter (ID) and the outer diameter (OD) are given). *Press* is outlet pressure. *Nb Pts* column contains the number of data points taken from the source. Total number of data points: 155. *Used in* column references other papers that used these data to calibrate or compare models (L: Levy 1967; SZ: Saha and Zuber 1974; LB: Lee and Bankoff 1998; C: Cai et al. 2021; LJ: Lee and Jeong 2022).

6.2.3 Comparing the data points to other references

Here the datapoints that I collected are compared with datapoints from the literature. Figure 6.2 is a comparison with Saha and Zuber 1974, figure 6.3 with Cai et al. 2021 and figure 6.4 with Lee and Jeong 2022.

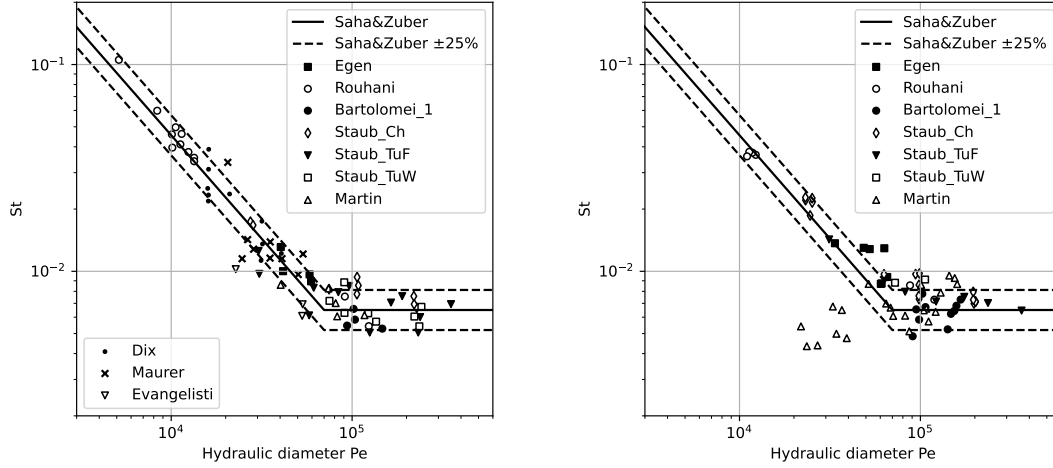


Figure 6.2: Comparison between the data presented in the original Saha and Zuber 1974 article and my data collection. **Left:** Peclet vs Stanton at OSV on the Saha and Zuber database. Compare with figure 2 from Saha and Zuber 1974. **Right:** Peclet vs Stanton at OSV, using the datapoints that I collected from the sources cited in Saha and Zuber 1974. I considered the void fraction measurements in Maurer 1960 and Evangelisti and Lupoli 1969 not precise enough to determine X_{OSV} . Furthermore, Dix 1971 defined the OSV as the point where bubbles are able to cross the channel, which is different from the one I selected, i.e. using the plot of the average void fraction as a function of X . This is why these 3 sources are absent from the database. The points collected here are consistent with those of Saha and Zuber, apart from a group of low- St low- Pe_h datapoints from Martin 1972 that come from high-pressure channels with a small hydraulic diameter.

I was not able to obtain the original data from other authors who compared different models, but the plots presented by Saha and Zuber 1974 (figure 6.2), Cai et al. 2021 (figure 6.3) and Lee and Jeong 2022 (figure 6.4) are reproduced. The plots are close to those of these authors, which yields a good level of confidence in the data collection.

6.2.4 System-scale analysis

Using the classical approach for OSV pioneered by Saha and Zuber 1974, the Stanton number at OSV as a function of the Peclet number calculated using the hydraulic and heated diameter D_h and D_{he} for all of the runs of the database is plotted in figure 6.5.

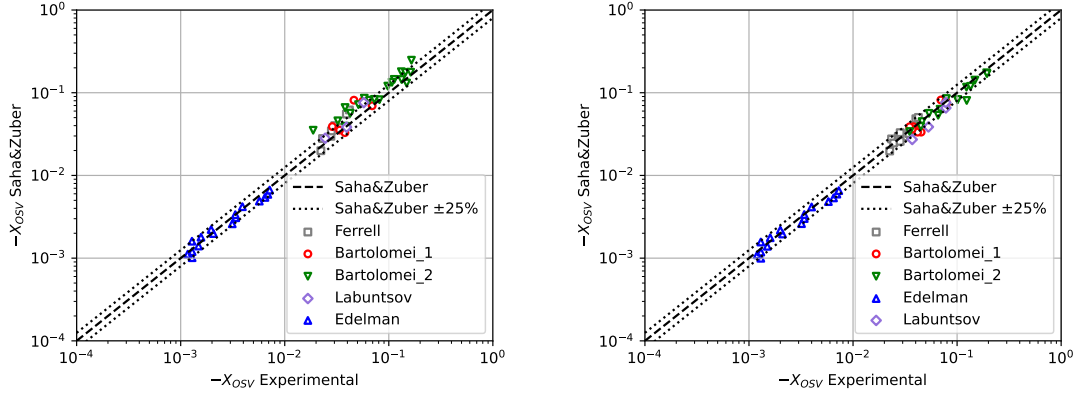


Figure 6.3: Comparison between the data presented in the article from Cai et al. 2021 and my data collection. **Left:** X_{OSV} prediction by the Saha and Zuber correlation vs experimental data on the Cai et al. database. Compare with figure 2.(a) from Cai et al. 2021. **Right:** X_{OSV} prediction by the Saha and Zuber correlation vs experimental data, using the data points collected here and that are used in Cai et al. 2021. The points collected here are consistent with those of Cai et al.

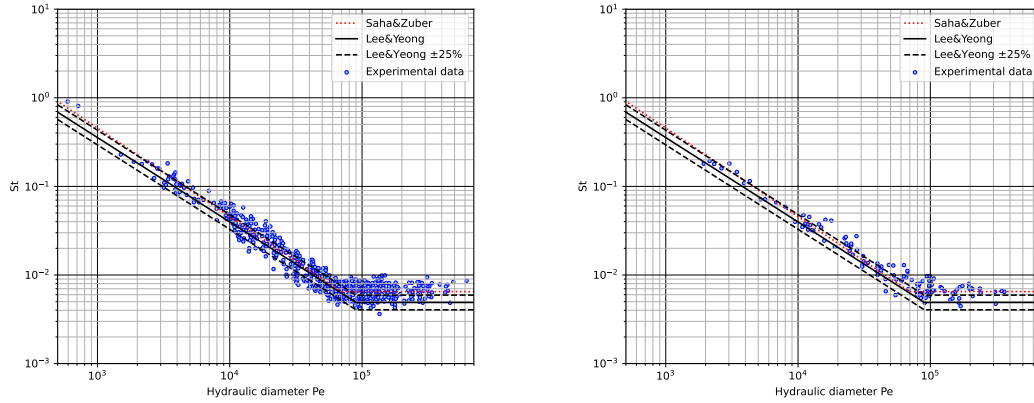


Figure 6.4: Comparison between the Lee and Jeong 2022 article and my data collection. **Left:** Peclet vs Stanton at OSV on the Lee and Jeong database. Compare with figure 11 from Lee and Jeong 2022. 499 datapoints collected. **Right:** Peclet vs Stanton at OSV, using the datapoints collected here and that are cited in Lee and Jeong 2022. I have much fewer datapoints (155 in total vs 972), as I decided not to use many references in their database. The points that are plotted seem consistent though the sources that they come from cannot be identified.

D_h and D_{he} are different for annular geometries (Rouhani and Zeitoun) and channels heated on one side (Staub_Ch). Using D_{he} , the Saha and Zuber correlation remains valid for $Pe_h > 7 \cdot 10^4$, as it is a constant Stanton region and St is independent of the diameter. This is no longer the case for $Pe_h < 7 \cdot 10^4$: data points are shifted to the right as $D_{he} \geq D_h$. While it seems logical that the characteristic length scale for high- Pe_h region is D_h , it is counter-intuitive in the

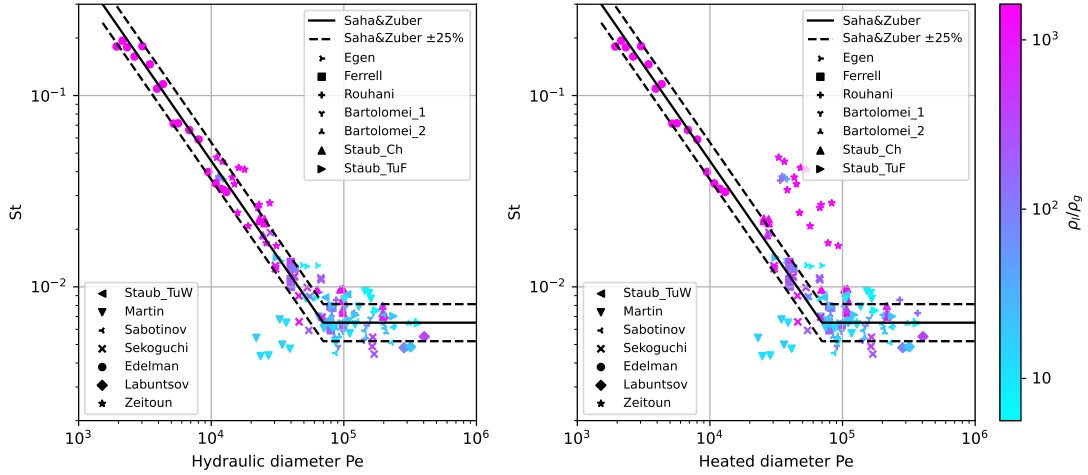


Figure 6.5: How the collected data fits the OSV the Saha and Zuber 1974 correlation. **Left:** Stanton number at OSV as a function of the Peclet number defined with the hydraulic diameter D_h . **Right:** Stanton number at OSV as a function of the Peclet number defined with the heated diameter D_{he} . The Saha and Zuber correlation is valid for the hydraulic diameter, not the heated diameter.

low- Pe_h region. According to SZ this region is dominated by thermal conduction and not turbulent effects, which is why the Nusselt number is constant. If this were the case, D_{he} would be the obvious relevant length scale candidate.

The transition from their so-called thermally controlled to detachment controlled regions is at $Pe_h = 7 \cdot 10^4$, though the temperature profile should be turbulent from $Pe_h \gtrsim 1 \cdot 10^3$. Even if the transition is thermally controlled, the characteristic thermal diffusivity for $1 \cdot 10^3 \lesssim Pe_h \lesssim 7 \cdot 10^4$ is the turbulent viscosity, not the molecular diffusivity $\lambda_l/(\rho_l C_{p,l})$, so a constant Nu here is unexpected.

The characteristic temperature used in equation 6.2 is the bulk liquid temperature. One would expect the near-wall liquid temperature to play a great role in the OSV, as it is a near-wall phenomenon.

Finally, the density ratio, i.e. pressure, seems to have no impact on the outcome, though it is extremely important in the near-wall dynamics. At high pressures, bubbles no longer stick to the surface but start sliding as they nucleate (Kossolapov 2021). Bubble diameters are very pressure-dependent (Kossolapov et al. 2024). The OSV is therefore not directly related to precise near-wall bubble dynamics.

6.3 CFD-scale approach

6.3.1 Transforming average-scale data to CFD-scale data

It was shown in section 4.3 that the temperature profile follows a log-law even in subcooled developed boiling flow (equation 4.4):

$$\Theta_+^s(y_+) = (T_s - T_l(y))/T_* = 2.12 \log(y_+) + \beta \quad (6.3)$$

Where $T_* = q_w / (\rho_l C_p u_\tau)$. This expression can be generalized in any developed boiling flow (equation 4.6):

$$\Theta_+^s(y_+) = \max(0, 2.12 \log(y_+) + \beta) \quad (6.4)$$

Where β varies along the axial position. One way to interpret this temperature profile is that $T_l(y) = T_s$ while $2.12 \log(y_+) + \beta < 0$, i.e. while:

$$y_+ \leq y_{+,c} = \exp\left(-\frac{\beta}{2.12}\right) \quad (6.5)$$

My goal in this section is to identify a critical value $y_{+,c}$ so that the OSV occurs when the thickness of the saturated layer $y_{+,s}$ reaches $y_{+,c}$. An interpretation of such a criterion is presented in figure 6.6.

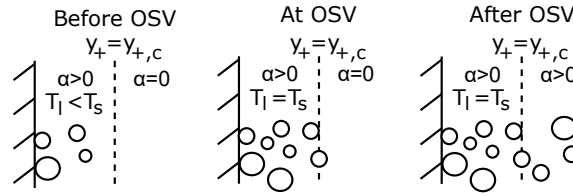


Figure 6.6: Physical interpretation of equation 6.5. After onset of nucleate boiling but before OSV, vapor is produced at the wall but in limited quantity due to condensation and stays at small y_+ . At OSV, $T_l(y_+ < y_{+,c}) \simeq T_s$ and void can enter the flow. After OSV, vapor leaves the near-wall layer and the temperature can reach T_s for higher y_+ .

This approach is similar to the critical heat flux model developed by Nop et al. 2021, where the authors show that in highly subcooled atmospheric-pressure flows the boiling crisis is reached when a thick enough fluid layer reaches saturation temperature.

In order to work more easily with the temperature profiles, in practice I will look for:

$$\beta_{OSV} = -2.12 \log(y_{+,c}) \quad (6.6)$$

So that at OSV the liquid temperature profile is:

$$\Theta_+^s(y_+) = \max(0, 2.12 \log(y_+) + \beta_{OSV}) \quad (6.7)$$

The OSV database is transformed from the form $X_{OSV}(\text{Test section}, P, G, q_w)$ to the form $\beta_{OSV}(\text{Test section}, P, G, q_w)$. The first step is to calculate u_τ for all of the data points. For tubes, the McAdams et al. 1942 correlation was used for high bulk Reynolds number $Re_h = \frac{D_h u_{\text{bulk}}}{\nu_l}$. The Blasius 1913 formulation was used for low Re_h :

$$\begin{cases} u_\tau = u_{\text{bulk}}(0.184 Re_h^{-0.2}/8)^{1/2} & \text{if } Re_h > 3 \cdot 10^4 \\ u_\tau = u_{\text{bulk}}(0.316 Re_h^{-0.25}/8)^{1/2} & \text{if } Re_h \leq 3 \cdot 10^4 \end{cases} \quad (6.8)$$

For channels, u_τ is determined so that the bulk velocity is correct using the log-law hypothesis along the width of the channel. For annular geometries, simulations are run with the $k - \omega$ turbulence model using the TrioCFD code (Angeli et al.

2015). The impact of an error on u_τ on the prediction of the OSV is discussed in section 6.3.2.

For given values of β , u_τ and the physical properties of the fluids, the bulk liquid temperature is evaluated. It is calculated by averaging the discharge over the flow's cross-section:

$$T_{\text{bulk}} = \frac{\langle u_{lz}(y)T_l(y) \rangle}{\langle u_{lz}(y) \rangle} \quad (6.9)$$

For the local temperature field, equation 6.4 is used. For tube and two-wall heated channels, the log-law is used for the liquid temperature across the whole width. For single-heated channels and annular flows, the temperature in the middle of the channel is used for the non-heated half.

For all flows, the local velocity used is the Reichardt 1951 single-phase adaptive wall law:

$$\begin{aligned} u_l(y_+) &= u_\tau u_+(y_+) \\ u_+(y_+) &= \frac{1}{\kappa} \log(1 + 0.4y_+) + 7.8 \left(1 - \exp\left(-\frac{y_+}{11}\right) - \frac{y_+}{11} \exp\left(-\frac{y_+}{3}\right) \right) \end{aligned} \quad (6.10)$$

To find β_{OSV} , the value of β at OSV, for each point in the database, a dichotomy on the value of β is performed so that the quality calculated for β_{OSV} is X_{OSV} :

$$\frac{h_l(T_{\text{bulk}}(\beta_{OSV})) - h_{ls}}{h_{gs} - h_{ls}} = X_{OSV}(\text{Test section}, P, G, q_w). \quad (6.11)$$

6.3.2 A simple CFD-scale correlation

As the target application is high- Pe_h flows in nuclear reactors, I concentrate on data where $Pe_h > 5 \cdot 10^4$. This limit was chosen as it is slightly lower than the $Pe_h = 7 \cdot 10^4$ transition in the Saha and Zuber correlation. It should therefore encompass all turbulent-driven points from their correlation. Furthermore, only geometries where all walls are heated are selected for the calibration step, as they have symmetrical temperature fields: tube and two-heated channel data is retained. Annular and single-heated channel data are used for the final model validation.

I strive to correlate β_{OSV} with the local flow conditions and key dimensionless numbers, i.e. u_τ , Pr and ρ_l/ρ_v . As the goal is to determine a CFD-scale correlation, the Peclet or Reynolds numbers for example cannot be used. Figure 6.7 shows β_{OSV} as a function of u_τ , with the color scale representing the density ratio. The Prandtl number was left out as its variation is very small across the database: the latter contains only one source with another fluid than water. No correlation is apparent in this plot.

In order to determine the optimal value of β_{OSV} , rather than taking the mean value the value that minimizes the mean average error (MAE) is determined. Results can be seen in figure 6.8. An interesting takeaway from this figure is also that the MAE is not extremely sensitive to the value of β_{OSV} . Therefore, for simplicity's sake, I will use:

$$\beta_{OSV} = -7 \quad (6.12)$$

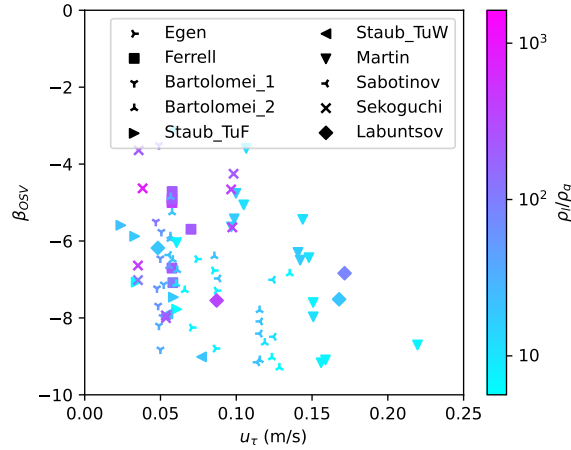


Figure 6.7: β at OSV vs friction velocity calculated for runs where $Pe_h > 5 \cdot 10^4$ and all wall of the test section are heated. The color scale represents the density ratio.

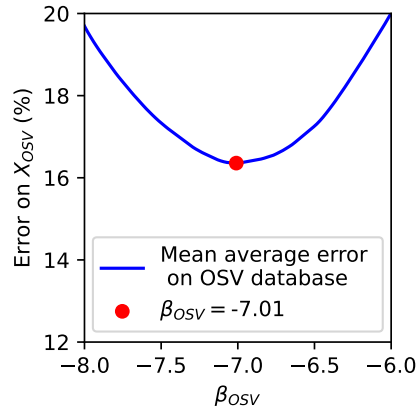


Figure 6.8: Mean average error on the high- Pe_h fully heated OSV database for different values of β_{OSV} . The MAE is not extremely sensitive to β_{OSV} . The optimal value is in the middle range of the ones seen in figure 6.7.

To verify the robustness of this correlation in industrial codes, where the friction velocity u_τ is not necessarily well predicted up to a few percent, the effect of a change on u_τ on the predicted X_{OSV} is calculated (figure 6.9). Changing u_τ by 10% has a smaller effect on X_{OSV} , which means the correlation is robust.

More complex regressions performed using the Uranie platform (Blanchard et al. 2018) marginally improve the MAE on X_{OSV} by a few %. However, this improvement was judged to small to justify the additional complexity. This also presents a risk of over-fitting the data, therefore a constant β_{OSV} is used.

According to equation 6.5, the saturated liquid layer thickness at OSV is then:

$$y_{+,c} = 27 \simeq 30 \quad (6.13)$$

Before OSV, T_l in this liquid sublayer is smaller than T_s and no void leaves it. At OSV, the boundary layer reaches T_s and significant void can be produced.

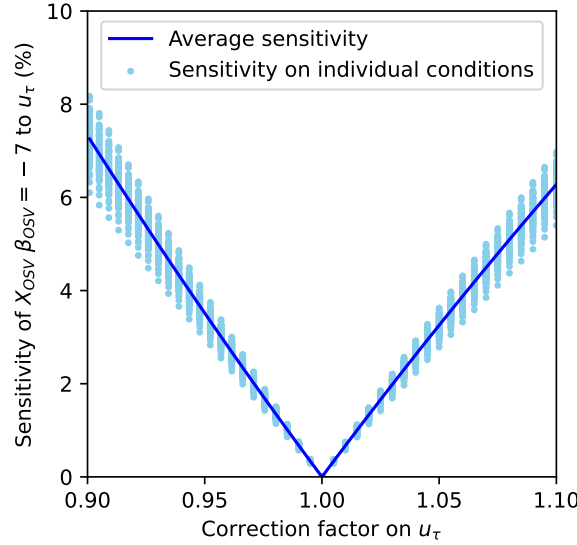


Figure 6.9: Sensitivity of X_{OSV} predicted using $\beta_{OSV} = -7$ when changing u_τ .

After OSV, the temperature can reach T_s outside the sublayer and vapor reaches regions that are far from the wall.

This $y_{+,c} = 30$ boundary layer size is coherent with the findings of Nop et al. 2021. They find that in a water channel with 25K subcooling, the boiling crisis occurs when a boundary layer of thickness $\delta = \frac{80\nu_l}{u_\tau}$ reaches saturation temperature. This limit is three times higher than the one at which OSV is predicted in the proposed model.

Recently, Kossolapov et al. 2024 measured bubble sizes at the wall in flow boiling for various pressures. The maximum dimensionless bubble size at the wall they observed was $\delta_+ = 30$. This is coherent with the current work, that finds a saturated layer up to $y_{+,c} = 30$.

The single-phase velocity log-law in a near-wall region is valid for $y_+ > 30$ (Pope 2000). This is the same value as our $y_{+,c} = 30$, which is remarkable but difficult to interpret.

6.3.3 Comparing the β_{OSV} -based correlation to the literature

A comparison between the prediction of X_{OSV} using different models for $Pe_h > 5 \cdot 10^4$ including annular and single-heated channel data is presented in figure 6.10. The MAE obtained on the partial database (15.77%) is comparable to that of the Saha and Zuber correlation (16.9%). Furthermore, as the error in the determination of the experimental X_{OSV} is of around 10%, the observed MAE's are of an acceptable order of magnitude. A local, CFD-scale OSV correlation valid at high Pe_h has therefore successfully been built.

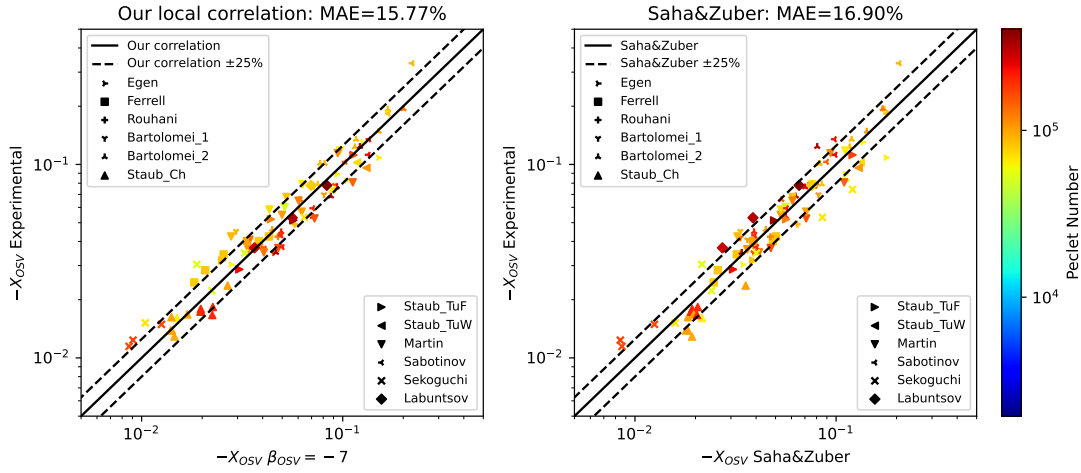


Figure 6.10: Comparison between models and experimental data for $Pe_h > 10^4$. **Left:** predicting X_{OSV} using $\beta_{OSV} = -7$. **Right:** Saha and Zuber 1974 correlation. Color scale: Pe_h number. The β_{OSV} -based correlation has a comparable MAE to the Saha and Zuber correlation.

Figure 6.11 plots the predicted results for $\beta_{OSV} = -7$ against those of Saha and Zuber 1974. The MAE (14.57%) is similar to that with the experimental data. This means that the $\beta_{OSV} = -7$ correlation is not simply a local version of the SZ correlation, or else the MAE would be significantly smaller than for the experimental comparison. This correlation is *different* and will predict different results in similar conditions.

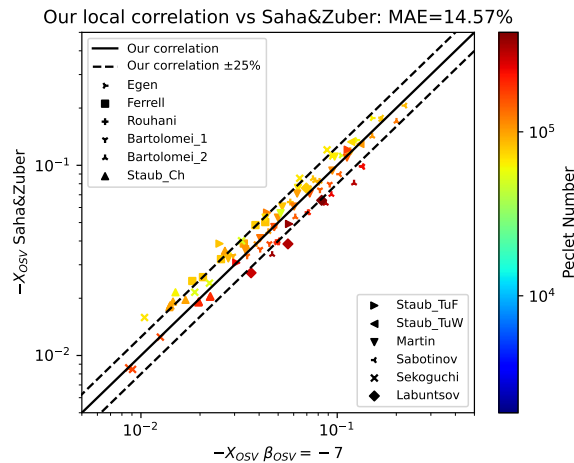


Figure 6.11: Comparison between $\beta_{OSV} = -7$ model and Saha and Zuber 1974 for $Pe_h > 5 \cdot 10^4$.

To check the validity range of the proposed correlation, the results it predicts are plotted on the complete OSV database and compared with those of Saha and Zuber (Figure 6.12). Some low- Pe_h runs with very small X_{OSV} coming from Edelman and

Elias 1981 are badly predicted using $\beta_{OSV} = -7$. For all of these points, grayed in figure 6.12, $Re_h < 2 \cdot 10^3$ and $Pe_h < 3.5 \cdot 10^3$. These points are eliminated for the calculation of the MAE. This gives a lower boundary of the validity domain of the correlation. It is therefore valid for virtually all turbulent flows, which is more coherent than the $Pe_h = 7 \cdot 10^4$ limit found in the Saha and Zuber correlation.

In situations where $Re_h > 2 \cdot 10^3$, the MAE in the proposed correlation is slightly larger than for the Saha and Zuber correlation: 21.85% vs 18.89%. However, there is only one fitted constant in my model, β_{OSV} , while there are two in SZ. The additional errors in the proposed correlation come from low- Pe_h annular flows ($Pe_h \sim 1 \cdot 10^4$), i.e. the data of Rouhani 1966a, Rouhani 1966b and Zeitoun 1994. However, high- Pe_h ($> 10^5$) predictions for the Rouhani data are consistent with the experimental results.

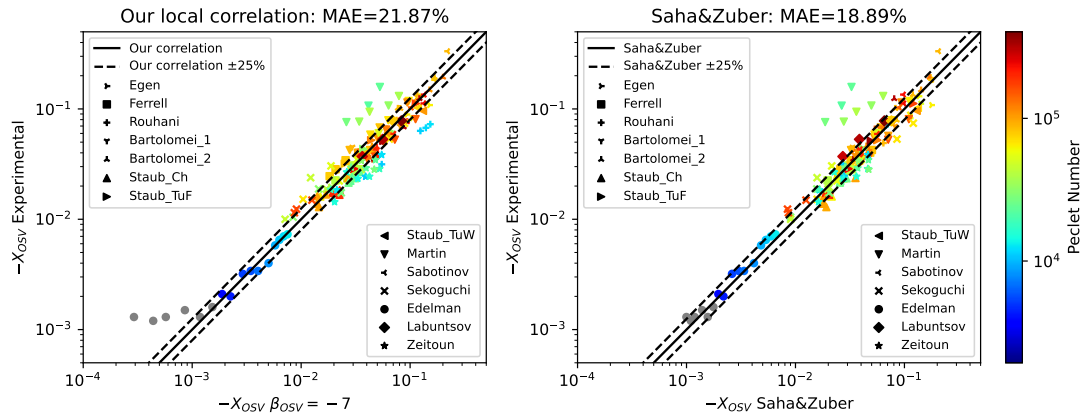


Figure 6.12: Comparison between models and experimental data all experimental data. **Left:** predicting X_{OSV} using $\beta_{OSV} = -7$. **Right:** Saha and Zuber 1974 correlation. Color scale: Pe_h number. Grey points: $Re_h < 2000$. The MAE is calculated only using points where $Re_h > 2000$.

6.4 Use for Heat Flux Partitioning

6.4.1 Heat flux partitions used for comparisons with the literature

In this section, only developed flows are studied. The single-phase heat transfer law used for all heat flux partitions is from Kader 1981. A detailed description can be found in 2.2.1.

The first model chosen as a reference is the original Kurul and Podowski 1990 formulation. A detailed description can be found in 2.2.5.

The second model is a modified version of the Kurul and Podowski 1990 formulation, that is the default option in the Neptune_CFD code (Guelfi et al. 2007). A detailed description can be found in Favre 2023 and Mimouni et al. 2016b. The

only difference with the original Kurul and Podowski formulation is the calculation of the departure diameter, that requires the bulk liquid velocity u_{bulk} as an input.

$$d_{\text{departure}} = 2.4 \cdot 10^{-5} P^{0.709} \frac{a}{\sqrt{b\phi}} \quad (6.14)$$

$$a = \frac{(T_w - T_s)\lambda_l}{2\rho_v(h_{vs} - h_{ls})\sqrt{\frac{\pi\lambda_w}{C_{pw}\rho_w}}} \quad (6.15)$$

Where λ_w is the wall conductivity, C_{pw} the wall heat capacity and ρ_w the wall density.

$$b = \begin{cases} \frac{T_s - T_l(y)}{2\left(1 - \frac{\rho_v}{\rho_l}\right)} & \text{if } St \leq 0.0065 \\ \frac{T_s - T_l(y)}{2\left(1 - \frac{\rho_v}{\rho_l}\right)} \frac{(1 - A_{\text{bubbles}})q_{\text{SP}}(y) + q_{\text{quench}} + q_{w,l \rightarrow v}}{\rho_l C_{p,l} u_{\text{bulk}}^{0.0065}} & \text{if } St > 0.0065 \end{cases} \quad (6.16)$$

Where $St = \frac{(1 - A_{\text{bubbles}})q_{\text{SP}}(y) + q_{\text{quench}} + q_{w,l \rightarrow v}}{\rho_l C_{p,l} u_{\text{bulk}} (T_s - T_l(y))}$ is defined using the bulk velocity.

$$\phi = \max\left(1, \left(\frac{u_{\text{bulk}}}{0.61}\right)^{0.47}\right) \quad (6.17)$$

6.4.2 Physical interpretation of a stationary developing boiling flow

Figure 6.13 presents the different physical mechanisms occurring in a developing boiling flow. The flow enters as subcooled liquid (column ①, first row). The temperature profile is a single-phase profile (second row). The wall temperature is below the saturation temperature (third row), and increases progressively.

The ONB occurs when the wall becomes hotter than saturation temperature. The wall temperature quickly reaches a constant value and does not evolve as boiling picks off (Garnier et al. 2001). Between ONB and OSV (column ②), the temperature profiles follow equation 6.4, like those of figure 4.5, with β becoming smaller and smaller. At a very local scale, bubbles nucleate at the wall and immediately condense. However, at a scale larger than that of the nucleating bubbles, which is the focus of this chapter, all of the heat flux keeps enters the liquid phase and no vapor is produced.

After the OSV, the heat flux is split between heating the liquid and evaporation (column ③). The void fraction departs from 0. The temperature in the first element, at $y_{+,1}$, keeps increasing.

When it reaches saturation temperature, all of the heat flux is used for evaporation (column ④). At first, the flow remains in subcooled boiling, as the core has not reached saturation temperature (pictured in the second row). The flow transitions to saturated boiling subsequently.

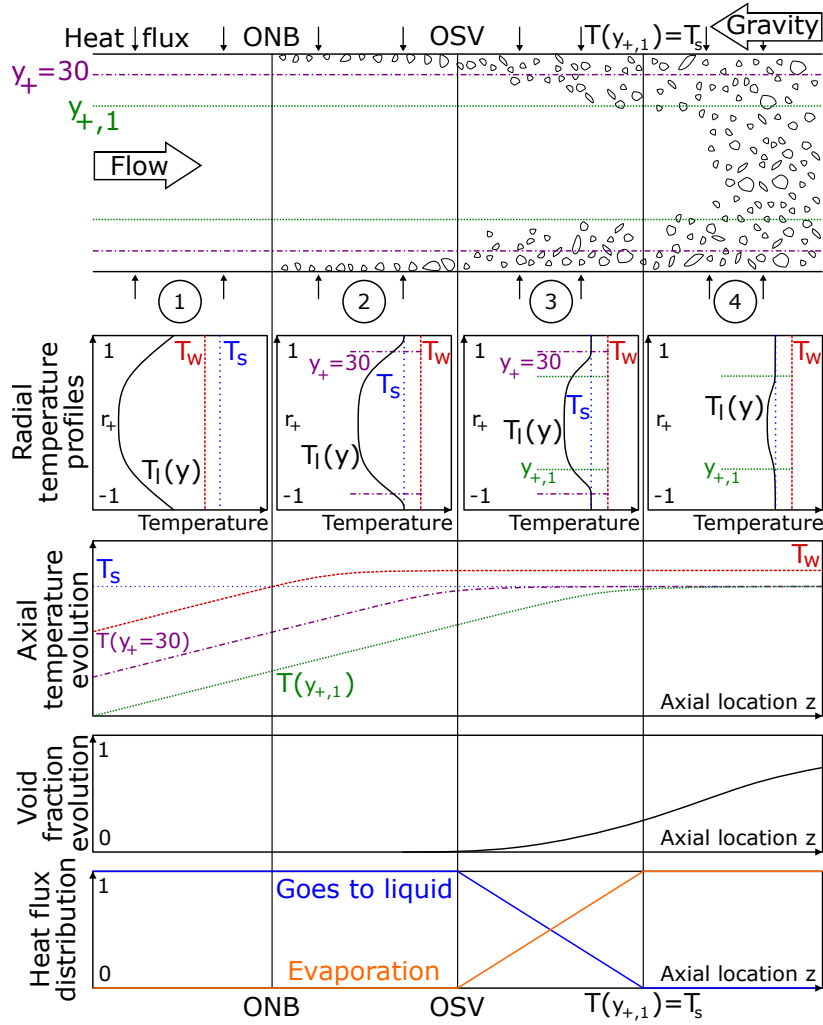


Figure 6.13: Physical interpretation of a stationary developing boiling flow. $T(y_+ = 30)$ is the average temperature in the boundary layer. $y_{+,1}$ is the dimensionless size of the first wall cell in a simulation. Onset of nucleate boiling (ONB) occurs when wall temperature passes saturation temperature. Onset of significant void (OSV) happens when the liquid temperature in the turbulent boundary layer reaches saturation temperature.

6.4.3 OSV-based heat flux partition

The physical mechanisms explained in the previous section are used to construct a heat flux partition.

In single-phase flow (region ① in figure 6.13), the heat flux at the wall is, for any distance to the wall y :

$$q_{SP} = \frac{(T_w - T_l(y))\rho_l C_{p,l} u_\tau}{\Theta_+^w(y_+)} = H_{l,SP}(y_+)(T_w - T_l(y)) \quad (6.18)$$

Where $H_{l,SP}(y_+)$ is the single-phase heat transfer coefficient calculated using the Kader 1981 correlation (see section 2.2.1).

Between the ONB and the OSV (region ②) the total heat flux q_w will follow a boiling-flow correlation that depends of the wall temperature T_w . For water, that of Jens and Lottes 1951 or Thom et al. 1965 can be used. For other fluids, the Frost and Dzakowic 1967 formulation can do nicely (from Delhaye 2008). It was shown to give very consistent results with the DEBORA database (Gueguen 2013). If another correlation is more appropriate for a given fluid or local conditions, as long as it only depends on near-wall quantities it can be used in this HFP without impacting the methodology. The aforementioned correlations for wall heat flux in boiling flow read:

$$\begin{aligned} q_{\text{Boil,Jens\&Lottes}} &= \left(\frac{T_w - T_s}{25} \exp(P/62) \right)^4 \\ q_{\text{Boil,Thom et al.}} &= \left(\frac{T_w - T_s}{22.65} \exp(P/87) \right)^2 \\ q_{\text{Boil,Frost\&Dzakowic}} &= \frac{\lambda_{l_s}(h_{q_s} - h_{l_s})\rho_v}{8\sigma T_s} \left(\frac{T_w - T_s}{Pr_s} \right)^2 \end{aligned} \quad (6.19)$$

Where Pr_s is the Prandtl number at saturation, λ_{l_s} the liquid conductivity at saturation and σ the surface tension. The pressure P must be in bar in the Jens and Lottes 1951 and Thom et al. 1965 formulations.

Combining equations 6.3 and 6.12, the heat transfer coefficient to the liquid at the OSV is:

$$H_{l,\text{OSV}}(y_+) = \frac{\rho_l C_{p,l} u_\tau}{\Theta_+^s(y_+, \beta = -7)} = \frac{\rho_l C_{p,l} u_\tau}{2.12 \log(y_+) - 7} \quad (6.20)$$

And the heat transfer towards the liquid phase at OSV is, at any distance y from the wall:

$$q_{l,\text{OSV}} = H_{l,\text{OSV}}(y_+)(T_s - T_l(y)) \quad (6.21)$$

Therefore, while the following inequality holds, the flow has not reached OSV and all of the heat flux remains in the liquid:

$$q_w < H_{l,\text{OSV}}(y_+)(T_s - T_l(y)) \quad (6.22)$$

The OSV occurs when inequality 6.22 no longer holds, i.e. when $T_l(y)$ has increased sufficiently. This is equivalent to being saturated for $y_+ < 30$. After this point (③), I use the same methodology as the system-scale models discussed previously (section 6.1). This requires assuming that after the OSV, the heat transfer coefficient towards the liquid stays the same. This is a strong hypothesis. I believe this is a lower bound on the heat transfer coefficient: as bubbles nucleate, grow and move away from the surface they are bound to increase the agitation and heat transfer efficiency compared with the situation at OSV. This enables the calculation of the heat flux towards the liquid phase. The heat flux towards evaporation is then the difference with the total heat flux:

$$\begin{cases} q_{lw} &= H_{l,\text{OSV}}(T_s - T_l(y)) \\ q_{w,l \rightarrow v} &= q_w - H_{l,\text{OSV}}(T_s - T_l(y)) \end{cases} \quad (6.23)$$

Finally, once the near-wall cell has reached saturation temperature, all of the heat flux enters the evaporation term (region ④).

If $y_+ < 30$ in the near-wall cell, then vapor production will begin when $T_l = T_s$, before the OSV. I recommend that $y_+ \geq 100$ at in the near-wall cells to use the model. Similar limitations also exists for mechanistic HFP's. If the wall cell is smaller than the bubble departure diameter, the near-wall models described are no longer valid.

Combining all of these elements, a heat flux partitioning algorithm can be built. When the wall temperature is known, the inputs are y_1 , u_τ , T_w , $T_l(y_1)$ and the physical properties of the liquid. y_1 is the size of the near-wall cell. The steps of the algorithm are the following:

1. Construct a mesh so that $y_{+,1} \geq 100$
2. Calculate single-phase heat flux q_{SP} using the Kader 1981 heat transfer coefficient (equation 6.18, see 2.2.1 for details)
3. Calculate total boiling heat flux q_{Boil} using a total heat flux correlation (equation 6.19)
4. If $T_l(y_1) \geq T_s$: $q_w = q_{\text{Boil}}$ goes into the evaporation term (region ④)
5. Else if $q_{\text{SP}} \geq q_{\text{Boil}}$: $q_{\text{SP}} = q_w$ goes into the liquid phase (region ①)
6. Else $q_w = q_{\text{Boil}}$; calculate $H_{l,\text{OSV}} = \frac{\rho_l C_{p,l} u_\tau}{\Theta_+^s(y_{+,1})}$
 - a) If $q_{l,\text{OSV}} = H_{l,\text{OSV}}(T_s - T_l(y_1)) > q_w$, q_w goes into the liquid phase (region ②)
 - b) Else the heat transfer to the liquid phase is $H_{l,\text{OSV}}(T_s - T_l(y_1))$ and the evaporation term is $q_w - H_{l,\text{OSV}}(T_s - T_l(y_1))$ (region ③)

The algorithm is shown in figure 6.14.

As $q_{\text{SP}} < q_{l,\text{OSV}}$, a condensed way to write steps 4 to 6 of this algorithm is:

$$\begin{aligned}
 q_{l,\text{OSV}} &= \max\left(0, \frac{\rho_l C_{p,l} u_\tau (T_s - T_l(y_1))}{2.12 \log(y_{+,1}) - 7}\right) \\
 q_w &= \max(q_{\text{SP}}, q_{\text{Boil}}) \\
 q_{lw} &= \min(q_w, q_{l,\text{OSV}}) \\
 q_{w,l \rightarrow v} &= q_w - q_{lw}
 \end{aligned} \tag{6.24}$$

This presents a clear numerical advantage compared to classical HFP's for constant heat flux boundary conditions: steps 2, 3 and 5 can be skipped in this case. As T_w is not needed for the other steps, this means avoiding a Newton algorithm to determine the partition. This saves computation time and is easier to implement in a code.

From a physics standpoint, this guaranties a better calculation of the total heat flux than mechanistic models, as correlations directly fitted on experimental data are more precise. Furthermore, given the simplicity of the model it is easy to anticipate and interpret the outputs and the physical mechanisms at play.

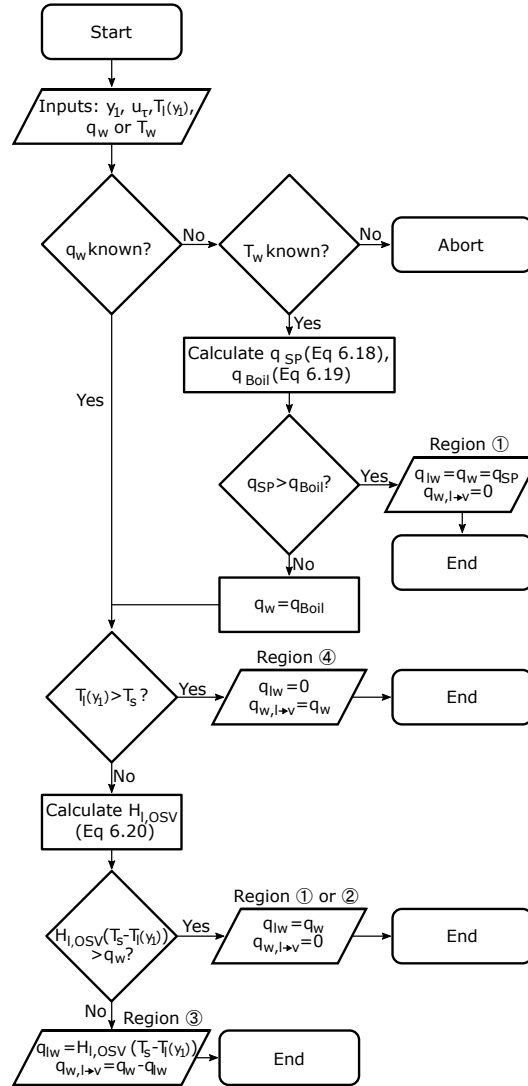


Figure 6.14: Different steps of OSV-based heat flux partition algorithm for a fixed heat flux or a fixed wall temperature boundary condition. Inputs of the algorithm are distance to the wall in the near-wall cell y_1 , friction velocity u_τ , local liquid temperature $T_l(y_1)$ and either total heat flux q_w either wall temperature T_w . Outputs are evaporation heat flux $q_{w,l \rightarrow v}$ and heat flux entering liquid phase q_{lw}

The heat transfer coefficient is dependent on u_τ . In this work, I only used models developed for single-phase flows. However, if reliable models for wall friction in bubbly flow are developed, comparable to that of Ramstorfer et al. 2005, u_τ will be affected. If u_τ changes between the ONB and the OSV, the situation could require either re-calibrating the model, or keep using the single-phase u_τ for the thermal equation. If it changes after the OSV, this would affect the HFP after the OSV and the model would need additional verification. For now, I recommend to use this model solely with u_τ calculated from a single-phase correlation for the OSV and HFP calculations for the moment, though a multiphase formulation of u_τ could be used in the momentum equation.

One option to reduce the impact of the near-wall cell size on the partition would be to determine for which β all of the heat flux would be used for liquid evaporation and none would be transferred directly for the liquid. Calling β_{evap} such a number, $\beta_{\text{evap}} < \beta_{\text{OSV}}$ is always verified. The temperature in the near-wall cell above which all of the heat flux is used for evaporation can then be calculated:

$$T_{l,\text{evap}}(y_1) = T_s - \frac{q_w}{\rho_l C_{p,l} u_\tau} (2.12 \log(y_{+,1}) + \beta_{\text{evap}}) \quad (6.25)$$

Finally, this temperature could be used to rescale q_{lw} after the OSV:

$$q_{lw} = H_{l,\text{OSV}}(T_s - T_l(y_1)) \frac{T_{l,\text{evap}}(y_1) - T_l(y_1)}{T_{l,\text{evap}}(y_1) - T_{l,\text{OSV}}(y_1)} \quad (6.26)$$

As long as $y_{+,1} > \exp(-\frac{\beta_{\text{evap}}}{2.12})$, the heat flux partition should no longer depend on the mesh size. However, no methodology to determine this β_{evap} has been proposed so this method cannot be implemented.

6.4.4 Comparing the OSV-based HFP with some from the literature

As the wall temperature, bulk liquid temperature and heat flux are the quantities most often measured in heat transfer experiments (Jens and Lottes 1951; Thom et al. 1965; Garnier et al. 2001), the predicted wall temperature for a given heat flux is the main point of reference for a heat transfer model (Kommajosyula 2020; Favre 2023). The proposed model only predicts the partition and used external correlations for the heat transfer. It is therefore as good at predicting the wall temperature as the external correlation used, and it cannot be validated with this type of data.

Measurements of the destination of heat fluxes, to see if they go towards the liquid phase or evaporation, are few. To the best of my knowledge, such experiments were only conducted at MIT (Richenderfer et al. 2018; Kossolapov 2021; Kossolapov et al. 2024) with a 10 mm×10 mm heater. However, the model proposed here is based on the assumption that the liquid thermal boundary layer is developed. These experiments therefore cannot be used to validate the OSV-based HFP.

The best that can be done is to compare the predicted fluxes with models from the literature, i.e. the original Kurul and Podowski 1990 formulation and the Neptune_CFD Kurul and Podowski (Favre 2023). To simplify notations, these will be called original KP and Neptune_CFD KP in the rest of this chapter. These comparisons are conducted on data from the DEBORA experiment (Garnier et al. 2001). The liquid temperature used as an input is the one measured closest to the wall in the experiment. The y used to calculate y_+ and $\Theta_+^s(y_+)$ in the proposed model and the single-phase heat transfer in all models is the one at which this liquid temperature is measured, i.e. $y = 0.55$ mm. The corresponding $y_{+,1}$ are between 354 and 1140. The Frost and Dzakowic 1967 correlation is used for the total heat flux in the OSV-based model.

Figure 6.15 presents the effect of the wall temperature on the predicted heat flux for four different (Mass flux, Pressure, Liquid temperature) combinations. In the first row, one can see that the total heat flux predicted by the OSV-based model (orange line) is much closer to the experimental measure (red point) than the other models. This is thanks to the use of the Frost and Dzakowic 1967 correlation. The difference between experimental heat fluxes and those predicted by the KP-based models is huge: the original KP is 3-10 times too high and the Neptune_CFD KP 1.5 to 5 times too low. The OSV-based model and the Neptune_CFD model follow the single-phase solution at low wall superheats on the section where they are superimposed. The inflection in the curve of the OSV-based model, at $T_w - T_s \sim 1.5$ K in the first column for the G2P14W16 run, marks the activation of the boiling model, where $q_{SP} \simeq q_{Boil}$. On the other hand, the original KP departs almost immediately from the single-phase solution.

The second row presents the effect of the wall temperature on the fraction of heat flux entering the liquid. The original KP model begins producing vapor as soon as the wall temperature exceeds saturation temperature. I believe this behavior to be non-physical. The OSV-based HFP needs a non-zero wall superheat before producing vapor, because of the $q_{l,OSV} = H_{l,OSV}(T_s - T_l(y)) > q_w$ criterion. As expected, this occurs after the inflection for the total heat flux, at $T_w - T_s \sim 3$ K in the first column (vs $T_w - T_s \sim 1.5$ K). As the most common boundary condition for industrial applications is an imposed heat flux, the heat flux fraction entering the liquid phase as a function of the total heat flux is also plotted (third row). This shifts the Neptune_CFD model to the left compared with the second row, as its total heat flux is smaller for a same wall superheat. For a same heat flux, the OSV-based HFP predicts a much higher fraction of heat entering the liquid phase than the KP-based models.

Figure 6.16 focuses on the practical case of imposed-heat flux conditions. In the first row, the predicted wall temperatures as a function of the liquid subcooling are presented. One can observe the transition from the single-phase regime at the right of each plot, where the subcooling is high and the wall temperature smaller than saturation temperature (black dashed line) to the boiling regime at the left of each plot. The predicted single-phase wall temperatures are the same for all 3 models, as they all use the Kader 1981 law. In the boiling regime, the three curves separate. The original KP predicts a wall superheat two times too small. The proposed model is consistent with experimental data, but this is thanks to the use of the Frost and Dzakowic 1967 correlation. The Neptune_CFD KP over-predicts the wall superheat by a factor 2. The difference between experimental temperatures and temperatures predicted by the KP-based models is huge. On the experimental data, once the wall temperature has passed the saturation temperature there is a clear change of slope and the wall temperature becomes nearly constant (second and fourth columns, i.e. G2P26W16 and G5P26W24). The inflection in the OSV-based model is slightly sharper than the experimental data, but much closer to the experiment than KP-based models. The proposed model is also the only one that predicts a constant wall temperature as the subcooling changes.

The second row of figure 6.16 presents the heat flux fraction entering the liquid

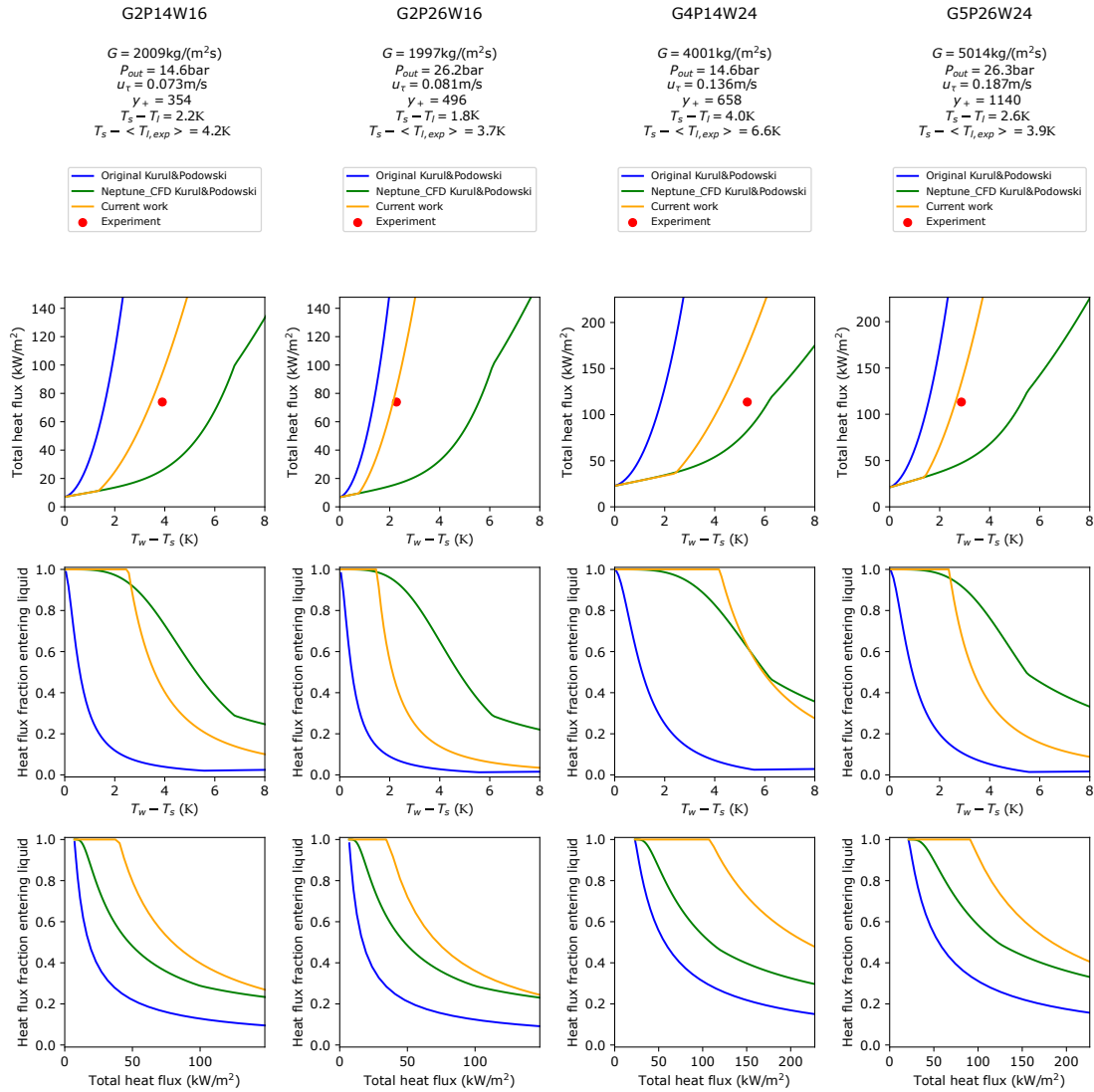


Figure 6.15: Impact of the wall temperature on the heat flux predicted by the original Kurul and Podowski 1990 and Neptune_CFD Kurul and Podowski model (Favre 2023) and the current work vs data from the DEBORA experiment (Cubizolles 1996). Each column represents a different (Mass flux, Pressure, Liquid temperature) combination given in the legend. **First row:** total heat flux as a function of wall superheat. **Second row:** fraction of heat flux entering the liquid phase as a function of the wall superheat. **Third row:** fraction of heat flux entering the liquid phase as a function of the total heat flux.

as a function of the subcooling, also for a fixed heat flux. The OSV-based model transitions smoothly from sending all of the heat flux to the liquid phase at high subcoolings to evaporating the whole heat flux close to saturation temperature. The KP-based models keep heating the liquid after saturation temperature is reached. This should create a liquid overheat in the simulations, which was never measured in the DEBORA experiment. Both KP models begin evaporation as soon as the

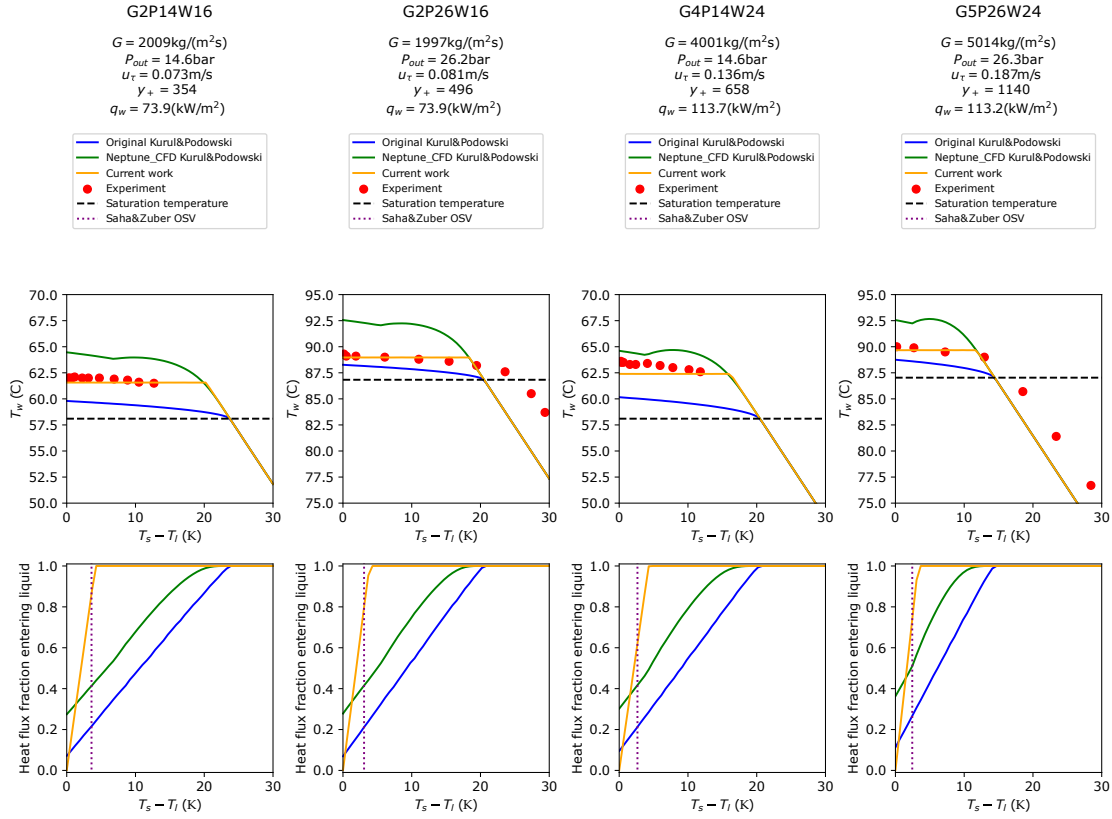


Figure 6.16: Impact of the total heat flux on the wall temperature and heat flux partitioning predicted by the original Kurul and Podowski 1990 and Neptune_CFD Kurul and Podowski model (Favre 2023) and the current work vs data from the DEBORAs experiment (Cubizolles 1996). Each column represents a different (Mass flux, Pressure, Heat flux) combination given in the legend. **First row:** Wall temperature as a function of liquid subcooling at y_+ given in the legend. **Second row:** fraction of heat flux entering the liquid phase as a function of liquid subcooling. The dashed vertical lines represent the liquid subcooling at y_+ when the Saha and Zuber 1974 criterion is reached for these conditions.

wall temperature goes above the saturation temperature: there is no zone between the ONB and the OSV where no vapor is produced. For the proposed model, vapor production begins for much lower subcoolings, around 5 K in the different plots and not 20 K. The local liquid temperatures at the wall where the Saha and Zuber 1974 criterion is reached in the bulk are plotted as purple vertical dashed lines in figure 6.16. This temperature is calculated by interpolation of experimental data, knowing the thermodynamic quality and liquid temperature at the wall in the experiments. The beginning of vapor production in the OSV-based HFP is consistent with the Saha and Zuber 1974 criterion, and is very far for the KP models. The latter are therefore expected to significantly over-predict the void fraction for high subcoolings compared with experimental results.

In this section, I have shown that the OSV-based HFP predicts a more phys-

ical heat flux distribution between phases than formulations from the literature, especially at high and low subcoolings, and a coherence with the Saha and Zuber 1974 OSV model. It also enables the use of total boiling heat flux correlations that have good wall temperature predictions. More generally, I believe that to verify the physical coherence of a heat flux partitioning model, one must check that:

- Significant vapor production does not begin as soon as the wall temperature exceeds saturation temperature, but the transition is smooth.
- For a given wall temperature, the total heat flux in the boiling region is only marginally dependent on the subcooling, as is the case in experiments.
- When the liquid temperature tends towards saturation temperature, all the energy is transferred towards evaporation.
- When the liquid subcooling increases and the bulk enthalpy reaches the Saha and Zuber criterion, the fraction of heat evaporating should not be significant.

6.4.5 Bubble departure diameter calculation

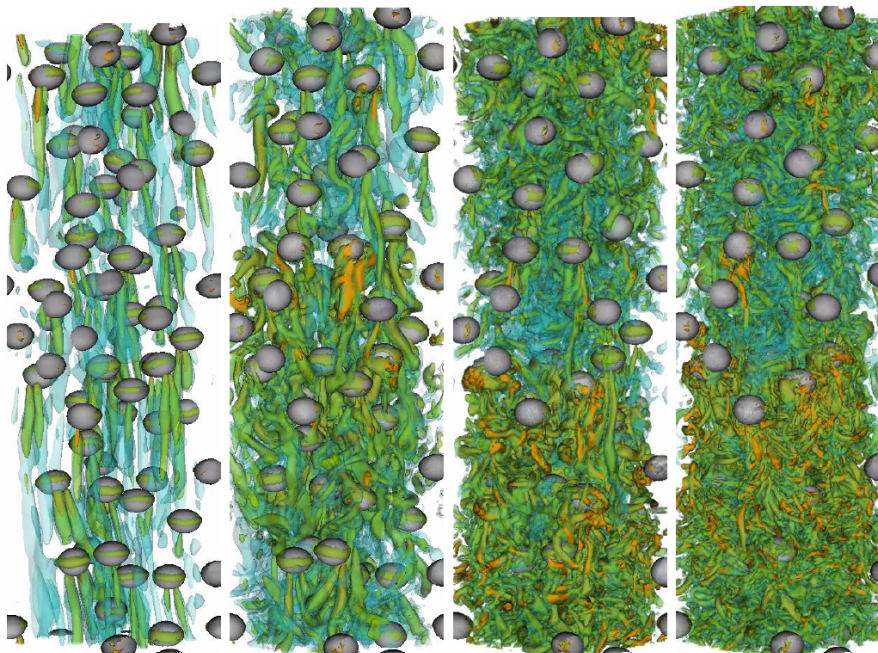
As no mechanistic modeling is conducted in this model, no departure diameter is calculated. This is not an issue in this thesis, as no interfacial area transport equation is used. However, it is problematic for most two-phase sets of closures (Guelfi et al. 2007; Liao et al. 2018).

Both mechanistic and fitted departure diameter calculation methodologies need the wall temperature as an input (Ünal 1976; Mazzocco et al. 2018; Kommajosyula 2020; Favre et al. 2023). If, in the simulation, the wall temperature is given, then it is possible to calculate the departure diameter. If the heat flux is enforced, one can use a total heat flux correlation to calculate the wall temperature (Jens and Lottes 1951; Thom et al. 1965; Frost and Dzakowic 1967), and feed it in the departure diameter model.

6.5 Conclusion

I have developed an OSV model validated for tube, channel and annular geometries, for Peclet numbers ranging from $3.5 \cdot 10^3$ to $4 \cdot 10^5$ and pressures from 1 bar to 147 bar. This model is simple, has only one fitted coefficient, and performs as well as the Saha and Zuber 1974 correlation. It can be used to implement a straightforward heat flux partition. The next step is to build a set of bulk closures adapted to high-pressure conditions.

CHAPTER 7



6% void fraction is already a lot... Image from Cluzeau 2019.

Improving bulk flow closures

In chapter 5, I have shown that interfacial force closure laws validated in atmospheric-pressure adiabatic flows are no longer valid in pressurized water reactor similarity conditions.

This is not necessarily surprising, as most of these models are used outside of their validity domain. Pressurized water reactor flows are extremely turbulent, have low surface tensions and density ratios. When boiling occurs in some accidental conditions they have high void fractions and can resemble emulsions (Hosler 1967; François et al. 2011).

In this chapter, building on the DEBORA database simulations of chapter 5 and the heat flux partition of chapter 6, I propose a new set of closures for the bulk terms of these flows, using a minimalistic physics-base approach that takes into account the particularities of pressurized water reactor flows. The set of closures built in this chapter is summarized in section 7.7.

Most of the text of this chapter was adapted from Reiss et al. 2024a.

Contents

7.1	Relative velocity inversion	121
7.2	Deformed bubble hypothesis	121
7.3	Drag force	124
7.4	Lift force	125
7.5	Turbulent dispersion force	126
7.6	Condensation	129
7.6.1	Formulating a condensation term that does not require bubble diameter modeling	129
7.6.2	DEBORA Simulation result comparison with different energy closures	132
7.6.3	Condensation database	136
7.6.4	Bartolomei simulation result comparison	140
7.7	Complete model	143

7.1 Relative velocity inversion

The axial relative velocity plays a key role in most closure terms. It is part of the formulation of the drag and lift forces. It is used in the calculation of the Wobble and bubble Reynolds numbers, and thus influences the condensation, drag, lift and turbulent dispersion coefficients. A detailed analysis of the relative velocity in the imposed-diameter simulations in the DEBORA database will now be carried out. It is shown in figure 7.1 for test tube III-G3P26W23.

The first column contains the results for the baseline case (closures of table 2.1). The axial relative velocity is positive at the wall, becomes negative as the bubbles move away from the wall and becomes positive again at the core of the flow. This is due to bubble inertia in the simulation: the velocity of bubbles in the near-wall cell is smaller than the velocity of the liquid in the core. As bubbles migrate towards the pipe center, their inertia prevents them from accelerating immediately, hence the negative relative velocity. This effect is exacerbated if vapor is produced with zero velocity, i.e. if a momentum source $-\Gamma_{l \rightarrow v} \vec{u}_v$ is added in the near-wall cell (center column in figure 7.1).

This behavior has direct effects on many interfacial terms: it cancels out or inverts the sign of the lift force, and reduces the turbulent dispersion force and condensation. There are very few experiments where gas and liquid velocities were measured in identical configurations (Roy et al. 2002; François et al. 2021). To the best of my knowledge, the gas velocities were never measured lower than the liquid ones underneath the experimental error. I therefore believe the relative velocity inversion to be non-physical and strive to prevent it in simulations.

Test tube III is thus run without the virtual mass term to reduce the inertia of the vapor (right column in figure 7.1). The relative velocity remains positive. Therefore, an unintended effect of the virtual mass force in boiling-flow simulations is to reduce or invert the relative velocity, this modifying all bulk closures. All further simulations are carried out without virtual mass.

7.2 Deformed bubble hypothesis

In order to evaluate if bubbles are deformed or not in the flow, two Weber numbers are plotted in figure 7.2. The first, We , is defined using the relative velocity and accounts for the effect of the drag force on bubble deformation. The second, We_ϵ , represents the impact of turbulent velocity fluctuations at the scale of the bubbles when their diameter is comparable to the turbulent length scales in the inertial range:

$$\begin{aligned} We &= \frac{\rho_l d_b \|\vec{u}_g - \vec{u}_l\|^2}{\sigma} \\ We_\epsilon &= \frac{\rho_l d_b (\epsilon d_b)^{2/3}}{\sigma} \end{aligned} \quad (7.1)$$

In this computation d_b comes from the experimental measurements. The other physical quantities come from the simulations carried using the baseline set of closures, but without the virtual mass force, and enforcing the experimental diameter as in chapter 5.

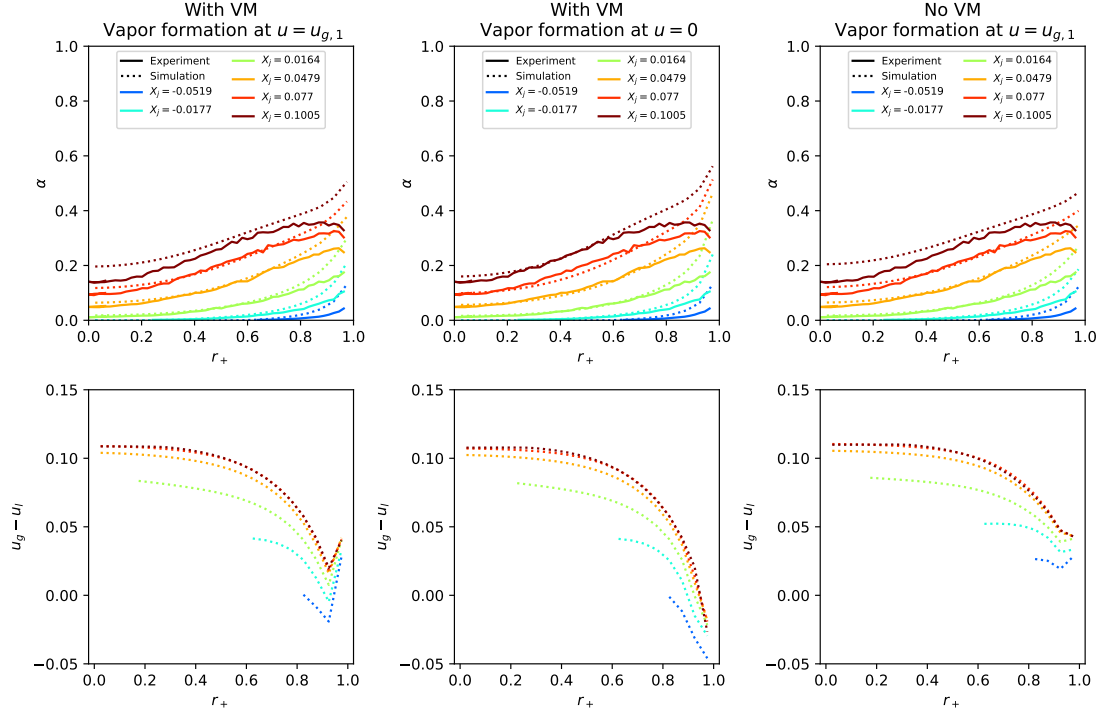


Figure 7.1: Void fraction and relative axial velocity results for test tube III-G3P26W23, for three different configurations. **Left:** with virtual mass and vapor formation at first-cell velocity. **Center:** with virtual mass and vapor formation at zero velocity. **Right:** without virtual mass and vapor formation at first-cell velocity.

The drag Weber number We is smaller than 1 in the near-wall region, which means that the bubbles should be spherical according to this criterion. In the core, it varies between 2 and 3. For such Weber numbers, bubbles should be deformed (Wallis 1974). The turbulence-driven Weber number We_c has an opposite behavior: it is large in the near-wall region and diminishes in the core. Bubbles experience significant deformation when $We_c \geq 2$ (Hinze 1955; Risso and Fabre 1998; Masuk et al. 2021). Therefore, on all three test tube bubbles are in a region where they are deformed due to their rise or due to turbulence.

Furthermore, as the void fraction increases, for a same average bubble size, the distance between bubbles decreases. If bubbles are assumed to be spherical and monodisperse, the densest possible configuration is face-centered cubic. The relationship between the void fraction, bubble diameter and distance between bubbles is then:

$$\frac{\frac{\pi}{6} d_b^3 \frac{1}{6}}{\frac{\sqrt{2}}{12} (d_b + d_{dist})^3} = \alpha_v \quad (7.2)$$

The distance between two bubbles d_{dist} can then be expressed as a function of the void fraction:

$$\frac{d_{dist}}{d_b} = \sqrt[3]{\frac{\pi}{3\sqrt{2}} \frac{1}{\alpha_v}} - 1 \quad (7.3)$$

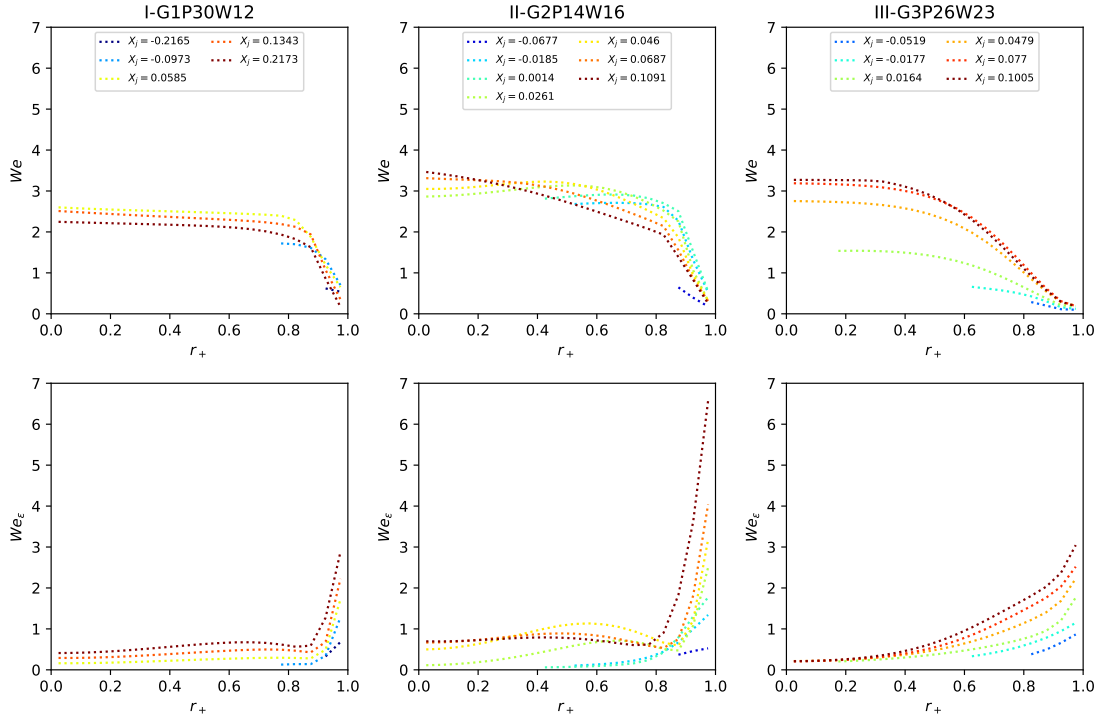


Figure 7.2: Weber numbers from DEBORA experiment simulations using the experimental diameters as input but without the virtual mass force. See equation 7.1 for definitions, figure 5.1 for void fraction comparison with the experiment and table 5.1 for simulation configurations. **Top row:** Weber numbers defined using the relative velocities. **Middle row:** Weber numbers defined using the turbulent velocity fluctuations at the scale of the bubbles.

The dimensionless distance between bubbles is plotted as a function of α_v in figure 7.3. $d_{dist} \simeq 1.5d_b$ for $\alpha_v = 0.06$, $d_{dist} \simeq d_b$ for $\alpha_v = 0.1$, and $d_{dist} \simeq 1/2d_b$ for $\alpha_v = 0.2$. For such void fractions many bubbles are almost touching each other. Figure 7.4 presents DNS results for periodic bubble swarms at $\alpha_v = 0.06$ from Cluzeau 2019 where this contact between bubbles is visible. $\alpha_v > 0.1$ in almost all of the DEBORA database (see figure 5.1). In flow boiling, bubble agitation and turbulence mean that they necessarily collide, which will also lead to bubble deformation.

I call *deformed bubble hypothesis* the hypothesis that in flow boiling in PWR conditions, bubbles are deformed, i.e. non-spherical, for $\alpha_v > 0.1$ by the combined effects of turbulence, drag and crowding. As this void fraction is easily achieved, I will consider in the rest of this work that bubbles are always deformed in pressurized water reactor flows.

Finally, the crowding that occurs for $\alpha_v > 0.1$ will have impacts on interfacial force and heat transfer correlations compared with the most commonly used forms based on measurements on single bubbles, though the means to quantify them are lacking.

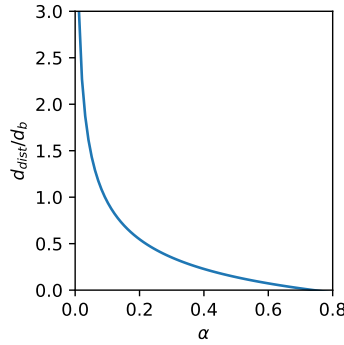


Figure 7.3: Distance between two spherical bubbles in a compact packing as a function of the void fraction.

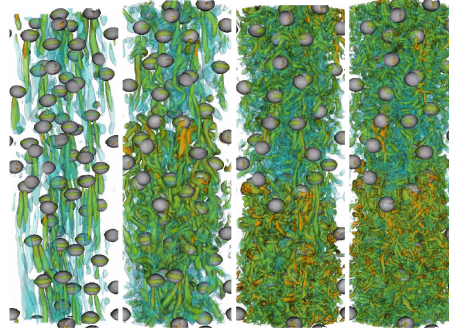


Figure 7.4: DNS of periodic bubble swarms with $\alpha_v = 0.06$. From left to right $Re_b \approx 100, 200, 400, 600$. Reproduced with permission from Cluzeau 2019.

7.3 Drag force

Bubble rise velocity increases with bubble diameter until the later becomes similar to the capillary length. It then becomes independent of the diameter as the bubbles deform (Clift et al. 2013). The drag force formulations most commonly used in the literature take this effect into account by having a drag coefficient that depends on the bubble Reynolds number and diameter. As shown by Sugrue 2017, when the bubbles are sufficiently deformed the air-water relative velocity becomes independent of the bubble diameter for all historical formulations (Ishii and Zuber 1979; Tomiyama et al. 1998; Bozzano and Dente 2001). The relative velocity for deformed bubbles is given by Ishii and Zuber 1979:

$$u_{r,IZdef} = \|\vec{u}_g - \vec{u}_l\| = \sqrt{2} \left(\frac{g\sigma(\rho_l - \rho_g)}{\rho_l^2} \right)^{1/4} \quad (7.4)$$

Figure 7.5 shows the rise velocity for Tomiyama et al. 1998 drag force, the deformed Ishii and Zuber 1979 formulation, and a modification of the latter: $\min(1, d_b/L_c) \cdot u_{r,IZdef}$. All 3 formulations are very similar for large diameters and the contaminated Tomiyama et al. 1998 relative velocity can be approached

by:

$$u_{r,Tcont} \approx \min(1, d_b/L_c) \cdot u_{r,IZdef} \quad (7.5)$$

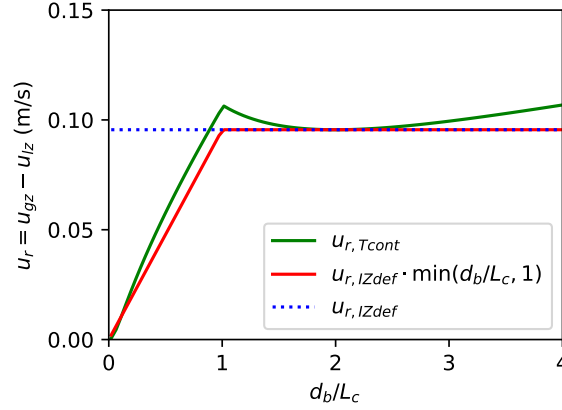


Figure 7.5: Bubble rise velocity for different drag formulations as a function of the dimensionless bubble diameter for 26 bar R12. All physical properties are taken at saturation temperature.

Ishii and Zuber 1979 also proposed a drag force formulation for deformed bubbles, that is equivalent to enforcing the bubble rise velocity given in equation 7.4. It is independent of the bubble diameter. This formulation will be used in the set of closures proposed here, as I consider that bubbles are systematically deformed in nuclear reactor conditions:

$$\begin{aligned} \vec{F}_{\text{drag}} &= -\frac{3}{4}C_D \frac{\alpha_v \rho_l}{d_b} \|\vec{u}_g - \vec{u}_l\| (\vec{u}_g - \vec{u}_l) \\ C_D &= \frac{2}{3} \frac{d_b}{L_c}, \quad L_c = \sqrt{\frac{\sigma}{g(\rho_l - \rho_v)}} \end{aligned} \quad (7.6)$$

As a sidenote, one can modify the expression of the Wobble number using this. Injecting $u_{r,IZdef} \cdot \min(d_b/L_c, 1)$ inside the formulation yields:

$$\begin{aligned} W_o &= \frac{(\rho_l - \rho_g) g d_b^2}{\sigma} \frac{k}{(u_{r,IZdef} \cdot \min(d_b/L_c, 1))^2} \\ &= \max(L_c/d_b, 1)^2 \frac{k}{u_{r,IZdef}^2} \end{aligned} \quad (7.7)$$

7.4 Lift force

The lift coefficient is positive for shear flow around a spherical bubble, and becomes negative for deformed bubbles (Legendre and Magnaudet 1998; Tomiyama et al. 2002; Sugrue 2017). Furthermore, as discussed in section 5.1, the void fraction profiles in the DEBORA experiment can only be explained by the presence of a negative lift coefficient in the 2-fluid model. In figure 5.1, the lift force seems to have an impact for $\alpha_v \gtrsim 0.3$. I therefore build a lift coefficient that is dependent on the void fraction, as the packing effect will increase bubble deformation. This approach is similar to the one of Yoon et al. 2017. It is equal to 0 up to $\alpha_v = 0.25$,

as there is no proof of the impact of lift on the flow in this region. I propose the following evolution for C_L . The coefficient drops linearly to a value of -0.2 , in-between the minimal values proposed by Tomiyama et al. 2002 (-0.25) and Sugrue 2017 (-0.15). It returns to 0 for very high void fractions for numerical stability. The $C_L(\alpha_v)$ function is plotted in figure 7.6, and the coefficient is worth:

$$C_L = \begin{cases} 0 & \text{if } \alpha_v < 0.25 \\ \max(-0.2, -0.7 \cdot (\alpha_v - 0.25)) & \text{if } 0.25 \leq \alpha_v < 0.7 \\ \alpha_v - 0.9 & \text{if } 0.7 \leq \alpha_v < 0.9 \\ 0 & \text{if } 0.9 \leq \alpha_v \end{cases} \quad (7.8)$$

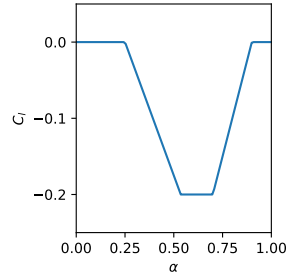


Figure 7.6: The lift coefficient proposed in this work as a function of the void fraction.

A comparison between the results of simulations using the Sugrue 2017 lift and the lift coefficient that I propose is presented in figure 7.7. Results are significantly improved on cases II-G2P14W16 and III-G3P26W23. However they are deteriorated for the higher thermodynamic qualities in I-G1P30W12. There is an inversion of the slope of $\alpha_v(r_+)$ when α_v becomes larger than ~ 0.3 , which is expected given that C_L becomes negative at $\alpha_v = 0.25$.

As this lift coefficient depends solely on the void fraction, the resulting lift coefficient is independent of the bubble diameter.

7.5 Turbulent dispersion force

In appendix D, I show using a series of simplifying hypotheses that the Burns turbulent dispersion amounts to considering the dispersed phase as a passive scalar. However, due to bubble cramming, the turbulent dispersion is expected to be larger at high void fractions, and increase with α_v .

Furthermore, it can be seen in the bottom row of figure 7.7 that in high-void fraction saturated situations the slope of the simulated void fraction distribution is larger than that of the experiment. This is apparent for $X_j = 0.1343$ and $X_j = 0.2173$ in test tube I, $X_j = 0.046$ and $X_j = 0.0687$ in test tube II and $X_j = 0.077$ in test tube III. In subcooled regions, this can be an issue with the condensation and heat flux partition.

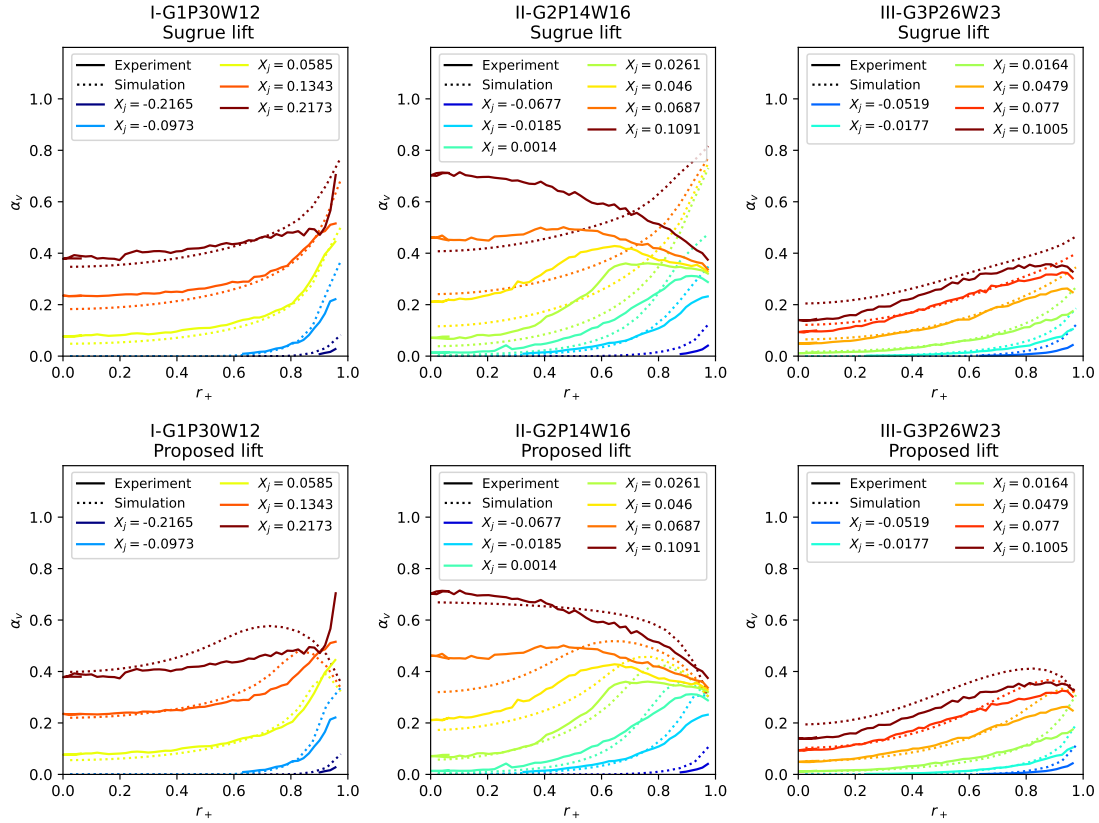


Figure 7.7: Comparison between the Sugrue 2017 lift coefficient (top row) and the one proposed here (equation 7.8, bottom row in this figure). Simulations are run using: no virtual mass, deformable Ishii and Zuber 1979 drag force, Burns et al. 2004 turbulent dispersion force, Kurul and Podowski 1990 heat flux partition and Ranz and Marshall 1952 interfacial heat transfer.

I therefore propose to keep the Burns et al. 2004 formulation at low void fractions and increase the turbulent dispersion coefficient when the void fraction increases. This yields the following formulation:

$$C_{TD} = \frac{1}{\max(0.1, 1 - \alpha_v)} C_{TD, \text{Burns}} \quad (7.9)$$

Figure 7.8 presents a comparison between a simulation with the Burns et al. 2004 turbulent dispersion force and the modified version that proposed here. Simulation results are improved, especially for high void fractions.

The Burns et al. 2004 turbulent dispersion coefficient contains a term in C_D/d_b (see equation 2.21). As the Ishii and Zuber 1979 deformed bubble drag coefficient is used, and as it contains d_b , the resulting turbulent dispersion force is independent of the bubble diameter. The set of momentum closures proposed in this thesis is therefore independent of d_b .

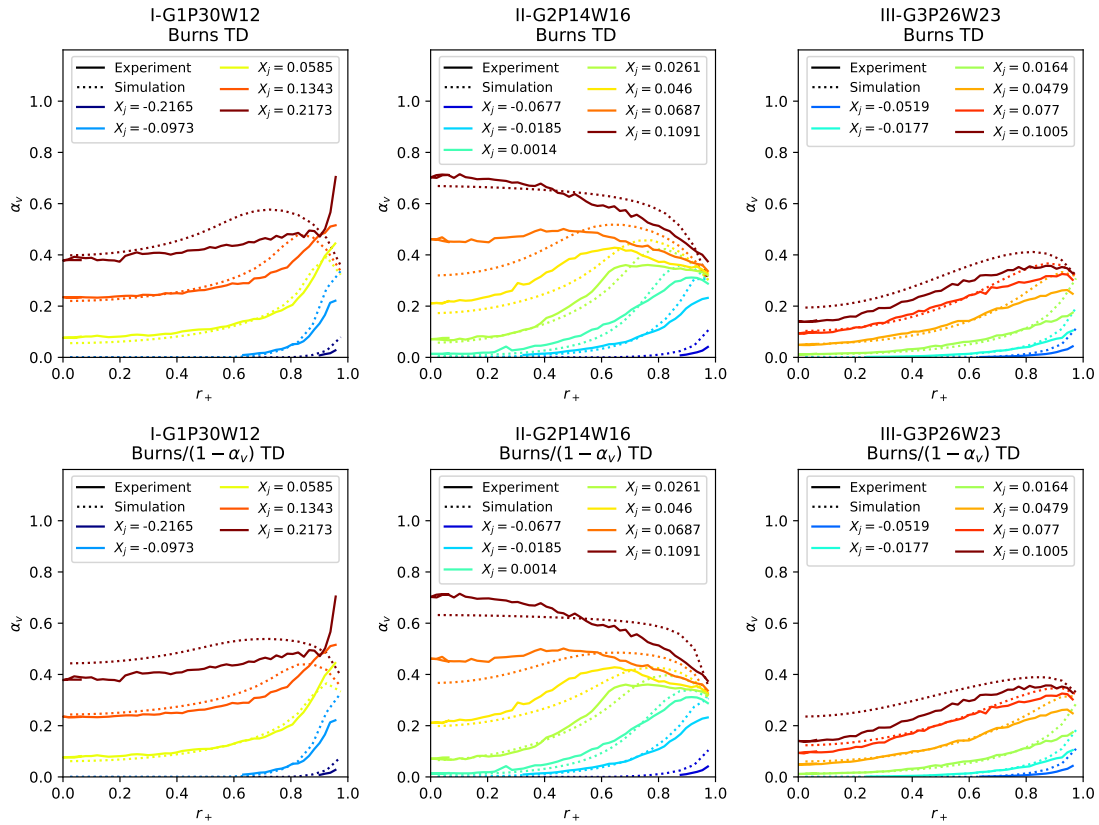


Figure 7.8: Comparison between the Burns et al. 2004 turbulent dispersion force and the one proposed here (equation 7.9, bottom row in this figure). Simulations are run using: no virtual mass, deformable Ishii and Zuber 1979 drag force, equation 7.8 lift force, Kurul and Podowski 1990 heat flux partition and Ranz and Marshall 1952 interfacial heat transfer.

7.6 Condensation

7.6.1 Formulating a condensation term that does not require bubble diameter modeling

We recall the general formulation of the condensation term from equation 2.24:

$$q_{ki} = a_i \frac{\lambda_l}{d_b} (T_g - T_l) Nu_b = \frac{6\alpha_v}{d_b} \frac{\lambda_l}{d_b} (T_g - T_l) Nu_b \quad (7.10)$$

All interfacial heat flux models proposed in the literature have this same aspect. The differences between the various formulations proposed in the literature lie only in the bubble Nusselt numbers. Nu_b is the most relevant quantity to compare models.

In high-void fraction flow boiling, bubbles are polydisperse, bump into each other, coalesce and break. These micro-scale mechanisms, which are not understood well enough to be modeled, impact the condensation and interfacial heat transfer terms.

None of the other closures proposed in this chapter require bubble diameter modeling through an interfacial area transport equation (Yao and Morel 2004) or population balance model (Krepper et al. 2008). I therefore aim to build a correlation that does not require bubble diameter modeling. In the DEBORA database, the measured bubble diameters were mostly close to the capillary length $L_c = \sqrt{\frac{\sigma}{g(\rho_l - \rho_v)}}$, and all of them were between $0.25L_c$ and $2L_c$. For test tubes I, II and III, L_c was 0.4, 0.65 and 0.45 mm (compare with figure 5.2 bottom line). In all three test tubes, $d_b < L_c$ if $T_s - T_l > 1$ K, i.e. in subcooled regions where condensation is non-negligible bubbles are smaller than L_c . The capillary length is therefore chosen as the bubble diameter length scale for the interfacial area evaluation ($a_i \sim 6\alpha_v/L_c$ in 7.10). This approach is used for bubbly-flow condensation in the system-scale codes RELAP-7 (Berry et al. 2018) and TRACE-5 (NRC 2010), widely used in the nuclear industry. When the distance between bubbles (equation 7.3) is larger than the capillary length, the latter is used as the characteristic temperature diffusion length (d_b in 7.10). When it is smaller, the former is used. This yields:

$$q_{ki} = \alpha_v Nu_{\text{fit}} \frac{6\lambda_l}{L_c^2} \frac{1}{\min\left(1, \sqrt[3]{\frac{\pi}{3\sqrt{2}} \frac{1}{\min(\alpha_v, 0.6)}} - 1\right)} (T_v - T_l) \quad (7.11)$$

With Nu_{fit} a fitted constant bubble Nusselt number. $Nu_{\text{fit}} = 30$ was found to be an optimal value on the DEBORA database by analyzing the condensation behavior in locations where the liquid was saturated in the near-wall region, i.e. where the heat flux partition no longer influenced the flow dynamics. $\frac{\pi}{3\sqrt{2}} \approx 0.74$. As the cubic root term in equation 7.11 goes to 1 as $\alpha_v \rightarrow \frac{\pi}{3\sqrt{2}}$, $\min(\alpha_v, 0.6)$ is included for numerical stability. When $\alpha_v = 0.6$, the heat transfer coefficient is multiplied by ~ 10 compared with low-volume fraction cases and in practice the liquid is at saturation temperature.

This correlation is not equivalent to using the capillary length as bubble diameter and using a Nusselt correlation from the literature. The intermediate quantity that is the bubble diameter is not fitted on any data. Only the total interfacial heat flux is. The interfacial heat flux can be correct with bubble diameters significantly larger or smaller than L_c .

This expression is compared to classical correlations from the literature: Ranz and Marshall 1952; Chen and Mayinger 1992; Zeitoun et al. 1995; Kim and Park 2011. As discussed in section 2.2, all of them are based on equation 7.10. The specificity of each correlation then lies in the Nusselt number formulation, that can depend on the Prandtl, bubble Reynolds or Jacob numbers:

$$\begin{aligned}
Nu_{\text{Ranz\&Marshall}} &= 2 + 0.6Re_b^{0.5}Pr^{0.33} \\
Nu_{\text{Chen\&Mayinger}} &= 0.185Re_b^{0.7}Pr^{0.5} \\
Nu_{\text{Zeitoun et al.}} &= 2.04Re_b^{0.61}\alpha^{0.328}Ja^{-0.308} \\
Nu_{\text{Kim\&Park}} &= 0.2575Re_b^{0.7}Ja^{-0.2043}Pr^{-0.4564}
\end{aligned} \tag{7.12}$$

Where $Ja = \frac{\rho_l C_{pl} \|T_{\text{sat}} - T_i\|}{\rho_g h_{lg}}$ is the Jacob number.

All these correlations contain the bubble Reynolds number, i.e. the bubble diameter and relative velocity. If the Tomiyama et al. 1998 drag formulation is used in a simulation as in the baseline set of closures, $u_{gz} - u_{lz} \propto d_b$ when $d_b \lesssim L_c$ and $u_{gz} - u_{lz}$ is independent of d_b when $d_b \gtrsim L_c$ (figure 7.5). Therefore, $Re_b \propto d_b^2$ when $d_b \lesssim L_c$ and $Re_b \propto d_b$ when $d_b \gtrsim L_c$. Table 7.1 compares the dependence of the interfacial heat flux on the bubble diameter for different correlations. The dependence on the bubble diameter remains, but is much less significant than $q_{ki} \propto d_b^{-2}$ that is visible in equation 7.10, particular in subcooled regions where $d_b < L_c$.

Reference	$d_b \lesssim L_c$	$d_b \gtrsim L_c$
Ranz and Marshall 1952	$q_{ki} \propto d_b^{-1}$	$q_{ki} \propto d_b^{-1.5}$
Chen and Mayinger 1992	$q_{ki} \propto d_b^{-0.6}$	$q_{ki} \propto d_b^{-1.3}$
Zeitoun et al. 1995	$q_{ki} \propto d_b^{-0.78}$	$q_{ki} \propto d_b^{-1.39}$
Kim and Park 2011	$q_{ki} \propto d_b^{-0.6}$	$q_{ki} \propto d_b^{-1.3}$
Current work	$q_{ki} \propto d_b^0$	$q_{ki} \propto d_b^0$

Table 7.1: Dependence of the interfacial heat transfer on the diameter for various correlations from the literature and for the current work.

The Nusselt as a function of the bubble diameter for different conditions is presented in the top row of figure 7.9. The inflection in the plots from the literature at $d_b \approx L_c$ come from the relative velocity becoming constant from this point. The bottom row contains the heat transfer coefficient compared to that of the Ranz and Marshall 1952 correlation. Correlations from the literature yield very different Nusselt numbers and heat transfer coefficients: the Zeitoun et al. 1995 expression can be five times higher than that of Ranz and Marshall 1952 or Kim and Park 2011, with the Chen and Mayinger 1992 correlation in the middle of the ballpark. The relative heat transfer of the proposed condensation compared with that of

Ranz and Marshall 1952 has an inflection at $d_b \approx L_c$, again as the relative velocity plateaus. In all conditions with R12, the proposed expression is in the inter-model uncertainty range.

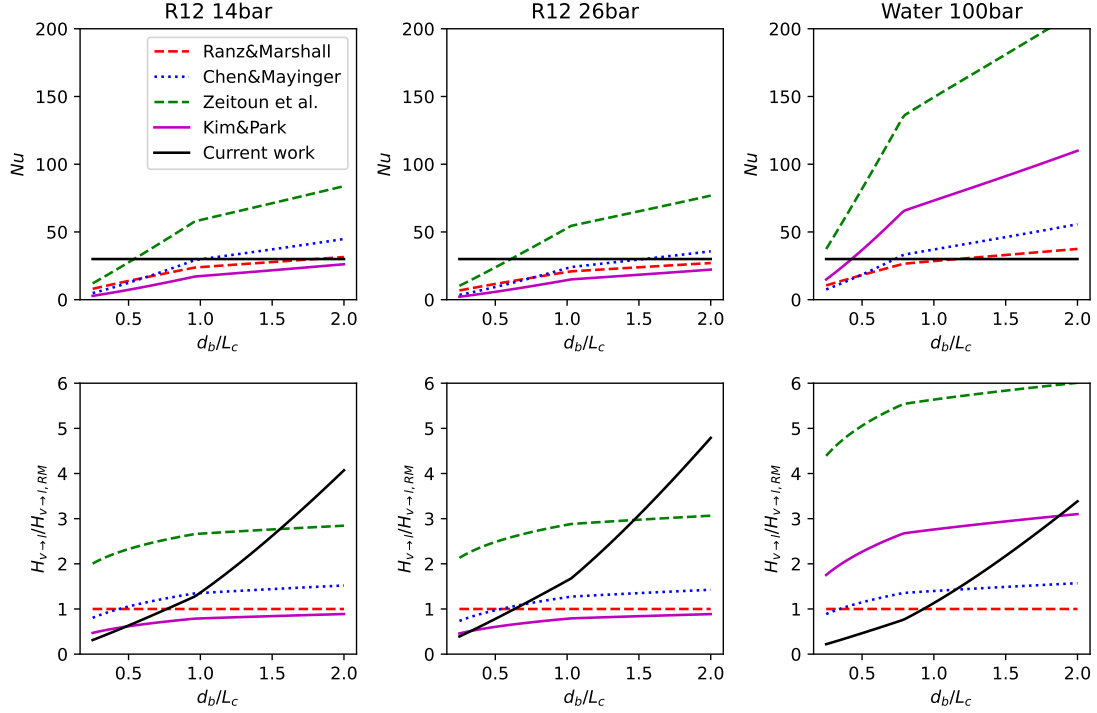


Figure 7.9: Comparison between different correlations used for interfacial condensation (Ranz and Marshall 1952, Chen and Mayinger 1992, Zeitoun et al. 1995, Kim and Park 2011 and current work). The relative velocity between the phases was chosen so that the contaminated Tomiyama et al. 1998 drag force compensates buoyancy. A 5 K subcooling and 0.1 void fraction were used for the Zeitoun et al. 1995 and Kim and Park 2011 formulations. **Top row:** Nusselt number as a function of the bubble diameter nondimensionalized by the capillary length. **Bottom row:** Heat transfer coefficient over Ranz and Marshall 1952 heat transfer coefficient (chosen as reference) for different correlations. **Left:** Results in the conditions of test tube II-G2P14W16, i.e. boiling water reactor similarity. **Center:** Results in the conditions of test tube III-G3P26W23, i.e. pressurized water reactor similarity. **Right:** Results for water at 100 bar.

For water the bubble Nusselt numbers from the literature are around two times larger than for R12. However, if $Nu_{\text{fit}} = 30$ is used for water then the heat transfer is lower than the correlations from the literature for $d_b > L_c$. This constant bubble Nusselt number may require adjustment to water flows in the future.

7.6.2 DEBORA Simulation result comparison with different energy closures

In order to compare the prediction of the thermal closure terms proposed in this thesis, i.e. the heat flux partition proposed in chapter 6 with Kurul and Podowski 1990 and the condensation proposed in section 7.6 with Kurul and Podowski 1990, simulations are run on low-void fraction conditions of the DEBORA database. The momentum closure terms already presented in this chapter are used, i.e.: no virtual mass, deformable Ishii and Zuber 1979 drag force, equation 7.8 lift force, and equation 7.9 turbulent dispersion force. The VDF numerical scheme and 2D axi-symmetric meshes that have 20 radial and 500 axial elements. The predicted void fractions and liquid temperatures are presented in figures 7.10 and 7.11 as a function of the dimensionless radius r_+ ($r_+ = 0$ at the center and $r_+ = 1$ at the wall). The three configurations presented are:

- Kurul and Podowski 1990 HFP and Ranz and Marshall 1952 condensation;
- The OSV-based HFP and Ranz and Marshall 1952 condensation;
- The OSV-based HFP and the proposed condensation (equation 7.11).

Heat flux partitions are compared first. The first three lines compare the experimental data (●) with the Kurul and Podowski 1990 and Ranz and Marshall 1952 models (—), and the OSV-based HFP and Ranz and Marshall 1952 (---), and the proposed HFP and condensation (■■■). For the lowest entrance temperatures (first row), the experimental void fraction at the wall is around 2%. The Kurul and Podowski 1990 model significantly over-predicts the void fraction for high subcoolings, as it sends a large part of the heat flux in the vapor phase (see figure 6.16). The OSV-based HFP, on the other hand, does not yet predict vapor formation, apart for case G2P26W16 (second column). For higher entrance temperatures (second and third rows), void fraction predictions are very satisfying, and closer to the experimental data than the Kurul and Podowski 1990 model. As the entrance temperature increases, the difference between the model proposed here and Kurul and Podowski 1990 decreases: the subcooling decreases and the OSV-based HFP sends more and more energy in the evaporation term. As $T_s - T_l$ keeps decreasing, the HFP will have less and less impact, and will no longer have any when $T_l = T_s$ in the first computation cell, where all of the energy will be used for evaporation. The bottom row contains liquid temperature predictions for both models, as well as liquid temperature measurements for runs G2P14W16 and G2P24W16 (first two columns). The liquid temperature is under predicted with the Kurul and Podowski 1990 model. With the OSV-based HFP, more energy is injected in the liquid and less in the vapor phase. This leads to higher liquid temperatures in the bulk, by up to 1C. The temperature prediction is significantly improved.

The proposed condensation model is now compared with that of Ranz and Marshall 1952. The former slightly larger void fractions, which is expected given the relative heat transfer coefficients shown in figure 7.9. The difference between

the two sets of models is very small, and insufficient on the DEBORA database to justify the use of an IATE or population balance model for diameter prediction with the added complexity and uncertainty that it warrants.

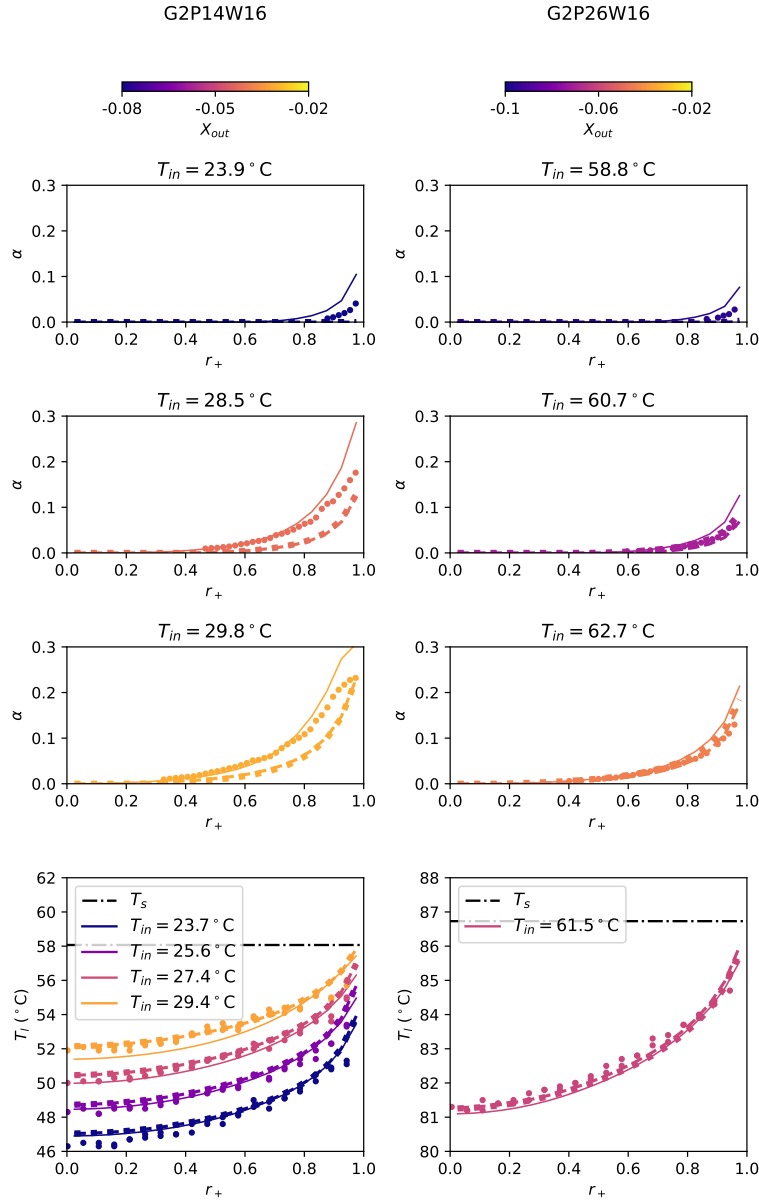


Figure 7.10: Comparison of local void fraction and liquid temperatures from DEBORA experimental data (\bullet) and TrioCFD simulations with the set of momentum closures proposed in this thesis and different heat and mass transfer closure terms: the baseline choice ($-$) (Kurul and Podowski 1990 and Ranz and Marshall 1952), an intermediate choice ($--$) (OSV HFP and Ranz and Marshall 1952) and the proposed closure terms (\blacksquare) (OSV HFP and equation 7.11). **Rows 1-3** present the experimental and simulated void fractions for the three coolest entrance temperatures for each test tube. **Bottom row:** simulated temperatures for each test tube. Though the entrance temperatures are different than for the void fraction data, they respect the same color scale. **Left column:** test tube G2P14W16, where $G = 2035 \text{ kg}/(\text{m}^2\text{s})$, $P = 14.59 \text{ bar}$ and $q_w = 73.9 \text{ kW}/\text{m}^2$. **Right column:** test tube G2P26W16, where $G = 2048 \text{ kg}/(\text{m}^2\text{s})$, $P = 26.15 \text{ bar}$ and $q_w = 73.9 \text{ kW}/\text{m}^2$.

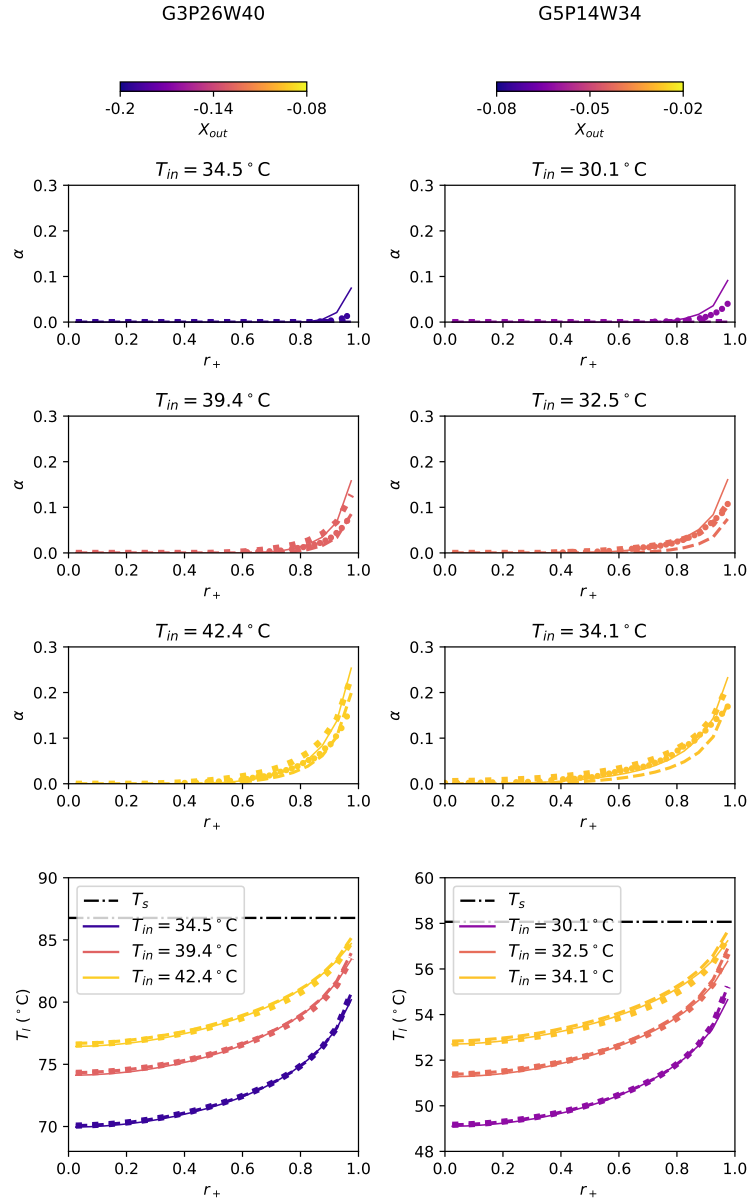


Figure 7.11: Comparison of local void fraction and liquid temperatures from DEBORA experimental data (●) and TrioCFD simulations with the set of momentum closures proposed in this thesis and different heat and mass transfer closure terms: the baseline choice (—) (Kurul and Podowski 1990 and Ranz and Marshall 1952), an intermediate choice (---) (OSV HFP and Ranz and Marshall 1952) and the proposed closure terms (⋯) (OSV HFP and equation 7.11). **Rows 1-3** present the experimental and simulated void fractions for the three coolest entrance temperatures for each test tube. **Bottom row:** simulated temperatures for each test tube. There is no liquid temperature available for these test tubes, therefore only simulated data is presented. **Left column:** test tube G3P26W40, where $G = 3050 \text{ kg}/(\text{m}^2\text{s})$, $P = 26.17 \text{ bar}$ and $q_w = 188.1 \text{ kW}/\text{m}^2$. **Right column:** test tube G5P14W34, where $G = 5077 \text{ kg}/(\text{m}^2\text{s})$, $P = 14.59 \text{ bar}$ and $q_w = 161.7 \text{ kW}/\text{m}^2$.

7.6.3 Condensation database

In the condensation correlations from the literature that are compared in section 7.6, the calculated Nusselt number is larger for water than for R12 (see figure 7.9). These clues indicate that the $Nu_b = 30$ coefficient calculated on the R12 DEBORA database is probably insufficient for condensation in water flows. A closer look into condensation in high-pressure water flows is taken in this section.

In order to separate the effect of the condensation from those of the heat flux partition, a possible experimental approach is to inject vapor in subcooled liquid and measure the downstream evolution of the flow, in particular void fraction and liquid temperature. This has been carried out by various groups (Bartolomei and Gorburov 1969; Lucas and Prasser 2007; Lucas et al. 2013). However, it is extremely difficult to simulate the injection in itself using two-fluid CFD because of the complex geometry. Lucas and Prasser 2007 and Lucas et al. 2013 overcome this difficulty by measuring all of the parameters required to set an entrance boundary condition in a CFD simulation. However, this still does not exactly represent flow boiling configurations, in particular the liquid temperature and void fraction radial distributions.

The ideal experiment to isolate condensation is a heated pipe with local void fraction measurements downstream of the end of this pipe. To the best of my knowledge, no such measurements are available in the literature for high-pressure water flows. However, Mimouni et al. 2017 and Ustinenko et al. 2008 have run CFD simulations for code validation on experiments where the average void fraction on the cross-section of the pipe was measured downstream of the heated length, for three test conditions. Avdeev and Pekhterev 1986 simulated condensation in high-pressure boiling water for 45 test conditions after heated sections from three different experimental sources. I collected the data and test conditions from these sources: Bartolomei et al. 1980, Zakharova et al. 1984 and Labuntsov et al. 1976. The range of conditions covered in these experiments can be found in table 7.2.

Source	G	P	q_w	D_h
Bartolomei et al. 1980	1000-2000 kg/(m ² s)	68.9-108 bar	800-1200 kW/m ²	12.03 mm
Zakharova et al. 1984	~800 kg/(m ² s)	30-70 bar	600 kW/m ²	30 mm
Labuntsov et al. 1976	370-2960 kg/(m ² s)	20-100 bar	600-1200 kW/m ²	12.1 mm

Table 7.2: Experimental range of the data used by Avdeev and Pekhterev 1986. The precise conditions of each run are given in figures 7.12 and 7.13 along with the experimental results.

Simulations are run on this database with the OSV-based heat flux partition and different Nusselt numbers between 30 and 90. The set of momentum closures employed is the same as in section 7.6.2. The VDF numerical scheme with an axisymmetric mesh is used. The number of radial elements is calibrated so all elements have the same width and the $y_{+,1} > 100$ criterion in the first element is respected. It therefore depends on the mass flux of each test. The number of axial elements is adjusted so that their aspect ratio in the flow is 10 in the inlet section and 5 in and downstream of the heated section. The length of the non-heated inlet region

is adjusted so that $z/D_h > 50$, and the heated length and downstream length depend of the experimental conditions. The mean average error on the void fraction prediction was minimized for $Nu_b = 65$. Simulation results for $Nu_b = 30$, the optimal value on the DEBORA database, and $Nu_b = 65$, can be found in figures 7.12 and 7.13. The quality of the void fraction predictions varies over the database.

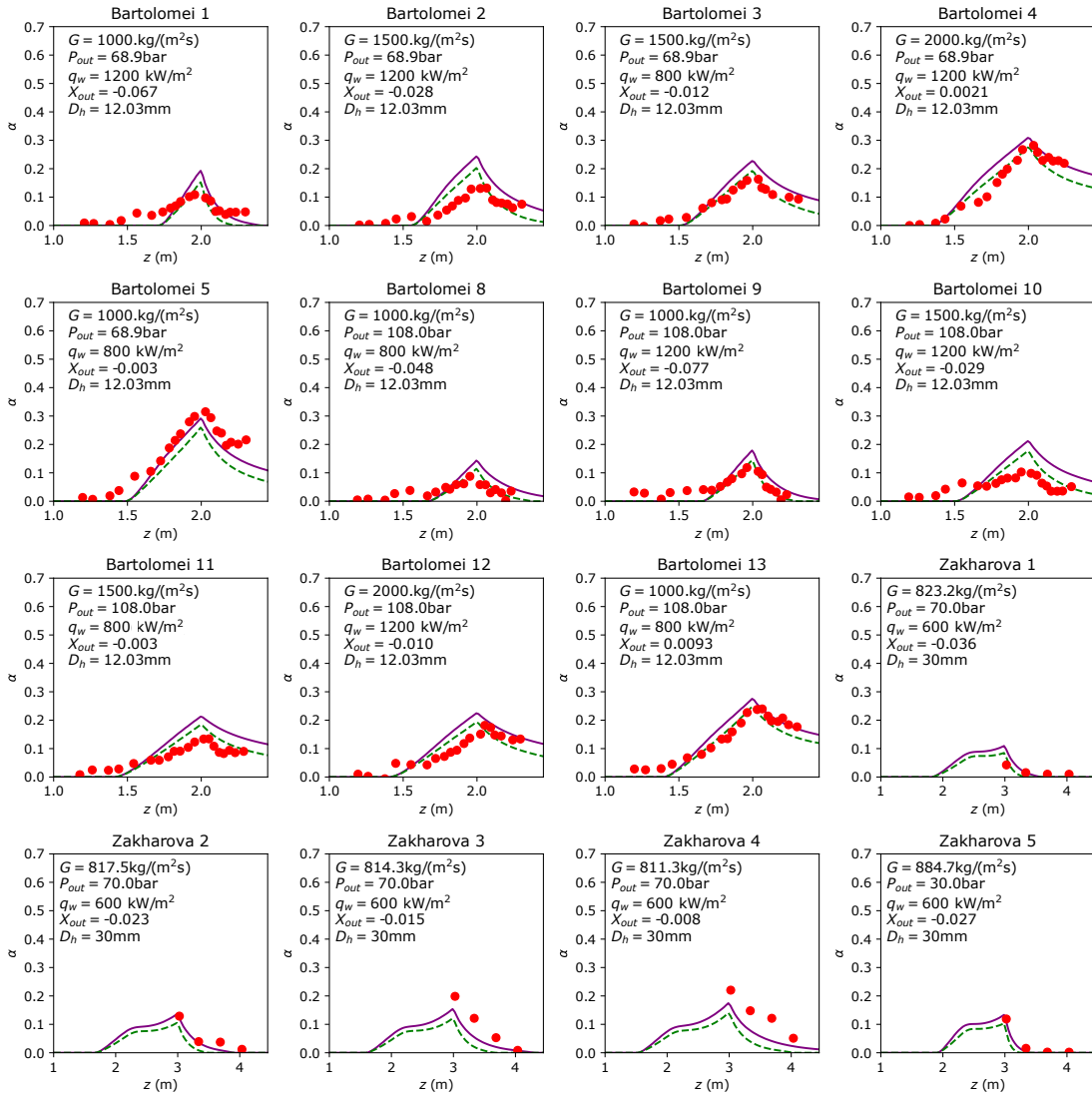


Figure 7.12: Comparison of average void fraction in condensing bubbly flow for experimental data (●) and TrioCFD simulations. The models used are the ones built in chapters 7 and 6, with $Nu_b = 30$ (—) and $Nu_b = 65$ (---). The data is from Bartolomei et al. 1980 and Zakharova et al. 1984, with the same run numbers as in Avdeev and Pekhterev 1986.

In figures 7.12 and 7.13, the condensation rate does not clearly double between $Nu_b = 30$ and $Nu_b = 65$. This would be the case if a system or a component-scale code was considered (section 1.2.2). However, with TrioCFD simulations are run with at a local scale with significant void fraction and temperature differences along

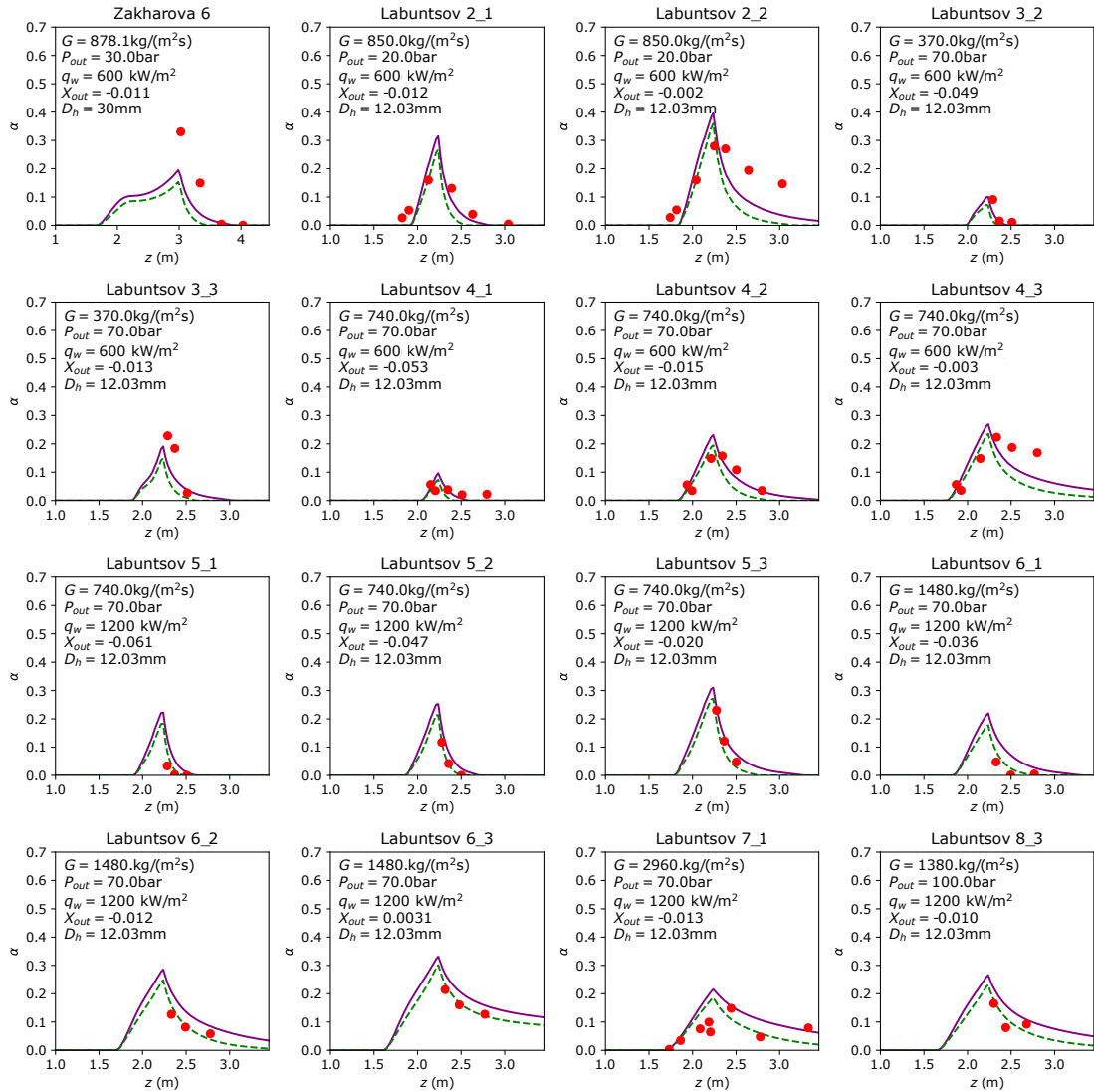


Figure 7.13: Comparison of average void fraction in condensing bubbly flow for experimental data (●) and TrioCFD simulations. The models used are the ones built in chapters 7 and 6, with $Nu_b = 30$ (—) and $Nu_b = 65$ (---). The data is from Zakharova et al. 1984 and Labuntsov et al. 1976, with the same run numbers as in Avdeev and Pekhterev 1986.

the radius of the pipe. The condensation rate is proportional to the void fraction and the subcooling. The subcooling is maximal in the core and the void fraction in the near-wall region. The condensation rates depend on how these quantities are radially distributed and it is difficult to predict exactly how increasing the Nusselt number will impact the flow, hence the possibly counter-intuitive behavior.

Access to specific condensation data for other fluids is not available, in particular for other refrigerant fluids like R22, R113 or R134A that can be used to mimic the behavior of water like R12 (Staub et al. 1969, Roy et al. 2002, François et al. 2021). As these freon-based fluids have physical properties that are close to those of R12,

$Nu_b = 30$ determined on the DEBORA database is selected to simulate them. This yields the final Nusselt numbers used in this thesis.

$$\begin{aligned} Nu_{b,\text{freon}} &= 30 \\ Nu_{b,\text{H}_2\text{O}} &= 65 \end{aligned} \tag{7.13}$$

7.6.4 Bartolomei simulation result comparison

The Bartolomei and Chanturiya 1967 and Bartolomei et al. 1982 experiments consist the measure of the average void fraction for as a function of the thermodynamic quality for 32 test tubes. These are part of the OSV database (see section 6.2.2). The test tube diameters, outlet pressures, mass fluxes and heat fluxes are varied. They are extensively used in the literature for CFD code validation (Shaver and Podowski 2015b; Colombo et al. 2019). The test conditions are given in table 7.3. The numbering of the test tubes is arbitrary as no test tube numbers were proposed in the original papers.

The same set of closures as in section 7.6.3 is used, with the VDF numerical scheme and 2D axi-symmetric meshes that have 20 radial and 350 axial elements. In order to show the impact of the heat flux partition and the condensation Nusselt number on the flow, simulations are run in three different conditions: with a Kurul and Podowski 1990 heat flux partition and $Nu_b = 30$, with the heat flux partition proposed in chapter 6 and $Nu_b = 30$ and with the OSV-based HFP and $Nu_b = 65$. Results are presented in figures 7.14 and 7.15.

Quantity	Range
Tube diameter	12, 15.4 and 24 mm
Pressure	15, 30, 45, 70, 110 and 150 bar
Mass flux	$\sim 450, 950, 1500$ and $2000 \text{ kg}/(\text{m}^2\text{s})$
Heat flux	380-2000 kW/m^2

Table 7.3: Range of the conditions for the test tubes in the Bartolomei and Chanturiya 1967 and Bartolomei et al. 1982 experiments.

The OSV predicted by the Kurul and Podowski 1990 model occurs too early. The simulated void fraction at the experimental OSV is extremely high, around 10% in most cases. The OSV-based HFP predicts an OSV that is coherent with the experimental results, greatly improving the simulations compared with the Kurul and Podowski 1990 model.

The void fraction predictions with the OSV-based HFP and with $Nu_b = 65$ are satisfying, and better than with $Nu_b = 30$. This validates this value for the bubble Nusselt number in water flows.

After the OSV in most cases the void fraction increases slightly faster with the proposed HFP than in the experiments. This could be an issue with the HFP: if the presence of a departed bubble layer increases the efficiency of the heat transfer towards the liquid, then the use of $H_{i,\text{OSV}}$ (equation 6.20) as the liquid heat transfer coefficient underestimates the transfer towards the liquid and overestimates vapor production. Other terms could be the cause of this discrepancy: the condensation term could be insufficient in the bulk, though it was calibrated on separate condensation experiments; a too low turbulent dispersion or lift force could prevent enough vapor from reaching the very subcooled regions near the core.

For high thermodynamic qualities, once all of the liquid has reached saturation temperature, all simulations converge to the same result.

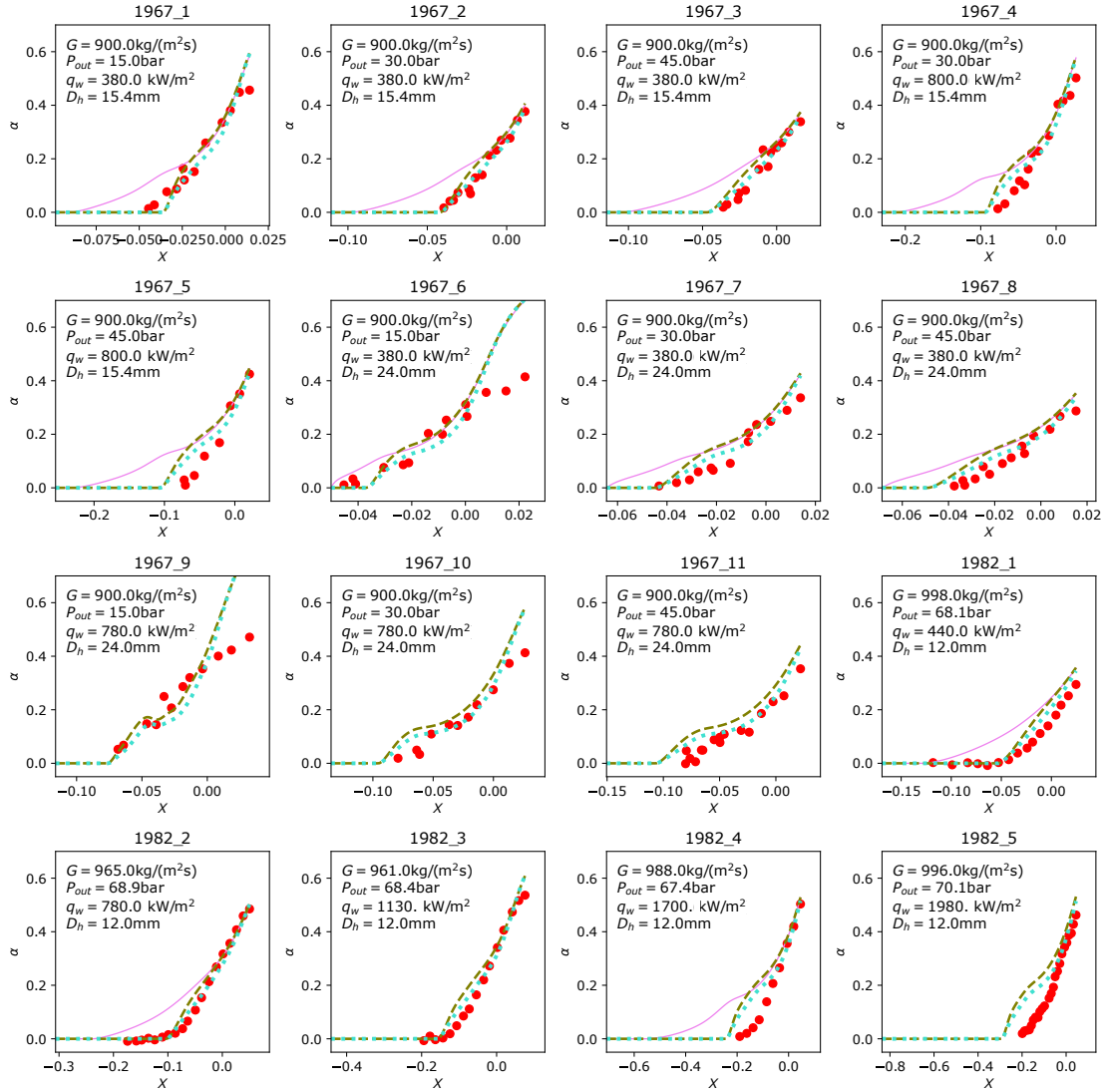


Figure 7.14: Comparison between the Bartolomei and Chanturiya 1967 and Bartolomei et al. 1982 experiments (●) and CFD simulations with three sets of closures: the Kurul and Podowski 1990 HFP with $Nu_b = 30$ (—), the OSV-based HFP with $Nu_b = 30$ (---) and the OSV-based HFP with $Nu_b = 65$ (---). Each box represents a different test tube. The simulation conditions are given in the legend.

The three test tubes in which the simulation is furthest from the experimental results are 1967_1, 1967_6 and 1967_9. These are all at only 15 bar outlet pressure. The test tubes at 30 bar also present some discrepancy in the outlet region. The set of closures built in this thesis is based on the DEBORA database, which is in similarity with water flows between 70 bar and 170 bar. It is therefore unsurprising to observe such behaviors. As test tubes at 45 bar are well predicted, for now the proposed set of models is therefore only valid in high-pressure flows with $P > 45$ bar.

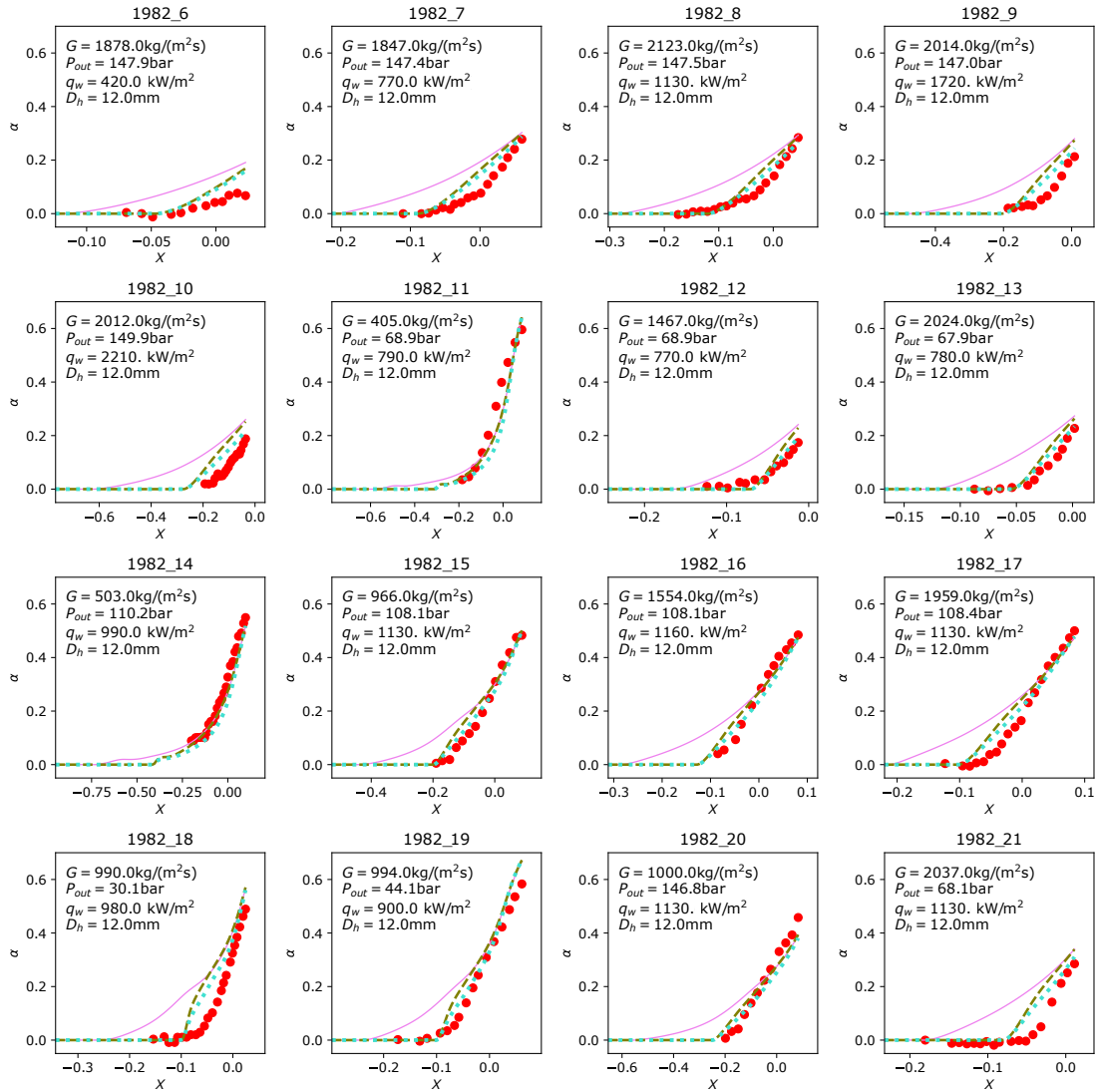


Figure 7.15: Comparison between the Bartolomei et al. 1982 experiments (●) and CFD simulations with three sets of closures: the Kurul and Podowski 1990 HFP with $Nu_b = 30$ (—), the OSV-based HFP with $Nu_b = 30$ (---), and the OSV-based HFP with $Nu_b = 65$ (⋯). Each box represents a different test tube. The simulation conditions are given in the legend.

7.7 Complete model

Table 7.4 compares the different closure terms of the baseline model with this thesis' proposal. The expressions of the terms in the current proposal are more simple than those of the baseline set of closures. Furthermore, no bubble diameter modeling by an interfacial area transport equation or population balance model is required.

This approach makes the numerical implementation of such a set of closures easier. More importantly, it significantly simplifies the interpretation of the results from a multiphase CFD simulation. Each individual term is easier to read and understand. Furthermore, there is less retroaction between terms than in the baseline set of closures. This eases the understanding the root cause of discrepancies between experimental and simulated results, reduces the risk of error compensation and makes it possible to iteratively improve this set of models.

Having no explicit dependency on the bubble diameter may seem surprising for a CFD-scale code. To the best of my knowledge, no such approach has been proposed for a boiling flow. However, it is common in subchannel and system codes in the nuclear industry: RELAP (Berry et al. 2018), TRACE (NRC 2010), CTF (Salko Jr et al. 2023) or CATHARE-3 (Emonot et al. 2011) can be used to simulate boiling flows and do not use an interfacial area transport equation in this regime.

Figure 7.16 presents the links between the unknowns and the major terms for the proposal of the current work (full boxes and lines) and the standard approach (all boxes and lines) used by Favre et al. 2022, Alatrash et al. 2022, Pham et al. 2023 and Vlček and Sato 2023 for example. The dashed boxes and terms are links that are no longer present in the set of closures proposed in this thesis. Though the system of equations solved is greatly simplified, it remains relatively complex.

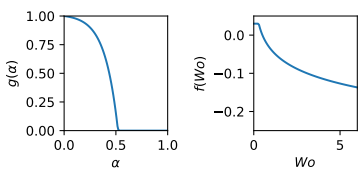
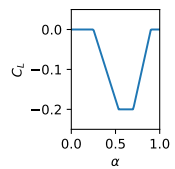
Term	Baseline closure	Current proposal
Drag	Tomiyama et al. 1998 $C_D = \max\left(\frac{24}{Re_b}(1 + 0.15Re_b^{0.687}), \frac{8Eo}{3Eo+12}\right)$	Ishii and Zuber 1979 deformable bubble $C_D = \frac{2}{3}d_b\sqrt{\frac{g(\rho_l-\rho_v)}{\sigma}}$
Lift	Sugrue 2017 $C_L = f(Wo) \cdot g(\alpha_v)$ 	Current work 
TD	Burns et al. 2004 $C_{TD} = \frac{3}{4}\frac{C_D}{d_b} \vec{u}_g - \vec{u}_l \frac{1}{w} \left(1 + \frac{\alpha_v}{\alpha_l}\right)$	Modified Burns et al. 2004 $C_{TD} = \frac{C_{TD,Burns}}{\max(0.1, 1-\alpha_v)}$
VM	Zuber 1964 adapted in current work $C_{VM} = \min\left(\frac{1}{2}\alpha_g, \frac{1}{2}\alpha_l\right)$	$C_{VM} = 0$
HFP	Kurul and Podowski 1990 $q_{SP} = (T_w - T_l(y)) \frac{\rho_l C_{pl} u_\tau}{\Theta_+^w(y_+)}$ $N_s = (210(T_w - T_s))^{1.8}$ $d_{b, \det} = 10^{-4} \cdot (T_w - T_s) + 0.0014$ $f_{dep} = \sqrt{\frac{4}{3} \frac{g(\rho_l - \rho_g)}{\rho_l d_{b, \det}}}$ $A_b = \min(1, \pi/4 \cdot N_s d_{b, \det}^2)$ $q_c = (1 - A_b) q_{SP}$ $q_q = 2A_b \lambda_l (T_w - T_l) \sqrt{\frac{f_{dep} \rho_l C_{pl}}{\pi \lambda_l}}$ $q_{wl} = q_c + q_q$ $q_{w, l \rightarrow v} = \frac{\pi}{6} f_{dep} d_{b, \det}^3 \rho_g h_l g N_s$ $q_w = q_c + q_q + q_{w, l \rightarrow v}$	Current work $q_{SP} = (T_w - T_l(y)) \frac{\rho_l C_{pl} u_\tau}{\Theta_+^w(y_+)}$ $q_{Boil} = \left(\frac{T_w - T_s}{22.65} \exp(P/87)\right)^2$ $q_{l, OSV} = \max\left(0, \frac{\rho_l C_{pl} u_\tau (T_s - T_l(y))}{2.12 \log(y_+) - 7}\right)$ $q_w = \max(q_{SP}, q_{Boil})$ $q_l = \min(q_w, q_{l, OSV})$ $q_{w, l \rightarrow v} = q_w - q_l$
Cond	Ranz and Marshall 1952 $q_{ki} = \frac{6\alpha_v \lambda_l (T_g - T_l)}{d_b^2} \left(2 + 0.6Re_b^{1/2} Pr^{1/3}\right)$	Current work $q_{ki} = \frac{6\alpha_v Nu_b \lambda_l g(\rho_l - \rho_v)(T_g - T_l)}{\sigma \min\left(1, \sqrt[3]{\frac{\pi}{3\sqrt{2}} \min(\alpha_v, 0.6)^{-1}}\right)}$ $Nu_{b, \text{freon}} = 30$ $Nu_{b, \text{H}_2\text{O}} = 65$

Table 7.4: Comparison of the closures from the baseline set of models with the proposed set of closures. *TD*: turbulent dispersion. *VM*: virtual mass. *HFP*: heat flux partition. *Cond*: condensation.

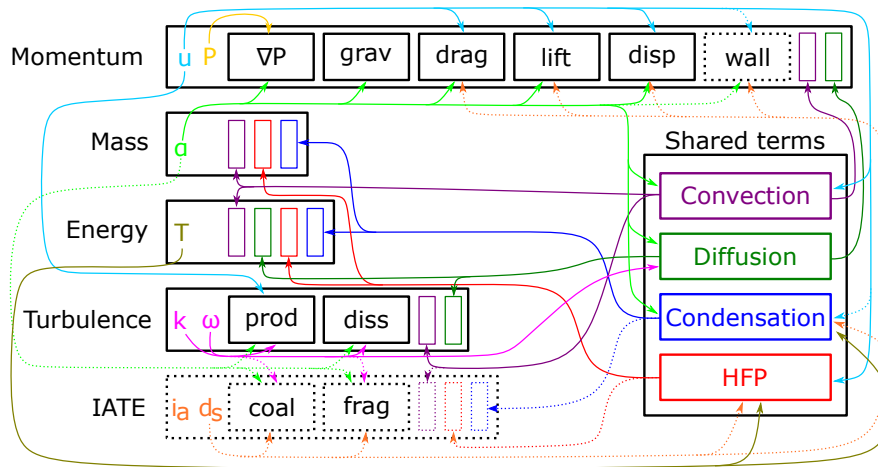
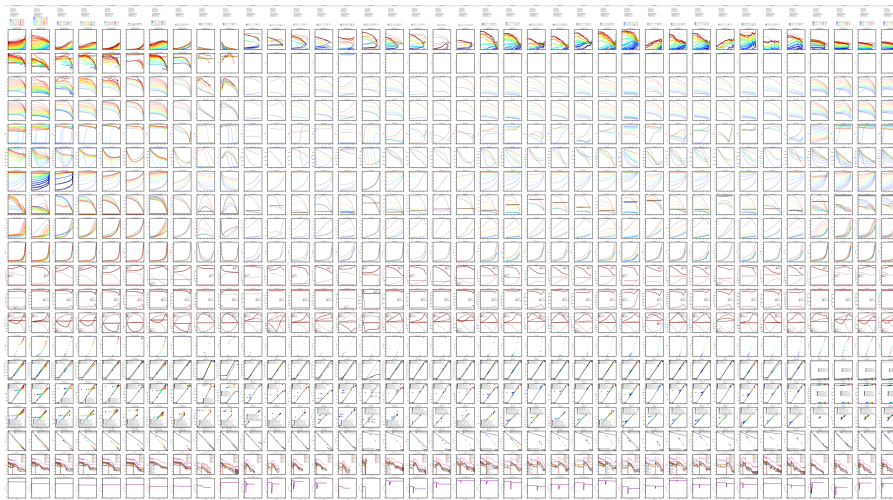


Figure 7.16: Comparison of the links between major terms and unknowns for the current work (full boxes and lines) and standard approaches (all boxes and lines; Favre et al. 2022; Alatrash et al. 2022; Pham et al. 2023; Vlček and Sato 2023). Each box aligned on the left represents a conservation equation. Each equation has unknowns, specific source terms, and terms that are shared between multiple equations. The latter are given in the box to the right. Each arrow represents an input from an unknown or a generic source term to an equation or a source term. For readability, the physical properties of the fluids are not represented in the figure, but they play a key role in all terms and are functions of the temperature and pressure. *grav* the gravity, *disp* the turbulent dispersion force, *prod* and *diss* the turbulence production and dissipation terms and *coal* and *frag* the bubble coalescence and fragmentation terms.

CHAPTER 8



The most natural way to visualize simulation results on a large database.

Simulations on the extended local database

This chapter compares the set of closure relations proposed in chapters 6 and 7 with an extended high-pressure validation database built during this thesis. In addition to the DEBORA runs, void fraction profiles were collected from St.-Pierre 1965, Staub et al. 1969, Martin 1969 and Chu et al. 2017. The multiple geometries and flow conditions covered by the experimental databases supports the applicability of the proposed set of closures to PWR conditions.

For clarity, only parts of each database are presented and discussed in this chapter. The complete simulation results with the minimalistic set of closures are shown in appendix F. I present at the end of this chapter a list of databases that I did not have the time to include in this thesis.

Contents

8.1	Building a large local high-pressure database	149
8.2	DEBORA	152
8.3	Saint-Pierre	156
8.4	Staub et al.	159
8.5	Martin	164
8.6	Chu et al.	170
8.7	Strengths and limits of the proposed set of closures	174
8.8	Other databases that can be used for multi-phase CFD validation	175

8.1 Building a large local high-pressure database

Pressurized water reactor subchannels can be seen as the combination of 3 different elementary shapes (see figure 8.1):

- A tube, in the center of a subchannel, that has a maximum velocity in its center (blue disk in figure 8.1).
- An annulus, around a rod, in which there is more space for the vapor to escape than the heating surface (green annulus in figure 8.1).
- A 3 mm-wide rectangular channel, between two rods, which is a very confined space where the flow is slowest (red rectangle in figure 8.1).

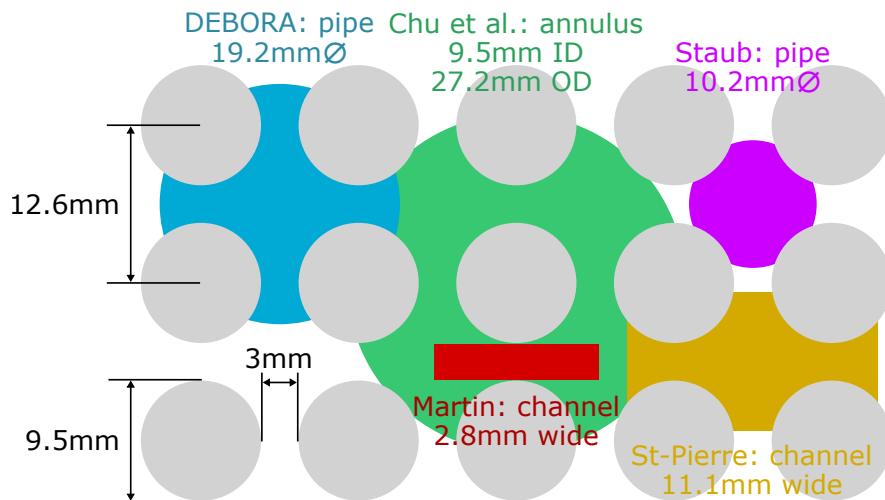


Figure 8.1: Diagram of a pressurized water reactor subchannel (fuel rods are in grey) and dimensions of the different experiments used for validation of CFD codes.

This chapter begins with a partial validation of the proposed set of closures, shown in table 7.4, in the tube geometry of the DEBORA database (section 8.2). However, validation is required for the two other elementary geometries, in high-pressure conditions. I believe that in order to simulate correctly a PWR or BWR rod bundle, one must be able to simulate all three of these shapes.

In addition to the DEBORA database, I found four boiling-flow sources in the literature that propose such data. Their cross-section geometries are included in figure 8.1. Simulation results for each of these sources will be presented in a separate section:

- The oldest database of this type is from St.-Pierre 1965 (section 8.3, gold rectangle). X-ray attenuation measurements were performed in a water-filled 11.2 mm-wide channel at different heights. The pressures are up to 50 bar, not as high as in reactors but non-negligible. Flow conditions are slow.

- Staub et al. 1969 used X-ray attenuation at BWR pressures on a cylindrical test section (section 8.4, magenta disk). The chordal void fraction, and not the local void fraction, is measured and the data quite noisy. They carried out similar experiments with R22 refrigerant fluid, going at PWR-similarity pressures.
- Martin 1969 performed X-ray attenuation measurements in water-filled boiling 2 mm and 2.8 mm- wide channels at BWR and PWR pressures (section 8.5, red rectangle). He measured the average void fraction along the width of the channel for different inlet temperatures and conditions, building test tubes.
- The Chu et al. 2017 experiments (section 8.6, green annulus) are relatively recent experimental results in a R134A annular channel, in which they were able to change the altitude of measuring plane. Void fractions, gas velocities and bubble diameters were measured using optical probes.

Though it is publicly available, the data from St.-Pierre 1965, Staub et al. 1969 and Martin 1969 are seldom used in the literature. I believe that this is due to the fact that when these experiments took place, CFD-scale codes were not available due to computational limitations. Only section-averaged codes had begun to appear. Therefore, the data that was most valuable for modeling was averaged, and local data is only found in the appendix of these reports. Some authors, like Marchaterre et al. 1960, did not even include the local data they measured in their appendix, and one cannot use it for CFD code validation.

Figure 8.2 shows the Reynolds and Boiling numbers for every test tube in the five databases. Values for PWR's and BWR's in operating conditions and reactivity induced transients from NEA 2022 are also included. Real-life incidents depend on multiple parameters like the fuel burnup, the reactor power at the moment of the accident or the rod location in the core. The values selected for reactors are indicative and can vary significantly from one configuration to another.

The experimental database built in this thesis covers well BWR steady-state and incidental operating conditions in multiple geometries. For PWR's however it does not cover the highest transient heat fluxes in hot zero power rod ejection accidents in terms of boiling number.

In the following sections, simulation results that use the set of closure laws from section 7.7 are presented. The VDF numerical scheme is used, with an axisymmetric for annular and round cross-sections and in 2D for rectangular channels. The number of radial elements is calibrated so all elements have the same width and the $y_{+,1} > 100$ criterion in the first element is respected. It therefore depends on the mass flux of each test tube. The maximum number of radial elements is set at 20 and the minimum at 5. The number of axial elements is adjusted so that each element is 5 mm long for the St.-Pierre 1965, Staub et al. 1969 and Martin 1969 simulations, and 10 mm long for DEBORA and Chu et al. 2017 simulations.

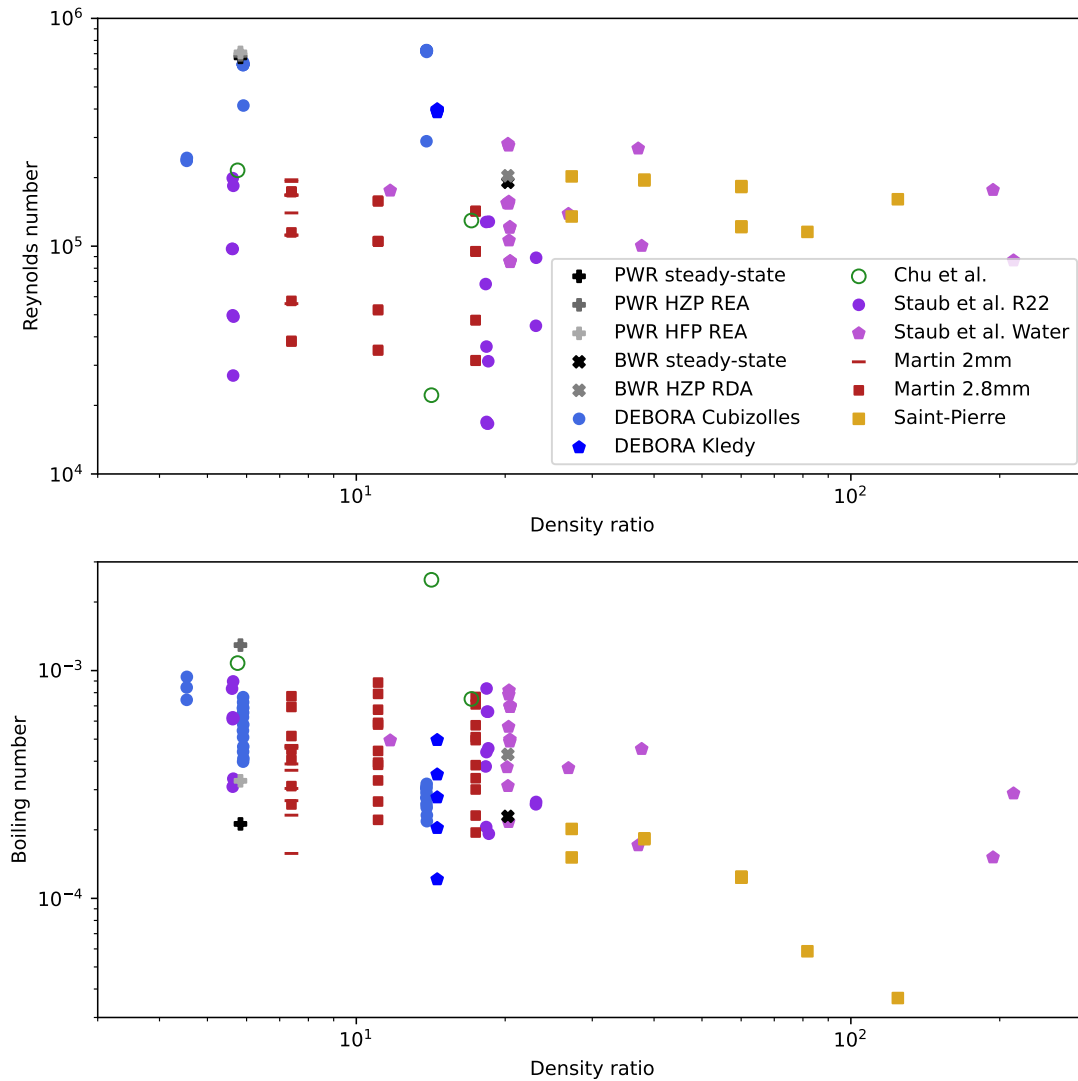


Figure 8.2: Dimensionless numbers for each test tube in the high-pressure CFD-grade database. **Top:** Reynolds number as a function of density ratio ρ_l/ρ_v . **Bottom:** Boiling number as a function of density ratio. The conditions for every test tube can be found in tables 4.2, 4.3, 8.1, 8.2, 8.3, 8.4, 8.5 and 8.6. HZP REA: Hot Zero Power Rod Ejection Accident. CZP REA: Cold Zero Power Rod Ejection Accident. HZP RDA: Hot Zero Power Rod Drop Accident. The characteristic heat fluxes chosen for reactor conditions are the following: PWR steady-state: 800 kW/m². PWR HZP REA: 5000 kW/m². PWR HFP REA: 1300 kW/m². BWR steady-state: 500 kW/m². BWR HZP RDA: 1000 kW/m².

8.2 DEBORA

The three test tubes from the DEBORA database that were investigated closely in chapters 5 and 7 are simulated first. Their conditions are shown in table 5.1. Void fraction results are shown in figure 8.3, and detailed results are shown for test tube II-G2P14W16 in figure 8.4.

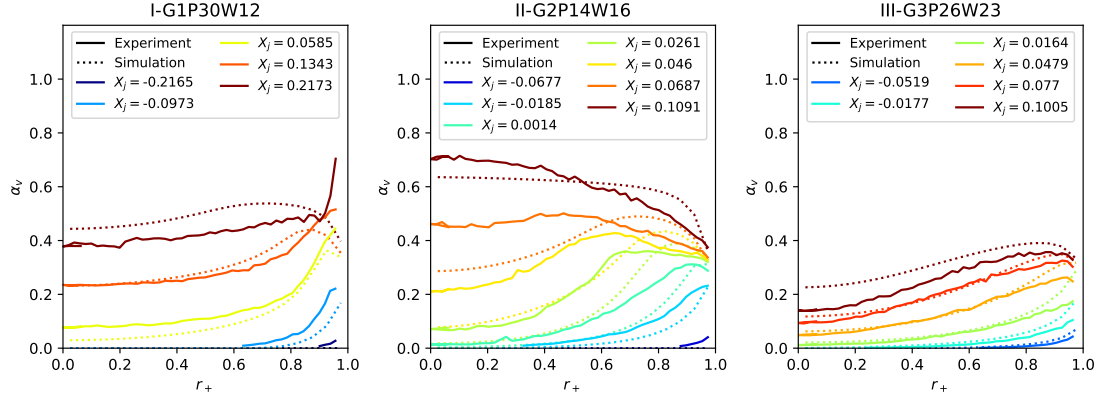


Figure 8.3: Void fraction simulation results on three test tubes from the DEBORA database for the set of closures proposed in this paper. The conditions of the runs are given in table 5.1. Compare with figure 5.1 that uses the baseline set of closures.

The simulation predictions are improved compared to the baseline model for test tubes II and III, and are of a similar quality for test tube I, despite the fact that the experimental diameter is no longer used to close the system of equations. In particular, the void fraction predictions are improved in the near-wall region. This region is critical for the prediction of the critical heat flux with CFD codes (Mimouni et al. 2016a).

The detailed predictions for test tube II-G2P14W16 can be compared with figure 5.2. The liquid temperature and gas velocity predictions are improved (figure 8.4 upper right and center left). The lift force is significantly larger in the radial force balance than in the baseline closure (figure 8.4 lower right). It pulls bubbles towards the center of the pipe, and is opposed to the drag and turbulent dispersion forces. The simulated radial vapor velocities are therefore much closer to those interpolated in section 4.5. The radial forces are much stronger than in the baseline set of closures (compare with figure 5.2 lower right).

Simulation results for the six test tubes simulated in figure 5.3 are shown in figure 8.5, that can be compared with figure 5.3. Results for cases G2P26W16 and G5P14W29 are of similar precision as with the baseline set of models, with much simpler closure laws. Predictions for the four other test tubes are significantly improved, particularly at low void fraction where α_v is no longer overestimated in the near-wall region. The OSV-based heat flux partition is probably the key reason for this improvement. These results are in line with those of figure 8.3.

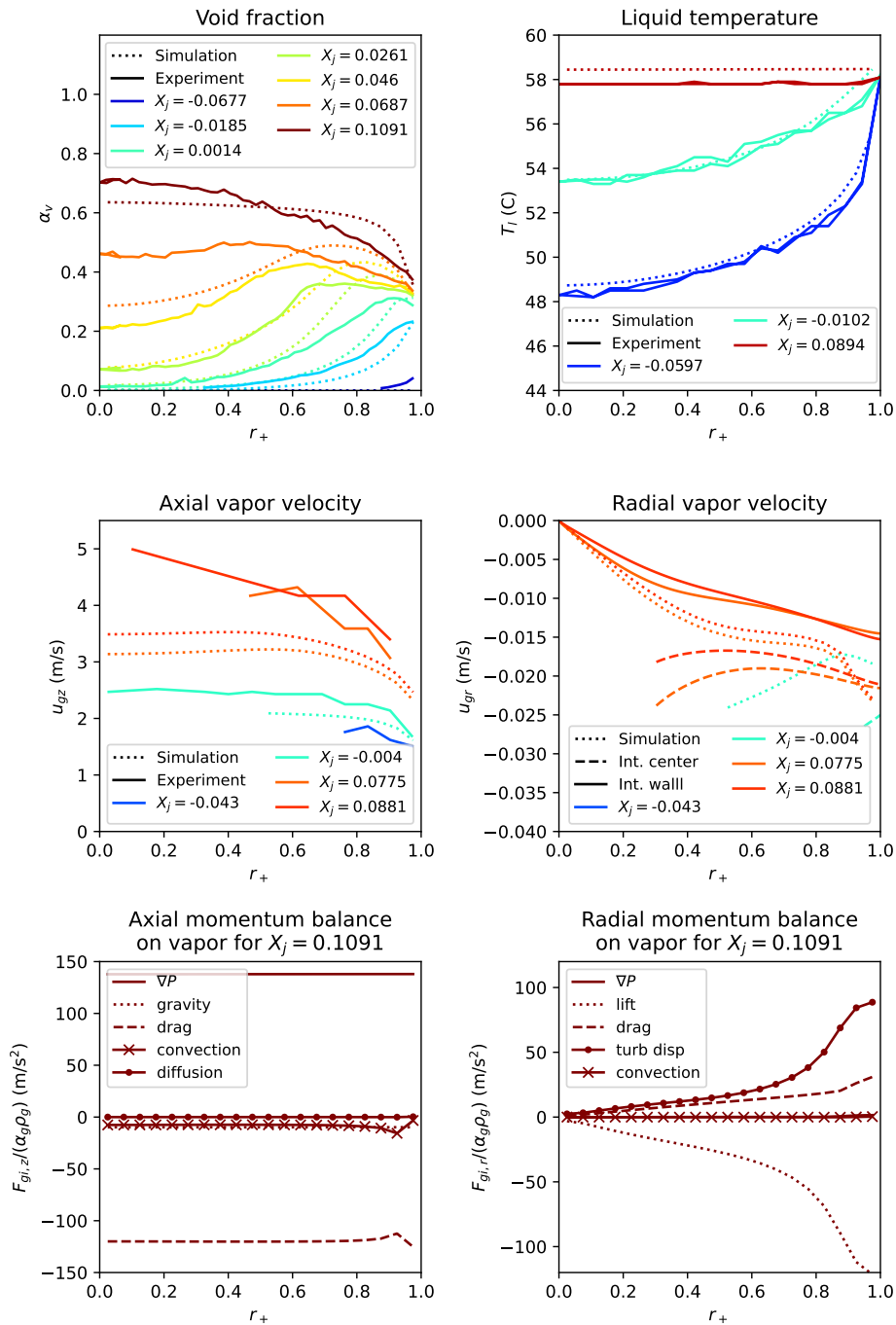


Figure 8.4: Detailed results of simulations on test tube II-G2P14W16 of the DEBORA setup using the proposed set of closures. Simulated radial and axial vapor velocities were only plotted when $\alpha_v > 0.02$. The force balances shown are divided by $\alpha_v \rho_v$ so that regions with different void fractions can be compared with ease. Compare with figure 5.2 that uses the baseline set of closures.

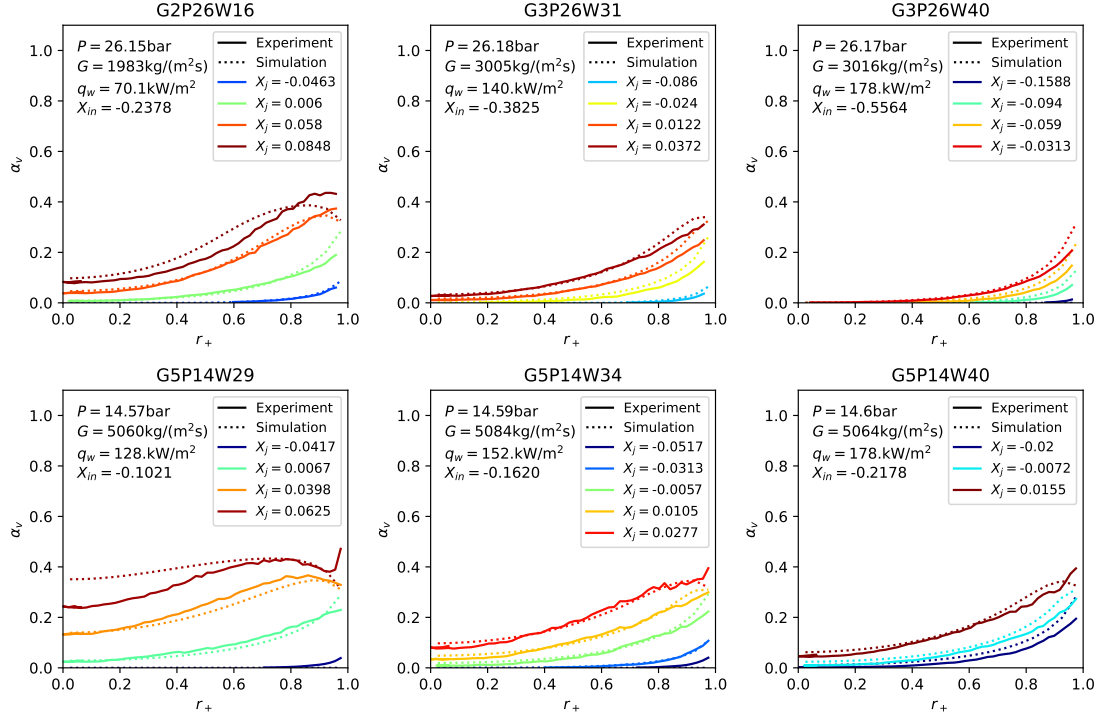


Figure 8.5: Simulated and experimental void fraction profiles for DEBORA test tubes with the proposed set of closures. The test conditions for each series can be found in table 4.2. Compare with figure 5.3 that uses the baseline set of closures.

To evaluate the precision of the predictions on other quantities than the void fraction, results from 3 test tubes from Kledy 2018 are presented in figure 8.6. Two of these test tubes only have one inlet temperature. Void fraction, gas velocity, liquid velocity and liquid temperature are measured. The simulation results are quite satisfying for test tubes G3P14Q48. The predicted void fraction in test tube G3P14Q200 is higher than the experiment and the predicted liquid temperature is lower. This suggests either insufficient condensation in the code or excessive boiling due to the heat flux partition.

For test G3P14Q110, measurements were carried out in two different campaigns. In the first, data for $X_j = 0.002$ was measured. In the second, the rest of the experimental data of this test tube was measured. It can be seen in the central column that void fraction measurements for $X_j = -0.01$ are superimposed with those of $X_j = 0.002$, though the liquid temperatures are different. This inconsistency makes the average void fraction measurements difficult to interpret.

In G3P14Q110, α_v at the wall is much larger in the experiment at high qualities, suggesting that the void fraction at which the lift force becomes active is too small for this test tube.

The velocity profiles in the experiment and in the simulations are flatter at high wall heat fluxes than at low heat fluxes. I believe this to be due to a buoyancy effect in the near-wall region as that is where the void fraction peak is.

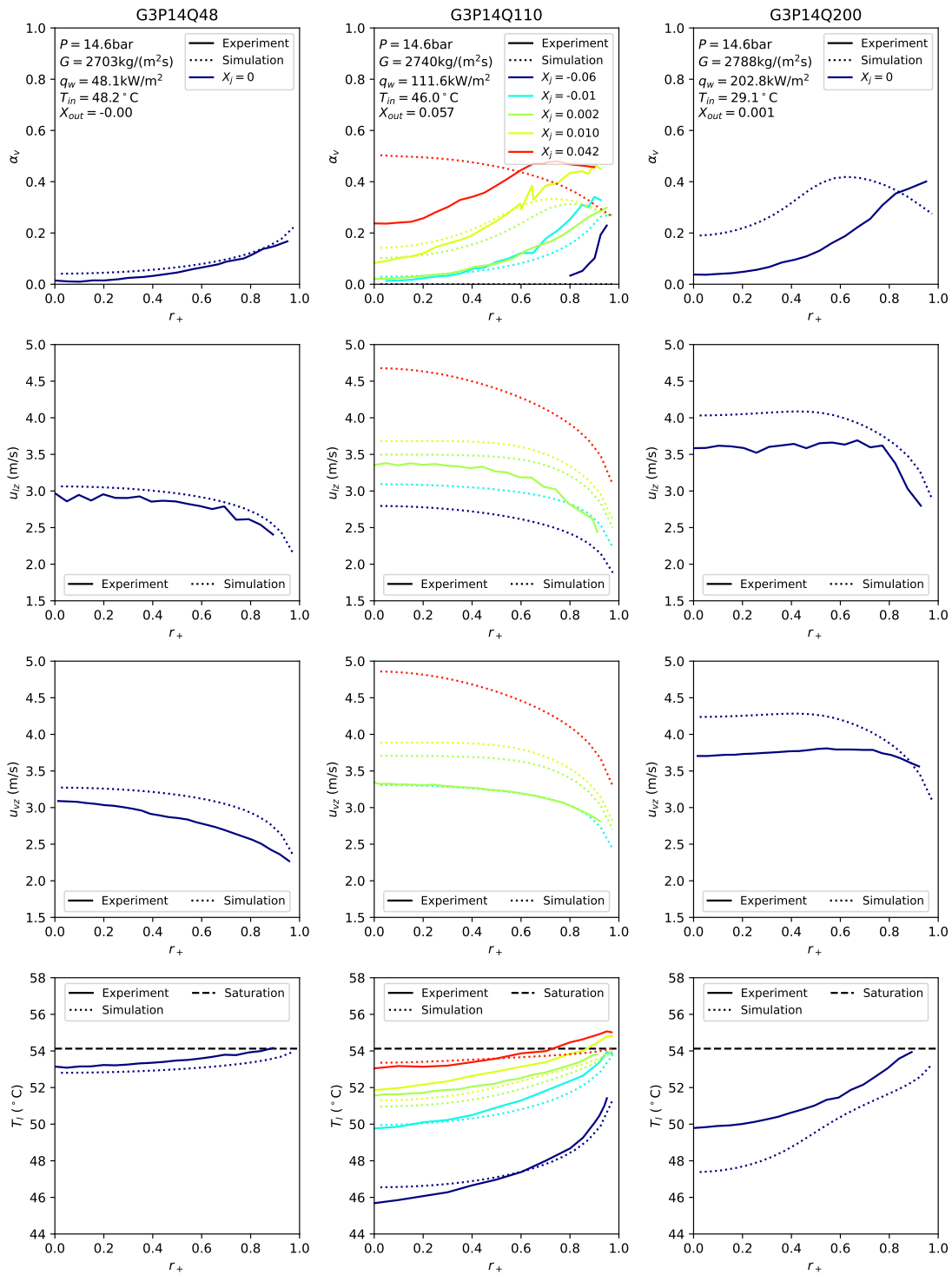


Figure 8.6: Simulated and experimental void fraction profiles for three Kledy 2018 test tubes with the proposed set of closures. The test conditions for each series are given in the figure.

8.3 Saint-Pierre

The St.-Pierre 1965 experiment consists in void fraction measurements through radiography. The beam goes through the whole width of the largest side of a 11 mm by 44 mm rectangular test section. For each inlet condition, the measuring apparatus was moved up and down the 1.25 m-long test section. The main aim of their study was to study boiling-water reactor conditions, therefore they used water up to 50 bar. Much of the report is focused on oscillating power conditions, but steady-state measurements were taken as well. These are the ones exploited in this section. They were used by Shaver and Podowski 2015a for multi-phase CFD validation. They have particularly high inlet qualities, i.e. they are very close to saturation from the entrance.

Table 8.1 lists the test conditions of the steady-state St.-Pierre 1965 tests. The operating pressure are much lower than in PWR conditions, between 13 and 55 bar. The mass fluxes are also relatively slow, between 500 and 1000 kg/(m²s), and the heat fluxes small, between 70 and 300 kW/m². Simulations are run on a 2D grid half the width of the small side of the test section, and the mesh size is chosen to respect $y_+ > 100$ in the first element due to the OSV heat flux partition. Complete simulation results for all of these tests can be found in appendix F. In this section, the tests marked with a ✓ will be analyzed.

Number	P_{out} bar	G kg/(m ² s)	q_w kW/(m ²)	X_{max}	Presented here
1	13.8	1004	71.9	0.008	✓
2	20.7	652	71.9	0.011	✓
4	27.6	640	143.8	0.026	
6				0.014	
7		960	215.8	0.026	
8				0.012	
9	41.4	925	287.7	0.035	
10				0.021	
12	55.2	593	143.8	0.025	✓
13		889	287.7	0.037	✓

Table 8.1: List of test tubes in the St.-Pierre 1965 boiling-flow database. Each (Pressure, Mass flux, Heating power) triplet is given for the experimental configuration, which is in water. The test tube numbers are the ones used in the original paper. The final column lists the test tubes that are investigated in detail in this section. The simulation and experimental results for the others can be found in appendix F. Some test tubes have very similar conditions, apart from the outlet quantity: (4,6), (7,8) and (9,10).

The simulated void fraction results for each test analyzed in this section are given in figure 8.7. Experimental results have two lines for each altitude of measure, as the radiography instrumentation went on each side of the channel. The difference between both lines gives a measure of experimental uncertainty. At the highest pressures, for tests 12 and 13, the predicted void fraction profiles are in rather good

agreement with the experimental results. The difference is extremely small for the lowest and highest measuring points. In the intermediate region, the experimental void fraction profiles are flatter than the simulated ones. This is also the main issue in all of the lower-pressure runs, i.e. 1, 2, 8 and 12. This could be due to an insufficient turbulent dispersion. Considering the effects of bubble-induced turbulence, which could be non-negligible here where flows are slower and bubbles larger than in nuclear reactor conditions could be a lead to improve the modeling.

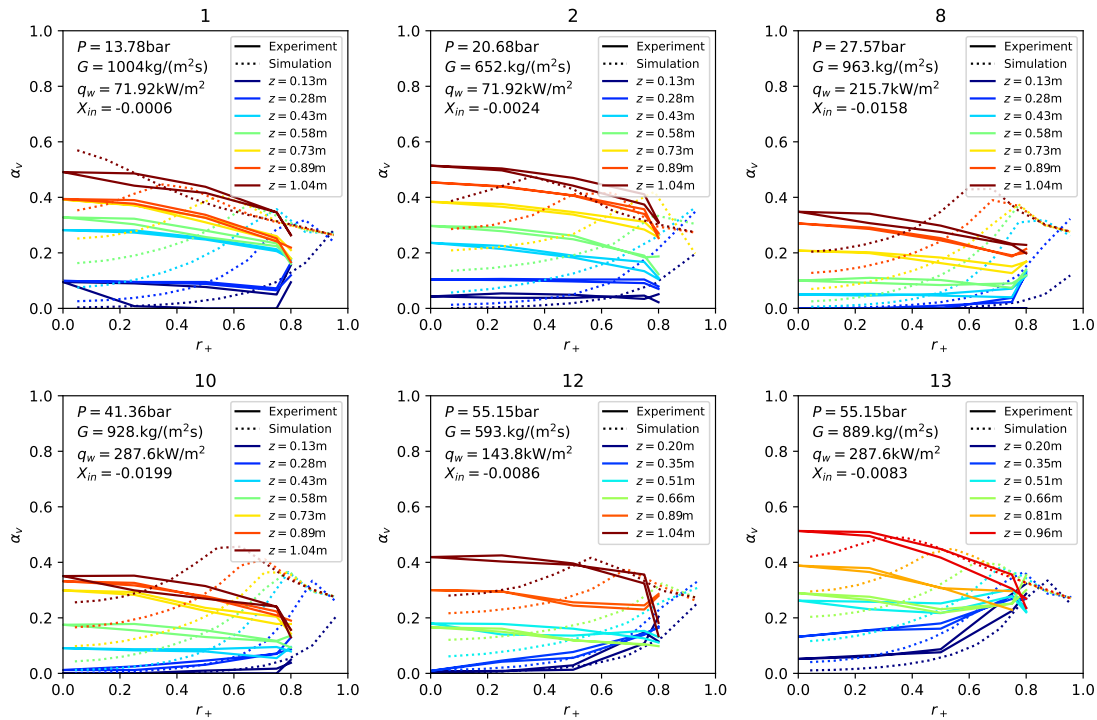


Figure 8.7: Simulated and experimental void fractions for six cases of the St.-Pierre 1965 experimental database. The altitude of each measuring point is given with reference to the inlet of the test section.

Detailed results of test 13 are plotted in figure 8.8, because it is the one that is closest to nuclear reactor conditions. In addition to the void fraction profiles that are in good agreement with the experiment, one can see that the axial velocity fields are flattened by the buoyancy of the vapor. At $z = 0.435$, the velocity profile is even inverted, with a peak closer to the wall than at the core. This behavior seems reasonable and is observed in velocity measurements in channels heated on a single wall (Estrada-Perez and Hassan 2010). However, to the best of my knowledge such axial velocities have not been measured in tubes or channels heated on both sides in the literature. As expected given the inlet conditions, the liquid temperature fields are extremely close to saturation temperature from the start. Radial vapor velocities are fairly independent on the altitude of the measuring section. Radial forces are much smaller than axial forces.

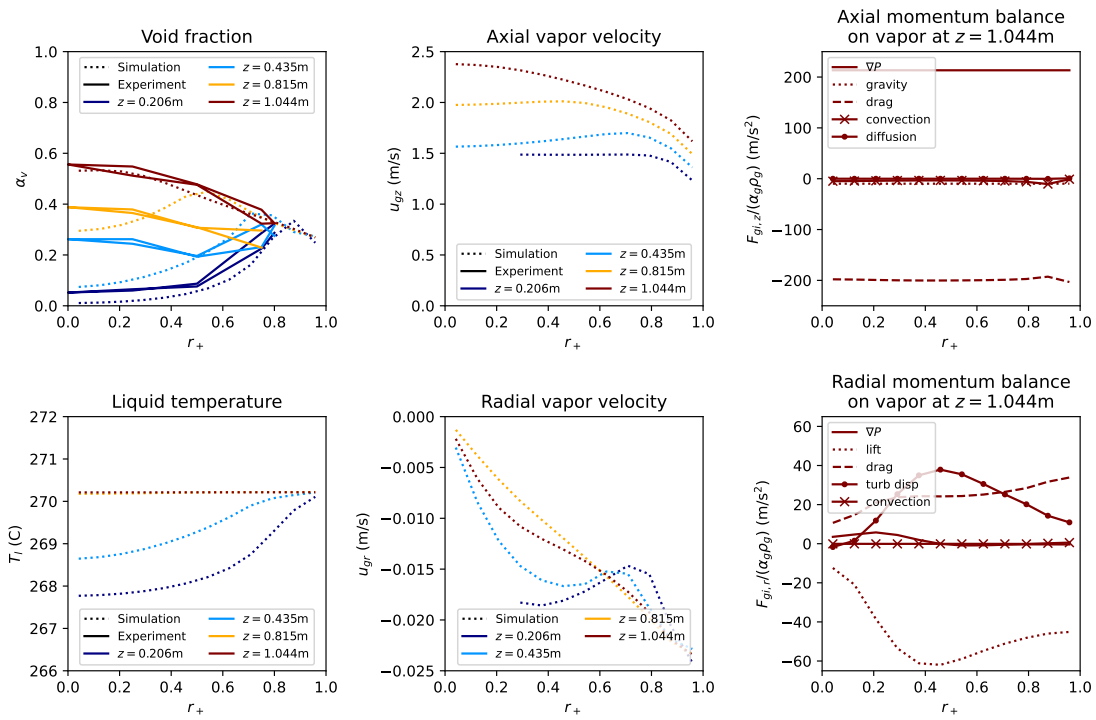


Figure 8.8: Focus on the predictions of the proposed set of closures for St.-Pierre 1965 test 13. The flow conditions are given in table 8.1. The altitude of each measuring point is given with reference to the inlet of the test section.

8.4 Staub et al.

The Staub et al. 1969 report contains three independent sections where void fraction measurements were carried out using radiography in different conditions. The first section focuses on a one-side heated channel at atmospheric pressure. As I focus on high-pressure data in this thesis, I did not look into this section further. The second and third sections contain measurements in a 11 mm-diameter round pipe, with respectively reactor-similarity R22 and with high-pressure water. For each inlet condition, the measuring apparatus was moved up and down the 1.5 m-long test section. Complete simulation results for all of these tests can be found in appendix F. Simulations of the water test runs then those of the R22 runs are presented.

Number	P_{out} bar	G kg/(m ² s)	q_w kW/(m ²)	X_{max}	Presented here
III-5	~8.5	1356	~800	0.097	✓
III-6		2699		0.039	
III-9	42	1037	800	0.142	✓
III-8		2765		0.038	
III-7	55.9	1328	800	0.114	✓
III-12	69.7	770	800	0.181	✓
III-12A				0.217	
III-14A				0.216	
III-21		955	1180	0.277	✓
III-16		1090	800	0.139	
III-18				0.145	
III-13		1400	800	0.106	
III-19			1180	0.207	
III-23			1670	0.187	
III-11		2500	800	0.039	✓
III-20			1180	0.100	✓
III-22		104.0	1394	890	0.120

Table 8.2: List of water test tubes in the Staub et al. 1969 boiling-flow database. Each (Pressure, Mass flux, Heating power) triplet is given for the experimental configuration. The test tube numbers are the ones used in the original paper. The final column lists the test tubes that are investigated in detail in this section. The simulation and experimental results for the others can be found in appendix F. Some test tubes have very similar conditions: (III-12,III-12A,III-14A), (III-16,III-18).

As the test section is circular, they do not measure directly the void fraction but the chordal void fraction, i.e. the integration of the void fraction over the path of the beam. In the near-wall region, this is the near-wall void fraction. In the center, this is an average void fraction over the whole pipe. This method yields relatively high experimental errors in the near-wall region for two reasons. First, the thickness of the steel pipe is larger there. Second, the thickness of fluid is

smaller. Both of these effects decrease the signal and increase noise. This means that it is difficult to extract information on low void fractions from this data, as it is where the errors are the largest. As in each axial location, measurements were carried out on both sides of the pipe, i.e. for positive and negative axial locations, I decided to only keep data points that have coherent measurements on both sides, i.e. a less than 5% difference in the chordal void fraction. To compare simulated local void fractions to measured chordal void fractions, the local void fractions are integrated to chordal ones. In each figure, the simulated local void fractions are plotted in thin dotted lines and the simulated chordal void fractions in thick dotted lines. The chordal profiles are much more regular than the local ones.

Table 8.2 lists the test conditions with water as operating fluid of the Staub et al. 1969 tests. The operating pressure are around BWR conditions, mainly at 80 bar, with one test at 104 bar. The mass fluxes are close to reactor conditions, up to 2500 kg/(m²s), and the heat fluxes around 1000 kW/m². Simulations are run on a 2D-axisymmetric grid half the width of the small side of the test section, and the mesh size is chosen so that $y_+ > 100$ in the near-wall cell.

Figure 8.9 presents the effect of increasing system pressure on simulated and experimental void fraction profiles in test tubes with identical mass and heat fluxes. Both simulated and experimental profiles become flatter as pressure increases. This is expected as the volume of vapor produced for similar conditions decreases with pressure. The code behaves surprisingly well in test case III-6, which is at only 10 bar and knowing that the behavior for the 15 bar-Bartolomei and Chanturiya 1967 test cases in section 7.6.3 was very different from experimental results.

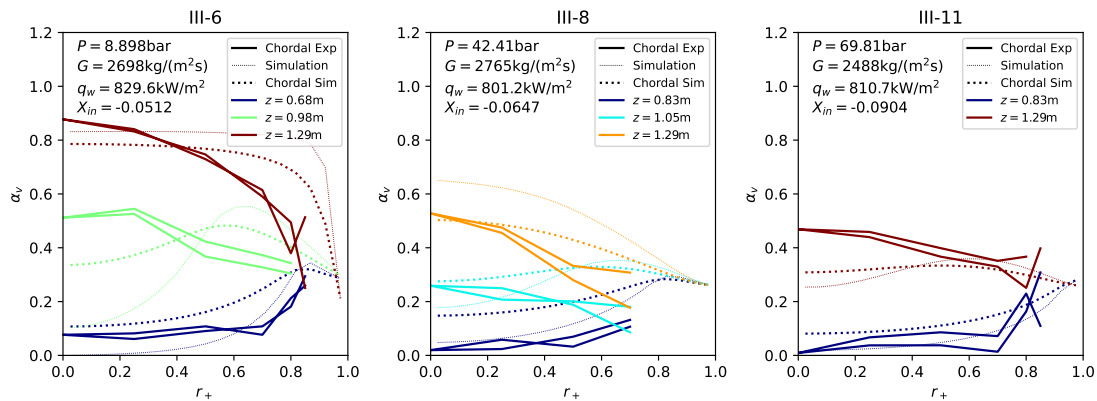


Figure 8.9: Effect of the system pressure on the simulated and experimental void fractions in the water Staub et al. 1969 experimental database. The altitude of each measuring point is given with reference to the inlet of the test section.

Figure 8.10 presents the effect of increasing the mass flux. Qualitatively, increasing G also seems to flatten the profiles, which is observed in the experiments and in the simulations. This is expected by the increased turbulent dispersion. The simulated void fraction profiles are much larger than the experimental ones in test tubes III-12 and III-13. In test tube III-12, the simulations are at saturation for $z = 1.13 \text{ m}$. As the simulated average void fraction is 20% higher than the

experiment, this means that there is probably an error on the energy conservation in the given experimental conditions.

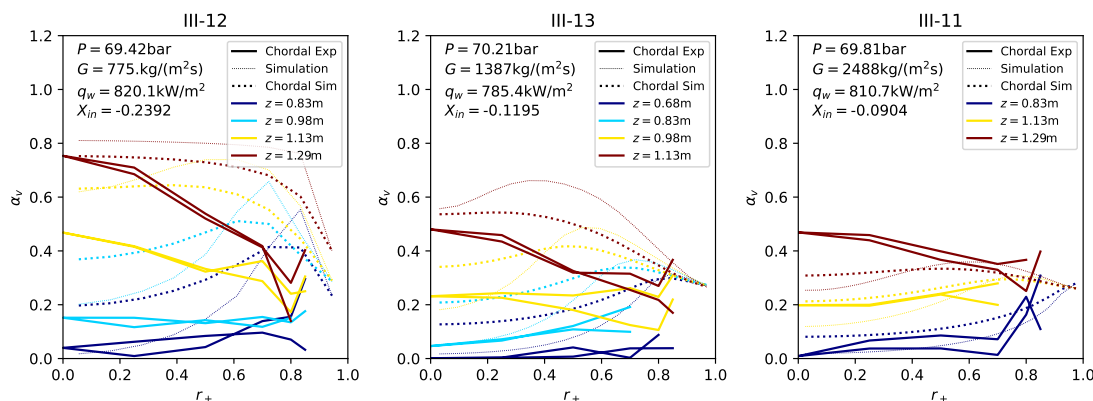


Figure 8.10: Effect of the mass flux on the simulated and experimental void fractions in the water Staub et al. 1969 experimental database. The altitude of each measuring point is given with reference to the inlet of the test section.

Figure 8.11 presents the effect of increasing the wall heat flux on the flow. One would expect effects to be significant in the subcooled region. However, there are no data points in this region for test tube III-20.

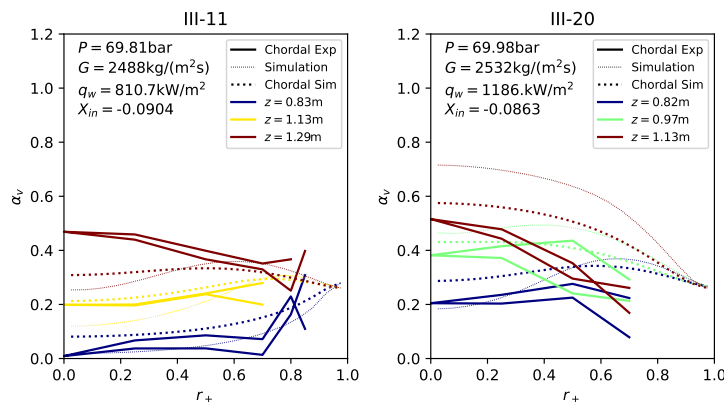


Figure 8.11: Effect of the wall heat flux on the simulated and experimental void fractions in the water Staub et al. 1969 experimental database. The altitude of each measuring point is given with reference to the inlet of the test section.

Table 8.3 lists the test conditions with R22 as operating fluid of the Staub et al. 1969 tests. The operating pressure are at BWR and PWR similarity conditions. The mass fluxes are lower than the water tests, between 300 and 1300 kg/(m²s), and the heat fluxes between 200 and 600 kW/m² in water similarity.

Contrarily to the water experiments, the test matrix does not contain a set of test tubes where a single parameter of the (P, G, q_w) triplet varies. This makes it impossible to interpret the effect of changing these parameters using the experimental data. Simulation results for the Staub et al. 1969 R22 tests are presented

Number	P_{out}	P_{out,H_2O}	G	G_{H_2O}	q_w	q_{w,H_2O}	X_{max}	Presented here
		bar	kg/(m ² s)		kW/(m ²)			
IV-S-8	11.9	(63.1)	529	(680)	24.3	(273)	0.05	
IV-S-7			1052	(1353)	49.6	(556)	0.096	
IV-S-6	14.5	(75.6)	180	(231)	20.2	(224)	0.329	✓
IV-S-9					0.328			
IV-S-5			25.9	(287)	0.369	✓		
IV-S-3			26.2	(291)	0.197			
IV-S-1			392	(502)	29.1	(323)	0.214	✓
IV-S-2			736	(943)	47.3	(525)	0.125	✓
IV-S-4			1385	(1770)	47	(520)	0.074	
IV-S-10							0.08	
IV-S-14	33	(157.6)	183	(227)	18.7	(193)	0.234	✓
IV-S-12			335	(415)	23.4	(242)	0.186	✓
IV-S-16							0.218	
IV-S-11			658	(817)	46.7	(483)	0.153	✓
IV-S-15							62.2	

Table 8.3: List of R22 test tubes in the Staub et al. 1969 boiling-flow database. Each (Pressure, Mass flux, Heating power) triplet is given for the experimental R134A configuration and the Water equivalent using the scaling criterion presented in section 4.1. All of these test tubes are used in this chapter.

in figure 8.12. On most test tubes, the simulation had not passed the point of onset of significant void where the first experimental void fractions were measured. Furthermore, the high-void fraction simulations of test IV-S-6, IV-S-1 and IV-S-2 are flatter than the experimental data. This is an opposite behavior than in section 8.3, where low-mass flux simulations at BWR pressures had profiles that were not as flat as the simulations. The other simulated void fraction profiles are relatively coherent with the experimental results.

All in all, the simulation results on this database are qualitatively rather good but the experimental data is not sufficiently precise for quantitative conclusions to be drawn.

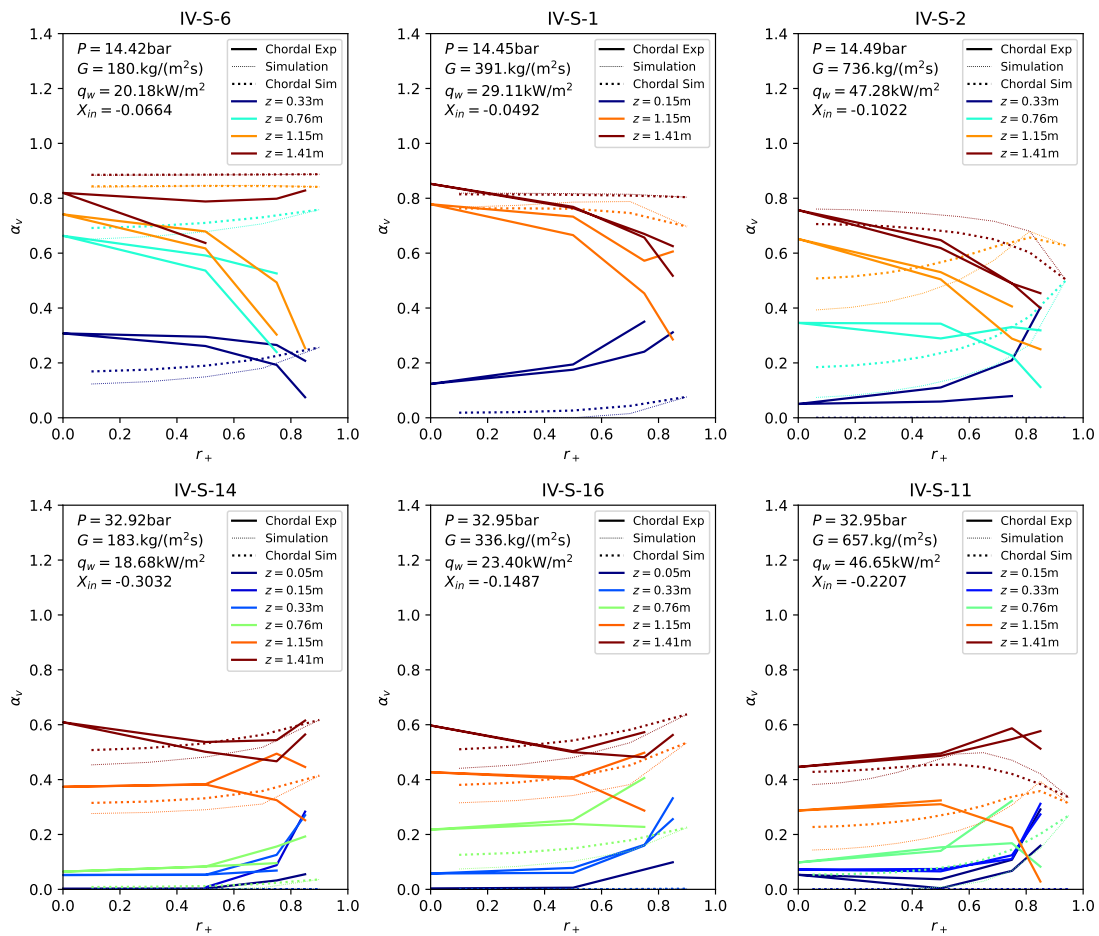


Figure 8.12: Simulated and experimental void fractions for six cases of the R22 Staub et al. 1969 experimental database. The altitude of each measuring point is given with reference to the inlet of the test section.

8.5 Martin

The Martin 1969 experiment consists in void fraction measurements through radiography. The beam goes through the whole width of the largest side of a 50 by 2 mm and a 50 by 2.8 mm channel. The 2 mm-wide test section was 1.5 m-long and the 2.8 mm-wide one 1.008 m. The width of the channel will be written w in this section. The equivalent altitude methodology was used, i.e. for each set of (w, P, G, q_w) conditions, multiple inlet temperatures were used. This methodology is explained in detail in section 4.4. The measuring apparatus was 129 mm upstream of the outlet of the test section. Averaged measurements on this database have been used in the literature by Saha and Zuber 1974 for their OSV criterion for example. However, to the best of my knowledge the local data has never been exploited in a CFD code.

One void fraction is measured every 25 μm along the width of the channel. The void fraction profiles in this database therefore have ~ 100 points when there is vapor in the core. The recorded data is therefore of extremely high quality, and it should be possible to apply the radial velocity methodology from section 4.5 to it. 37 test tubes were recorded in total. In almost every test tube, the void fraction is wall-peaked at low outlet qualities and core-peaked at higher qualities. The void fraction at the wall is almost independent of the flow quality and the average void fraction for a given test tube, but is different for each test tube.

Table 8.4 lists the test conditions of the steady-state Martin 1969 tests in a 2 m-wide section. The operating pressure are in PWR conditions, at 137 bar. The mass fluxes are high, above 2000 $\text{kg}/(\text{m}^2\text{s})$, and the heat fluxes between 500 and 1000 kW/m^2 .

Number	Width mm	P_{out} bar	G $\text{kg}/(\text{m}^2\text{s})$	q_w $\text{kW}/(\text{m}^2)$	X_{max}	Presented here
31	2	137.3	1012	500	0.395	✓
33			2020	500	0.132	
34B				1000	0.257	
34C			2531	1000	0.238	
34A			3030	517	0.122	
35A				1001	0.229	
32A			3500	1541	0.168	
35B				1013	0.186	
32B				1493	0.139	

Table 8.4: List of 2 mm-wide water test tubes in the Martin 1969 boiling-flow database. Each (Pressure, Mass flux, Heating power) triplet is given for the experimental configuration. The test tube numbers are the ones used in the original paper. The order in which they are given is meant to regroup similar test tubes. The final column lists the test tubes that are investigated in detail in this section. The simulation and experimental results for the others can be found in appendix F.

Number	Width mm	P_{out} bar	G kg/(m ² s)	q_w kW/(m ²)	X_{max}	Used in		
20	2.8	78.5	500	216	0.145			
25				415	0.275			
22			750	416	0.186			
24				770	0.235			
26			1500	421	0.076			
28				1109	0.245			
29				1663	0.166			
21			2240	751	0.121		✓	
30				1096	0.138		✓	
23		1619		0.07				
46		107.9	495	207	0.137			
36				425	0.388			
38			744	419	0.183			
37				750	0.168			✓
43			1490	418	0.072			✓
42				747	0.186			
44				1099	0.181			✓
45			2240	1681	0.092			✓
41				756	0.069			✓
40	1097			0.138	✓			
39	1683	0.078						
14	137.3	495	216	0.136				
11			415	0.167				
8		743	0.22					
5		1485	0.072					
1		2240	752	0.109				
3			1092	0.13		✓		
15			1684	0.122				

Table 8.5: List of 2.8 mm-wide water test tubes in the Martin 1969 boiling-flow database. Each (Pressure, Mass flux, Heating power) triplet is given for the experimental configuration. The test tube numbers are the ones used in the original paper. The final column lists the test tubes that are investigated in detail in this section. The simulation and experimental results for the others can be found in appendix F.

Table 8.5 lists the test conditions of the steady-state Martin 1969 tests in a 2.8 m-wide section. The operating pressure varies from BWR to PWR conditions, from 78.5 to 137 bar. The mass and heat fluxes cover a much wider range than for the 2 mm tests, respectively from 500 to 2240 kg/(m²s) and between 200 and 1600 kW/m².

Simulations are run on a 2D grid half the width of the small side of the test section. The mesh size is chosen so that $y_+ > 100$ in the near-wall cell. Complete simulation results for all of these tests can be found in appendix F. In this section, the tests marked with a \checkmark will be analyzed.

A detailed examination of test 21, chosen arbitrarily, is carried out first (figure 8.13). The void fraction profiles are in good agreement with the experiment, transitioning from wall-peaked to core-peaked. This is in great part due to the lift coefficient becoming negative as α_v increases (equation 7.8). The liquid remains subcooled while the void fraction is wall-peaked, and becomes saturated around when the void becomes core-peaked. Contrarily to the St.-Pierre 1965 cases, axial vapor velocities remain core-peaked. This is probably due to the high mass flux. u_{vz} achieves very high values, up to 10 m/s, as the void fraction increases. This is expected through mass conservation.

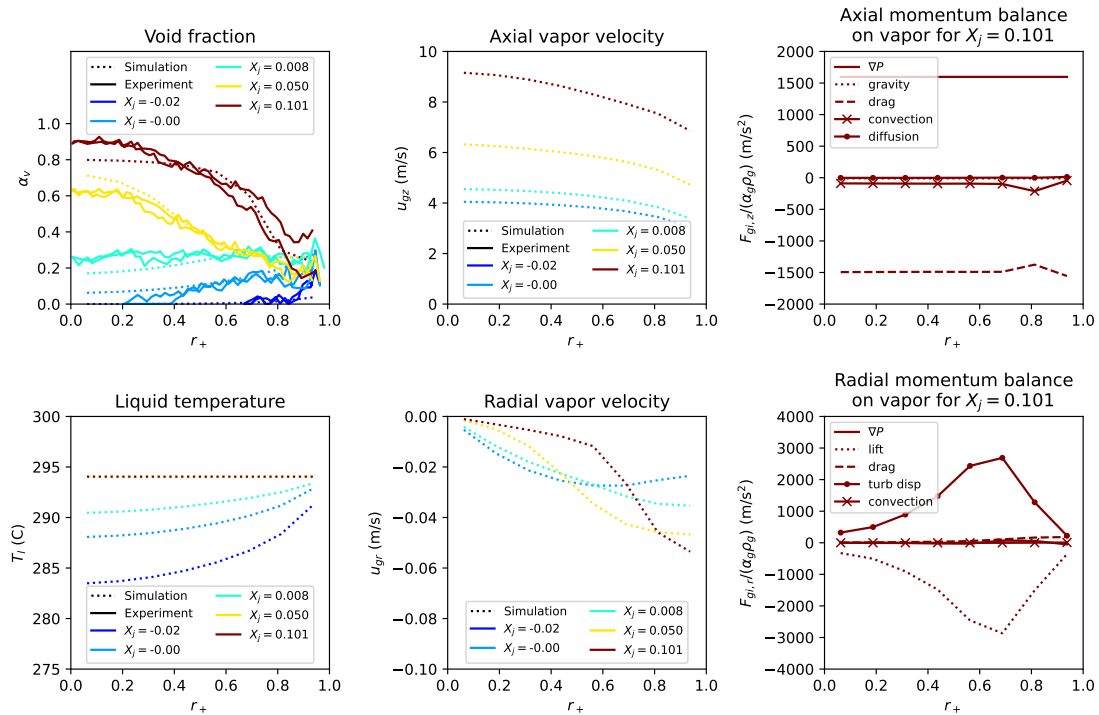


Figure 8.13: Focus on the predictions of the proposed set of closures for Martin 1969 test 21. The channel is 2.8 mm wide, $P = 78.5$ bar, $G=2240$ kg/(m²s) and $q_w = 751$ kW/m²

The radial force balance is surprising for two main reasons. First, the drag force is negligible before the lift and turbulent dispersion forces. Second, the radial forces are larger than the axial forces. This is due to the slimmness of the channel: as it is

10 times thinner than in the DEBORA experiment, the vorticity and therefore the lift force are 10 times larger. This can explain why radial velocities have a more exotic shape than the ones in figures 8.4 and 8.8. As one can no longer assume that the radial force balance is small before the axial forces, the methodology presented in section 2.3 to derive a 3 dimensional drift velocity from the force balance can no longer be used.

Figure 8.14 presents the effect of channel width on the void fraction profiles. It is the only set of (P, G, q_w) conditions where a comparison is possible. At low void fractions, for the same outlet quality $X_j \sim 0$, the 2 mm-channel has a lower void fraction than the 2.8 mm-channel in the experiments and simulations. This means that a larger part of the channel is at saturation before boiling begins, which is expected as the channel is less wide. It is difficult to see a clear effect of the channel width on higher void fractions ($X_j \sim 0.09$), where the simulated profiles are relatively far from the experiments. The void fraction at the wall is too large, i.e. the lift coefficient seems to become negative too early in the simulation.

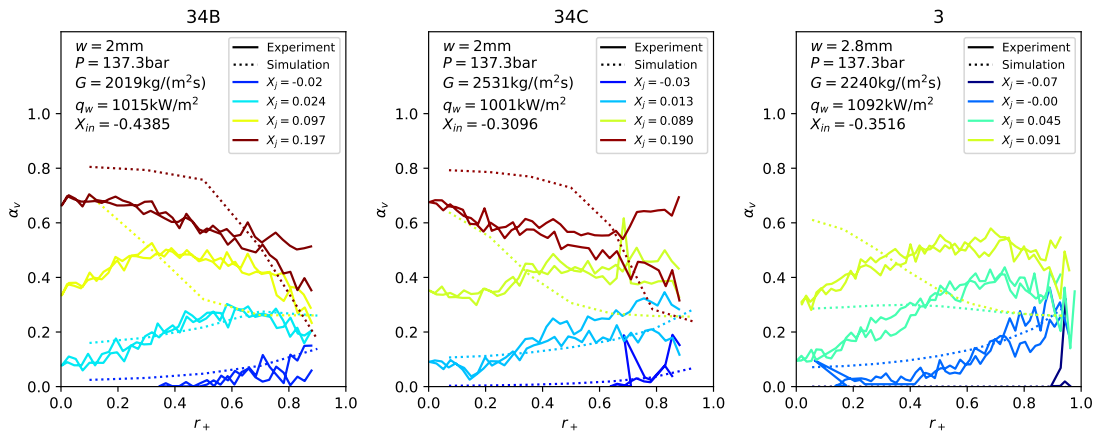


Figure 8.14: Effect of the channel width on the simulated and experimental void fractions in the water Martin 1969 experimental database. The altitude of each measuring point is given with reference to the inlet of the test section.

Figure 8.15 presents the effect of the outlet pressure on the void fraction profiles. The (w, G, q_w) conditions are the same on all three figures. For similar outlet qualities $X_j \sim 0$ or $X_j \sim 0.1$, the void fraction decreases with P . This is a direct effect of the decreasing density ratio and is exacerbated at high qualities where the effect of subcooling is smaller. The void fraction profiles are well predicted for test tubes 30 and 40, but not for test tube 1: the maximum void fraction at the wall seems to increase with the pressure in the experiments but not in the simulations.

Figure 8.16 presents the effect of the heat flux on the void fraction profiles. The (w, P, G) conditions are the same in all three subfigures. For similar outlet qualities ($X_j \sim 0$), the void fraction is as expected larger at higher heat fluxes in the experiments and in the simulation. α_v at the wall also increases with q_w in the experiment. This is expected, as more vapor is produced at the wall. However, the

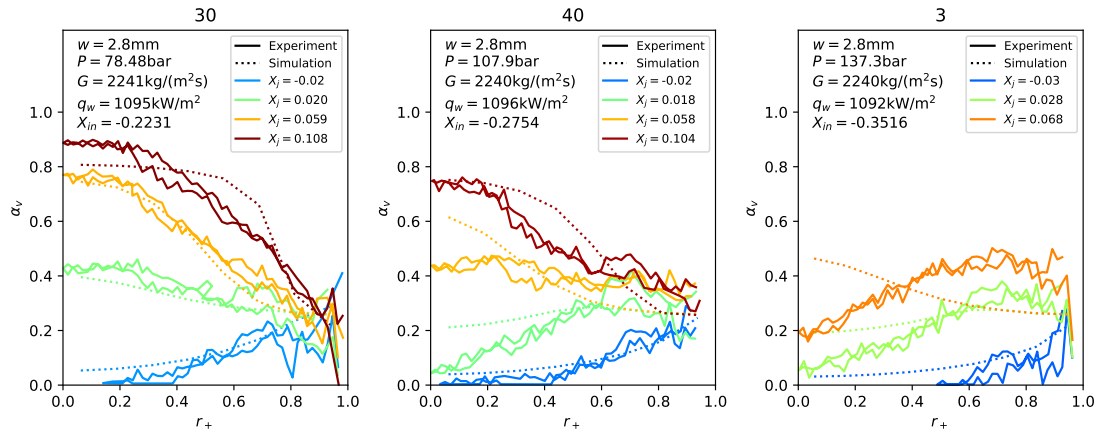


Figure 8.15: Effect of the outlet pressure on the simulated and experimental void fractions in the water Martin 1969 experimental database. The altitude of each measuring point is given with reference to the inlet of the test section.

increase is moderate: it goes from ~ 0.3 to ~ 0.4 as the wall heat flux is multiplied by four. In the simulations however it remains the same.

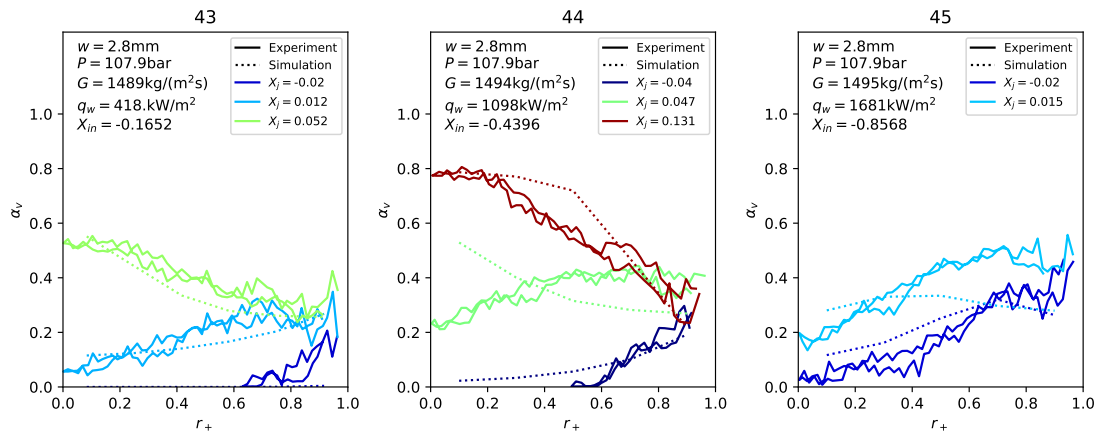


Figure 8.16: Effect of the heat flux on the simulated and experimental void fractions in the water Martin 1969 experimental database. The altitude of each measuring point is given with reference to the inlet of the test section.

Figure 8.17 presents the effect of the mass flux on the void fraction profiles. The (w, P, q_w) conditions are the same on both rows of the figure. For similar outlet qualities, the void fraction profiles are flatter in the simulations and experiments. This is expected due to turbulent dispersion and was observed in section 8.4 on Staub et al. 1969 data. Increasing the flow velocity also seems to decrease the experimental void fraction at the wall. This would be coherent with the Sugrue 2017 lift coefficient, which becomes more negative when the turbulent intensity of the flow increases. However, it remains the same with the proposed set of closures.

Globally, on the Martin 1969 database, the proposed set of closures gives very

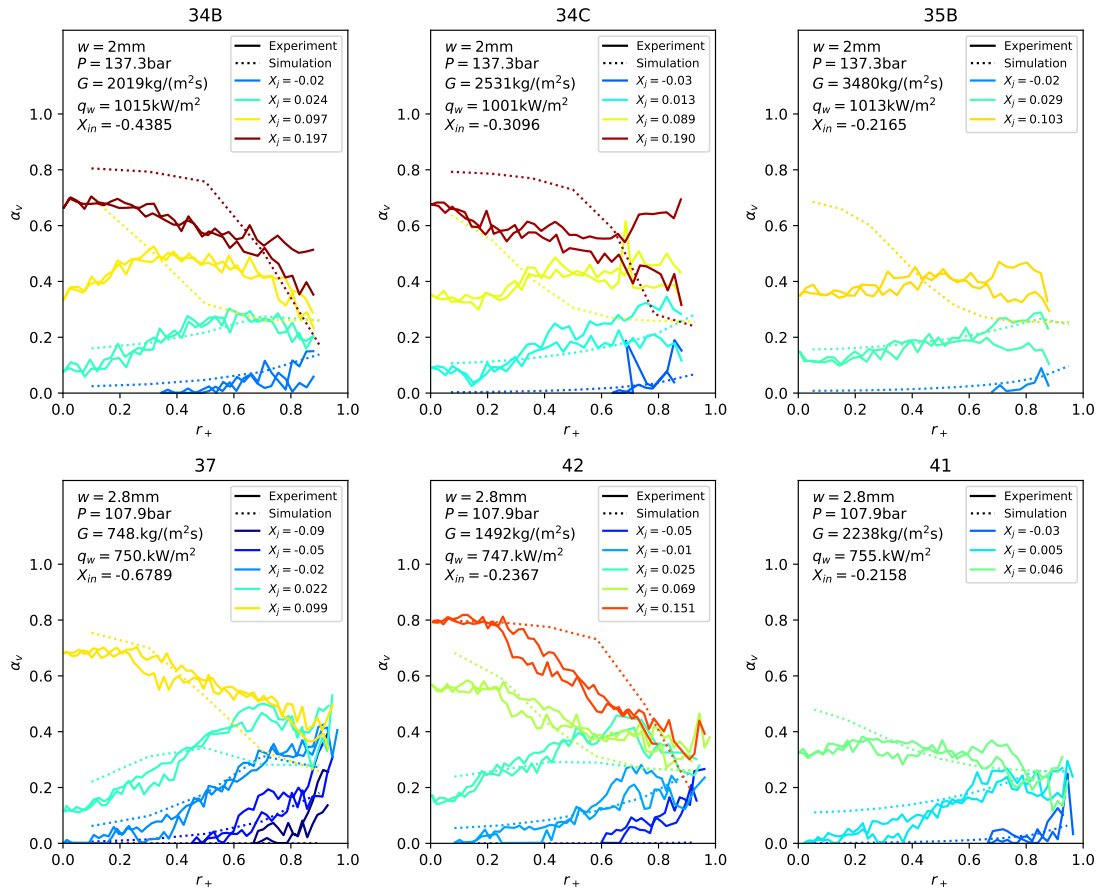


Figure 8.17: Effect of the mass flux on the simulated and experimental void fractions in the water Martin 1969 experimental database. The altitude of each measuring point is given with reference to the inlet of the test section.

good void fraction predictions at low qualities, when $\alpha_v < 0.2$, and relatively good results for $\alpha_v \geq 0.2$.

8.6 Chu et al.

Chu et al. 2017 carried out double-optical probe measurements in a 9.5 mm outer diameter 27.2 mm inner diameter annular geometry. The shape of this annulus compared to a PWR subchannel is shown in figure 8.1. The fluid used is R134A, in similarity conditions with water. This experiment follows those of Lee et al. 2002, Situ et al. 2004 and Lee et al. 2009, with water at low pressures in a similar test section. For each inlet condition, the measuring apparatus was moved up and down the 1.750 m-long heated section. This experiment was used by Alatrash et al. 2022 for multi-phase CFD validation. The recorded data is therefore of extremely high quality, and it should be possible to apply the radial velocity and coalescence-breakup methodologies from section 4.5 and appendix C to it.

Table 8.6 lists the test conditions of the steady-state Chu et al. 2017 tests. The operating pressures are PWR and BWR-similarity conditions, between 13 and 27 bar for R134A. The mass fluxes are also relatively slow, between 166 and 1000 kg/(m²s). The heat fluxes are similar to reactor conditions, between 800 and 1500 kW/m² in water equivalent. Simulations are run on a 2D axisymmetric grid that is the width of the annulus, with only the inner wall that is heated. The mesh size is chosen so that $y_+ > 100$ in the near-wall cell. Complete simulation results for all of these tests can be found in appendix F.

Number	P_{out}	P_{out,H_2O}	G	G_{H_2O}	q_w	q_{w,H_2O}	X_{max}
	bar		kg/(m ² s)		kW/(m ²)		
Test_01	12.9	(79.6)	1049	(1490)	120.4	(1615)	-0.046
Test_02	14.9	(91.2)	166	(235)	60.6	(807)	-0.026
Test_03	26.9	(155.9)	1072	(1480)	120.7	(1532)	-0.0378

Table 8.6: List of test tubes in the Chu et al. 2017 boiling-flow database. Each (Pressure, Mass flux, Heating power) triplet is given for the experimental R134A configuration and the Water equivalent using the scaling criterion presented in section 4.1. All of these test tubes are used in this chapter.

Figure 8.18 presents simulation results for all three cases of this database. The void fraction predictions of the proposed set of closures are much smaller than in the experiment. This is due to either an excessive condensation or to insufficient evaporation in the heat flux partition. The OSV-based heat flux partition could be offset by the fact that in this experiment the flow begin to boil just after the entrance of the heated section, i.e. before the thermal boundary layer is developed. The shape of the void fraction profiles are very close to those of the experiment however, which means that the radial velocities and radial force balance is probably coherent. The measured bubble diameters are very close to the capillary length, which further justifies my choice to use it as reference length for bubble condensation.

Finally, the predicted experimental and simulated vapor velocities are all wall-peaked. This is due to the combination of buoyancy, as discussed in section 8.3, and the annular geometry itself. In annular channels, the zone where the velocity

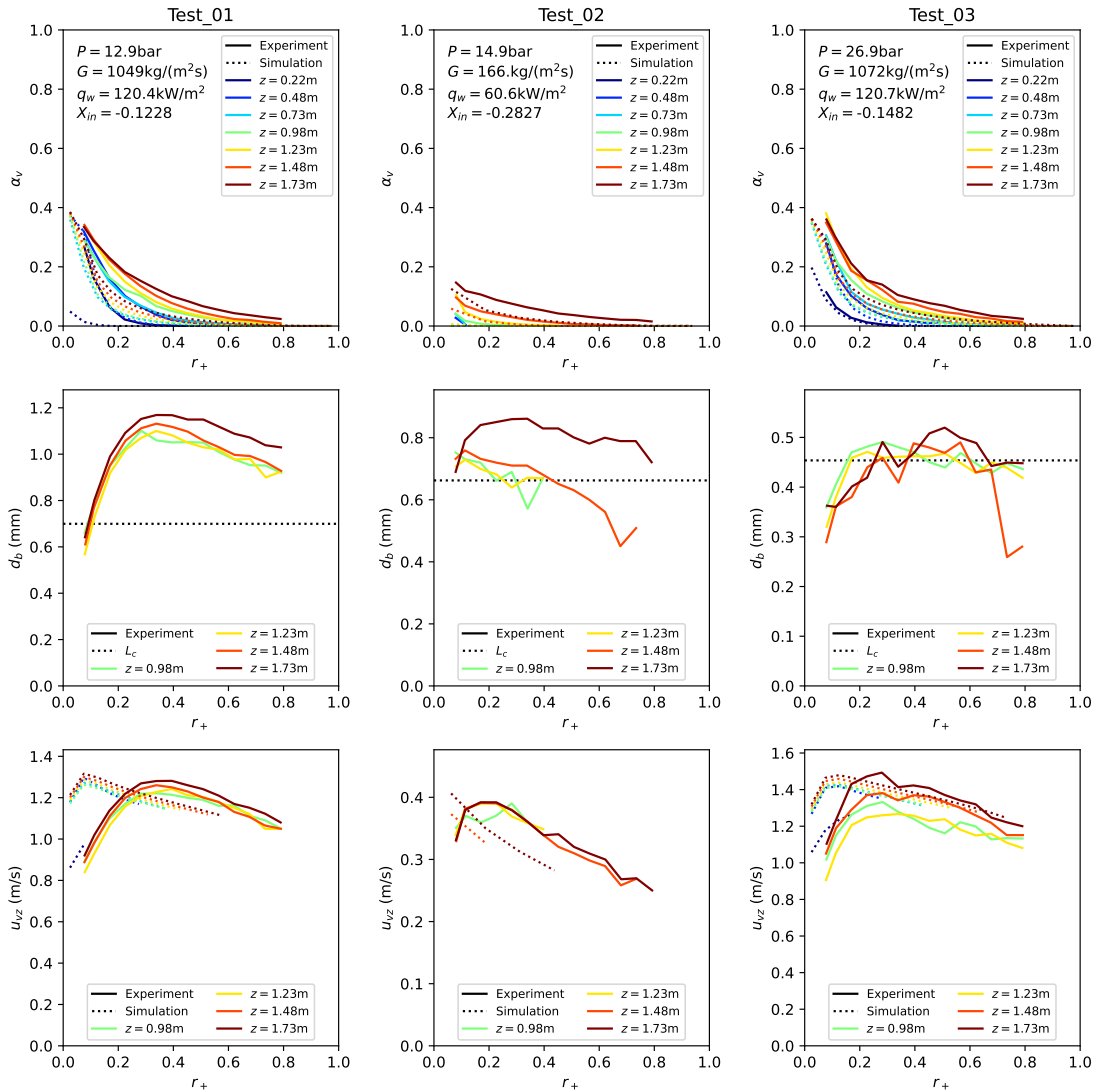


Figure 8.18: Simulated and experimental void fractions for all three cases of the Chu et al. 2017 experimental database. The altitude of each measuring point is given with reference to the inlet of the test section. As the set of closures proposed does not include bubble diameter prediction, the capillary length is plotted in the middle row, which is the characteristic length scale in the proposed condensation correlation (equation 7.11).

is highest is closer to the inner wall. This can be seen in the simulations of the liquid velocity even before boiling begins. This is due to a smaller perimeter on the inside pipe, which reduces drag relative to the outside pipe. However, the profiles predicted by the proposed set of closures in the boiling region are more skewed towards the center than the experimental results. This effect is exacerbated in Test_02, which is the slowest of the three. This discrepancy can be caused by the following phenomena:

- Not taking into account the fact that the nucleating vapor has zero veloc-

ity, and taking out the virtual mass term. The trade-offs of this choice are discussed at length in section 7.1.

- Not taking into account the friction on the vapor phase due to the bubble-induced friction in the near-wall region. This could play a key role at low flow velocities, like that of the Test_02. Multiple formulations from the literature include that of Ramstorfer et al. 2005, which is based on the experiments of Gabillet et al. 2002.
- Not modeling bubble induced turbulence. The relative importance of bubble-induced turbulence relative to shear-induced turbulence becomes significant for bubble numbers $b = \frac{\alpha_g \|\vec{u}_g - \vec{u}_l\|^2}{u_{SP}^{\prime 2}} \gtrsim 0.5$ (Almeras et al. 2017). In slower flows, u'_{SP} becomes smaller while $\alpha_g \|\vec{u}_g - \vec{u}_l\|^2$ remains of the same magnitude. In Test_02 for example, $b \sim 10$, significantly larger than the threshold.
- Not having significant momentum diffusion in the vapor phase. The turbulent momentum diffusion in the vapor phase scales with $\nu_t \rho_v$, proportional to the vapor density, while all forces that are applied to the bubbles scale with the liquid density. Even in BWR similarity conditions, there is still an order of magnitude difference between the two.

The simulated quantities in Test_03 are now investigated in detail, as it is the closest to PWR conditions. Results are presented in figure 8.19. In addition to the void fraction and axial vapor velocity profiles already discussed, one can see that at $z = 0.23$ m the liquid temperature profile is not developed at all. Furthermore, as they are at saturation at the wall, this means that the heat flux partition will transform all of the wall heat flux into vapor. The condensation correlation is therefore probably responsible for the insufficient void fraction. As the simulated void fraction in the R134A tests of figure 8.6 was too large, I believe the culprit to not be the effect of the fluid properties on the Nusselt number but rather the influence of the low-velocity conditions of these tests. As for the St.-Pierre 1965 test 13, the predicted radial vapor velocity seems independent of the void fraction. Finally, radial forces are much smaller than axial forces.

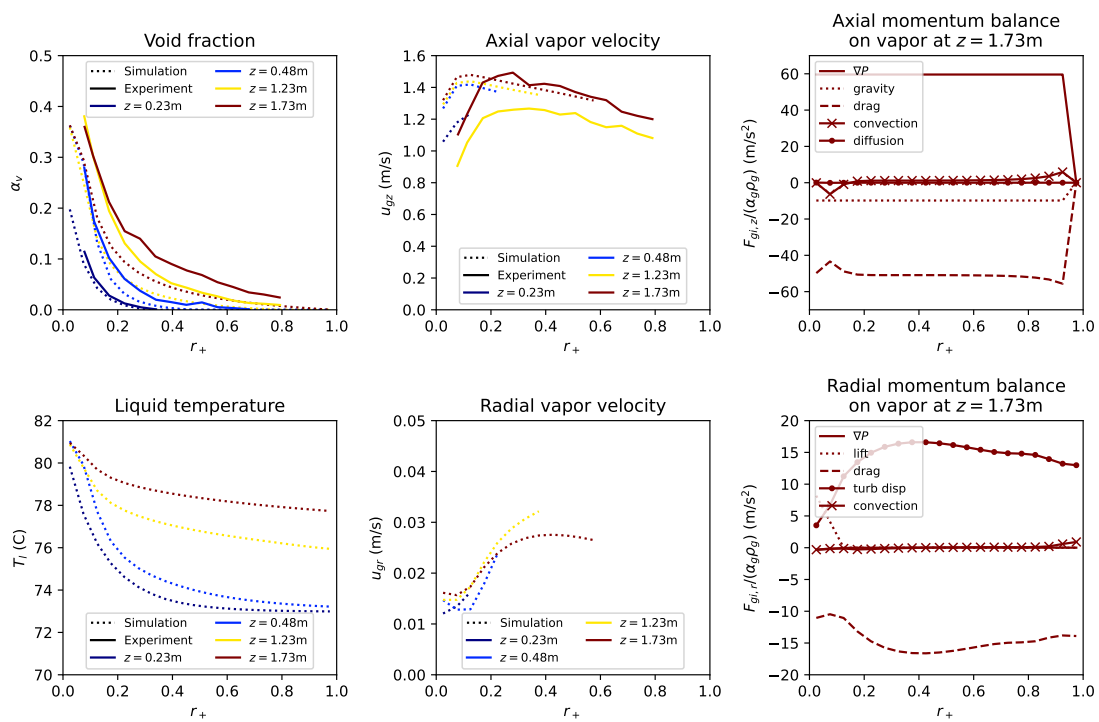


Figure 8.19: Focus on the predictions of the proposed set of closures for Chu et al. 2017 Test_03. The flow conditions are given in table 8.6. The altitude of each measuring point is given with reference to the inlet of the test section.

8.7 Strengths and limits of the proposed set of closures

The set of closures built in chapter 4 focusing on the DEBORA database is able to simulate multiple flow conditions and geometries, even though it is much simpler than traditional formulations (see figure 7.16). The OSV-based heat flux partition is able to correctly predict low-void fraction profiles. The proposed lift force lets flows transition smoothly from wall-peaked to core-peaked profiles as the void fraction increases, as seen in the experiments of St.-Pierre 1965, Staub et al. 1969, Martin 1969 and Cubizolles 1996. This wall-to-core peaked transition was also discussed by Marchaterre et al. 1960. It is difficult to make a fair comparison with simulation results from other codes and sets of closures, as in most cases the published validation databases are much smaller than the one presented here (Krepper et al. 2007; Ustinenko et al. 2008; Shaver and Podowski 2015b; Mimouni et al. 2017; Kommajosyula 2020).

However, there are still limits to this modeling:

- In the low-pressure flows presented in section 7.6 where $P < 15$ bar, the simulated average void fractions were far from the experimental data.
- In low-velocity flows ($G < 1000$ kg/(m²s)), simulated void fraction profiles could be too flat (figure 8.12) or not flat enough (figure 8.7).
- In the Chu et al. 2017 low-velocity flows, the predicted void fraction is smaller than in the experiment. This is coupled with an excessive vapor velocity in near-wall region.
- The maximum void fraction at the wall when the wall-to-core peaked void fraction profile transition occurs is fixed in the simulations but seems to depend on experimental conditions:
 - Increases with P
 - Decreases with G
 - Increases with q_w

I believe that additional modeling work on low-pressure and low-mas flux conditions is necessary to lift these limitations.

It would also be nice to understand the physical mechanism at play in the inversion of the void fraction profile at the wall. In a classical Euler-Euler framework this can only be explained by a negative lift coefficient. However, the reason why it should become negative at $\alpha_v \sim 0.3$ is unclear: do the vapor inclusions coalesce? Is the crowding directly responsible?

The only limit that concerns nuclear reactor operating conditions is that of the maximum void fraction at the wall, which isn't always well predicted. Therefore, in the next chapter focused on the critical heat flux the proposed set of closures will be assumed is validated in reactor conditions.

8.8 Other databases that can be used for multi-phase CFD validation

In this thesis, I simulated all boiling-flow high-pressure experiments with local measurements that I was able to find in the literature. To increase the size of the validation database, one must either look to non-local data or to other flow conditions. In this section, a list of boiling-flow experiments that could be used in this context is given.

Low-pressure experiments with local data include:

- In addition to their high-pressure pipe experiments presented in section 8.4, Staub et al. 1969 carried out boiling experiments in atmospheric-pressure water-filled channel heated on a single wall.
- Roy et al. carried out multiple studies in a refrigerant-filled annular geometry in the 1990's. The data is disseminated in multiple papers: Hasan et al. 1990b, Hasan et al. 1990a, Hasan et al. 1991, Roy et al. 1993, Roy et al. 1994, Roy et al. 1997, Roy et al. 1999, Roy et al. 2002 and Kang and Roy 2002.
- The works of Lee et al. 2002, Situ et al. 2004 and Lee et al. 2009 concern annular water atmospheric-pressure test sections with void fraction, vapor velocity and interfacial area measurements at different axial positions along the test section.
- Lucas and Prasser 2007 and Lucas et al. 2013 injected vapor in a subcooled pipe to isolate condensation from the near-wall boiling phenomena. They measured various physical quantities at different distances from the inlet: void fractions, bubble diameters and gas velocities.
- Estrada-Perez and Hassan 2010 carried out liquid velocity PTV measurements in a single-wall heated refrigerant rectangular channel.
- Ozar et al. 2013, Kumar et al. 2019 and Bottini et al. 2020 studied an ascending water flow between 1 and 10 bar with a heated annular section before a non-heated section. By measuring local void fractions, interfacial area concentrations and liquid temperatures in the non-heated section they extracted information on the condensation. In a follow-up study, Ooi et al. 2020 changed the test section from annular to circular after the heated section. This gives information on the effect of the change in geometry on local void fractions and interfacial area concentrations.

High-pressure non-local databases in simple geometries (tube, channel and annulus) can only be exploited to calibrate the condensation and boiling terms if there is a good level of confidence in the momentum closures, as in section 7.6.3. However, they can always be used to gain information on the limits of a set of closures, as shown in section 7.6.4. Multiple ascending flow databases were presented

in table 6.1. Some descending flow experiments, like Lobachev et al. 1973, can be found in the literature and could be very interesting to simulate.

Finally, going towards more complex rod bundle geometries would be an important step in model validation. Such experiments include:

- Hori 1994 carried out transient heating experiments in a subchannel geometry with void fraction measurements.
- Some campaigns on the DEBORA experiments studied the effect of a single mixing vane in a tube on boiling flow. This data has recently begun to be used for CFD validation (Favre et al. 2022; Favre 2023).
- The BFBT benchmark exercise contained void fraction measurements by sub-channel in BWR conditions that contained 60 to 64 heating rods (Neykov et al. 2006).
- The PSBT benchmark exercise contained void fraction measurements by sub-channel in boiling PWR conditions with 5 by 5 heating rods (Rubin et al. 2012).
- Recent void fraction measurements using tomography in a 3 by 3 refrigerant-filled PWR rod bundle (Taş et al. 2023a; Taş et al. 2023b).

Towards CHF prediction

CHAPTER 9

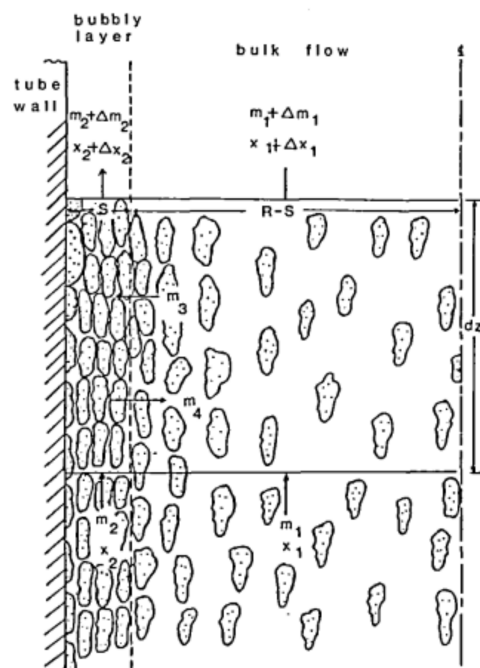


Diagram of the Weisman and Pei 1983 bubble crowding CHF model.

A critical heat flux criterion for R12 subcooled flow

In this chapter, the CFD set of models built in chapters 6 and 7 and validated in chapter 8 is used to extract information on flow conditions at the boiling crisis. The chapter begins with a literature review of various ways the CHF can be determined (section 9.1). The DEBORA CHF database used in this chapter is presented (section 9.2). The conditions in which the boiling crisis (BC) is reached are simulated with TrioCFD (section 9.3). Simulation results are then used to build a near-wall CHF criterion valid in subcooled flow (section 9.4). The limits of this model are then discussed (section 9.5).

Contents

9.1	CHF prediction approaches from the literature	181
9.1.1	Empirical correlations	181
9.1.2	Mechanistic dry-out	182
9.1.3	Pool boiling DNB	182
9.1.4	Mechanistic departure from nucleate boiling	183
9.1.5	The case of the transition region	186
9.2	DEBORA critical heat flux measuring campaigns	187
9.3	CFD Simulations of conditions at CHF in the DEBORA database	187
9.4	A simple CHF correlation for subcooled high-pressure freon-R12	191
9.4.1	Linking β at the outlet of the tube to the CHF	191
9.4.2	Assessing the precision of the proposed model	192
9.4.3	Sensitivity to change in mesh size	194
9.4.4	A conservative criterion for saturated flow	196
9.5	Limits of the proposed correlation	197

9.1 CHF prediction approaches from the literature

This section presents a short literature review of different methods used in the literature to predict the critical heat flux in various flow conditions. The thesis of Nop 2020 contains a thorough literature review of proposed DNB mechanisms and should be referred to for more details.

To predict if a flow has passed the CHF, system and subchannel codes currently in use in the nuclear industry use correlations and look-up tables that are valid for all regimes (section 9.1.1). A great deal of effort has also been put into building mechanistic approaches to predict dry-out (section 9.1.2), pool boiling DNB (section 9.1.3), and flow boiling DNB (section 9.1.4). The latter is the main focus of this review section. The case of the transition regime, for which no predictive mechanistic model currently exists, is also discussed (section 9.1.5).

9.1.1 Empirical correlations

The importance of preventing boiling crises in nuclear reactors has led to the production of a large amount of experimental CHF data. Typical campaigns consist in measuring the steady-state CHF for a given heated test section. For a given experimental run, the pressure and mass flux are imposed. One can then either:

- For a given heat flux, incrementally increase the inlet temperature until thermocouples located at the outlet of the pipe measure a wall temperature increase.
- For a given inlet temperature, incrementally increase the heat flux until thermocouples located at the outlet of the pipe measure a wall temperature increase.

Compiling a large amount of experimental data, the heat flux can be expressed in analytical fitting formulas like the Westinghouse W3 correlation (Todreas and Kazimi 2021 page 558), valid for circular cross-sections. The outlet quality X_{out} is usually used to measure the thermal conditions rather than the inlet temperature, though the two are equivalent. The CHF models then take the form:

$$q_{CHF} = f(P, G, X_{out}, L, \text{cross-section}) \quad (9.1)$$

Where L is the test section length and *cross-section* refers to the cross-section geometry and hydraulic diameter. It is usually round, annular, rectangular or an assembly. For a given geometry, pressure and mass flow rate the $q_{CHF}(X_{out})$ function is often plotted, as in figure 9.1. Celata et al. 1994 can be referred to for an assessment of different CHF formulations valid in circular cross-sections.

Another way to build an empirical formulation is through look-up tables. Groeneveld et al. 2007 built the one that is most widely used today. The normalized root mean square error of the Groeneveld et al. 2007 look-up table is 7.1% with constant inlet conditions. It is discussed in more detail in section 10.1.

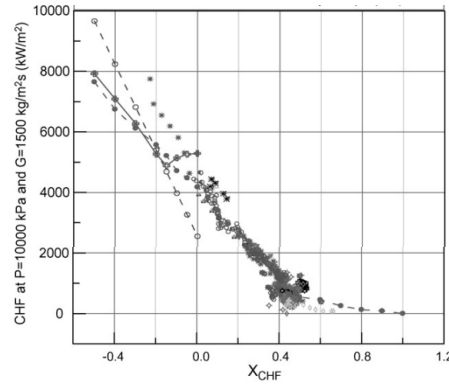


Figure 9.1: $q_{CHF}(X_{out})$ function on a subset of the Groeneveld et al. 2007 database. Reproduced from Groeneveld et al. 2007.

The use of machine learning algorithms on such large experimental databases could significantly reduce the errors of empirical correlations. Preliminary results are encouraging, with normalized root mean square errors that can be divided by two compared with the LUT (Helmryd Grosfilley et al. 2023). However, the possibility of using machine learning algorithms for safety demonstration leads to questions on explainability and model predictions in regions where few data points are available.

9.1.2 Mechanistic dry-out

Historical models for dry-out in annular regime have sought to evaluate a critical film thickness underneath which the film evaporates and the boiling crisis is triggered (Chun et al. 2003). For the prediction to be accurate, a code or a model must also be able to predict the film thickness in the flow. This problem is far from easy. It depends on the local flow quality. Determining the friction between the vapor and the film is key to know the velocities and the film dynamics. The volume of droplets entrained by the flow can also significantly alter the thickness.

Recent experiments by Morse et al. 2024 stressed the importance of dynamic phenomena, i.e. wave transport on the liquid film, for the DO. The surface can become dry in the trough a wave and be rewetted by its peak.

This highlights the complexity of determining the precise dynamics leading to the boiling crisis even in situations where most sources in the literature agree on the main mechanism. As shown in the next section, for DNB the community has not yet reached such an agreement.

9.1.3 Pool boiling DNB

To the best of my knowledge, the first mechanistic model for CHF was proposed by Zuber 1958 during his thesis. He considered pool boiling on a flat surface. He proposed that all of the heat flux is used for evaporation, which gives the vapor volume production. Vapor forms a blanket or a film above the surface. It is evac-

uated through vapor jets caused by the Rayleigh-Taylor instability (Taylor 1950), which sets the distance between jets. The ascending velocity of vapor and the descending velocity of fluid must ensure mass conservation. At the interface between both phases, Zuber proposes that when the heat flux, vapor production and relative velocity are sufficiently large, a Kelvin-Helmoltz instability occurs. The vapor jets then fuse, preventing the evacuation of vapor from the blanket and triggering the CHF. The conditions in which the Kelvin-Helmoltz instability appears gives an analytical CHF formulation. The proposed mechanism is hydrodynamic, not thermal, and involves the movement of fluid that is far from the surface.

A recent pool boiling experiment by Alvarez and Bucci 2024 looks into the effect of the height of liquid on the value of the pool boiling CHF. The authors find that at atmospheric pressure the value of CHF is independent of the height of the water column as long as it is larger than 4.0 mm, which is similar to the capillary length of water at atmospheric pressure (2.7 mm). They conclude that the mechanism that causes CHF for depths larger than 4 mm is bubble coalescence and interactions in the near-wall region, and do not observe the vapor columns hypothesized by Zuber 1958.

These two examples, though not directly relevant for the case of pressurized water reactors, present clearly one question that is asked when investigating DNB mechanisms: is the DNB a local phenomenon, triggered by mechanisms happening at the wall, or a larger-scale phenomenon that involves flow dynamics in far-off regions? Another debate is determining if the DNB is hydrodynamically-driven, i.e. happens when vapor can no longer be removed from the wall, or thermally-driven, i.e. happens when the liquid is at or over saturation temperature.

9.1.4 Mechanistic departure from nucleate boiling

Mass balance in a near-wall sublayer Weisman and Pei 1983 propose that the boiling crisis occurs when the near-wall void fraction exceeds 0.82. This criterion, or similar ones, has been directly used in CFD codes (Zhang et al. 2015; Mimouni et al. 2016a; Pothukuchi et al. 2019). However, Weisman and Pei 1983 sought to close their model in a simpler fashion. They carry out a vapor mass balance in the near-wall region. The vapor removal from the sublayer depends on the flow turbulent velocity fluctuations. It is constant for a given mass flow rate and is entirely hydrodynamic: no condensation is considered. The vapor production depends on the Levy 1967 OSV criterion coupled with a Lahey 1978 system-scale approach. Such models were discussed at length in sections 6.1 and 6.2.1. Vapor production therefore increases with the bulk liquid subcooling, and the criterion obtained depends on the bulk enthalpy.

Momentum balance in a near-wall sublayer Tong 1968 studies a momentum balance in the near-wall region. He calculates the flow skin friction $\rho_l u_\tau^2$ and the momentum generated by vapor formation through boiling $1/\rho_v (q_w/h_{lv})^2$. He proposes that the critical heat flux is reached when the two quantities are of the

same order of magnitude. A dimensionless constant function of the flow quality is fitted on experimental data. The final expression is:

$$q_{CHF,Tong-68} = (1.76 - 7.433X + 12.222X^2) h_{lv} u_\tau \rho_l \quad (9.2)$$

Energy balance in a near-wall sublayer Tong 1971 later proposed a model based on an energy balance in a near-wall liquid layer of a certain thickness. The axial evolution of the energy in this region can be computed analytically with assumptions. The boiling crisis occurs when this region is close enough to saturation, which translates into a criterion on the bulk subcooling.

Using experimental data on a short heater in highly subcooled flow, Nop et al. 2021 proposed that the boiling crisis occurs when a homogeneous liquid mantle reaches saturation temperature. The mantle thickness at CHF is shown to be only a function of turbulent quantities, without the presence of near-wall bubble models:

$$\delta_{CHF} = 180 \frac{\lambda}{\rho_l C_{p,l} u_\tau} = 180 \frac{1}{Pr} \frac{\nu_l}{u_\tau} \quad (9.3)$$

This equation can be used to determine the steady-state CHF:

$$q_{CHF,Nop} = \frac{(h_{ls} - h_l(T_{in})) u'_y(\delta_{CHF})}{1 - \exp\left(-Pe \frac{G^+ L}{Pr e}\right)} \quad (9.4)$$

Where u'_y are the normal turbulent velocity fluctuations at a distance δ_{CHF} from the wall, $\frac{G^+}{Pr} = 3.75 \cdot 10^{-4}$, L is the heated length and e the channel half width. The average error on the prediction of the CHF is around 5% on their data. Roumet et al. 2023 extended this approach to longer heaters, with mixed success. The main issue is that for large enough heating lengths, the bulk liquid temperature is no longer homogeneous and this influences the cooling of the mantle.

Liquid sublayer dryout Lee and Mudawar 1988 proposed that bubbles ejected from the wall coalesce and form a vapor blanket. It would be separated from the wall by a liquid sublayer. They investigate the mass and energy balance of the sublayer, that is cooled by the bulk flow. The boiling crisis occurs when the whole sublayer is depleted.

The CHF in this situation depends on the liquid bulk subcooling through the energy exchange term between the bulk and the blanket.

Kelvin-Helmholtz instability Based on experimental observations Galloway and Mudawar 1993 proposed that the vapor produced at the wall forms a blanket that is destabilized by the Kelvin-Helmholtz instability, generating a wavy aspect with patches of dry wall and a wetting front just before the CHF is reached. The boiling crisis occurs when the momentum of the produced vapor, which increases with the heat flux, overcomes the pressure difference created by the curvature of the waves.

The CHF depends on the liquid bulk subcooling through the vapor evaporation term: to produce vapor, the liquid in the wetting front must be heated to saturation then evaporated. The mass flux of vapor produced at the wall is considered to be $\Gamma_{w,l \rightarrow v} = q_w / (h_{lv} + C_{p,l}(T_s - T_{\text{bulk}}))$.

Criterion based on high-resolution near-wall data Recently, Zhang et al. 2022 carried out high-resolution measurements in pool boiling and flow boiling conditions near CHF. The quantities they determined were:

- The nucleation site density N_{sites} ;
- The average bubble footprint diameter d_{foot} ;
- The product of average bubble growth time and detachment frequency $f_{\text{departure}} t_{\text{growth}}$.

By combining these data, they built a criterion for the critical heat flux in flow and pool boiling conditions. The boiling crisis occurs when nucleating bubbles occupy all of the space on the surface of their heater, i.e. when:

$$C_{CHF} = N_{\text{sites}} \frac{\pi}{4} d_{\text{foot}}^2 f_{\text{departure}} t_{\text{growth}} \simeq 1 \quad (9.5)$$

These experiments are extremely interesting, and show that the triggering of the boiling crisis depends on local quantities, at the wall. This contradicts the mechanisms proposed in many of the aforementioned models.

Favre 2023 applied this model at a CFD scale using the 2-fluid NEPTUNE_CFD code with the default set of models on the DEBORA database. He obtained $C_{CHF} > 1$ after 0.5 m of the 3.5 m-long heated section for a test where the CHF was not reached experimentally. This was certainly because the models part of the heat flux partition were not appropriate. The criterion kept increasing up to 3.5 as liquid temperature in the near-wall cell neared saturation, and became constant when it had reached it for the last 0.5 m of the test section. Using the set of heat flux partition closures that he developed, he obtained $C_{CHF} = 0.8$ at the outlet for the same test run.

This shows that the Zhang et al. 2022 criterion is difficult to use in a CFD code in high-pressure conditions because it highly depends on correlations for many terms: the nucleation site density, bubble footprint diameter and growth and detachment time. Various proposals exist in the literature, and reliable formulations are not currently available in PWR conditions. It is interesting to note that the evolution of C_{CHF} in such a framework is mainly governed by the liquid temperature in the near-wall cell, which controls the key terms in most heat flux partitions (see section 2.2.5 and 6.4.1). This criterion will not evolve in saturated flow with current correlations, making it practical only in conditions where the flow is sub-cooled in the near-wall region. As the liquid temperature in the near-wall cell is mesh-dependent, it will be as well.

Taking a step back on approaches from the literature The different DNB mechanistic models have presented in this section are very different from one another. Each proposes its own key mechanism. Though different mechanisms can occur in different situations, these are not compatible with each other in the same conditions. Some also disagree with experimental observations. For example, no vapor blanket was observed in the CHF tests of Kossolapov et al. 2020. The difficulty of determining the precise near-wall dynamics in flow boiling have already been discussed in section 6.1. As the DNB is approached, which is a very sudden phenomenon, it can only increase.

Most of these models are based on small-scale hydrodynamic modeling at an intermediate distance from the wall. Intermediate, because apart for the Zhang et al. 2022 model the dynamics on the wall are not taken into account and because the bulk only indirectly influences the outcome.

Sublayer-based models consider a homogeneous bulk temperature. As shown in section 4.3, in flow boiling the temperature profile is logarithmic as in single-phase flow. The hypothesis of a discrete number of thermal zones is therefore very debatable, apart in the case of Nop et al. 2021 who focuses on very short heaters where the flow is not developed.

It is interesting that though the different authors propose hydrodynamic models, the bulk temperature is always a key parameter. In most models, it influences the vapor production which in turn is linked to the CHF. The final versions of the models are thermal, as they depend on the bulk quality. Though they have different derivation methods, many models share characteristics in the final formulations, in particular dependencies on h_{lv} and u_{τ} . Most are fitted on $q_{CHF}(X_{CHF})$ experimental data, which could explain the relatively good performance of these correlations given that at most one describes the correct physical mechanism.

9.1.5 The case of the transition region

The CHF can be reached in the transition regime. This is when the flow is saturated, at the minimum in the near-wall region, but the flow quality is insufficient for the it to have reached the annular regime where dry-out occurs (section 9.1.2). The existence of this region is certain as the $q_{CHF}(X_{CHF})$ plot presented in figure 9.1 is continuous from $X_{CHF} = -0.4$ to $X_{CHF} = 0.4$. In theory, the different hydrodynamics-based DNB models presented in section 9.1.4 should be applicable to this regime. However, as they were derived at a system scale and depend on the bulk to be subcooled for the instabilities that they propose to evolve along the heated length, they are not applicable to saturated flows.

This is also true for the Zhang et al. 2022 criterion: classical correlations for nucleation site density of bubble departure do not change if the flow is saturated in the near-wall region, as seen in the work of Favre 2023.

Mimouni et al. 2016a propose to use the Weisman and Pei 1983 $\alpha_{CHF} = 0.82$ criterion with a CFD code to predict DNB. This could work in a saturated region. However, such a method requires precise modeling of near-wall dynamics, where interfacial forces are modified compared with the bulk (Shi and Rzehak 2020). It

also could be sensible to mesh refinement, as it is the case for Mimouni et al. 2016a. It was observed in chapter 8 that in flow boiling experiments on multiple experimental databases the void fraction at the wall becomes independent from the outlet quality. Simulating correctly wall-bounded void fractions, as in the experiments, will be hardly compatible with a high-void fraction CHF criterion. Finally, DEBORA test G1P30W12 presents an interesting behavior (figure F.1). The experimental void fraction profile for the two highest outlet qualities gives the impression that the transition can be brutal and sudden between the wall-bounded regime and film boiling where the void fraction increases.

9.2 DEBORA critical heat flux measuring campaigns

In addition to the void fraction, Sauter mean diameter, vapor velocity and liquid temperature measurements discussed in chapter 4, several CHF measuring campaigns were conducted on the DEBORA test loop (Garnier 1992; Chichoux 1993).

The total number of datapoints is around 200. These tests were conducted in the same 3.5 m-long, 19.2 mm-diameter R12-filled pipe. The critical heat flux as a function of the inlet subcooling was measured in various (G, P) configurations. G went from 1000 to 5000 kg/(m²s) and P went from 10 to 30 bar. As remarked by Mimouni et al. 2016a, both authors used test sections in different materials and this had very little impact on the flow. Figure 9.2 presents experimental results from this database. Low-quality CHF ($X_{CHF} < 0$) in the database, which is probably in the subcooled DNB regime, occurs mainly at high pressures and flow rates.

At low mass fluxes ($G = 1000$ kg/(m²s)) $q_{CHF}(X_{CHF})$ is extremely dependent on P . For $G = 3000$ kg/(m²s) $q_{CHF}(X_{CHF})$ seems independent of the pressure, and for $G = 5000$ kg/(m²s) it is difficult to be conclusive.

At $P = 14$ bar the minimum CHF for a given quality occurs at $G = 3000$ kg/(m²s), i.e. $q_{CHF}(X_{CHF})$ has a complex shift when the mass flux changes. For higher pressures, the CHF increases with G .

I decided to use the DEBORA CHF database as a reference to study the boiling crisis as the set of closures developed in chapter 7 is well validated on local data from DEBORA (chapter 8).

9.3 CFD Simulations of conditions at CHF in the DEBORA database

In order to build a CHF correlation, this database is simulated with the set of closures presented in chapter 7. The inlet temperature, pressure and mass flux for the CHF conditions are enforced. The heat flux is taken as 95% of the CHF, to be coherent with the enthalpy flux analysis presented in section 4.2. The VDF numerical scheme is used with an axisymmetric mesh that contains 500 axial and 20

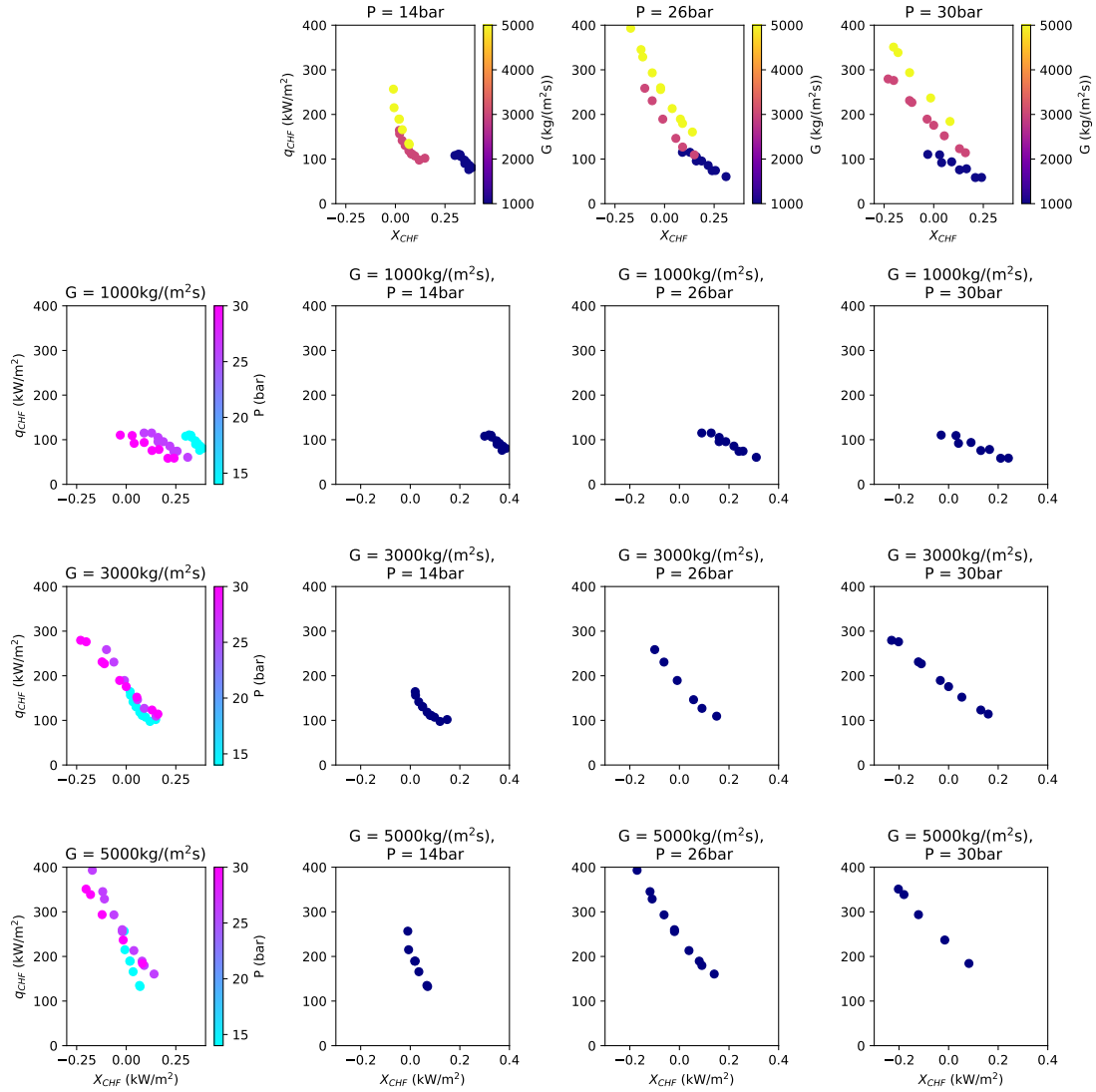


Figure 9.2: Experimental DEBORA CHF values for some selected conditions. Each subplot represents $q_{CHF}(X_{CHF})$ functions. **Top row:** influence of the mass flux on the CHF at various pressures. **Left column:** influence of the pressure on the CHF at various mass fluxes. **Other subplots:** $q_{CHF}(X_{CHF})$ functions for a given (G, P) configuration. Each column represents data for a given value of P and each row for a given value of G .

radial elements. The first cell distance to the wall is therefore 0.24 mm, and y_+ in the first cell between 175 and 600 depending on the flow velocity.

Figure 9.3 presents the first analysis of the outputs of these simulations. The void fraction in the near-wall cell at the outlet $\alpha_{CHF,1}$ is plotted as a function of the critical heat flux q_{CHF} . The void fraction globally diminishes as the heat flux increases, but the data is very scattered. As expected, a criterion like the one of Weisman and Pei 1983 cannot be used with the set of closures proposed in this thesis to determine the CHF.

The top subplots in figure 9.3 seem to indicate that the pressure and mass flux

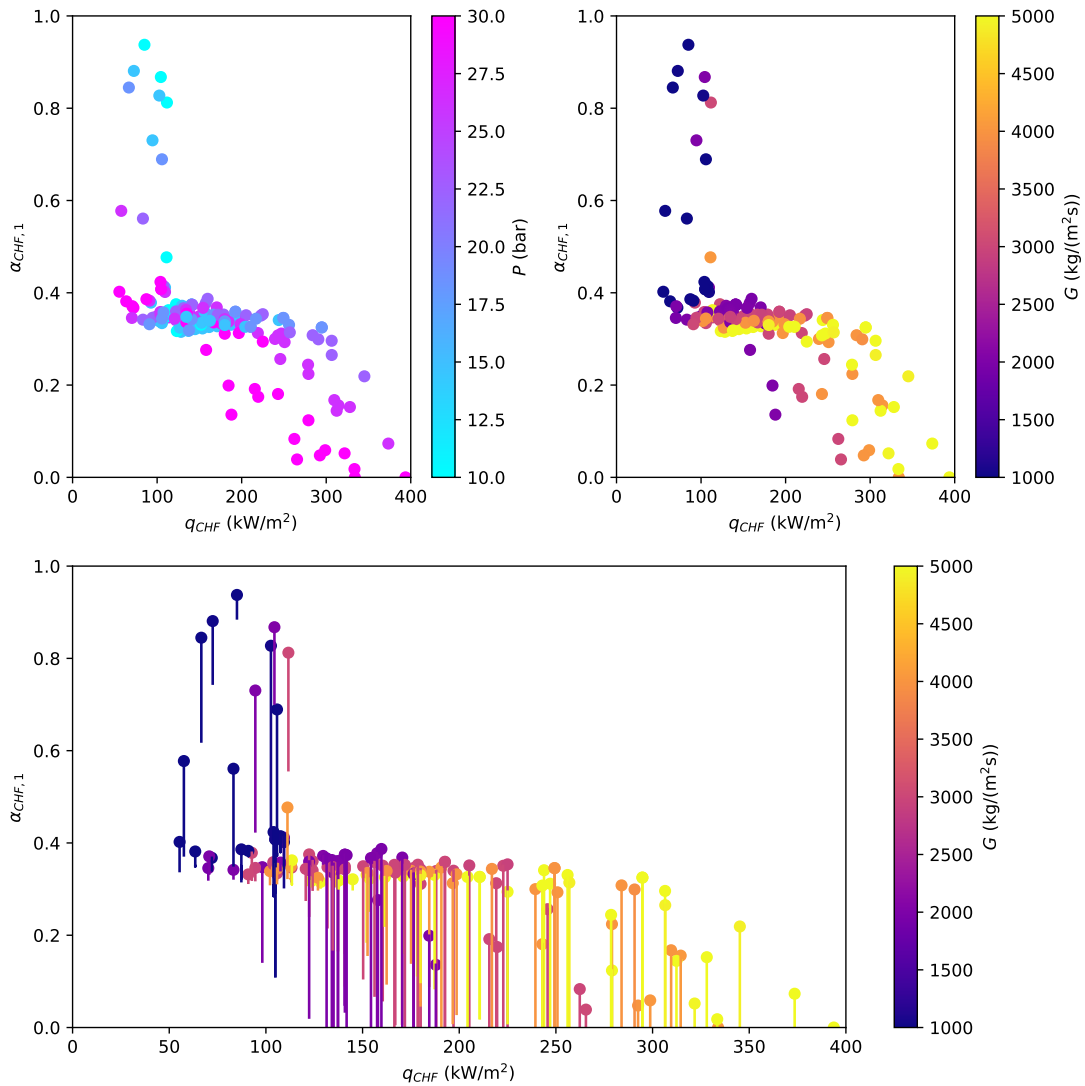


Figure 9.3: Void fraction in the near-wall cell at the outlet of the boiling section as a function of the critical heat flux. **Top left:** influence of the pressure on the outcome. **Top right:** influence of the mass flux on the outcome. **Bottom:** void fraction in the near-wall cell at the outlet (circle) and void fraction in the near-wall cell for 1 m before the outlet (lines).

have an influence on the plot for $\alpha_{CHF,1} \lesssim 0.35$. For a large subset of data points, the near-wall cell void fraction seems independent of the heat flux.

The bottom subplot in figure 9.3 presents, in addition to the near-wall void fraction at the outlet (circles), the evolution of the near-wall cell void fraction for 1 m upstream of the outlet (line). If the line is short, the near-wall cell void fraction does not change significantly as the flow evolves and cannot be used as a predictive criterion for the boiling crisis. If the line is long, it is feasible to use the near-wall cell void fraction. For $q_{CHF} < 200 \text{ kW/m}^2$, many conditions have short lines. This makes predicting the CHF using $\alpha_{v,1}$ impractical in these regions.

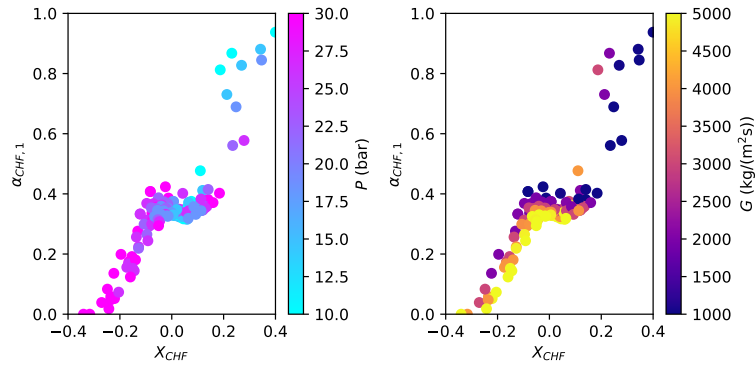


Figure 9.4: Void fraction in the near-wall cell at the outlet of the boiling section as a function of the flow quality at the boiling crisis. **Left:** influence of the system pressure. **Right:** influence of the mass flux.

$\alpha_{CHF,1}$ is plotted as a function of X_{CHF} in figure 9.4. The data is concentrated around a single curve, which indicates the relevance of looking into thermal effects. However, X_{CHF} is a non-local quantity. One could investigate the liquid temperature in the near-wall cell, but it will significantly depend on the mesh refinement. In the next section, I therefore look into a quantity that characterizes the near-wall temperature and is independent of the mesh: the flow boiling thermal-log law constant β , already discussed at length in section 4.3, in chapter 6 and in appendix B.

9.4 A simple CHF correlation for subcooled high-pressure freon-R12

9.4.1 Linking β at the outlet of the tube to the CHF

We recall that the liquid temperature profile follows a log-law even in subcooled developed boiling flow (section 4.3 equation 4.4):

$$\Theta_+^s(y_+) = \frac{T_s - T_l(y)}{T_*} = 2.12 \log(y_+) + \beta \quad (9.6)$$

Where $T_* = q_w / (\rho_l C_p u_\tau)$.

Thanks to TrioCFD simulation of CHF runs, all components of this equation are known apart from β . β can therefore be calculated in the near-wall cell at the boiling crisis at the outlet of the heated section:

$$\beta_{CHF,1} = \frac{T_s - T_l(y_1)}{T_*} - 2.12 \log(y_{+,1}) \quad (9.7)$$

Figure 9.5 presents $\beta_{CHF,1}$ calculated in this way as a function of the CHF with three different colormaps: one on the friction velocity u_τ , one on the system pressure P and one on the void fraction in the near-wall cell $\alpha_{v,1}$. I arbitrarily decide to only look at cases where the near-wall cell subcooling is larger than 1 K. 51 of the 156 simulated cases fall in this category.

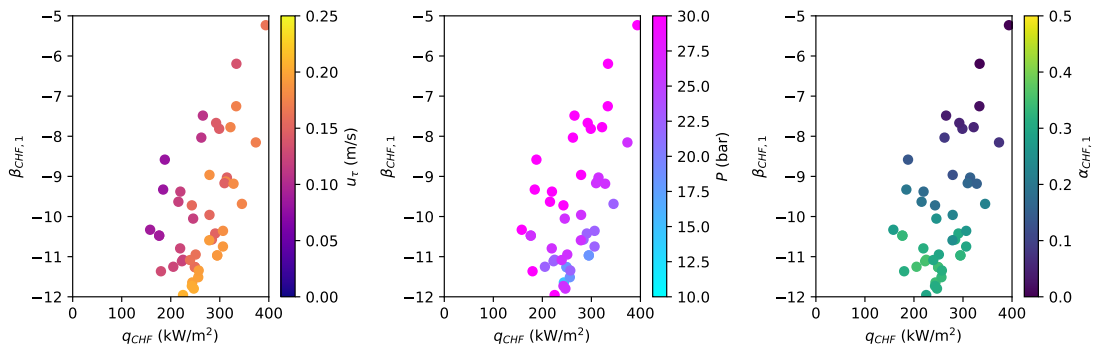


Figure 9.5: β_{CHF} at the outlet for every run subcooled in the near-wall cell, defined as $T_s - T_{l,1} > 1$ K. **Left:** effect of friction velocity in the near-wall cell. **Center:** effect of outlet pressure. **Right:** effect of the void fraction in the near-wall cell.

The first element of interest is that the values of $\beta_{CHF,1}$ are coherent with the OSV criterion developed in chapter 6, though both databases were built completely independently. Only two datapoints, for very high heat fluxes, have $\beta_{CHF,1} > -7$.

The parameter that seems to influence the CHF the most is the friction velocity u_τ . $\beta_{CHF,1}(q_{CHF})$ seems to form lines for different values of u_τ . I will therefore concentrate on this to build a CHF criterion. Higher subcoolings have larger values of $\beta_{CHF,1}$. This is coherent with the void fraction in the near-wall cell $\alpha_{CHF,1}$ being larger at low $\beta_{CHF,1}$.

At the system scale, the boiling number $Bo = \frac{q_w}{Gh_{lv}}$ is often considered a relevant dimensionless quantity for the CHF value (Ahmad 1973). However, it is a non-local quantity. One can look at a local version of the boiling number, built with the friction velocity and that should be independent of mesh size:

$$\Phi_{loc} = \frac{q_w}{\rho_l u_\tau h_{lv}} \quad (9.8)$$

This parameter was key in the formulation obtained by Tong 1968. While in his version of the correlation he used the a global friction velocity correlation, here u_τ is calculated by the CFD simulation. CFD codes should be able to calculate coherent values in any geometry without knowing the overall structure of the flow.

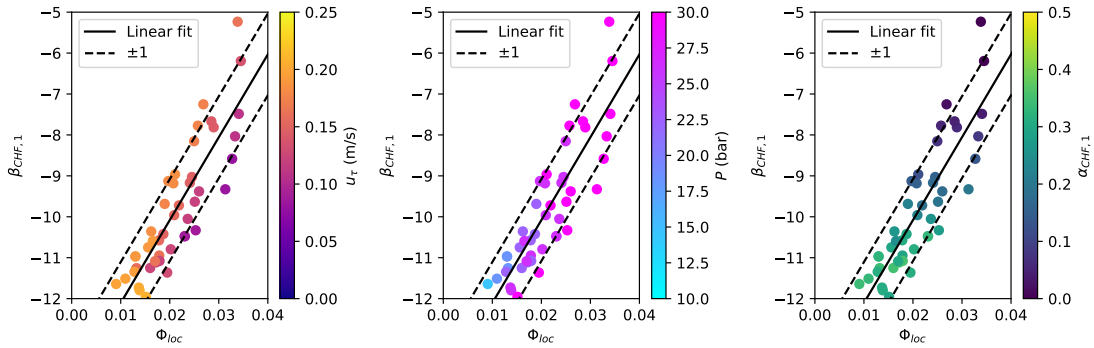


Figure 9.6: β_{CHF} as a function of Φ_{loc} in the near-wall cell at the outlet of the test section for every subcooled run (see equation 9.8 for definition). **Left:** effect of friction velocity in the near-wall cell. **Center:** effect of outlet pressure. **Right:** effect of the void fraction in the near-wall cell.

$\beta_{CHF,1}$ is plotted as a function of Φ_{loc} with different colormaps in figure 9.6. The datapoints line up rather well. A significant influence of u_τ remains visible (figure 9.6 left). The values of $\Phi_{loc} \sim 0.02$ may seem high compared with typical boiling numbers that are between 10^{-4} and 10^{-3} (see figure 8.2). This is due to u_τ being of the order of 20 times smaller than the bulk velocity.

Using a linear fit, if $T_s - T_l(y_1) > 1$ K the CHF occurs when:

$$\beta < \beta_{CHF,1} = \frac{\Phi_{loc} - 0.0698}{0.00494} \quad (9.9)$$

9.4.2 Assessing the precision of the proposed model

To evaluate the precision of this model, simulations are run with the experimental conditions, but a longer heated section. It is prolonged by 1 m, up to 4.5 m in total. At each point along the heated section, β in the near-wall cell is evaluated. If the criterion given in equation 9.9 is verified, the boiling crisis z -position is considered to have been reached. The position of the boiling crisis for the runs that respect this criterion is given at the left of figure 9.7. It is compared to the friction velocity u_τ (vertical axis) and the system pressure (colormap). One can see that the boiling

crisis is predicted close to the outlet of the test section. All points are located between 3 and 4 m downstream of the inlet. The distribution of the points seems independent of the pressure. However, there is a clear dependency on the friction velocity u_τ , which is also visible in the left plot of figure 9.6. The means square error (MSE) and normalized mean square error (NMSE) for a quantity x given in the legend are defined as:

$$\begin{aligned} \text{MSE} &= \sqrt{\langle (x_{sim} - x_{exp})^2 \rangle} \\ \text{NMSE} &= \sqrt{\langle \frac{(x_{sim} - x_{exp})^2}{x_{exp}^2} \rangle} \end{aligned} \quad (9.10)$$

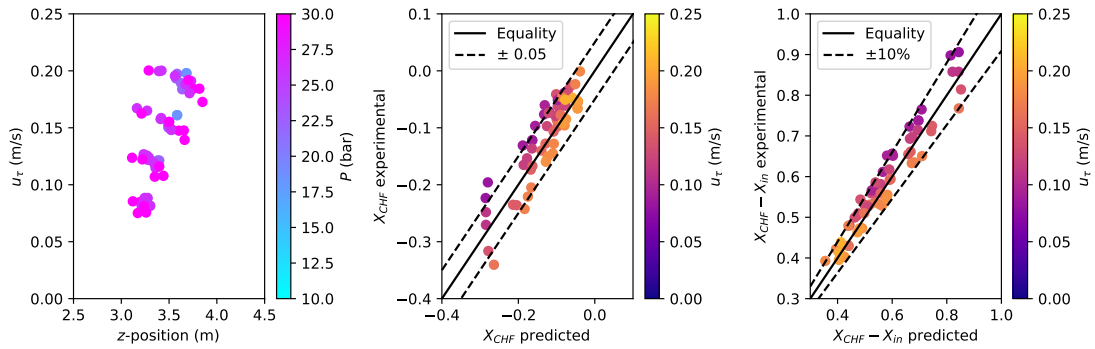


Figure 9.7: Evaluation of the precision of the subcooled CHF model proposed in equation 9.9. **Left:** position of the boiling crisis predicted by equation 9.9. **Center:** X_{CHF} calculated using the z -position of the boiling crisis. The MSE is 0.036. **Right:** change in quality between the inlet and the boiling crisis. The NMSE is 5.8%.

The central plot of figure 9.7 presents the predicted quality at CHF vs the experimental data. The agreement is relatively good, and the mean square error on X_{CHF} 0.036. The right plot presents the increase in quality between the inlet and the predicted CHF. The normalized mean square error on this quantity is 5.8%.

Some datapoints were lost between the linear fit shown in figure 9.6 and figure 9.7. In the simulations, they had $T_s - T_l(y_1) < 1$ before verifying the criterion given in equation 9.9.

There are some high-quality CHF datapoints that respect equation 9.9 in regions where $T_s - T_l(y_1) < 1$, in particular at low Φ_{loc} . This can lead to very small predicted z_{CHF} . I stress that it is essential to always check that the liquid is subcooled in the near-wall cell before applying the CHF criterion. The 1 K chosen arbitrarily may need to be adjusted in the future depending on simulation results. It can filter out different runs depending on the size of the near-wall cells, as larger near-wall cells have higher liquid temperatures in flow boiling.

In the previous simulations, the predicted altitude and quality at which the boiling crisis occurs were compared for a given wall heat flux. I now seek to compare the CHF predicted for a tube with a given inlet temperature with experimental data. This case is of particular interest to the nuclear industry: the temperature of the flow entering assemblies is set by that of the secondary circuit (see section 1.1.1).

This would ideally require a dichotomic algorithm on the heat flux in the heated section until the predicted CHF occurs at the outlet of the test section. However this has a high computational cost.

The methodology described in figure 9.8 is therefore applied. In addition to the simulation at q_{CHF} that was already analyzed, a second simulation is run for a heat flux 5% higher (step ①). The axial positions at which the boiling crisis is predicted in each configuration z_{CHF} and $z_{CHF,105\%}$ are then calculated (step ②). The $q_{CHF}(z)$ function is supposed relatively regular near the end of the test section. The critical heat flux is interpolated using the altitude at the outlet of the test section z_{out} (step ③) :

$$q_{CHF,sim} = q_{CHF,exp} \left(1 + 0.05 \frac{z_{out} - z_{CHF}}{z_{CHF,105} - z_{CHF}} \right) \quad (9.11)$$

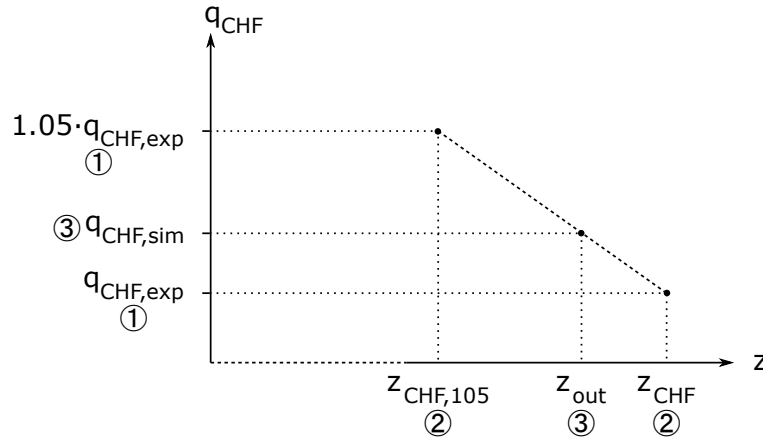


Figure 9.8: Diagram of the method used to determine the CHF for a given inlet temperature.

Results for the CHF calculation in a given configuration are given in figure 9.9. The predicted CHF is fairly close to the experimental values. The normalized mean square error calculated is 4.1%. It is of the same magnitude but smaller than the NMSE on $X_{CHF} - X_{in}$. It is also two times smaller than the NMSE in the Groeneveld et al. 2007 look-up table.

This very good prediction of the CHF can seem surprising given the dispersion of the $\beta_{CHF,1}(\Phi_{loc})$ data in figure 9.6. Figure B.5 contained the axial evolution of β for test tubes with much smaller wall heat fluxes. For test G2P26W16, which remains subcooled at the outlet, β goes from 0 to -18 over 2.5 m. For this test tube, an error of ~ 1 on the prediction of β , i.e. what is expected from figure 9.6, would result in an error of $\sim 5\%$ on the prediction of $X_{CHF} - X_{in}$.

9.4.3 Sensitivity to change in mesh size

In order to evaluate the sensitivity to change in mesh size, a series of simulations using the same setup as in section 9.4.2 are run. These have a heated section

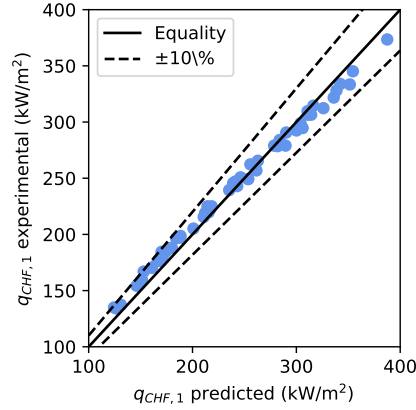


Figure 9.9: Experimental CHF plotted against the CHF predicted in subcooled flow for a given inlet temperature using the method described in figure 9.8. The NMSE on the data is 4.1%.

that is 1 m longer than in the experiment to determine the quality at which the boiling crisis occurs. The number of radial cells was reduced from 20 to 12. I decided to increase rather than reduce the mesh size so that the near-wall cells would remain still respect the $T_s - T_l(y_1) > 1$ subcooling criterion. A comparison between the predicted values of β_{CHF} at the outlet of the test section for both meshes, the predicted z -position at which equation 9.9 is verified and the resulting X_{CHF} is presented in figure 9.10. There is a visible difference in the simulated β_{CHF} for $\beta_{CHF} < -11$. However, the predicted boiling crisis position and thermodynamic quality are very similar for both cases. The difference is smaller than between predicted and experimental values (figure 9.7).

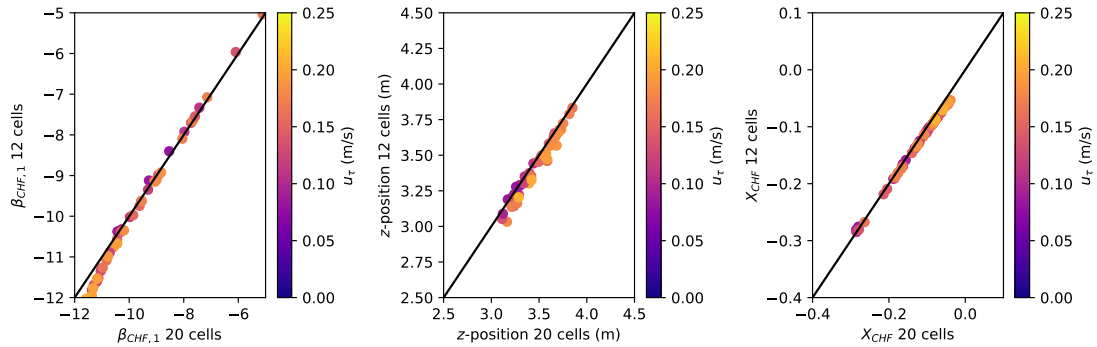


Figure 9.10: Evaluation of the sensitivity to change in mesh size of the CHF model proposed in this chapter. **Left:** β_{OSV} at the outlet of the test section for 12 and 20 radial cell meshes. The difference between the two becomes visible for $\beta_{OSV} < -11$. **Center:** z -position of the boiling crisis predicted by equation 9.9 for 12 and 20 radial cell meshes. The difference between both simulations is not significant. **Right:** X_{CHF} predicted by equation 9.9 for 12 and 20 radial cell meshes. The difference between both simulations is not significant.

9.4.4 A conservative criterion for saturated flow

We now take a look at the datapoints that are not encompassed in the $T_s - T_{l,1} > 1$ K criterion used to determine if the near-wall cell is subcooled. Figure 9.11 shows where they are located in a $\alpha_{CHF,1}(X_{CHF})$ and a $\alpha_{CHF,1}(q_{CHF})$ plane.

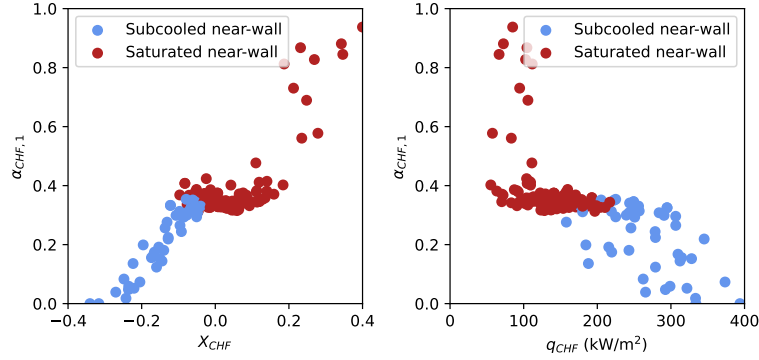


Figure 9.11: Locations of the CHF datapoints that are saturated and subcooled in the near-wall cell with respect to figures 9.3 and 9.4.

As expected, the datapoints that are subcooled in the near-wall region have low outlet qualities ($X_{CHF} < -0.05$) and high heat fluxes. The others all have a minimum void fraction at the wall of 0.32. A conservative criterion on the whole database is therefore:

$$\begin{cases} \beta < \beta_{CHF,1} = \frac{\Phi_{loc} - 0.0579}{0.00373} & \text{if } T_s - T_{l,1} > 1 \text{ K} \\ \alpha_v > 0.32 & \text{if } T_s - T_{l,1} \leq 1 \text{ K} \end{cases} \quad (9.12)$$

However, the void fraction criterion will be very sensitive to any adjustment of the α_v -dependent lift force proposed in section 7.4.

9.5 Limits of the proposed correlation

A simple model to predict the critical heat flux in subcooled flow at a CFD scale was built. It is based on relevant dimensionless quantities, β_{OSV} and Φ_{loc} , that have already proven key to predict boiling phenomena in chapter 6 of this thesis and in the literature (Tong 1968, Nop et al. 2021). On the subcooled database, the mean square error on X_{CHF} is 0.036. The NSME on q_{CHF} for a given inlet temperature is 4.1%, which is surprisingly low with regard to experimental uncertainty in the determination of the CHF. The model is also robust to a change in mesh size.

One must keep in mind that the heated length on the DEBORA database is fairly large at 3.5 m. This makes the error on the predicted CHF for a given X_{CHF} smaller, and could be part of the reason why the proposal has such slow MSE. Another part is that only one experimental database was used. As described by Groeneveld et al. 2007, there can be a large variability between databases for CHF prediction.

The correlation proposed has the following limits:

- The fluid used to calibrate this model was R12, and not high-pressure water as is found in PWR's. This limitation will be addressed in chapter 10, where a similar analysis is carried out on the Groeneveld et al. 2007 database.
- The correlation was tested in a single geometry, the circular pipe used in the DEBORA experiment. In chapter 10, pipes of different diameters and an annular channel will be investigated.
- This work does not give an understanding of what occurs at the CHF. The underlying fundamental mechanism could be a hydrodynamic instability (Lee and Mudawar 1988), bubble coalescence on the wall (Zhang et al. 2022) or something else entirely.
- The predicted liquid temperature profiles varies less between different sets of closures in CFD codes than void fraction distributions. This can be seen by comparing figures 5.2 and 8.4 for example. However, the proposed CHF model is bound to be sensitive to the set of closures that are selected in a CFD framework. This has not been evaluated.
- It must be verified more thoroughly that the criterion is never met in up-stream regions in high-quality CHF conditions.
- As the criterion is solely energy-based, no progress has been made on the prediction of the CHF in the transition regime where the flow is saturated.
- The way this model will behave for larger values of Φ_{loc} , where the CHF should still be subcooled DNB, is not known. Either the OSV criterion will no longer be respected, or the $\beta_{CHF,1}(\Phi_{loc})$ dynamics will change. This could be of particular interest in low-void fraction high-subcooling conditions, like those investigated by Nop et al. 2021, where the OSV was not apparent at the CHF.

CHAPTER 10

Pressure [kPa]	Mass Flux [kg m ⁻² s ⁻¹]	CHF [kW m ⁻²]																											
		11000	9572	7966	6675	5958	5076	4002	3360	2680	1910	1409	1138	922	772	414	404	329	294	221	109	66	35	0					
12000	3500	11000	9572	7966	6675	5958	5076	4002	3360	2680	1910	1409	1138	922	772	414	404	329	294	221	109	66	35	0					
12000	4000	11291	9679	8449	7028	6239	5226	4061	3326	2680	1904	1456	1244	1077	923	693	586	454	361	251	131	70	36	0					
12000	4500	11695	10442	8797	7329	6398	5397	4163	3353	2698	1927	1529	1363	1174	1007	862	685	539	418	294	154	75	38	0					
12000	5000	12117	10836	9117	7579	6726	5903	4418	3473	2772	2010	1637	1431	1254	1154	921	726	573	465	341	183	82	40	0					
12000	5500	12466	11071	9431	7831	7005	6089	4517	3728	2908	2140	1857	1621	1469	1345	1105	909	704	564	401	214	91	43	0					
12000	6000	13176	11559	9762	8050	7166	6226	4603	3885	3160	2229	1966	1781	1627	1472	1264	1065	868	721	483	252	105	49	0					
12000	6500	14034	12051	10061	8249	7390	6426	4668	3941	3128	2355	2150	1949	1811	1623	1447	1220	1023	852	558	290	122	57	0					
12000	7000	14607	12508	10487	8532	7609	6605	4731	4011	3182	2432	2217	2093	1955	1750	1554	1342	1126	945	622	326	140	66	0					
12000	7500	14975	12908	10907	8703	7863	6710	4821	4080	3250	2490	2284	2170	2077	1921	1676	1441	1227	1034	683	356	152	72	0					
12000	8000	15432	13296	11407	8898	8033	6904	4932	4219	3398	2627	2737	2527	2420	2168	1912	1606	1370	1142	749	384	162	76	0					
X→	-0.50	-0.40	-0.30	-0.20	-0.15	-0.10	-0.05	0.00	0.05	0.10	0.15	0.20	0.25	0.30	0.35	0.40	0.45	0.50	0.60	0.70	0.80	0.90	1						
14000	0	3505	3372	3240	3113	3046	2965	2846	2654	2242	1848	1544	1296	1129	992	884	799	736	691	585	384	202	113	0					
14000	50	3908	3676	3552	3413	3338	3250	3129	2951	2557	2195	1919	1710	1527	1363	1230	1114	1035	930	790	565	310	185	0					
14000	100	4244	4060	3897	3721	3617	3500	3371	3206	2909	2586	2290	1961	1791	1575	1469	1262	1193	1023	811	595	342	204	0					
14000	300	4479	4268	4074	3858	3727	3586	3448	3301	2996	2701	2358	2100	1970	1756	1651	1481	1308	1143	842	615	347	217	0					
14000	500	4680	4404	4184	3876	3713	3545	3401	3249	3001	2641	2373	2089	1825	1559	1422	1273	1087	1017	319	298	192	119	0					
14000	750	5155	4929	4487	3917	3666	3417	3241	3066	2841	2505	2177	1849	1591	1332	1131	885	769	502	265	135	79	77	0					
14000	1000	6001	5568	4960	4089	3670	3378	3049	2693	2399	2051	1731	1466	1244	1017	854	745	649	295	224	102	67	49	0					
14000	1500	6787	6145	5185	4364	3798	3406	3003	2583	2218	1807	1498	1200	971	765	555	196	180	138	119	53	43	34	0					
14000	2000	7188	6465	5394	4496	3995	3628	3201	2696	2221	1751	1444	1121	879	603	419	176	126	108	93	58	41	26	0					
14000	2500	7630	6781	5986	4902	4465	4006	3595	2832	2224	1773	1391	1024	831	564	312	213	139	119	102	62	42	27	0					
14000	3000	7824	7031	6139	5394	4701	4236	3320	2894	2333	1831	1396	1082	865	604	318	275	237	201	146	80	47	31	0					
14000	3500	8111	7338	6268	5532	4884	4356	3417	2963	2433	1897	1444	1140	927	710	491	420	340	281	200	108	61	32	0					
14000	4000	8229	7457	6488	5706	5185	4498	3518	2992	2511	2029	1603	1307	1103	854	722	590	467	365	245	125	65	33	0					
14000	4500	8718	7543	6537	5730	5344	4748	3789	3092	2558	2105	1709	1449	1207	1005	835	676	558	421	287	148	70	34	0					
14000	5000	8978	7649	6594	5732	5451	4912	3963	3214	2692	2161	1745	1510	1280	1062	916	746	599	465	329	174	76	36	0					
14000	5500	9249	7760	6609	5753	5505	4944	4043	3419	3026	2433	1989	1746	1475	1298	1107	940	746	572	380	206	87	40	0					
14000	6000	9831	8166	6738	5864	5509	4956	4110	3463	3170	2575	2209	1986	1656	1420	1253	1082	893	709	468	242	101	47	0					
14000	6500	10687	8715	6808	5894	5553	4972	4129	3544	3208	2617	2326	2201	1908	1609	1448	1241	1034	834	539	280	118	55	0					
14000	7000	11414	9448	7169	6008	5694	4993	4140	3605	3202	2682	2339	2261	2018	1745	1566	1343	1129	924	603	317	136	64	0					
14000	7500	12199	10064	7714	6137	5700	5016	4159	3729	3240	2689	2350	2270	2120	1836	1638	1433	1216	1013	666	347	148	70	0					
14000	8000	12874	10581	8108	6231	5878	5214	4370	3809	3276	2806	2508	2342	2217	2033	1803	1565	1338	1116	733	376	159	75	0					
X→	-0.50	-0.40	-0.30	-0.20	-0.15	-0.10	-0.05	0.00	0.05	0.10	0.15	0.20	0.25	0.30	0.35	0.40	0.45	0.50	0.60	0.70	0.80	0.90	1						
16000	0	2869	2780	2691	2603	2556	2500	2417	2276	1978	1667	1411	1199	1036	903	820	739	668	640	535	317	165	82	0					

Extract from the Groeneveld et al. 2007 CHF look-up table.

Subcooled CHF in the Groeneveld database

The work carried out in chapter 9 is extended to high-pressure water flows in different geometries. The Groeneveld et al. 2007 CHF database that is used in this chapter is presented (section 10.1). A similar methodology as in chapter 9 is carried out and a CHF criterion for subcooled flow is built (section 10.3). The results are less convincing than those on the DEBORA database. A single criterion for R12 and water flows is then investigated: the one proposed by Nop et al. 2021 is evaluated and another is proposed (section 10.4). The PATRICIA experiment for the boiling crisis in transient RIA-like conditions is simulated and the CHF criteria evaluated in these conditions (section 10.5). Possible next steps for CHF modeling in this framework are proposed (section 10.6).

Contents

10.1	The Groeneveld database	201
10.1.1	Presentation	201
10.1.2	Analysis of raw experimental data	201
10.1.3	A representative sample for subcooled flow	205
10.2	Simulation setup	206
10.3	The CHF in subcooled high-pressure developed water flow	207
10.4	Towards a single criterion for two different fluids	210
10.4.1	Evaluating the Nop criterion on both fluids	210
10.4.2	Proposed model for both fluids	212
10.4.3	Summary of investigated local subcooled CHF models	213
10.5	Simulations of PATRICIA transient flows	215
10.5.1	Transient CHF models from the literature	215
10.5.2	The PATRICIA experimental database	215
10.5.3	Steady-state PATRICIA results	216
10.5.4	Transient PATRICIA results	216
10.6	Perspectives	221

10.1 The Groeneveld database

10.1.1 Presentation

The Groeneveld et al. 2007 look-up table (LUT) is one of the most widely used methods to determine the CHF in a heated circular pipe. It is based on $\sim 24,781$ data points from 82 different sources. The q_{CHF} for discrete values of (P, G, X_{out}) triplets is calculated from the experimental data. One can directly refer to the LUT to determine the CHF at the closest point to the conditions of interest. The LUT can also be loaded into a software so that the CHF can be interpolated in between those discrete values.

The issue with building a look-up table is that a limited number of parameters can be considered for it to remain readable. In particular, the CHF is considered independent of the heated length, which can have an impact. Furthermore, the experimental data contains various pipe diameters, from 3 to 25 mm. The CHF is rescaled to 8 mm data as it is the most common in the database through a formula that can also lead to errors:

$$q_{CHF} = q_{CHF, D_h=8 \text{ mm}} \left(\frac{D_h}{8 \text{ mm}} \right)^{-1/2} \quad (10.1)$$

Due to these limitations and errors in experimental conditions, the normalized root mean square error of the CHF prediction with constant inlet temperature is 7.1%.

The data used to build the LUT was recently published (Groeneveld 2019). The analysis and simulations carried out in this chapter are based on this raw dataset, and not on LUT interpolations.

10.1.2 Analysis of raw experimental data

In this subsection, the CHF trends that can be seen in the database are discussed. $q_{CHF}(X_{CHF})$ data is plotted in different configurations. In order to understand the separate impact of various parameters, the data that have similar P , G and D are grouped. I have not seen the database discussed in this way in the literature.

Figure 10.1 presents the dynamics for an 8 mm-diameter pipe. For each (P, G) couple, the dynamics described by Groeneveld et al. 2007 are visible: for $X_{CHF} \lesssim 0$, a steep slope that corresponds to the DNB region. The slope then straightens in the transition region. For a certain X_{CHF} that depends on the flow conditions but lies between 0.3 and 0.7 here, the slope becomes extremely steep and the boiling crisis (BC) seems entirely determined by the quality and not by the heat flux.

The top row in the figure shows the impact of G at three different pressures. At $P = 70$ bar, q_{CHF} is largest for smallest G for a given X_{CHF} . At $P = 147$ bar, q_{CHF} seems independent of G . At $P = 177$ bar, q_{CHF} is minimal for smaller G .

The left row of the figure shows the impact of changing the system pressure at a constant G . At the lowest mass fluxes, q_{CHF} is maximal for smallest pressures. At $G = 4000 \text{ kg}/(\text{m}^2\text{s})$, q_{CHF} seems independent of the pressure for $X_{CHF} > 0$.

The underlying causes of this complex behavior are not clear for us. The conditions that are closest to those of nuclear reactors are $G = 4000 \text{ kg}/(\text{m}^2\text{s})$ and

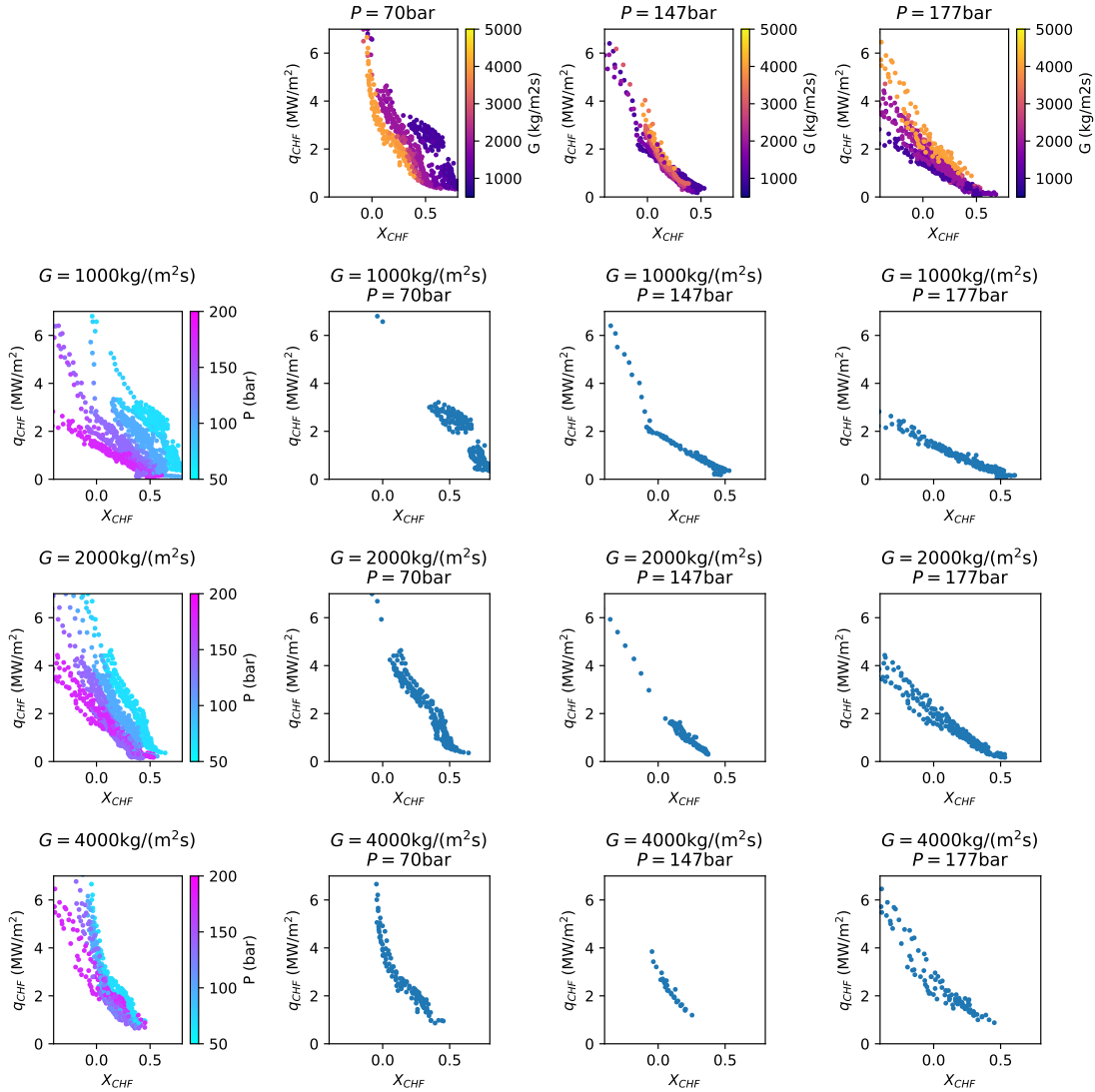


Figure 10.1: Critical heat flux data for 8 mm-diameter pipes from Groeneveld 2019. Experimental data is grouped in classes of P and G that encompass data at $\pm 5\%$ compared with the values that are given in the legend. **Top row:** influence of the mass flux on the CHF at various pressures. **Left column:** influence of the pressure on the CHF at various mass fluxes. **Other subplots:** $q_{CHF}(X_{CHF})$ functions for a given (G, P) configuration. Each column represents data for a given P and each row for a given G .

$P = 147$ bar. These are the locations in which the dynamics of $X_{CHF}(q_{CHF})$ seems independent of G and P , i.e. where the trends seem most simple.

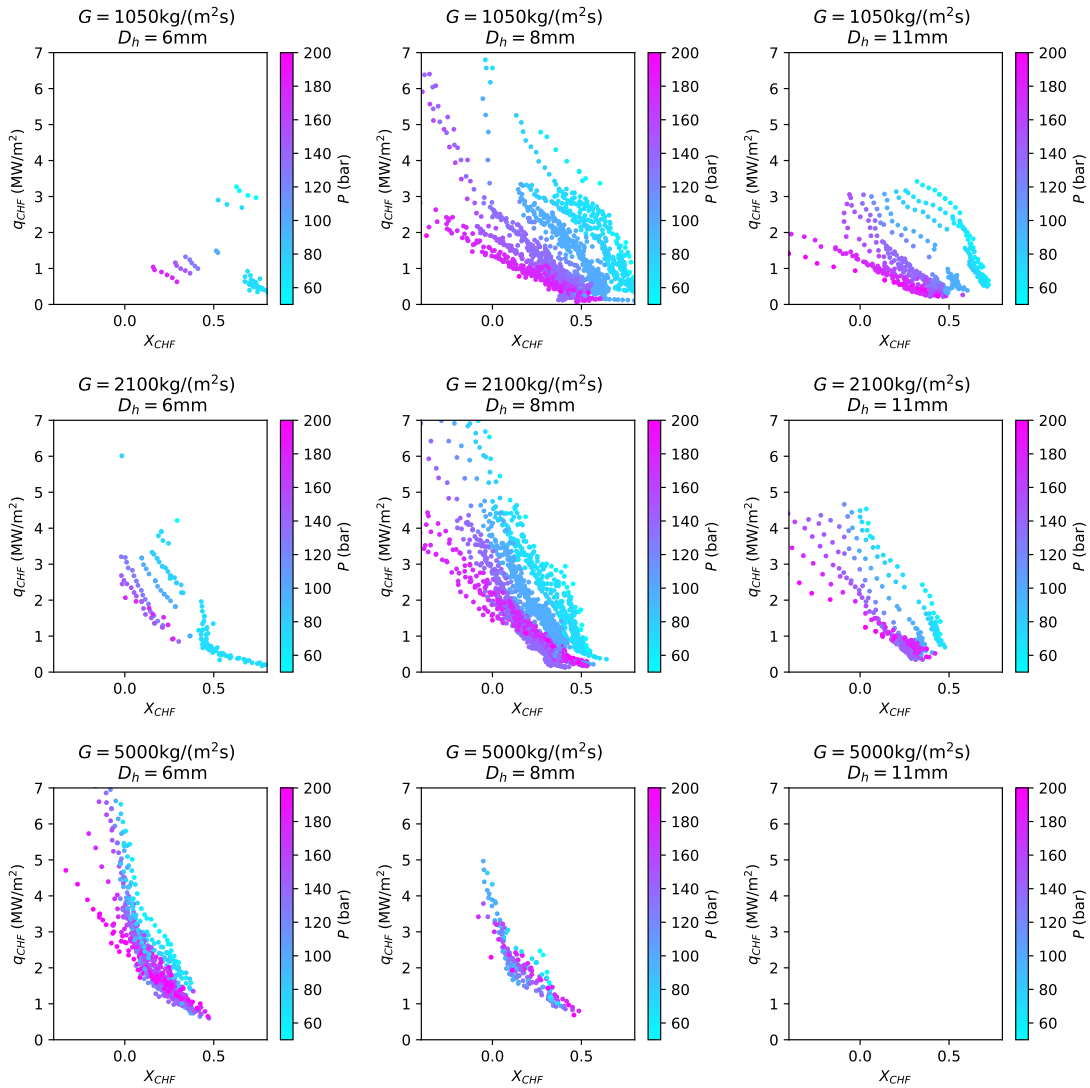


Figure 10.2: Effect of the system pressure on critical heat flux data from Groeneveld 2019. Experimental data is grouped in classes of G and D_h that encompass data at $\pm 5\%$ compared with the values that are given in the legend. Each column represents data for a given D_h and each row for a given G .

Figure 10.2 shows the effect of the system pressure in different (G, D_h) configurations. No clear trend on the experimental quantities is visible when changing the test section diameter. As above, increasing the mass flux gathers the data on similar lines. For $G = 5000 \text{ kg}/(\text{m}^2\text{s})$, q_{CHF} still varies significantly with the pressure when $X_{CHF} < 0$.

The effect of the mass flux in different (P, D_h) configurations is shown in figure 10.3. As in figure 10.1, for all three diameters investigated at $P = 147 \text{ bar}$ the data collapses together, and seems to have very different behaviors at higher and lower pressures. At $P = 70 \text{ bar}$, the influence of the mass flux also seems to diminish for low flow qualities. At $P = 178 \text{ bar}$, it seems to increase for low flow

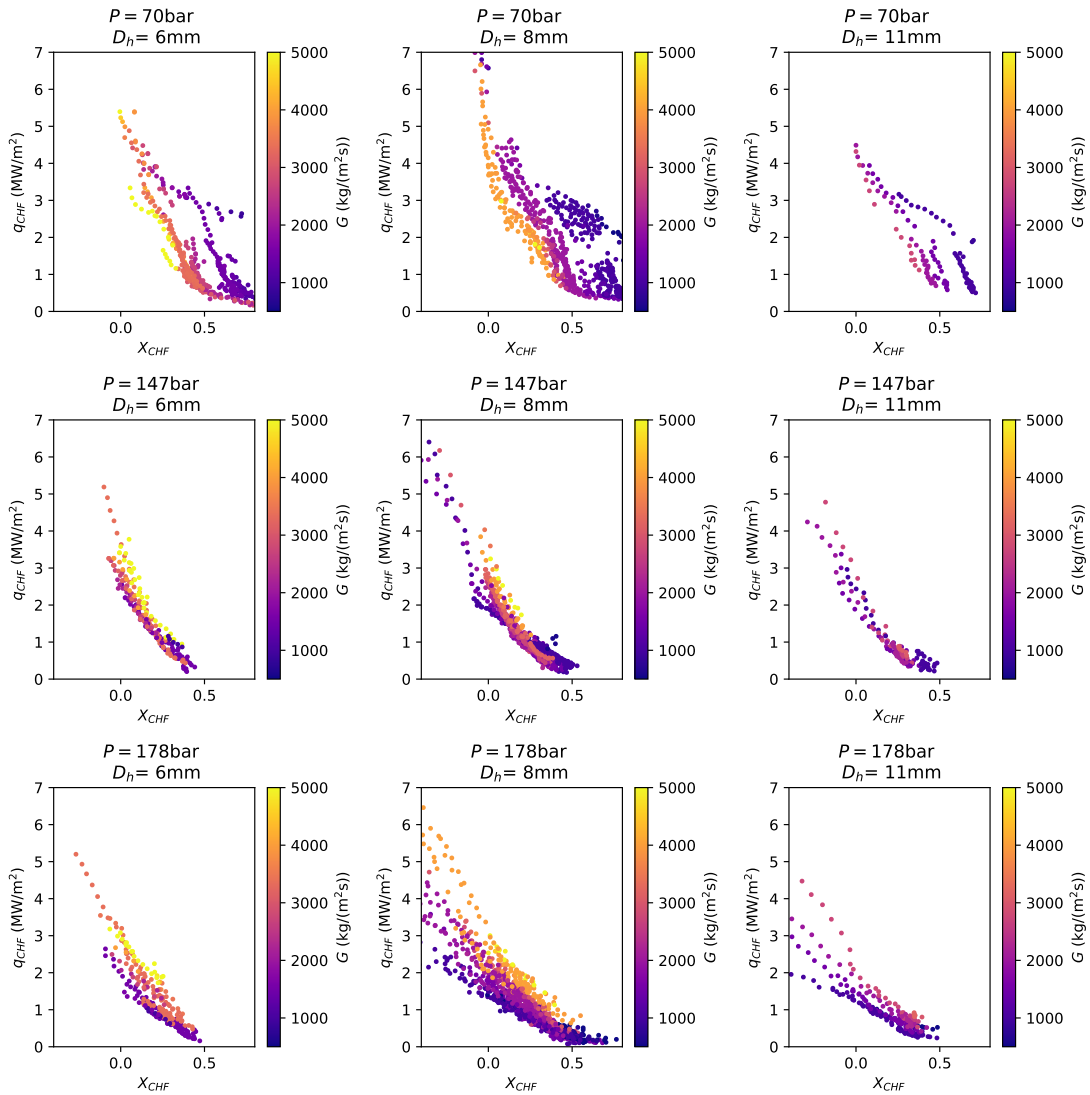


Figure 10.3: Effect of the mass flux on critical heat flux data from Groeneveld 2019. Experimental data is grouped in classes of P and D_h that encompass data at $\pm 5\%$ compared with the values that are given in the legend. Each column represents data for a given D_h and each row for a given P .

qualities. One cannot identify a visible effect of changing the test section diameter.

Figure 10.4 presents the impact of the section diameter in different (P, G) configurations. In all of the plotted data, the effect of the tube diameter on the flow is much less significant than what was seen in figures 10.2 and 10.3 with the pressure and mass flux. The general trend seems to be that for a given CHF increasing the diameter reduces X_{CHF} . This is expected as for smaller pipes the core will heat up more easily for similar near-wall temperatures.

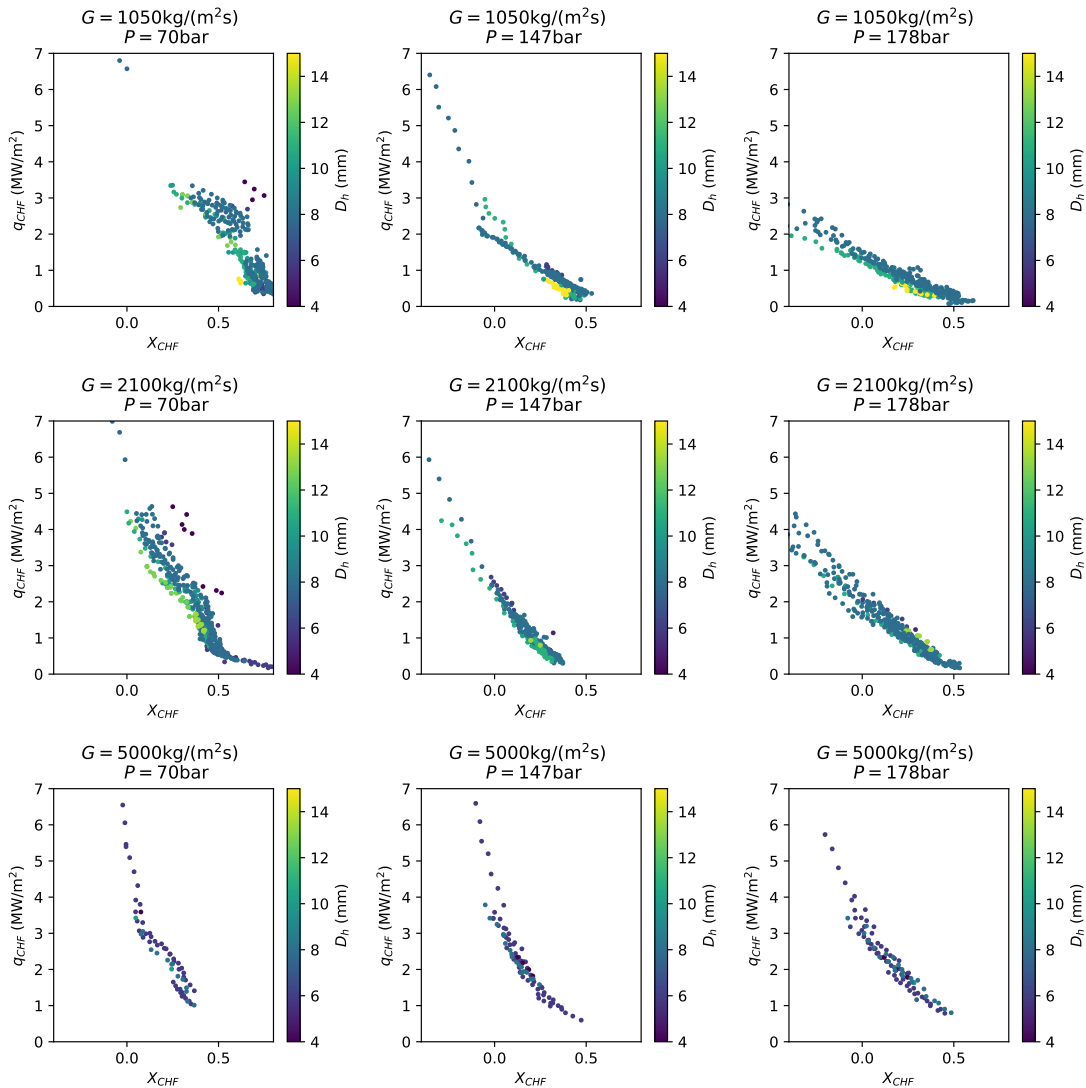


Figure 10.4: Effect of the pipe hydraulic diameter on critical heat flux data from Groeneveld 2019. Experimental data is grouped in classes of P and G that encompass data at $\pm 5\%$ compared with the values that are given in the legend. Each column represents data for a given P and each row for a given G .

10.1.3 A representative sample for subcooled flow

In order to extend the subcooled CHF model from chapter 9 to high-pressure water flow, a similar methodology is used and CFD simulations are run in pipes to analyze the simulated quantities in the near-wall region. I therefore concentrate on low-quality runs, where $X_{CHF} < 0.05$ and the flow has a good chance of being subcooled in the near-wall region. This limits the size of the Groeneveld 2019 database to 2856 points. To keep a reasonable computation cost, ~ 300 runs are selected from the database.

To this end, the simplest method would be to randomly select 300 conditions

from the 2856. However, around half of these points are in 8 mm diameter pipes. As can be seen in figures 10.1, 10.2, 10.3 and 10.4, some sets of (P, G, D) triplets have many more $X_{CHF}(q_{CHF})$ than others.

To extract a subset that is representative of the diversity of experiments, the domain is partitioned in a number of (P, G, D) triplets that contain multiple CHF points. For each triplet, the point with the lowest $X_{CHF,min}$ is included. The point with the next smallest X_{CHF} so that it is larger than $X_{CHF,min} + 0.03$ is then selected. This process is repeated until $X_{CHF} = 0.05$ is reached. This enables a homogeneous and automatic sampling of the database. A step of 0.03 was chosen to obtain ~ 300 points in total. It can be adjusted to select more or less points. Adding a small number of points randomly selected, in total 374 runs are simulated.

10.2 Simulation setup

The set of closures that used is the one developed in chapter 7. The VDF axisymmetric numerical scheme is selected. For each tube, a $50D_h$ -long unheated section is simulated for the RANS turbulence to develop before the inlet. As in section 9.4.2, a longer heated length than in the experiment is simulated to post-process the axial location where the BC occurs. Depending on the hydraulic diameter, the simulated test section is between 1.5 and 2 times the length of the experimental one. This is sufficient to locate the boiling crisis. A $10D_h$ -long unheated outlet section is also simulated. The number of radial cells was set so that $y_{+,1} \simeq 150$ in the near-wall cell. The number of radial cells is then set to at least 5 and at most 20. The number of axial cells was determined for them to have an aspect ratio of 10 in the non-heated sections and 5 in the heated section. Each run therefore has its own geometry, number of radial and axial elements.

10.3 The CHF in subcooled high-pressure developed water flow

Figure 10.5 presents the simulated $\alpha_{CHF,1}$ of the various simulations on the Groenewald 2019 database. One can see that the simulated void fractions are significantly larger than on the DEBORA database (figure 9.4), and on the water test tubes conditions simulated in chapter 8. This can have two different root causes.

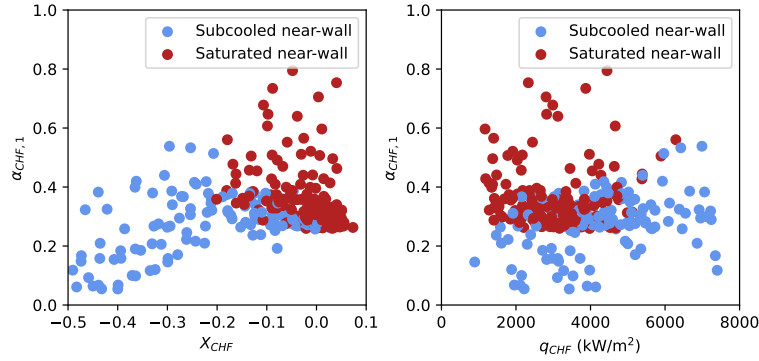


Figure 10.5: Void fraction in the near-wall cell as a function of the CHF (**left**) and the quality at CHF (**right**). The subcooled points are defined as having $T_s - T_l(y_1) > 3$ K.

The first possibility is that the simulated conditions in the code are adequate, i.e. near experimental data if there were any in these conditions. This would mean that at these heat fluxes the void fraction distributions are different than in the ones that were simulated in chapter 8. There were no conditions in water flow in geometries of hydraulic diameter around 8 mm and where the heat flux is as high. The largest wall heat flux simulated was on the Martin 1969 database, and it was 3500 MW/m², for a 4 mm D_h . Figure 8.2 showed that the conditions for PWR RIA applications were at the edge of the local void fraction database.

The second possibility is that the vapor predictions are wrong. This would impact any void-fraction based criterion. However, as discussed in section 9.5, the liquid temperature profiles vary much less from one simulation to another than void fraction ones, apart very close to saturation. As in section 9.4, I will concentrate on the liquid temperature field in the near-wall cell and the associated $\beta_{CHF,1}$. To limit the risk of bad temperature predictions interfering with the analysis, the criterion that defines sufficient subcooling to calculate $\beta_{CHF,1}$ is arbitrarily increased from 1 to 3 K.

$\beta_{CHF,1}$ as a function of the critical heat flux and of Φ_{loc} (defined in equation 9.8) is plotted in figure 10.6. The $\beta_{CHF,1}(\Phi_{loc})$ data does not collapse as well on a line as in figure 9.6, but the correlation is improved compared with the $\beta_{CHF,1}(q_{CHF})$ plot. One can also notice that the β_{OSV} -based OSV criterion (chapter 6) is respected for every datapoint, which is also reassuring.

It should also be noted that there is no clear correlation between $\beta_{CHF,1}$ and the tube hydraulic diameter. This is also reassuring, as the desired local correlation

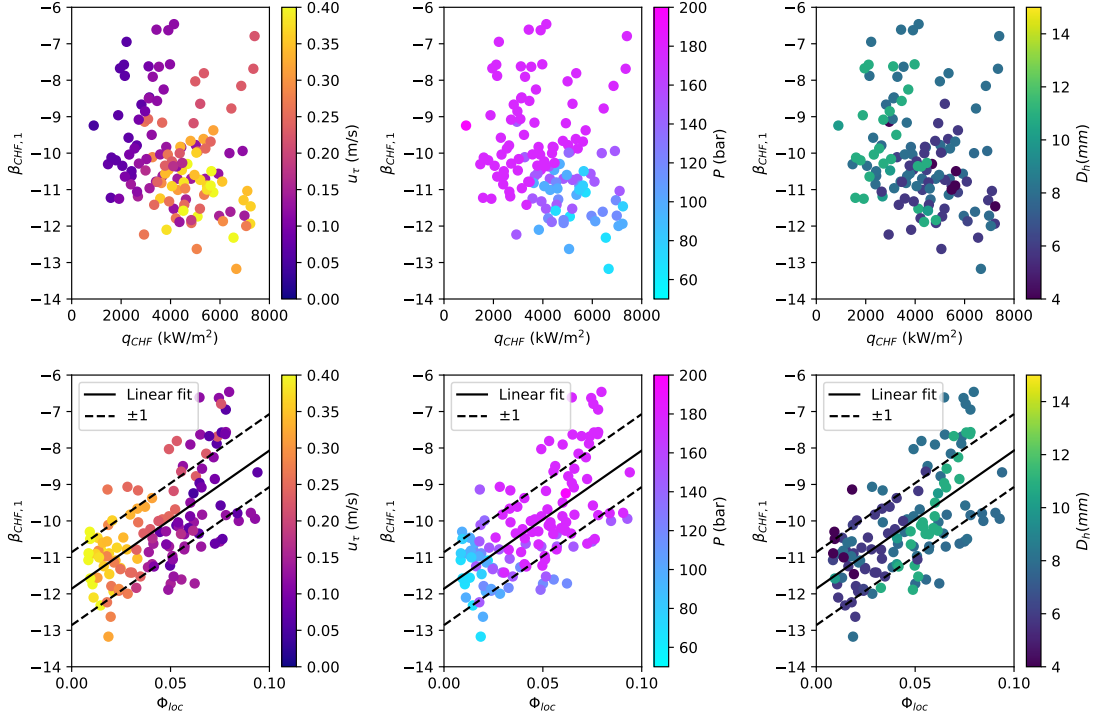


Figure 10.6: $\beta_{CHF,1}$ as a function of the CHF (top row) and the local boiling number defined in equation 9.8 (bottom row). **Left column:** effect of friction velocity in the near-wall cell. **Center column:** effect of outlet pressure. **Right column:** effect of the hydraulic diameter in the near-wall cell. Compare with figures 9.5 and 9.6 for the DEBORA database.

must be independent of the channel geometry.

Using a linear fit, one can calculate that if $T_s - T_l(y_1) > 3$ K, the CHF occurs when:

$$\beta < \beta_{CHF,1} = \frac{\Phi_{loc} - 0.313}{0.0264} \quad (10.2)$$

For each simulation, one can now look for the most upstream point at which the criterion defined in equation 10.2 is verified. This yields the altitude at which the BC in the code is predicted for a given q_{CHF} . The quality at the CHF and the difference between the inlet and CHF quality can then be calculated. Results are presented in figure 10.7. The mean square error (MSE) and normalized mean square error (NMSE) were defined in equation 9.10.

The quality of the prediction is far worse than on the DEBORA database. Many of the datapoints used for the interpolation in figure 10.6 pass the $T_s - T_l(y_1) < 3$ K criterion before the criterion from equation 10.2, and do not appear in figure 10.7. Many of those that do appear pass the equation 10.2 too soon, i.e. they were underneath the fit in the bottom row of figure 10.6. This is why the average predicted altitude is smaller than the pipe heated length, which makes the proposed criterion conservative.

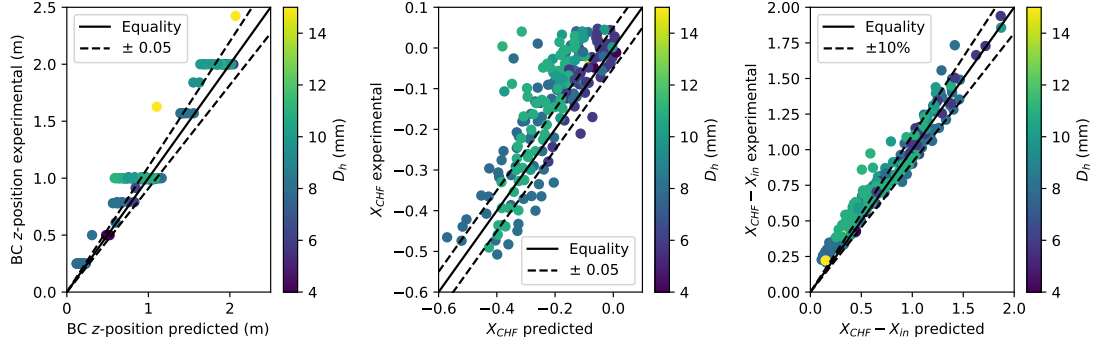


Figure 10.7: Evaluation of the precision of the subcooled CHF model proposed in equation 10.2. **Left:** position of the predicted boiling crisis in simulations. **Center:** X_{CHF} calculated using the z -position of the boiling crisis. The MSE is 0.107. **Right:** change in quality between the inlet and the boiling crisis. The NMSE is 18%. The colormap used concerns the hydraulic diameter of the flow. See figure 9.7 for comparison with the DEBORA database.

Another reason why the results are different than in figure 9.7 is that the void fraction is larger in the near-wall cell. This increases the liquid and vapor velocities, and u_τ . Φ_{loc} will decrease for a given wall heat flux, therefore the predicted β_{CHF} will decrease as the flow ascends. As β decreases as well, this will make the equation 10.2 criterion less selective.

The predicted quantities do not seem biased at a first glance by the diameter of the channel. This cannot be taken for granted, as D_h plays a key role in the simulations. In addition to changing the heat balance, as in system and component scale codes, it influences the gradients, therefore the vorticity and all interfacial forces. This was acutely visible in chapter 8. However, more precise predictions are needed to guarantee that the β_{CHF} -based approach intrinsically takes into account the effect of D_h .

Using the methodology explained in section 9.4.2, the critical heat flux for a given inlet temperature is calculated. Results are shown in figure 10.8, along with predictions from the Groeneveld et al. 2007 LUT and the W3 correlation for reference (see section 9.1.1).

The CHF predictions using equation 10.2 are significantly less precise than on the DEBORA database (see figure 9.9). The exact reason for this is unclear, but the main possibilities are:

- The proposed method to infer the CHF criterion could be valid, but the set of closures for the two-fluid model could be less adapted to these conditions than those of the DEBORA database;
- $\beta_{CHF,1}$ could be well predicted, but the correlation was not inferred in an optimal manner from the available data.

Though the CHF prediction points are scattered, there are no points for which the predicted CHF is more than 10% larger than the experimental one: the proposed

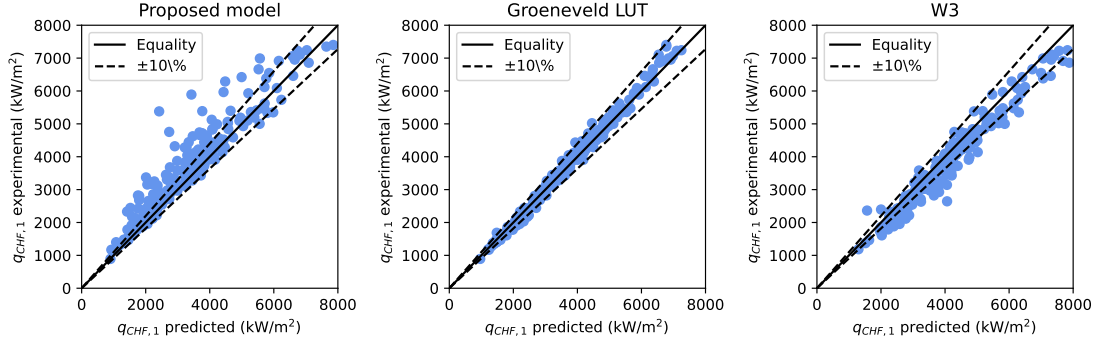


Figure 10.8: Comparison of the CHF predictions for a given inlet temperature of the subcooled CHF model proposed in equation 10.2 (**left**) with the Groeneveld et al. 2007 LUT (**center**) and the W3 CHF correlation (**right**, Todreas and Kazimi 2021). The respective NMSE are 15.2%, 4.4% and 9.8%.

correlation is conservative. A 15% NMSE is not that large. For these reasons, I believe that $\beta_{CHF,1}$ is the correct parameter to investigate, and that the good results obtained in chapter 9 were not a coincidence.

The LUT itself has a 4.4% MSE on the subcooled datapoints selected for simulation. This is less than the MSE on the whole database, which is at 7.1%. This means that in very subcooled conditions, the CHF is more consistent than on the rest of the database.

The W3 correlation does not perform that well, with an MSE of 9.8%. The CHF is overpredicted in high heat flux conditions. However, it is used here outside of its validity range, which is normally for $-0.15 < X_{out} < 0.15$.

10.4 Towards a single criterion for two different fluids

The $\beta_{CHF,1}(\Phi_{loc})$ plots built for DEBORA (figure 9.6) and Groeneveld 2019 (figure 10.6) show that the values of $\beta_{CHF,1}$ at CHF were similar in both databases though the values of Φ_{loc} were different.

This indicates that Φ_{loc} is not the universal relevant dimensionless quantity, and that another expression of β_{CHF} should be pursued. In this section, the Nop et al. 2021 criterion is evaluated on both databases before proposing another one is proposed.

10.4.1 Evaluating the Nop criterion on both fluids

Nop et al. 2021 showed that the point of DNB could be calculated in a subcooled channel as the moment where a liquid layer of a certain thickness reaches saturation temperature (equation 9.3).

This criterion can be transformed as a criterion on β_{CHF} :

$$\beta_{CHF} = -2.12 \log \left(\frac{180}{Pr} \right) \quad (10.3)$$

Using the simulations carried out on the DEBORA and Groeneveld 2019 CHF databases, the altitude at which the BC occurs according to this correlation can be evaluated and the local quality at CHF, the quality variation along the test tube and the CHF for constant quality inlet temperature inferred. Results are presented in figure 10.9.

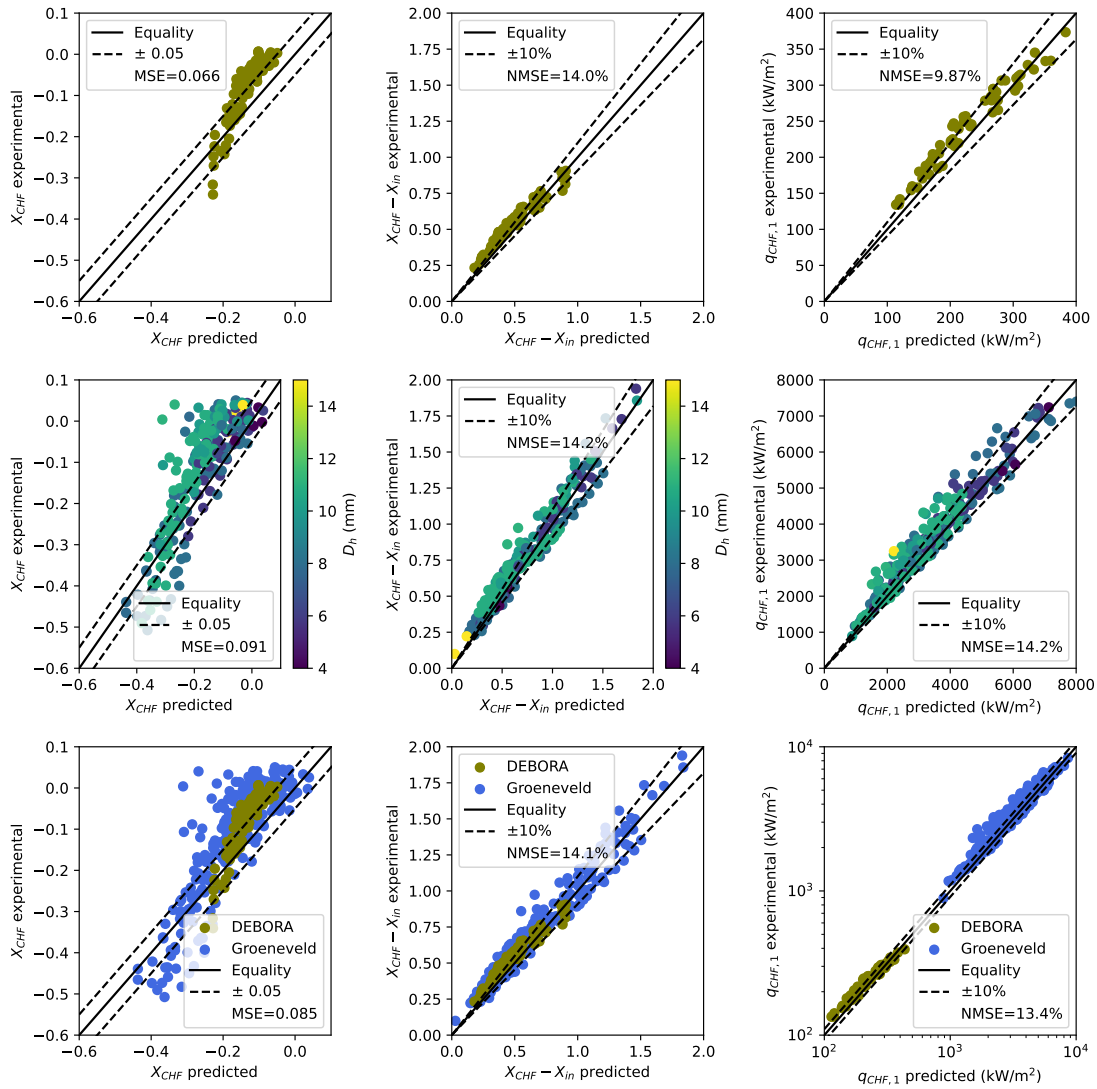


Figure 10.9: Comparison of X_{CHF} and q_{CHF} predictions for the Nop et al. 2021 model (equation 10.3). **Top row:** DEBORA database. **Middle row:** Groeneveld 2019 database. **Bottom row:** both databases. **Left column:** X_{CHF} prediction. **Center column:** $X_{CHF} - X_{in}$ prediction. **Right column:** $q_{CHF}(T_{in})$ prediction.

The predicted qualities and CHF are fairly similar to the experimental values for both fluids. It must be stressed that these results are obtained without any

fitting on my part. The Nop et al. 2021 criterion, based on atmospheric-pressure highly subcooled flow in 1cm-long heater, was simply applied to high-pressure developed pipe flow with 2 different fluids and multiple experimental sources. This indicates that the mechanism of DNB is the same in the Groeneveld 2019 high-subcooling database, for which there are no near-wall precise measurements, as in the Kossolapov et al. 2020 experiments. The very small difference between the results on DEBORA and Groeneveld 2019 and the fact that the CHF predictions cover two orders of magnitude data also stresses that we are looking at relevant dimensionless quantities.

However, the plot of the predicted vs experimental X_{CHF} (left column in figure 10.9) shows a clear bias: the predicted CHF varying over a much smaller interval than the experimental one. In order to improve on this model, an alternative model is proposed in the following section.

10.4.2 Proposed model for both fluids

For boiling flows, the Prandtl number can have a significant importance in heat exchanges and in condensation heat transfer. It is around 3 for the R12 and between 0.85 and 1.7 for the high-water pressure flows investigated here.

The $\beta_{CHF}(\Phi_{loc})$ plot for both fluids had a similar aspect but different maximum and minimum values of Φ_{loc} (figures 9.6 and 10.6). In the Nop et al. 2021 DNB criterion, the thickness of the saturated layer at DNB decreases when Pr increases. This means that fluids that transmit heat less efficiently need a smaller saturated layer for the BC to occur, which is expected. The smaller the size of the saturated layer, the larger β_{CHF} . For larger values of Pr , β_{CHF} should therefore be larger. This is coherent with the difference between $\beta_{CHF}(\Phi_{loc})$ plots on the DEBORA and Groeneveld et al. 2007 databases (figures 9.6 and 10.6).

I therefore propose to plot β_{CHF} as a function of $\Phi_{loc}Pr$. Pr will influence the sublayer thickness in the same direction as equation 10.3. For a same heat flux, β_{CHF} will be larger, i.e. the sublayer will be smaller, for larger Pr . Results are plotted in figure 10.10.

The data from both plots collapse on the same line. Interestingly, the data from Groeneveld 2019 is nearer to the interpolation than in the $\beta_{CHF}(\Phi_{loc})$ fit carried out earlier (figure 10.6). This confirms the relevance of taking the Prandtl number into account in this way.

The resulting interpolation gives:

$$\beta_{CHF} = \frac{\Phi_{loc}Pr - 0.46}{0.039} \quad (10.4)$$

This criterion is now used to predict X_{CHF} , $X_{CHF} - X_{in}$ and q_{CHF} . Results can be found in figure 10.11.

The proposed correlation has less bias but more dispersal than that of Nop 2020. The results of both databases collapse on the same lines, and the errors in the prediction are smaller.

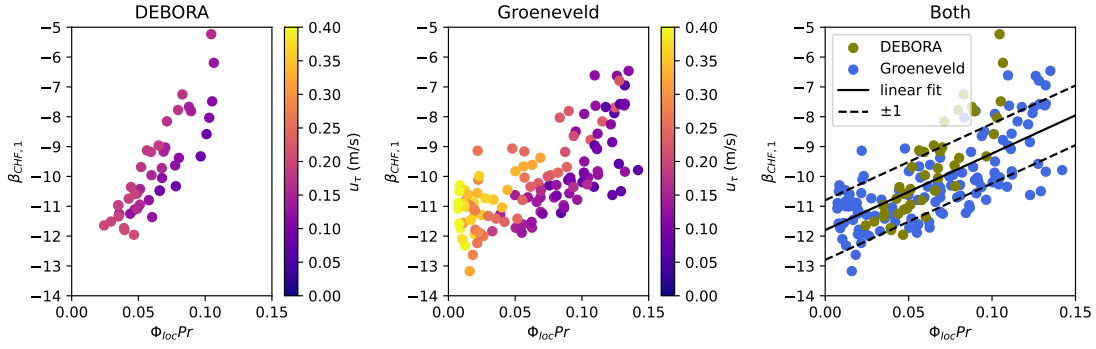


Figure 10.10: β_{CHF} at the outlet of the simulated test sections as a function of $\Phi_{loc}Pr$. **Left column:** DEBORA database. **Center column:** Groeneveld 2019 database. **Right column:** All data.

In order to arrive at a definitive conclusion on the relevance of the models of equations 10.3 and 10.4, more fluids would nevertheless be required to explore a larger part of the Prandtl spectrum.

10.4.3 Summary of investigated local subcooled CHF models

Table 10.1 contains a summary of the errors of all of the methods used here to predict the CHF.

Quantity	Database	LUT	R12 $\beta_{CHF}(\Phi_{loc})$ Eq 9.9	Water $\beta_{CHF}(\Phi_{loc})$ Eq 10.2	Nop Eq 10.3	$\beta_{CHF}(\Phi_{loc}Pr)$ Eq 10.4
X_{CHF}	DEBORA	NA	0.036	NA	0.067	0.046
MSE	Groeneveld	0.061	NA	0.107	0.092	0.103
$X_{CHF} - X_{in}$	DEBORA	NA	5.8%	NA	14%	7.7%
NMSE	Groeneveld	8.0%	NA	18%	14%	16%
$q_{CHF}(T_{in})$	DEBORA	NA	4.1%	NA	9.8%	6.0%
NMSE	Groeneveld	4.4%	NA	15.2%	14%	13%

Table 10.1: Error on the prediction of X_{CHF} and NMSE on the predictions of $X_{CHF} - X_{in}$ and $q_{CHF}(T_{in})$ on the DEBORA and Groeneveld databases

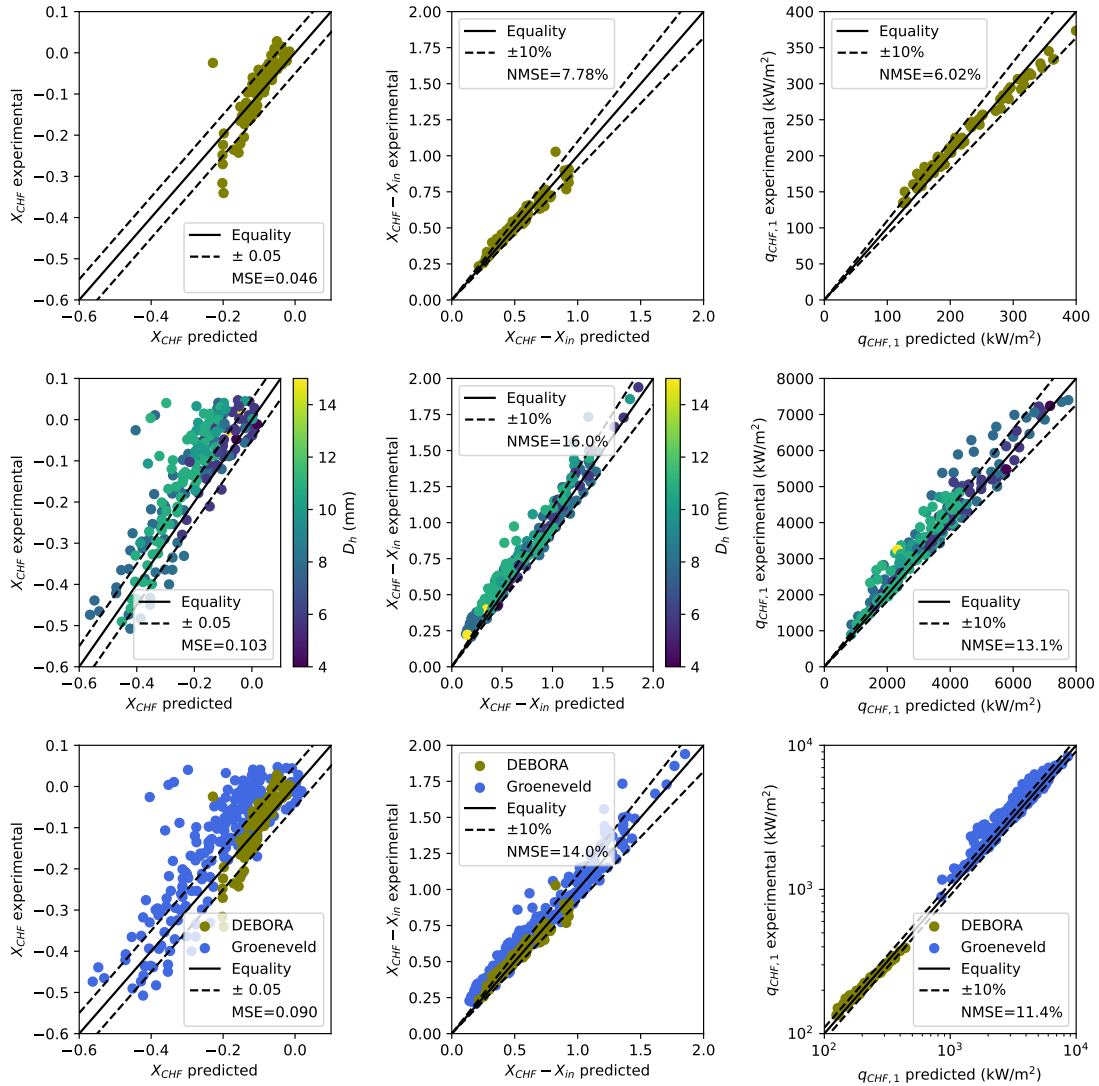


Figure 10.11: Comparison of X_{CHF} and q_{CHF} predictions for the proposed model valid across multiple fluids (equation 10.4). **Top row:** DEBORA database. **Middle row:** Groeneveld 2019 database. **Bottom row:** both databases. **Left column:** X_{CHF} prediction. **Center column:** $X_{CHF} - X_{in}$ prediction. **Right column:** $q_{CHF}(T_{in})$ prediction.

10.5 Simulations of PATRICIA transient flows

10.5.1 Transient CHF models from the literature

Section 9.1.4 presented a large variety of existing steady-state DNB models. Nop 2020 also reviewed various transient CHF models. Those that he discusses take into account transient effects in the liquid sublayer dryout model (Serizawa 1983), which is already questionable. The authors carry out analytical time-dependent heat and mass balances in the sublayer.

Nop et al. 2021 developed an analytical model for short heaters in highly sub-cooled transient flow. The steady-state CHF criterion found (equation 10.3) remains valid if one carries out a time-dependent enthalpy balance in the sublayer. This is an indication that the approach used here, also based on a saturated sublayer thickness, has a good chance to remain relevant. However, the sublayer thickness evaluated depends on the hypothesis that the liquid temperature profile is developed, at least in the near-wall cell, which is not necessarily the case for fast transients.

10.5.2 The PATRICIA experimental database

Test section The PATRICIA loop was built at CEA and designed to understand the clad-to-coolant heat transfer for RIA's (Bessiron 2007). It is extensively used in the RIA literature (NEA 2022). It has operated in flow and pool boiling conditions, but only flow boiling is investigated in this thesis.

The test section consists in a 0.6 m-long annulus. It is heated through the inner rod which has an 8.8 mm inner diameter and a 9.5 mm outer diameter. The channel outer diameter is 14.2 mm. It can be pressurized up to 155 bar. The mass flux can reach 3500 kg/(m²s). Transient heat fluxes can be applied. Time-dependent inner wall temperatures were measured using four thermocouples located on the inside of the heating tube. In this section, only data from the highest thermocouple, located 5 mm before the end of the heated section, is analyzed.

The first test configurations were stationary, to determine the steady-state CHF in this annular configuration. Transient tests were carried out at around 150 bar and 3200 kg/(m²s) in four main configurations where the initial liquid subcooling and transient shape were varied. The initial subcooling could be low (20 K) or high (60 K). In the fast transient, the power would increase during 100 ms, reaching a peak around 10-15 MW/m², then decrease during 200 ms. In the slow transient, the power would increase during 500 ms, reaching a peak around 15 MW/m², then decrease during 1000 ms.

Simulation setup To run simulations, the PolyMAC numerical scheme is selected. The mesh is a 2°-wide annulus. It contains 20 radial elements. The height of the mesh cells was set to 1 mm. The total simulated height was 1.2 m.

In order to take into account transient effects, a coupled simulation with the solid domain is run. The experimental volumetric power in the pipe is injected

between $z = 0.5$ m and $z = 1.1$ m. The power injection begins after enough physical time in the simulation for the turbulent flow to be developed.

10.5.3 Steady-state PATRICIA results

Figure 10.12 presents the steady-state conditions and simulation results on the PATRICIA database. The left subplot shows $q_{CHF}(X_{CHF})$ data for these runs, which is coherent with the shape of such data from figure 10.1 for example. The right subplot shows β_{CHF} as a function of $\Phi_{loc}Pr$ and a comparison with equation 10.4. There is a bias in the data, β_{CHF} in PATRICIA being systematically larger than the model. However, this is within the data spread of figure 10.10, the trend is well captured and the flow remains subcooled at the outlet. β_1 can therefore be used as a reference to analyze transient conditions.

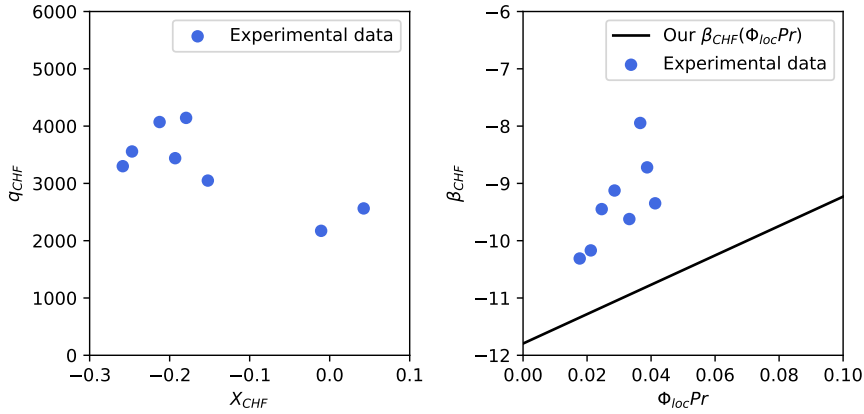


Figure 10.12: Steady-state CHF results in PATRICIA (Bessiron 2007). In all runs, $P \simeq 150$ bar and $G \simeq 3000$ kg/(m²s). **Left:** $q_{CHF}(X_{CHF})$ plot for the stationary runs. **Right:** $\beta_{CHF,1}$ as a function of the local boiling number times the Prandtl number for stationary runs and comparison with equation 10.4.

10.5.4 Transient PATRICIA results

Transient simulations are now run on the PATRICIA database. All tests have $P \simeq 150$ bar and $G \simeq 3000$ kg/(m²s). Three tests are analyzed here:

- Test 55: long heating pulse (~ 500 ms ascent) and low initial subcooling (20 K);
- Test 58: long heating pulse (~ 500 ms ascent) and high initial subcooling (60 K);
- Test 69: short heating pulse (~ 100 ms ascent) and high initial subcooling (60 K).

Simulation results can be found in figures 10.13, 10.14 and 10.15. For each run, the heating power is plotted as a function of time. The injected power is compared to the power transmitted from the rod to the fluid. The simulated and experimental inside wall temperatures as a function of time are also shown. β_{CHF} for the Nop et al. 2021 criterion and the one proposed in equation 10.4 are calculated. They are compared with the time-dependent β_1 calculated in the near-wall cell using the liquid temperature and wall heat flux. Finally, radial wall and liquid temperature profiles at the altitude of the top thermocouple as well as axial wall temperature profiles at different times are presented.

Run 55 (figure 10.13) does not experimentally exceed the CHF. This is coherent with the predicted values of β_1 , that always remain high over the CHF criterion. The power transferred to the flow has a short delay compared with the one transferred to the rod, which is expected. Liquid and solid temperatures at the inlet temperature before the simulation, increase during the transient and fall back to the inlet temperature. One can clearly see that the liquid heats more in the near-wall region than in the bulk. The axial wall temperature heats in a similar fashion along the heated section, but the inlet cools significantly faster than the outlet.

However, the predicted wall temperatures are significantly smaller than in the experiment. This can be due to an overestimation of the heat transfer coefficient in boiling flow using the Jens and Lottes 1951 correlation. Testing other wall heat transfer correlations, like that of Thom et al. 1965, could be a way to improve these results.

Run 58 has a similar behavior as run 55 (figure 10.14), but starts with a lower inlet temperature and has a significantly larger maximum heating power. The predicted wall temperatures are in excellent agreement with the experimental data. β_1 decreases sharply as the liquid temperature and heating power increase and goes back up as the flow cools. It remains over both CHF criteria. This is coherent with the good wall temperature predictions.

Run 69 has a much shorter power step and a higher maximum injected power than the other two (figure 10.15). Both CHF criteria are exceeded. Given the delay for the wall temperature decrease compared with the power pulse profile, this run exceeds the CHF. The simulation crashed at $t = 116\text{ms}$. This is probably due to too much vapor production at this point in time. One can clearly see that the liquid heats more in the near-wall region than in the bulk, which is still at the inlet temperature at the time of the crash.

If the heat transfer coefficient was reduced in the code after the DNB occurs, far less vapor would be produced which would contribute to stabilizing the simulation.

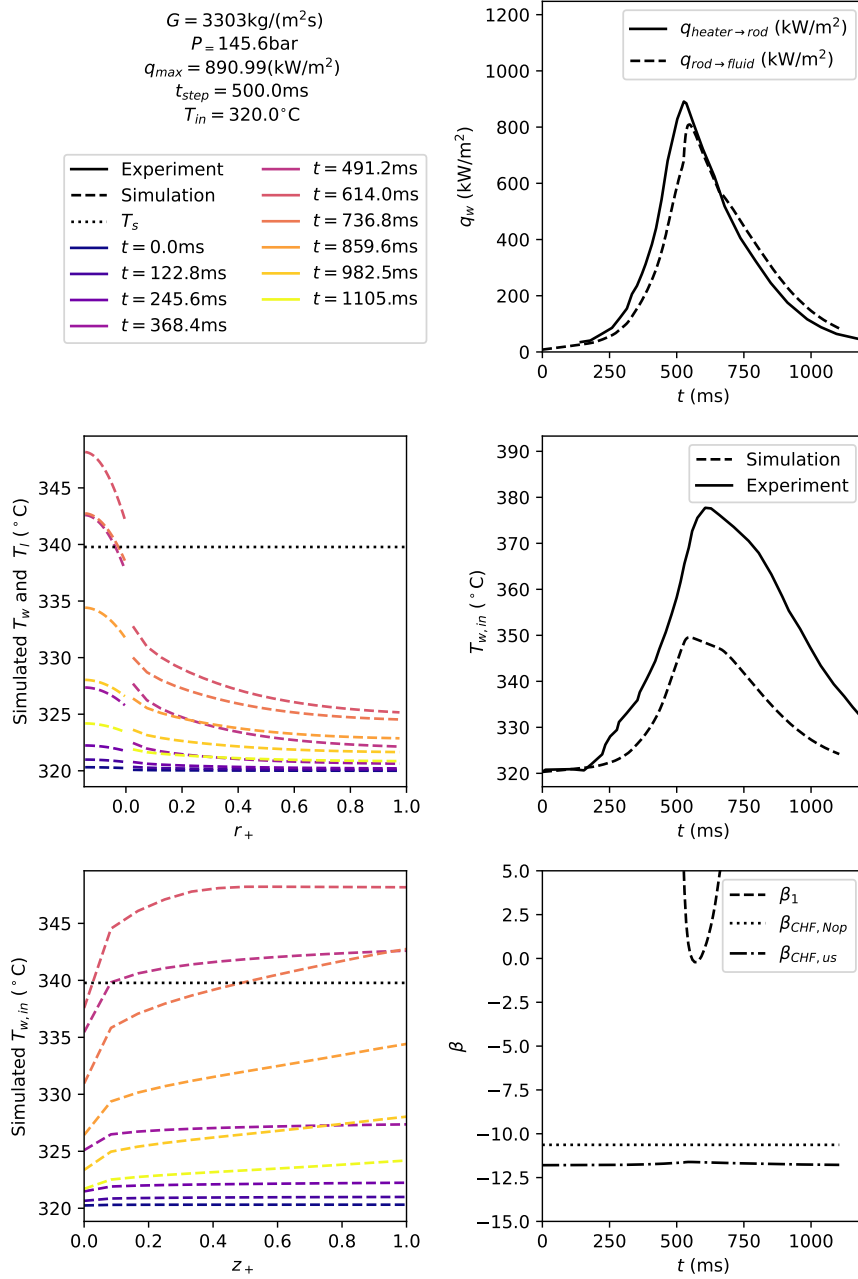


Figure 10.13: Simulation results for transient PATRICIA run 55. **Right column top and center:** time evolution of the heating power and inside wall temperature. **Right column bottom:** time evolution of the simulated β in the near-wall cell and comparison with the Nop et al. 2021 model and the model proposed in equation 10.4. **Left column center:** radial wall (for $r_+ \leq 0$) and liquid (for $r_+ > 0$) temperature profiles at different times. **Left column bottom:** axial wall temperature profile at different times 5 mm before the outlet. $z_+ = 0$ at the inlet of the heated section and $z_+ = 1$ at the outlet.

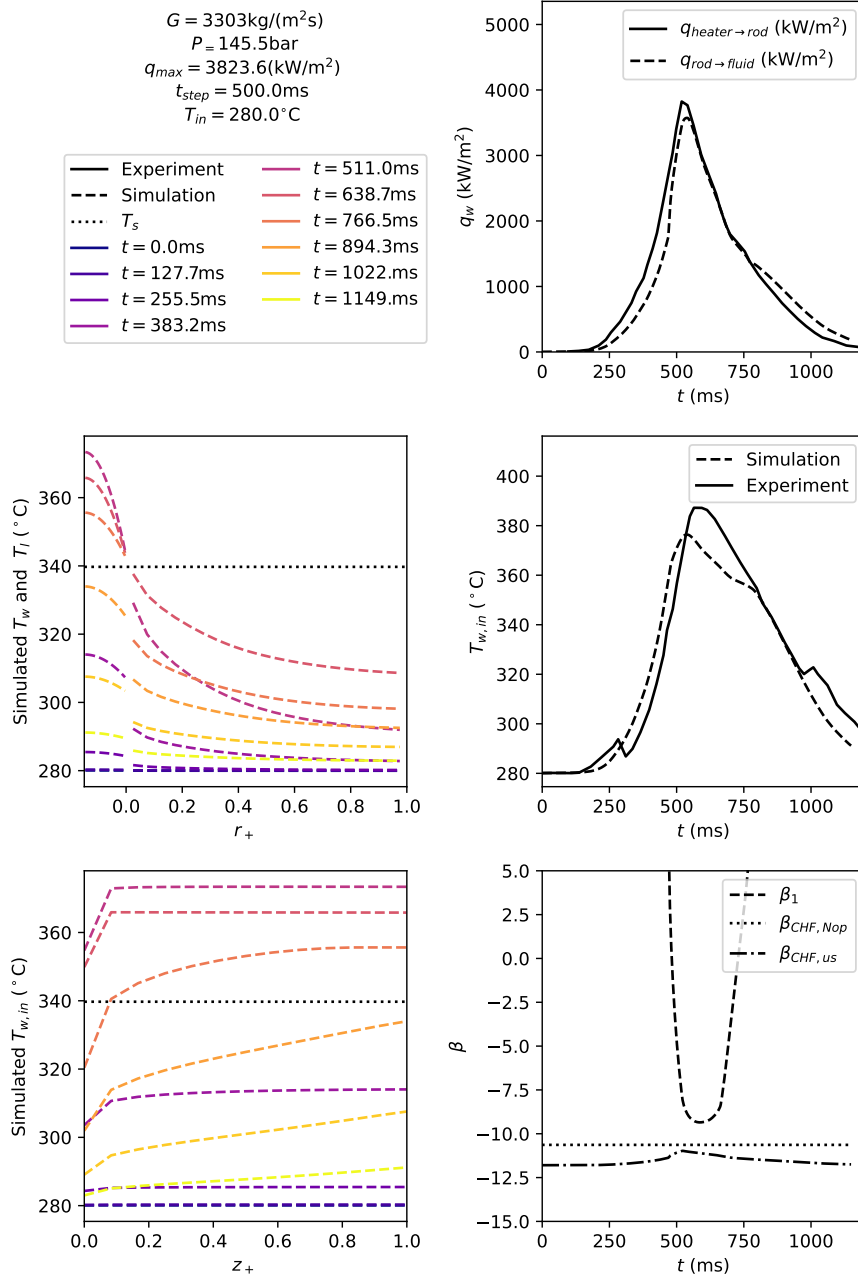


Figure 10.14: Simulation results for transient PATRICIA run 58. **Right column top and center:** time evolution of the heating power and inside wall temperature. **Right column bottom:** time evolution of the simulated β in the near-wall cell and comparison with the Nop et al. 2021 model and the model proposed in equation 10.4. **Left column center:** radial wall (for $r_+ \leq 0$) and liquid (for $r_+ > 0$) temperature profiles at different times. **Left column bottom:** axial wall temperature profile at different times 5 mm before the outlet. $z_+ = 0$ at the inlet of the heated section and $z_+ = 1$ at the outlet.

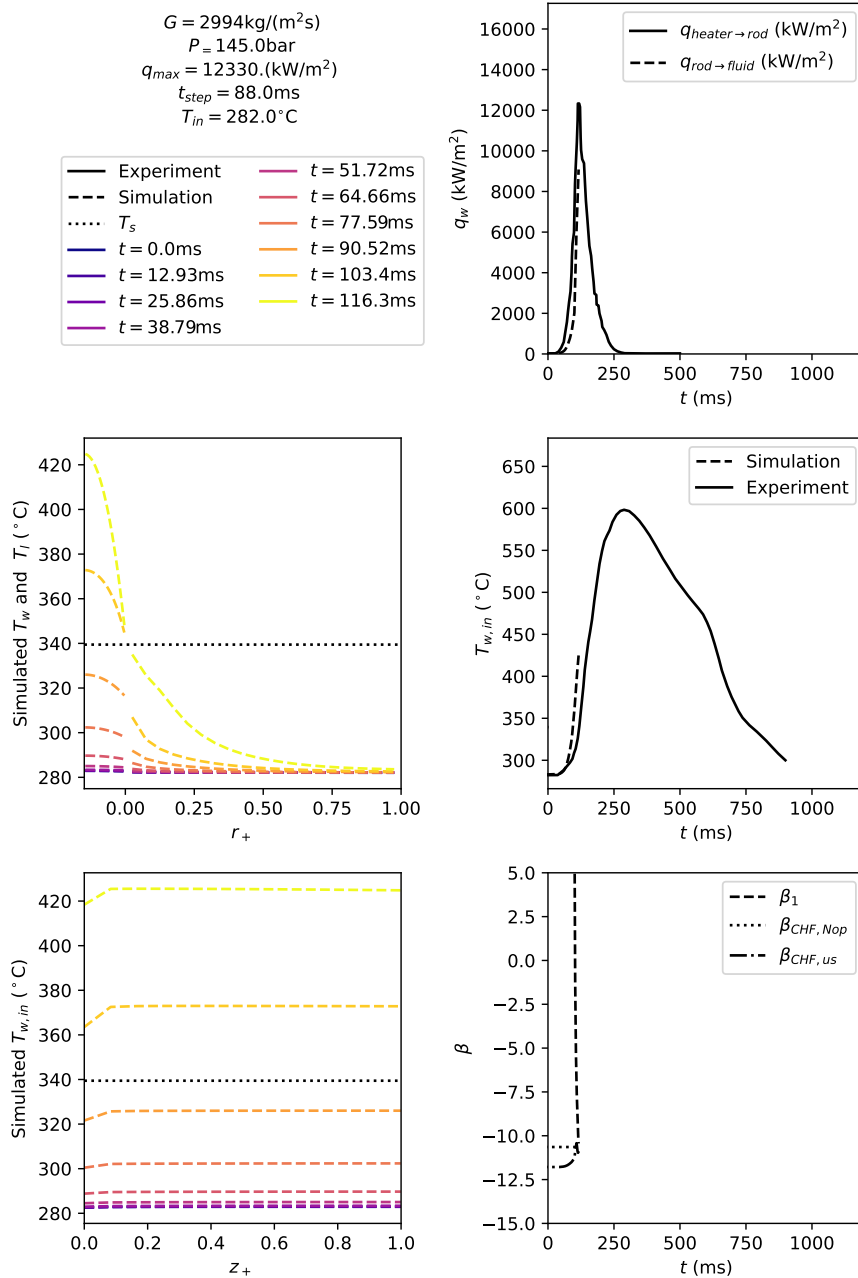


Figure 10.15: Transient temperature predictions in PATRICIA run 69. **Right column top and center:** time evolution of the heating power and inside wall temperature. **Right column bottom:** time evolution of the simulated β in the near-wall cell and comparison with the Nop et al. 2021 model and the model proposed in equation 10.4. **Left column center:** radial wall (for $r_+ \leq 0$) and liquid (for $r_+ > 0$) temperature profiles at different times. **Left column bottom:** axial wall temperature profile at different times 5 mm before the outlet. $z_+ = 0$ at the inlet of the heated section and $z_+ = 1$ at the outlet.

10.6 Perspectives

Applying the methodology from chapter 9, the departure from nucleate boiling in subcooled flow on the Groeneveld 2019 database was investigated, looking closely at the saturated liquid layer at a scale smaller than the near-wall cell. This is coherent with the work of Nop et al. 2021 that was conducted in very different conditions (low-pressure short ITO heater). The saturated sublayer was also the key parameter to build the β_{OSV} -based OSV criterion (chapter 6). Work still needs to be done to understand exactly what happens in the sublayer. Nevertheless, I believe that the sublayer thickness β is an interesting quantity that should continue to be studied and evaluated in the future.

The errors in the prediction of the CHF and critical qualities (table 10.1) are still significantly larger than reference empirical formulations from the literature. However, the approach presented in this chapter is based on a dimensionless quantity, β_{CHF} . Different formulations that give encouraging results on both R12 and high-pressure water flow were tested: that of Nop et al. 2021 and the one proposed in equation 10.4. These contain only two fitted coefficients.

The first transient simulations are very encouraging and give good results when the BC does not occur. It could also be seen that the CHF criteria were exceeded for a short power pulse in transient flow.

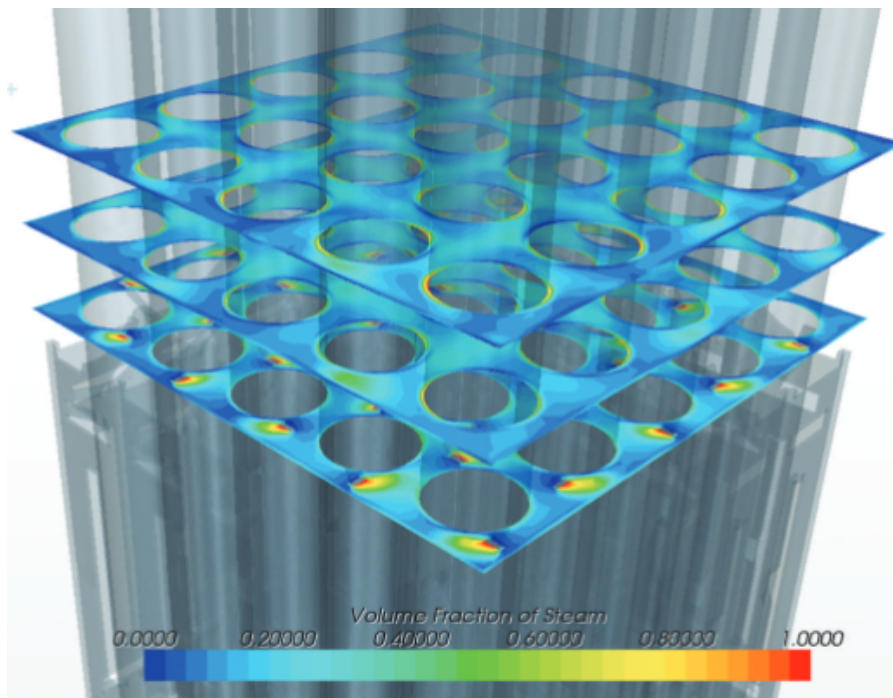
In order to improve modeling of subcooled boiling crisis using a near-wall saturated layer, the following steps can be carried out:

- Improve the closure laws for high-heat flux and high-shear conditions. It was seen in figure 10.5 that in the near-wall cell much higher void fractions were achieved than in any point on the extended validation database (chapter 8). In this context, the capillary length could no longer be a relevant scale for condensation for subcooled CHF data from Groeneveld et al. 2007. However, CFD-scale interfacial area validation data is lacking for such high heat flux conditions to adjust closure laws.
- A way of dodging such a difficulty would be to carry out an analytical analysis of β_{CHF} with a similar method as that of chapter 6 for the OSV. Figure B.5 in appendix B gives an indication of up to which point the $\beta(z)$ function can be considered linear, which would enable to go farther than the OSV.
- Evaluating more clearly the sensitivity of models proposed to changes in mesh size. However, as for the OSV criterion it seems difficult to adapt these criteria to situations where $y_{+,1} < 100$.
- Extending this analysis to more fluids, in particular with different Pr numbers. In the CHF databases it goes from 0.85 to 3. The work of Ahmad 1973, who identified scaling distortions on channel-scale CHF data, contains many references that could be exploited.
- To evaluate the capacity of the set of closures and CHF criteria to represent developing flow, it could be tested against CHF data for short pipes,

with heating lengths of $\sim 10D_h$ for example. Groeneveld et al. 2007 left this data out of the LUT as they anticipated that developing flow effects would affect the precision of the table. However, at a CFD scale it should be possible to simulate how the short length affects the radial liquid temperature distribution and through this $\beta_{CHF,1}$.

- Transient effects that could occur on a smaller scale than the first element cannot currently be taken into account. To do this, one could build a time-dependent subgrid model of the saturated layer with a similar method as Nop et al. 2021. The main difference would be that the saturated layer would not exchange energy with the complete bulk but only with the first element.
- Extending the DNB model to lower pressure experiments in stationary and transient conditions would be extremely interesting. Relevant data includes the work of Nyer 1969 and Chavagnat et al. 2022. The fact that the Nop et al. 2021 model works relatively well without any modification for high-pressure data is encouraging in this regard.
- An additional step towards the industrial application would be multi-physics transient simulations. Data from the CABRI experimental reactor could be used for validation (Biard et al. 2020; Labit et al. 2021b).

CHAPTER 11



Future work: CFD simulations of boiling flow with mixing vane grids. Image: void fraction distribution downstream of a MVG in a simulation of the PSBT benchmark, reproduced from Lo and Osman 2012.

Conclusion

11.1 Main results

11.1.1 Numerical contributions

During this thesis, I contributed to developing an Euler-Euler open-source multiphase CFD module in TrioCFD (chapter 2). A Reynolds averaged Navier-Stokes two-fluid framework that can solve a mass, momentum and energy equation for an arbitrary number of phases was implemented in two different numerical schemes: VDF, that enables good performance on Cartesian and axisymmetric grids, and PolyMAC, that can handle arbitrary polynomial meshes. Multiple multiphase closures were implemented: drag, lift, turbulent dispersion and wall repulsion forces, as well as condensation terms and heat flux partitions. Some of these closures came from the literature, some were proposed in this thesis. The flexibility of TrioCFD will enable future researchers to try out many more combinations of models.

The Euler-Euler solver was adapted to easily implement a drift-flux model, which yielded very similar results as the two-fluid model for a drift velocity based on a force balance (chapter 3). In boiling nuclear-reactor condition pipes, using one or the other does not significantly change the simulation results, apart from the contribution of the virtual mass that was not included in the final set of closures. Though conceptual debates between the defenders of both approaches will certainly remain, there is no pragmatic need to oppose them.

11.1.2 Exploiting experimental databases

In this manuscript I strove to extract as much information as possible on the physics of boiling flows from experimental databases through reconstructions and without extensive simulations. On the DEBORA database, the first step was to show the validity of the test tube hypothesis, which allowed me to build (r,z) maps of void fraction and Sauter mean diameter (section 4.4). I determined the liquid temperature profiles through an energy balance, and calculated the radial phase

velocities through an integration (appendix B). This approach also enabled me to determine the coalescence-breakup term from experimental void fraction and interfacial area data in saturated regions of the flow. I then proposed a simple return-to-equilibrium model for this term (appendix C). For such reconstructions to be possible, I believe that it is key to systematically measure data to be able to reconstruct axial profiles, either through placing probes at different altitudes or using a test tube methodology.

Building an extensive onset of significant void database that contains data from multiples sources enabled me to build a simple CFD-scale criterion through physical analysis (chapter 6). It was then used to build a heat flux partition adapted to flow boiling that is much easier to implement and interpret than more classical approaches.

I also took data from the literature to build a large high-pressure CFD-scale database used to evaluate the strengths and limits of the models developed in TrioCFD (chapter 8).

Table 11.1 lists all of the experimental databases exploited in this thesis. Part of the data used and the analysis carried out is available on my GitHub page: <https://github.com/CoReiss>.

Database	Source of data	Use
Adiabatic bubbly flow	Hibiki et al. 2001; Colin et al. 2012	Validation of baseline closures (sec 3.2)
DEBORA	Cubizolles 1996; Garnier et al. 2001; Kledy 2018	Experimental reconstruction (app B, app C), evaluation of baseline closures (chap 5), building new set of closures (chap 7, 8), subcooled CHF criterion (chap 9)
Onset of significant void	See table 6.1	CFD OSV criterion and resulting HFP (chap 6)
High-pressure condensation	Avdeev and Pekhterev 1986	Water Nusselt number calibration (sec 7.6)
High-pressure CFD-grade boiling flow	St.-Pierre 1965; Staub et al. 1969; Martin 1969; Chu et al. 2017	Validation of proposed closures (chap 8)
Critical heat flux	Groeneveld et al. 2007	Subcooled CHF criterion (chap 10)

Table 11.1: Summary of the experimental databases used in this thesis.

11.1.3 Using simulations to understand physics

A baseline set of closures was validated for single-phase flow and in two-phase atmospheric-pressure adiabatic conditions (chapter 3).

Evaluating the baseline set of closures in the PWR-similarity conditions of the DEBORA database showed that atmospheric-pressure closure terms are not valid in PWR conditions (chapter 5).

I showed that in reactor conditions bubbles are deformable, i.e. non-spherical. This enabled me to propose a set of drag, lift, turbulent dispersion and condensation closures that improves simulation results compared with the baseline model. No bubble diameter modeling is required, which simplifies the implementation and eases the interpretation of the simulation results (chapter 7).

To build a model for the critical heat flux (CHF), I simulated experiments to obtain physical quantities in the near-wall region at the boiling crisis (chapter 9, 10). Using an analysis of the thermal boundary layer that is similar to the one carried out on the onset of significant void database, I built an empirical CHF criterion for stationary flows where the liquid remains subcooled in the near-wall region. It predicts the CHF with $\sim 10\%$ precision for high-pressure water and R12 flows.

11.1.4 Methodological contributions

How building a new code helped modeling efforts Many of the researchers with whom I discussed my work doubted the usefulness of developing a new multi-phase Euler-Euler framework as many solutions exist, that are open source, commercial or carried by the French nuclear industry. Developing the TrioCFD multi-phase module undoubtedly made me spend less time on the physical closures than if I had not done so. However, adding the closure terms one by one made me question the relevance of the ones commonly used in the literature and was key in developing the semi-empirical minimalistic set of closures. Furthermore, having total control on the code and understanding every building block from the numerical scheme to the physical laws enabled me to easily test multiple closures and adjustments.

Importance of having an explainable code In all of the simulations that I ran, I strove to avoid the black-box effect, i.e. I always wanted to understand why the code predicts what it predicts. Code interpretability is essential in order to understand the root causes of simulation-experiment discrepancies, and to continue improving the closures. It is part of the reasons why I chose to decouple many terms from each other: drag and lift from bubble diameter and condensation from relative velocity for example. However, I was not able to completely rid the minimalistic set of closures from these effects: in ascending flow, the turbulent dispersion and lift force are always linked in the radial force balance. Having less retroactive effects reduces the amount of terms whose bad modeling can cause non-physical behaviors and error compensation.

It limits the risk of the code behaving in completely unexpected ways. This can be important in a safety demonstration: the computational cost of Multi-phase CFD codes discourages the use of uncertainty propagation methodologies that are common with system-scale codes in loss-of-cooling accidents for example. Furthermore, due to the interactions between different terms, it is difficult to imagine a set

of closures that would be systematically conservative for nuclear safety. Conceptual work remains to be done to determine how to take into account the modeling uncertainties, which remain important in multi-phase flow, in safety demonstrations without unreasonable computational costs.

Using simple closures to leverage experimental data Small-scale DNS and LES are inaccessible for now due to their computational costs in reactor conditions with Reynolds numbers around 200 000. The heat and pressure conditions in PWR's prevent us from building precise experiments. I believe that leveraging the experiments that we have is the key to going forwards in the short and medium term, by adjusting the simplest possible sets of closures to these results, rather than using closures calibrated at atmospheric pressure on single bubbles in stagnant tanks. Using such a minimalistic approach means accepting that we do not yet understand the full complexity of boiling flows and all of the interdependent micro-mechanisms that they comprise. It also means using what we are sure of as starting points: the conservation equations, the liquid thermal log-law, the system-scale OSV correlations.

Closure calibration and code validation Though I used it extensively in this thesis, I do not like the term *validation* when applied to multi-phase CFD. For me, a code can be validated when we are relatively confident in its predictions. Given the strong differences between different multi-phase CFD codes and simple boiling-flow experiments, and given the fact that no safety demonstration has yet contained Euler-Euler RANS simulations, before we can validate TrioCFD we must understand the physics and the phenomena at play and calibrate the different closure terms.

I strongly believe that if we build two different small-scale experiments to represent similar nuclear reactor conditions, the differences between the experiments will probably be much smaller than between the experiments and the reactor. Even if a code is well calibrated on the first experiment, if results are not satisfying on the second then the code is probably unable to reproduce correctly reactor flows. If we factor in the differences in geometries and flow conditions from different set-ups, this means that no experimental database used for the analysis, calibration and validation of a model can be too big. Leveraging simultaneously as many experiments as possible to prevent over-fitting is essential, even if it means using system-scale and component-scale data in conditions where no CFD-grade data is available.

Analyzing existing experimental data to extract new information Part of the multi-phase CFD community believes that experimental data can be separated in three categories:

- Time-dependent extremely precise local data, including high-speed videos, that is necessary to understand the underlying physical phenomena in multi-phase flows.

- Less precise local data, like that of the DEBORA database. When judged to be *CFD-grade*, it can be exploited for code calibration.
- Data that has more uncertainty or that is at a system scale. It can be used for validation but not for calibration.

I believe to have shown through DEBORA reconstructions and exploitation of OSV and condensation databases that the border between these grades of data is fuzzy, and that creative physics-based data treatment can enable us to extract a lot of information from experiments that are not necessarily CFD-grade. We do not need to wait for PIV measurements or DNS in nuclear reactor conditions to better understand the boiling heat transfer from the fuel rods to the flow.

11.2 Perspectives

Statistical methodologies One of the main limits of this work is that I did not carry out an error propagation on the minimalistic set of closures and the high-pressure local database, either on the uncertainties of the experimental conditions or on the fitting coefficients proposed for the models of chapter 7. This is essential both to calibrate efficiently the models and to quantify their limitations.

Physical modeling of boiling flows Though I focused on high-pressure high-velocity flows in reactivity induced accident conditions, many more conditions are important for nuclear reactor safety. Being able to simulate a transition to annular flow with sharp interface models will be essential to simulate steam generators and boiling water reactors. Work is ongoing at the lab on low-pressure and low-velocity bubbly flows, which can take place in used-fuel pools, loss of coolant accidents or in various heat exchangers.

In these conditions, some of the modeling hypothesis made for the reactor condition set of closures are no longer valid. In particular, bubble-induced turbulence (BIT) is sure to play a key role. An internship on BIT took place in 2023 at the lab. This work must still be extended to boiling flows where the boiling-induced shear stress in the near-wall region isn't well understood. Another thing to look out for is the importance of the turbulent momentum diffusion in the vapor phase, which I believe should play a role. However, as it scales in ρ_v and all interfacial forces scale in ρ_l it is always negligible in the simulations.

It could also be necessary to introduce an interfacial area transport equation (IATE) for these conditions if the simplified momentum and condensation closures no longer hold. Implementing the model presented in appendix C and testing it at different pressures would be a first step in this direction.

Horizontal and tilted boiling flows are found in numerous applications, from CANDU fission reactors to cooling channels in fusion reactors. They also have a very different physics than ascending flows, from the near-wall boiling dynamics to the critical heat flux and even the definition of forces (appendix A). Extending the

minimalistic approach to these conditions would be of great scientific and practical interest.

Improving the CHF criterion The critical heat flux criterion proposed in chapter 10 only works for flows that are subcooled at the wall. However, the CHF can also be reached in saturated conditions. Dry-out models linked to the liquid film thickness have a better track record than departure from nucleate boiling models in the literature, but much work remains to be done on the progressive transition between the two regimes where the flow is saturated near the wall but not yet annular. The void fraction in the near-wall region could be a key parameter in this regime, but in the set of closures proposed in chapter 7 the near-wall void fraction is almost constant. A different set of closures, and in particular a different lift coefficient that could depend on other local quantities than the void fraction, could be required to predict this regime efficiently.

The initial aim of this PhD was to study the critical heat flux in transient conditions, which differs significantly from that of stationary conditions. The proposed departure from nucleate boiling model is linked to the thickness of the saturated thermal boundary layer. Though I had encouraging results with a β_{CHF} -based model on short transients (section 10.5), I believe that it can be improved. Working on a sub-grid model to determine the time-dependent saturated thermal boundary layer thickness could enable us to better capture transient effects. Research on this subject is ongoing in another thesis at CEA Saclay.

Industrial conditions To go towards complex industrial geometries with grids, one approach would be to improve the calculation speed and robustness of TrioCFD. Multiphase closure terms have been coded in the PolyVEF numerical scheme, better suited to such geometries than the ones used in this thesis (PolyMAC and VDF), though the numerical verification and validation has not been finished yet. The second option and possibly easier is to directly implement them in reference industrial codes to run such tests.

Experiments Numerical simulations would have no meaning without experimental databases to compare them to. Building a public reference database for multi-phase flow experiments, on the model of the NASA turbulence modeling resource, would be a great service to the community. Digitizing data with a homogeneous format is a fastidious but necessary step in this direction. Being able to trace and collect old but valuable data, for example from *Teploenergetika* journal, is also important.

In addition to exploring new geometries and flow conditions, future CFD-grade nuclear reactor condition experiments could include the following setups that are different from the currently predominant measurements at the outlet of the heated section in ascending flow:

- Carrying out measurements downstream of the heated section in saturated conditions. This could enable us to reconstruct the bubble diameter evolution

and the momentum balance independently of condensation and wall boiling effects.

- Looking into descending flows with high liquid velocities ($\gtrsim 1$ m/s). This would be of great interest to understand radial bubble movement in reactor conditions: all things being equal, in downwards flow the lift force would have an opposite sign. It should therefore push bubbles on the wall for high void fractions ($\alpha_v > 0.3$). If descending flow void fraction profiles turn out to be core-peaked, this would mean that the lift force is not the primary driver of a core-peaked profile in ascending flow.
- Slightly tilting pipes or channels to add gravity in the radial direction, to have a well-known force to compare with radial lift and turbulent dispersion.
- Asymmetrically heating a pipe or a channel to create a void fraction gradient in the hope of calibrating turbulent dispersion.

11.3 What I learned

Multidisciplinary work was a key part of my thesis, with physics and coding sprinkled with a little bit of math and nuclear engineering. It is one of the specificities of the nuclear industry. In this context, I am convinced of the importance of talking with as many people as possible, inside and outside of one's organization. In addition to being fun, this helped me learn a lot, find help when I needed it and get quick feedback from different perspectives.

Devising a simple quick and dirty test to try out a wacky idea is always worth it, even if it often fails. It was heart-wrenching but essential to discard work that did not pan out and resist to the sunken cost effect.

The George Box quote "All models are wrong. Some are useful." applies very well to my PhD. The set of closures that I propose is not an absolute truth, but a possibly useful step towards a multi-phase CFD set of closures that can be useful for nuclear reactor design and safety.

Whatever my future work, scientific or not, I plan to uphold the guiding principles that I had during this PhD: understanding the essence of what is happening, sharing my work widely, listening to all feedback and keeping in mind its context and finality.

References

- Abbrecht, Peter H and Stuart W Churchill (1960). “The thermal entrance region in fully developed turbulent flow”. In: *AIChE Journal* 6.2, pp. 268–273. DOI: [10.1002/aic.690060220](https://doi.org/10.1002/aic.690060220).
- Ahmad, SY (1973). “Fluid to fluid modeling of critical heat flux: a compensated distortion model”. In: *International Journal of Heat and Mass Transfer* 16.3, pp. 641–662. DOI: [10.1016/0017-9310\(73\)90229-9](https://doi.org/10.1016/0017-9310(73)90229-9).
- Alatrash, Yazan, Yun-Je Cho, Han-Young Yoon, Chul-Hwa Song, and In-Cheol Chu (2022). “Experimental and numerical investigation of local bubble parameters for subcooled flow boiling in a pressurized annulus”. In: *International Journal of Heat and Mass Transfer* 194, p. 123040. DOI: [10.1016/j.ijheatmasstransfer.2022.123040](https://doi.org/10.1016/j.ijheatmasstransfer.2022.123040).
- Almeras, Elise, Varghese Mathai, Detlef Lohse, and Chao Sun (2017). “Experimental investigation of the turbulence induced by a bubble swarm rising within incident turbulence”. In: *J. Fluid Mech.* 825, pp. 1091–1112. DOI: [10.1017/jfm.2017.410](https://doi.org/10.1017/jfm.2017.410).
- Alm eras, Elise, Varghese Mathai, Chao Sun, and Detlef Lohse (May 2019). “Mixing induced by a bubble swarm rising through incident turbulence”. In: *International Journal of Multiphase Flow* 114, pp. 316–322. DOI: [10.1016/j.ijmultiphaseflow.2019.03.014](https://doi.org/10.1016/j.ijmultiphaseflow.2019.03.014).
- Alvarez, Rodrigo Cavalcanti and Matteo Bucci (2024). “The influence of liquid height to bubble size ratio on the boiling crisis in pool boiling”. In: *Journal of Physics: Conference Series*. Vol. 2766. 1. IOP Publishing, p. 012138. DOI: [10.1088/1742-6596/2766/1/012138](https://doi.org/10.1088/1742-6596/2766/1/012138).
- Angeli, Pierre-Emmanuel, Ulrich Bieder, and Gauthier Fauchet (2015). “Overview of the TrioCFD code: Main features, V&V procedures and typical application to nuclear engineering”. In: *NURETH-16*. DOI: [10.1615/978-1-56700-099-3.590](https://doi.org/10.1615/978-1-56700-099-3.590). URL: <https://cea.hal.science/cea-02500815>.

- Anglart, H. and O. Nylund (1996). “CFD application to prediction of void fraction distribution in two-phase bubbly flows in rod bundles”. In: *Nuclear Engineering and Design* 163. DOI: [10.1016/0029-5493\(95\)01160-9](https://doi.org/10.1016/0029-5493(95)01160-9).
- Anglart, H., O. Nylund, N. Kurul, and M.Z. Podowski (1997). “CFD prediction of flow and phase distribution in fuel and assemblies with spacers”. In: *Nuclear Engineering and Design* 177, pp. 215–228. DOI: [10.1016/S0029-5493\(97\)00195-7](https://doi.org/10.1016/S0029-5493(97)00195-7).
- Anne, R. D. and D. R. H. Beattie (1996). “Net Vapour Generation Onset During High Velocity Subcooled Boiling Flow: A Simple Turbulence-Based Prediction Method”. In: *Heat and Mass Transfer Australasia*. Ed. by Begel House Inc., pp. 503–509. DOI: [10.1615/978-1-56700-099-3.590](https://doi.org/10.1615/978-1-56700-099-3.590).
- Ansys Fluent Theory Guide* (Jan. 2022). ANSYS, Inc.
- Antal, S. P., R. T. Lahey, and J. E. Flaherty (1991). “Analysis of Phase Distribution in Fully Developed Laminar Bubbly Two-Phase Flow”. In: *Int. J. Multiphase Flow* 17.5, pp. 635–652. DOI: [10.1016/0301-9322\(91\)90029-3](https://doi.org/10.1016/0301-9322(91)90029-3).
- Aouadi, Aroua, Ghazi Bellakhal, and Jamel Chahed (2019). “Effect of the turbulent contribution of the interfacial momentum transfer on the bubbles dynamics and void fraction distribution in vertical bubbly jets”. In: *International Journal of Multiphase Flow* 114, pp. 82–97. DOI: [10.1016/j.ijmultiphaseflow.2019.01.018](https://doi.org/10.1016/j.ijmultiphaseflow.2019.01.018).
- Al-Arabi, M (1982). “Turbulent heat transfer in the entrance region of a tube”. In: *Heat Transfer Engineering* 3.3-4, pp. 76–83. DOI: [10.1080/01457638108939586](https://doi.org/10.1080/01457638108939586).
- Avdeev, Alexandr Alexandrovich and VP Pekhterev (1986). “Vapor condensation in non-equilibrium bubble flows”. In: *Teplofizika Vysokikh Temperatur* 24.6, pp. 1125–1131.
- Bacq, Pierre-Loïc, Antoine Gerschenfeld, and Michael Ndjinga (2023). “Poly-MAC: Staggered Finite Volume Methods on General Meshes for Incompressible Navier–Stokes Problems”. In: *International Conference on Finite Volumes for Complex Applications*. Springer, pp. 149–156. DOI: [10.1007/978-3-031-40864-9_9](https://doi.org/10.1007/978-3-031-40864-9_9).
- Baglietto, Emilio, Etienne Demarly, and Ravikishore Kommajosyula (Mar. 2019). “Boiling crisis as the stability limit to wall heat partitioning”. In: *Applied Physics Letters* 114.10, p. 103701. DOI: [10.1063/1.5080724](https://doi.org/10.1063/1.5080724).
- Bartolomei, G. G., G. I. Batashova, V. G. Brantov, et al. (1980). *Heat and Mass Transfer-IV.T.5, p. 38*. ITMO Academy of Sciences of the BSSR Mink.
- Bartolomei, G. G. and V. I. Gorburov (1969). “Experimental Investigation of Steam Condensation in Subcooled Liquid”. In: *Thermal Engineering (english translation of Teploenergetica)* 16.12, pp. 58–62.

- Bartolomei, G.G., V. G. Brantov, Y. S. Molochnikov, Y.V. Kharitonov, V. A. Solodkii, G.N. Batashova, and V. N. Mikhailov (1982). “An experimental investigation of true volumetric vapor content with subcooled boiling in tubes”. In: *Thermal Engineering (english translation of Teploenergetica)* 29.3, pp. 132–135. URL: <https://theses.hal.science/tel-04496140>.
- Bartolomei, G.G. and V. M. Chanturiya (1967). “Experimental study of true void fraction when boiling subcooled water in vertical tubes.” In: *Thermal Engineering (english translation of Teploenergetica)* 14.2, pp. 123–128.
- Basu, Nilanjana, Gopinath R Warriar, and Vijay K Dhir (2005). “Wall heat flux partitioning during subcooled flow boiling: Part 1—model development”. In: *J. Heat Transfer* 127.2, pp. 131–140. DOI: <https://doi.org/10.1115/1.1842784>.
- Bazin, Clément (2023). “Numerical and experimental studies of two-phase flows interacting with a bundle of tubes”. PhD thesis. Institut Polytechnique de Paris.
- Bazin, P, P Clement, R Deruaz, D Dumont, Ph Gully, and B Noel (1990). “Investigation of PWR accident situations at BETHSY facility”. In: *Nuclear engineering and design* 124.3, pp. 285–297. DOI: [10.1016/0029-5493\(90\)90297-B](https://doi.org/10.1016/0029-5493(90)90297-B).
- Béguin, C., É. Pelletier, and S. Étienne (2016). “Void fraction influence on added mass in a bubbly flow”. In: *European Journal of Mechanics B/Fluids* 56, pp. 28–45. DOI: [10.1016/j.euromechflu.2015.11.008](https://doi.org/10.1016/j.euromechflu.2015.11.008).
- Bell, Ian H, Jorrit Wronski, Sylvain Quoilin, and Vincent Lemort (2014). “Pure and pseudo-pure fluid thermophysical property evaluation and the open-source thermophysical property library CoolProp”. In: *Industrial & engineering chemistry research* 53.6, pp. 2498–2508. DOI: [10.1021/ie4033999](https://doi.org/10.1021/ie4033999).
- Bellet, Serge, Nicolas Goreaud, and Norbert Nicaise (2005). “Evolution of design methodologies for next generation of reactor pressure vessels and extensive role of thermal-hydraulic numerical tools”. In: *Nuclear technology* 152.2, pp. 196–209. DOI: [10.13182/NT05-A3670](https://doi.org/10.13182/NT05-A3670).
- Bergeaud, V. and V. Lefebvre (2010). “SALOME. A software integration platform for multi-physics, pre-processing and visualisation.” In: *Proceedings of SNA + MC2010: Joint international conference on supercomputing in nuclear applications + Monte Carlo Tokyo*.
- Berry, Ray A, John W Peterson, Hongbin Zhang, Richard C Martineau, Haihua Zhao, Ling Zou, David Andrs, and Joshua Hansel (2018). *Relap-7 theory manual*. Tech. rep. Idaho National Lab.(INL), Idaho Falls, ID (United States).
- Bessiron, Vincent (Feb. 2007). “Modelling of Clad-to-Coolant Heat Transfer for RIA Applications”. In: *Journal of Nuclear Science and Technology* 44.2, pp. 211–221. DOI: [10.1080/18811248.2007.9711275](https://doi.org/10.1080/18811248.2007.9711275).

- Bestion, D., D. Lucas, M. Boucker, H. Anglart, I. Tiselj, and V. Bartosiewicz (2009). “Some lessons learned from the use of Two-Phase CFD for Nuclear Reactor Thermalhydraulics”. In: *The 13th International Topical Meeting on Nuclear Reactor Thermal Hydraulics (NURETH-13)*.
- Biard, Bruno, Vincent Chevalier, Claude Gaillard, Vincent Georgenthum, Quentin Grando, Jerome Guillot, Lena Lebreton, Christelle Manenc, Salvatore Mirotta, and Nathalie Monchalin (2020). “Reactivity Initiated Accident transient testing on irradiated fuel rods in PWR conditions: The CABRI International Program”. In: *Annals of Nuclear Energy* 141, p. 107253. DOI: [10.1016/j.anucene.2019.107253](https://doi.org/10.1016/j.anucene.2019.107253).
- Bieder, Ulrich, François Falk, and Gauthier Fauchet (2014). “LES analysis of the flow in a simplified PWR assembly with mixing grid”. In: *Progress in Nuclear Energy* 75, pp. 15–24. DOI: [10.1016/j.pnucene.2014.03.014](https://doi.org/10.1016/j.pnucene.2014.03.014).
- Blanchard, J. B., G. Damblin, J. M. Martinez, G. Arnaud, and F. Gaudier (2018). “The Uranie platform: an open-source software for optimisation, meta-modelling and uncertainty analysis”. In: *arXiv preprint arXiv:1803.10656*. DOI: [10.1051/epjn/2018050](https://doi.org/10.1051/epjn/2018050).
- Blasius, Heinrich (1913). “Das aehnlichkeitsgesetz bei reibungsvorgängen in flüssigkeiten”. In: *Mitteilungen über Forschungsarbeiten auf dem Gebiete des Ingenieurwesens: insbesondere aus den Laboratorien der technischen Hochschulen*. Springer, pp. 1–41.
- Board, U.S. Atomic Energy Commission. SL-1 Accident Investigation (1961). *SL-1 Accident: Atomic Energy Commission Investigation Board Report, Joint Committee on Atomic Energy, Congress of the United States, June 1961*. HeinOnline: U.S. Congressional documents. U.S. Government Printing Office. URL: <https://books.google.fr/books?id=oHcdxQEACAAJ>.
- Bois, G, P Fillion, F François, A Burlot, A Ben Hadj Ali, A Khaware, J Sanyal, M Rehm, B Farges, F Vinauger, et al. (2024). “Benchmark DEBORA: Assessment of MCFD compared to high-pressure boiling pipe flow measurements”. In: *International Journal of Multiphase Flow* 179, p. 104920. DOI: [10.1016/j.ijmultiphaseflow.2024.104920](https://doi.org/10.1016/j.ijmultiphaseflow.2024.104920).
- Bottini, Joseph L, Longxiang Zhu, Zhiee Jhia Ooi, Taiyang Zhang, and Caleb S Brooks (2020). “Experimental study of boiling flow in a vertical heated annulus with local two-phase measurements and visualization”. In: *International Journal of Heat and Mass Transfer* 155, p. 119712. DOI: [10.1016/j.ijheatmasstransfer.2020.119712](https://doi.org/10.1016/j.ijheatmasstransfer.2020.119712).
- Bozzano, G. and M. Dente (2001). “Shape and terminal velocity of single bubble motion a novel and approach”. In: *Computers and Chemical Engineering*. DOI: [10.1016/S0098-1354\(01\)00636-6](https://doi.org/10.1016/S0098-1354(01)00636-6).

- Broughton, James M, Pui Kuan, David A Petti, and EL Tolman (1989). “A scenario of the Three Mile Island unit 2 accident”. In: *Nuclear Technology* 87.1, pp. 34–53. DOI: [10.13182/NT89-A27637](https://doi.org/10.13182/NT89-A27637).
- Burns, Alan D., Thomas Frank, Ian Hamill, and Jun-Mei Shi (2004). “The Favre Averaged Drag Model for Turbulent Dispersion in Eulerian Multi-Phase Flows”. In: *5th International Conference on Multiphase Flow*. Vol. 4, pp. 1–17. URL: http://www.drthfrank.de/publications/2004/Burns_Frank_ICMF_2004_final.pdf.
- Cai, Chang, Issam Mudawar, Hong Liu, and Xi Xi (2021). “Assessment of void fraction models and correlations for subcooled boiling in vertical upflow in a circular tube”. In: *International Journal of Heat and Mass Transfer* 171. DOI: <https://doi.org/10.1016/j.ijheatmasstransfer.2021.121060>.
- Carlson, Jan-Renee, Veer N. Vatsay, and Jeery Whitey (2015). “Node-Centered Wall Function Models for the Unstructured Flow Code Fun3D”. In: *22nd AIAA Computational Fluid Dynamics Conference*, p. 2758.
- Cebeci, Tuncer (2013). *Analysis of turbulent flows with computer programs*. Butterworth-Heinemann.
- Celata, GP, M Cumo, and A Mariani (1994). “Assessment of correlations and models for the prediction of CHF in water subcooled flow boiling”. In: *International journal of heat and mass transfer* 37.2, pp. 237–255. DOI: [10.1016/0017-9310\(94\)90096-5](https://doi.org/10.1016/0017-9310(94)90096-5).
- Chavagnat, F, Raksmy Nop, BA Phillips, Nicolas Dorville, Marie-Christine Duluc, and Matteo Bucci (2022). “Investigation of transient subcooled flow boiling and critical heat flux in a narrow rectangular channel”. In: *19th international topical meeting on Nuclear Reactor Thermal Hydraulics (NURETH-19)*.
- Chen, Y. M. and F. Mayinger (1992). “Measurement of Heat Transfer at the Phase Interface of Condensing Bubbles”. In: *Int. J. Multiphase Flow* 18.6, pp. 877–890. DOI: [10.1016/0301-9322\(92\)90065-0](https://doi.org/10.1016/0301-9322(92)90065-0).
- Chichoux, Ch. (1993). *Essais de crise d'ébullition en tube 19.2 mm, acierinoxydable 316 TI, longueur chauffante 3.5m*. Tech. rep. DRN/DTP/STR/LETC/93-132. CEA Internal Report.
- Chu, In-Cheol, Seung-Jun Lee, Young Jung Youn, Jong Kuk Park, Hae Seob Choi, Dong-Jin Euh, and Chul-Hwa Song (2017). “Experimental evaluation of local bubble parameters of subcooled boiling flow in a pressurized vertical annulus channel”. In: *Nuclear Engineering and Design* 312, pp. 172–183. DOI: [10.1016/j.nucengdes.2016.06.027](https://doi.org/10.1016/j.nucengdes.2016.06.027).
- Chuang, Tien-Juei and Takashi Hibiki (Oct. 2017). “Interfacial forces used in two-phase flow numerical simulation”. In: *International Journal of Heat and Mass Transfer* 113, pp. 741–754. DOI: [10.1016/j.ijheatmasstransfer.2017.05.062](https://doi.org/10.1016/j.ijheatmasstransfer.2017.05.062).

- Chun, Ji-Han, Won-Jae Lee, Cheol Park, and Un-Chul Lee (2003). “Development of the critical film thickness correlation for an advanced annular film mechanistic dryout model applicable to MARS code”. In: *Nuclear engineering and design* 223.3, pp. 315–328. DOI: [10.1016/S0029-5493\(03\)00079-7](https://doi.org/10.1016/S0029-5493(03)00079-7).
- Clift, Roland, John R Grace, and Martin E Weber (2013). *Bubbles, drops, and particles*. Ed. by Academic Press. Courier Corporation.
- Cluzeau, A. du, G. Bois, N. Leoni, and A. Toutant (2022). “Analysis and modelling of bubble-induced agitation from direct numerical simulation of homogeneous bubbly flows”. In: *Physical review fluids* 7. DOI: [10.1103/PhysRevFluids.7.044604](https://doi.org/10.1103/PhysRevFluids.7.044604).
- Cluzeau, Antoine Du (Oct. 2019). “Modélisation physique de la dynamique des écoulement sà bulles par remontée d’échelle à partir de simulations fines”. PhD thesis. Université de Perpignan Via Domitia. URL: <https://theses.hal.science/tel-02336611>.
- Cohen, Caroline, Timothée Mouterde, David Quéré, and Christophe Clanet (2015). “Capillary muscle”. In: *Proceedings of the National Academy of Sciences* 112.20, pp. 6301–6306. DOI: [10.1073/pnas.1419315112](https://doi.org/10.1073/pnas.1419315112).
- Cole, Robert (1960). “A photographic study of pool boiling in the region of the critical heat flux”. In: *AIChE Journal* 6.4, pp. 533–538. DOI: <https://doi.org/10.1002/aic.690060405>.
- Colin, Catherine, Jean Fabre, and Arjan Kamp (Sept. 2012). “Turbulent bubbly flow in pipe under gravity and microgravity conditions”. In: *Journal of Fluid Mechanics* 711, pp. 469–515. DOI: [10.1017/jfm.2012.401](https://doi.org/10.1017/jfm.2012.401).
- Colin, Catherine and Dominique Legendre (2002). “Bubble distribution in turbulent shear flows: experiments and numerical simulations on single bubbles”. In: *International Conference on Multiphase Flow*.
- Collier, John G and John R Thome (1994). *Convective boiling and condensation*. Clarendon Press.
- Colombo, Marco, Ronak Thakrar, Michael Fairweather, and Simon P Walker (2019). “Assessment of semi-mechanistic bubble departure diameter modelling for the CFD simulation of boiling flows”. In: *Nuclear Engineering and Design* 344, pp. 15–27. DOI: [10.1016/j.nucengdes.2019.01.014](https://doi.org/10.1016/j.nucengdes.2019.01.014).
- Colombo, Marco, Daniele Vivaldi, and Jean Baccou (2023). “Prediction of the flow patterns in a steam generator tube bundle configuration with all-flow-regime CFD models”. In: *The 20th International Topical Meeting on Nuclear Reactor Thermal Hydraulics (NURETH-20)*.
- Coste-Delclaux, Mireille, Cheikh Diop, Anne Nicolas, and Bernard Bonin (2013). *Neutronique*. Ed. by Le Moniteur. CEA Saclay; Groupe Moniteur.

- Cubizolles, Géraud (1996). “Etude Stereologique de la Topologie des Ecoulements Diphasiques a Haute Pression”. PhD thesis. Ecole Centrale Lyon. URL: https://inis.iaea.org/collection/NCLCollectionStore/_Public/48/007/48007225.pdf.
- D’Auria, F and GM Galassi (2010). “Scaling in nuclear reactor system thermal-hydraulics”. In: *Nuclear Engineering and Design* 240.10, pp. 3267–3293. DOI: [10.1016/j.nucengdes.2010.06.010](https://doi.org/10.1016/j.nucengdes.2010.06.010).
- Deike, Luc, Stephane Popinet, and W Kendall Melville (2015). “Capillary effects on wave breaking”. In: *Journal of Fluid Mechanics* 769, pp. 541–569. DOI: [10.1017/jfm.2015.103](https://doi.org/10.1017/jfm.2015.103).
- Del Valle, Victor H. and D. B. R. Kenning (1985). “Subcooled flow boiling at high heat flux”. In: *International Journal of Heat and Mass Transfer* 28.10, pp. 1907–1920. DOI: [https://doi.org/10.1016/0017-9310\(85\)90213-3](https://doi.org/10.1016/0017-9310(85)90213-3).
- Delhaye, Jean-Marc (2008). *Thermohydraulique des réacteurs*. EDP Sciences.
- Dix, G. E. (1971). *Vapor void fractions for forced convection with subcooled boiling at low flow rates*. Tech. rep. GE Report.
- Doherty, J, P Ngan, J Monty, and M Chong (2007). “The development of turbulent pipe flow”. In: *16th Australasian Fluid Mechanics Conference*. School of Engineering, The University of Queensland.
- Driver, David M. and H. Lee Seegmiller (1985). “Features of a Reattaching Turbulent Shear Layer in Divergent Channel flow”. In: *AIAA Journal* 23.2, pp. 163–171. ISSN: 1533-385X. DOI: [10.2514/3.8890](https://doi.org/10.2514/3.8890). URL: <https://doi.org/10.2514/3.8890>.
- Edelman, Z. and E. Elias (1981). “Void fraction distribution in low flow rate subcooled boiling”. In: *Nuclear Engineering and Design* 66.3, pp. 375–382. DOI: [https://doi.org/10.1016/0029-5493\(81\)90167-9](https://doi.org/10.1016/0029-5493(81)90167-9).
- Egen, Richard A., David A. Dingee, and Joel W. Chastain (1957). *Vapor formation and behavior in boiling heat transfer*. Tech. rep. BMI-1163. Battelle Memorial Inst., Columbus, Ohio.
- Emonot, P., A. Souyri, J.L. Gandrille, and F. Barré (May 2011). “CATHARE-3: A new system code for thermal-hydraulics in the context of the NEPTUNE project”. In: *Nuclear Engineering and Design*. ISSN: 0029-5493. DOI: [10.1016/j.nucengdes.2011.04.049](https://doi.org/10.1016/j.nucengdes.2011.04.049).
- Estrada-Perez, C.E. and Y.A. Hassan (Sept. 2010). “PTV experiments of subcooled boiling flow through a vertical rectangular channel”. In: *International Journal of Multiphase Flow* 36.9, pp. 691–706. DOI: [10.1016/j.ijmultiphaseflow.2010.05.005](https://doi.org/10.1016/j.ijmultiphaseflow.2010.05.005).
- Evangelisti, Roberto and Paolo Lupoli (1969). “The Void Fraction in an Annular Channel at Atmospheric Pressure”. In: *International Journal of Heat and Mass*

Transfer 12, pp. 699–711. DOI: [https://doi.org/10.1016/0017-9310\(69\)90004-0](https://doi.org/10.1016/0017-9310(69)90004-0).

- Fajeau, M (1969). “Flica: a code for the thermodynamic study of a reactor or a test loop; Programme FLICA etude thermodynamique d’un reacteur ou d’une boucle d’essai”. In.
- Fang, Jun, Michel Rasquin, and Igor A Bolotnov (2017). “Interface tracking simulations of bubbly flows in PWR relevant geometries”. In: *Nuclear Engineering and Design* 312, pp. 205–213. DOI: [10.1016/j.nucengdes.2016.07.002](https://doi.org/10.1016/j.nucengdes.2016.07.002).
- Fang, Jun, Dillon R Shaver, Ananias Tomboulides, Misun Min, Paul Fischer, Yu-Hsiang Lan, Ronald Rahaman, Paul Romano, Sofiane Benhamadouche, Yassin A Hassan, et al. (2021). “Feasibility of full-core pin resolved CFD simulations of small modular reactor with momentum sources”. In: *Nuclear Engineering and Design* 378, p. 111143.
- Favre, L., C. Colin, S. Pujet, and S. Mimouni (Sept. 2023). “An updated force balance approach to investigate bubble sliding in vertical flow boiling at low and high pressures”. In: *International Journal of Heat and Mass Transfer* 211, p. 124227. ISSN: 0017-9310. DOI: [10.1016/j.ijheatmasstransfer.2023.124227](https://doi.org/10.1016/j.ijheatmasstransfer.2023.124227).
- Favre, Luc (2023). “Modeling and simulation of the boiling crisis within PWR at CFD scale”. PhD thesis. Institut National Polytechnique de Toulouse-INPT. URL: <https://theses.hal.science/tel-04244931>.
- Favre, Luc, Stéphane Puget, Stéphane Mimouni, and Catherine Colin (2022). “NEPTUNE_CFD simulations of DEBORA-Promoteur experiments: boiling freon in a vertical pipe with mixing vanes”. In: *The 19th International Topical Meeting on Nuclear Reactor Thermal Hydraulics (NURETH-19)*.
- Ferrell, J.K. (1964). *A Study of Convection Boiling Inside Channels*. Tech. rep. North Carolina State University, Raleigh, North Carolina. DOI: <https://doi.org/10.2172/4598223>.
- Foglia, J. J., F. G. Peter, H. M. Epstein, R. O. Wooton, D. A. Dingee, and J. W. Chastain (1961). *Boiling-water Void Distribution and Slip Ratio in Heated Channels: Final Report to Joint US-Euratom Research and Development Board*. Tech. rep. BMI-1517. Battelle Memorial Institute.
- Folsom, Charles P, Colby B Jensen, Richard L Williamson, Nicolas E Woolstenhulme, Heng Ban, and Daniel M Wachs (2016). *BISON modeling of reactivity-initiated accident experiments in a static environment*. Tech. rep. Idaho National Lab.(INL), Idaho Falls, ID (United States).
- Franck, T., S. Jain, A.A. Matyushenko, and A.V. Garbaruk (2012). “The OECD/NEA MATHIS-H benchmark - CFD analysis of water flow through a 5x5 rod bundle with spacer grids using Ansys Fluent and Ansys CFX”. In: *CFD4NRS-4, Conference on Experimental Validation and Application of CF-*

Dand CMFD Codes in Nuclear Reactor Technology, OECD/NEA and IAEA Workshop.

- Francois, F and G Berthoud (2003). “Extension of the compensated distortion method to the critical heat flux modelling in rectangular inclined channel”. In: *International journal of heat and mass transfer* 46.14, pp. 2673–2684. DOI: [10.1016/S0017-9310\(03\)00028-0](https://doi.org/10.1016/S0017-9310(03)00028-0).
- François, Fabrice, Jean-Marc Delhaye, and Philippe Clément (2011). “The Distribution Parameter C0 in the Drift Modeling of forces convective boiling”. In: *Multiphase Science and technology* 23.1, pp. 77–100. DOI: [10.1615/MultScienTechn.v23.i1.40](https://doi.org/10.1615/MultScienTechn.v23.i1.40).
- François, Fabrice, Henda Djeridi, Stéphane Barre, and Michel Kledy (2021). “Measurements of void fraction, liquid temperature and velocity under boiling two-phase flows using thermal-anemometry”. In: *Nuclear Engineering and Design* 381, p. 111359. DOI: <https://doi.org/10.1016/j.nucengdes.2021.111359>.
- Frost, W and GS Dzakowic (1967). *An extension of the method for predicting incipient boiling on commercially finished surfaces*. Ed. by ASME. ASME.
- Gabillet, C., C. Colin, and J. Favre (2002). “Experimental study of bubble injection in a turbulent and boundary layer”. In: *International Journal of Multiphase Flow* 28, pp. 553–578. DOI: [10.1016/S0301-9322\(01\)00075-1](https://doi.org/10.1016/S0301-9322(01)00075-1).
- Galloway, JE and I Mudawar (1993). “CHF mechanism in flow boiling from a short heated wall—II. Theoretical CHF model”. In: *International journal of heat and mass transfer* 36.10, pp. 2527–2540. DOI: [10.1016/S0017-9310\(05\)80191-7](https://doi.org/10.1016/S0017-9310(05)80191-7).
- Garnier, C., M. Lance, and J.L. Marie (2002). “Measurement of local flow characteristics in buoyancy-driven bubbly flow at high void fraction”. In: *Experimental Thermal and Fluid Science* 26, pp. 811–815. DOI: [10.1016/S0894-1777\(02\)00198-X](https://doi.org/10.1016/S0894-1777(02)00198-X).
- Garnier, J. (1992). *Essais de crise d'ébullition en tube 19.2 mm*. Tech. rep. STR/LETC/91 · 45. CEA.
- Garnier, J., E. Manon, and G. Cubizolles (2001). “Local measurements on flow boiling of refrigerant 12 in a vertical tube”. In: *Multiphase Science and Technology* 13.1&2. DOI: <http://dx.doi.org/10.1615/MultScienTechn.v13.i1-2.10>.
- Gerschenfeld, Antoine and Yannick Gorsse (2022). “Development of a Robust multiphase flow solver on General Meshes; application to sodium boiling at the subchannel scale”. In: *NURETH-19*.
- Groeneveld, DC (2019). *Critical heat flux data used to generate the 2006 groeneveld lookup tables*. Tech. rep. Tech. rep., United States Nuclear Regulatory Commission.
- Groeneveld, DC, JQ Shan, AZ Vasić, LKH Leung, Ahmet Durmayaz, J Yang, SC Cheng, and A Tanase (2007). “The 2006 CHF look-up table”. In: *Nuclear*

engineering and design 237.15-17, pp. 1909–1922. DOI: <https://doi.org/10.1016/j.nucengdes.2007.02.014>.

- Gueguen, Jil (2013). “Contribution à la modélisation multidimensionnelle des écoulements bouillants convectifs en conduite haute pression pour l’application au cas des réacteurs à eau pressurisée”. PhD thesis. Université de Grenoble. URL: <https://theses.hal.science/tel-01685226/>.
- Guelfi, Antoine, Dominique Bestion, Marc Boucker, Pascal Boudier, Philippe Fillion, Marc Grandotto, Jean-Marc Hérard, Eric Hervieu, and Pierre Péturaud (July 2007). “NEPTUNE: A New Software Platform for Advanced Nuclear Thermal Hydraulics”. In: *Nuclear Science and Engineering* 156.3, pp. 281–324. DOI: [10.13182/nse05-98](https://doi.org/10.13182/nse05-98).
- Gundersen, Hans Jørgen G and EB Jensen (1983). “Particle sizes and their distributions estimated from line-and point-sampled intercepts. Including graphical unfolding”. In: *Journal of Microscopy* 131.3, pp. 291–310. DOI: [10.1111/j.1365-2818.1983.tb04256.x](https://doi.org/10.1111/j.1365-2818.1983.tb04256.x).
- Ha, Tae-Wook, Byong-Jo Yun, and Jae Jun Jeong (2020). “Improvement of the subcooled boiling model for thermal-hydraulic system codes”. In: *Nuclear Engineering and Design* 364.110641. DOI: <https://doi.org/10.1016/j.nucengdes.2020.110641>.
- Harlow, F.H. and J.E. Welch (1965). “Numerical Calculation of Time-Dependent Viscous Incompressible Flow of Fluid with Free Surface”. In: *Physics of Fluids* 8, pp. 2182–2189. DOI: [10.1063/1.1761178](https://doi.org/10.1063/1.1761178).
- Harlow, Francis H and Anthony A Amsden (1968). “Numerical calculation of almost incompressible flow”. In: *Journal of Computational Physics* 3.1, pp. 80–93. DOI: [10.1016/0021-9991\(68\)90007-7](https://doi.org/10.1016/0021-9991(68)90007-7).
- Hasan, A., R. P. Roy, and S. P. Kalra (1990a). “Heat transfer measurements in turbulent liquid flow through a vertical annular channel”. In: *Journal of Heat Transfer (Transactions of the ASME (American Society of Mechanical Engineers), Series C)* 112.1, pp. 247–250. DOI: [10.1115/1.2910354](https://doi.org/10.1115/1.2910354).
- (1991). “Some Measurements in Subcooled Boiling of Refrigerant-113”. In: *Journal of Heat Transfer* 113.1, pp. 216–223. DOI: [10.1115/1.2910527](https://doi.org/10.1115/1.2910527).
- (1990b). “Experiments on subcooled flow boiling heat transfer in a vertical annular channel”. In: *International journal of heat and mass transfer* 33.10, pp. 2285–2293. DOI: [10.1016/0017-9310\(90\)90127-G](https://doi.org/10.1016/0017-9310(90)90127-G).
- Hasan, Altaf (1991). “Turbulent subcooled boiling and nonboiling flow through a vertical concentric annular channel”. PhD thesis. Arizona State University.
- Helmryd Grosfilley, Emil, Gustav Robertson, Jerol Soibam, and Jean-Marie Le Corre (2023). “Investigation of Machine Learning Regression Techniques to Pre-

- dict Critical Heat Flux over a Large Parameter Space”. In: *20th International Topical Meeting on Nuclear Reactor Thermal Hydraulics (NURETH-20)*.
- Herer, Christophe, Achim Beisiegel, Pierre Imbert, David A Farnsworth, and Friedrich Burtak (2005). “Comparison of PWR fuel assembly CHF tests obtained at three different test facilities”. In: *The 11th International Topical Meeting on Nuclear Reactor Thermal-Hydraulics (NURETH-11)*.
- Hibiki, T and M Ishii (2000a). “One-group interfacial area transport of bubbly flows in vertical round tubes”. In: *International Journal of Heat and Mass Transfer* 43.15, pp. 2711–2726. DOI: [10.1016/S0017-9310\(99\)00325-7](https://doi.org/10.1016/S0017-9310(99)00325-7).
- Hibiki, Takashi and Mamoru Ishii (2000b). “Two-group interfacial area transport equations at and bubbly-to-slug flow transition”. In: *Nuclear Engineering and Design* 202, pp. 39–76. DOI: [10.1016/S0029-5493\(00\)00286-7](https://doi.org/10.1016/S0029-5493(00)00286-7).
- (July 2003). “Active nucleation site density in boiling systems”. In: *International Journal of Heat and Mass Transfer* 46.14, pp. 2587–2601. DOI: [10.1016/s0017-9310\(03\)00031-0](https://doi.org/10.1016/s0017-9310(03)00031-0).
- (Nov. 2007). “Lift force in bubbly flow systems”. In: *Chemical Engineering Science* 62.22, pp. 6457–6474. DOI: [10.1016/j.ces.2007.07.034](https://doi.org/10.1016/j.ces.2007.07.034).
- Hibiki, Takashi, Mamoru Ishii, and Zheng Xiao (2001). “Axial interfacial area transport of vertical bubbly flows”. In: *International Journal of Heat and Mass Transfer* 44, pp. 1869–1888. DOI: [10.1016/S0017-9310\(00\)00232-5](https://doi.org/10.1016/S0017-9310(00)00232-5).
- Hinze, Julius O (1955). “Fundamentals of the hydrodynamic mechanism of splitting in dispersion processes”. In: *AIChE journal* 1.3, pp. 289–295. DOI: [10.1002/aic.690010303](https://doi.org/10.1002/aic.690010303).
- Hirt, Cyril W and Billy D Nichols (1981). “Volume of fluid (VOF) method for the dynamics of free boundaries”. In: *Journal of computational physics* 39.1, pp. 201–225. DOI: [10.1016/0021-9991\(81\)90145-5](https://doi.org/10.1016/0021-9991(81)90145-5).
- Hori, K (1994). “Transient Void Fraction Measurement in a Single Channel Simulating One Channel of a PWR Fuel Assembly”. In: *Proc. of Nuclear Thermal Hydraulics, ANS Winter Meeting, 1994*.
- Hosler, E R (Jan. 1967). *Flow patterns in high pressure two-phase (steam-water) flow with heat addition*. Tech. rep. WAPD-T-1824. Bettis Atomic Power Lab., Pittsburgh, Pa. URL: <https://www.osti.gov/biblio/4844120>.
- Ishii, Mamoru and Takashi Hibiki (2006). *Thermo-fluid dynamics of two-phase flow*. Springer Science and Business Media.
- Ishii, Mamoru and Novak Zuber (1979). “Drag Coefficient and Relative Velocity in Bubbly, Droplet or Particulate Flows”. In: *AIChE Journal* 25.5. DOI: <https://doi.org/10.1002/aic.690250513>.

- Jasak, Hrvoje (2009). “OpenFOAM: Open source CFD in research and industry”. In: *International journal of naval architecture and ocean engineering* 1.2, pp. 89–94. DOI: [10.2478/IJNAOE-2013-0011](https://doi.org/10.2478/IJNAOE-2013-0011).
- Jens, Wayne Henry and P. A. Lottes (1951). *Analysis of heat transfer, burnout, pressure drop and density data for high-pressure water*. Tech. rep. No. ANL-4627. Argonne National Lab.(ANL), Argonne, IL (United States). DOI: [10.2172/4421630](https://doi.org/10.2172/4421630).
- Jeong, JJ, HY Yoon, IK Park, and HK Cho (2010). “The CUPID code development and assessment strategy”. In: *Nuclear Engineering and Technology* 42.6, pp. 636–655.
- Kader, B.A. (1981). “Temperature and concentration profiles in fully turbulent boundary layers”. In: *Int. J. Heat Mass Transfer* 24.9, pp. 1541–1544. DOI: [https://doi.org/10.1016/0017-9310\(81\)90220-9](https://doi.org/10.1016/0017-9310(81)90220-9).
- Kader, B.A. and A.M. Yaglom (1972). “Heat and mass transfer laws for fully turbulent wall flows”. In: *Int. J. Heat Mass Transfer* 15, pp. 2329–2351. DOI: [https://doi.org/10.1016/0017-9310\(72\)90131-7](https://doi.org/10.1016/0017-9310(72)90131-7).
- Kalitzin, Georgi, Gorazd Medic, Gianluca Iaccarino, and Paul Durbin (Mar. 2005). “Near-wall behavior of RANS turbulence models and implications for wall functions”. In: *Journal of Computational Physics* 204.1, pp. 265–291. DOI: [10.1016/j.jcp.2004.10.018](https://doi.org/10.1016/j.jcp.2004.10.018).
- Kamp, A.M., A.K. Chesters, C. Colin, and J. Fabre (2001). “Bubble coalescence in turbulent flows : A mechanistic model for turbulence-induced coalescence applied to microgravity bubbly pipe flow”. In: *International Journal of Multiphase Flow* 27, pp. 1363–1396. DOI: [10.1016/S0301-9322\(01\)00010-6](https://doi.org/10.1016/S0301-9322(01)00010-6).
- Kang, S. and R. P. Roy (2002). “Vapor Phase Measurements in Subcooled Boiling Flow”. In: *J. Heat Transfer* 124.6, pp. 1207–1209. DOI: [10.1115/1.1517269](https://doi.org/10.1115/1.1517269).
- Kim, Seong-Jin and Goon-Cherl Park (2011). “Interfacial heat transfer of condensing bubble in subcooled boiling flow at low pressure”. In: *International Journal of Heat and Mass Transfer* 54, pp. 2962–2974. DOI: [10.1016/j.ijheatmasstransfer.2011.03.001](https://doi.org/10.1016/j.ijheatmasstransfer.2011.03.001).
- Kledy, Michel (2018). “Developpemet d’une methode de mesure du champ de vitesse et de temperature liquide en ecoulement diphasique en conditions reacteurs ou simulantes”. PhD thesis. Universite Grenoble Alpes. URL: <https://theses.hal.science/tel-02905447>.
- Kledy, Michel, Fabrice François, Henda Djeridi, Stephane Barre, and Jean-Marc Delhaye (2021). “Toward a local drift flux model for high-pressure, subcooled, convective boiling flows”. In: *International Journal of Heat and Mass Transfer* 177. DOI: [10.1016/j.ijheatmasstransfer.2021.121506](https://doi.org/10.1016/j.ijheatmasstransfer.2021.121506).

- Knopp, Tobias, Thomas Alrutz, and Dieter Schwamborn (2006). “A grid and flow adaptive wall-function method for RANS turbulence modelling”. In: *Journal of Computational Physics* 220, pp. 19–40. DOI: [10.1016/j.jcp.2006.05.003](https://doi.org/10.1016/j.jcp.2006.05.003).
- Kok, J.C. (1999). *Resolving the dependence on free-stream values for the k-omega turbulence model*. Tech. rep. NLR-TP-99295. National Aerospace Laboratory NLR. DOI: <https://doi.org/10.2514/2.1101>.
- Kok, J.C. and S.P. Spekreijse (2000). *Efficient and accurate implementation of the k-omega turbulence model in the NLR multi-block Navier-Stokes system*. Tech. rep. NLR-TP-2000-144. National Aerospace Laboratory NLR.
- Kolev, NI (1985). “Comparisons of the RALIZA-2/02 two-phase flow model with experimental data”. In: *Nuclear engineering and design* 85.2, pp. 217–237. DOI: [https://doi.org/10.1016/0029-5493\(85\)90288-2](https://doi.org/10.1016/0029-5493(85)90288-2).
- Kommajosyula, Ravikishore (2020). “Development and assessment of a physics-based model for subcooled flow boiling with application to CFD”. PhD thesis. Massachusetts Institute of Technology. URL: <https://dspace.mit.edu/handle/1721.1/129051>.
- Končar, Boštjan, C Morel, S Mimouni, L Vyskocil, and MC Galassi (2011). “Computational Fluid Dynamics Modeling of Boiling Bubbly Flow for Departure from Nucleate Boiling Investigations”. In: *Multiphase Science and Technology* 23.2, p. 165. DOI: [10.1615/MultScienTechn.v23.i2-4.40](https://doi.org/10.1615/MultScienTechn.v23.i2-4.40).
- Kossolapov, A., F. Chavagnat, R. Nop, N. Dorville, B. Phillips, J. Buongiorno, and M. Bucci (Oct. 2020). “The boiling crisis of water under exponentially escalating heat inputs in subcooled flow boiling at atmospheric pressure”. In: *International Journal of Heat and Mass Transfer* 160, p. 120137. DOI: [10.1016/j.ijheatmasstransfer.2020.120137](https://doi.org/10.1016/j.ijheatmasstransfer.2020.120137).
- Kossolapov, Artyom (2021). “Experimental Investigation of Subcooled Flow Boiling and CHF at Prototypical Pressures of Light Water Reactors”. PhD thesis. Massachusetts Institute of Technology. URL: <https://dspace.mit.edu/handle/1721.1/151891>.
- Kossolapov, Artyom, Matthew T Hughes, Bren Phillips, and Matteo Bucci (2024). “Bubble departure and sliding in high-pressure flow boiling of water”. In: *Journal of Fluid Mechanics* 987, A35. DOI: [10.1017/jfm.2024.405](https://doi.org/10.1017/jfm.2024.405).
- Kraus, Adam, Elia Merzari, Thomas Norddine, Oana Marin, and Sofiane Benhamadouche (2021). “Large Eddy Simulation of a 5×5 rod bundle: Impacts of a central control rod thimble tube”. In: *Nuclear Engineering and Design* 381, p. 111337. DOI: [10.1016/j.nucengdes.2021.111337](https://doi.org/10.1016/j.nucengdes.2021.111337).
- Krepper, E., P. Ruyer, M. Beyer, D. Lucas, H.-M. Prasser, and N. Seiler (2009). “CFD Simulation of Polydispersed Bubbly Two-Phase Flow around an Obstacle”. In: *Science and Technology of Nuclear Installations* 2009, pp. 1–12. DOI: [10.1155/2009/320738](https://doi.org/10.1155/2009/320738).

- Krepper, Eckhard, Matthias Beyer, Dirk Lucas, and Martin Schmidtke (Aug. 2011). “A population balance approach considering heat and mass transfer—Experiments and CFD simulations”. In: *Nuclear Engineering and Design* 241.8, pp. 2889–2897. DOI: [10.1016/j.nucengdes.2011.05.003](https://doi.org/10.1016/j.nucengdes.2011.05.003).
- Krepper, Eckhard, Bostjan Koncar, and Yury Egorov (2007). “CFD modelling of subcooled boiling—Concept, validation and application to fuel assembly design”. In: *Nuclear Engineering and Design* 237. DOI: [10.1016/j.nucengdes.2006.10.023](https://doi.org/10.1016/j.nucengdes.2006.10.023).
- Krepper, Eckhard, Dirk Lucas, Thomas Frank, Horst-Michael Prasser, and Phil J. Zwart (July 2008). “The inhomogeneous MUSIG model for the simulation of polydispersed flows”. In: *Nuclear Engineering and Design* 238.7, pp. 1690–1702. DOI: [10.1016/j.nucengdes.2008.01.004](https://doi.org/10.1016/j.nucengdes.2008.01.004).
- Krull, Benjamin, Richard Meller, Matej Tekavčič, and Fabian Schlegel (2024). “A filtering approach for applying the two-fluid model to gas-liquid flows on high resolution grids”. In: *Chemical Engineering Science* 290, p. 119909. DOI: [10.1016/j.ces.2024.119909](https://doi.org/10.1016/j.ces.2024.119909).
- Kumar, Vineet, Zhiee Jhia Ooi, and Caleb S Brooks (2019). “Forced convection steam-water experimental database in a vertical annulus with local measurements”. In: *International Journal of Heat and Mass Transfer* 137, pp. 216–228. DOI: [10.1016/j.ijheatmasstransfer.2019.03.099](https://doi.org/10.1016/j.ijheatmasstransfer.2019.03.099).
- Kurul, N. and M.Z. Podowski (1990). “Multidimensional effects in forced convection subcooled boiling”. In: *International Heat Transfer Conference Digital Library*. Ed. by Begel House Inc., pp. 21–26. DOI: <http://dx.doi.org/10.1615/IHTC9.40>.
- Labit, J-M, N Marie, O Clamens, and E Merle (2021a). “Multiphysics CATHARE2 modeling and experimental validation methodology against CABRI transients”. In: *Nuclear Engineering and Design* 373, p. 110836. DOI: [10.1016/j.nucengdes.2020.110836](https://doi.org/10.1016/j.nucengdes.2020.110836).
- (2021b). “Transient heat exchanges under fast Reactivity-Initiated Accident”. In: *Nuclear Engineering and Design* 373, p. 110917. DOI: [10.1016/j.nucengdes.2020.110917](https://doi.org/10.1016/j.nucengdes.2020.110917).
- Labunsov, D. A., A. G Lobachev, E. A. Zakharova, and B. A. Kol’chugin (1974). “Influence of subcooling of liquid at the inlet of a heated channel on true volumetric steam content”. In: *Thermal Engineering (english translation of Teploenergetica)* 21.9, pp. 22–24.
- Labunsov, D. A., R. I. Soeiev, A. G. Lobachev, et al. (1976). *In the book: Heat transfer and hydrodynamics in energy, Vol. 35, p. 88*.
- Labunsov, D.A., A.G. Lobachev, B.A. Kol’chugin, and E.A. Zakharova (1984). “The main principles of variation in vapour content of equilibrium and non-

- equilibrium two-phase flows in channels of different geometry”. In: *Thermal Engineering (english translation of Teploenergetica)* 31.9, pp. 506–508.
- Lahey, R.T. (1978). “A Mechanistic Subcooled Boiling Model”. In: *Proc. Sixth Int. Heat Transfer Conference*. Vol. 1, pp. 293–297. DOI: <http://dx.doi.org/10.1615/IHTC6.600>.
- Lahey, Richard T., Emilio Baglietto, and Igor A. Bolotnov (2021). “Progress in multiphase computational fluid dynamics”. In: *Nuclear Engineering and Design*. DOI: <https://doi.org/10.1016/j.nucengdes.2020.111018>.
- Laviéville, Jérôme, Nicolas Mérigoux, Mathieu Guingo, Cyril Baudry, and Stéphane Mimouni (2017). “A Generalized turbulent dispersion model for bubbly flow numerical simulation in NEPTUNE CFD”. In: *Nuclear Engineering and Design* 312, pp. 284–293. DOI: [10.1016/j.nucengdes.2016.11.003](https://doi.org/10.1016/j.nucengdes.2016.11.003).
- Lebas, Romain, Thibault Menard, Pierre-Arnaud Beau, Alain Berlemont, and François-Xavier Demoulin (2009). “Numerical simulation of primary break-up and atomization: DNS and modelling study”. In: *International Journal of Multiphase Flow* 35.3, pp. 247–260. DOI: [10.1016/j.ijmultiphaseflow.2008.11.005](https://doi.org/10.1016/j.ijmultiphaseflow.2008.11.005).
- Lee, CH and I Mudawar (1988). “A mechanistic critical heat flux model for subcooled flow boiling based on local bulk flow conditions”. In: *International Journal of Multiphase Flow* 14.6, pp. 711–728. DOI: [10.1016/0301-9322\(88\)90070-5](https://doi.org/10.1016/0301-9322(88)90070-5).
- Lee, S. C. and S. G. Bankoff (1998). “A comparison of predictive models for the onset of significant void at low pressures in forced-convection subcooled boiling”. In: *KSME International Journal* 12.504-513. DOI: <https://doi.org/10.1007/BF02946366>.
- Lee, Tae Beom and Young Hoon Jeong (2022). “Improvement of the subcooled boiling model using a new net vapor generation correlation inferred from artificial neural networks to predict the void fraction profiles in the vertical channel”. In: *Nuclear Engineering and Technology* 54, pp. 4776–4797. DOI: <https://doi.org/10.1016/j.net.2022.07.031>.
- Lee, Tae-Ho, Rong Situ, Takashi Hibiki, Hyun-Sik Park, Mamoru Ishii, and Michitsugu Mori (2009). “Axial developments of interfacial area and void concentration profiles in subcooled boiling flow of water”. In: *International Journal of Heat and Mass Transfer* 52.1-2, pp. 473–487. DOI: [10.1016/j.ijheatmasstransfer.2008.05.038](https://doi.org/10.1016/j.ijheatmasstransfer.2008.05.038).
- Lee, TH, GC Park, and DJ Lee (2002). “Local flow characteristics of subcooled boiling flow of water in a vertical concentric annulus”. In: *International Journal of Multiphase Flow* 28.8, pp. 1351–1368. DOI: [10.1016/S0301-9322\(02\)00026-5](https://doi.org/10.1016/S0301-9322(02)00026-5).

- Legendre, Dominique, Jacques Boreee, and Jacques Magnaudet (1998). “Thermal and dynamic evolution of a spherical bubble moving steadily in a superheated or subcooled liquid”. In: *Physics of Fluids*. DOI: [10.1063/1.869654](https://doi.org/10.1063/1.869654).
- Legendre, Dominique and Jacques Magnaudet (1998). “The lift force on a spherical bubble in a viscous linear shear flow”. In: *J. Fluid Mech.* 368, pp. 81–126. DOI: [10.1017/S0022112098001621](https://doi.org/10.1017/S0022112098001621).
- Leoni, Nicolas (2022). “Bayesian inference of model error for the calibration of two-phase CFD codes”. PhD thesis. Institut polytechnique de Paris. URL: <https://theses.hal.science/tel-03654787v1>.
- Leoni, Nicolas, Olivier Le Maitre, Maria-Giovanna Rodio, and Pietro Marco Congedo (2024). “Bayesian calibration with adaptive model discrepancy”. In: *International Journal for Uncertainty Quantification* 14.1. DOI: [10.1615/Int.J.UncertaintyQuantification.2023046331](https://doi.org/10.1615/Int.J.UncertaintyQuantification.2023046331).
- Levy, Salomon (1967). “Forced convection subcooled boiling—prediction of vapor volumetric fraction”. In: *International journal of heat and mass transfer* 10.7, pp. 951–965. DOI: [https://doi.org/10.1016/0017-9310\(67\)90071-3](https://doi.org/10.1016/0017-9310(67)90071-3).
- Liao, Yixiang, Eckhard Krepper, and Dirk Lucas (July 2019). “A baseline closure concept for simulating bubbly flow with phase change: A mechanistic model for interphase heat transfer coefficient”. In: *Nuclear Engineering and Design* 348, pp. 1–13. DOI: [10.1016/j.nucengdes.2019.04.007](https://doi.org/10.1016/j.nucengdes.2019.04.007).
- Liao, Yixiang, Tian Ma, Liu Liu, Thomas Ziegenhein, Eckhard Krepper, and Dirk Lucas (Oct. 2018). “Eulerian modelling of turbulent bubbly flow based on a baseline closure concept”. In: *Nuclear Engineering and Design* 337, pp. 450–459. DOI: [10.1016/j.nucengdes.2018.07.021](https://doi.org/10.1016/j.nucengdes.2018.07.021).
- Lo, Simon and Joseph Osman (2012). “CFD modeling of boiling flow in PSBT 5×5 bundle”. In: *Science and Technology of Nuclear Installations* 2012.1, p. 795935. DOI: [10.1155/2012/795935](https://doi.org/10.1155/2012/795935).
- Lobachev, A. G., B. A. Kol’chugin, E. A. Zakharova, and G. G. Kruglikhina (1973). “Investigating the true Volumetric Steam Contents in a Heated Tube with Rising and Falling Motion of a Two-Phase Flow”. In: *Thermal Engineering (english translation of Teploenergetica)*.
- Lubchenko, Nazar, Ben Magolan, Rosie Sugrue, and Emilio Baglietto (Jan. 2018). “A more fundamental wall lubrication force from turbulent dispersion regularization for multiphase CFD applications”. In: *International Journal of Multiphase Flow* 98, pp. 36–44. DOI: [10.1016/j.ijmultiphaseflow.2017.09.003](https://doi.org/10.1016/j.ijmultiphaseflow.2017.09.003).
- Lucas, D, M Beyer, and L Szalinski (2013). “Experimental database on steam–water flow with phase transfer in a vertical pipe”. In: *Nuclear Engineering and Design* 265, pp. 1113–1123. DOI: [10.1016/j.nucengdes.2013.10.002](https://doi.org/10.1016/j.nucengdes.2013.10.002).

- Lucas, D., R. Rzehak, E. Krepper, Th. Ziegenhein, Y. Liao, S. Kriebitzsch, and P. Apanasevich (Apr. 2016). “A strategy for the qualification of multi-fluid approaches for nuclear reactor safety”. In: *Nuclear Engineering and Design* 299, pp. 2–11. DOI: [10.1016/j.nucengdes.2015.07.007](https://doi.org/10.1016/j.nucengdes.2015.07.007).
- Lucas, Dirk and Horst-Michael Prasser (2007). “Steam bubble condensation in sub-cooled water in case of co-current vertical pipe flow”. In: *Nuclear Engineering and Design* 237.5, pp. 497–508. DOI: [10.1016/j.nucengdes.2006.09.004](https://doi.org/10.1016/j.nucengdes.2006.09.004).
- Luo, Hean and Hallvard F Svendsen (1996). “Theoretical model for drop and bubble breakup in turbulent dispersions”. In: *AIChE journal* 42.5, pp. 1225–1233. DOI: [10.1002/aic.690420505](https://doi.org/10.1002/aic.690420505).
- Lyczkowski, Robert W (2010). “The history of multiphase computational fluid dynamics”. In: *Industrial & Engineering Chemistry Research* 49.11, pp. 5029–5036. DOI: [10.1021/ie901439y](https://doi.org/10.1021/ie901439y).
- Mahaffy, John H (1982). “A stability-enhancing two-step method for fluid flow calculations”. In: *Journal of Computational Physics* 46.3, pp. 329–341. DOI: [10.1016/0021-9991\(82\)90019-5](https://doi.org/10.1016/0021-9991(82)90019-5).
- Manninen, Mikko, Veikko Taivassalo, and Sirpa Kallio (1996). *On the mixture model for multiphase flow*. Tech. rep. VTT Energy.
- Manon, Etienne (2000). “Contribution à l’analyse et à la modélisation locale des écoulements bouillants sous-saturés dans les conditions des réacteurs à eau sous pression”. PhD thesis. Châtenay-Malabry, Ecole centrale de Paris.
- Marchaterre, J. F., M. Petrick, P.A. Lottes, R.J. Weatherhead, and W. S. Flinn (1960). *Natural and Forced-Circulation Boiling Studies*. Tech. rep. A.N.L.-5735. Argonne National Laboratory.
- Marfaing, O., M. Guingo, J. Laviéville, G. Bois, N. Méchitoua, N. Méricoux, and S. Mimouni (2016). “An analytical relation for the void fraction distribution in a fully developed bubbly flow in a vertical pipe”. In: *Chemical Engineering Science* 152, pp. 579–585. DOI: [10.1016/j.ces.2016.06.041](https://doi.org/10.1016/j.ces.2016.06.041).
- Martin, Robert (1969). “Mesure du taux de vide à haute pression dans un canal chauffant”. INIS RN:36002834. PhD thesis. Centre d’études nucléaires de Grenoble.
- (1972). “Measurement of the local void fraction at high pressure in a heating channel”. In: *Nuclear Science and Engineering* 48.2, pp. 125–138. DOI: <https://doi.org/10.13182/NSE72-A22466>.
- Martin, Robert P and Larry D O’Dell (2005). “AREVA’s realistic large break LOCA analysis methodology”. In: *Nuclear Engineering and Design* 235.16, pp. 1713–1725. DOI: [10.1016/j.nucengdes.2005.02.004](https://doi.org/10.1016/j.nucengdes.2005.02.004).
- Martinez, P and J Galpin (2014). “CFD modeling of the EPR primary circuit”. In: *Nuclear Engineering and Design* 278, pp. 529–541.

- Masuk, Ashik Ullah Mohammad, Ashwanth KR Salibindla, and Rui Ni (2021). “Simultaneous measurements of deforming Hinze-scale bubbles with surrounding turbulence”. In: *Journal of Fluid Mechanics* 910, A21. DOI: <https://doi.org/10.1017/jfm.2020.933>.
- Maurer, G. W. (1960). “A method of predicting steady-state boiling vapor fractions in reactor coolant channels”. In: *Bettis Technical Review* WAPD-BT-19, pp. 59–70.
- Mazzocco, T., W. Ambrosini, R. Kommajosyula, and E. Baglietto (Feb. 2018). “A reassessed model for mechanistic prediction of bubble departure and lift off diameters”. In: *International Journal of Heat and Mass Transfer* 117, pp. 119–124. ISSN: 0017-9310. DOI: [10.1016/j.ijheatmasstransfer.2017.09.105](https://doi.org/10.1016/j.ijheatmasstransfer.2017.09.105).
- McAdams, WH, WK Woods, and LC Heroman Jr (1942). “Vaporization inside horizontal tubes—II benzene-oil mixtures”. In: *Transactions of the American Society of Mechanical Engineers* 64.3, pp. 193–199. DOI: <https://doi.org/10.1115/1.4019013>.
- Menter, Florian R. (1993). “Zonal Two Equation k- ϵ , Turbulence Models for Aerodynamic Flows”. In: *American Institute of Aeronautics and Astronautics 24th Fluid Dynamics Conference*. AIAA 93-2906. American Institute of Aeronautics and Astronautics.
- Mesina, George L (2016). “A history of RELAP computer codes”. In: *Nuclear Science and Engineering* 182.1, pp. v–ix. DOI: [10.13182/NSE16-A38253](https://doi.org/10.13182/NSE16-A38253).
- Meunier, Philippe (2001). *La caractérisation des couvercles de cuve déposés. Réacteurs EDF REP 900 MWE/1300 MWE*. Tech. rep. EDF.
- Mimouni, S., C. Baudry, M. Guingo, J. Lavieville, N. Merigoux, and N. Mechtoua (Apr. 2016a). “Computational multi-fluid dynamics predictions of critical heat flux in boiling flow”. In: *Nuclear Engineering and Design* 299, pp. 28–36. DOI: [10.1016/j.nucengdes.2015.07.017](https://doi.org/10.1016/j.nucengdes.2015.07.017).
- Mimouni, Stephane, William Benguigui, Solène Fleau, Arnaud Foissac, Mathieu Guingo, Mickael Hassanaly, Jérôme Lavieville, Jeanne Malet, Namane Méchtoua, Nicolas Mérigoux, et al. (2017). “Dispersed two-phase flow modelling for nuclear safety in the NEPTUNE_CFD code”. In: *Science and Technology of Nuclear Installations* 2017. DOI: [10.1155/2017/3238545](https://doi.org/10.1155/2017/3238545).
- Mimouni, Stephane, William Benguigui, Jerome Lavieville, Nicolas Merigoux, Mathieu Guingo, Cyril Baudry, and Olivier Marfaing (2016b). “New nucleation boiling model devoted to high pressure flows”. In: *ICMF-2016-9th International Conference on Multiphase Flow*. URL: https://www.researchgate.net/publication/304303168_New_nucleation_boiling_model_devoted_to_high_pressure_flows.

- Montout, Michaël (2009). “Contribution au développement d’une Approche Prédictive Locale de la crise d’ébullition”. PhD thesis. Institut National Polytechnique de Toulouse.
- Morel, Christophe, Pierre Ruyer, Nathalie Seiler, and Jerome M. Lavieville (Jan. 2010). “Comparison of several models for multi-size bubbly flows on an adiabatic experiment”. In: *International Journal of Multiphase Flow* 36.1, pp. 25–39. DOI: [10.1016/j.ijmultiphaseflow.2009.09.003](https://doi.org/10.1016/j.ijmultiphaseflow.2009.09.003).
- Morse, Roman W, Jason Chan, Evan T Hurlburt, Jean-Marie Le Corre, Arganthaël Berson, Gregory F Nellis, and Kristofer M Dressler (2024). “A new paradigm for the role of disturbance waves on film dryout and wall heat transfer in annular two-phase flow”. In: *International Journal of Heat and Mass Transfer* 219, p. 124812.
- Nasto, Alice, P-T Brun, and AE Hosoi (2018). “Viscous entrainment on hairy surfaces”. In: *Physical Review Fluids* 3.2, p. 024002. DOI: [10.1103/PhysRevFluids.3.024002](https://doi.org/10.1103/PhysRevFluids.3.024002).
- NEA (2022). *State-of-the-art Report on Nuclear Fuel Behaviour Under Reactivity-initiated Accident Conditions (RIA SOAR)*. OECD Publishing, Paris.
- Neykov, D, F Aydogan, L Hochreiter, H Utsuno, F Kasahara, E Sartori, and M Martin (2006). “NUPEC BWR Full-size Fine-mesh Bundle Test (BFBT) Benchmark: Volume I: Specifications”. In: *OECD Papers* 6.7, pp. 1–132.
- Nguyen, Thanh-Binh and Tomio Okawa (2024). “Experimental validation of the mechanism and condition for the onset of significant void in subcooled flow boiling”. In: *International Journal of Heat and Mass Transfer* 219.124881. DOI: <https://doi.org/10.1016/j.ijheatmasstransfer.2023.124881>.
- Nop, R., M.-C. Duluc, N. Dorville, A. Kossolapov, F. Chavagnat, and M. Bucci (Oct. 2021). “An energy model for the transient flow boiling crisis under highly subcooled conditions at atmospheric pressure”. In: *International Journal of Thermal Sciences* 168, p. 107042. DOI: [10.1016/j.ijthermalsci.2021.107042](https://doi.org/10.1016/j.ijthermalsci.2021.107042).
- Nop, Raksmy (2020). “Experimental investigation and modeling of the transient flow boiling crisis of water at moderate pressure and high subcooling”. PhD thesis. Université Paris-Saclay. URL: <https://theses.hal.science/tel-03081992>.
- NRC (n.d.). *How Nuclear Reactors Work*. URL: <https://www.nrc.gov/reactors/power/pwrs.html>.
- NRC, US (2010). *TRACE v5. 0 theory manual, field equations, solution methods, and physical models*. Tech. rep. United States Nucl. Regul. Comm. URL: <https://www.nrc.gov/docs/ML1200/ML120060218.pdf>.

- Nukiyama, Shiro (1966). “The maximum and minimum values of the heat Q transmitted from metal to boiling water under atmospheric pressure”. In: *International Journal of Heat and Mass Transfer* 9.12, pp. 1419–1433. DOI: [10.1016/0017-9310\(66\)90138-4](https://doi.org/10.1016/0017-9310(66)90138-4).
- Nyer, Marcel (1969). “Étude des phénomènes thermiques et hydrauliques accompagnant une excursion rapide de puissance sur un canal chauffant”. In: *PhD thesis, Univ. de Grenoble*.
- Ooi, Zhiee Jhia, Taiyang Zhang, and Caleb S Brooks (2020). “Experimental dataset with high-speed visualization for vertical upward steam-water flow with transition from annulus to circular channel”. In: *International Journal of Heat and Mass Transfer* 161, p. 120281. DOI: [10.1016/j.ijheatmasstransfer.2020.120281](https://doi.org/10.1016/j.ijheatmasstransfer.2020.120281).
- Ozar, B, CS Brooks, T Hibiki, and M Ishii (2013). “Interfacial area transport of vertical upward steam–water two-phase flow in an annular channel at elevated pressures”. In: *International Journal of Heat and Mass Transfer* 57.2, pp. 504–518. DOI: [10.1016/j.ijheatmasstransfer.2012.10.059](https://doi.org/10.1016/j.ijheatmasstransfer.2012.10.059).
- Park, I.K., H.K. Cho, H.Y. Yoon, and J.J. Jeong (2009). “Numerical effects of the semi-conservative form of momentum equations for multi-dimensional two-phase flows”. In: *Nuclear Engineering and Design* 239, pp. 2365–2371. DOI: <https://doi.org/10.1016/j.nucengdes.2009.06.011>.
- Pham, Monica, Guillaume Bois, Fabrice François, and Emilio Baglietto (Sept. 2023). “Assessment of State-of-the-art multiphase CFD modeling for subcooled flow boiling in reactor applications”. In: *Nuclear Engineering and Design* 411, p. 112379. ISSN: 0029-5493. DOI: [10.1016/j.nucengdes.2023.112379](https://doi.org/10.1016/j.nucengdes.2023.112379).
- Pope, Stephen B. (Aug. 2000). *Turbulent Flows*. Cambridge University Press. DOI: [10.1017/cbo9780511840531](https://doi.org/10.1017/cbo9780511840531).
- Pothukuchi, Harish, S Kelm, BSV Patnaik, BVSSS Prasad, and H-J Allelein (2019). “CFD modeling of critical heat flux in flow boiling: Validation and assessment of closure models”. In: *Applied thermal engineering* 150, pp. 651–665.
- Prince, Michael J. and Harvey W. Blanch (1990). “Bubble Coalescence and Break-Up in Air-Splarged Bubble Columns”. In: *AIChE Journal*. DOI: [10.1002/aic.690361004](https://doi.org/10.1002/aic.690361004).
- Qi, Yinghe, Shiyong Tan, Noah Corbitt, Carl Urbanik, Ashwanth KR Salibindla, and Rui Ni (2022). “Fragmentation in turbulence by small eddies”. In: *Nature communications* 13.1, p. 469. DOI: [10.1038/s41467-022-28092-3](https://doi.org/10.1038/s41467-022-28092-3).
- Ramstorfer, Franz, Bernd Breitscha del, Helfried Steiner, and Gunter Brenn (2005). “Modelling of the near-wall liquid velocity field in subcooled boiling flow”. In: *Heat Transfer Summer Conference*. Vol. 47322, pp. 323–332. DOI: <https://doi.org/10.1115/HT2005-72182>.

- Ranz, W. E. and W.R. Marshall (1952). “Evaporation from drops”. In: *Chem. Eng. Prog.* 48.3, pp. 141–146.
- Reichardt, H. (1951). “Vollständige Darstellung der turbulenten Geschwindigkeitsverteilung in glatten Leitungen”. In: *Z. angew. Math. Mech.* 31.7, pp. 208–219. DOI: <https://doi.org/10.1002/zamm.19510310704>.
- Reiss, Corentin (2024). *Burns turbulent dispersion considers the dispersed phase as a passive scalar*. HAL archive. URL: <https://hal.science/hal-04494644>.
- Reiss, Corentin, Antoine Gerschenfeld, and Catherine Colin (2024a). “Boiling-flow multiphase CFD simulations for nuclear reactor conditions without interfacial area transport equation”. In: *Nuclear Engineering and Design* 428. DOI: [10.1016/j.nucengdes.2024.113453](https://doi.org/10.1016/j.nucengdes.2024.113453).
- (2024b). “Heat flux partition based on onset of significant void”. In: *International Journal of Multiphase Flow* 181. DOI: [10.1016/j.ijmultiphaseflow.2024.104972](https://doi.org/10.1016/j.ijmultiphaseflow.2024.104972). URL: <https://hal.science/hal-04524455>.
- Reiss, Corentin, Antoine Gerschenfeld, Elie Saikali, Yannick Gorsse, and Alan Burlot (2024c). “Presenting the multi-phase solver implemented in the open source TrioCFD code based on the TRUST HPC platform”. In: *EPJ Web Conf.* Vol. 302. Joint International Conference on Supercomputing in Nuclear Applications + Monte Carlo (SNA + MC 2024) 03001. DOI: [10.1051/epjconf/202430203001](https://doi.org/10.1051/epjconf/202430203001).
- Richenderfer, Andrew, Artyom Kossolapov, Jee Hyun Seong, Giacomo Saccone, Etienne Demarly, Ravikishore Kommajosyula, Emilio Baglietto, Jacopo Buongiorno, and Matteo Bucci (2018). “Investigation of subcooled flow boiling and CHF using high-resolution diagnostics”. In: *Experimental Thermal and Fluid Science* 99, pp. 35–58. DOI: <https://doi.org/10.1016/j.expthermflusci.2018.07.017>.
- Risso, Frédéric and Jean Fabre (1998). “Oscillations and breakup of a bubble immersed in a turbulent field”. In: *Journal of Fluid Mechanics* 372, pp. 323–355. DOI: <https://doi.org/10.1017/S0022112098002705>.
- Riviere, Aliénor, Wouter Mostert, Stéphane Perrard, and Luc Deike (2021). “Sub-Hinze scale bubble production in turbulent bubble break-up”. In: *Journal of Fluid Mechanics* 917, A40. DOI: [10.1017/jfm.2021.243](https://doi.org/10.1017/jfm.2021.243).
- Rouhani, S. Z. (1966a). *Void Measurements in the Regions of Sub-Cooled and Low-Quality Boiling Part 1. Low Mass Velocities*. Tech. rep. AE-238. Aktiebolaget Atomenergi. URL: <https://www.osti.gov/etdeweb/biblio/20949499>.
- (1966b). *Void Measurements in the Regions of Sub-Cooled and Low-Quality Boiling Part 2. Higher Mass Velocities*. Tech. rep. AE-239. Aktiebolaget Atomenergi. URL: <https://www.osti.gov/etdeweb/biblio/20949498>.

- Roumet, Elie, Raksmy Nop, Nicolas Dorville, and Marie-Christine Duluc (2023). “Towards modeling the impact of the aspect ratio in an energy model describing the transient flow boiling at high subcooling”. In: *ICMF 2023-11th International Conference on Multiphase Flow*.
- Roy, R. P., V. Velidandla, S.P. Kalra, and P. Peturaud (1994). “Local measurements in the two-phase region of turbulent subcooled boiling flow”. In: *ASME Journal of Heat and Mass Transfer* 116.3, pp. 660–669. DOI: <https://doi.org/10.1115/1.2910920>.
- Roy, R. P., A. Hasan, and S. P. Kalra (1993). “Temperature and velocity fields in turbulent liquid flow adjacent to a bubbly boiling layer”. In: *International journal of multiphase flow* 19.5, pp. 765–795. DOI: [10.1016/0301-9322\(93\)90042-S](https://doi.org/10.1016/0301-9322(93)90042-S).
- Roy, R. P., S. Kang, and J. A. Zarate (1999). “Measurement of the thermal and velocity fields in the liquid phase of turbulent subcooled bubbly boiling flow”. In: *ASME International Mechanical Engineering Congress and Exposition*. DOI: [10.1115/IMECE1999-1133](https://doi.org/10.1115/IMECE1999-1133).
- Roy, R. P., V. Velidandla, and S. P. Kalra (1997). “Velocity field in turbulent subcooled boiling flow”. In: *J. Heat Transfer* 119, pp. 754–766. DOI: [10.1115/1.2824180](https://doi.org/10.1115/1.2824180).
- Roy, R.P., S. Kang, J.A. Zarate, and A. Laporta (2002). “Turbulent Subcooled Boiling Flow—Experiments and Simulations”. In: *J. Heat Transfer* 124.1, pp. 73–93. DOI: <https://doi.org/10.1115/1.1418698>.
- Rubin, A, A Schoedel, M Avramova, H Utsuno, S Bajorek, and A Velazquez-Lozada (2012). *Oecd/nrc benchmark based on nupec pwr sub-channel and bundle test (psbt). volume i: Experimental database and final problem specifications*. Tech. rep. Organisation for Economic Co-Operation and Development.
- Rumsey, Chris, Brian Smith, and George Huang (June 2010). “Description of a Website Resource for Turbulence Modeling Verification and Validation”. In: *40th Fluid Dynamics Conference and Exhibit*. DOI: [10.2514/6.2010-4742](https://doi.org/10.2514/6.2010-4742). URL: <https://doi.org/10.2514/6.2010-4742>.
- Ruyer, Pierre and Nathalie Seiler (2009). “Advanced model for polydispersion in size in boiling flows”. In: *La Houille blanche*. DOI: [10.1051/lhb/2009046](https://doi.org/10.1051/lhb/2009046).
- Rzehak, Roland and Eckhard Krepper (2013). “CFD modeling of bubble-induced turbulence”. In: *International Journal of Multiphase Flow* 55, pp. 138–155. DOI: [10.1016/j.ijmultiphaseflow.2013.04.007](https://doi.org/10.1016/j.ijmultiphaseflow.2013.04.007).
- Sabotinov, L. (1974). “Experimental investigation of the void fraction at subcooled boiling for different heat flux profiles along the channel”. PhD thesis. Moscow Power Engineering Institute, Chair “Nuclear Power Plants”, Moscow.

- Saha, Pradip and Novak Zuber (1974). “Point of Net Vapor Generation and Vapor Void Fraction in Subcooled Boiling”. In: *International Heat Transfer Conference Digital Library*. Ed. by Begel House Inc., pp. 175–179. URL: <https://www.nrc.gov/docs/ML1733/ML17338A800.pdf>.
- Saikali, Elie, Gilles Bernard-Michel, Anne Sergent, Christian Tenaud, and R Salem (2019). “Highly resolved large eddy simulations of a binary mixture flow in a cavity with two vents: Influence of the computational domain”. In: *International journal of hydrogen energy* 44.17, pp. 8856–8873. DOI: [10.1016/j.ijhydene.2018.08.108](https://doi.org/10.1016/j.ijhydene.2018.08.108).
- Saikali, Elie, Pierre Ledac, Adrien Bruneton, Anida Khizar, Christophe Bourcier, Gilles Bernard-Michel, Erwan Adam, and Deborah Houssin-Agbomson (2021). “Numerical modeling of a moderate hydrogen leakage in a typical two-vented fuel cell configuration”. In: *International Conference of Hydrogen Safety*.
- Sakurai, A. (2000). “Mechanisms of transitions to film boiling at CHF’s in subcooled and pressurized liquids due to steady and increasing heat inputs”. In: *Nuclear Engineering and Design* 197, pp. 301–356. DOI: [10.1016/S0029-5493\(99\)00314-3](https://doi.org/10.1016/S0029-5493(99)00314-3).
- Salibindla, Ashwanth K. R., Ashik Ullah Mohammad Masuk, Shiyong Tan, and Rui Ni (May 2020). “Lift and drag coefficients of deformable bubbles in intense turbulence determined from bubble rise velocity”. In: *Journal of Fluid Mechanics* 894. DOI: [10.1017/jfm.2020.244](https://doi.org/10.1017/jfm.2020.244).
- Salko Jr, Robert, Maria Avramova, Aaron Wysocki, Belgacem Hizoum, Aysenur Toptan, Jianwei Hu, Nathan Porter, Taylor S Blyth, Christopher A Dances, Ana Gomez, et al. (2023). *CTF Theory Manual: Version 4.3*. Tech. rep. Oak Ridge National Laboratory (ORNL), Oak Ridge, TN (United States). URL: <https://www.osti.gov/biblio/1994732>.
- Sato, Y, M Sadatomi, and K Sekoguchi (1981). “Momentum and heat transfer in two-phase bubble flow—I. Theory”. In: *International Journal of Multiphase Flow* 7.2, pp. 167–177. DOI: [10.1016/0301-9322\(81\)90003-3](https://doi.org/10.1016/0301-9322(81)90003-3).
- Sekoguchi, Kotohiko, O. Tanaka, S. Esaki, and T. Imasaka (1980). “Prediction of void fraction in subcooled and low quality boiling regions”. In: *Bulletin of JSME* 23.183, pp. 1475–1482. DOI: <https://doi.org/10.1299/jsme1958.23.1475>.
- Serizawa, Akimi (1983). “Theoretical prediction of maximum heat flux in power transients”. In: *International journal of heat and mass transfer* 26.6, pp. 921–932. DOI: [10.1016/S0017-9310\(83\)80116-1](https://doi.org/10.1016/S0017-9310(83)80116-1).
- Shaver, D. R. and M. Z. Podowski (2015a). “Modeling of Interfacial and Forces for Bubbly and Flows in Subcooled and Boiling Conditions”. In: *Transactions of the American Nuclear Society*. Vol. 113. 1, pp. 1368–1371.
- Shaver, Dillon, Aleks Obabko, Ananias Tomboulides, Victor Coppo-Leite, Yu-Hsiang Lan, MiSun Min, Paul Fischer, and Christopher Boyd (2020). *Nek5000*

Developments in Support of Industry and the NRC. Tech. rep. ANL/NSE-20/48. Argonne National Laboratory.

Shaver, DR and MZ Podowski (2015b). “Modeling and validation of forced convection subcooled boiling”. In: *NURETH-16*, pp. 4112–4125.

Shi, Pengyu and Roland Rzehak (Jan. 2020). “Lift forces on solid spherical particles in wall-bounded flows”. In: *Chemical Engineering Science* 211, p. 115264. DOI: [10.1016/j.ces.2019.115264](https://doi.org/10.1016/j.ces.2019.115264).

Situ, Rong, Takashi Hibiki, Xiaodong Sun, Ye Mi, and Mamoru Ishii (2004). “Axial development of subcooled boiling flow in an internally heated annulus”. In: *Experiments in Fluids* 37, pp. 589–603. DOI: [10.1007/s00348-004-0855-6](https://doi.org/10.1007/s00348-004-0855-6).

St.-Pierre, Carl C. (1965). *Frequency-response analysis of steam voids to sinusoidal power modulation in a thin-walled boiling water coolant channel*. Tech. rep. ANL-7041. Argonne National Laboratory.

Stasiuk, Mark V, Claude Jaupart, R Stephen, and J Sparks (1993). “Influence of cooling on lava-flow dynamics”. In: *Geology* 21.4, pp. 335–338. DOI: [10.1130/0091-7613\(1993\)021%3C0335:IOCOLF%3E2.3.CO;2](https://doi.org/10.1130/0091-7613(1993)021%3C0335:IOCOLF%3E2.3.CO;2).

Staub, F. W., G. E. Walmet, and R. O. Neimi (1969). *Heat Transfer and Hydraulics: the Effects of Subcooled Voids. Final Report, February 1967–June 1969*. Tech. rep. NYO-3679-8; EURAEC-2120. General Electric Co., Schenectady, NY Research and Development Center; General Electric Co., San Jose, Calif. Atomic Power Equipment Dept. URL: <https://www.osti.gov/biblio/4766327>.

Sugrue, Rosemary (2017). “A Robust Momentum Closure Approach for Multiphase Computational Fluid Dynamics Applications”. PhD thesis. Massachusetts Institute of Technology.

Sungkorn, R, JJ Derksen, and JG Khinast (2011). “Modeling of turbulent gas–liquid bubbly flows using stochastic Lagrangian model and lattice-Boltzmann scheme”. In: *Chemical engineering science* 66.12, pp. 2745–2757. DOI: [10.1016/j.ces.2011.03.032](https://doi.org/10.1016/j.ces.2011.03.032).

Sussman, Mark, Peter Smereka, and Stanley Osher (1994). “A level set approach for computing solutions to incompressible two-phase flow”. In: *Journal of Computational physics* 114.1, pp. 146–159. DOI: [10.1006/jcph.1994.1155](https://doi.org/10.1006/jcph.1994.1155).

Tag, Sibel (2024). “A comprehensive review of numerical and experimental research on the thermal-hydraulics of two-phase flows in vertical rod bundles”. In: *International Journal of Heat and Mass Transfer* 221, p. 125053. DOI: [10.1016/j.ijheatmasstransfer.2023.125053](https://doi.org/10.1016/j.ijheatmasstransfer.2023.125053).

Tag, Sibel, Stephan Boden, Ronald Franz, Yixiang Liao, and Uwe Hampel (Mar. 2023a). “An experimental study of boiling two-phase flow in a vertical rod bundle with a spacer grid-Part 1: Effects of mass flux and heat flux”. In:

Experimental Thermal and Fluid Science 145, p. 110903. DOI: [10.1016/j.expthermflusci.2023.110903](https://doi.org/10.1016/j.expthermflusci.2023.110903).

Taş, Sibel, Stephan Boden, Ronald Franz, Yixiang Liao, and Uwe Hampel (Nov. 2023b). “An experimental study of boiling two-phase flow in a vertical rod bundle with a spacer grid-Part 2: Effects of vane angle”. In: *Experimental Thermal and Fluid Science* 149, p. 111000. DOI: [10.1016/j.expthermflusci.2023.111000](https://doi.org/10.1016/j.expthermflusci.2023.111000).

Taylor, Geoffrey Ingram (1950). “The instability of liquid surfaces when accelerated in a direction perpendicular to their planes. I”. In: *Proceedings of the Royal Society of London. Series A. Mathematical and Physical Sciences* 201.1065, pp. 192–196.

Tecchio, Cassiano (2022). “Experimental study of boiling: characterization of near-wall phenomena and bubble dynamics”. PhD thesis. Université Paris-Saclay. URL: <https://theses.hal.science/tel-03859592/>.

Tentner, Adrian, Prasad Vegendla, Ananias Tomboulides, Aleks Obabko, Elia Merzari, and Dillon Shaver (2018). “Advances in modeling critical heat flux in LWR Boiling flows with the NEK-2P CFD code”. In: *Proceedings of the 2018 26th International Conference on Nuclear Engineering ICONE26*.

Thom, J. R. S., W. Walker, T. A. Fallon, and G. F. S. Reising (1965). “Paper 6: boiling in sub-cooled water during flow up heated tubes or annuli”. In: *Proceedings of the institution of mechanical engineers, conference proceedings*. Ed. by England: Sage Publications Sage UK: London. Vol. 180-3, pp. 226–246. DOI: [https://doi.org/10.1016/0301-9322\(81\)90040-9](https://doi.org/10.1016/0301-9322(81)90040-9). URL: <https://www.osti.gov/biblio/4263900>.

Thomas, RM (1981). “Bubble coalescence in turbulent flows”. In: *International Journal of Multiphase Flow* 7.6, pp. 709–717. DOI: [10.1016/0301-9322\(81\)90040-9](https://doi.org/10.1016/0301-9322(81)90040-9).

Tinc, Q, F David, and P Racle (1994). “THYC, un code de thermohydraulique 3D pour les générateurs de vapeur, les échangeurs de chaleur et les condenseurs: développements récents et cas de validation”. In: *Rapport technique, EDF R&D*.

Todreas, Neil E. and Mujid S. Kazimi (2021). *Nuclear Systems I: Thermal Hydraulic Fundamentals*. CRC press.

Tomiyama, Akio (1998). “Struggle with computational bubble dynamics”. In: *Multiphase Science and Technology* 10, pp. 369–405. DOI: [10.1615 / MultScienTechn.v10.i4.40](https://doi.org/10.1615/MultScienTechn.v10.i4.40).

Tomiyama, Akio, Isao Kataoka, Iztok Zun, and Tadashi Sakaguchi (1998). “Drag Coefficients of Single Bubbles under Normal and Micro Gravity Conditions”. In: *JSME International Journal Series B Fluids and Thermal Engineering*. DOI: [10.1299/jsmeb.41.472](https://doi.org/10.1299/jsmeb.41.472).

- Tomiyama, Akio, Hidesada Tamai, Iztok Zun, and Shigeo Hosokawa (2002). “Transverse migration of single bubbles in simple and shear flows”. In: *Chemical Engineering Science* 57, pp. 1849–1858. DOI: [10.1016/S0009-2509\(02\)00085-4](https://doi.org/10.1016/S0009-2509(02)00085-4).
- Tomiyasu, Kunihiro, Tomoyuki Sugiyama, and Toyoshi Fuketa (2007). “Influence of cladding-peripheral hydride on mechanical fuel failure under reactivity-initiated accident conditions”. In: *Journal of Nuclear Science and Technology* 44.5, pp. 733–742.
- Tong, L Sç (1971). *Theoretical analyses of subcooled boiling crisis*. Tech. rep.
- Tong, LS (1968). “Boundary-layer analysis of the flow boiling crisis”. In: *International Journal of Heat and Mass Transfer* 11.7, pp. 1208–1211. DOI: [10.1016/0017-9310\(68\)90037-9](https://doi.org/10.1016/0017-9310(68)90037-9).
- Tryggvason, Grétar, Bernard Bunner, Asghar Esmaeeli, Damir Juric, N Al-Rawahi, W Tauber, J Han, S Nas, and Y-J Jan (2001). “A front-tracking method for the computations of multiphase flow”. In: *Journal of computational physics* 169.2, pp. 708–759. DOI: [10.1006/jcph.2001.6726](https://doi.org/10.1006/jcph.2001.6726).
- Ünal, H.C. (1976). “Maximum bubble diameter, maximum bubble-growth time and bubble-growth rate during the subcooled nucleate flow boiling of water up to 17.7 MN/m²”. In: *International Journal of Heat and Mass Transfer*. DOI: [https://doi.org/10.1016/0017-9310\(76\)90047-8](https://doi.org/10.1016/0017-9310(76)90047-8).
- Ustinenko, V, M Samigulin, A Ioilev, S Lo, A Tentner, A Lychagin, A Razin, V Girin, and Ye Vanyukov (2008). “Validation of CFD-BWR, a new two-phase computational fluid dynamics model for boiling water reactor analysis”. In: *Nuclear Engineering and Design* 238.3, pp. 660–670. DOI: [10.1016/j.nucengdes.2007.02.046](https://doi.org/10.1016/j.nucengdes.2007.02.046).
- Vlček, Daniel and Yohei Sato (2023). “Sensitivity analysis for subcooled flow boiling using Eulerian CFD approach”. In: *Nuclear Engineering and Design* 405, p. 112194. DOI: <https://doi.org/10.1016/j.nucengdes.2023.112194>.
- Wallis, Graham B (1974). “The terminal speed of single drops or bubbles in an infinite medium”. In: *International Journal of Multiphase Flow* 1.4, pp. 491–511. DOI: [10.1016/0301-9322\(74\)90003-2](https://doi.org/10.1016/0301-9322(74)90003-2).
- Weisman, J and BS Pei (1983). “Prediction of critical heat flux in flow boiling at low qualities”. In: *International Journal of Heat and Mass Transfer* 26.10, pp. 1463–1477. DOI: [10.1016/S0017-9310\(83\)80047-7](https://doi.org/10.1016/S0017-9310(83)80047-7).
- Wilcox, David C. (2006). *Turbulence Modeling for CFD*. DCW Industries.
- Wu, Q, S Kim, M Ishii, and SG Beus (1998). “One-group interfacial area transport in vertical bubbly flow”. In: *International Journal of Heat and Mass Transfer* 41.8-9, pp. 1103–1112. DOI: [10.1016/S0017-9310\(97\)00167-1](https://doi.org/10.1016/S0017-9310(97)00167-1).
- Yao, Wei and Christophe Morel (Jan. 2004). “Volumetric interfacial area prediction in upward bubbly two-phase flow”. In: *International Journal of Heat and Mass*

Transfer 47.2, pp. 307–328. DOI: [10.1016/j.ijheatmasstransfer.2003.06.004](https://doi.org/10.1016/j.ijheatmasstransfer.2003.06.004).

Yoon, S.-J., G. Agostinelli, and E. Baglietto (2017). “Assessment of multiphase CFD with zero closure model for boiling water reactor fuel assemblies”. In: *17th International Topical Meeting on Nuclear Reactor Thermal Hydraulics*.

Yuan, C., F. Laurent, and R.O. Fox (Sept. 2012). “An extended quadrature method of moments for population balance equations”. In: *Journal of Aerosol Science* 51, pp. 1–23. DOI: [10.1016/j.jaerosci.2012.04.003](https://doi.org/10.1016/j.jaerosci.2012.04.003).

Zakharova, E. A., B. A. Kol’chugin, A. G. Lobachev, et al. (1984). *In the book: Boiling and condensation. Vol. 8., p. 132*. Publishing house. Rzhsk polytechnic institute Riga.

Zeitoun, O., M. Shoukri, and V. Chatoorgoon (1995). “Interfacial Heat Transfer Between Steam Bubbles and Subcooled Water in Vertical Upward Flow”. In: *J. Heat Transfer* 117.2, pp. 402–407. DOI: <https://doi.org/10.1115/1.2822536>.

Zeitoun, Obida M. (1994). “Subcooled flow boiling and condensation”. PhD thesis. McMaster University.

Zhang, Limiao, Chi Wang, Guanyu Su, Artyom Kossolapov, Gustavo Matana Aguiar, Jee Hyun Seong, Florian Chavagnat, Bren Phillips, Md Mahamudur Rahman, and Matteo Bucci (2022). “A unifying criterion of the boiling crisis”. In: *Nature Communications*. DOI: [doi:10.1038/s41467-023-37899-7](https://doi.org/10.1038/s41467-023-37899-7).

Zhang, Rui, Tenglong Cong, Wenxi Tian, Suizheng Qiu, and Guanghui Su (2015). “Prediction of CHF in vertical heated tubes based on CFD methodology”. In: *Progress in Nuclear Energy* 78, pp. 196–200.

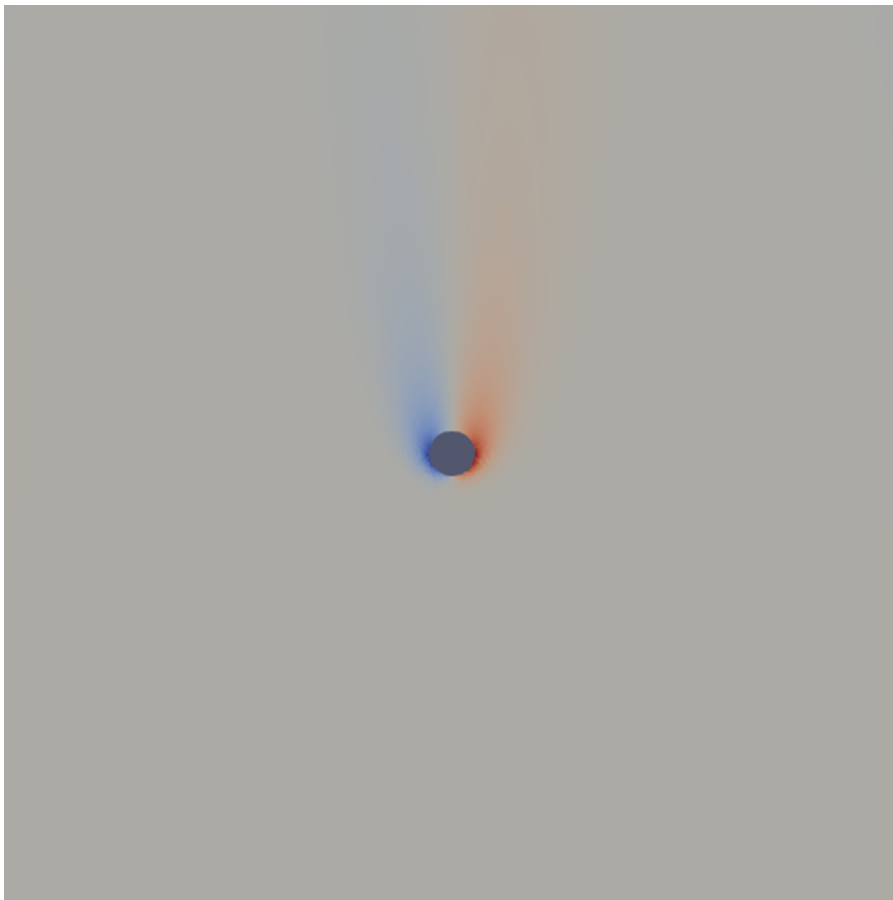
Zuber, N. (1964). “On the dispersed two-phase flow in the laminar flow regime”. In: *Chemical Engineering Science* 19, pp. 897–917. DOI: [10.1016/0009-2509\(64\)85067-3](https://doi.org/10.1016/0009-2509(64)85067-3).

Zuber, Novak (1958). “On the stability of boiling heat transfer”. In: *Transactions of the American Society of Mechanical Engineers* 80.3, pp. 711–714. DOI: [10.1115/1.4012484](https://doi.org/10.1115/1.4012484).

Zuber, Novak and J ASME Findlay (1965). “Average volumetric concentration in two-phase flow systems”. In: *J. Heat Transfer*. 87.4, pp. 453–468. DOI: [10.1115/1.3689137](https://doi.org/10.1115/1.3689137).

Appendix

APPENDIX A



Radial velocity fields in the wake of a 2D bubble.

A

Horizontal flow lift force differs from vertical flow lift force

Seen from a bubble's frame of reference, horizontal and vertical flows have different flow fields around the bubble. The pressure field at the bubble surface will therefore probably be different as well, as will the lift force. However the lift force as defined by standard formulations is the same in both cases.

Using TrioCFD, I run crude 2D simulations of a box with a fixed circular bubble sporting a slip boundary condition. One configuration corresponds to horizontal flow and another to vertical flow, with the same relative velocity and bulk vorticity. I then postprocess the pressure fields to obtain the lift coefficients for 4 different bubble Reynolds numbers. My preliminary results indicate a 20% difference in the lift coefficient for horizontal flow. As the calculation is different from a 3D case, the amplitude of this difference cannot be extrapolated to any real-life situations. However, the existence of a non-negligible difference confirms the relevance of looking at the 3D situation. I then suggest different ways in which this study could go forwards.

Contents

A.1	Introduction	262
A.2	Simulation setup	263
A.3	Results and discussion	265
A.4	Conclusion	267

A.1 Introduction

Formulation of the lift force The general formulation for the lift force from the liquid on a bubble in a Lagrangian framework is (Tomiya et al. 2002; Legendre and Magnaudet 1998):

$$\vec{F}_{\text{lift}} = -C_L \rho_l \alpha_g \frac{\pi d_b^2}{6} (\vec{u}_g - \vec{u}_l) \wedge (\nabla \wedge \vec{u}_l) \quad (\text{A.1})$$

The general formulation for the lift force from the liquid on the bubbles in an Euler-Euler framework is (Hibiki and Ishii 2007; Sugrue 2017):

$$\vec{F}_{\text{lift}} = -C_L \rho_l \alpha_g (\vec{u}_g - \vec{u}_l) \wedge (\nabla \wedge \vec{u}_l) \quad (\text{A.2})$$

Gabillet et al. issue This work stems from attempts to simulate the Gabillet et al. 2002 experiments using two-phase adiabatic CFD. A diagram of the setup is presented in figure A.1. It is made of a horizontal channel in which water flows. This channel is much wider than it is high, so the flow is essentially 2D. A porous medium is located at the bottom of the channel. Air is injected through this media into the channel. The goal of the experiment was to mimic the dynamic effects of flow boiling in a horizontal channel.

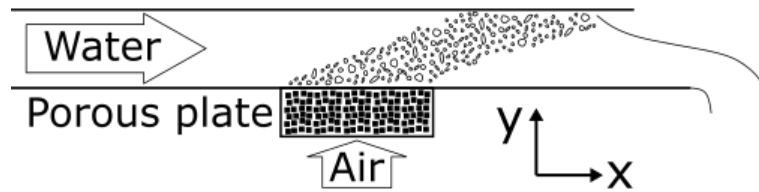


Figure A.1: Diagram of the Gabillet et al. 2002 experiment

Bubbles are formed at the wall, so start out at a zero velocity. They rise and are accelerated to the horizontal velocity of the liquid. As bubbles are injected in the channel and rise, the relative velocity between the gas and the liquid is vertical. According to the classical lift formulations presented above, this results in a horizontal lift force. Taking into account the lift force significantly downgraded the results of early calculations: bubbles had a much too high horizontal velocity.

Flow seen from the bubble To understand where these discrepancies between the effect of the lift force in horizontal and vertical flow come from, the flow is studied in the bubble frame of reference.

Seen from the bubble's frame of reference, the two situations described in figure A.2 have different flow fields. The force applied on the bubble by the liquid depends on the pressure field at the bubble surface. This pressure field will probably be different in these two situations. However, the lift force as defined by standard formulations described above is the same in both cases.

A.2 Simulation setup

I wanted to run fast simulations to obtain an order of magnitude of the impact of changing from horizontal to vertical flow on the lift force.

I run 2D simulations on the geometry presented in figure A.3. The calculation domain is a square box containing a circular bubble. A slip boundary condition is imposed on the bubble surface. An automatic triangular mesher is used to build

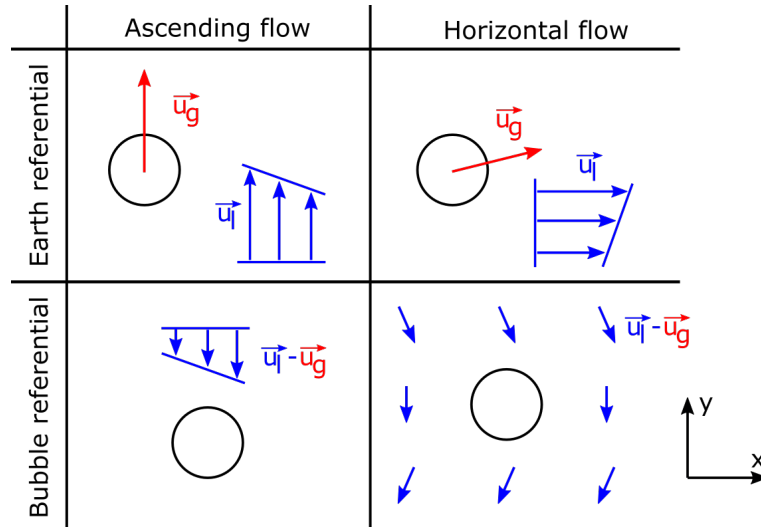


Figure A.2: Flow in the ascending and horizontal situations, seen from the frame of reference of earth and that of the bubble. According to the standard lift force formulations for lagrangian and eulerian frameworks, the lift force in both cases are the same even though the flow field around the bubble is very different.

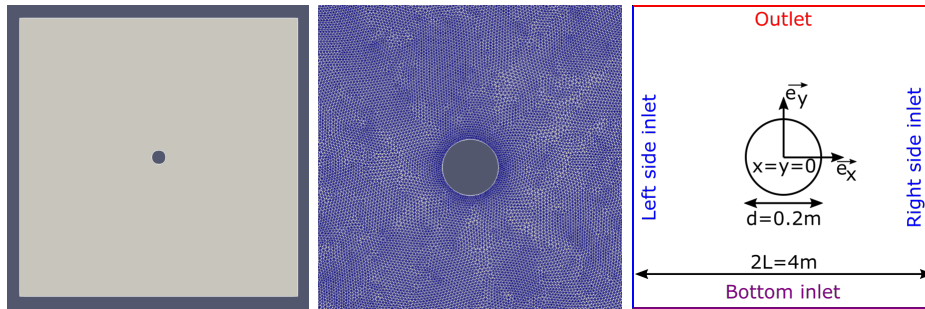


Figure A.3: **Left:** Geometry of the simulated domain. **Center:** close-up view of the mesh near the bubble. **Right:** diagram of the simulated domain (not at scale).

the $\sim 200\,000$ element-mesh. A close-up view is presented in figure A.3. The VEF module of TrioCFD is used to solve the incompressible Navier-Stokes equations.

The top boundary was an imposed-pressure outlet in all simulations. A constant bulk velocity was set at the bottom boundary. Simulations were run with four Reynolds numbers, defined using the bubble diameter and bulk velocity $u = 1$ m/s: $Re = 1, 10, 40, 100$. Re was varied by changing the fluid viscosity. Simulations ran until reaching a steady-state. For each Reynolds number, 3 configurations were simulated (see table A.1). In the no-shear configuration, the boundary condition on the side and bottom walls is a velocity $\vec{u}(x, y) = u\vec{e}_y$. In the ascending configuration, the boundary condition is $\vec{u}(x, y) = (u + \omega x)\vec{e}_y$ where ω is the vorticity of the flow. In the horizontal configuration (which represents the velocity seen in the bubble frame of reference in horizontal liquid flow), the boundary condition is $\vec{u}(x, y) = u\vec{e}_y - \omega y\vec{e}_x$ where for a given Reynolds ω is the same as in the ascending configuration. ω was chosen such that for a box width $2L$, $\omega L = 0.1 \cdot u$, i.e.

$\omega = 0.05 \text{ s}^{-1}$ with $L = 2 \text{ m}$.

Configuration	No-shear	Ascending	horizontal
Bottom velocity	$u\vec{e}_y$	$u + \omega x\vec{e}_y$	$u\vec{e}_y + \omega L\vec{e}_x$
Side velocity	$u\vec{e}_y$	$u \pm \omega L\vec{e}_y$	$u\vec{e}_y - \omega y\vec{e}_x$

Table A.1: 3 calculation configurations ran in this study: the boundary condition changes.

For each simulation, the pressure field at the bubble surface is extracted from the code. This field is then integrated to obtain the forces on the bubble along the horizontal and vertical axis, i.e. lift and drag force.

A.3 Results and discussion

Results Simulated velocity fields in the 3 configurations at $Re=10$ are presented in figure A.4. As expected, one can see that in the ascending case, the y-velocity is lower to the left of the bubble and that in the horizontal case it is larger underneath the bubble.

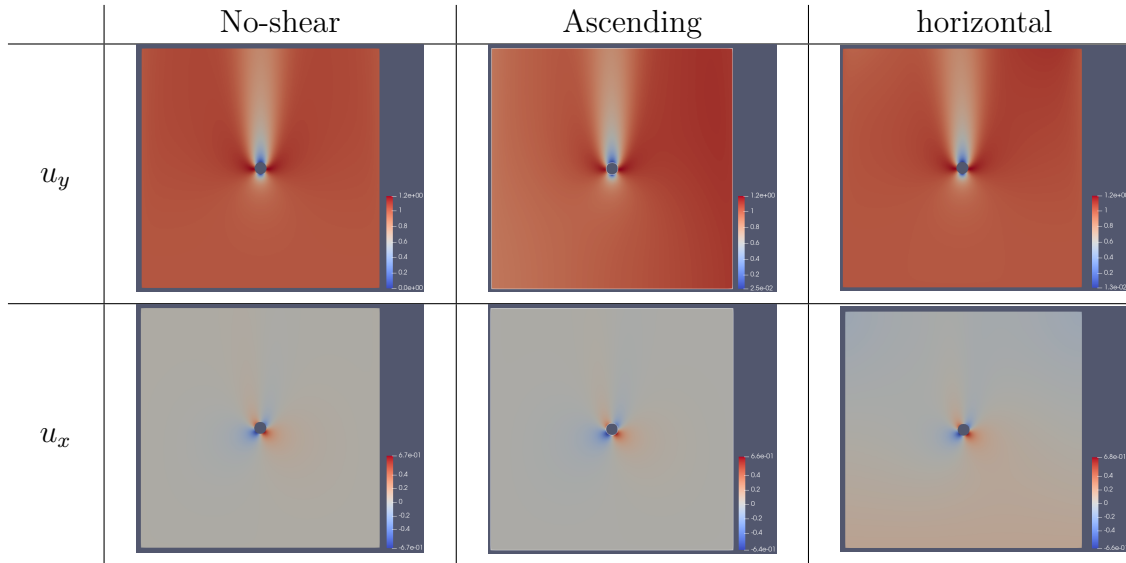


Figure A.4: Simulated velocity fields for the 3 simulation configurations at $Re=10$. y is the vertical axis and x the horizontal axis. The scales are to the right of the simulated boxes.

Figure A.5 shows the vorticity fields as a function of the angle around the bubble far from the bubbles for all 4 Reynolds numbers. The plots of the raw value of the vorticity show that the bubble influences the vorticity, even at a distance of 20 times the bubble radius. Therefore, no-shear vorticity is subtracted to obtain the vorticity induced by the boundary conditions. This shows that the vorticity remains close to the target value of 0.05s^{-1} on all plots.

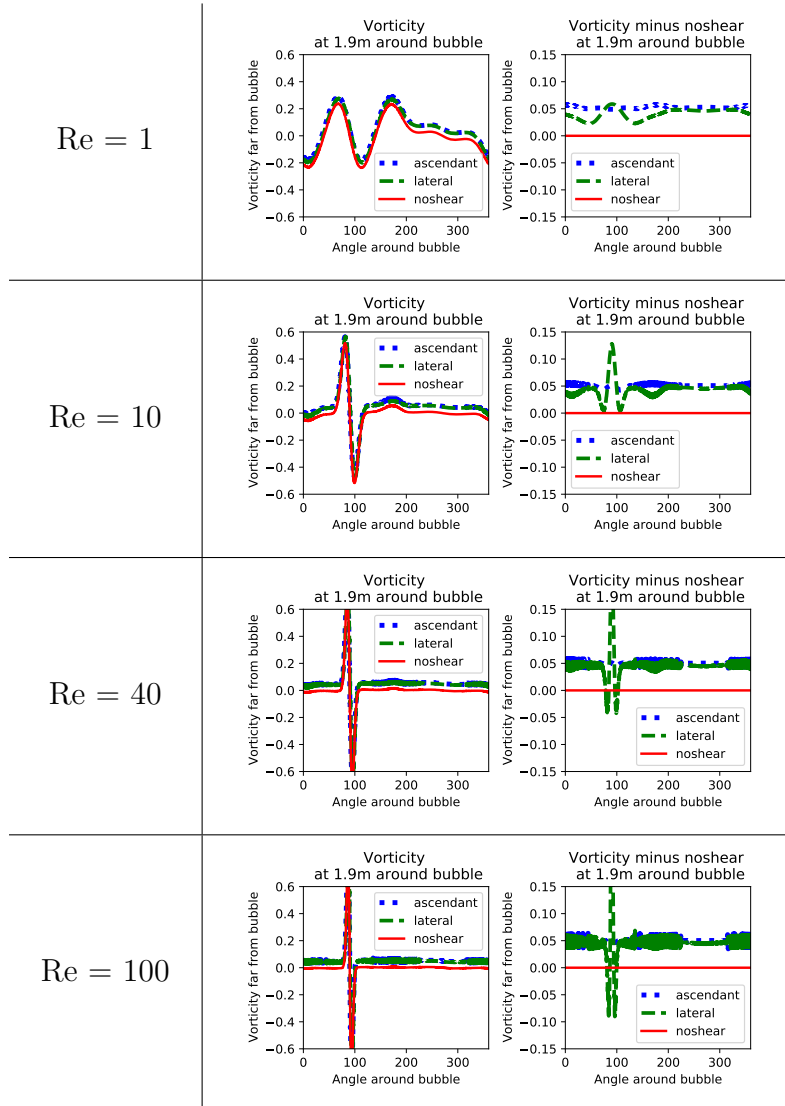


Figure A.5: Vorticity fields along a circle or radius $R = 1.9 \text{ m} = 0.95L$ around the bubbles, for each Reynolds number in each of the 3 configurations. Angle= 0° is along the x-axis. Angle= 90° is in the bubble wake, along the y-axis. **Plots on the left:** raw value of the vorticity. One can see that the bubble influences the vorticity, even at a distance of 20 times the bubble radius. **Plots on the right:** vorticity from which the no-shear vorticity was retracted. One can see that the vorticity remains close to the target value of 0.05s^{-1} on all plots, except in the bubble wake.

The pressure field around the bubble is then used to obtain the lift and drag coefficients in all configurations. These results are shown in figure A.6.

Discussion Concerning the drag coefficient, no standard case was available to compare these results (a cylinder with a slip boundary). However, they are in the same ballpark as no-slip sphere at similar Reynolds.

The vorticity varies more than I would like in the far-field flow, even when it is

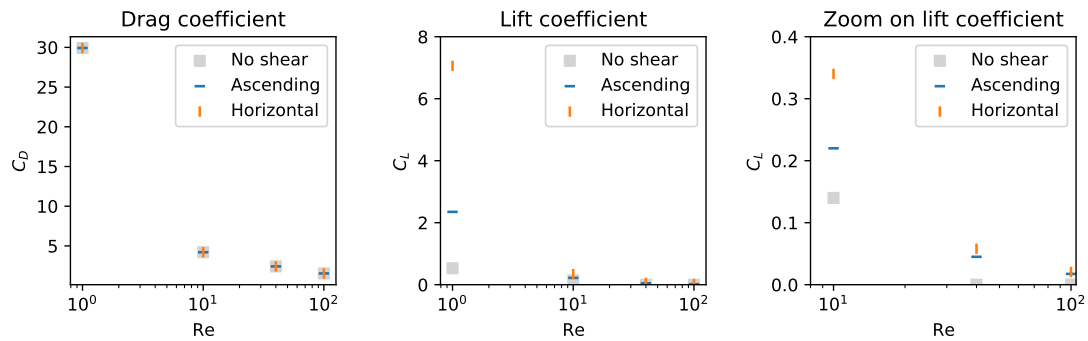


Figure A.6: Drag and lift coefficients obtained for different configurations for the 4 Reynolds numbers.

corrected by no shear results. I already greatly increased the size of the calculation domain compared with earlier simulations. To reduce this effect, one could keep increasing the size of the domain or use a different computation domain, with a similar method as Legendre and Magnaudet 1998.

The lift coefficient is non-zero for the no shear case at $Re=1$ and $Re=10$. This means that the boundary conditions were ill-chosen, or that the mesh was not refined enough. The results obtained with these Reynolds numbers will not be used to interpret the data.

For $Re=40$ and $Re=100$, there is a difference $\sim 20\%$ in the ascending and horizontal lift coefficients. This difference is non-negligible. It would be interesting to see if it holds up with less crude simulations and/or at higher Reynolds numbers.

A.4 Conclusion

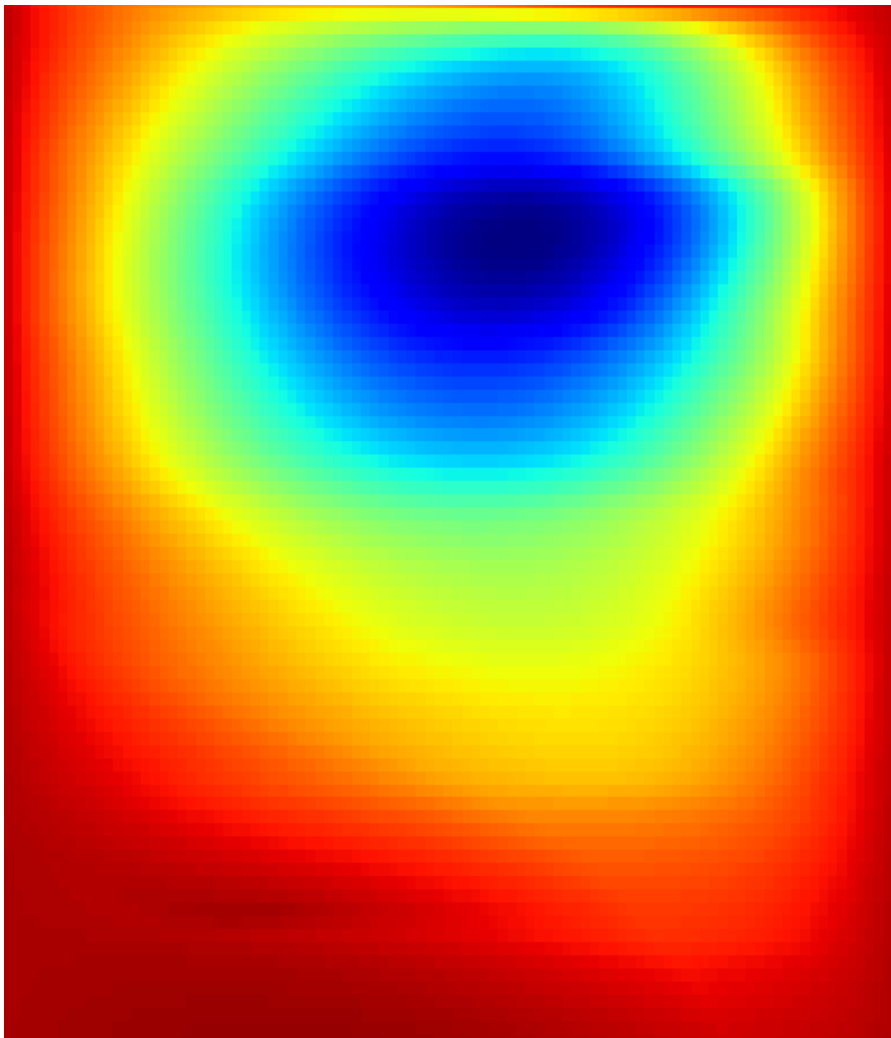
Next steps on this topic In order to improve our understanding on the effect of the angle between the relative velocity of the bubble and liquid and the liquid flow, the following steps could be taken. As this is not the topic of my PhD, I will not run such simulations or take part in such work. The following steps could nevertheless be carried out:

- **Sensitivity to simulation conditions:** I have not tested the sensitivity of the results to the simulation conditions, in particular the box size. This would be an important step in the verification process.
- **3D simulation:** The quick simulations I have ran are 2D, the results are sure to change in 3D.
- **Deformable bubbles:** Bubble deformation is a key contributor to the lift force (Legendre and Magnaudet 1998). Furthermore, an elongated bubble will be positioned differently compared to the flow for ascendant and horizontal cases: the change in lift coefficient could be greater at low surface tensions.

- **Continuum of the angle of the relative velocity:** Pipes can be set at any angle between a horizontal and vertical position. It may be possible to combine results on horizontal and vertical flow to obtain the lift force at a 45° angle for example.
- **Freely moving bubbles:** The IJK module of the TrioCFD software enables us to run front-tracking simulations on single bubbles or bubble swarms in various flow configurations (Cluzeau 2019). This could be taken advantage of this to study the coupled effect of bubble movement and the angle of the liquid flow relative to gravity.

Conclusion These crude simulations were intended as a proof of concept to see if more work on this topic could be interesting. I have shown that in these preliminary 2D calculations, there can be a difference in the lift coefficient on a bubble between a horizontal and a vertical flow. I believe this subject to be interesting both from a fundamental point of view (how the lift force depends on vorticity) and a practical one (boiling in horizontal or inclined flows).

APPENDIX B



Radial mixture velocity colormap on test tube G2P26W16 of the DEBORA database.

B

Reconstruction of velocity and temperature profiles in DEBORA

The instrumentation on the DEBORA database presented in section 4.2 makes it possible to obtain experimental void fractions, liquid temperatures, gas velocities and bubble Sauter mean diameters. In this section, I aim to obtain information on more physical quantities in the DEBORA experiment. To this end, I choose to focus on test tubes G2P14W16, G2P26W16 and G3P26W23, as they are presented in Garnier et al. 2001 and are the most often used in the literature.

Contents

B.1	Experimental data interpolation on a test tube	270
B.2	Axial velocity approximation	271
B.3	Radial mixture integration	273
B.4	Liquid temperature determination	274
B.5	Vapor and liquid radial velocity determination	275

B.1 Experimental data interpolation on a test tube

The bubble Sauter mean diameters and void fraction data for a given test tube depend on the radial position in the tube and on the inlet temperature. I begin by using the test tube hypothesis to express the void fraction and Sauter mean diameter measurements as functions of a radial and axial position in the test tube with the highest inlet temperature.

The data is interpolated as a function of (r, z) coordinates on the test tube. The interpolation yields the different physical quantities at 100 radial and axial points, located between $r = 0$ mm and $r = 9.6$ mm and between $z = 1$ m and $z = 3.5$ m, where $z = 0$ m is at the inlet of the heated section. To obtain a physically coherent behavior at altitudes where the void fraction is insufficient for an experimental

measure, $\alpha_v = 0$ is enforced. For the bubble diameter, the maximum diameter measurements at that same altitude is enforced: $d_b = d_{b,\max}(z)$.

Figures B.1 and B.2 presents a comparison between the interpolated and experimental values of void fraction and Sauter mean diameter as well as (r, z) colormaps for these tests.

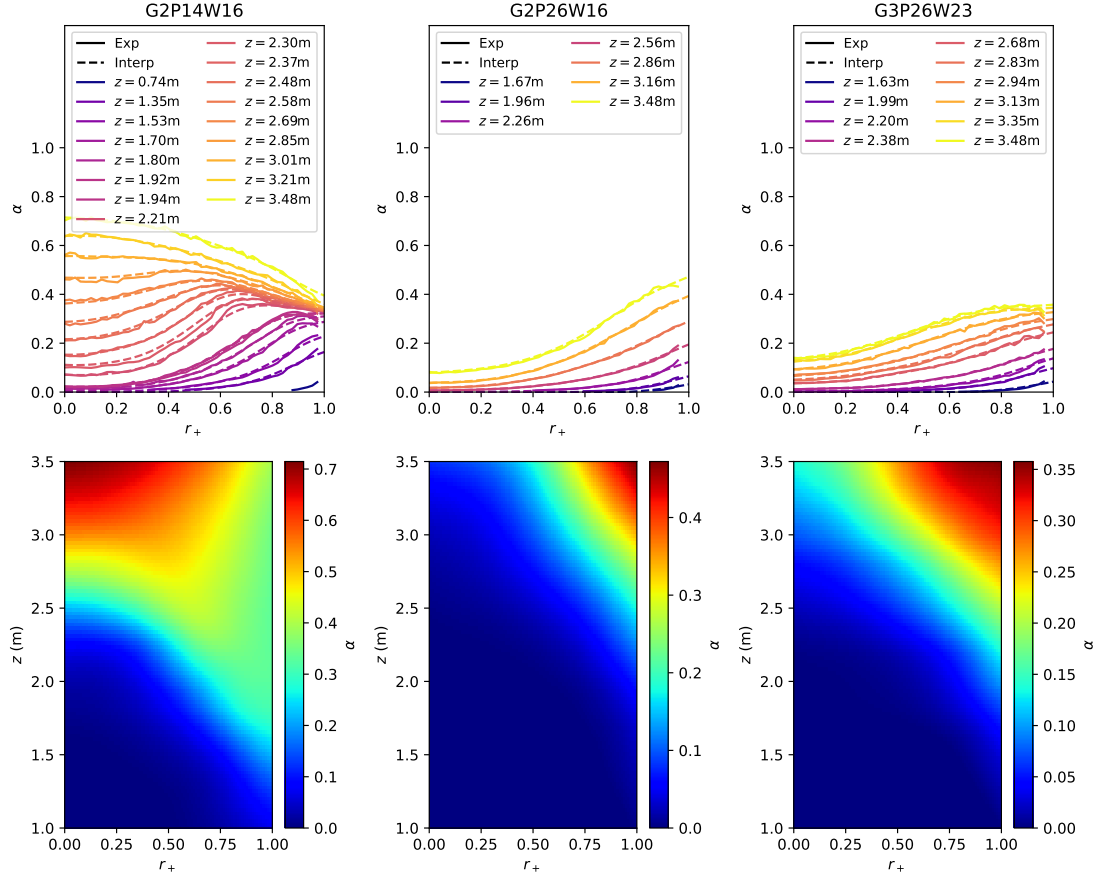


Figure B.1: Top row: comparison between the interpolated and experimental values of void fraction for 3 DEBORA test tubes. The experimental conditions are given in table 4.2. Bottom row: (r, z) colormap for these test tubes.

B.2 Axial velocity approximation

The mixture velocity is defined as:

$$\vec{u}_m = \frac{\alpha_v \rho_v \vec{u}_v + \alpha_l \rho_l \vec{u}_l}{\alpha_v \rho_v + \alpha_l \rho_l} \quad (\text{B.1})$$

The methodology developed by Gueguen 2013 and Kledy et al. 2021 is used to obtain approximated mixture axial velocity fields. Here, R is the pipe radius. For each interpolation altitude along the test tube, the steps of this methodology are the following:

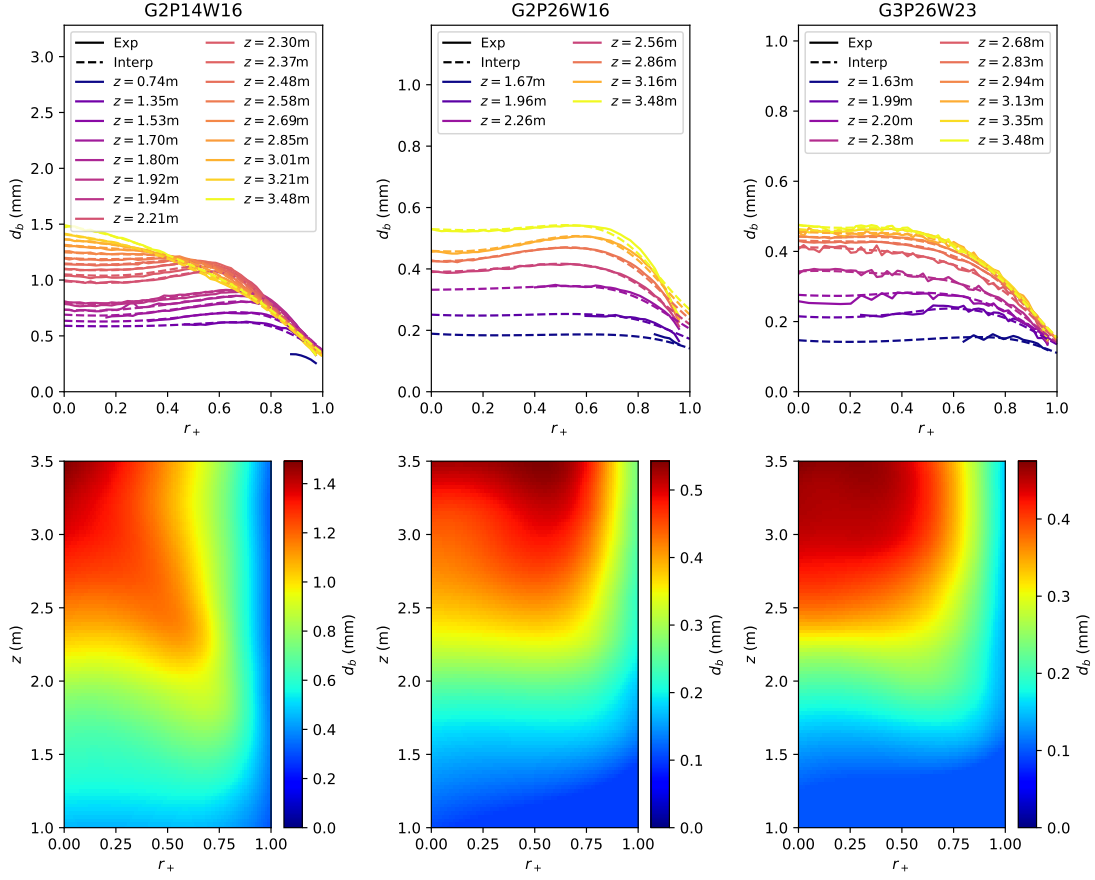


Figure B.2: Top row: comparison between the interpolated and experimental values of Sauter mean diameter for 3 DEBORA test tubes. The experimental conditions are given in table 4.2. Bottom row: (r, z) colormap for these test tubes.

1. Calculate the friction velocity u_τ using the McAdams et al. 1942 correlation:

$$u_\tau = u_{\text{bulk}}(0.316Re^{-0.25}/8)^{1/2} \quad (\text{B.2})$$

2. Calculate the radial profile of the turbulent diffusivity using the Reichardt 1951 correlation:

$$\nu_t(r) = \frac{0.41Ru_\tau}{6} \cdot \left(1 - \left(\frac{r}{R}\right)^2\right) \cdot \left(1 + 2\left(\frac{r}{R}\right)^2\right) \quad (\text{B.3})$$

3. Calculate the total local viscosity:

$$\mu_{\text{tot}}(r) = \rho_m \nu_t + \mu_l = (\alpha_v \rho_v + \alpha_l \rho_l) \nu_t + \mu_l \quad (\text{B.4})$$

4. Integrate the stationary axial velocity profile along r using $u_{mz} = 0$ at the wall as a boundary condition:

$$\partial_r u_{mz}(r) = \frac{1}{\mu_{\text{tot}}(r)} \left(\frac{-r \rho_l u_\tau^2}{R} \right) \quad (\text{B.5})$$

A comparison between the calculated mixture velocity and the experimental double optical probe measurements for the tests for which they are available is presented in figure B.3. The difference is significant for test tube G2P14W16, but reasonable for the others. As expected, vapor velocities are larger than the mixture velocities as bubbles rise faster than the liquid. A clear acceleration of the flow due to vapor formation and mass conservation can be seen.

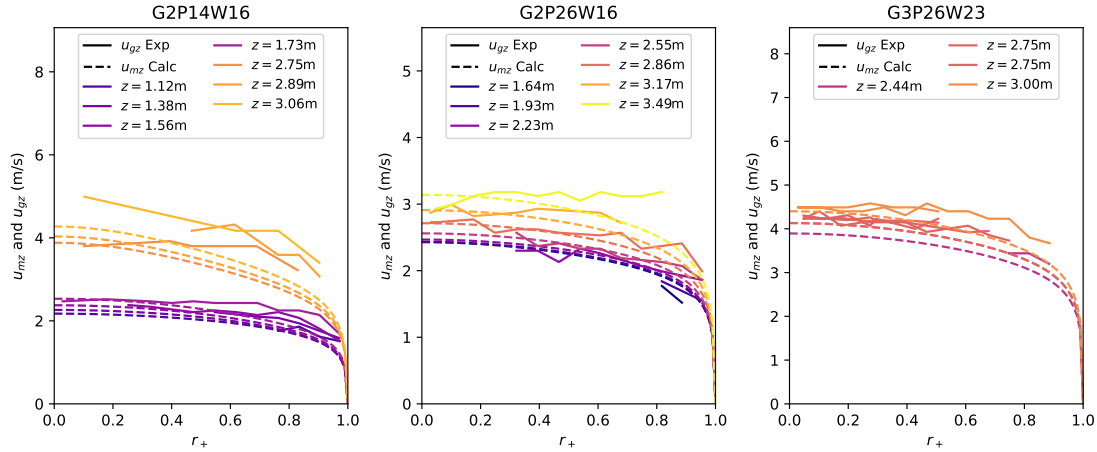


Figure B.3: Comparison between the axial mixture velocity integrated from the void fraction profiles and the experimental values of vapor velocity measured with double optical probes for 3 DEBORA test tubes. The experimental conditions are given in table 4.2.

In the remainder of this section, the axial mixture velocity is used as an approached axial vapor and liquid velocity. This is possible as the relative velocity expected in the conditions of the DEBORA conditions is ~ 0.1 m/s, well underneath the ~ 1 m/s bulk velocities.

B.3 Radial mixture integration

The mixture mass balance in cylindrical coordinates reads:

$$\partial_z(\rho_m u_{mz}) + \frac{1}{r} \partial_r(r \rho_m u_{mr}) = 0 \quad (\text{B.6})$$

As the void fraction distribution was interpolated and approached axial mixture velocity determined, this equation can be integrated to determine the mixture radial velocity, using $u_{rm} = 0$ at the center of the channel as a boundary condition. The results obtained are presented in figure B.4.

The important number of hypotheses made coming up to this point transpire in the colormaps, that are not as smooth as one could have hoped. Nevertheless, two regions can be identified on these figures. For low z , the mixture radial velocity is negative: vapor is forming at the wall and pushing the liquid towards the center of the channel. For higher z , vapor is going towards the center and liquid is pulled

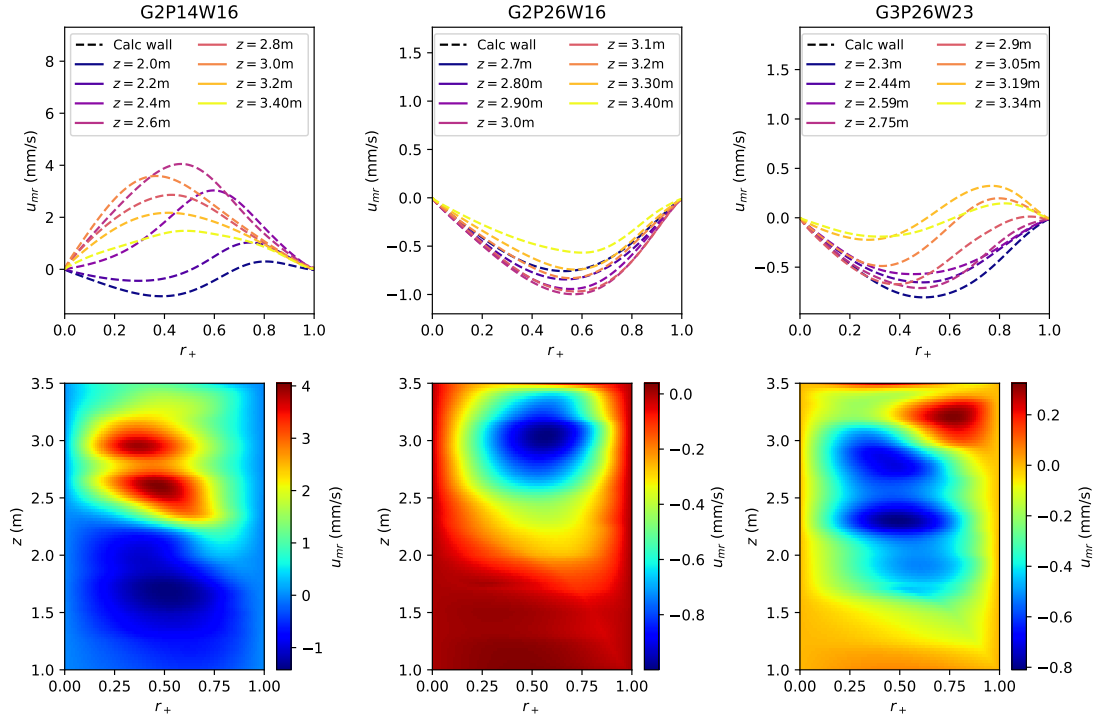


Figure B.4: Top row: integrated radial mixture velocity at various altitudes for 3 DEBORA test tubes. The experimental conditions are given in table 4.2. Bottom row: (r, z) colormap for these test tubes.

towards the wall of the channel. As liquid has a much larger density the mixture velocity is positive.

B.4 Liquid temperature determination

In this section, the liquid temperature fields in the complete test tubes is approached. Through a simple heat balance and assuming that the vapor is at saturation temperature, the total enthalpy flux on the pipe cross-section at a distance z from the inlet of the heated section is:

$$\begin{aligned}\Phi_{\text{tot}} &= G \cdot h_l(T_{\text{in}})\pi R^2 + 2\pi R z q_w \\ &= \int_{r=0}^R (\alpha_v(r)\rho_v h_{vs} u_{vz}(r) + \alpha_l \rho_l h_l(Tl(r))u_{lz}) \cdot dr\end{aligned}\quad (\text{B.7})$$

As experimental void fraction profiles and an approached axial mixture velocity that will be used as the axial vapor and liquid velocities are available, the only unknown term in this equation is the radial liquid temperature profile. However, as seen in equation 4.6 section 4.3), the liquid temperature follows a log-law in flow boiling. Therefore, the only unknown in this equation is the dimensionless liquid temperature parameter β .

A dichotomic algorithm is used to determine β at each interpolation altitude along the test tube. The axial profiles of β can be found in figure B.5. $\beta(z)$ decreases

linearly near the entrance of the tube, then the slope decreases slightly as boiling begins. Thermal energy is being stored in the vapor phase, which slows the liquid phase heating. The places along the tube where β is not plotted correspond to the altitude at which all of the liquid must be considered at saturation temperature for the energy balance to be respected. β is then no longer a relevant parameter.

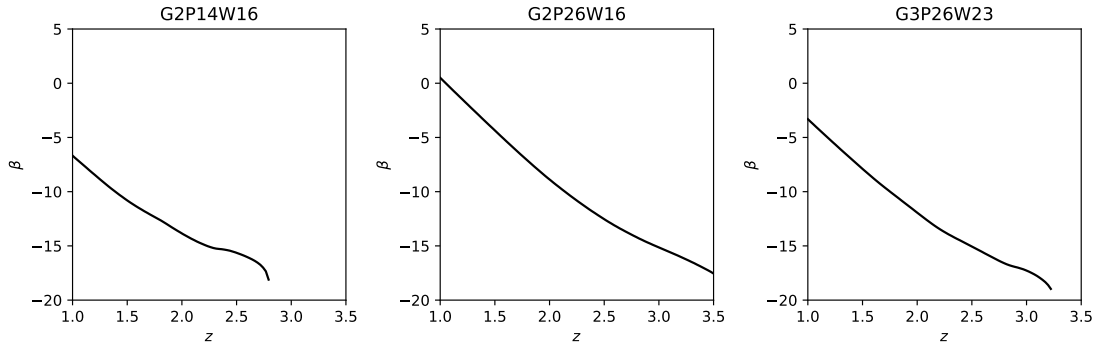


Figure B.5: Evolution of the boiling-flow thermal radial log-law parameter β as a function of the axial position in the test tube (see equation 4.6 for the definition of β). The experimental conditions are given in table 4.2.

The liquid temperature profiles obtained in this way are compared to the DEBORA experimental liquid temperature profiles in figure B.6, along with liquid temperature colormaps. The interpolated values are extremely close to experimental results, which comforts the use of this methodology.

B.5 Vapor and liquid radial velocity determination

The reason why the vapor or liquid mass balance equations cannot be used to integrate the radial velocities like the mixture mass equation is the presence of the phase change source term:

$$\nabla \cdot (\alpha_k \rho_k \vec{u}_k) = \sum_{m \neq k} \Gamma_{km} \quad (\text{B.8})$$

However, this term is zero in the region of the flow where the liquid temperature is at saturation. The vapor and liquid velocities are therefore integrated in the regions of the flow where the liquid is at saturation according to the energy balance.

The equation that is integrated is then:

$$\partial_z (\alpha_k \rho_k \vec{u}_{mz}) + \frac{1}{r} \partial_r (r \alpha_k \rho_k \vec{u}_{kr}) = 0 \quad (\text{B.9})$$

Two different boundary conditions can be selected to integrate these equations:

- At the center of the channel, the radial velocities are zero

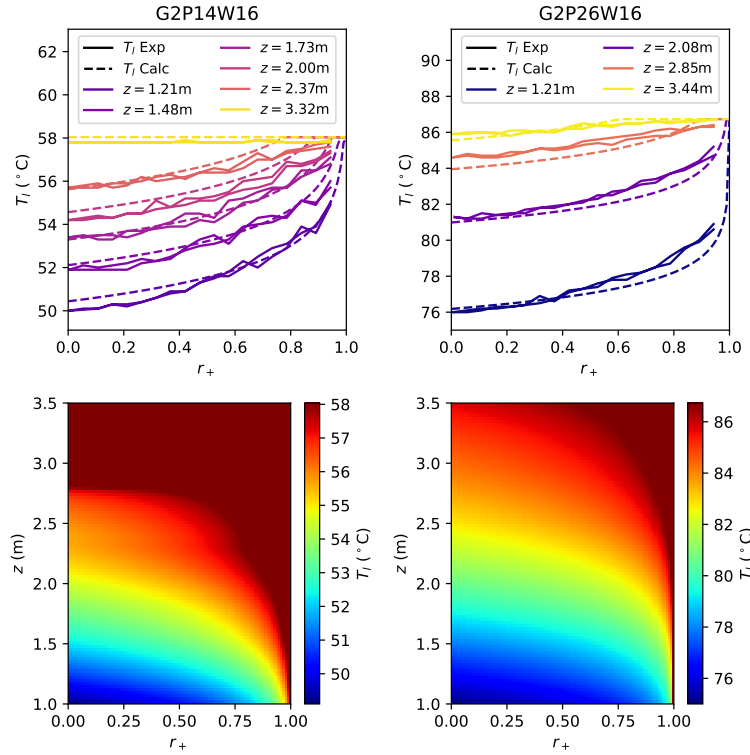


Figure B.6: **Top row:** comparison between experimental and calculated liquid temperatures at various altitudes for 2 DEBORA test tubes. The experimental conditions are given in table 4.2. **Bottom row:** (r, z) colormap for these test tubes.

- In the near wall region, as the flow is saturated, all of the wall heat flux is used for evaporation. The vapor mass production is then:

$$\Gamma_{w,lv} = \frac{q_w}{h_{vl}} \quad (\text{B.10})$$

Equation B.9 can be integrated from the center of the channel only in conditions where the liquid is at saturation on the width of the flow, but it can always be integrated from the wall. One of the issues encountered in the integration from the wall is that, due to the $1/r$ term in equation B.9, the solution diverges in the center of the channel. Therefore the wall-integrated solutions are cut off at $r_+ = 0.3$. The integrated vapor radial velocities obtained are presented in figure B.7, and the radial liquid velocities in figure B.8.

Both vapor velocity interpolations do not overlap in a satisfying way. This is certainly due to the real axial vapor velocity profile being different from the calculated axial mixture velocity. If high-quality vapor velocity measurements were available on the DEBORA database or on another, this methodology could be repeated using directly an interpolation of the experimental velocities. The difference in the two integration methods yields an approximate uncertainty on the radial velocity, which I will consider to be $\pm 50\%$.

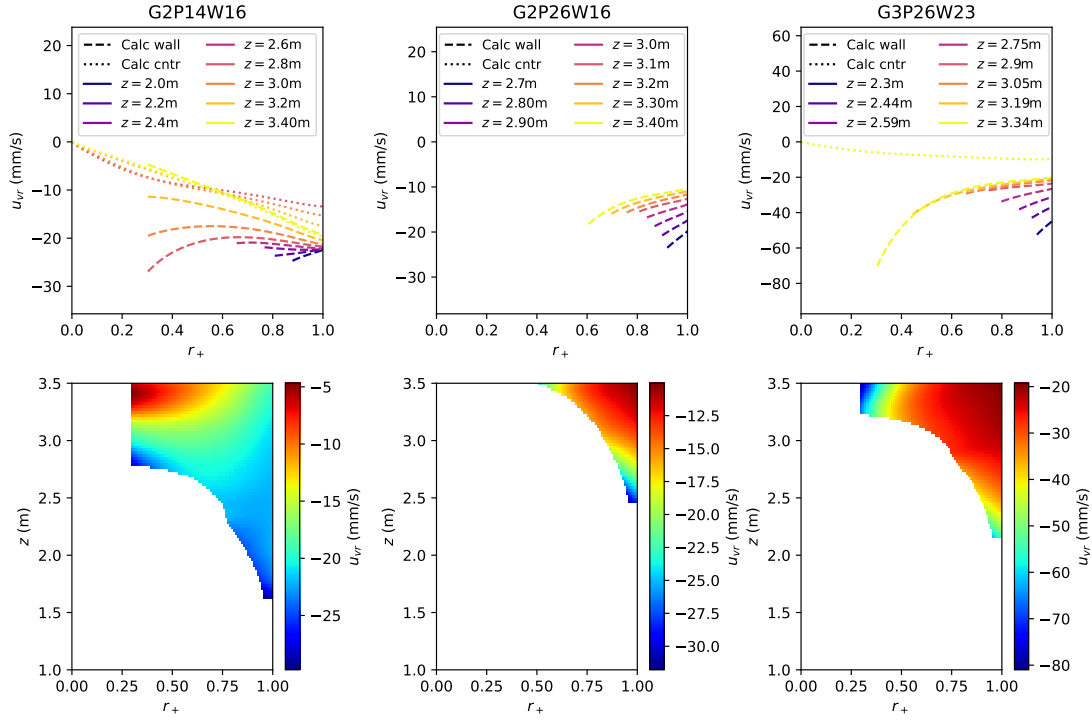


Figure B.7: **Top row:** calculated radial vapor velocity at various altitudes for 3 DEBOR test tubes. The experimental conditions are given in table 4.2. **Bottom row:** (r_+, z) colormap for these test tubes.

Nevertheless, the information obtained on the radial vapor velocities is interesting. At low void fractions the vapor accelerates as it moves away from the wall. This is coherent with a liquid turbulence-driven dispersion, as the turbulent viscosity increases far from the wall. The radial velocities are almost independent of r_+ for higher void fractions between $r_+ \simeq 0.4$ and $r_+ = 1$, apart for case G2P14W16.

The radial liquid velocities are much smaller than the vapor velocities, apart from the near-wall region. The differences between the integration from the center and the wall are smaller, perhaps suggesting that the liquid velocity profile is closer to the calculated axial mixture velocity. The liquid velocities are positive in the near-wall region, as liquid goes in the opposite direction as vapor, and can be negative for small r_+ as liquid is pushed away from the wall by the boiling.

I use these interpolated velocities in comparisons with two-fluid simulations in chapters 5 and 8.

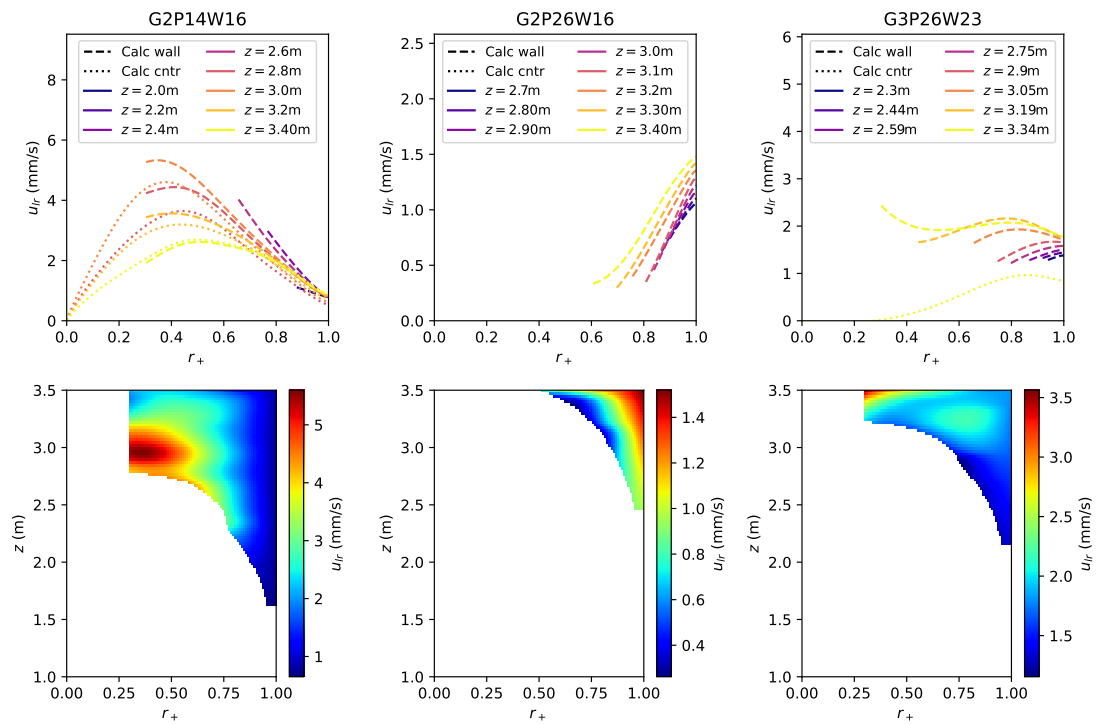


Figure B.8: Top row: calculated radial liquid velocity at various altitudes for 3 DEBORA test tubes. The experimental conditions are given in table 4.2. Bottom row: (r, z) colormap for these test tubes.

APPENDIX C



DNS of bubble breakup in turbulent flow from Riviere et al. 2021.

C

Analysis of bubble coalescence and breakup in DEBORA

This appendix presents results from the integration of the coalescence-fragmentation term on the DEBORA database. I then compare this integration to results from the literature and propose my own formulation. Many results from appendix B are used here.

Contents

C.1	Different frameworks to determine bubble diameter distributions	280
C.2	Coalescence-breakup term determination	281
C.3	Coalescence and breakup formulations from the literature . . .	282
C.4	A simple return-to-equilibrium proposal	286

C.1 Different frameworks to determine bubble diameter distributions

Various frameworks have been proposed in the literature to determine bubble diameters and bubble diameter distributions. The all include one or multiple transport equations, that can be of different types:

- One-group interfacial area transport equation (IATE): in this framework, bubbles are assumed to be monodisperse. The interfacial area of a given phase is the transported variable, and the bubble Sauter mean diameters calculated as:

$$d_b = \frac{6\alpha_g}{a_i} \tag{C.1}$$

The Yao and Morel 2004 and Hibiki and Ishii 2000a models are examples of this.

- Two-group interfacial area transport equation: Hibiki and Ishii 2000b proposed this framework where the vapor phase is split in two groups that have

mass, momentum and energy conservation equations solved separately. One group is made of small, spherical bubbles. The second contains larger deformable, non-spherical bubbles. A variety of coalescence and breakup mechanisms occur inside each group and between each group.

- Moment density transport: Kamp et al. 2001 proposed a model in which the moment densities of the bubble diameters are transported. The 0 moment is the bubble concentration and the 2 moment is proportional to the interfacial area.
- Population balance models: the works of Krepper et al. 2008 and Yuan et al. 2012 are part of this family of models. In this framework, the dispersed phase is divided into various population groups. Each group corresponds to a certain bubble diameter. The populations of each group are transported separately. Coalescence, breakup and coalescence change the population of the different groups.

Each framework includes coalescence and breakup formulations. In this section, I extend the integration methodology presented in appendix B to coalescence and breakup terms. The coalescence-breakup term in the DEBORA database are inferred from the experimental data in a one-equation interfacial area transport equation framework. Various formulations found in the literature are presented and their predictions compared with the inferred values. A simple return-to-equilibrium model that improves predictions is proposed.

C.2 Coalescence-breakup term determination

After the Sauter mean diameters were determined, the original dwell time distribution was lost. This data therefore cannot be used to infer the bubble size distributions for comparisons with population balance models Krepper et al. 2008; Yuan et al. 2012. In order to investigate these phenomena, the Yao and Morel 2004 interfacial area transport equation, which considers the bubble size distribution to be monodisperse, is used as a reference. It yields:

$$\begin{aligned}
 \partial_t a_i + \nabla \cdot (\vec{u}_v a_i) &= \frac{2}{3} \frac{a_i}{\alpha} \left(\frac{\Gamma_{vl}}{\rho_v} - \frac{\alpha_v}{\rho_v} \partial_t \rho_v \right) + \frac{36\pi}{3} \left(\frac{\alpha}{a_i} \right)^2 (\phi_{\text{coal}} + \phi_{\text{bkup}}) \\
 &= \frac{2}{3} \frac{a_i}{\alpha} \left(\frac{\Gamma_{vl}}{\rho_v} - \frac{\alpha_v}{\rho_v} \partial_t \rho_v \right) + \Phi_{\text{coal}} + \Phi_{\text{bkup}} \\
 &= \frac{2}{3} \frac{a_i}{\alpha} \left(\frac{\Gamma_{vl}}{\rho_v} - \frac{\alpha_v}{\rho_v} \partial_t \rho_v \right) + \Phi_{\text{coal-bkup}}
 \end{aligned}
 \tag{C.2}$$

As for the integration of the radial vapor velocities, in the regions where the liquid is at saturation temperature there is no condensation. The only unknown quantities in equation C.2 are the coalescence and breakup terms. In this section, I will consider them together, and integrate the coalescence-breakup $\Phi_{\text{coal-bkup}}$ term on the saturated domain. A colormap of this integration is presented in figure C.1.

$\Phi_{\text{coal-bkup}}$ is negative on almost all of the domain, which means that coalescence is much more present than breakup, as the former reduces the interfacial area and the latter increases it.

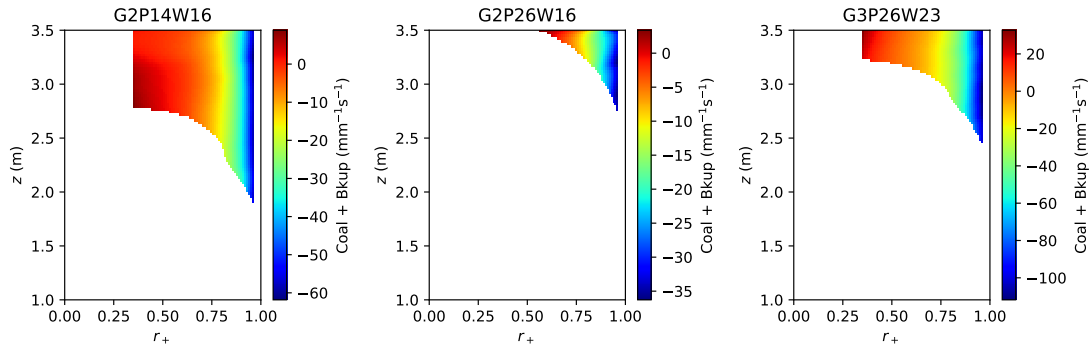


Figure C.1: (r, z) calculated (coal+breakup) term colormap for 3 DEBORA test tubes. The experimental conditions are given in table 4.2.

These integrated terms will now be compared to formulations from the literature.

C.3 Coalescence and breakup formulations from the literature

Five coalescence and fragmentation pairings proposed in the literature were selected for this analysis:

- Prince and Blanch 1990 coalescence and Luo and Svendsen 1996 breakup, used among others by Krepper et al. 2008.
- Yao and Morel 2004
- Ruyer and Seiler 2009
- Wu et al. 1998
- Hibiki and Ishii 2000a

In order to compare each effectively, these proposed terms are put into the IATE framework of equation C.2. In most of these formulations, the rate of dissipation of turbulent kinetic energy ϵ and the turbulent Weber number $We = \frac{\rho_l d_b^{5/3} \epsilon^{2/3}}{\sigma}$ play a part. All authors use a similar theoretical analysis. The coalescence term is taken as the product of bubble collision frequency by the coalescence probability. The breakup term is the frequency of bubble collisions with turbulent eddies by the breakup probability.

Prince & Blanch and Luo & Svendsen The Prince and Blanch 1990 coalescence is often used in population balance models Krepper et al. 2009 with the Luo

and Svendsen 1996 breakup. The Prince and Blanch 1990 turbulence-driven coalescence rate is:

$$\phi_{\text{coal, PB}} = -C_c \pi 2^{7/3} d_b^2 (\epsilon d_b)^{1/3} n^2 \exp\left(-0.14 \log\left(\frac{h_0}{h_f}\right) \sqrt{We}\right) \quad (\text{C.3})$$

Where $C_c = 0.356$, $h_0 = 10^{-4}\text{m}$ and $h_f = 10^{-4}\text{m}$ are the initial and final film thickness when two bubbles coalesce. The bubble number density n is related to the other terms by:

$$n = \frac{6\alpha_v}{\pi d_b^3} \quad (\text{C.4})$$

The Luo and Svendsen 1996 breakup reads:

$$\begin{aligned} \phi_{\text{bkup, LS}} &= C_b (1 - \alpha_v) \frac{\epsilon^{1/3}}{d_b^{2/3}} n \int_{\xi_{\min}}^1 \frac{(1+\xi)^2}{\xi^{11/3}} \exp\left(-\frac{b}{\xi^{11/3}}\right) d\xi \\ &= C_b (1 - \alpha_v) \frac{\epsilon^{1/3}}{d_b^{2/3}} n \frac{3}{11b^{8/11}} \left[\Gamma(8/11, b) - \Gamma(8/11, t_{\min}) \right] \\ &\quad + 2b^{3/11} \left[\Gamma(5/11, b) - \Gamma(5/11, t_{\min}) \right] \\ &\quad + b^{6/11} \left[\Gamma(2/11, b) - \Gamma(2/11, t_{\min}) \right] \\ b &= \frac{12c_f \sigma}{\beta \rho_l \epsilon^{2/3} d_b^{5/3}} \\ \xi_{\min} &= \frac{\lambda_{\min}}{d_b} \\ \lambda_{\min} &= C_2 \left(\frac{\nu_l}{\epsilon}\right)^{1/4} \\ t_{\min} &= b \xi_{\min}^{-11/3} \end{aligned} \quad (\text{C.5})$$

Where $C_b = 0.923$, $c_f = 2^{1/3} - 1 = 0.26$, $\beta = 2.05$, $C_2 = 11.4$ and $\Gamma(x, y)$ the lower incomplete Gamma function.

The coalescence-breakup adapted to an IATE is then:

$$\begin{aligned} \Phi_{\text{coal-bkup, PBLs}} &= a_i \frac{\epsilon^{1/3}}{d_b^{2/3}} \left(-\alpha_v \frac{2^{10/3}}{3} C_c \exp\left(-0.14 \log\left(\frac{h_0}{h_f}\right) \sqrt{We}\right) \right. \\ &\quad + \frac{1}{3} C_b (1 - \alpha_v) \frac{3}{11b^{8/11}} \left[\Gamma(8/11, b) - \Gamma(8/11, t_{\min}) \right] \\ &\quad + 2b^{3/11} \left[\Gamma(5/11, b) - \Gamma(5/11, t_{\min}) \right] \\ &\quad \left. + b^{6/11} \left[\Gamma(2/11, b) - \Gamma(2/11, t_{\min}) \right] \right) \end{aligned} \quad (\text{C.6})$$

Yao & Morel Yao and Morel 2004 propose a classical monodisperse interfacial area formulation. The coalescence and fragmentation models were originally written in a bubble number density form. Their coalescence model is:

$$\phi_{\text{coal, YM}} = -K_{c1} \frac{\epsilon^{1/3} \alpha_v^2}{d_b^{11/3}} \frac{1}{g(\alpha_v) + K_{c2} \alpha_v \sqrt{We/We_{cr}}} \cdot \exp\left(-K_{c3} \sqrt{\frac{We}{We_{cr}}}\right) \quad (\text{C.7})$$

Where $g(\alpha_v) = (\alpha_{\max}^{1/3} - \alpha_v^{1/3})/\alpha_{\max}^{1/3}$, $\alpha_{\max} = 0.52$, $K_{c1} = 2.86$, $K_{c2} = 1.922$, $K_{c3} = 1.017$ and $We_{cr} = 1.24$.

Their breakup model is:

$$\phi_{\text{bkup, YM}} = K_{b1} \frac{\epsilon^{1/3} \alpha_v (1 - \alpha_v)}{d_b^{11/3}} \frac{1}{1 + K_{b2} (1 - \alpha_v) \sqrt{We/We_{cr}}} \cdot \exp\left(-\frac{We_{cr}}{We}\right) \quad (\text{C.8})$$

Where $K_{b1} = 1.6$ and $K_{b2} = 0.42$.

The formulation to compare with the integration is:

$$\begin{aligned}\Phi_{\text{coal-bkup, YM}} &= \frac{36\pi}{3} \left(\frac{\alpha}{a_i}\right)^2 (\phi_{\text{bkup}} + \phi_{\text{coal}}) \\ &= a_i \frac{\epsilon^{1/3}}{d_b^{2/3}} \frac{\pi}{18} \left(-\frac{K_{c1}\alpha_v}{g(\alpha_v) + K_{c2}\alpha_v \sqrt{We/We_{cr}}} \cdot \exp\left(-K_{c3}\sqrt{\frac{We}{We_{cr}}}\right) \right. \\ &\quad \left. + K_{b1} \frac{1-\alpha_v}{1+K_{b2}(1-\alpha_v)\sqrt{We/We_{cr}}} \cdot \exp\left(-\frac{We_{cr}}{We}\right) \right)\end{aligned}\quad (\text{C.9})$$

Ruyer & Seiler The Ruyer and Seiler 2009 model is based on the hypothesis that the bubble size distribution is parabolic. In practice it behaves exactly like a one-group interfacial area equation. Morel et al. 2010 was used to obtain the formulation of the coalescence and fragmentation terms.

$$\begin{aligned}\Phi_{\text{coal, RS}} &= -a_i^{5/3} \epsilon^{1/3} \alpha_v^{1/3} \xi(Nc) \exp(-\sqrt{We}) \\ \xi(Nc) &= -0.18(1 + 0.34Nc + 0.199Nc^2) \\ Nc &= 1.81\sqrt{We}\end{aligned}\quad (\text{C.10})$$

$$\Phi_{\text{bkup, RS}} = 0.158 a_i \frac{\epsilon^{1/3}}{d_b^{2/3}} \left(1 - \left(\frac{We_{cr}}{3.17We}\right)^2\right) \sqrt{1 - \frac{We_{cr}}{3.17We}} \exp\left(-0.63\frac{We_{cr}}{We}\right) \quad (\text{C.11})$$

$$\begin{aligned}\Phi_{\text{coal-bkup, RS}} &= a_i \frac{\epsilon^{1/3}}{d_b^{2/3}} \left(-6^{2/3} \alpha_v \xi(Nc) \exp(-\sqrt{We})\right. \\ &\quad \left.+ 0.158 \left(1 - \left(\frac{We_{cr}}{3.17We}\right)^2\right) \sqrt{1 - \frac{We_{cr}}{3.17We}} \exp\left(-\frac{0.63We_{cr}}{We}\right)\right)\end{aligned}\quad (\text{C.12})$$

Wu et al. Wu et al. 1998 propose a classical monodisperse interfacial area formulation. It is written as bubble number density transport. Their coalescence model contains a turbulent and a wake entrainment term and is:

$$\begin{aligned}\phi_{\text{coal, Wu}} &= -C_{RC}(\epsilon d_b)^{1/3} d_b^2 n^2 \frac{1}{\alpha_{\max}^{1/3}(\alpha_{\max}^{1/3} - \alpha_v^{1/3})} \left(1 - \exp\left(-C \frac{\alpha_{\max}^{1/3} \alpha_v^{1/3}}{\alpha_{\max}^{1/3} - \alpha_v^{1/3}}\right)\right) \\ &\quad - C_{WE} d_b^2 n^2 u_r\end{aligned}\quad (\text{C.13})$$

Where $C_{RC} = 0.0565$, $C = 3$, $\alpha_{\max} = 0.65$ and $C_{WE} = 0.151$. u_r is the norm of the bubble drift velocity.

Their breakup model is:

$$\phi_{\text{bkup, Wu}} = C_{TI} \frac{\epsilon^{1/3}}{d_b^{2/3}} n \sqrt{1 - We/We_{cr}} \cdot \exp\left(-\frac{We_{cr}}{We}\right) \quad (\text{C.14})$$

Where $C_{TI} = 0.18$ and $We_{cr} = 2$.

The formulation to compare with the integration is:

$$\begin{aligned}\Phi_{\text{coal-bkup, Wu}} &= a_i \frac{\epsilon^{1/3}}{d_b^{2/3}} \frac{1}{3} \left[-C_{RC} 6\alpha_v \left(1 - \exp\left(-C \frac{\alpha_{\max}^{1/3} \alpha_v^{1/3}}{\alpha_{\max}^{1/3} - \alpha_v^{1/3}}\right)\right) \right. \\ &\quad \left. + C_{TI} \sqrt{1 - We/We_{cr}} \cdot \exp\left(-\frac{We_{cr}}{We}\right) \right] \\ &\quad - C_{WE} \frac{2\alpha_v}{\pi d_b} u_r\end{aligned}\quad (\text{C.15})$$

Hibiki & Ishii Hibiki and Ishii 2000a directly propose the coalescence and sink terms adapted for an IATE. Their coalescence term is:

$$\Phi_{\text{coal, HI}} = - \left(\frac{\alpha}{a_i} \right)^2 \Gamma_c \frac{\epsilon^{1/3} \alpha_v^2}{d_b^{11/3}} \frac{1}{\alpha_{\text{max}} - \alpha_v} \cdot \exp \left(-K_c \sqrt{We} \right) \quad (\text{C.16})$$

Where $\alpha_{\text{max}} = 0.52$, $\Gamma_c = 0.188$, $K_c = 1.29$

Their breakup term is:

$$\Phi_{\text{bkup, HI}} = \left(\frac{\alpha}{a_i} \right)^2 \Gamma_b \frac{\epsilon^{1/3} \alpha_v (1 - \alpha_v)}{d_b^{11/3}} \frac{1}{\alpha_{\text{max}} - \alpha_v} \cdot \exp \left(-\frac{K_b}{We} \right) \quad (\text{C.17})$$

Where $\Gamma_b = 0.264$ and $K_b = 1.37$.

This transforms into:

$$\begin{aligned} \Phi_{\text{coal-bkup, HI}} = & a_i \frac{\epsilon^{1/3}}{d_b^{2/3}} \frac{1}{216} \left(-\Gamma_c \frac{\alpha_v}{\alpha_{\text{max}} - \alpha_v} \cdot \exp \left(-K_c \sqrt{We} \right) \right. \\ & \left. + \Gamma_b \frac{1 - \alpha_v}{\alpha_{\text{max}} - \alpha_v} \cdot \exp \left(-\frac{K_b}{We} \right) \right) \end{aligned} \quad (\text{C.18})$$

Typical structure of coalescence and breakup formulations Combining all of the above formulations, one can identify a typical structure of coalescence and breakup correlations from the literature:

$$\begin{aligned} \Phi_{\text{coal-bkup, typical}} = & a_i \frac{\epsilon^{1/3}}{d_b^{2/3}} \left(-K_c f_c(\alpha_v, We) \cdot \exp \left(-\sqrt{\frac{We}{We_{cr,c}}} \right) \right. \\ & \left. + K_b f_b(\alpha_v, We) \cdot \exp \left(-\frac{We_{cr,b}}{We} \right) \right) \end{aligned} \quad (\text{C.19})$$

Where K_c , K_b , $We_{cr,c}$ and $We_{cr,b}$ are constants and f_c and f_b functions of the void fraction and Weber number. The exponential terms come from the coalescence and breakup probabilities if two bubbles collide together or if a bubble collides with a turbulent eddy. The f_c and f_b functions come from the collision frequency between bubbles or between a bubble and a turbulent eddy. The above coalescence-fragmentation combinations have ~ 10 fitted parameters each. They come from theoretical analysis, expert judgment, calibration on adiabatic air-water atmospheric-pressure pipe flows or on air-water stirred tanks. The functions f_c and f_b are difficult to interpret without plotting them graphically.

For a given (ϵ, α_v) combination, the coalescence and fragmentation make the interfacial area and bubble diameter evolve towards an equilibrium that is a function of ϵ and α_v . However, the equilibrium bubble diameter is not apparent in the equations.

Comparing the literature to the experiment All of the five coalescence and breakup formulations presented in section C.3 require the turbulent kinetic energy dissipation ϵ as inputs. To approach the values of ϵ , the Reichardt 1951 value of the turbulent diffusivity in a pipe are used (equation B.3). The turbulent kinetic energy is taken as (Kalitzin et al. 2005):

$$k(r) = u_\tau^2 \left(1 + 2 \frac{r}{R} \right) \quad (\text{C.20})$$

And its dissipation is calculated on all of the spatial interpolation points using:

$$\epsilon = 0.09 \frac{k^2}{\nu_t} \quad (\text{C.21})$$

This approach is extremely crude. I estimate the uncertainty on ϵ to be of the order of 50%. However, as it is always used in the power $2/3$, this softens the blow on the prediction of the formulations from the literature.

The Wu et al. 1998 formulation requires a bubble rise velocity. The Ishii and Zuber 1979 deformed bubble rise velocity is chosen as it is easy to calculate and independent of the bubble diameter. As flows in DEBORA are extremely turbulent, the wake entrainment coalescence should anyhow be negligible before the random collision coalescence.

The coalescence and breakup terms listed above can then be calculated. A comparison between the interpolated term and those from the literature is presented in figure C.2. The difference between the different terms from the literature covers two orders of magnitude. The Yao and Morel 2004 and Prince and Blanch 1990 and Luo and Svendsen 1996 terms are the closest to the interpolation, with Ruyer and Seiler 2009 having slightly too much coalescence. The uncertainty on the interpolation and the calculations of the terms from the literature being of the order of 50%, one cannot conclude which one is closest to the data. However, the Wu et al. 1998 and Hibiki and Ishii 2000a formulations are extremely far from the interpolation.

It is not because a multiphase CFD code uses a model that predicts $\Phi_{\text{coal-bkup}}$ to have larger negative values compared to the integration, i.e. too much coalescence, that the predicted bubble diameters will be too large. Many different terms come into play in an Euler-Euler set of closures. If the radial velocities or turbulent kinetic energy dissipation rate are different from those used in the integration or if the flow is not subcooled, then the predicted bubble diameter can very well be too small.

One must bear in mind that on these test tubes the coalescence dominates the breakup in the reconstructed values. Therefore, the results obtained do not enable a decisive conclusion on the relevance of the breakup terms from the literature.

C.4 A simple return-to-equilibrium proposal

Equation C.19 shows that the various coalescence and breakup terms from the literature have a similar structure though they predict extremely different outcomes. However, all of the forms of these terms are complex, which makes them difficult to interpret and calibrate, and can lead to implementation errors.

In this section, a simple model for the coalescence-fragmentation term is proposed. It takes the form of a recall to an equilibrium diameter that is calculated using the bubble rise and turbulent Weber numbers. The characteristic recall time scale chosen is $\epsilon^{1/3}/d_b^{2/3}$. A prefactor α_v is added to the equation as the more void

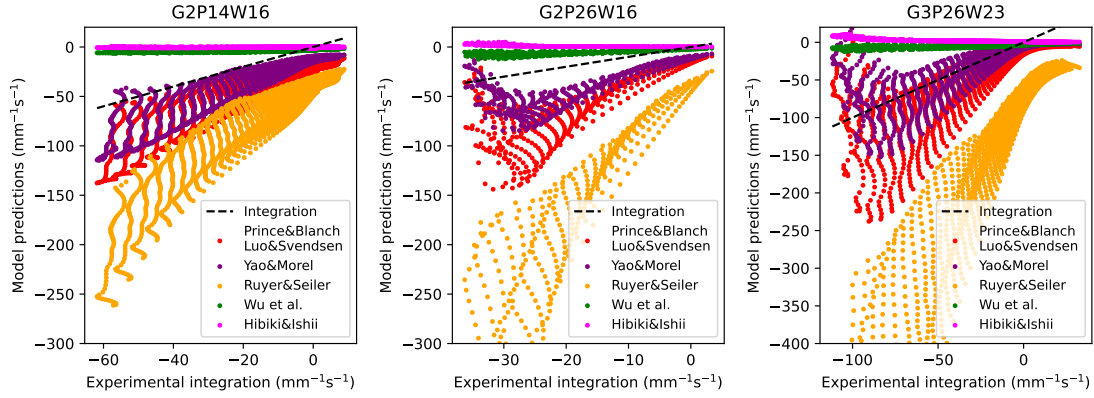


Figure C.2: Comparison between the (coalescence+breakup) term integrated from the void fraction and interfacial area experimental measurements and various formulations from the literature for 3 DEBORA test tubes. The experimental conditions are given in table 4.2.

there is, the more coalescence and breakup occurs.

$$\begin{aligned}
 \Phi_{\text{coal-bkup, proposed}} &= -\alpha_v K \frac{\epsilon^{1/3}}{d_b^{2/3}} (a_i - a_{i,\text{eq}}) \\
 a_{i,\text{eq}} &= \frac{6\alpha_v}{d_{b,\text{eq}}} \\
 d_{b,\text{eq}} &= \min(d_{b,\text{eq, turb}}, d_{b,\text{eq, rise}}) \\
 d_{b,\text{eq, rise}} &= We_{cr,\text{rise}} \frac{\sigma}{u_{r,\text{IZdef}}^2 \rho_l} \\
 u_{r,\text{IZdef}} &= \sqrt{2} \left(\frac{g\sigma(\rho_l - \rho_g)}{\rho_l^2} \right)^{1/4} \\
 d_{b,\text{eq, turb}} &= \left(We_{cr,\text{turb}} \frac{\sigma}{\epsilon^{2/3} \rho_l} \right)^{3/5}
 \end{aligned} \tag{C.22}$$

Where $K = 0.2$, $We_{cr,\text{rise}} = 4$ and $We_{cr,\text{turb}} = 3$. $We_{cr,\text{rise}}$ and $We_{cr,\text{turb}}$ are two critical Weber numbers that were adjusted so that:

- Their values are coherent with classical values from the literature (Wallis 1974; Hinze 1955; Risso and Fabre 1998; Masuk et al. 2021).
- The predicted coalescence-fragmentation term match the interpolated values.

The proposed model therefore contains two semi-fitted coefficients ($We_{cr,\text{rise}}$ and $We_{cr,\text{turb}}$) and one fitted coefficient (K).

Figure C.3 compares the results of the model presented in equation C.22 with those from the literature. In particular, the two bottom rows present log-scale histograms of the ratio of various formulations to the integrated (coalescence+breakup) term. The proposed model outperforms those of the literature. This is expected as it was calibrated on the DEBORA database.

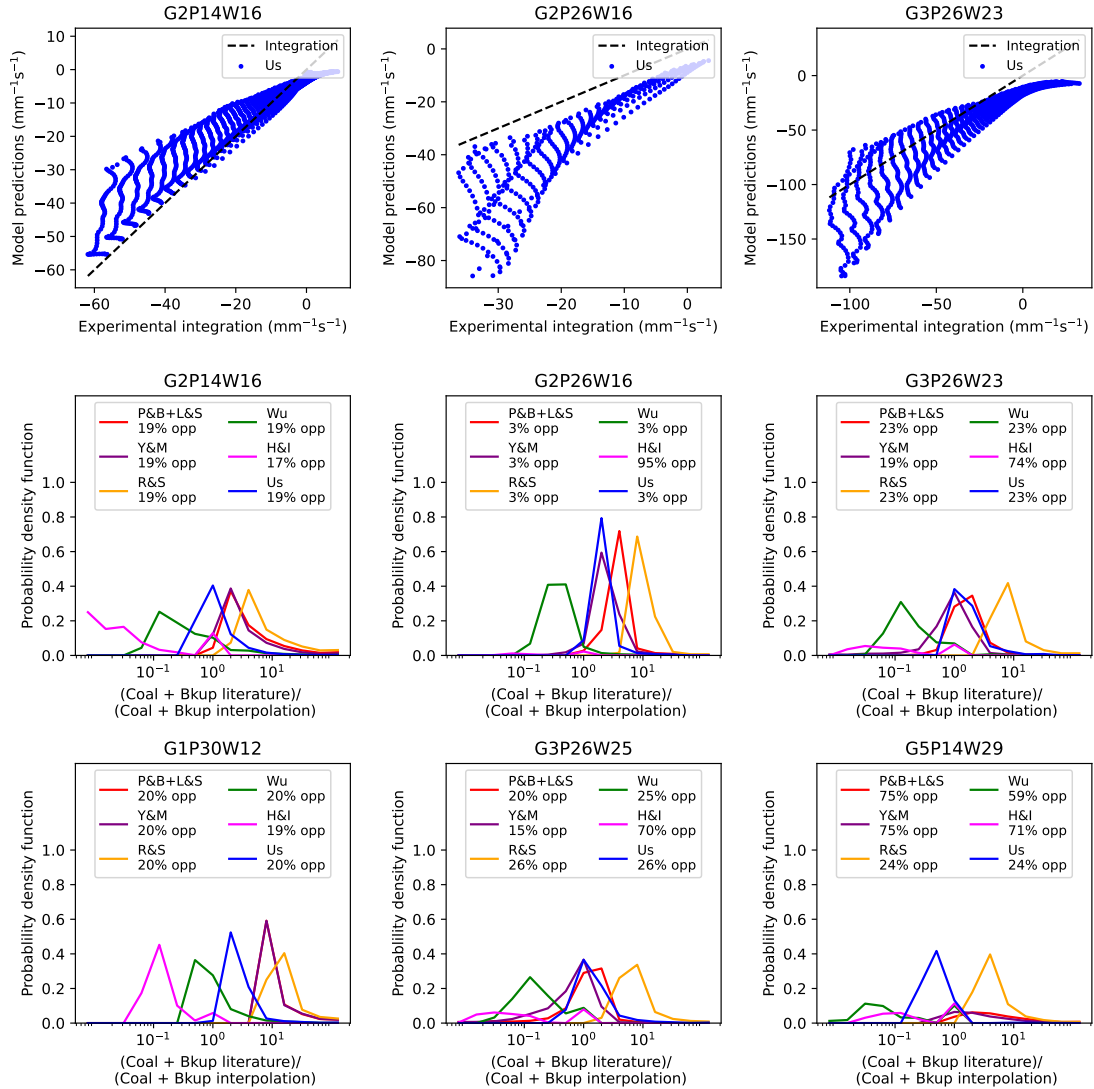
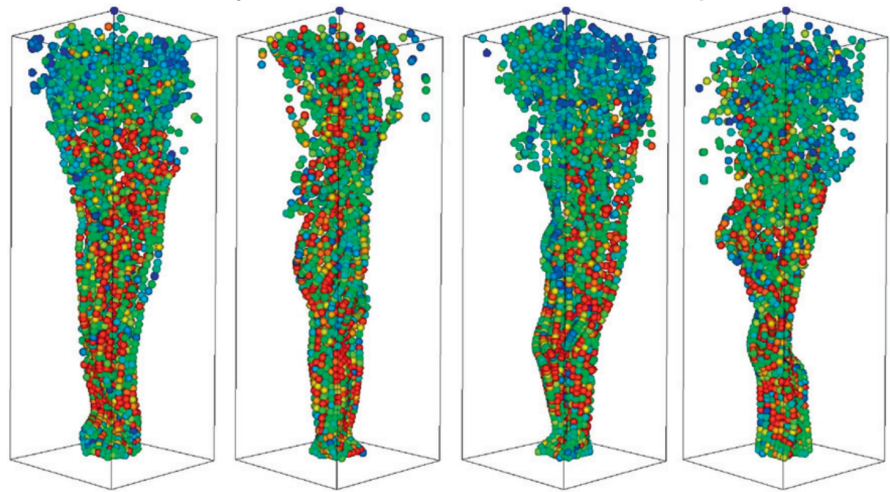


Figure C.3: **Top row:** comparison between the (coalescence+breakup) term integrated from the void fraction and interfacial area experimental measurements and the return-to-equilibrium formulation proposed in equation C.22 for 3 DEBORA test tubes. **Bottom rows:** log-scale histogram of the ratio of various formulations proposed in the literature to the integrated (coalescence+breakup) term. The proportion of terms that do not have the right sign is given in the legend, for these the ratio cannot be included in the log scale. The experimental conditions are given in table 4.2. P&B+L&S: Prince and Blanch 1990 coalescence and Luo and Svendsen 1996 breakup. Y&M: Yao and Morel 2004 coalescence and breakup. R&S: Ruyer and Seiler 2009 coalescence and breakup. Wu: Wu et al. 1998 coalescence and breakup. H&I: Hibiki and Ishii 2000a coalescence and breakup.

APPENDIX D



Lattice-Boltzman method simulation of a bubble column by Sungkorn et al. 2011.

D

Burns turbulent dispersion considers the dispersed phase as a passive scalar

This appendix discusses the practical effect of the Burns et al. 2004 turbulent dispersion force in bubbly flow. It was adapted from Reiss 2024.

Contents

D.1	Introduction	291
D.2	Analytical analysis	294
D.3	Simulation	296
D.4	Conclusion	297

In vertical ascending channel flow, the radial void fraction distribution results from an equilibrium between the lift, drag and turbulent dispersion forces. Appropriate experimental data to derive a formulation for the turbulent dispersion force in high-pressure fast-flowing PWR conditions should take out the lift force of this equilibrium. For example, if vapor was injected at the core of a wide pipe the lift force would be negligible as the vorticity would be zero. One could then study the spread of void fraction. The distribution would result from the equilibrium of the drag force and the turbulent dispersion. This has already been tested at atmospheric pressure (Colin and Legendre 2002) but as far as I know never in PWR conditions. Another possibility would be to study rectangular channels. If the channel section was 5.5 mm (x) by 55 mm (y), its hydraulic diameter would be the same as a PWR subchannel. If it were inclined at a small angle ($\sim 10\%$) around the x -axis, the void fraction distribution along the y -axis should be independent of the lift force as the y -section is wide. At equilibrium it will result from the balance between drag, gravity and turbulent dispersion. However, to the best of my knowledge such data is not currently available in the literature.

I therefore resort to a theoretical analysis of the Burns et al. 2004 turbulent dispersion force. It is the most commonly used turbulent dispersion in the two-fluid RANS bubbly-flow literature. However, its derivation is based on a series of hypotheses that are difficult to justify in industrial flows. In this section, it is shown that in low-void fraction vertical pipe flow, the Burns turbulent dispersion

formulation is equivalent to considering the radial movement of the gas phase like a passive scalar that follows turbulent eddies. This is not apparent in the derivation of the force. As bubbles in pressurized water reactor (PWR) conditions have a low Stokes number ($\sim 10^{-1}$), considering bubbles are transported by turbulence is a good approximation for bubble dispersion in pipe flow. This is a useful key to interpret void fraction dispersion results in two-fluid simulations. Therefore, the Burns turbulent dispersion force should be appropriate to represent bubble dispersion in low-void fraction PWR flows.

It should also be noted that the Burns et al. 2004 turbulent dispersion coefficient contains a term in C_D/d_b (see equation 2.21). As the Ishii and Zuber 1979 deformable bubble drag force is extensively used in this thesis (see equation 7.6), these two terms cancel out and the turbulent dispersion force is independent of the bubble diameter.

D.1 Introduction

Stokes number, turbulent time scale and dissipation rate The turbulent dispersion of a passive scalar is a stochastic process. A $k-\omega$ turbulence framework will be used here (Kok 1999), with ω the turbulent dissipation rate. A dye particle will follow eddies that move at a velocity $\sim \sqrt{k}$ for a time $\tau_{turb} = \frac{1}{\omega} = \frac{C_\mu k}{\epsilon}$ (Kok and Spekreijse 2000). The diffusion is characterized by a turbulent viscosity $\nu_t = k\tau_{turb}$. It is therefore surprising that most classical formulations for bubble dispersion hide τ_{turb} in the turbulent dispersion coefficient even though it is sure to play a part.

In a CFD simulation of the DEBORA experiment, ω is typically $10^2 - 10^3 \text{s}^{-1}$ (see figure 4.8). The turbulent time scale is therefore $\tau_{turb} \sim 10^{-3} - 10^{-2} \text{s}$.

Furthermore, the bubble response time will be in $\alpha_g \rho_g u_g / F_{drag}$, where F_{drag} is the drag force. So $\tau_{bubble} \sim C_D d_b \rho_g / (\rho_l u_r)$ with C_D the drag coefficient and d_b the bubble diameter (Tomiyama et al. 1998). In nuclear reactor conditions, $\rho_g / \rho_l \sim 0.1$, $d_b \sim 5 \cdot 10^{-4} \text{m}$, $u_r \sim 0.1 \text{ m/s}$, $C_D \sim 1$. Therefore, $\tau_{bubble} \sim 5 \cdot 10^{-5}$, $St_{bubble} \sim 10^{-2}$.

However, one must take into account the virtual mass force at the scale of the bubbles. The bubble inertia then increases and $\tau_{bubble} \sim C_{VM} C_d d_b / u_r$. Taking $C_{VM} \sim 0.5$ (Zuber 1964), $\tau_{bubble} \sim 2 \cdot 10^{-4}$, which reduces the difference with the turbulent time scale. $St_{bubble} \sim 10^{-1}$, still smaller than 1. Bubbles should then follow the liquid flow in the radial direction. In the axial direction, buoyancy creates a velocity difference.

General form of the turbulent dispersion force In this subsection, the following notation conventions are used:

- All forces written here are applied to the gas phase;
- X' is defined as the fluctuations of a quantity X , which yields $u_i = u_i + u'_i$, $P_i = P_i + P'_i$, $\alpha_i = \alpha_i + \alpha'_i$, etc.

The general form of the turbulent dispersion force is (see equation 2.21 in section 2.2):

$$\vec{F}_{TD} = -C_{TD}\rho_l k \nabla \alpha_g \quad (\text{D.1})$$

The instantaneous mass equation for the gas phase in a two-fluid adiabatic model reads Ishii and Hibiki 2006:

$$\frac{\partial \chi \rho_g}{\partial t} + \nabla \cdot (\chi \rho_g \vec{u}_g) = 0 \quad (\text{D.2})$$

With χ the phase indicator function, ρ_g the gas density and \vec{u}_g the gas velocity.

The Favre average, also called statistical average and phase average, of a quantity Φ is a mass and void fraction weighted average: $\langle \Phi \rangle_{Favre} = \frac{\langle \Phi \alpha \rho \rangle_{Time}}{\langle \alpha \rho \rangle_{Time}}$. It is usually used when going towards a RANS formulation (Ishii and Hibiki 2006). Favre-averaging the mass equation results in a convection equation on void fraction:

$$\frac{\partial \alpha_g \rho_g}{\partial t} + \nabla \cdot (\alpha_g \rho_g \langle \vec{u}_g \rangle_{Favre}) = 0 \quad (\text{D.3})$$

Derivation of the Burns et al. 2004 turbulent dispersion force This methodology is used indiscriminately to describe bubble and particle dispersion. The authors start from the two-phase momentum equation:

$$\frac{\partial \alpha_k \rho_k \vec{u}_k}{\partial t} + \nabla \cdot (\alpha_k \rho_k \vec{u}_k \otimes \vec{u}_k) = -\alpha_k \nabla P + \nabla \cdot [\alpha_k \mu_k \nabla \vec{u}_k] + \vec{F}_{ki} + \alpha_k \rho_k \vec{g} \quad (\text{D.4})$$

Where k can be either the liquid or the gas phase, \vec{F}_{ki} are the interfacial forces, \vec{g} the gravitational acceleration and μ_k the dynamic viscosity.

They then apply a Reynolds-Averaged Navier-Stokes methodology to the two-phase flow. They consider that the unstable contribution to the drag force is the only one that is non-negligible after averaging. Burns et al. write:

$$\vec{F}_{TD} = \langle \frac{3}{4} C_D \frac{\alpha_g \rho_l}{d_b} |\vec{u}_g - \vec{u}_l| \rangle \left(\frac{\langle \alpha'_g u'_g \rangle}{\alpha_g} - \frac{\langle \alpha'_l u'_l \rangle}{\alpha_l} - \frac{\langle a'_i (u'_g - u'_l) \rangle}{\langle a'_i \rangle} \right) \quad (\text{D.5})$$

They then apply an eddy viscosity hypothesis ($\langle \alpha'_k u'_k \rangle = -\frac{\nu_t}{Pr_t} \nabla \alpha_k$ with ν_t the turbulent viscosity and Pr_t the bubble turbulent Prandtl number) to arrive at their final formulation for two-phase flow:

$$\vec{F}_{TD} = - \langle \frac{3}{4} C_D \frac{\alpha_g \rho_l}{d_b} |\vec{u}_g - \vec{u}_l| \rangle \frac{\nu_t}{Pr_t} \left(\frac{1}{\alpha_g} + \frac{1}{\alpha_l} \right) \nabla \alpha_g \quad (\text{D.6})$$

However, this formulation is not usable as such as there is still an averaged value inside. The authors then do the following hypothesis to close the turbulent dispersion force:

$$\langle \frac{3}{4} C_D \frac{\alpha_g \rho_l}{d_b} |\vec{u}_g - \vec{u}_l| \rangle = \frac{3}{4} C_D \frac{\alpha_g \rho_l}{d_b} |\vec{u}_g - \vec{u}_l| \quad (\text{D.7})$$

Where the C_D used is that of the drag force of steady-state bubbles rising in the liquid $|\vec{u}_g - \vec{u}_l|$.

For this formulation to be valid, the following hypotheses must be met:

- The only non-negligible unstable contribution to the force balance is through the drag force. Other sources disagree with this hypothesis (Laviéville et al. 2017; Aouadi et al. 2019).
- The drag force formulation used in the fluctuating flow before the RANS step must be valid. A steady-state single-bubble formulation is most often used. This means in particular that:
 - The drag coefficient must be the same in the vertical and other directions, which is not necessarily the case for deformed bubbles;
 - The typical size of turbulent eddies is much larger than the size of bubbles, so they are faced with a uniform velocity field;
 - The typical time scale of eddies dispersing the bubbles is much larger than the time required for the drag force from the eddy on the bubble to reach its stationary value.
- The approximation used in equation D.7 is valid.

These hypotheses are not necessarily met in high-void fraction fast-flowing conditions.

Derivation of the Laviéville et al. 2017 turbulent dispersion force This methodology is used indiscriminately to describe bubble and particle dispersion. In this work, the turbulent dispersion formulation comes from an averaging of the Lagrangian equation of motion for a single bubble which is then transformed back in Eulerian coordinates.

The authors take into account many different forces acting on the bubbles: added mass, drag, lift and pressure variations (which, as with the application of the Burns et al. 2004 methodology, must have the same formulation in a fluctuating flow as in a stationary one).

Without going into detail as to how their formulation is derived, they make the following hypotheses:

- The fluctuations of single bubbles in a large amount of fluid are identical to those of a bubble swarm;
- The formulations on lift, drag and added mass forces evaluated on single bubbles in an undisturbed bulk used before RANS averaging are valid in unsteady high-void fraction flows;
- They can build a time scale of fluid turbulence along bubble trajectories and one for drag;
- $\langle u'_g u'_g \rangle$ and $\langle u'_g u'_l \rangle$ can be related to $\langle u'_l u'_l \rangle$ in all flow conditions through complex formulas that use the aforementioned time scales and an added mass coefficient.

As above, these hypotheses are not necessarily met in high-void fraction fast-flowing conditions.

D.2 Analytical analysis

Force equilibrium in a bubbly boiling pipe flow In the core region of bubbly boiling PWR-condition pipe flows, the radial lift and added mass forces, bubble inertia and the pressure gradient play a minor role. The radial bubble movement is piloted by the balance between the turbulent dispersion and the drag force (see figure 5.2). Furthermore, the axial velocity is much larger than the radial velocity. The radial drag force reads:

$$\vec{F}_{D,r} = -\frac{3}{4}C_D \frac{\alpha_g \rho_l}{d_b} |u_{g,z} - u_{l,z}| (u_{g,r} - u_{l,r}) \quad (\text{D.8})$$

Using the Burns formulation from equation D.6, one obtains:

$$\frac{3}{4}C_D \frac{\alpha_g \rho_l}{d_b} |u_{g,z} - u_{l,z}| (u_{g,r} - u_{l,r}) + \frac{3}{4}C_D \frac{\alpha_g \rho_l}{d_b} |u_g - u_l| \frac{\nu_t}{Pr_t} \left(\frac{1}{\alpha_g} + \frac{1}{\alpha_l} \right) \partial_r \alpha_g = 0 \quad (\text{D.9})$$

Therefore, the relative velocity of the vapor phase is:

$$u_{g,r} - u_{l,r} = -\frac{\nu_t}{Pr_t} \left(\frac{1}{\alpha_g} + \frac{1}{\alpha_l} \right) \partial_r \alpha_g \quad (\text{D.10})$$

Simplified situation I will now place myself in the following situation:

- The bubbles are in homogeneous isotropic liquid turbulence, with a turbulent diffusivity ν_t ;
- The bubble movement is piloted by the drag-dispersion equilibrium;
- There is no phase change or bubble injection in the area of interest;
- The flow is stationary;
- The volume masses ρ_l and ρ_g are constant;
- The vertical velocities are uniform.

This seemingly far-fetched situation is that of a vertical bulk liquid flow in a turbulent large tank where bubbles are injected upstream of the area of interest, as in the Alm eras et al. 2019 experiments. It is also not too different from the core region of a saturated bubbly pipe flow.

As the flow is stationary and has no phase change:

$$\nabla \cdot (\alpha_k \vec{u}_k) = 0 \quad (\text{D.11})$$

I will now place myself in a 2D channel, i.e. a pipe with a rectangular cross-section (Martin 1972). z is the vertical axis and x the horizontal axis along the small width. This leads to the following system of equations:

$$\begin{cases} (1) & u_{gz}\partial_z\alpha_g + \partial_x(\alpha_g u_{gx}) = 0 \\ (2) & -u_{lz}\partial_z\alpha_g + \partial_x((1 - \alpha_g)u_{lx}) = 0 \\ (3) & u_{g,x} - u_{l,x} = -\frac{\nu_t}{Pr_t} \left(\frac{1}{\alpha_g} + \frac{1}{1 - \alpha_g} \right) \partial_x\alpha_g \end{cases} \quad (D.12)$$

Integration u_{lx} is replaced by $u_{gx} - (u_{gx} - u_{lx})$ in (2) and equations (1) and (2) are integrated between 0 and X :

$$\begin{cases} (1) & u_{gz} \int_0^X (\partial_z\alpha_g) dx + \alpha_g(X)u_{gx}(X) - \alpha_g(0)u_{gx}(0) = 0 \\ (2) & -u_{lz} \int_0^X (\partial_z\alpha_g) dx + (1 - \alpha_g(X))u_{gx}(X) - (1 - \alpha_g(0))u_{gx}(0) \\ & = (1 - \alpha_g(X))(u_{gx}(X) - u_{lx}(X)) - (1 - \alpha_g(0))(u_{gx}(0) - u_{lx}(0)) \end{cases} \quad (D.13)$$

Doing (1) \cdot (1 - α_g) - $\alpha_g \cdot$ (2), injecting (3) and doing another derivation yields:

$$((1 - \alpha_g)u_{gz} + \alpha_g u_{lz}) \partial_z\alpha_g = \partial_x \left(\frac{\nu_t}{Pr_t} \partial_x\alpha_g \right) + \partial_x\alpha_g (u_{gz} - u_{lz}) \int_0^X \partial_z\alpha_g dx \quad (D.14)$$

The left-hand term and first right-hand term gives a radial diffusion equation in the convected fluid.

Big approximation I now suppose that axial velocity differences have little impact on the transverse flow. In other words, $u_{gz}, u_{lz} \gg u_{gz} - u_{lz}$. As $u_{gz} - u_{lz} \sim 0.1$ m/s in bubbly flow Sugrue 2017, this approximation is valid in a fast-flowing rectangular channel ($u_{lz} > 1$ m/s). This yields $\alpha_g u_{gx} \sim -(1 - \alpha_g)u_{lx}$ from equation D.12-(1) and D.12-(2). Equation D.12-(3) then becomes:

$$u_{g,x} - u_{l,x} = u_{g,x} + u_{g,x} \frac{\alpha_g}{1 - \alpha_g} = \frac{u_{g,x}}{1 - \alpha_g} = -\frac{\nu_t}{Pr_t} \left(\frac{1}{\alpha_g} + \frac{1}{1 - \alpha_g} \right) \partial_x\alpha_g \quad (D.15)$$

So:

$$\alpha_g u_{g,x} = -\frac{\nu_t}{Pr_t} \partial_x\alpha_g \quad (D.16)$$

Using equation D.12-(1) yields:

$$((1 - \alpha_g)u_{gz} + \alpha_g u_{lz}) \partial_z\alpha_g = \partial_x \left(\frac{\nu_t}{Pr_t} \partial_x\alpha_g \right) \quad (D.17)$$

This is the same equation as above, without the integral term: a radial diffusion equation in the convected fluid, with a diffusivity equal to the liquid turbulent viscosity.

This means that the integral term in equation D.14 represents the contribution of axial velocity difference between the two phases to the evolution of α_g . This is coherent with the fact that this term contains $u_{gz} - u_{lz}$ and $\partial_z\alpha_g$.

Big approximation in cylindrical coordinates The previous reasoning is expanded to cylindrical coordinates. The system to solve is:

$$\begin{cases} (1) & u_{gz}\partial_z\alpha_g + 1/r\partial_r(r\alpha_g u_{gr}) = 0 \\ (2) & -u_{lz}\partial_z\alpha_g + 1/r\partial_r(r(1-\alpha_g)u_{lr}) = 0 \\ (3) & u_{g,r} - u_{l,r} = -\frac{\nu_t}{Pr_t}\left(\frac{1}{\alpha_g} + \frac{1}{1-\alpha_g}\right)\partial_r\alpha_g \end{cases} \quad (\text{D.18})$$

A fast-flowing pipe flow is also considered, where $\alpha_g u_{gr} \sim -(1-\alpha_g)u_{lr}$. As above, $\alpha_g u_{g,x} = -\frac{\nu_t}{Pr_t}\partial_x\alpha_g$. And:

$$((1-\alpha_g)u_{gz} + \alpha_g u_{lz})\partial_z\alpha_g = 1/r\partial_r\left(r\frac{\nu_t}{Pr_t}\partial_r\alpha_g\right) \quad (\text{D.19})$$

Which is also a diffusion equation.

D.3 Simulation

The hypothesis that the Burns turbulent dispersion force disperses bubbles as if they were passive scalars in industrial geometries is tested in this section.

I simulate the following situation: a tube where bubbles are injected at the core (Colin and Legendre 2002). The multi-phase module of the TrioCFD code is used Angeli et al. 2015. The tube is 4 cm in diameter, 4 m long and a small amount of air is injected 2 m downstream of the entrance. Bubbles are 0.92 mm in diameter, and $Re_b \sim 100$. The liquid bulk velocity is 1 m/s and a $k-\omega$ turbulence model is used. The void fraction predicted by the code along the width of the pipe at different positions downstream of the inlet is compared.

The first simulated configuration is a 2-fluid model with drag, added mass, gravity and Burns turbulent dispersion forces. The lift force and a wall correction were left out to compare the Burns force with simple diffusion.

The second simulated configuration is a mixture model where the relative velocity $\vec{u}_g - \vec{u}_l$ can be enforced in the code (see section 2.3). Here, the following relative velocity is used:

$$\vec{u}_g - \vec{u}_l = u_{r,\text{Ishii-Zuber}} - \frac{\nu_t}{Pr_t\alpha_g}\nabla\alpha_g \quad (\text{D.20})$$

This amounts to directly enforcing equation D.10, and obtaining an effective diffusion equation on the vapor velocity. The momentum and mass equations for the mixture are then solved by the code.

The results of this simulation are shown in figure D.1. There are slight differences between both simulations. This is expected, as the conditions in which the approximation to obtain equation D.19 is valid are not completely satisfied. In particular, the axial velocities can no longer be considered constant along the width of the pipe. Furthermore, the added mass force was used. It plays a small part in the center of the pipe as bubbles accelerate after injection.

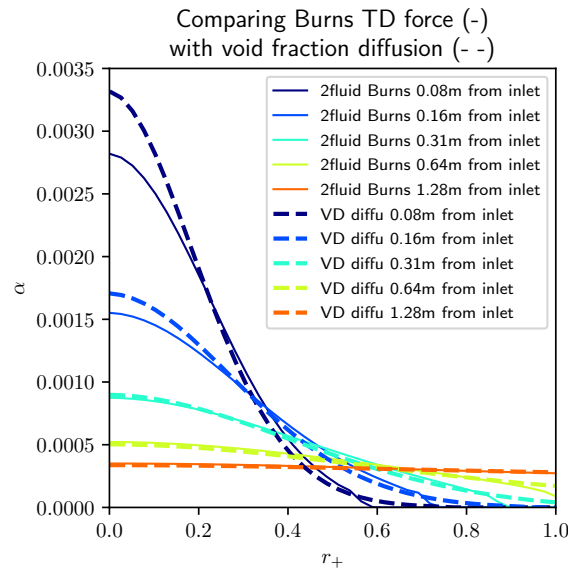


Figure D.1: Comparison between the simulation results obtained with the Burns turbulent dispersion in a 2-fluid model and a void-drift model enforcing passive scalar-like turbulent diffusion.

However, as the differences between outputs are small, this simulation reinforces the case for the Burns turbulent dispersion to amount to passive scalar turbulent diffusion in fast-flowing pipe flow. Considering the Stokes number of PWR-condition flows, this behavior is in line with what is expected from the flow at low void fractions.

D.4 Conclusion

Using an analytical analysis in a simplified situation and a drift-flux simulation, I show that the practical effect of the Burns et al. 2004 turbulent dispersion force in ascending bubbly flow is to treat the dispersed phase as a passive scalar. Though the hypotheses made in the derivation of this force are questionable, this effect is in line with what is expected in pressurized water reactors at low void fraction given the Stokes numbers in the flow.

APPENDIX E



E

Onset of significant void database

This section contains the onset of significant void database that I built during this thesis. It is used in chapter 6. It is split between tables E.1 and E.2. The data contained is accessible at https://github.com/CoReiss/CFD_OSV.

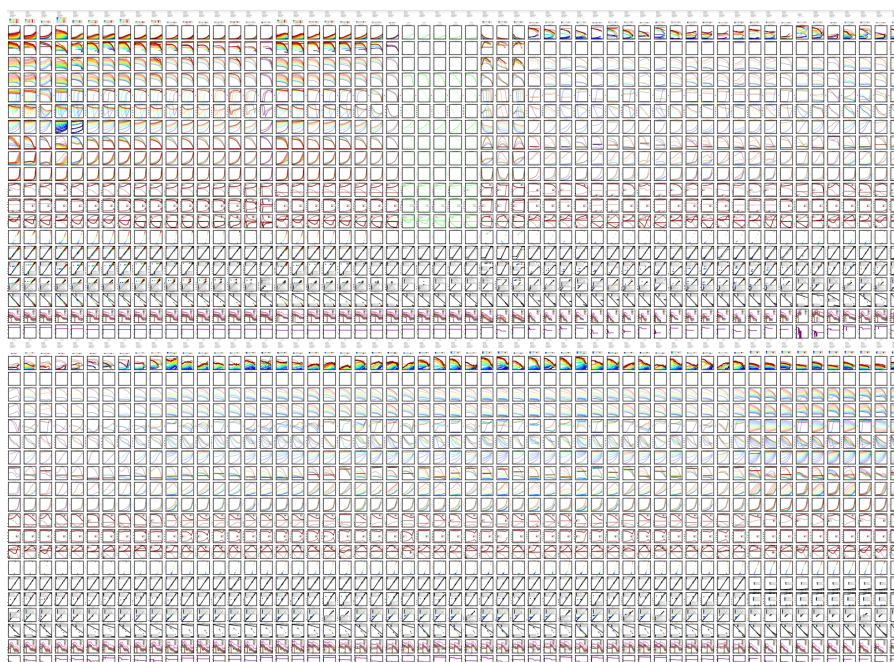
Source	Fluid	D_h mm	l_1 mm	l_2 mm	Geom.	P bar	G kg/(m ² s)	u_{in} m/s	q_w kW/m ²	X_{OSV}	$T_s - T_{OSV}$ °C
Egen	H ₂ O	4.72	2.6	25.4	Chan.	137.9	913		252		4.44
Egen	H ₂ O	4.72	2.6	25.4	Chan.	137.9	549		473		9.44
Egen	H ₂ O	4.72	2.6	25.4	Chan.	137.9	898		946		12.78
Egen	H ₂ O	4.72	2.6	25.4	Chan.	137.9	887		1261		17.78
Egen	H ₂ O	4.72	2.6	25.4	Chan.	137.9	1139		946		13.89
Egen	H ₂ O	4.72	2.6	25.4	Chan.	137.9	1145		1262		21.11
Egen	H ₂ O	4.72	2.6	25.4	Chan.	137.9	1145		1577		17.22
Ferrell	H ₂ O	11.8		11.8	Tube	4.14	540		363		11.67
Ferrell	H ₂ O	11.8		11.8	Tube	4.14	1065		363		12.22
Ferrell	H ₂ O	11.8		11.8	Tube	8.27	529		363		14.44
Ferrell	H ₂ O	11.8		11.8	Tube	8.27	529		366		12.78
Ferrell	H ₂ O	11.8		11.8	Tube	8.27	1059		243		10.56
Ferrell	H ₂ O	11.8		11.8	Tube	8.27	1059		681		18.89
Ferrell	H ₂ O	11.8		11.8	Tube	8.27	1059		451		16.11
Ferrell	H ₂ O	11.8		11.8	Tube	8.27	1059		363		13.33
Ferrell	H ₂ O	11.8		11.8	Tube	8.27	1318		678		18.89
Ferrell	H ₂ O	11.8		11.8	Tube	16.5	540		366		12.22
Ferrell	H ₂ O	11.8		11.8	Tube	16.5	1052		66		18.33
Rouhani	H ₂ O	13	12	25	Ann.	39.1	132		590		26.45
Rouhani	H ₂ O	13	12	25	Ann.	29.1	132		590		26.40
Rouhani	H ₂ O	13	12	25	Ann.	19.6	132		590		26.73
Rouhani	H ₂ O	13	12	25	Ann.	9.8	132		300		14.53
Rouhani	H ₂ O	13	12	25	Ann.	9.8	1060		890		22.71
Rouhani	H ₂ O	13	12	25	Ann.	9.8	1440		890		19.56
Bartolomei	1	H ₂ O	15.4		15.4	Tube	15	900		380	-0.0451
Bartolomei	1	H ₂ O	15.4		15.4	Tube	30	900		380	-0.0408
Bartolomei	1	H ₂ O	15.4		15.4	Tube	45	900		380	-0.0381
Bartolomei	1	H ₂ O	15.4		15.4	Tube	30	900		800	-0.0773
Bartolomei	1	H ₂ O	15.4		15.4	Tube	45	900		800	-0.0698
Bartolomei	1	H ₂ O	24		24	Tube	15	900		380	-0.0418
Bartolomei	1	H ₂ O	24		24	Tube	30	900		380	-0.037
Bartolomei	1	H ₂ O	24		24	Tube	45	900		380	-0.035
Bartolomei	1	H ₂ O	24		24	Tube	30	900		780	-0.0792
Bartolomei	1	H ₂ O	24		24	Tube	45	900		780	-0.078
Bartolomei	2	H ₂ O	12		12	Tube	68.9	985		1130	-0.1231
Bartolomei	2	H ₂ O	12		12	Tube	68.1	998		440	-0.0461
Bartolomei	2	H ₂ O	12		12	Tube	68.9	965		780	-0.101
Bartolomei	2	H ₂ O	12		12	Tube	68.4	961		1130	-0.1347
Bartolomei	2	H ₂ O	12		12	Tube	67.4	988		1700	-0.1924
Bartolomei	2	H ₂ O	12		12	Tube	147.9	1878		420	-0.0351
Bartolomei	2	H ₂ O	12		12	Tube	147.4	1847		770	-0.0686
Bartolomei	2	H ₂ O	12		12	Tube	147.5	2123		1130	-0.1237
Bartolomei	2	H ₂ O	12		12	Tube	68.9	1467		770	-0.0658
Bartolomei	2	H ₂ O	12		12	Tube	67.9	2024		780	-0.0448
Bartolomei	2	H ₂ O	12		12	Tube	108.1	966		1130	-0.1484
Bartolomei	2	H ₂ O	12		12	Tube	108.4	1959		1130	-0.0764
Bartolomei	2	H ₂ O	12		12	Tube	30.1	990		980	-0.0791
Bartolomei	2	H ₂ O	12		12	Tube	44.1	994		900	-0.1012
Bartolomei	2	H ₂ O	12		12	Tube	146.8	1000		1130	-0.1939
Bartolomei	2	H ₂ O	12		12	Tube	68.1	2037		1130	-0.0537
Staub	Ch	H ₂ O	11.45	6.3	63	Chan.	1.13		0.336	366	12.84
Staub	Ch	H ₂ O	11.45	6.3	63	Chan.	1.14		0.336	369	11.92
Staub	Ch	H ₂ O	11.45	6.3	63	Chan.	1.12		0.915	308	8.58
Staub	Ch	H ₂ O	11.45	6.3	63	Chan.	1.19		1.373	369	6.86
Staub	Ch	H ₂ O	11.45	6.3	63	Chan.	1.48		2.898	772	9.44
Staub	Ch	H ₂ O	11.45	6.3	63	Chan.	1.19		1.434	715	12.6
Staub	Ch	H ₂ O	11.45	6.3	63	Chan.	1.19		1.464	368	7.38
Staub	Ch	H ₂ O	11.45	6.3	63	Chan.	1.15		0.366	366	11.45
Staub	Ch	H ₂ O	11.45	6.3	63	Chan.	1.19		1.434	368	7.38
Staub	Ch	H ₂ O	11.45	6.3	63	Chan.	1.47		2.959	784	9.2
Staub	Ch	H ₂ O	11.45	6.3	63	Chan.	1.19		0.366	420	12.54
Staub	Ch	H ₂ O	11.45	6.3	63	Chan.	1.20		1.434	368	8.64
Staub	Ch	H ₂ O	11.45	6.3	63	Chan.	1.50		2.959	778	9.13
Staub	Ch	H ₂ O	11.45	6.3	63	Chan.	3.08		0.366	372	13.67
Staub	Ch	H ₂ O	11.45	6.3	63	Chan.	3.08		1.464	378	8.51
Staub	Ch	H ₂ O	11.45	6.3	63	Chan.	3.08		2.928	785	8.45
Staub	Ch	H ₂ O	11.45	6.3	63	Chan.	3.08		2.928	792	9.29
Staub	TuF	R22	10.16		10.16	Tube	14.4		0.168	20	-0.0434
Staub	TuF	R22	10.16		10.16	Tube	14.5		0.659	48	-0.0521
Staub	TuF	R22	10.16		10.16	Tube	14.5		1.251	49	-0.0287
Staub	TuF	R22	10.16		10.16	Tube	11.9		0.458	24	-0.0318
Staub	TuF	R22	10.16		10.16	Tube	32.9		0.702	62	-0.1119
Staub	TuF	R22	10.16		10.16	Tube	32.9		1.342	47	-0.0514
Staub	TuW	H ₂ O	10.16		10.16	Tube	68.9		1.129	1170	-0.1023
Staub	TuW	H ₂ O	10.16		10.16	Tube	68.9		1.647	1658	-0.0961

Table E.1: First half of the onset of significant void database. *Geom.* stands for geometry of the test section. Chan. and Ann. stand for channel and annulus. l_1 is the small characteristic length of the test section, i.e. channel small width or annulus internal diameter. l_2 is the large characteristic length of the test section, i.e. channel large width, annulus external diameter or tube diameter. The data in this table is from Egen et al. 1957, Ferrell 1964, Rouhani 1966a, Rouhani 1966b, Bartolomei and Chanturiya 1967, Bartolomei et al. 1982 and Staub et al. 1969.

Source	Fluid	D_h mm	l_1 mm	l_2 mm	Geom.	P bar	G kg/(m ² s)	u_{in} m/s	q_w kW/m ²	X_{OSV}	$T_s - T_{OSV}$ °C
Martin	H ₂ O	5.3	2.8	50	Chan.	78.48	2200		1100	-0.0549	
Martin	H ₂ O	5.3	2.8	50	Chan.	78.48	500		400	-0.1071	
Martin	H ₂ O	5.3	2.8	50	Chan.	78.48	1500		1100	-0.0789	
Martin	H ₂ O	5.3	2.8	50	Chan.	78.48	750		400	-0.0767	
Martin	H ₂ O	5.3	2.8	50	Chan.	78.48	750		750	-0.1073	
Martin	H ₂ O	5.3	2.8	50	Chan.	78.48	1500		1700	-0.1180	
Martin	H ₂ O	5.3	2.8	50	Chan.	78.48	1500		750	-0.0585	
Martin	H ₂ O	5.3	2.8	50	Chan.	107.91	500		200	-0.0759	
Martin	H ₂ O	5.3	2.8	50	Chan.	107.91	2200		750	-0.0351	
Martin	H ₂ O	5.3	2.8	50	Chan.	107.91	750		400	-0.0942	
Martin	H ₂ O	5.3	2.8	50	Chan.	107.91	1500		400	-0.0424	
Martin	H ₂ O	5.3	2.8	50	Chan.	107.91	1500		750	-0.0679	
Martin	H ₂ O	5.3	2.8	50	Chan.	107.91	2200		1100	-0.0650	
Martin	H ₂ O	5.3	2.8	50	Chan.	107.91	500		400	-0.1582	
Martin	H ₂ O	5.3	2.8	50	Chan.	107.91	2200		1700	-0.1144	
Martin	H ₂ O	5.3	2.8	50	Chan.	107.91	750		750	-0.1311	
Martin	H ₂ O	5.3	2.8	50	Chan.	137.34	750		400	-0.0603	
Martin	H ₂ O	5.3	2.8	50	Chan.	137.34	2200		1100	-0.0526	
Martin	H ₂ O	5.3	2.8	50	Chan.	137.34	2200		1700	-0.0808	
Martin	H ₂ O	3.84	2	50	Chan.	137.34	2000		1000	-0.0570	
Martin	H ₂ O	3.84	2	50	Chan.	137.34	3000		1000	-0.0370	
Sabotinov	H ₂ O	11.7		11.7	Tube	68.06	2037		1137		17.35
Sabotinov	H ₂ O	11.7		11.7	Tube	68.35	1547		1367		30.71
Sabotinov	H ₂ O	11.7		11.7	Tube	67.86	2023		785		12.49
Sabotinov	H ₂ O	11.7		11.7	Tube	68.06	1979		786		10.80
Sabotinov	H ₂ O	11.7		11.7	Tube	67.86	962		1688		56.56
Sabotinov	H ₂ O	11.7		11.7	Tube	107.97	1015		1723		80.83
Sabotinov	H ₂ O	11.7		11.7	Tube	107.68	2129		1723		29.87
Sabotinov	H ₂ O	11.7		11.7	Tube	107.98	2109		1718		24.42
Sekoguchi	H ₂ O	15.8		15.8	Tube	1.42	310		93	-0.0104	
Sekoguchi	H ₂ O	15.8		15.8	Tube	1.52	311		161	-0.0188	
Sekoguchi	H ₂ O	15.8		15.8	Tube	1.52	466		93	-0.0100	
Sekoguchi	H ₂ O	15.8		15.8	Tube	1.72	468		162	-0.0238	
Sekoguchi	H ₂ O	15.8		15.8	Tube	1.93	697		162	-0.0152	
Sekoguchi	H ₂ O	13.6		13.6	Tube	2.33	501		234	-0.0188	
Sekoguchi	H ₂ O	13.6		13.6	Tube	4.15	328		233	-0.0174	
Sekoguchi	H ₂ O	13.6		13.6	Tube	4.26	498		231	-0.0194	
Sekoguchi	H ₂ O	13.6		13.6	Tube	4.36	1919		228	-0.0115	
Sekoguchi	H ₂ O	13.6		13.6	Tube	4.36	1937		334	-0.0149	
Sekoguchi	H ₂ O	13.6		13.6	Tube	4.15	625		458	-0.0349	
Sekoguchi	H ₂ O	13.6		13.6	Tube	8.00	630		231	-0.0304	
Sekoguchi	H ₂ O	13.6		13.6	Tube	8.11	1937		217	-0.0124	
Sekoguchi	H ₂ O	13.6		13.6	Tube	16.21	607		231	-0.0223	
Sekoguchi	H ₂ O	11		11	Tube	8.21	974		1146	-0.0533	
Sekoguchi	H ₂ O	11		11	Tube	8.21	974		1628	-0.0742	
Edelman	H ₂ O	11.3		11.3	Tube	1	27.5		14.6	-0.0013	
Edelman	H ₂ O	11.3		11.3	Tube	1	30.5		16	-0.0012	
Edelman	H ₂ O	11.3		11.3	Tube	1	33		17.3	-0.0013	
Edelman	H ₂ O	11.3		11.3	Tube	1	37.5		20.3	-0.0015	
Edelman	H ₂ O	11.3		11.3	Tube	1	43		22.9	-0.0013	
Edelman	H ₂ O	11.3		11.3	Tube	1	49		25.8	-0.0016	
Edelman	H ₂ O	11.3		11.3	Tube	1	55.5		28.6	-0.0021	
Edelman	H ₂ O	11.3		11.3	Tube	1	61.5		31.9	-0.002	
Edelman	H ₂ O	11.3		11.3	Tube	1	74		38.1	-0.0032	
Edelman	H ₂ O	11.3		11.3	Tube	1	80		43.9	-0.0034	
Edelman	H ₂ O	11.3		11.3	Tube	1	97		49.2	-0.0034	
Edelman	H ₂ O	11.3		11.3	Tube	1	114		60.6	-0.004	
Edelman	H ₂ O	11.3		11.3	Tube	1	135		70.4	-0.0058	
Edelman	H ₂ O	11.3		11.3	Tube	1	153		78	-0.0065	
Edelman	H ₂ O	11.3		11.3	Tube	1	169		86.7	-0.007	
Edelman	H ₂ O	11.3		11.3	Tube	1	185		95.5	-0.0073	
Labuntsov	H ₂ O	34.3		34.3	Tube	5		2	1700	-0.078	
Labuntsov	H ₂ O	12.1		12.1	Tube	20		4	1160	-0.0371	
Labuntsov	H ₂ O	12.1		12.1	Tube	70		1	580	-0.0779	
Labuntsov	H ₂ O	12.1		12.1	Tube	70		4	1160	-0.053	
Zeitoun	H ₂ O	12.7	12.7	25.4	Ann.	1.14	161.2		214		9.80
Zeitoun	H ₂ O	12.7	12.7	25.4	Ann.	1.1	188.9		210		7.66
Zeitoun	H ₂ O	12.7	12.7	25.4	Ann.	1.18	239.5		208		9.90
Zeitoun	H ₂ O	12.7	12.7	25.4	Ann.	1.56	139		357		12.83
Zeitoun	H ₂ O	12.7	12.7	25.4	Ann.	1.07	181.3		357		12.53
Zeitoun	H ₂ O	12.7	12.7	25.4	Ann.	1.3	327.5		366		15.68
Zeitoun	H ₂ O	12.7	12.7	25.4	Ann.	1.23	283.1		479		15.50
Zeitoun	H ₂ O	12.7	12.7	25.4	Ann.	1.45	390.7		483		17.93
Zeitoun	H ₂ O	12.7	12.7	25.4	Ann.	1.2	224.5		593		15.28
Zeitoun	H ₂ O	12.7	12.7	25.4	Ann.	1.25	288.7		598		18.35
Zeitoun	H ₂ O	12.7	12.7	25.4	Ann.	1.37	348.9		603		14.98
Zeitoun	H ₂ O	12.7	12.7	25.4	Ann.	1.09	198.6		292		14.30
Zeitoun	H ₂ O	12.7	12.7	25.4	Ann.	1.1	202.7		467		13.06
Zeitoun	H ₂ O	12.7	12.7	25.4	Ann.	1.2	152.6		593		20.47

Table E.2: Second half of the onset of significant void database. *Geom.* stands for geometry of the test section. Chan. and Ann. stand for channel and annulus. l_1 is the small characteristic length of the test section, i.e. channel small width or annulus internal diameter. l_2 is the large characteristic length of the test section, i.e. channel large width, annulus external diameter or tube diameter. The data in this table is from Martin 1969, Sabotinov 1974, Sekoguchi et al. 1980, Edelman and Elias 1981, Labuntsov et al. 1984 and Zeitoun 1994.

APPENDIX F



There's always a bigger plot.

F

All local flow boiling simulation results

This appendix contains all simulation results using the set of closures presented in table 7.4 on the local database built during this thesis. The data comes from:

- Cubizolles 1996, part of the DEBORA database (test matrix in table 4.2).
- Kledy 2018, part of the DEBORA database (test matrix in table 4.3).
- St.-Pierre 1965 (test matrix in table 8.1).
- Staub et al. 1969 (test matrix in tables 8.3 and 8.2).
- Martin 1969 (test matrix in tables 8.4 and 8.5).
- Chu et al. 2017 (test matrix in table 8.6).

These experiments are described in detail and the simulation results discussed in chapter 8.

Test tubes III-5 from the Staub et al. 1969 database and 4 and 6 from St.-Pierre 1965 did not converge. This is not necessarily surprising, as the minimalistic set of closures was built for high-pressure conditions and these test tubes have pressures lower than 30 bar.

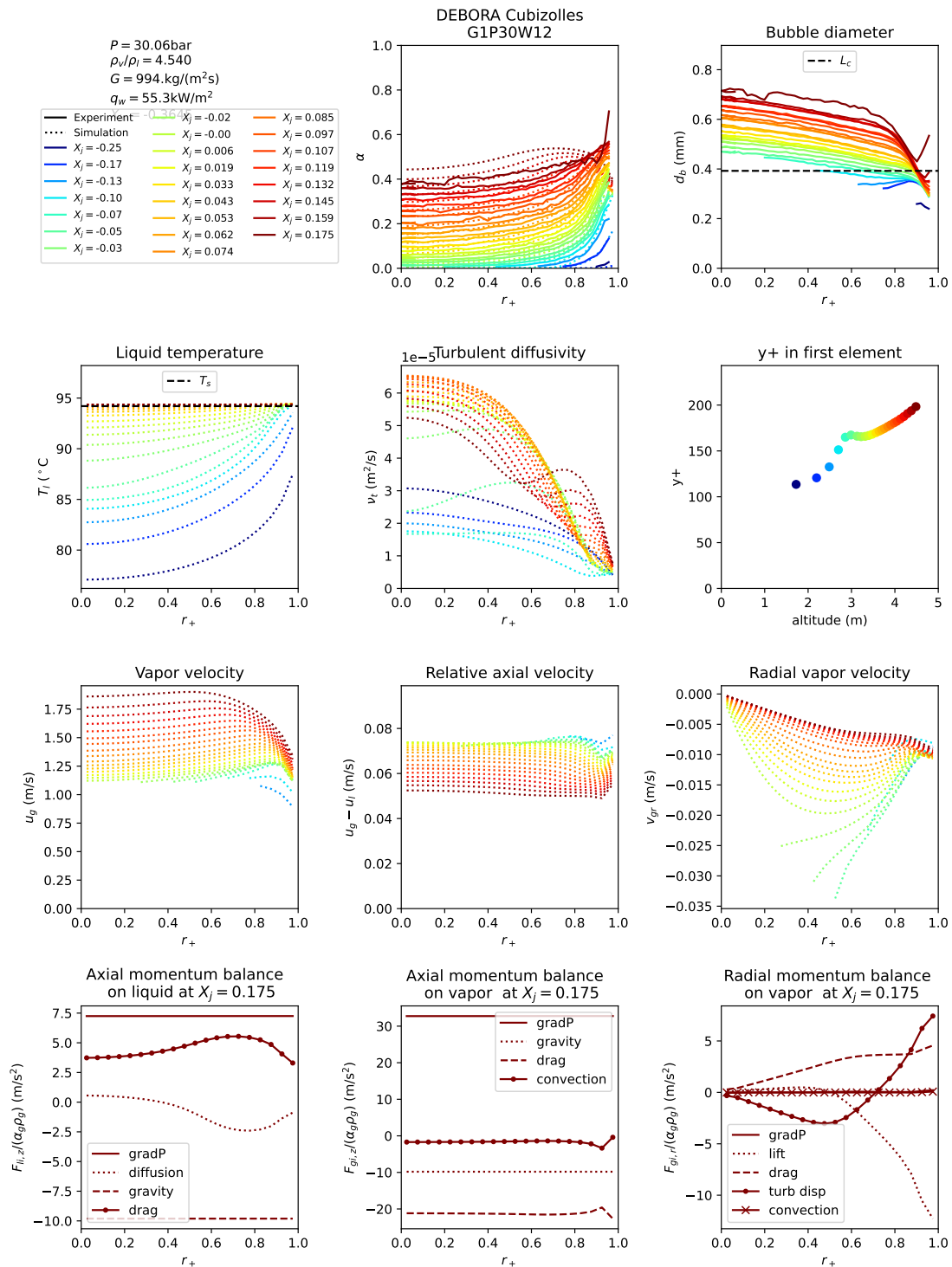


Figure F.1: Simulation results for test tube G1P30W12 of Cubizolles 1996. Experimental results are represented with a full line and simulations with a dashed line.

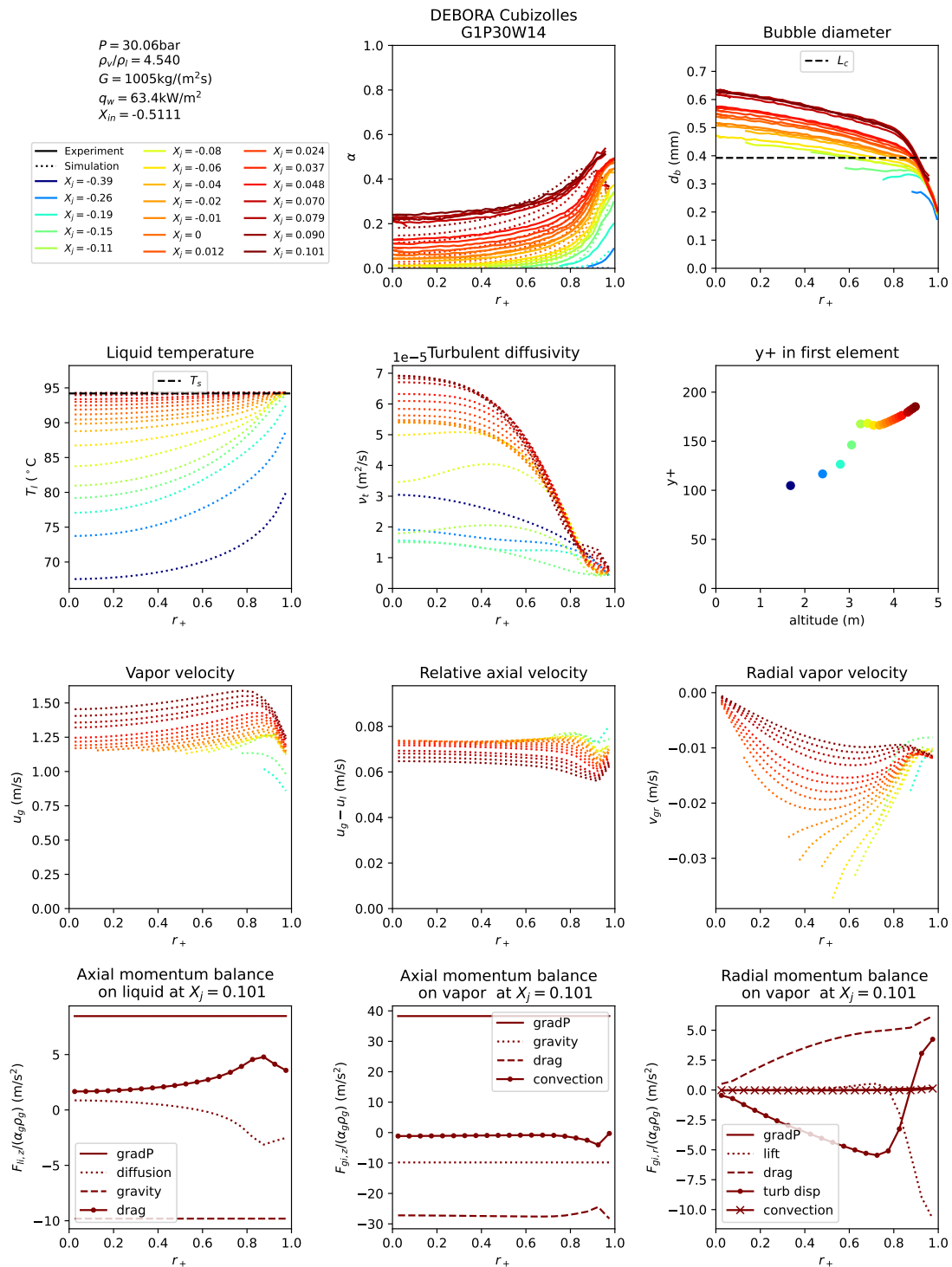


Figure F.2: Simulation results for test tube G1P30W14 of Cubizolles 1996. Experimental results are represented with a full line and simulations with a dashed line.

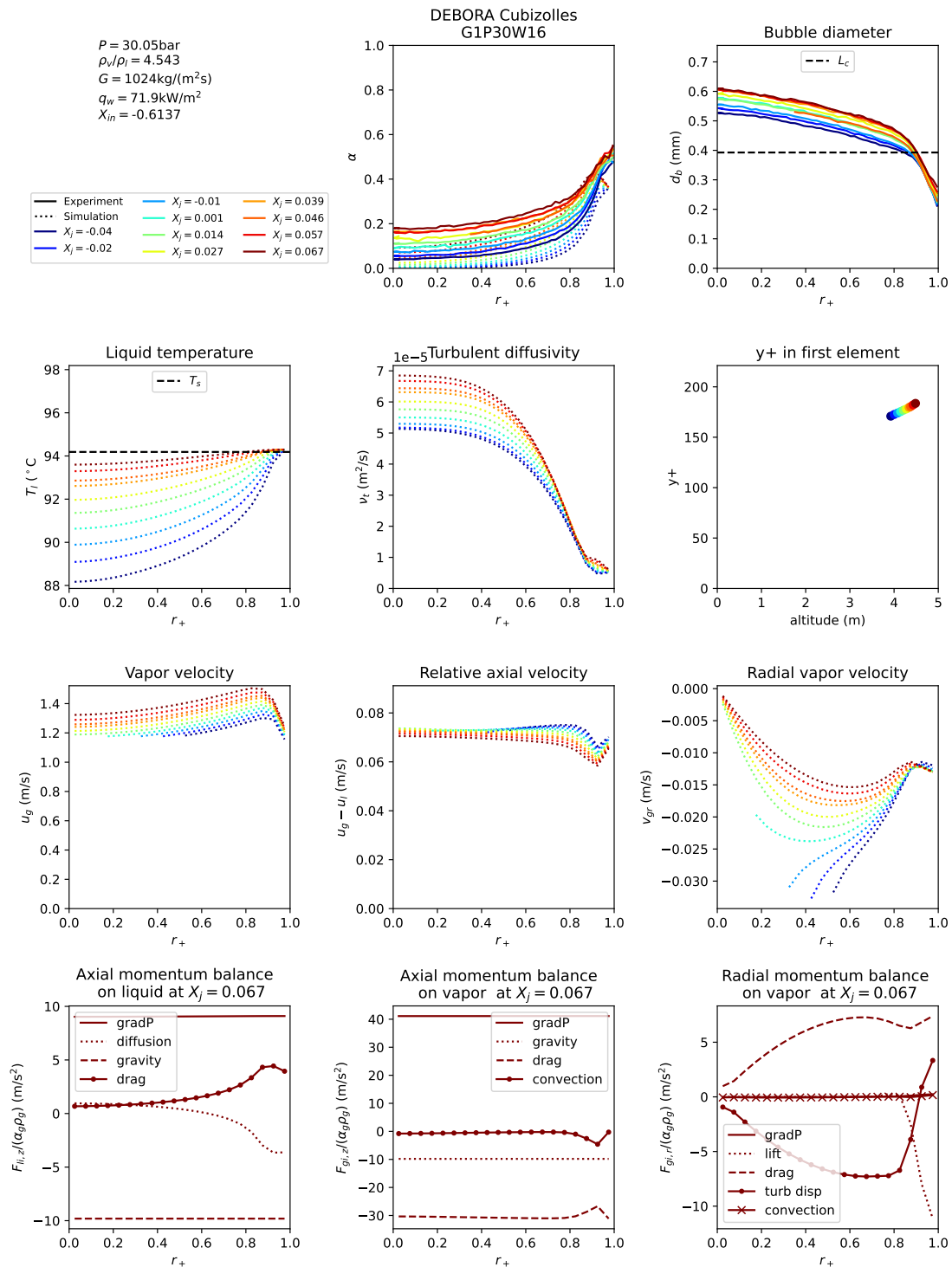


Figure F.3: Simulation results for test tube G1P30W16 of Cubizolles 1996. Experimental results are represented with a full line and simulations with a dashed line.

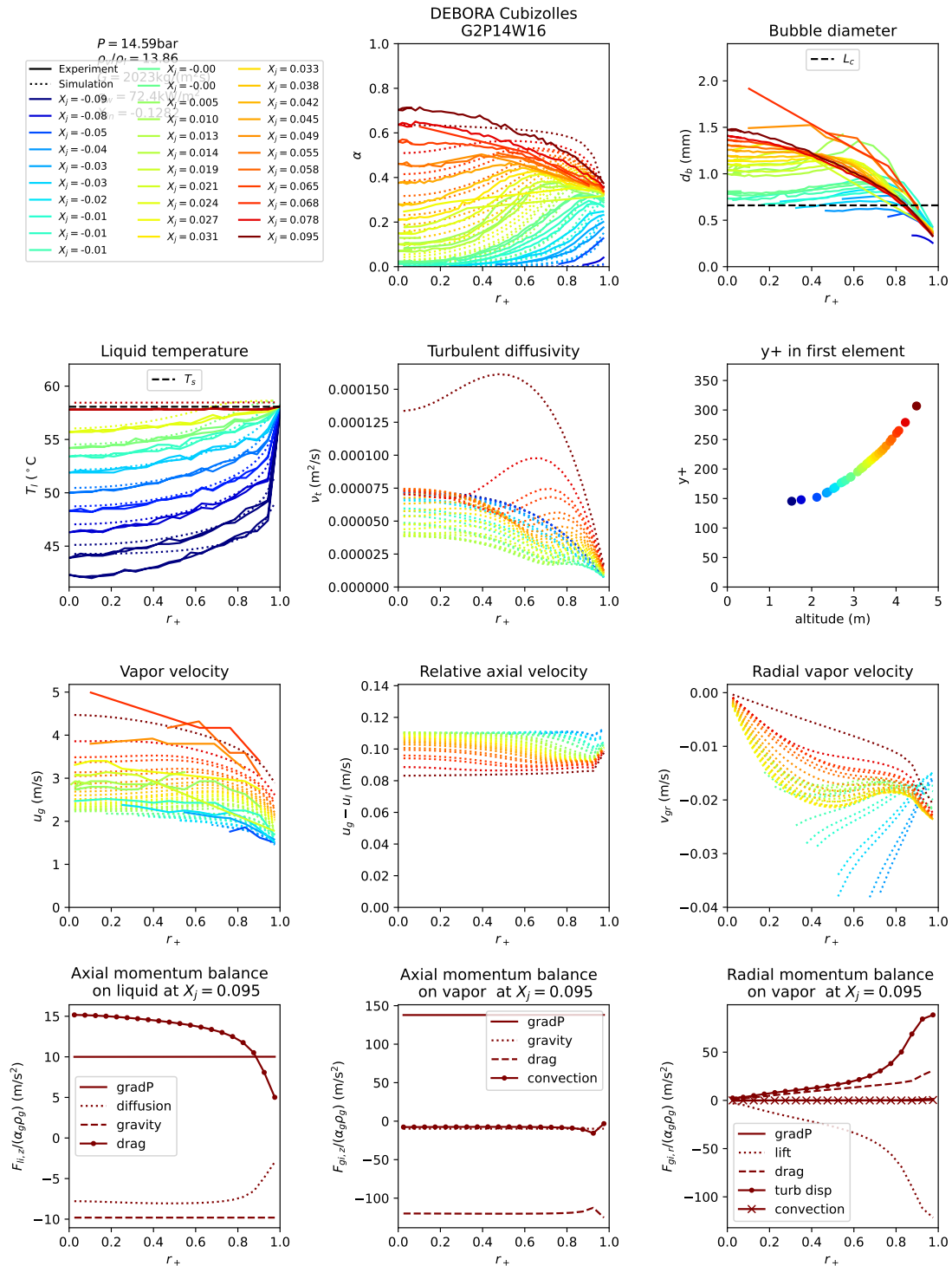


Figure F.4: Simulation results for test tube G2P14W16 of Cubizolles 1996. Experimental results are represented with a full line and simulations with a dashed line.

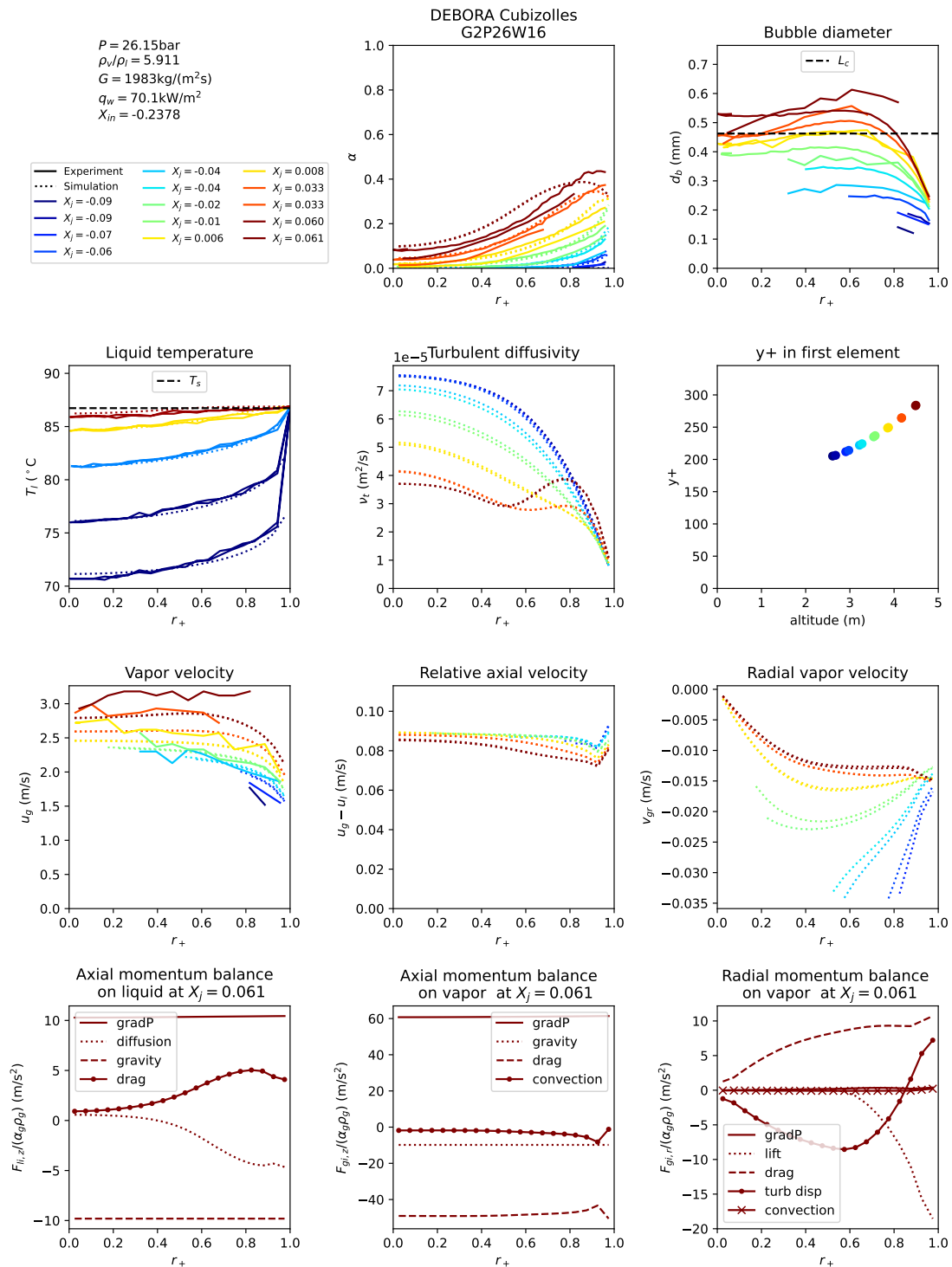


Figure F.5: Simulation results for test tube G2P26W16 of Cubizolles 1996. Experimental results are represented with a full line and simulations with a dashed line.

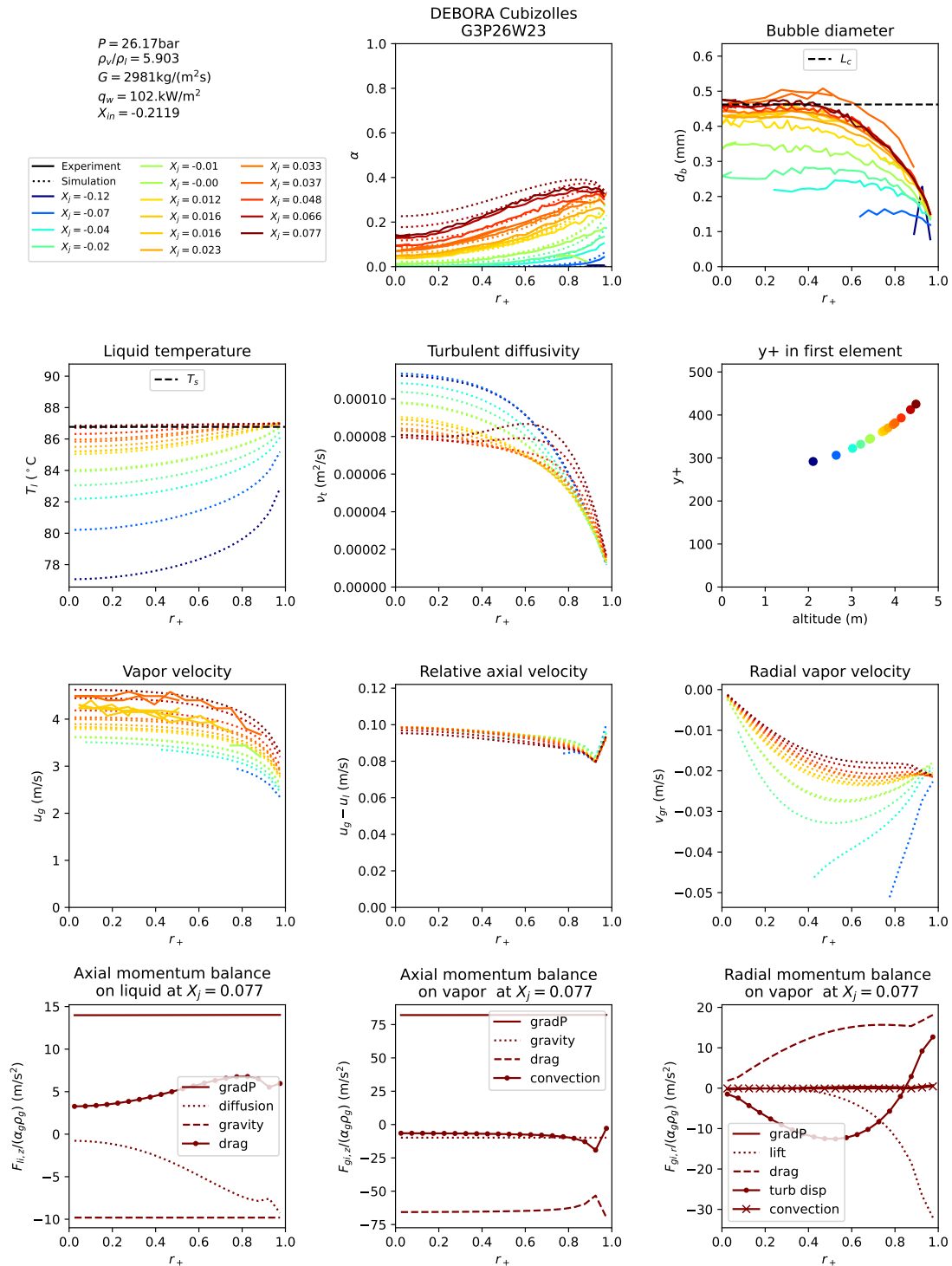


Figure F.6: Simulation results for test tube G3P26W23 of Cubizolles 1996. Experimental results are represented with a full line and simulations with a dashed line.

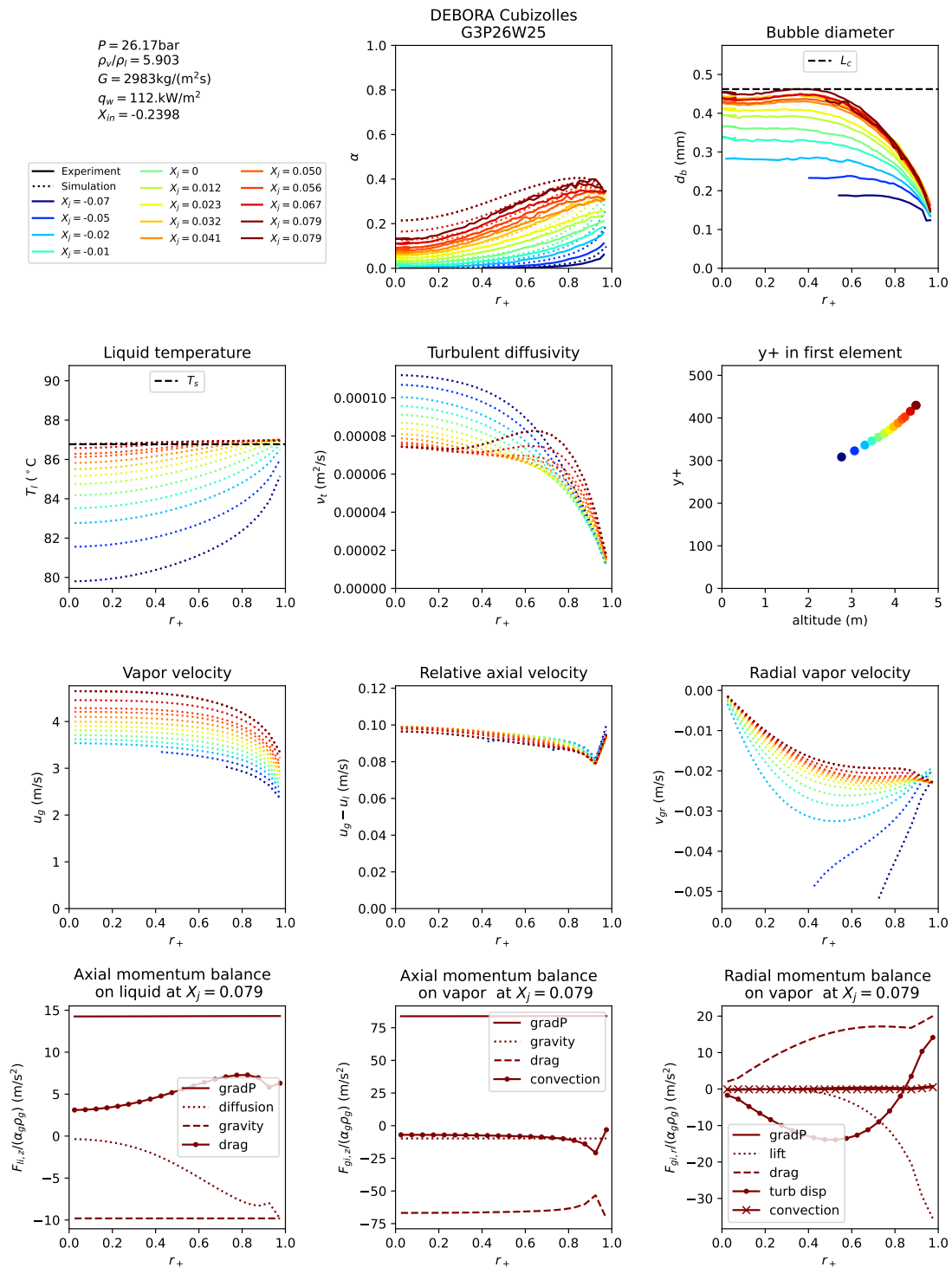


Figure F.7: Simulation results for test tube G3P26W25 of Cubizolles 1996. Experimental results are represented with a full line and simulations with a dashed line.

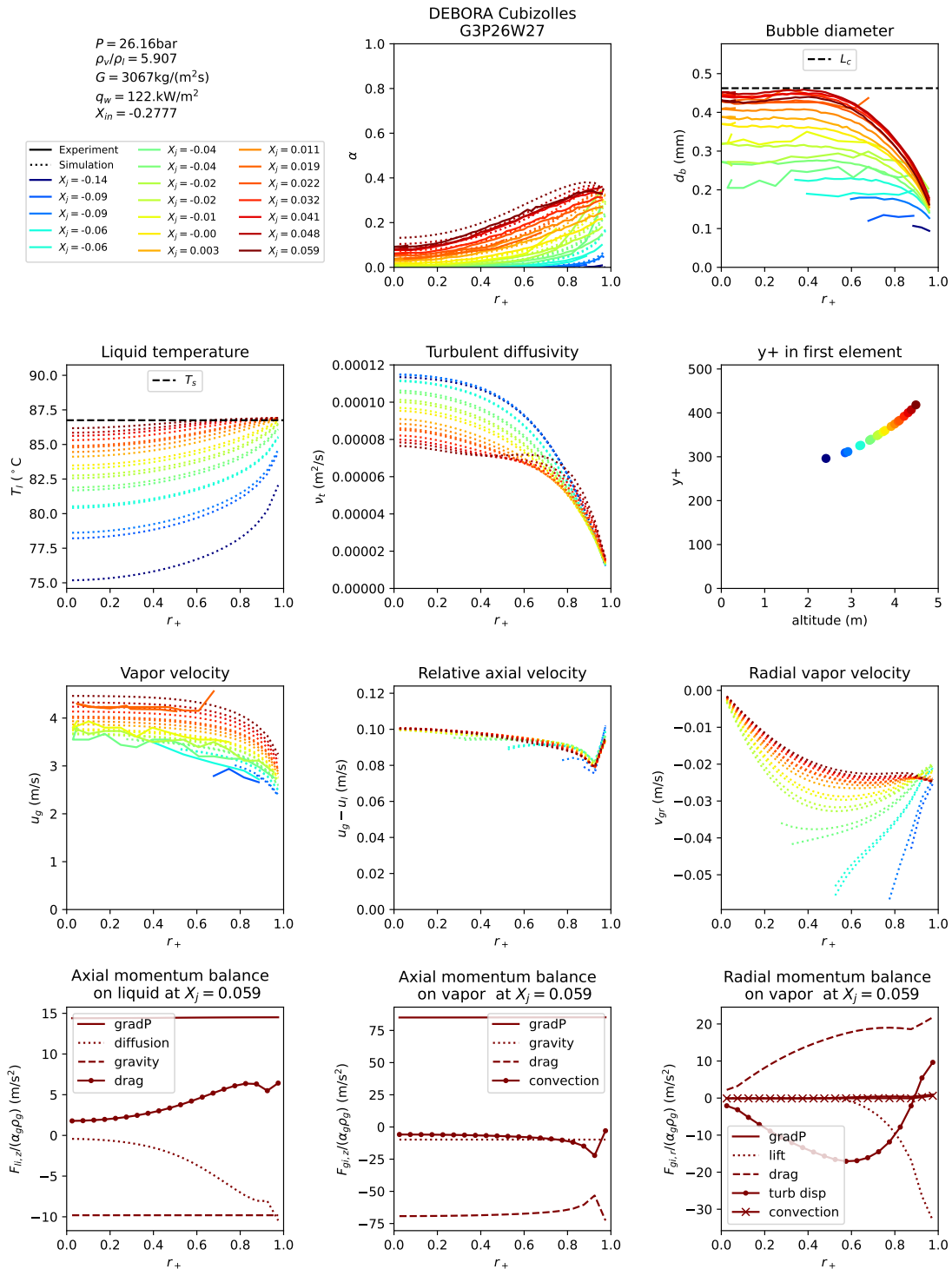
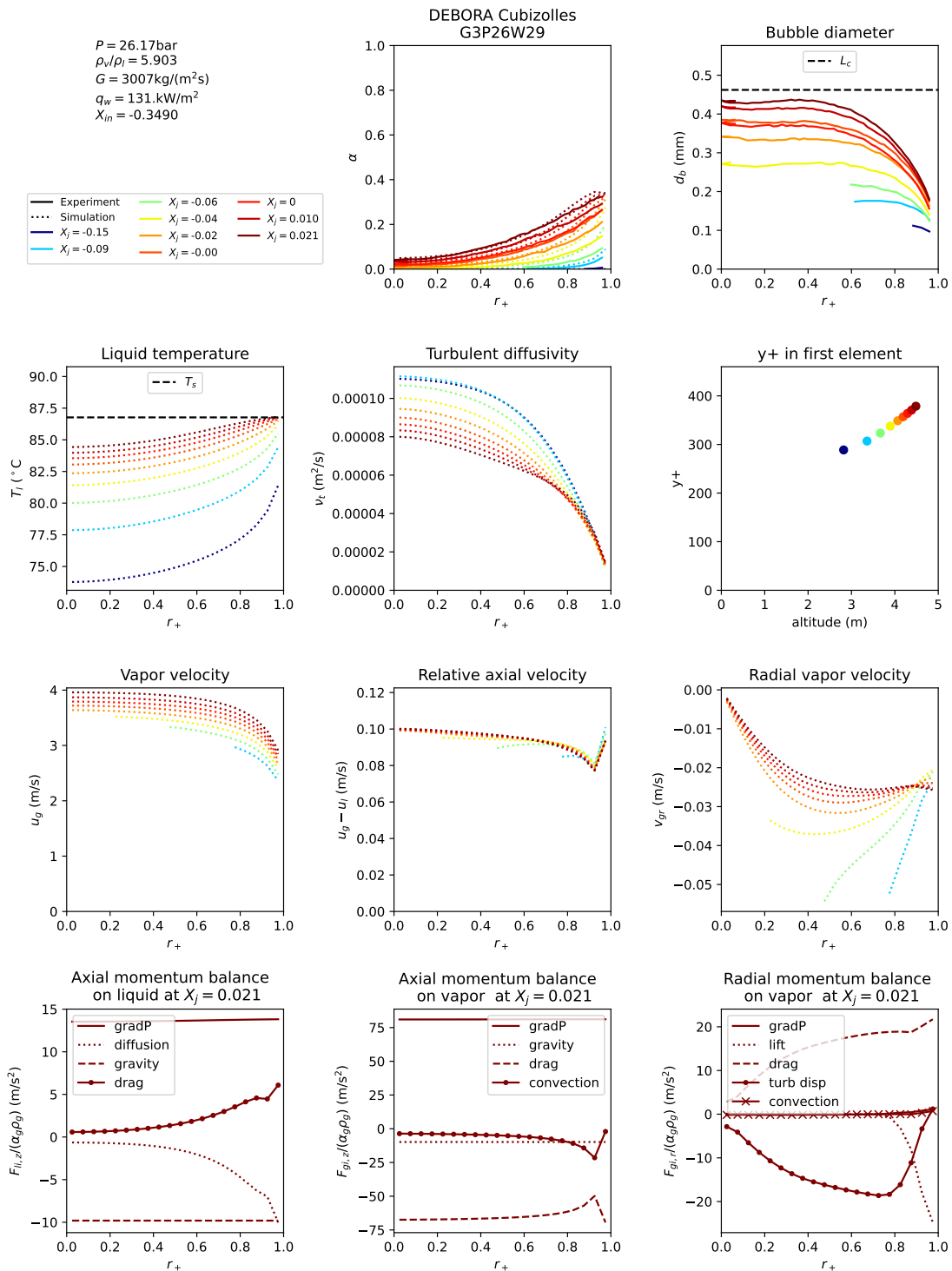
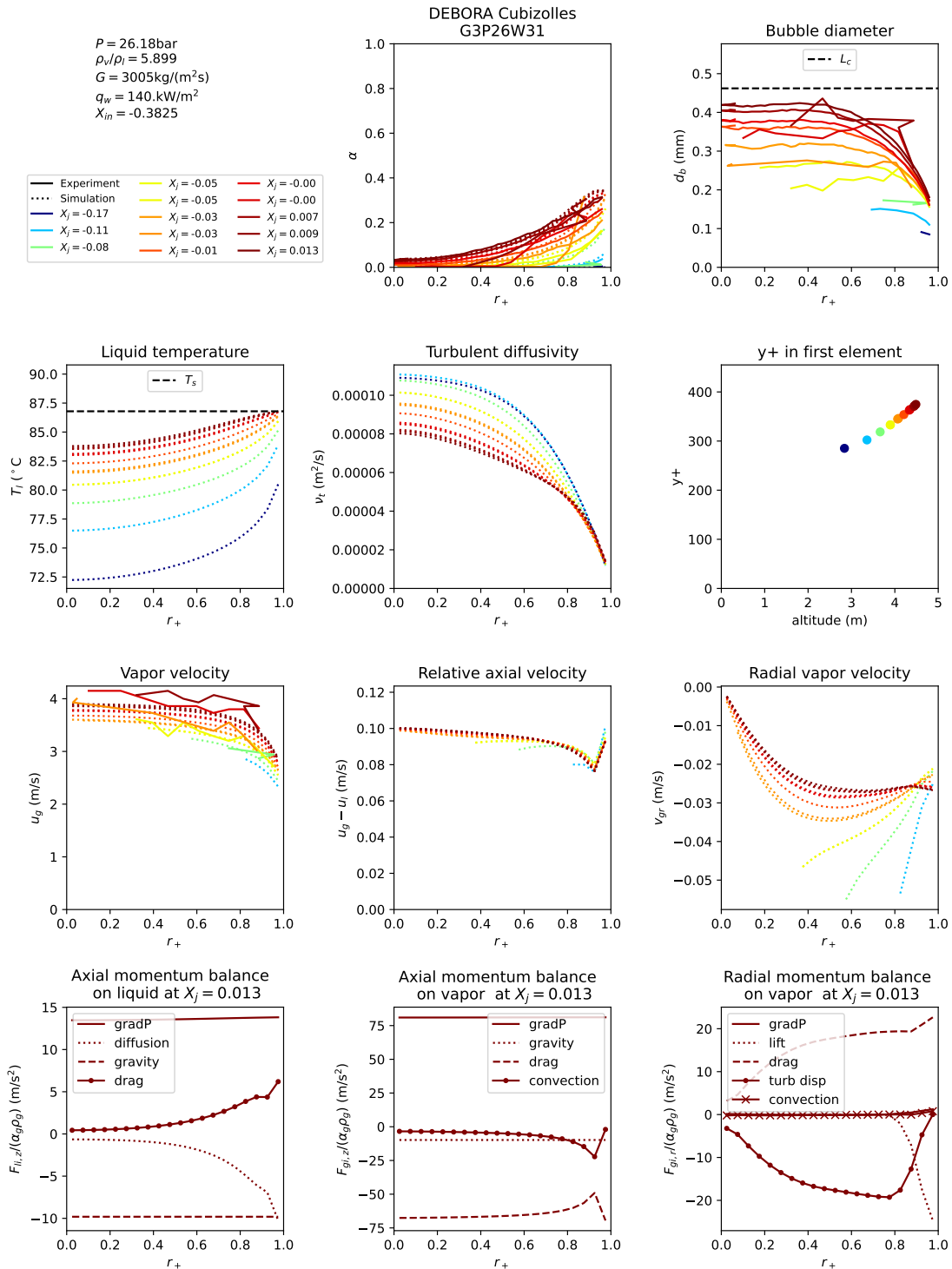


Figure F.8: Simulation results for test tube G3P26W27 of Cubizolles 1996. Experimental results are represented with a full line and simulations with a dashed line.





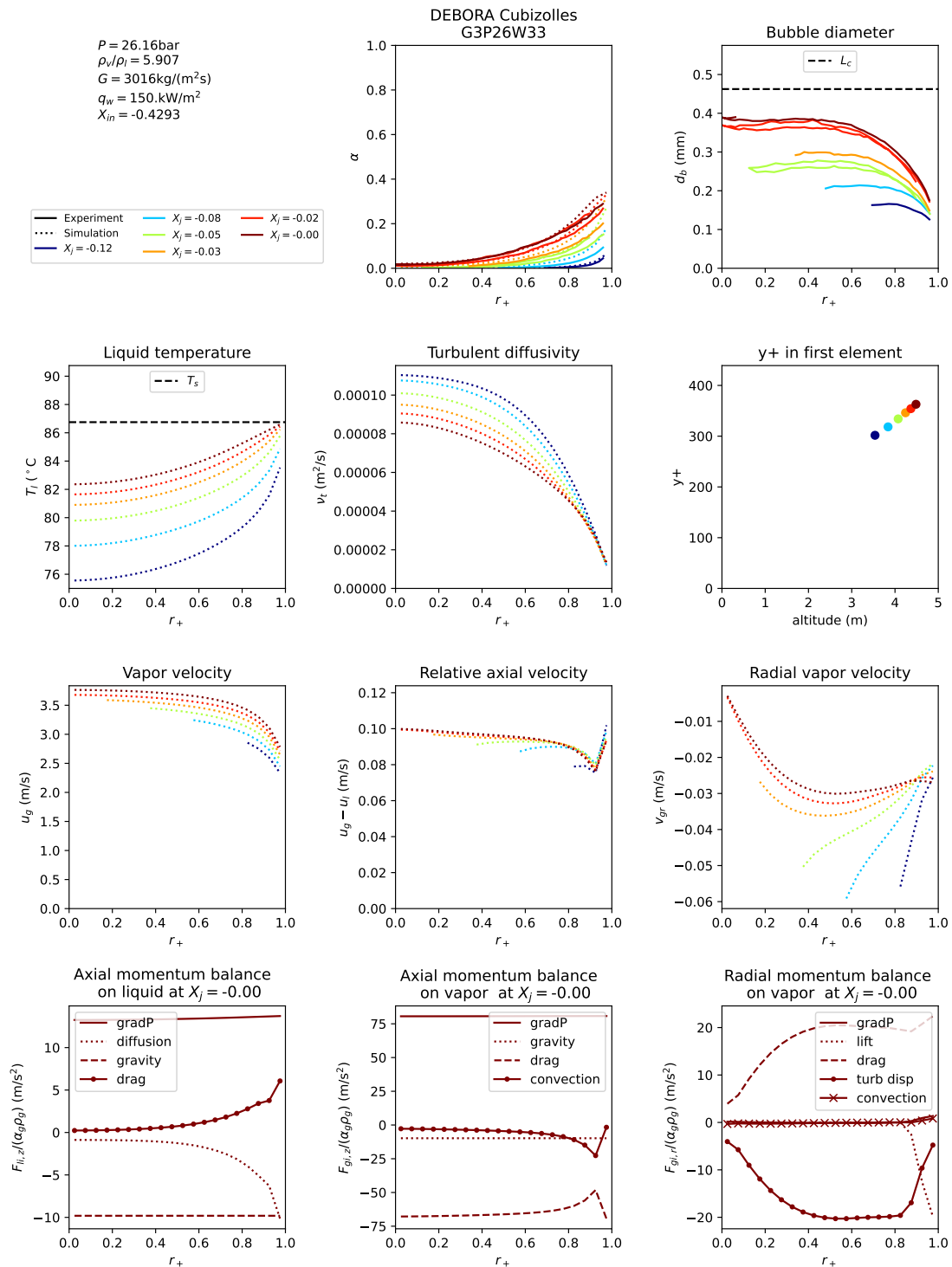


Figure F.11: Simulation results for test tube G3P26W33 of Cubizolles 1996. Experimental results are represented with a full line and simulations with a dashed line.

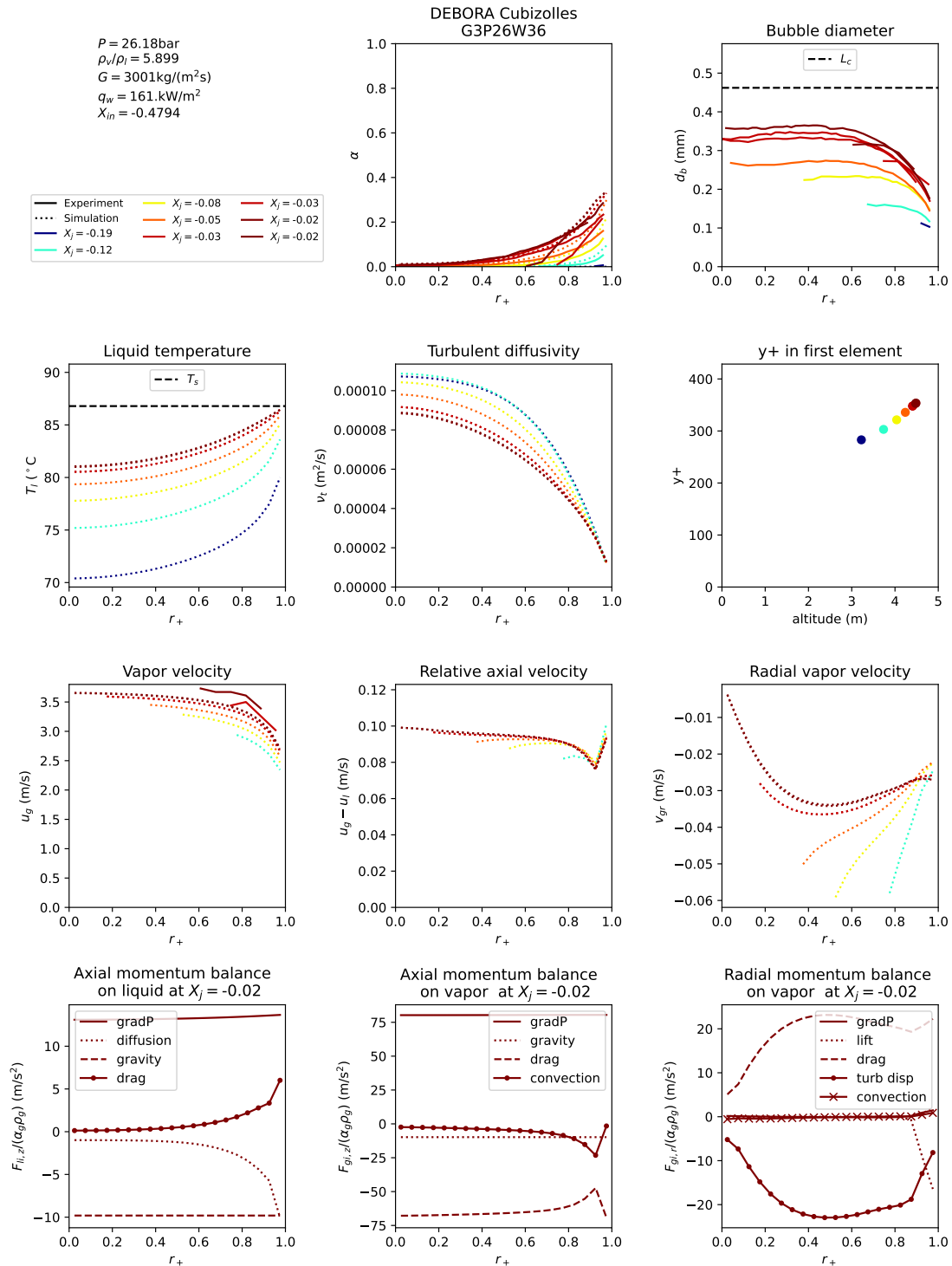


Figure F.12: Simulation results for test tube G3P26W36 of Cubizolles 1996. Experimental results are represented with a full line and simulations with a dashed line.

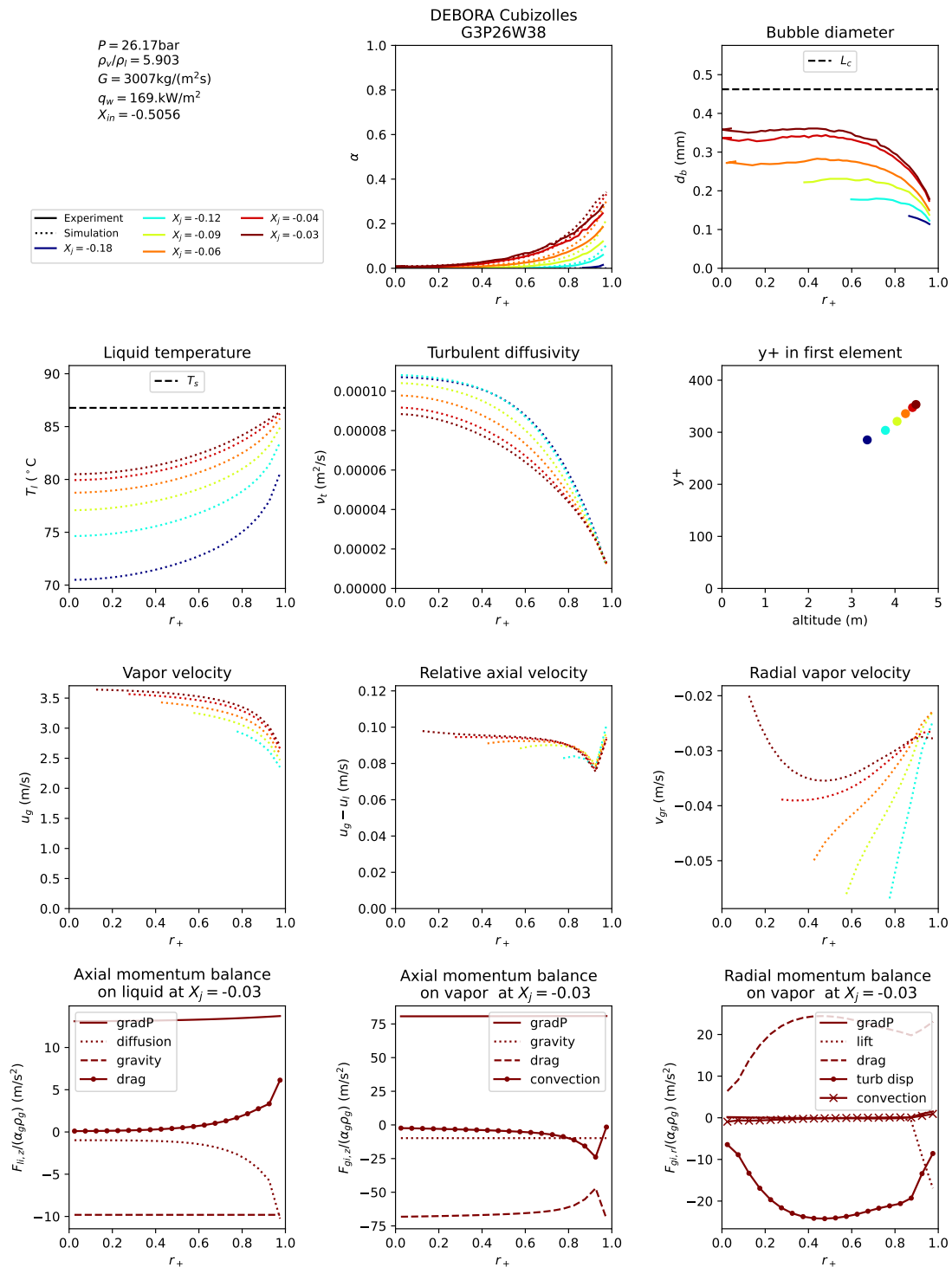
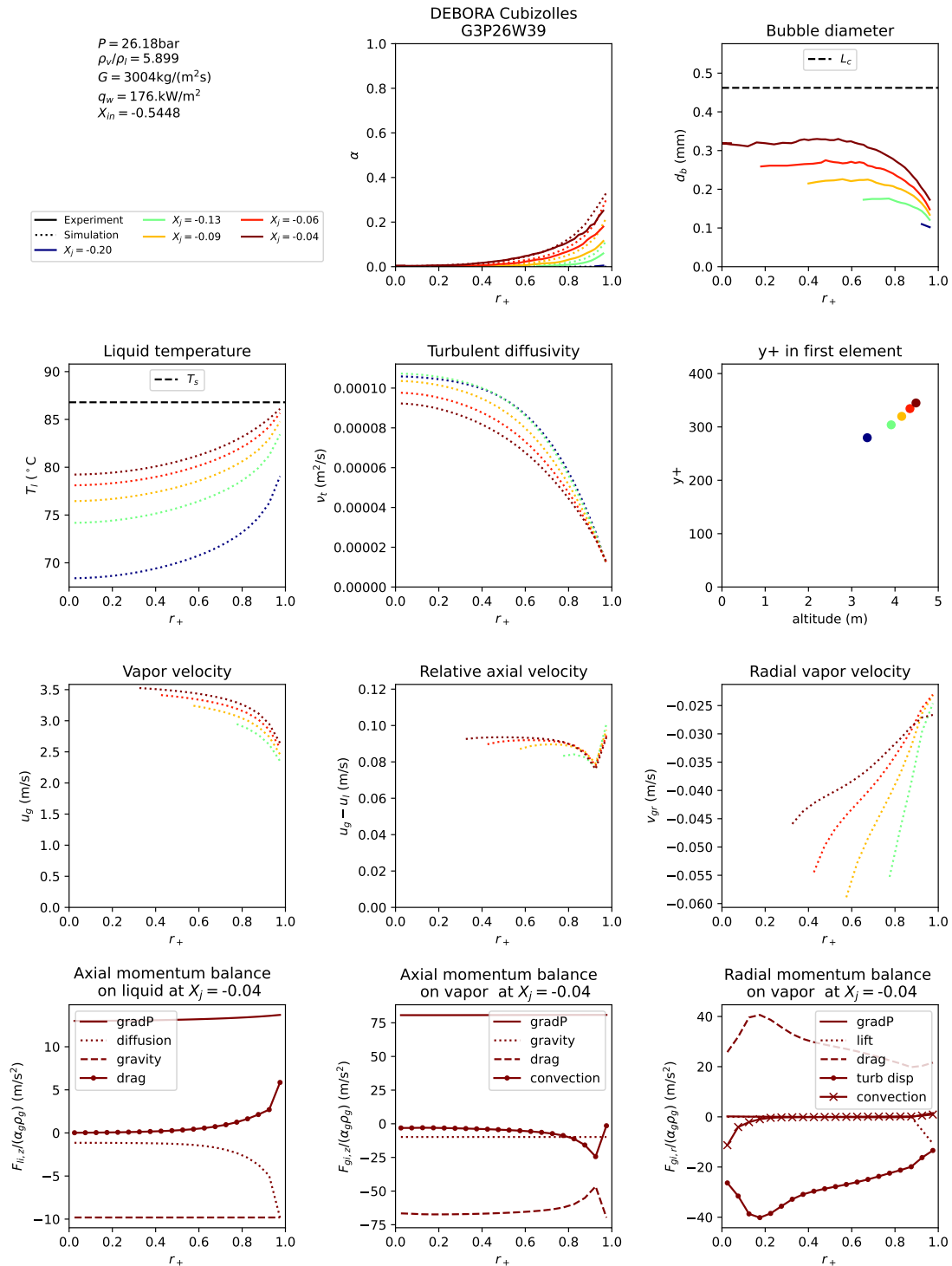
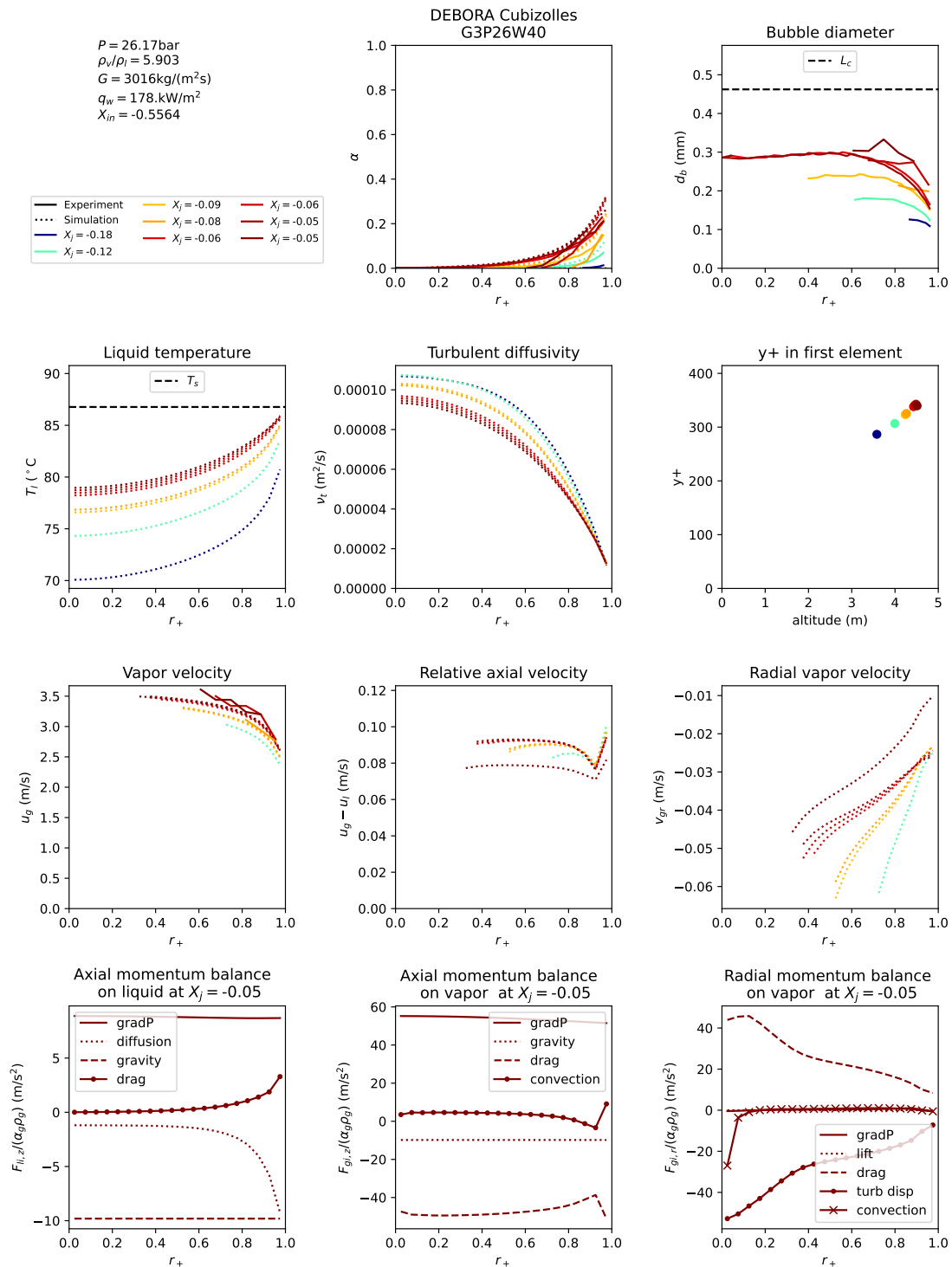


Figure F.13: Simulation results for test tube G3P26W38 of Cubizolles 1996. Experimental results are represented with a full line and simulations with a dashed line.





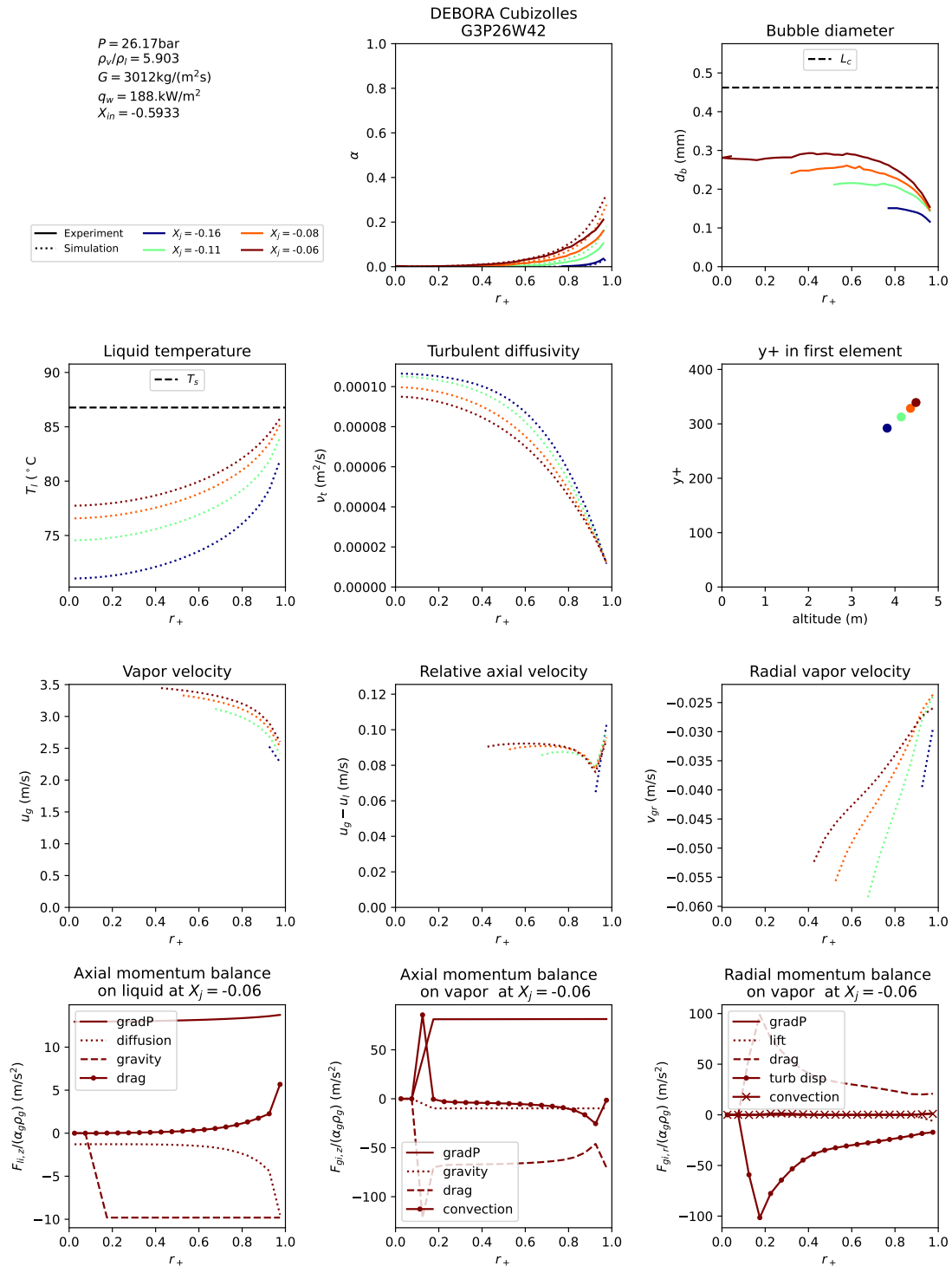


Figure F.16: Simulation results for test tube G3P26W42 of Cubizolles 1996. Experimental results are represented with a full line and simulations with a dashed line.

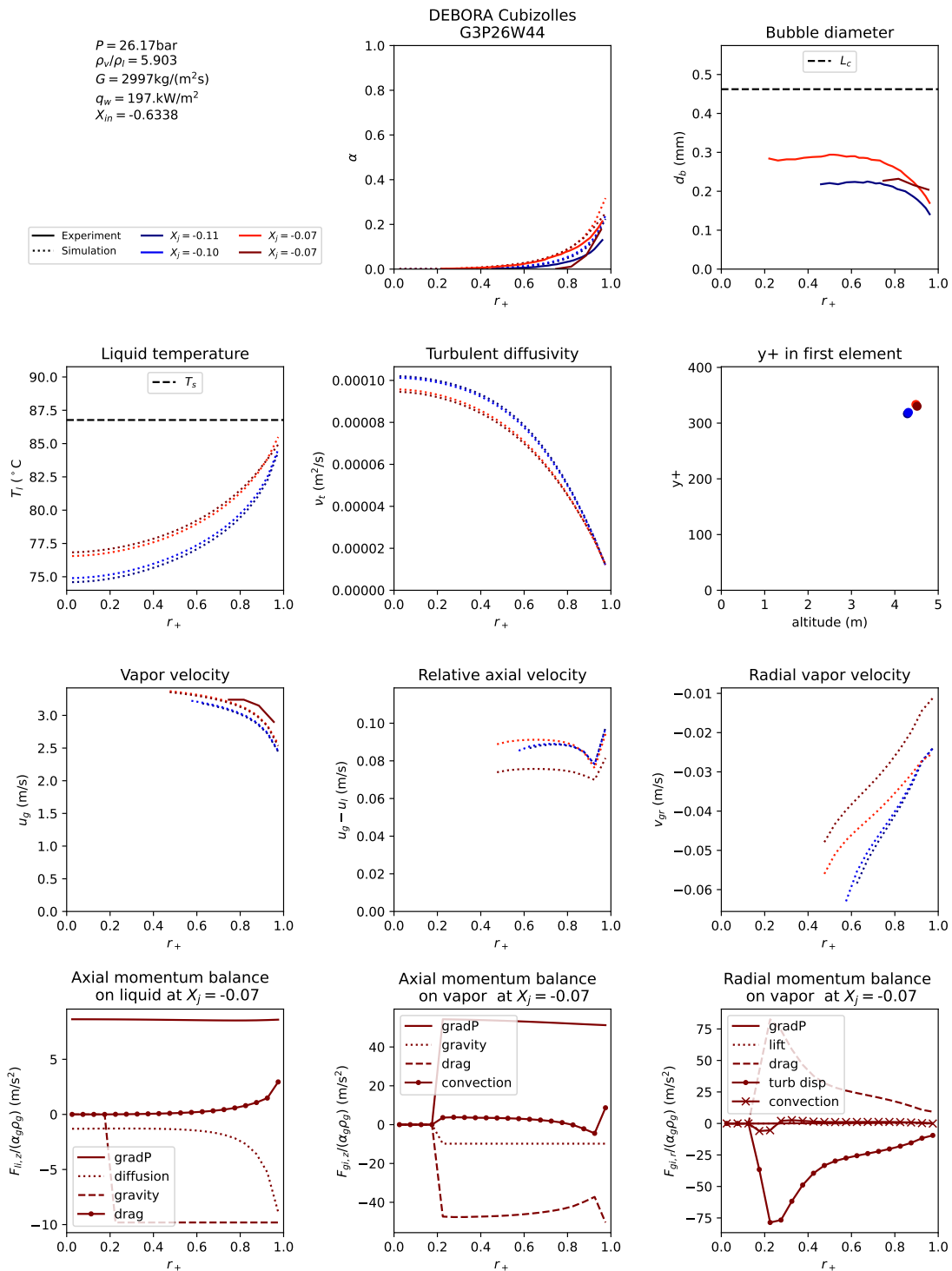


Figure F.17: Simulation results for test tube G3P26W44 of Cubizolles 1996. Experimental results are represented with a full line and simulations with a dashed line.

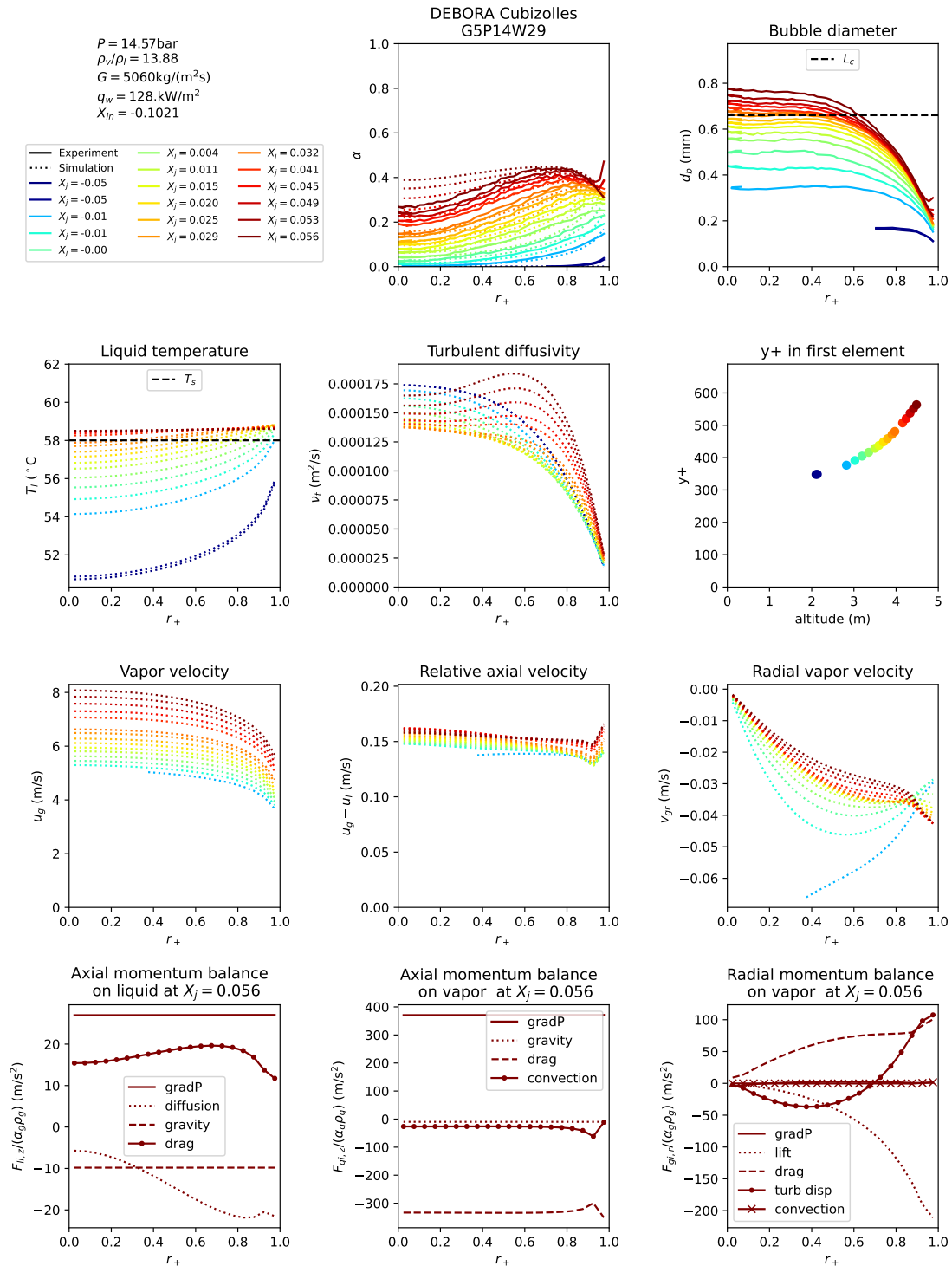


Figure F.18: Simulation results for test tube G5P14W29 of Cubizolles 1996. Experimental results are represented with a full line and simulations with a dashed line.

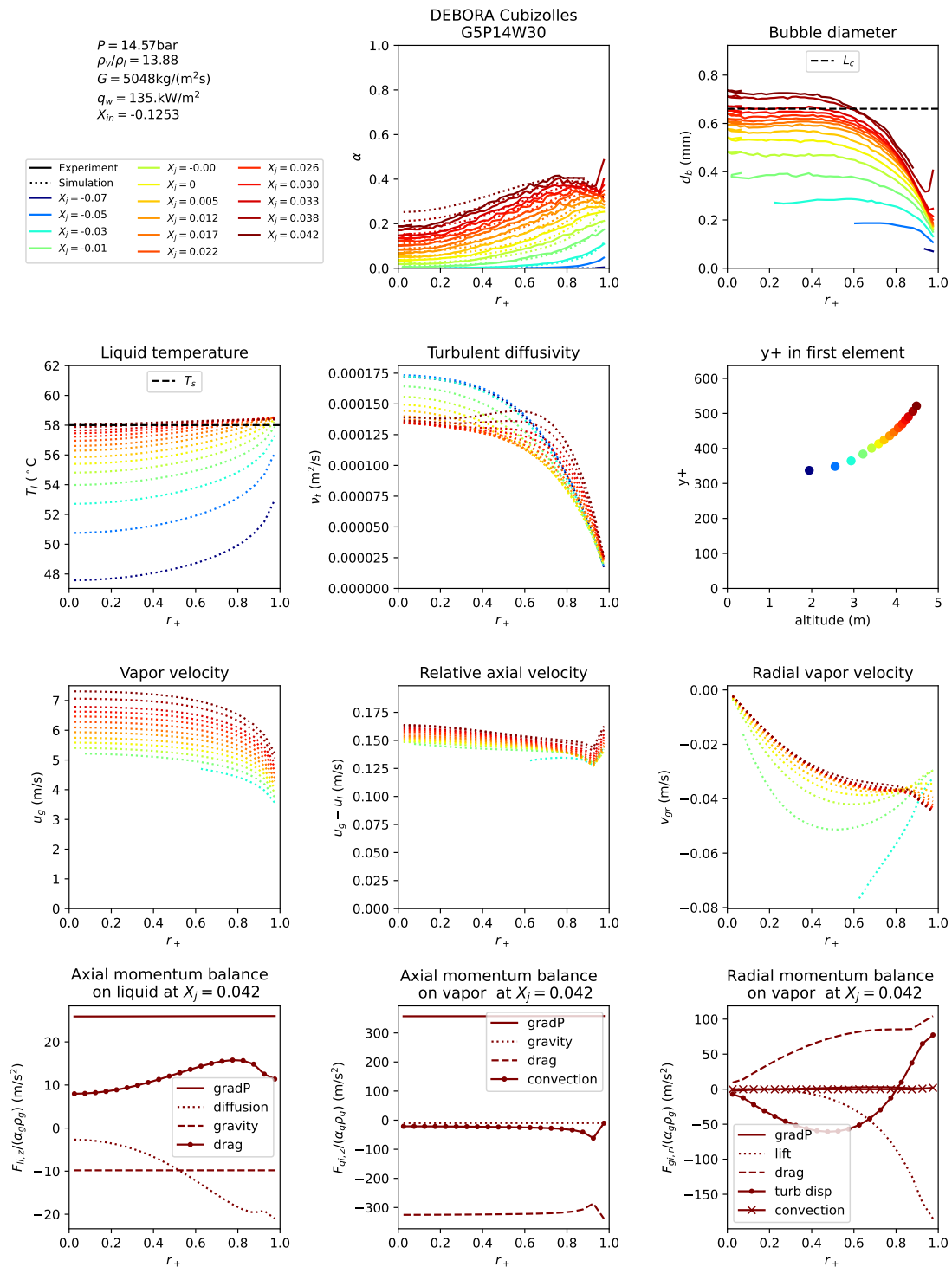
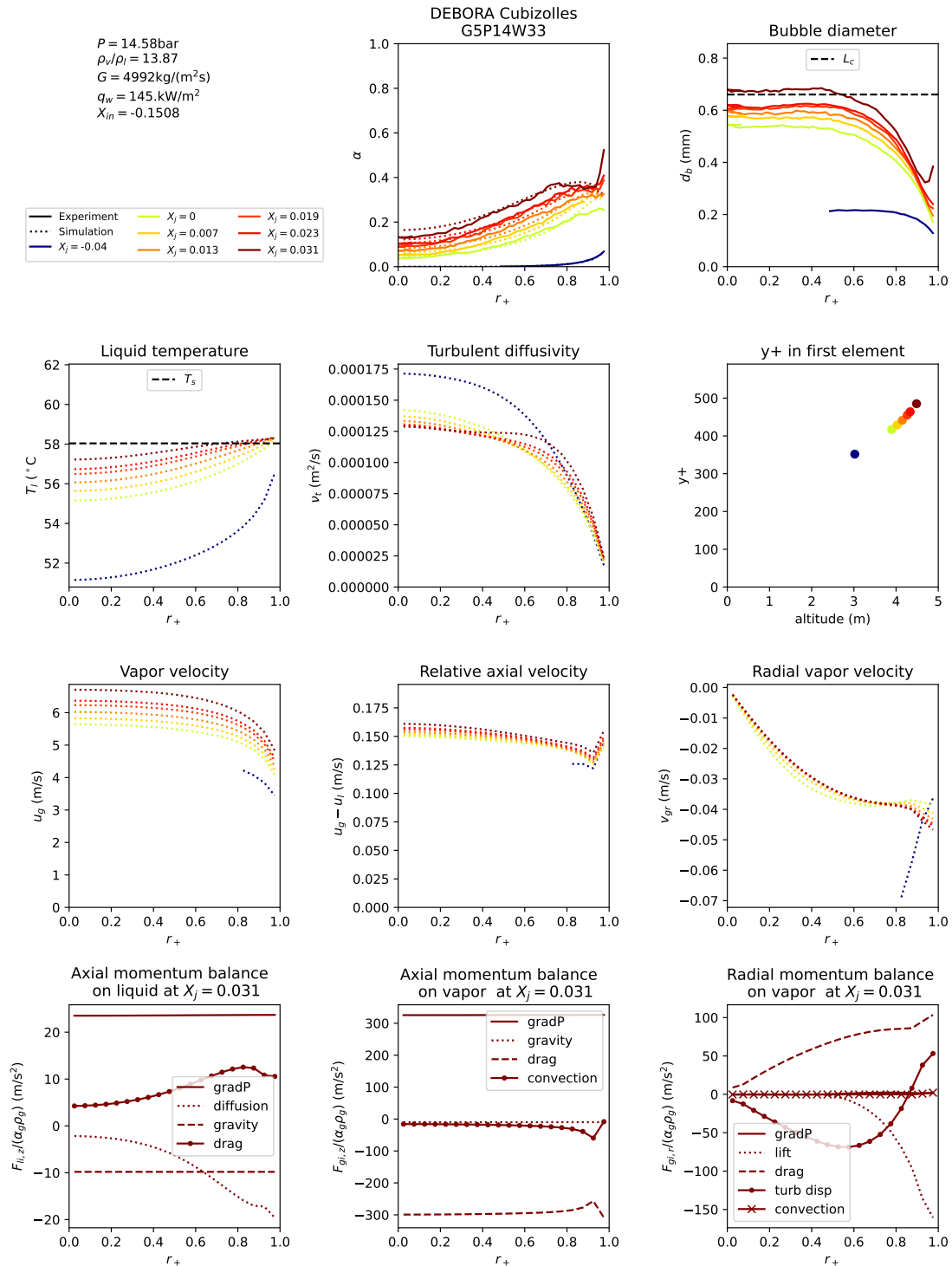


Figure F.19: Simulation results for test tube G5P14W30 of Cubizolles 1996. Experimental results are represented with a full line and simulations with a dashed line.



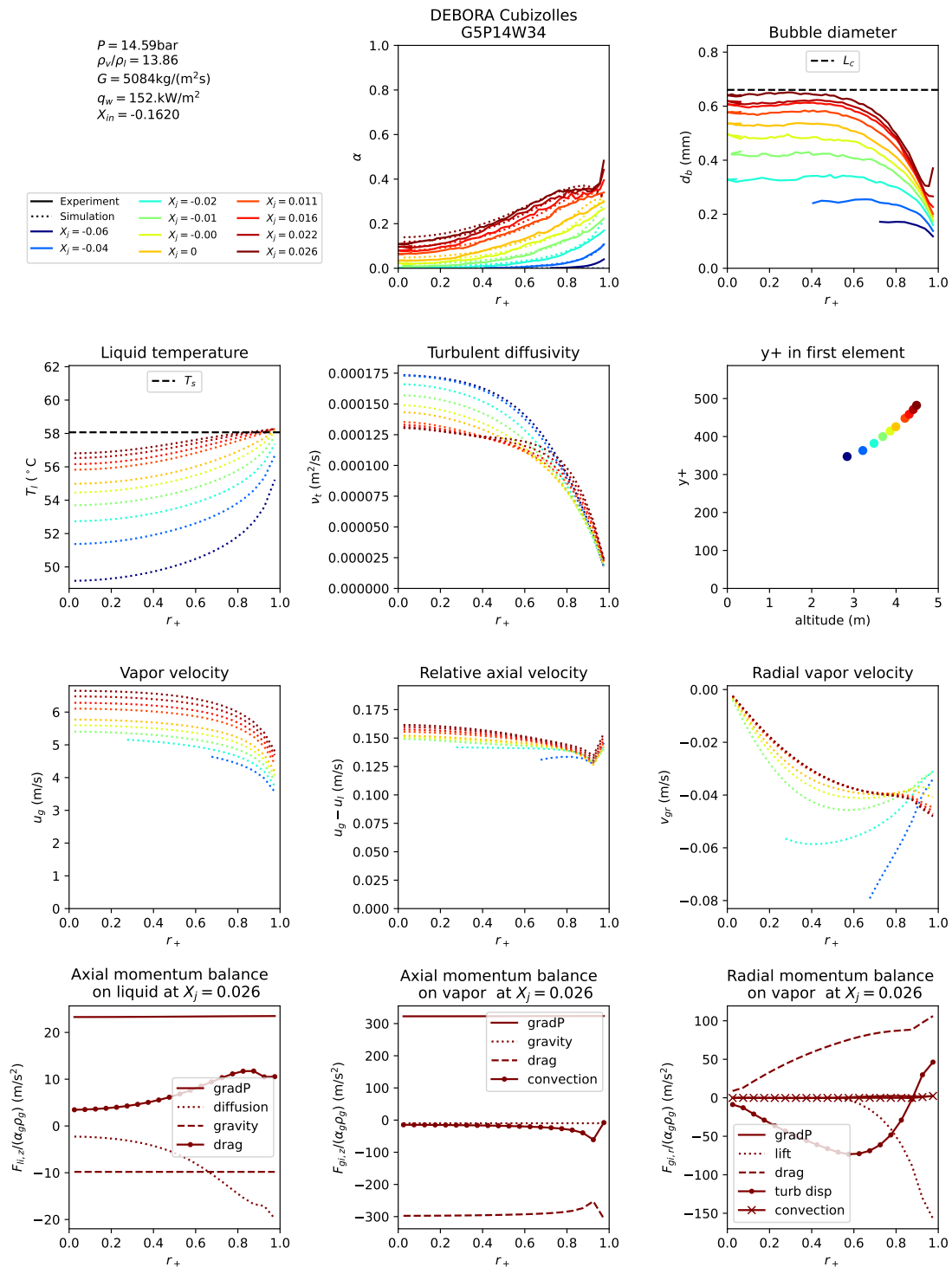
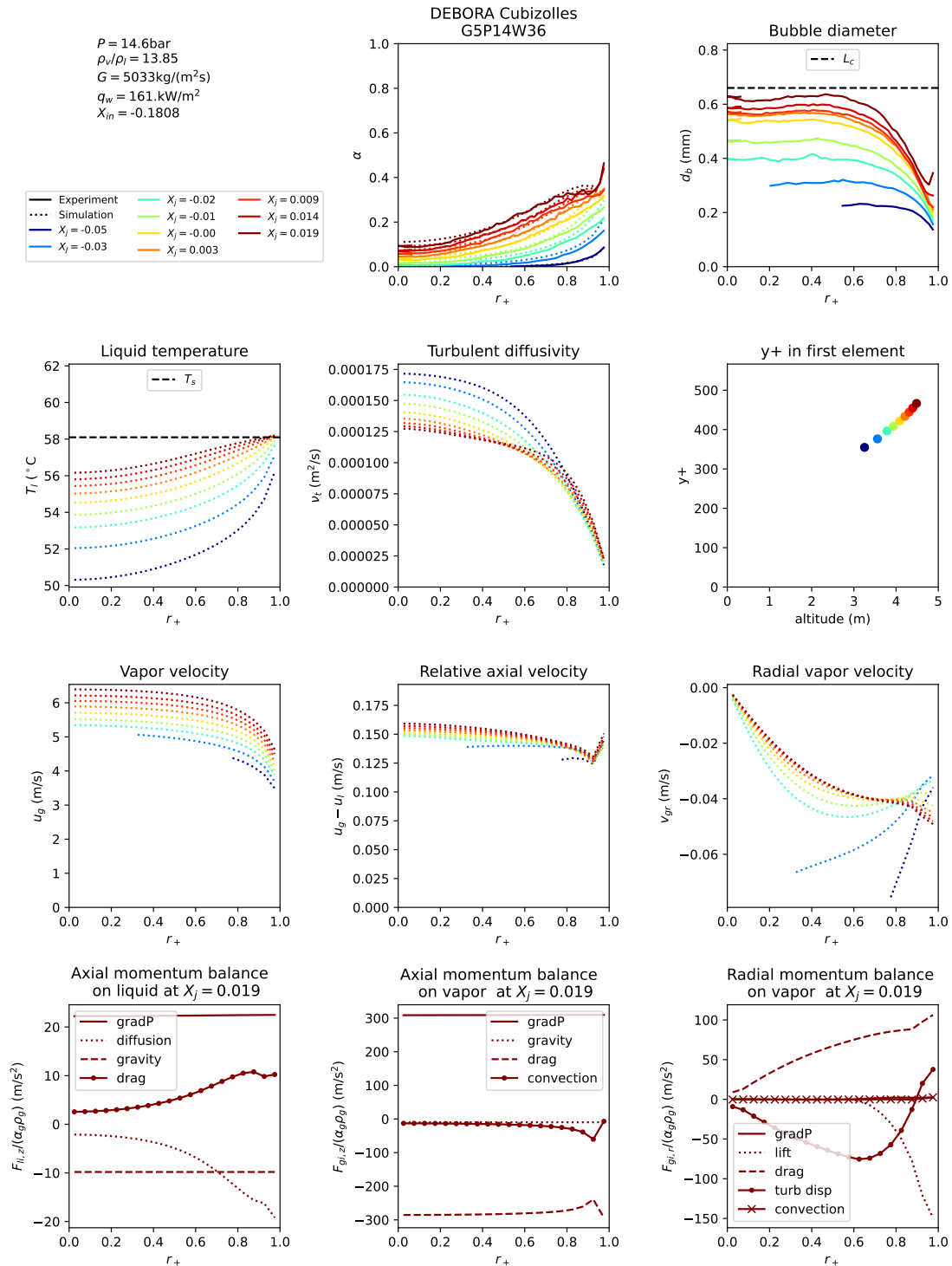


Figure F.21: Simulation results for test tube G5P14W34 of Cubizolles 1996. Experimental results are represented with a full line and simulations with a dashed line.



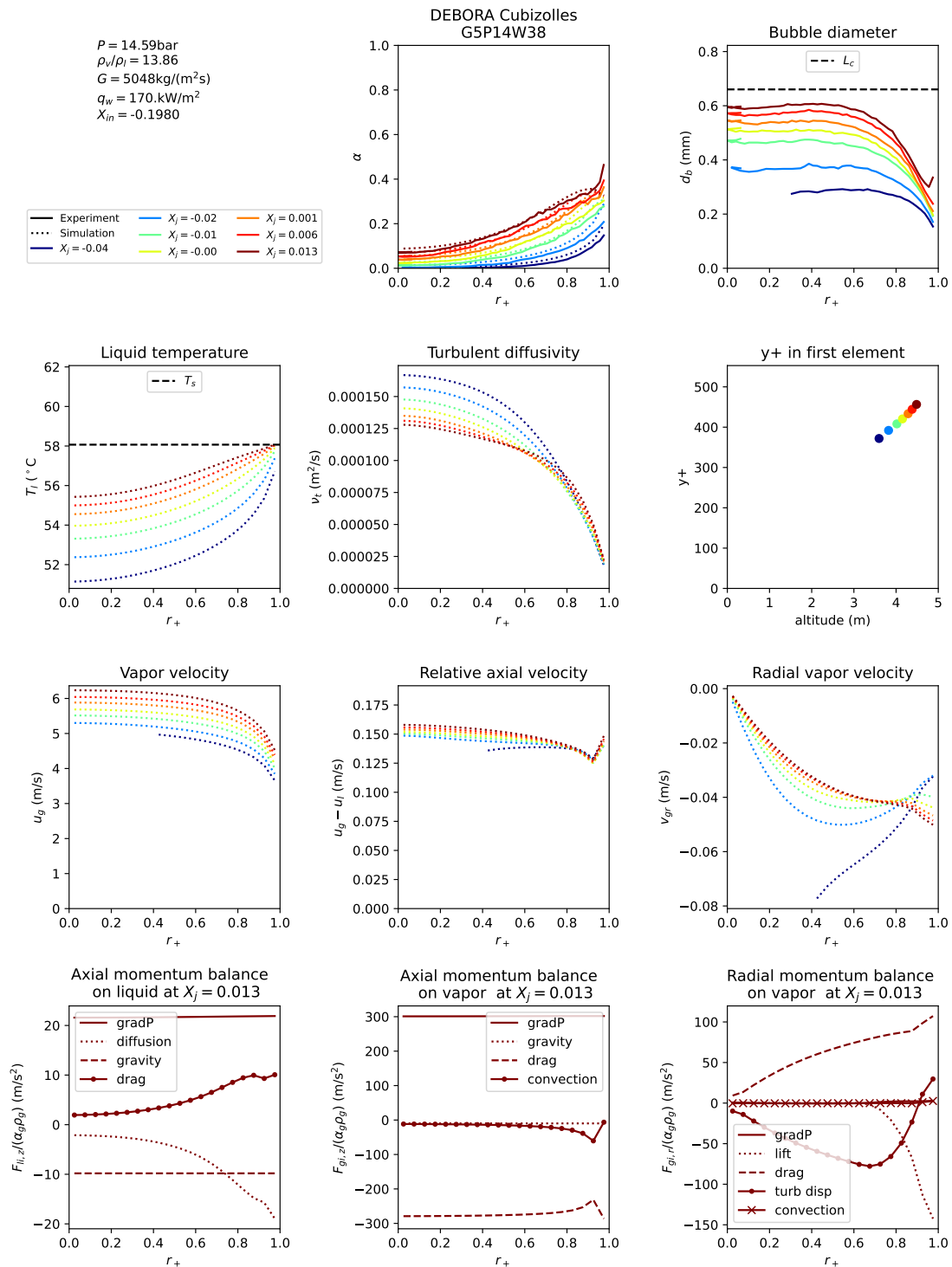


Figure F.23: Simulation results for test tube G5P14W38 of Cubizolles 1996. Experimental results are represented with a full line and simulations with a dashed line.

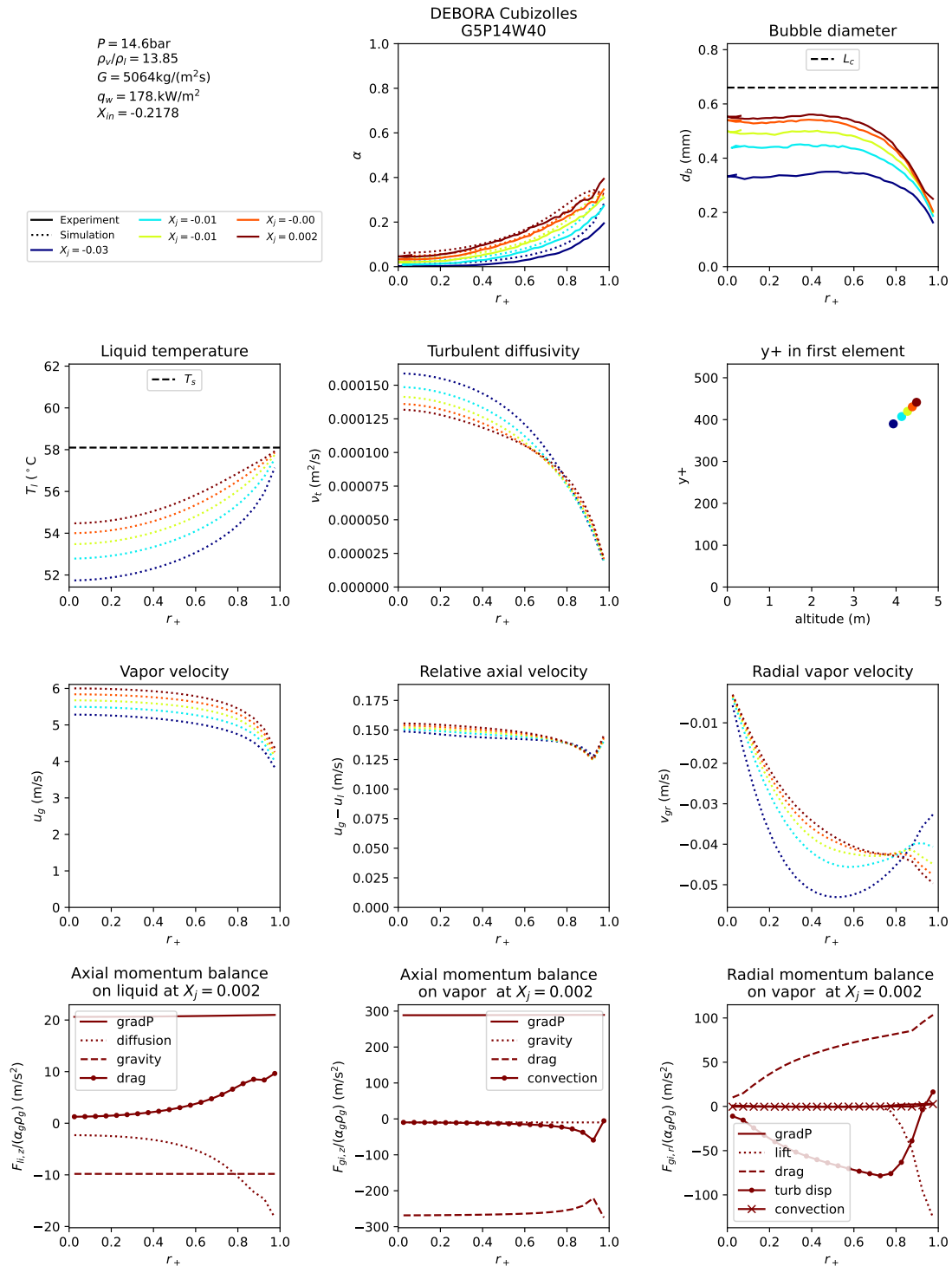


Figure F.24: Simulation results for test tube G5P14W40 of Cubizolles 1996. Experimental results are represented with a full line and simulations with a dashed line.

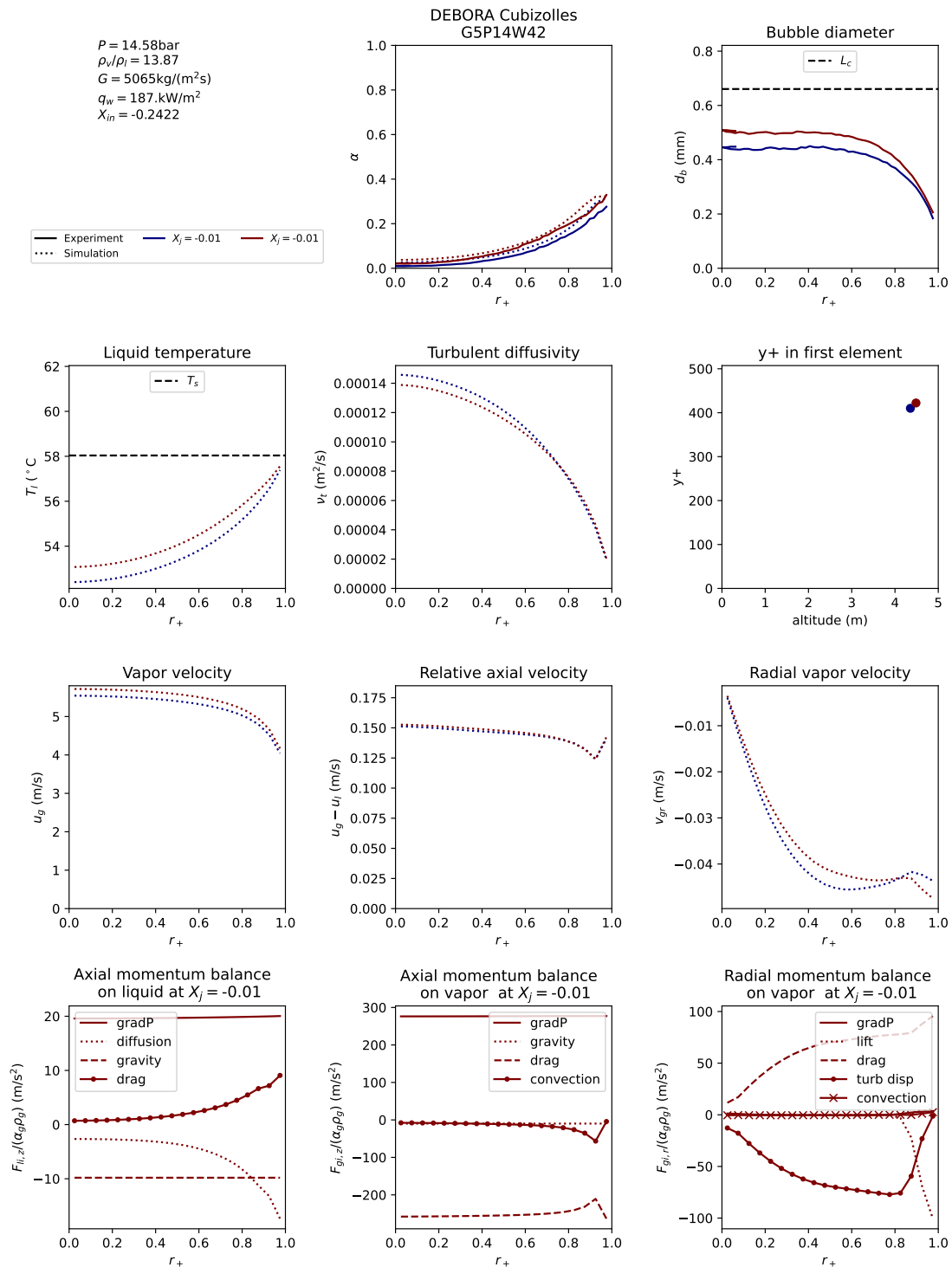


Figure F.25: Simulation results for test tube G5P14W42 of Cubizolles 1996. Experimental results are represented with a full line and simulations with a dashed line.

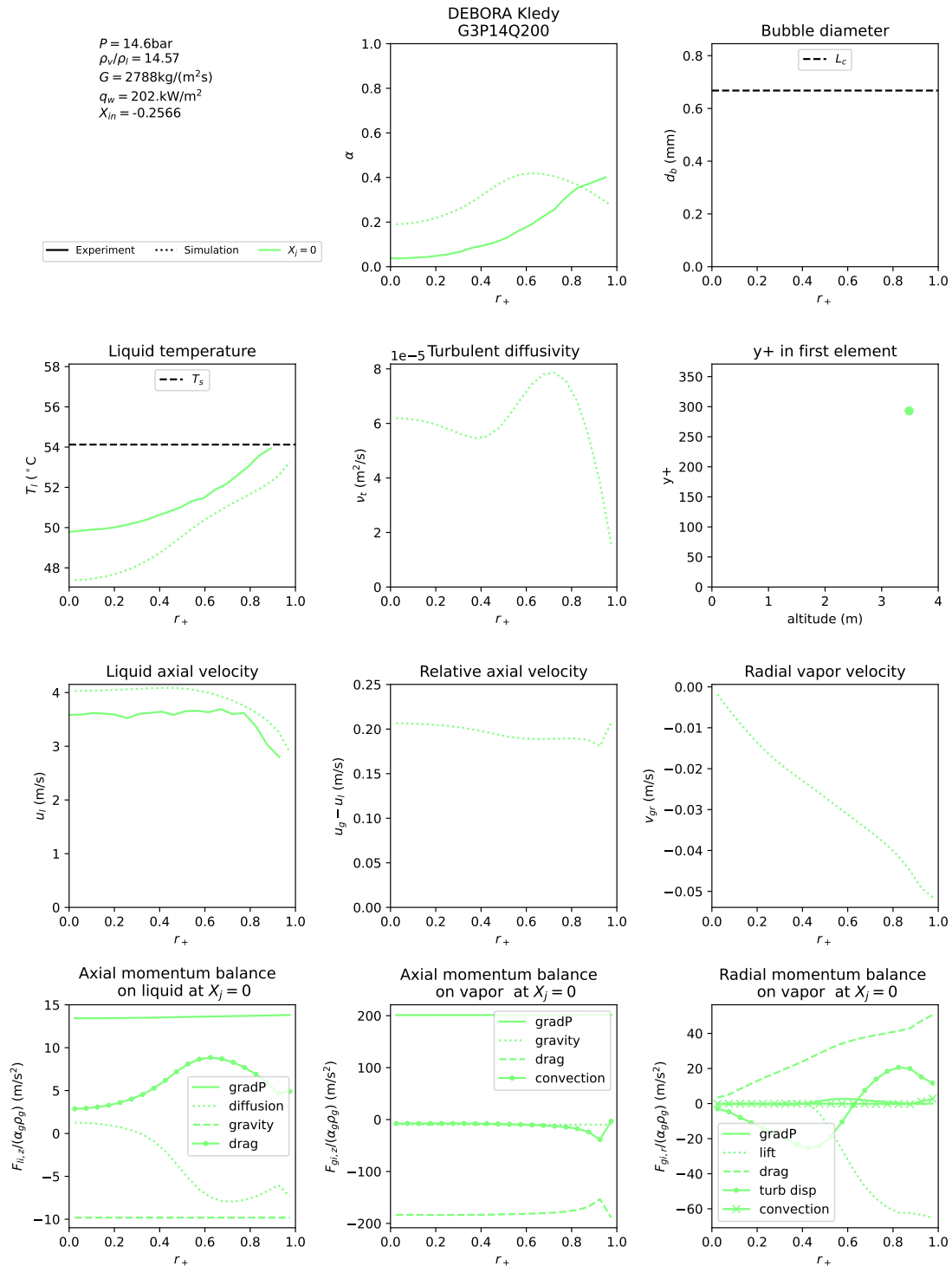


Figure F.26: Simulation results for test tube G3P14Q200 of Kledy 2018. Experimental results are represented with a full line and simulations with a dashed line.

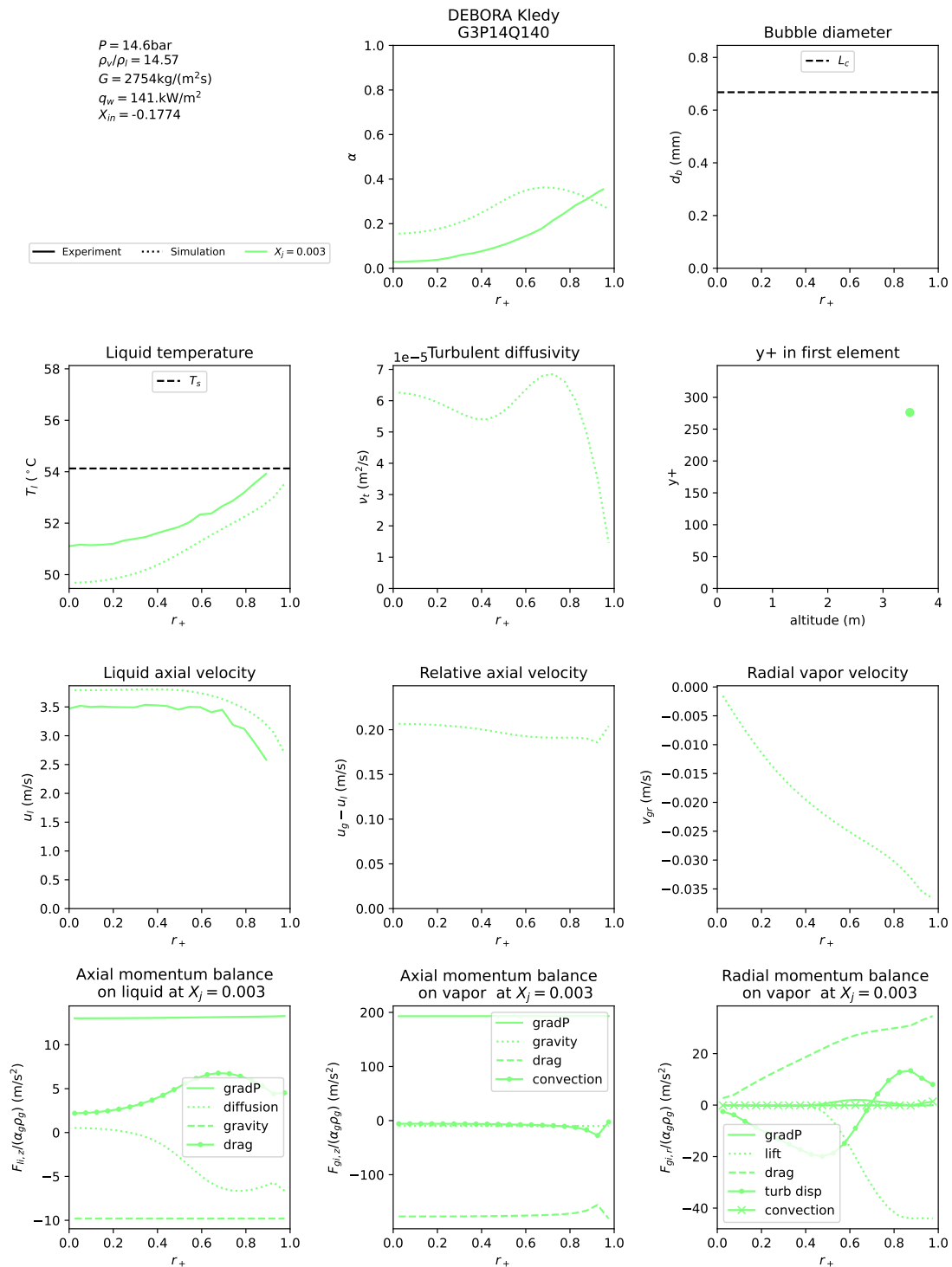


Figure F.27: Simulation results for test tube G3P14Q140 of Kledy 2018. Experimental results are represented with a full line and simulations with a dashed line.

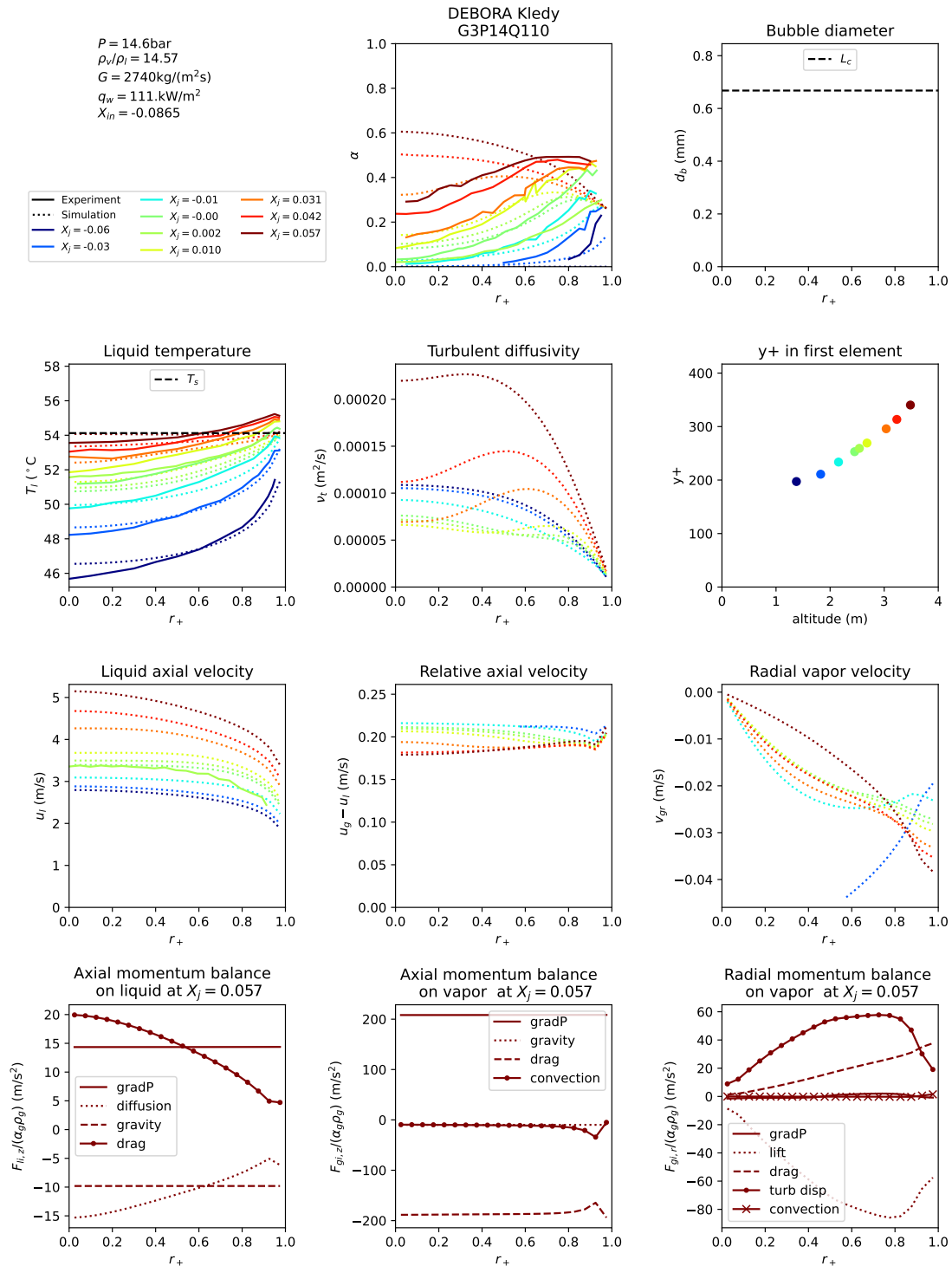


Figure F.28: Simulation results for test tube G3P14Q110 of Kledy 2018. Experimental results are represented with a full line and simulations with a dashed line.

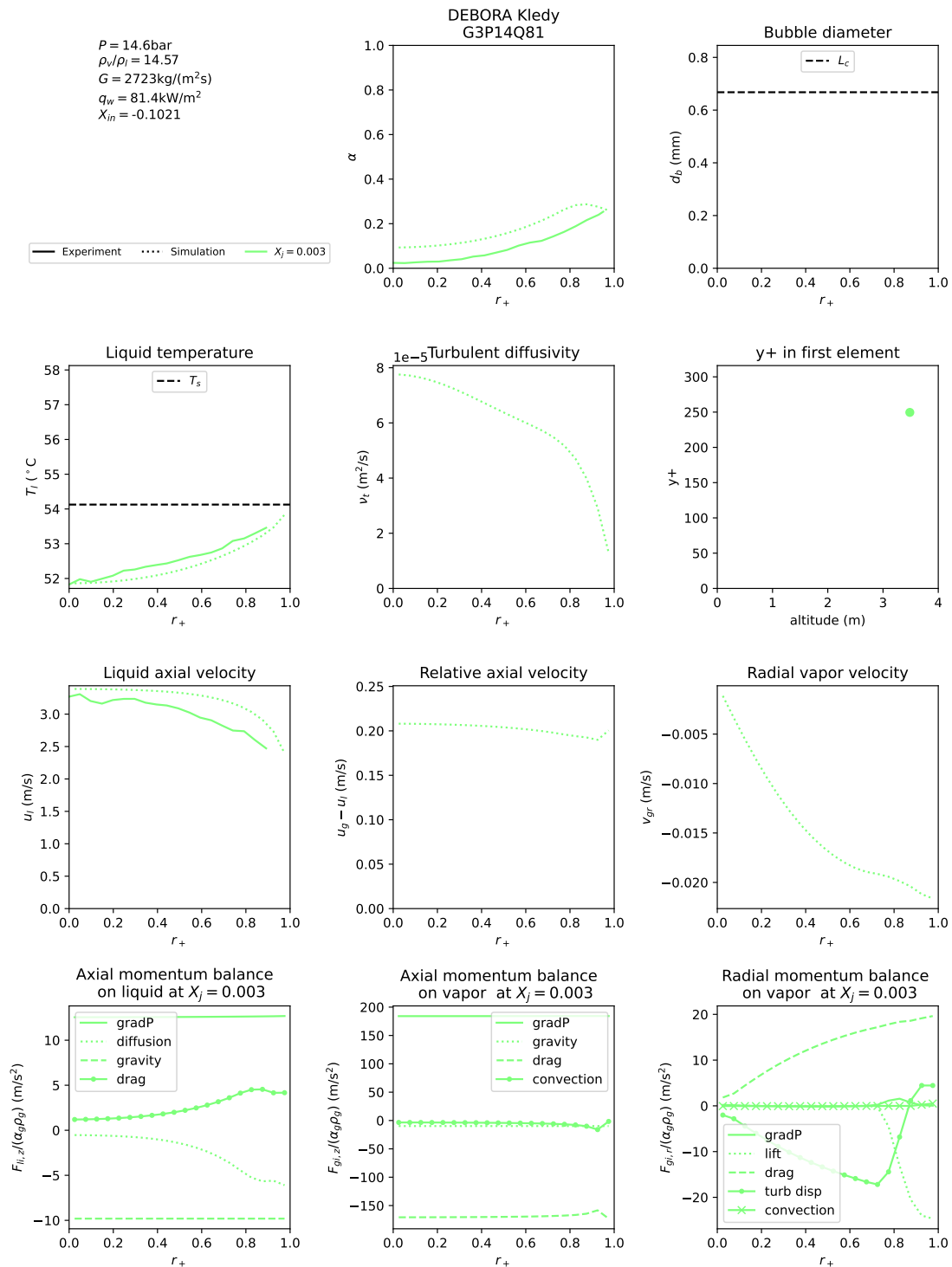


Figure F.29: Simulation results for test tube G3P14Q81 of Kledy 2018. Experimental results are represented with a full line and simulations with a dashed line.

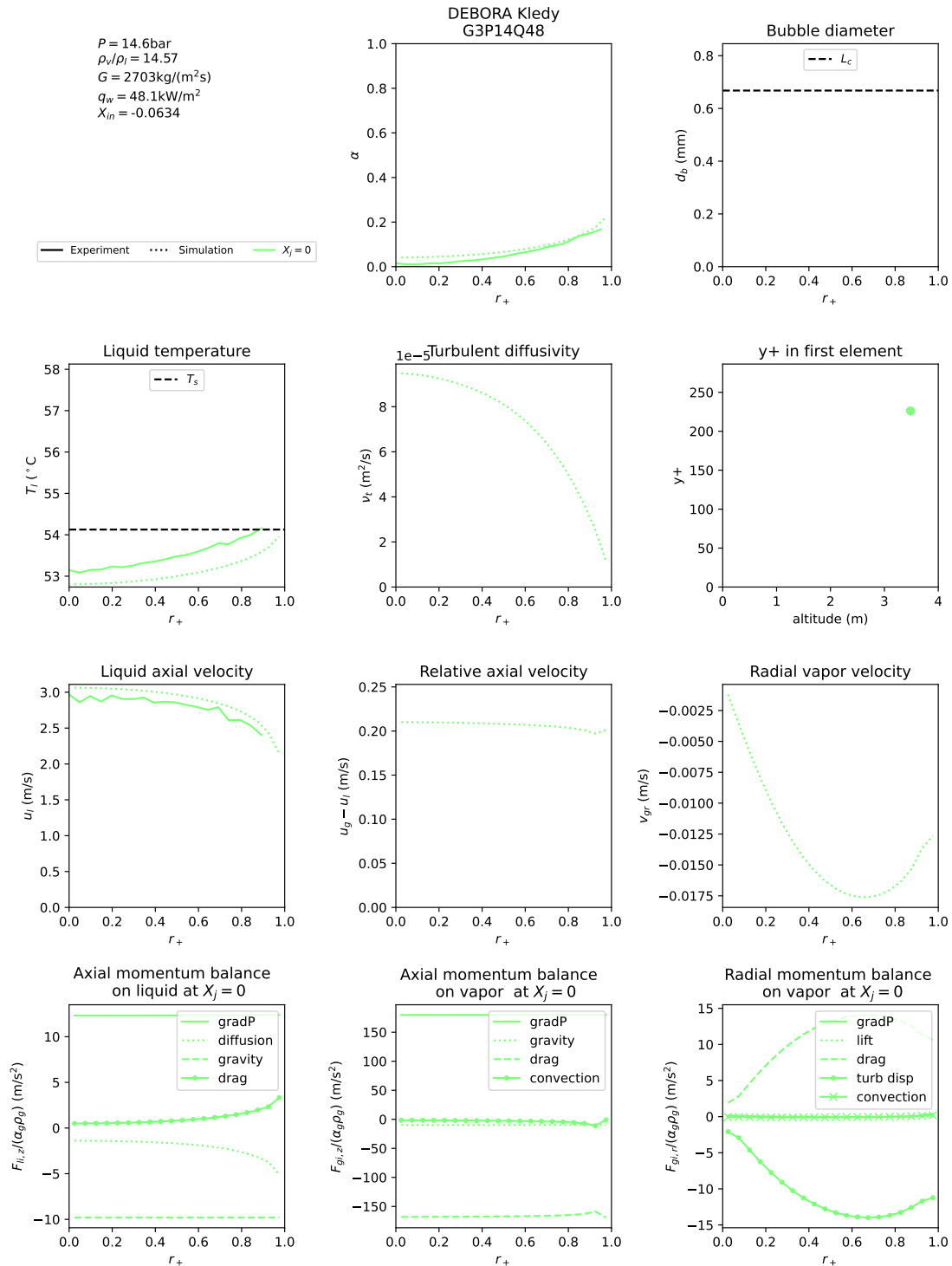


Figure F.30: Simulation results for test tube G3P14Q48 of Kledy 2018. Experimental results are represented with a full line and simulations with a dashed line.

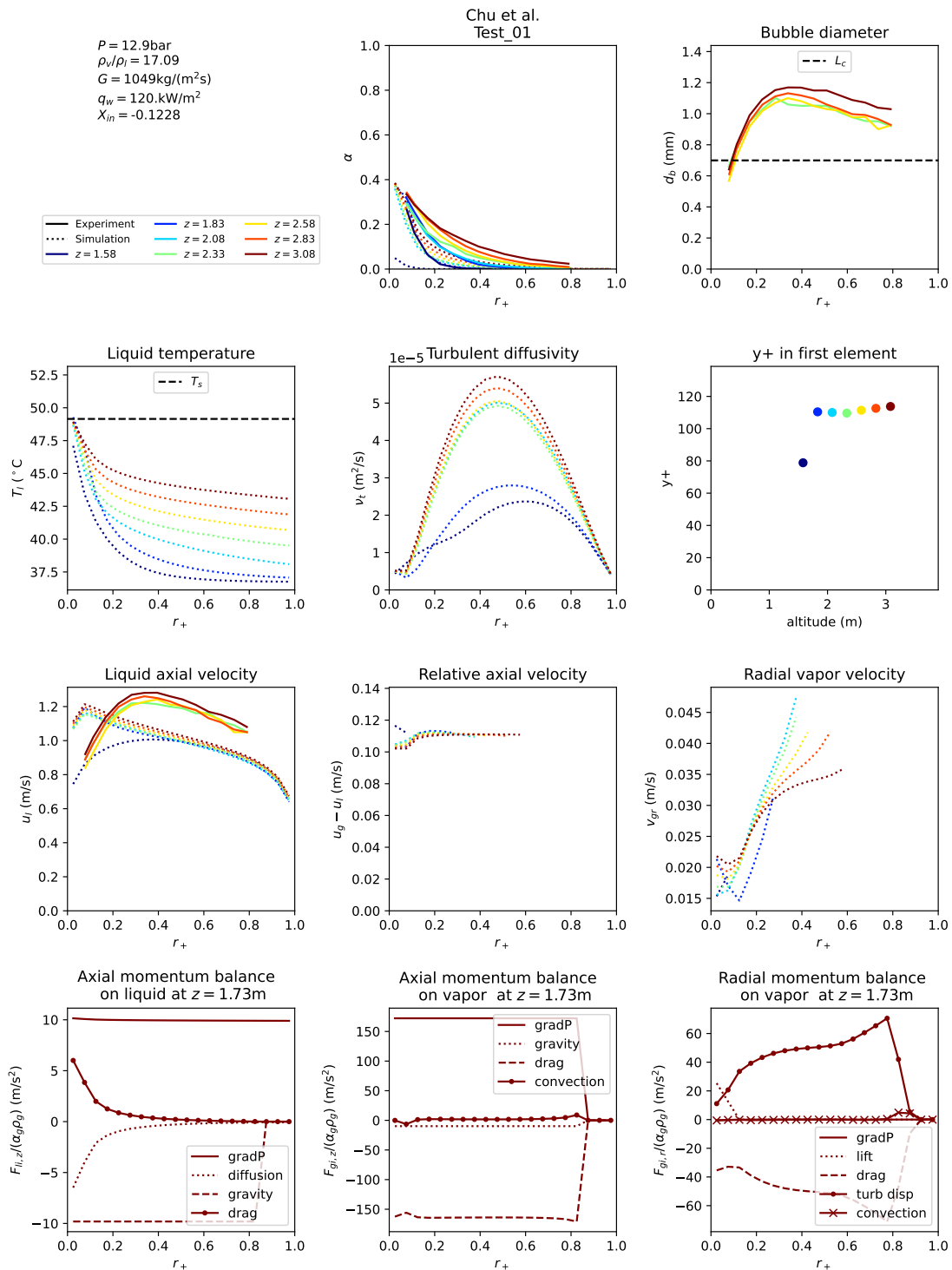


Figure F.31: Simulation results for test tube Test_01 of Chu et al. 2017. Experimental results are represented with a full line and simulations with a dashed line.

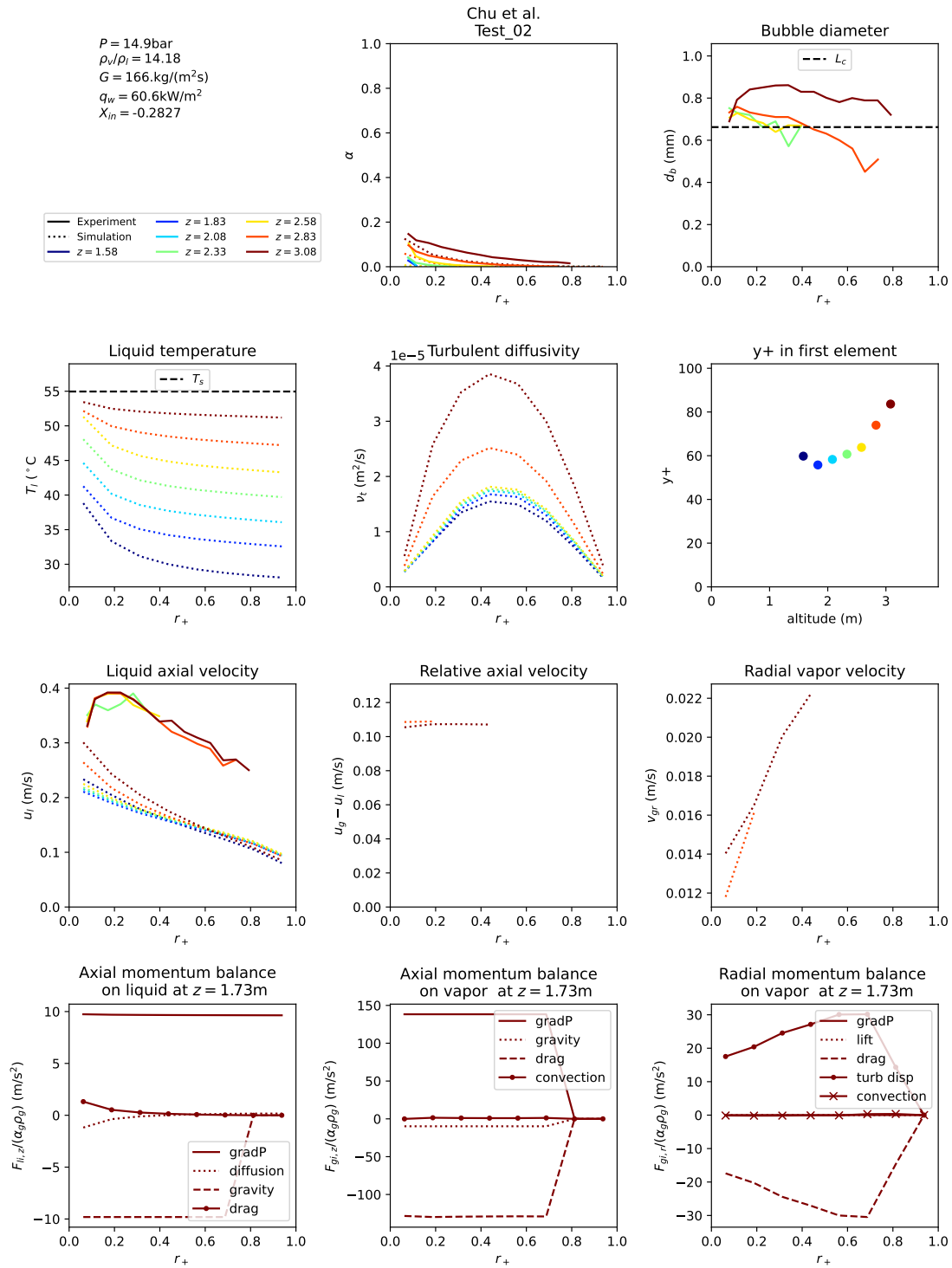


Figure F.32: Simulation results for test tube Test_02 of Chu et al. 2017. Experimental results are represented with a full line and simulations with a dashed line.

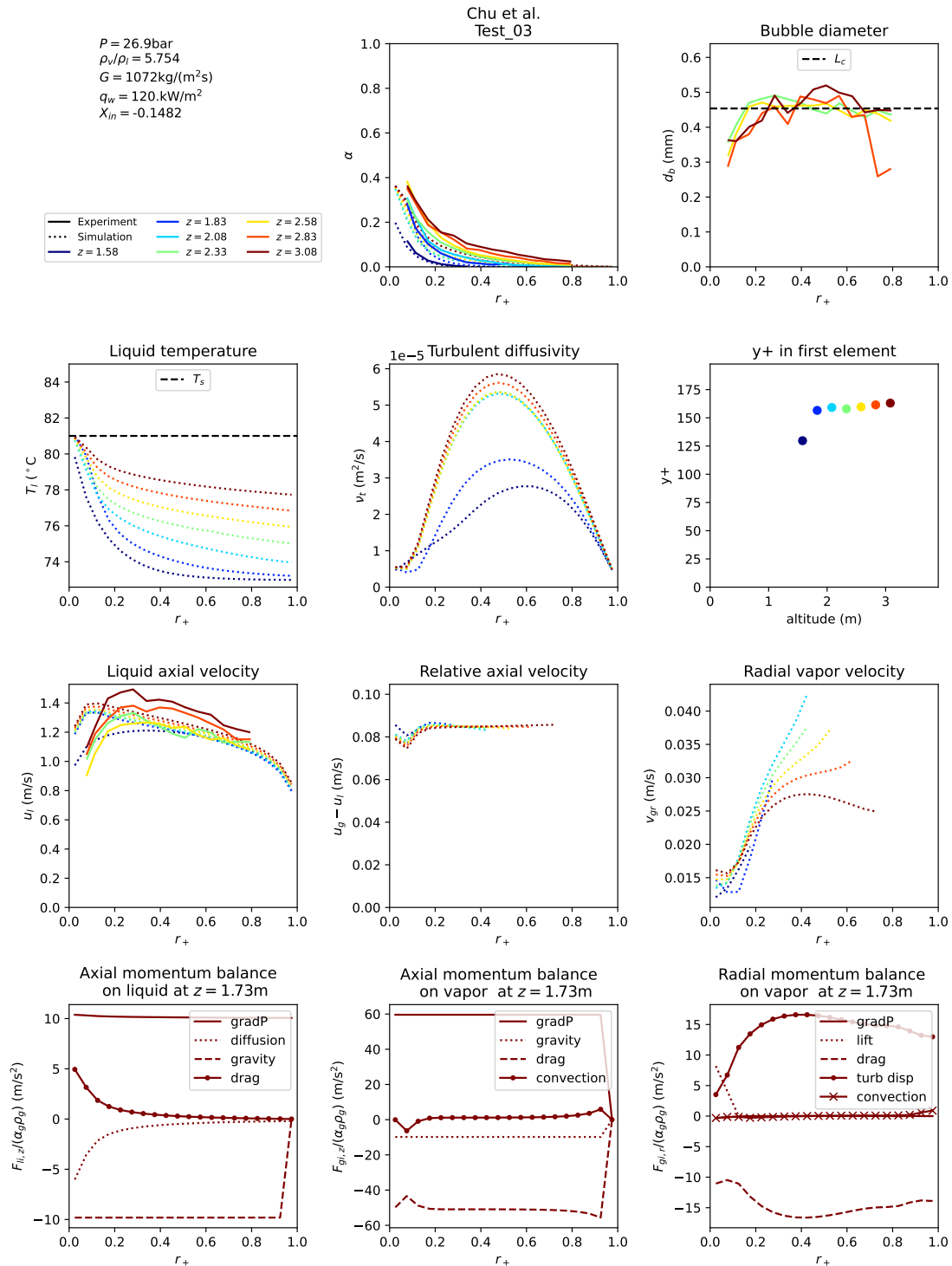


Figure F.33: Simulation results for test tube Test_03 of Chu et al. 2017. Experimental results are represented with a full line and simulations with a dashed line.

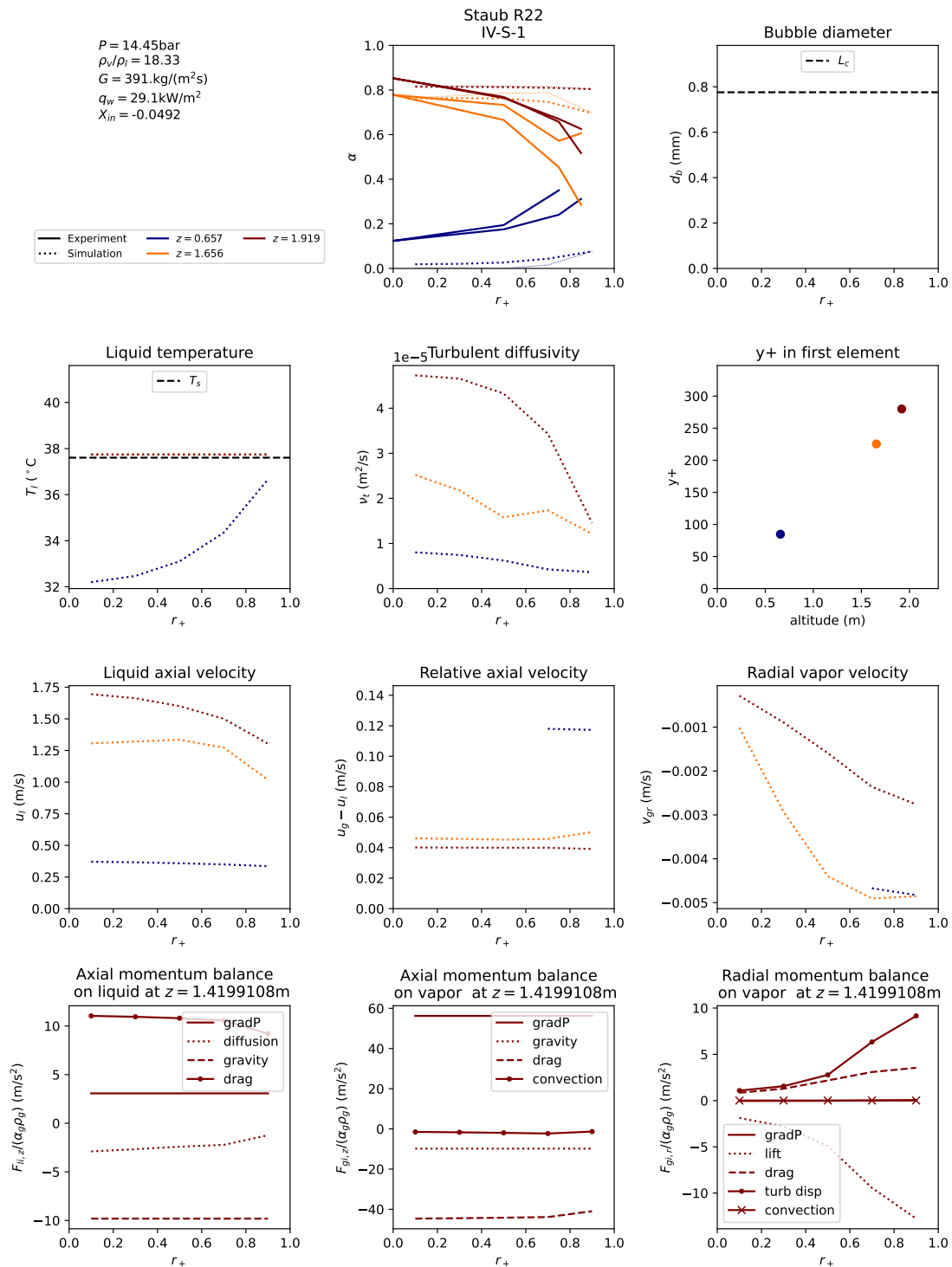


Figure F.34: Simulation results for test tube IV-S-1 of Staub et al. 1969. Experimental results are represented with a full line and simulations with a dashed line.

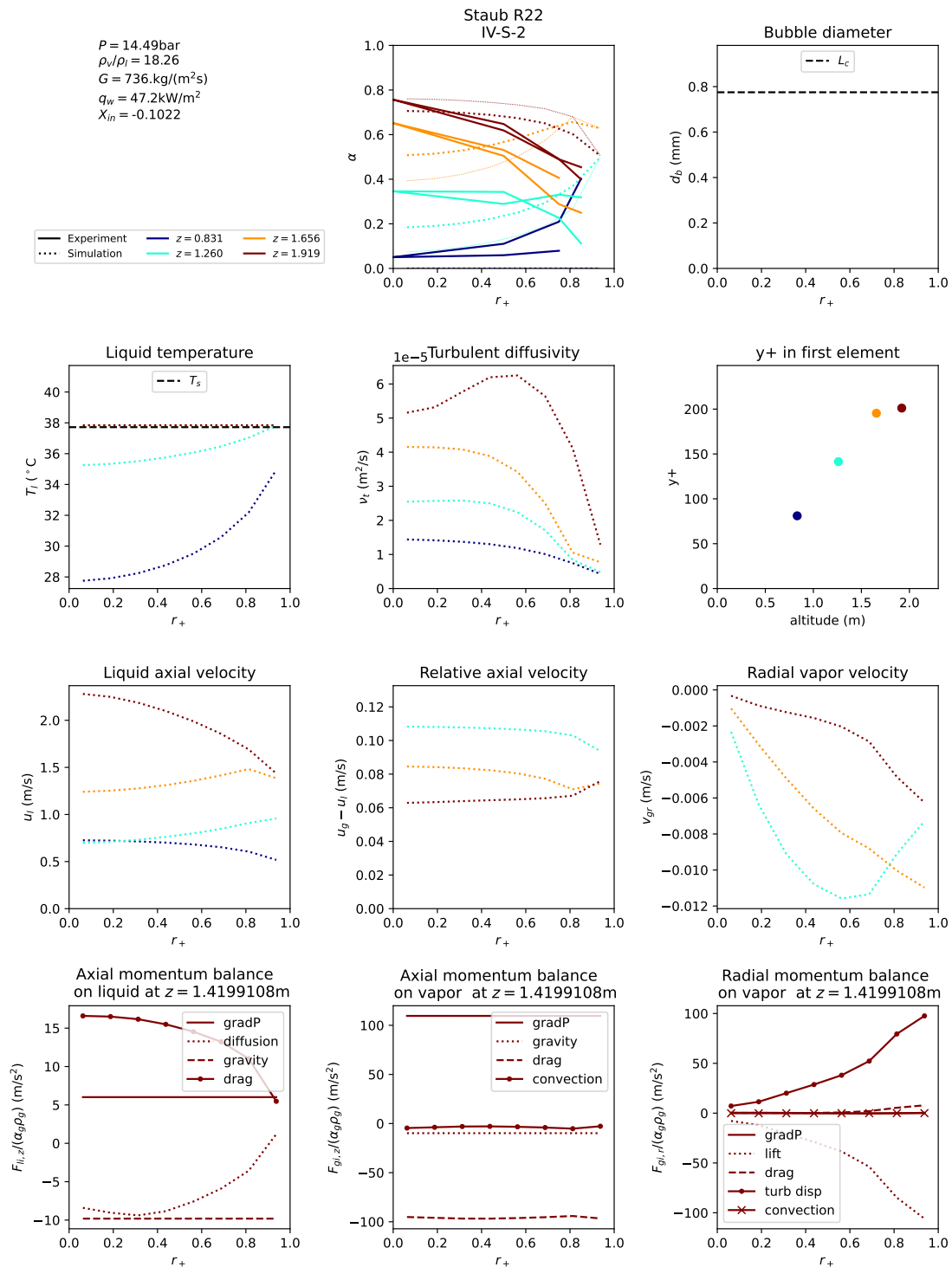


Figure F.35: Simulation results for test tube IV-S-2 of Staub et al. 1969. Experimental results are represented with a full line and simulations with a dashed line.

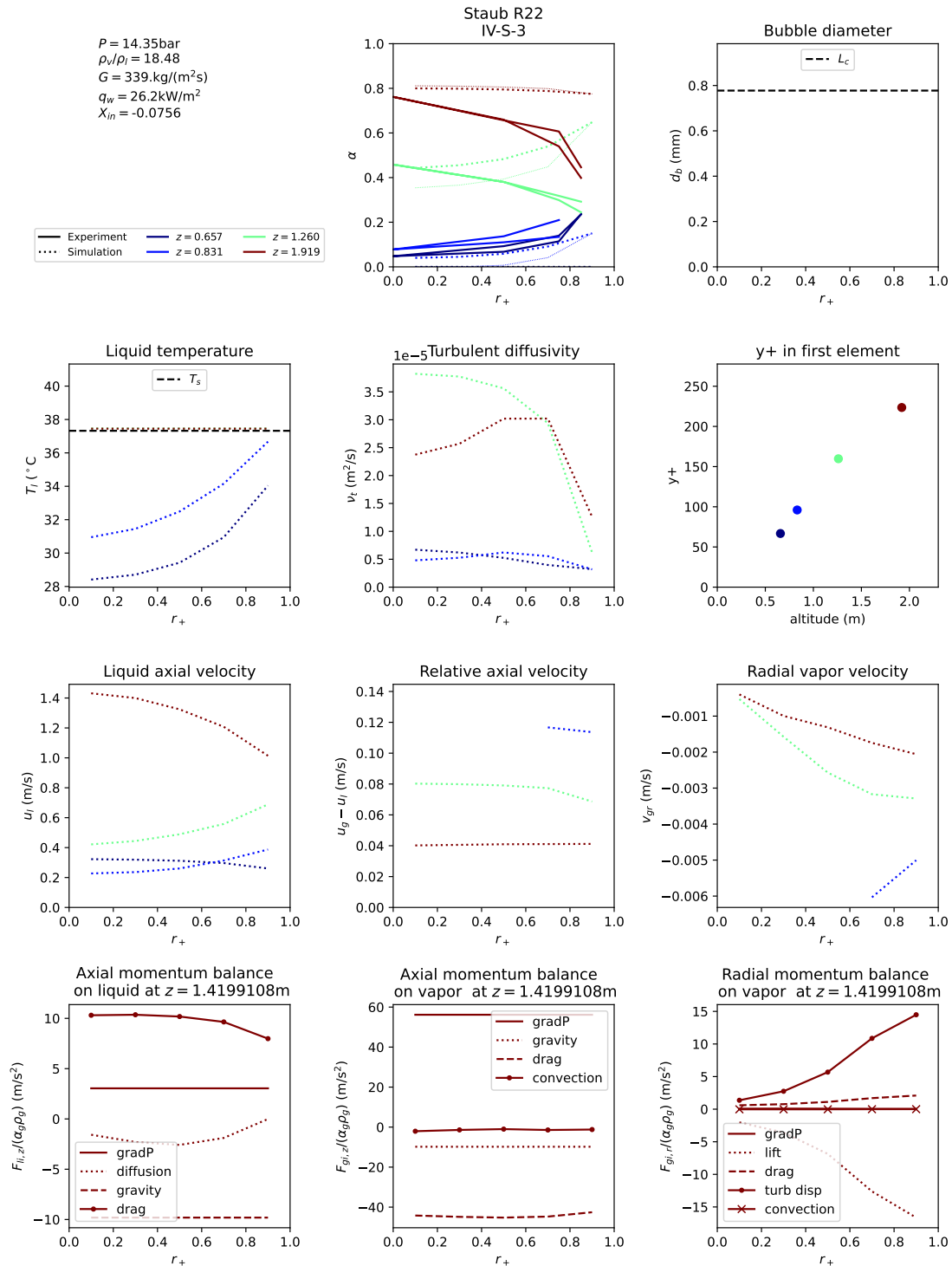


Figure F.36: Simulation results for test tube IV-S-3 of Staub et al. 1969. Experimental results are represented with a full line and simulations with a dashed line.

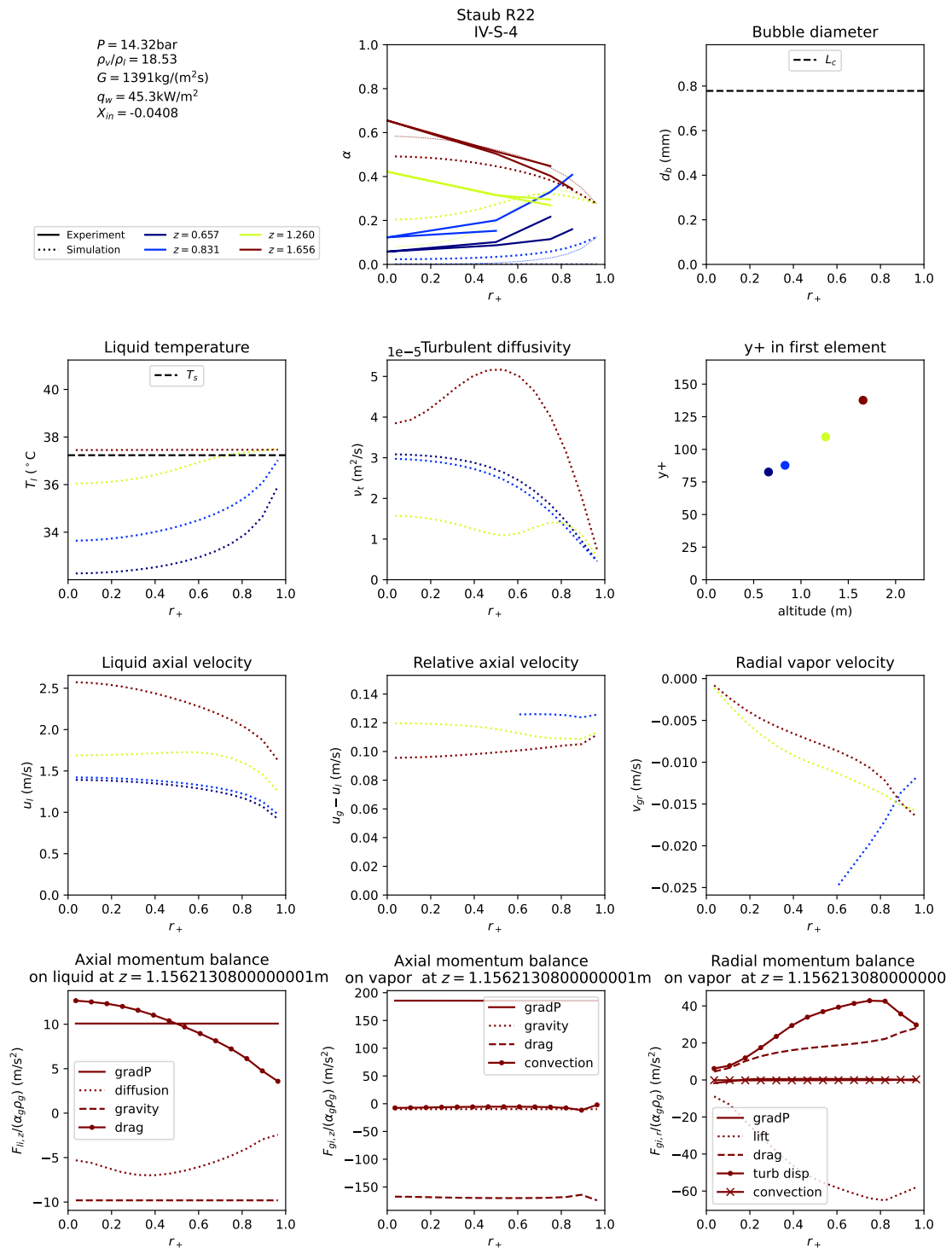


Figure F.37: Simulation results for test tube IV-S-4 of Staub et al. 1969. Experimental results are represented with a full line and simulations with a dashed line.

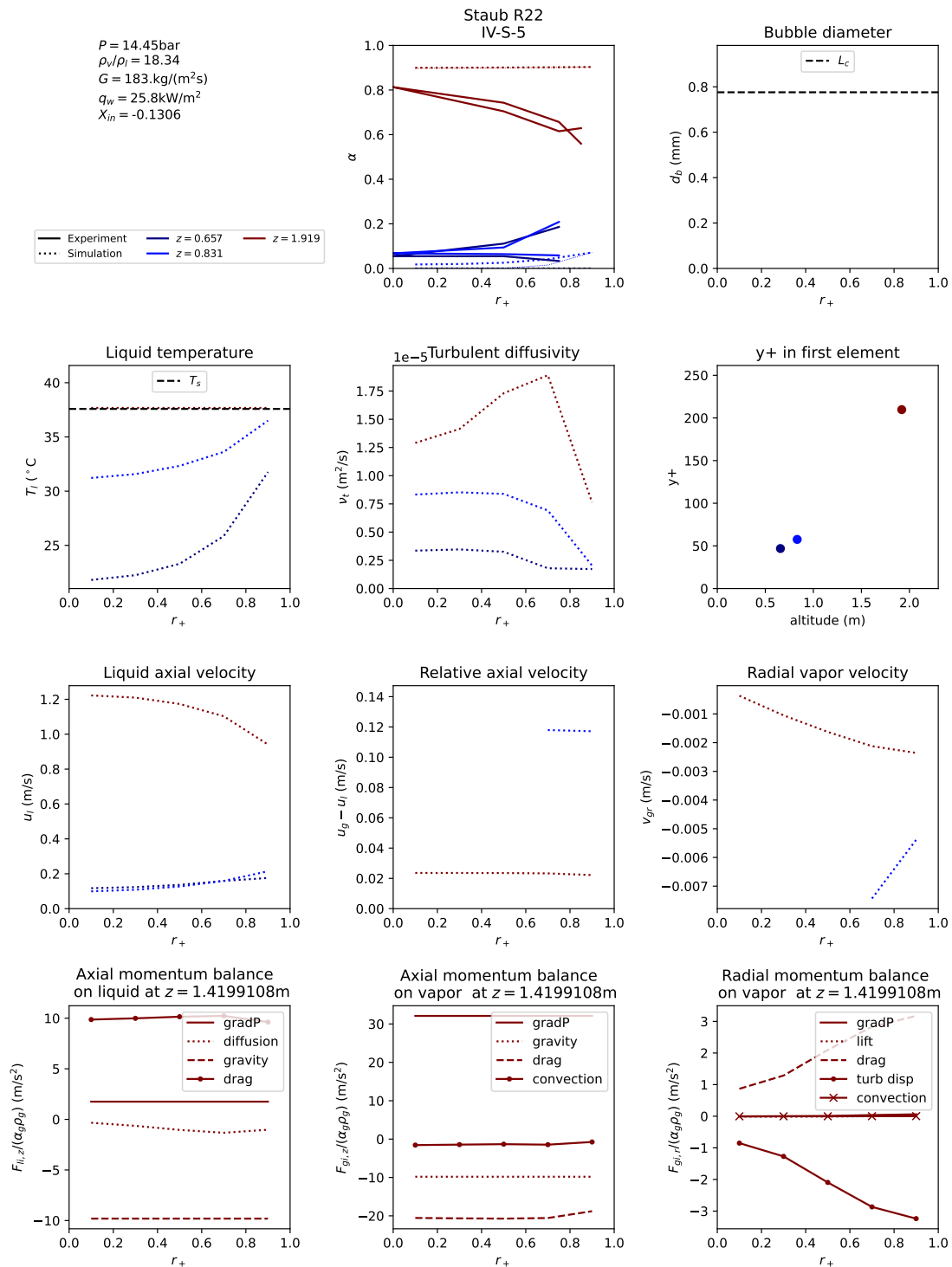


Figure F.38: Simulation results for test tube IV-S-5 of Staub et al. 1969. Experimental results are represented with a full line and simulations with a dashed line.

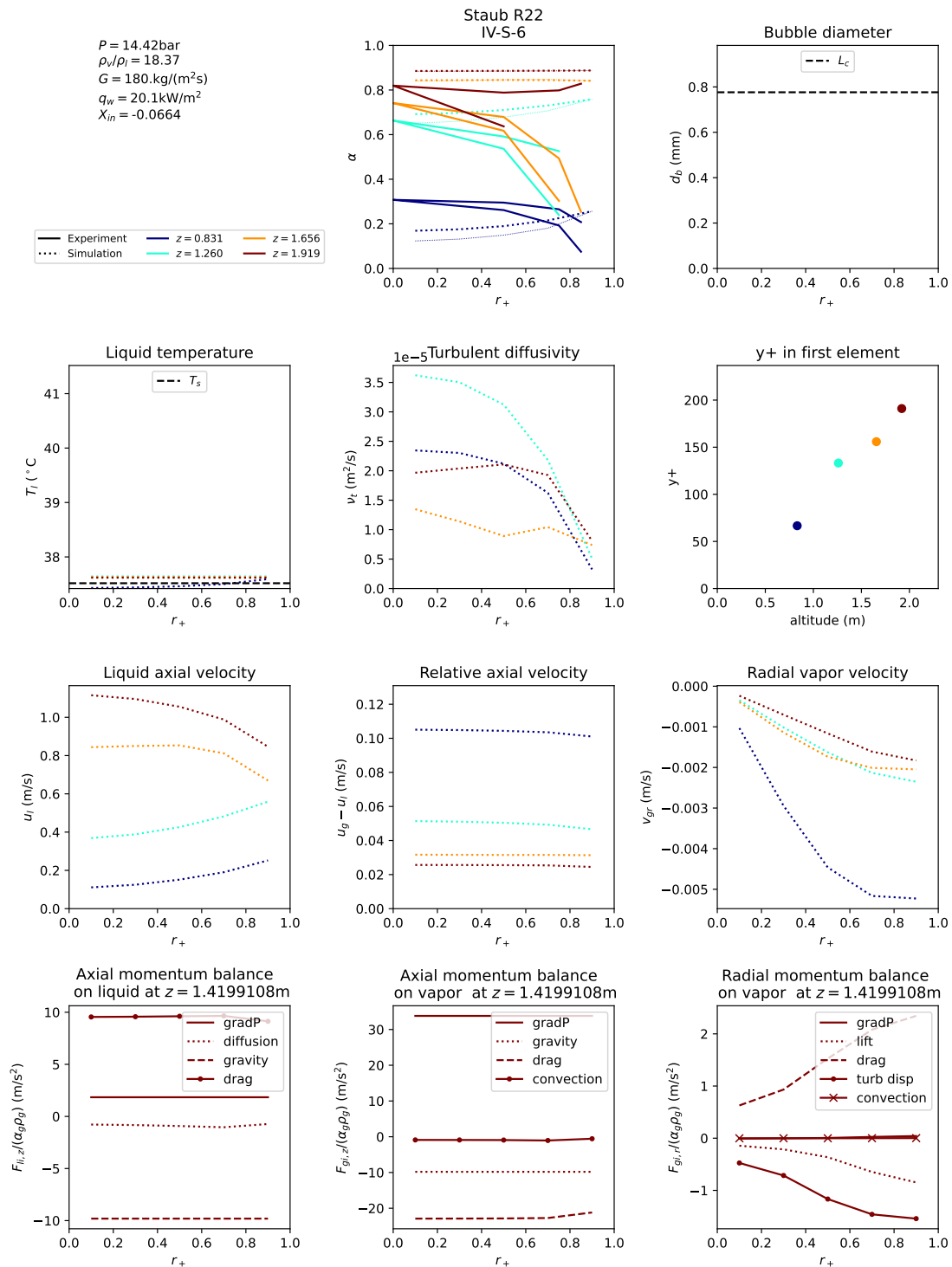


Figure F.39: Simulation results for test tube IV-S-6 of Staub et al. 1969. Experimental results are represented with a full line and simulations with a dashed line.

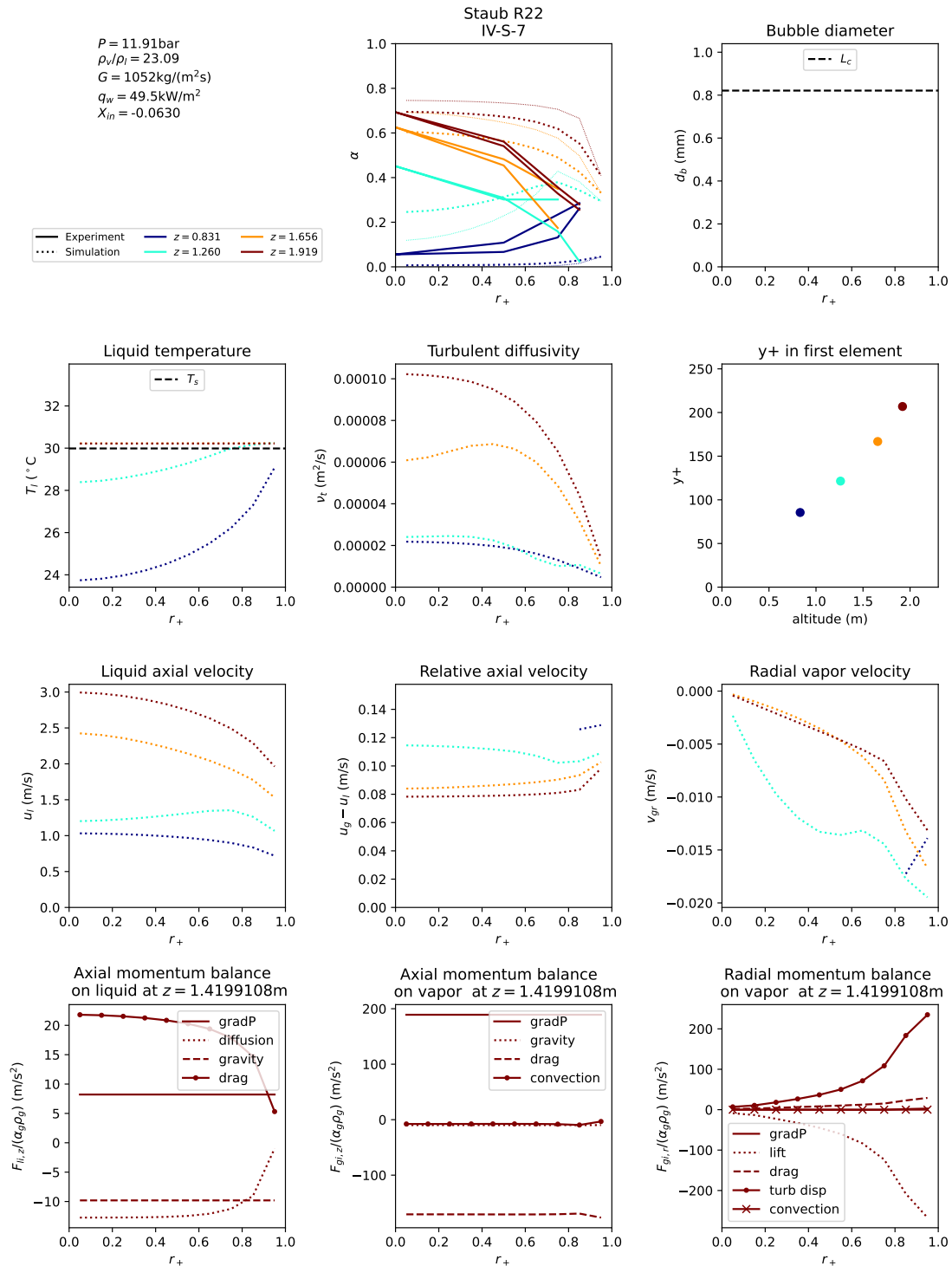


Figure F.40: Simulation results for test tube IV-S-7 of Staub et al. 1969. Experimental results are represented with a full line and simulations with a dashed line.

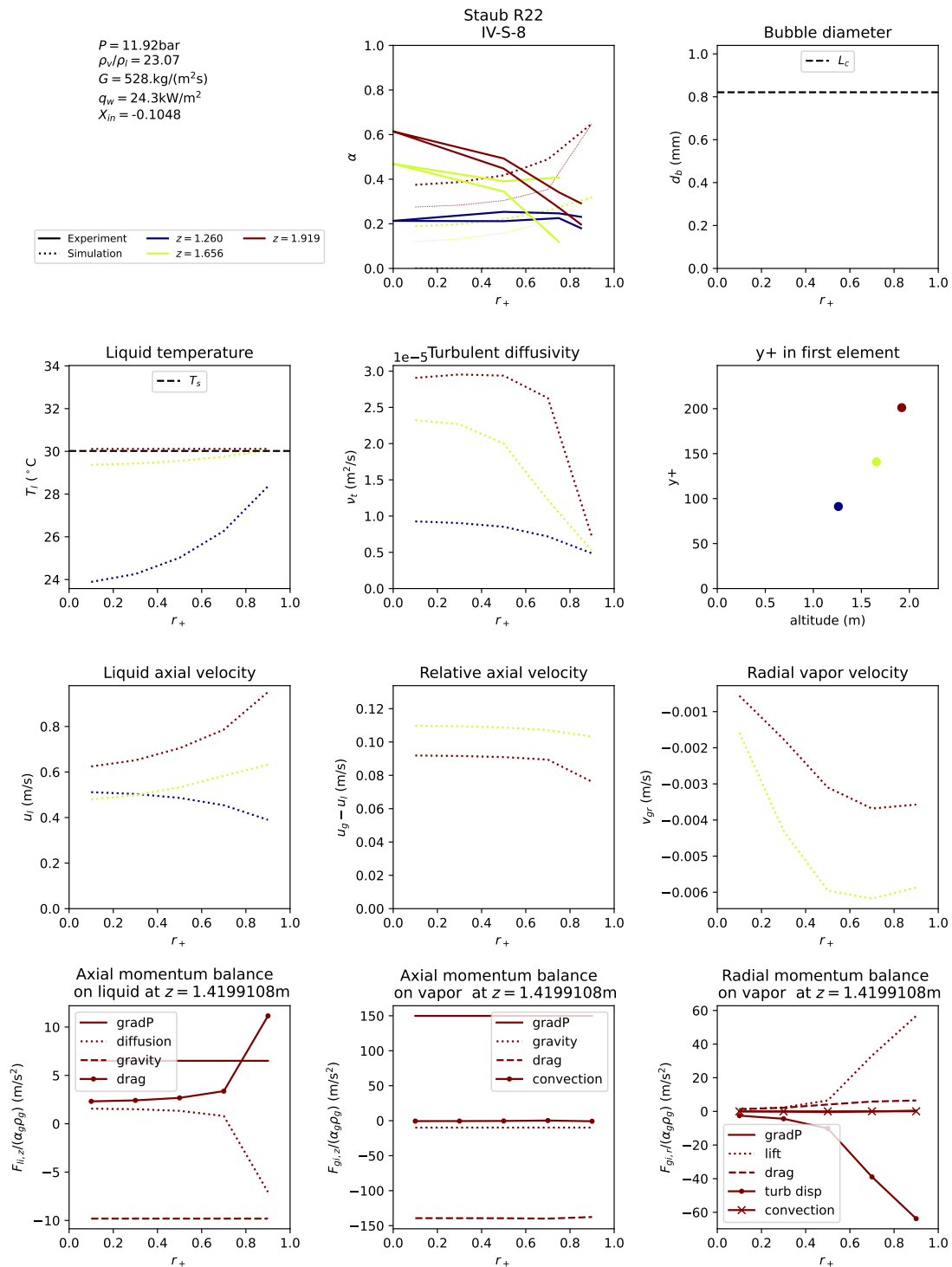
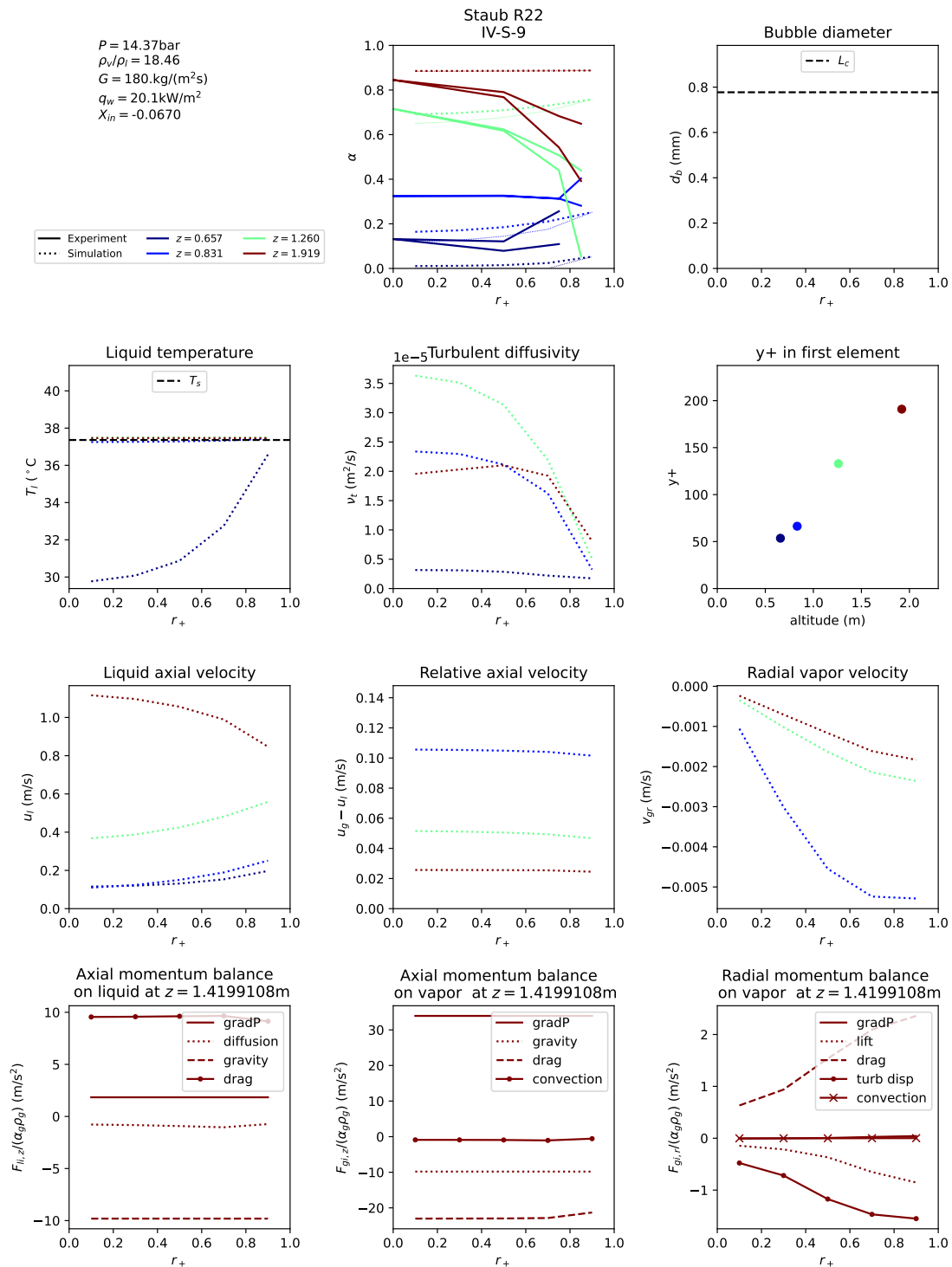


Figure F.41: Simulation results for test tube IV-S-8 of Staub et al. 1969. Experimental results are represented with a full line and simulations with a dashed line.



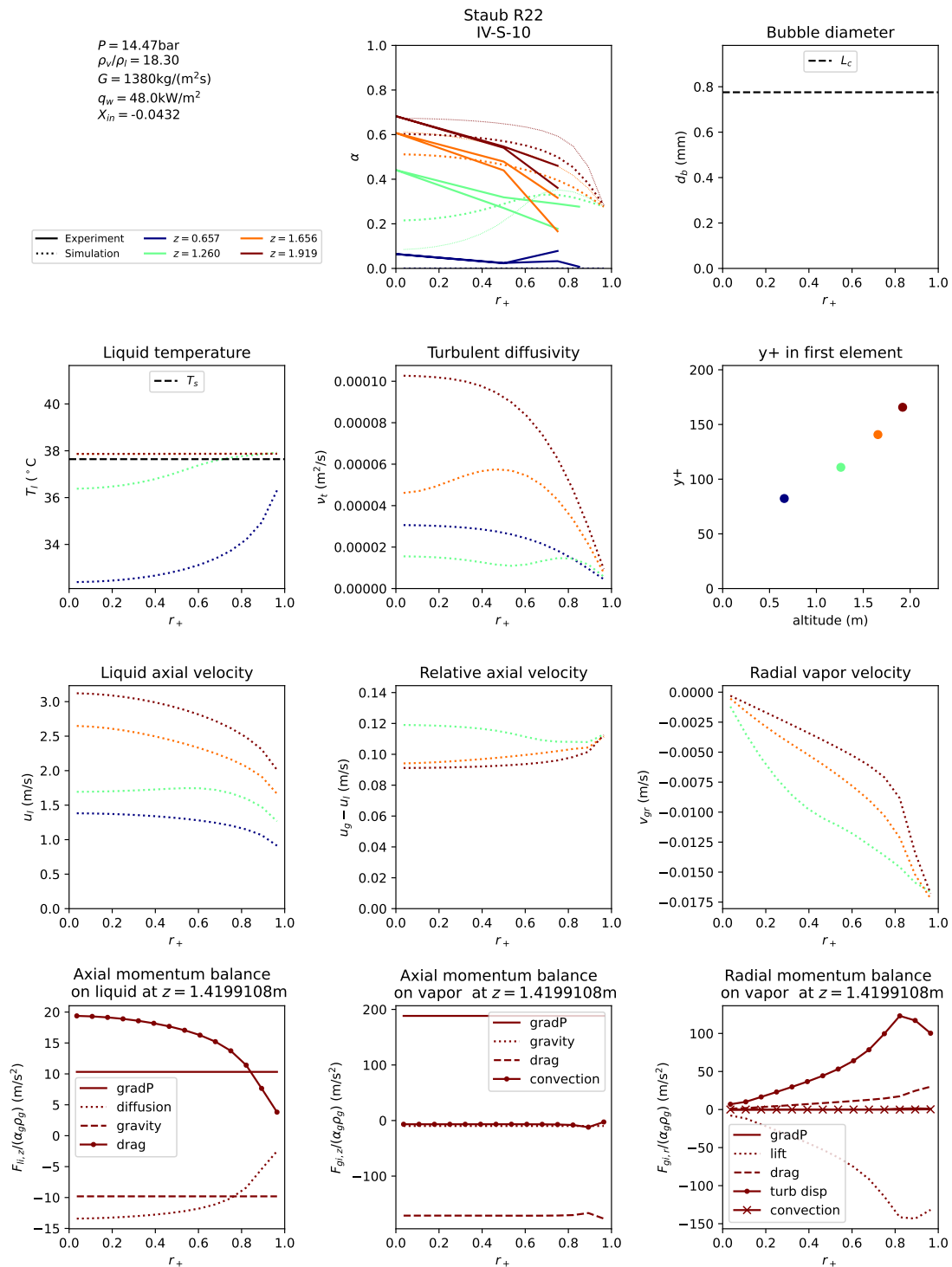
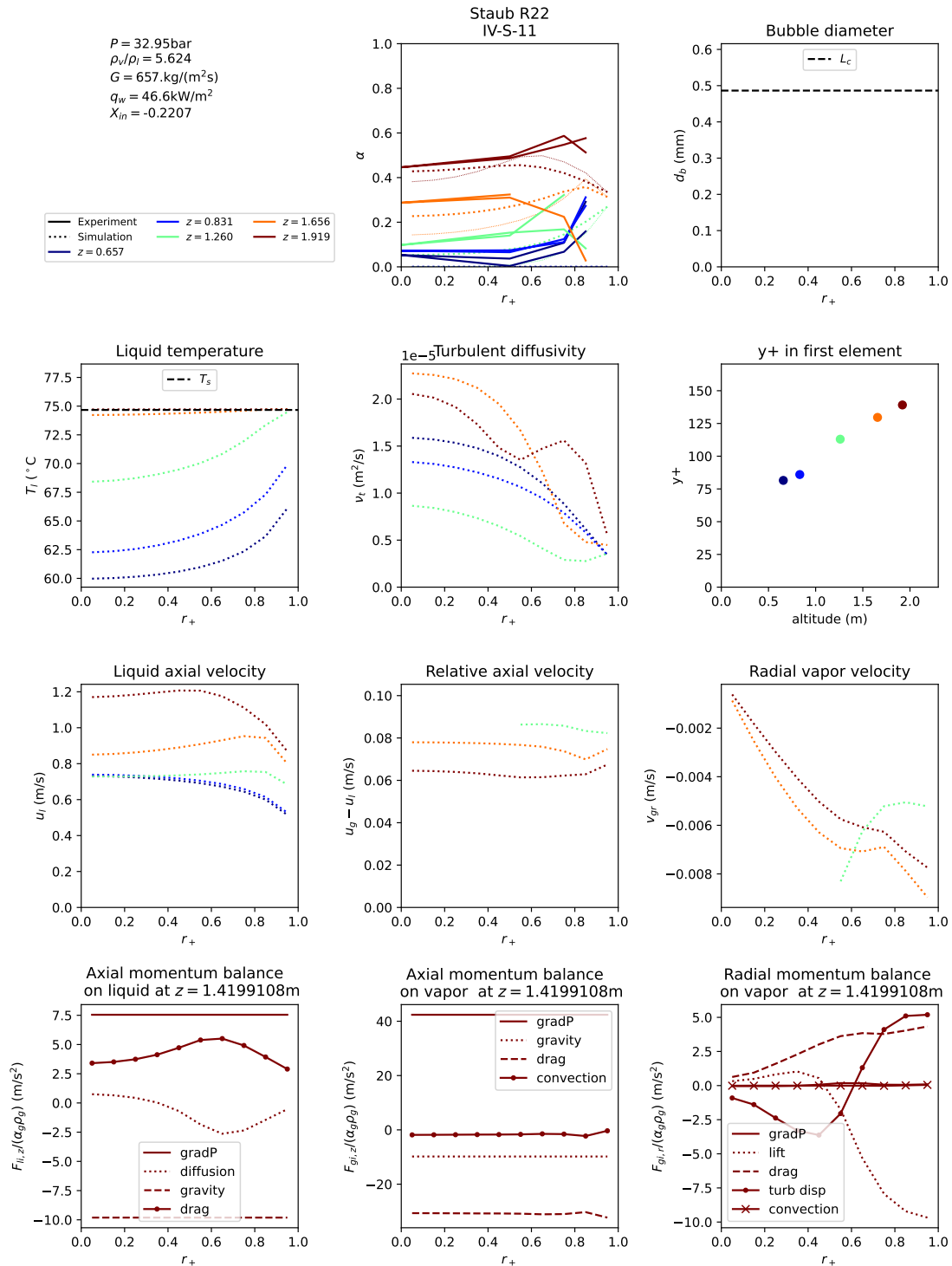


Figure F.43: Simulation results for test tube IV-S-10 of Staub et al. 1969. Experimental results are represented with a full line and simulations with a dashed line.



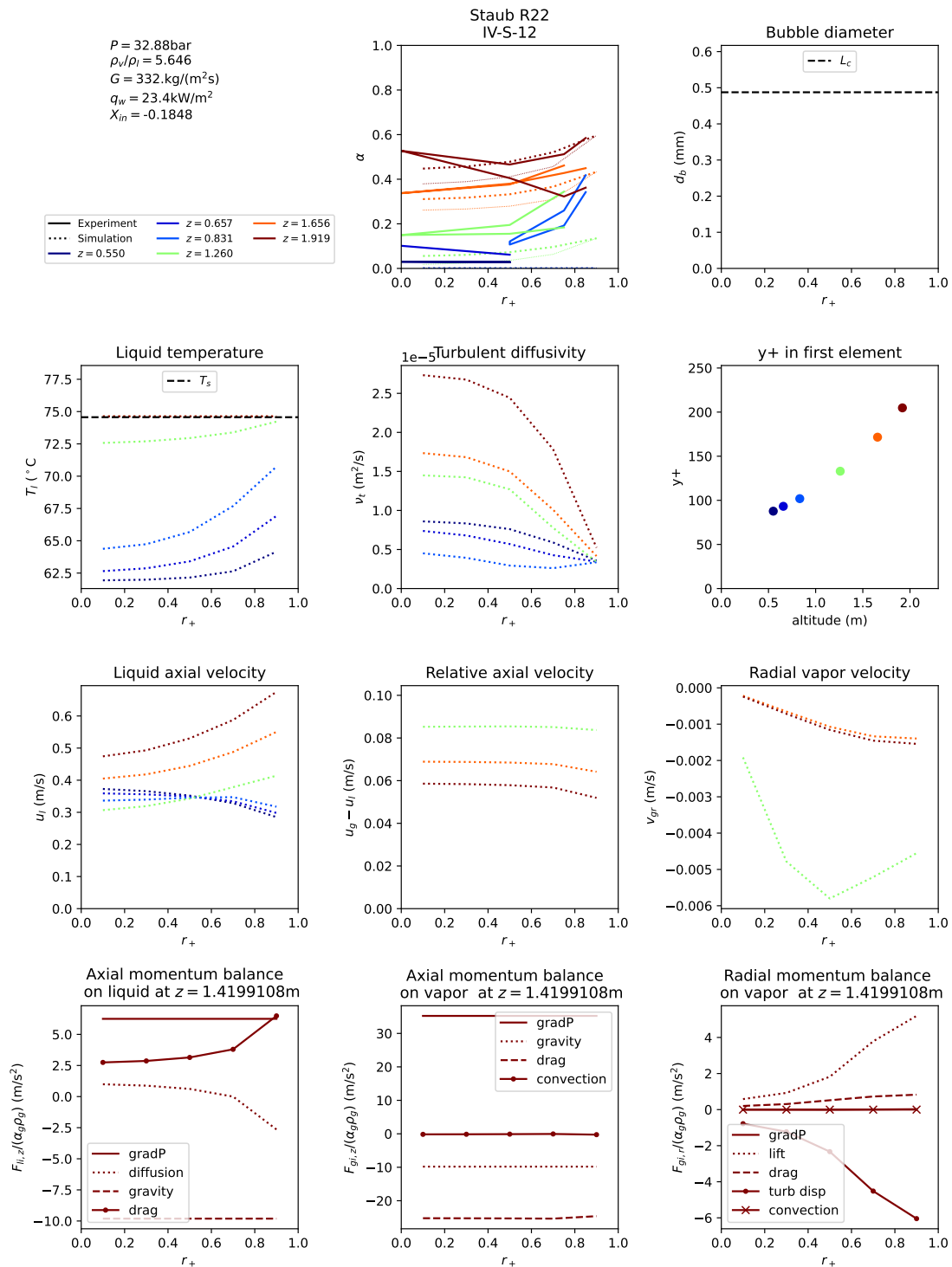


Figure F.45: Simulation results for test tube IV-S-12 of Staub et al. 1969. Experimental results are represented with a full line and simulations with a dashed line.

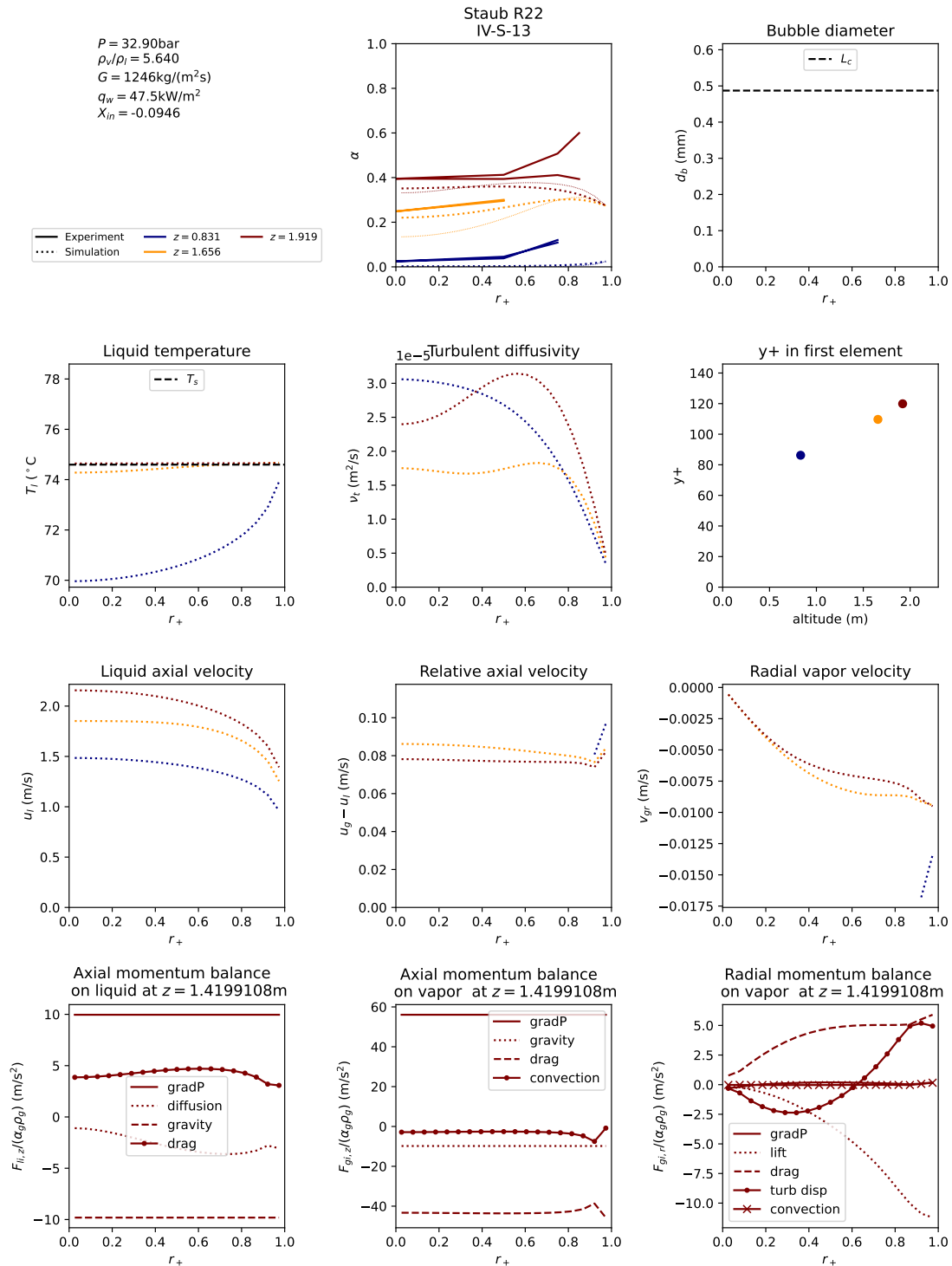


Figure F.46: Simulation results for test tube IV-S-13 of Staub et al. 1969. Experimental results are represented with a full line and simulations with a dashed line.

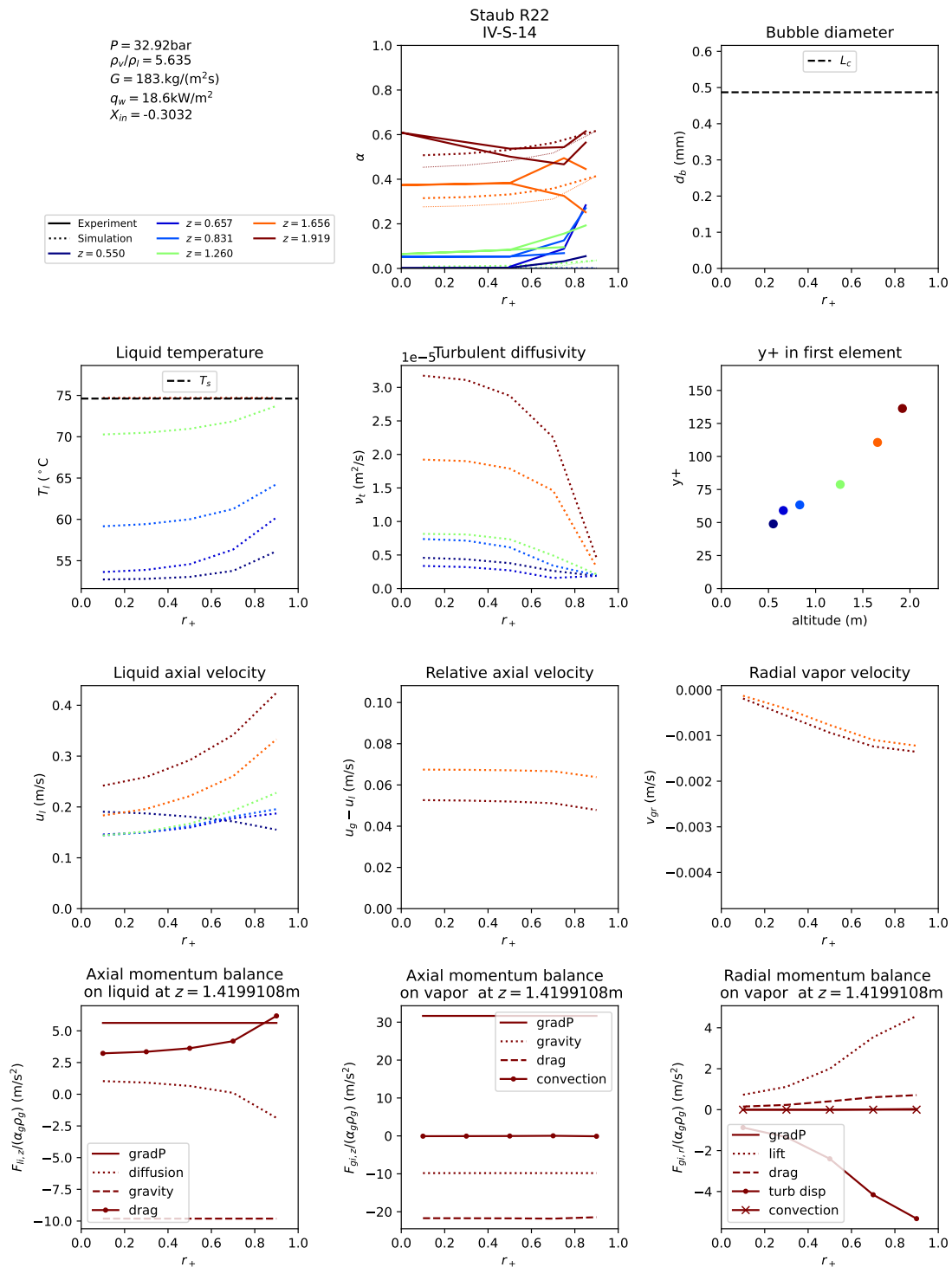


Figure F.47: Simulation results for test tube IV-S-14 of Staub et al. 1969. Experimental results are represented with a full line and simulations with a dashed line.

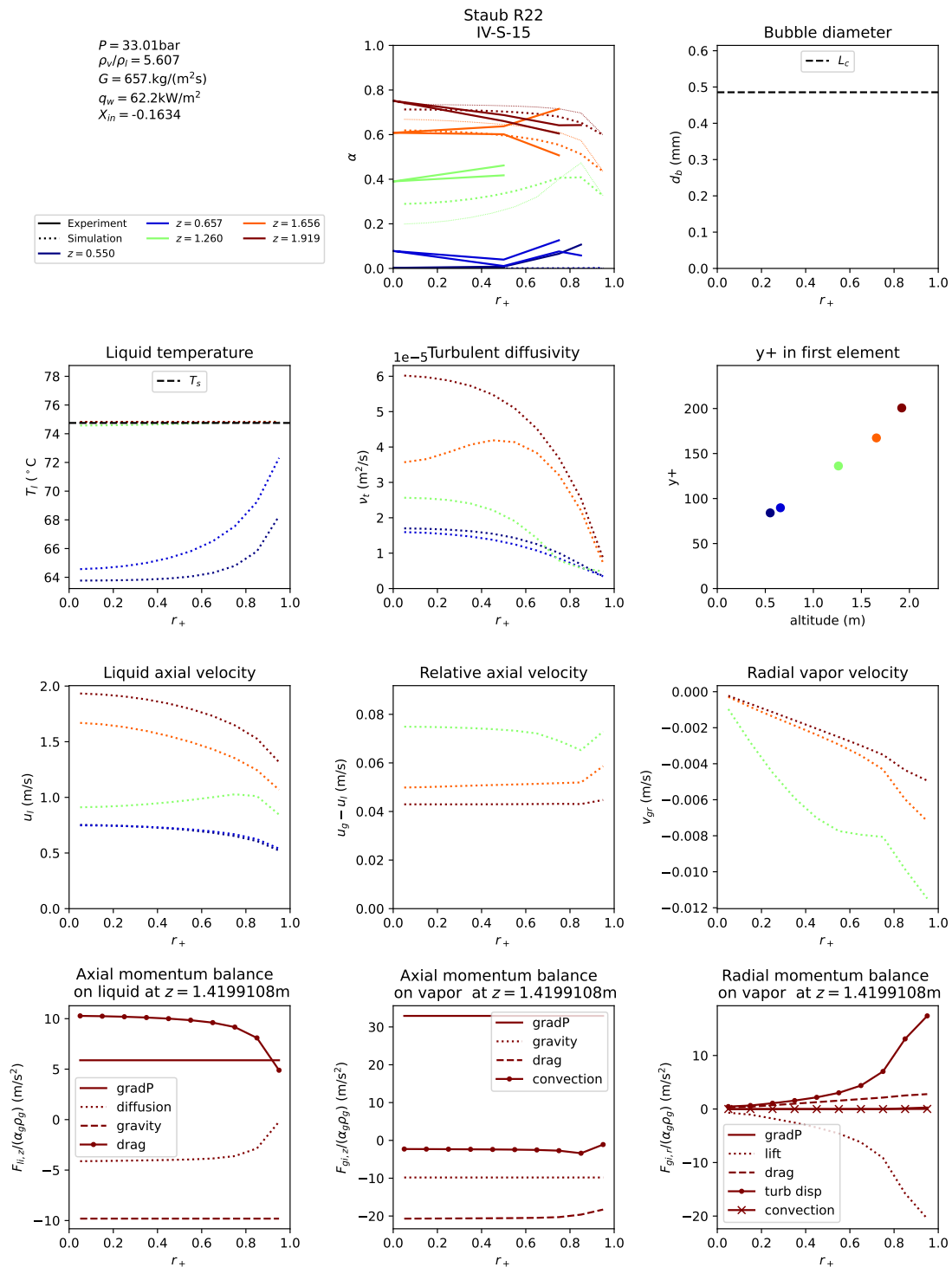


Figure F.48: Simulation results for test tube IV-S-15 of Staub et al. 1969. Experimental results are represented with a full line and simulations with a dashed line.

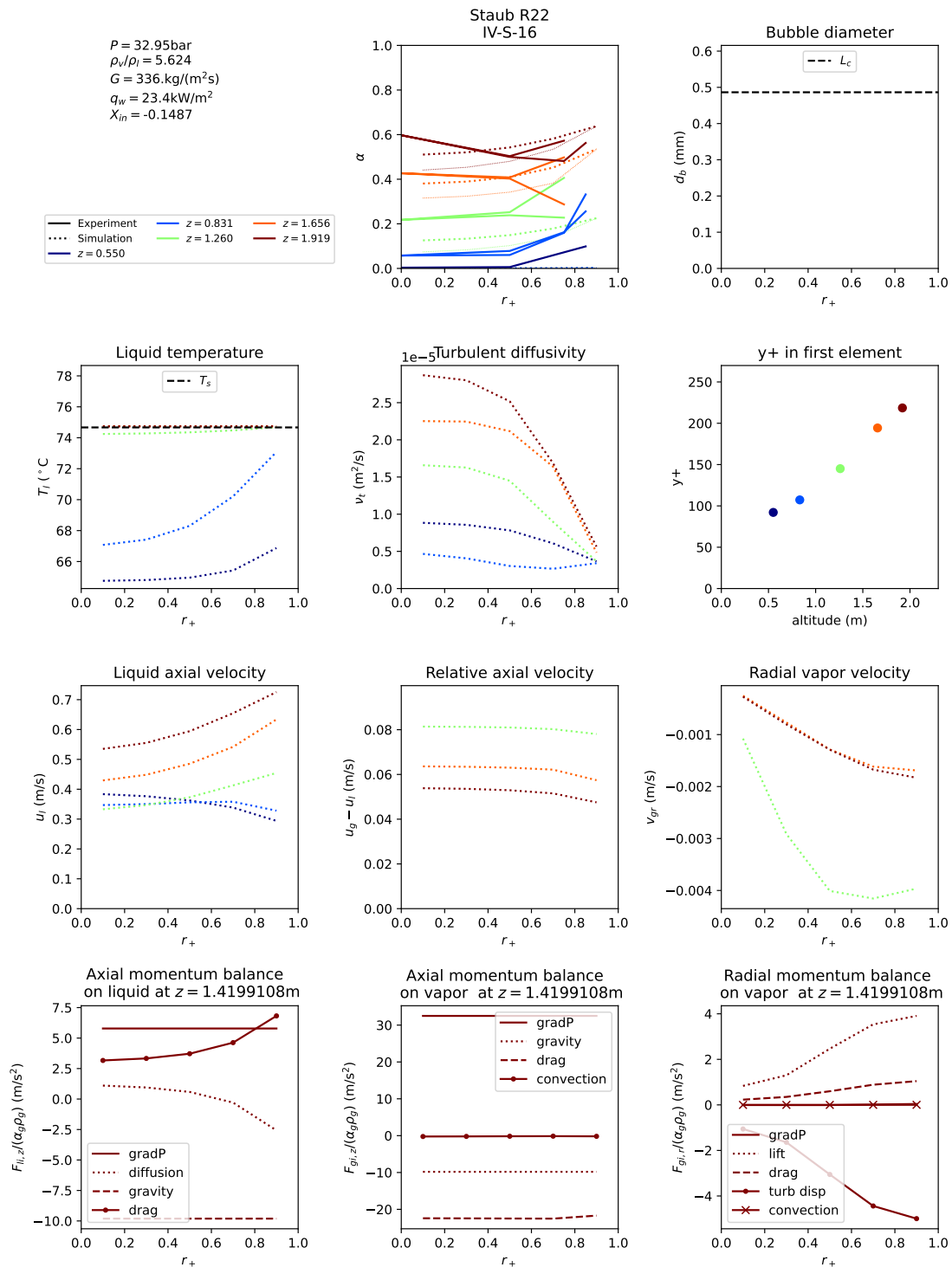


Figure F.49: Simulation results for test tube IV-S-16 of Staub et al. 1969. Experimental results are represented with a full line and simulations with a dashed line.

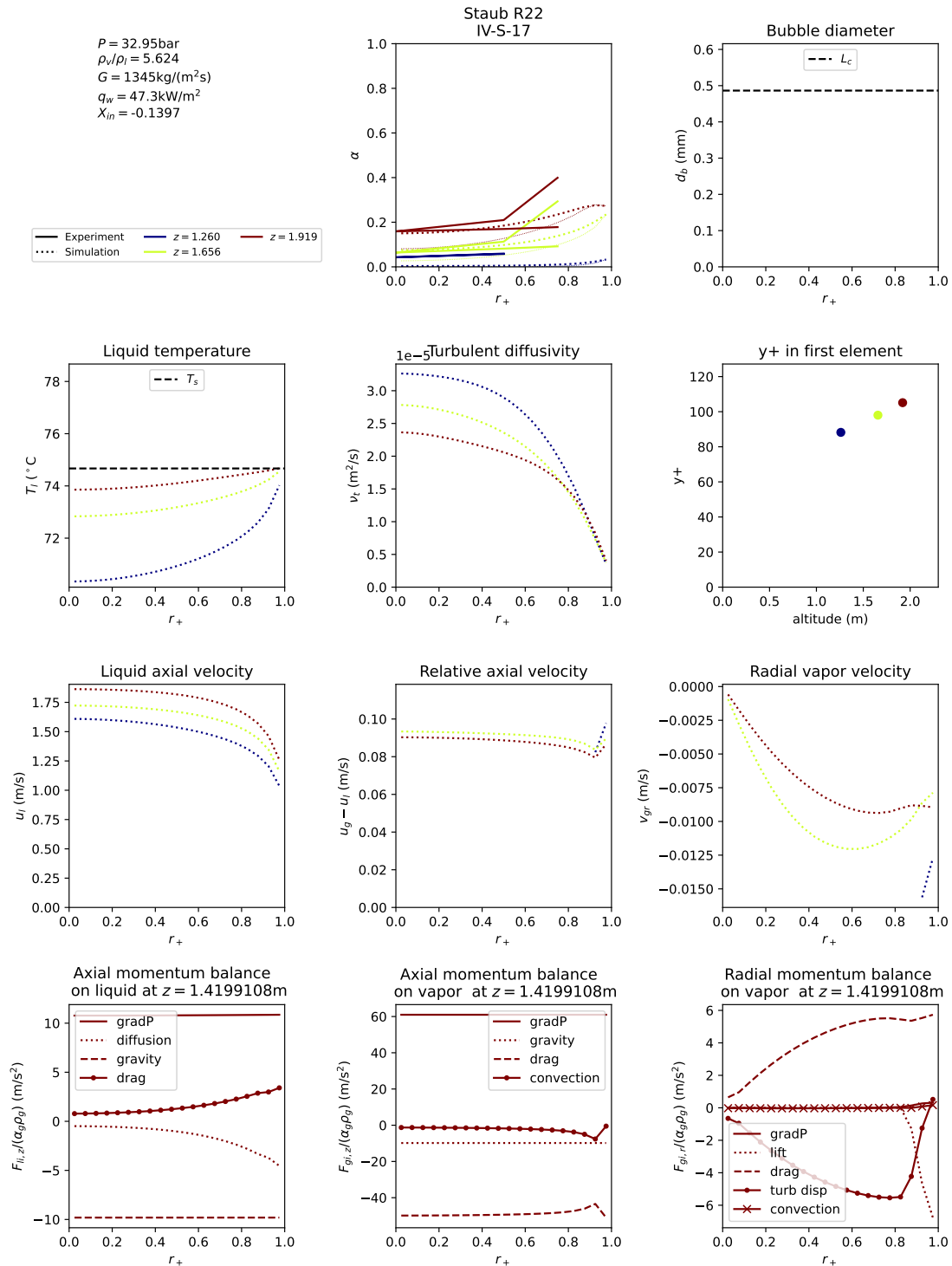


Figure F.50: Simulation results for test tube IV-S-17 of Staub et al. 1969. Experimental results are represented with a full line and simulations with a dashed line.

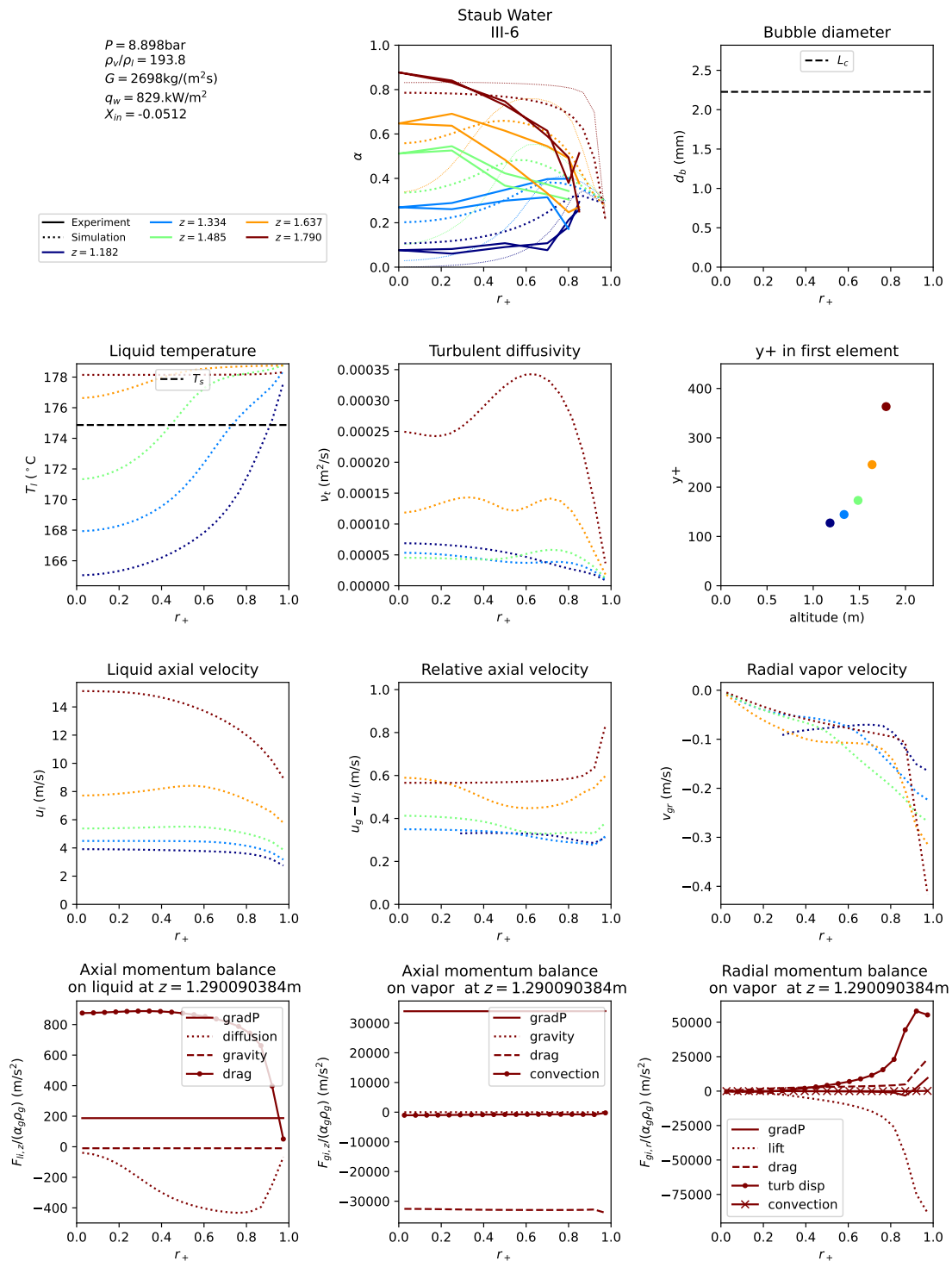


Figure F.51: Simulation results for test tube III-6 of Staub et al. 1969. Experimental results are represented with a full line and simulations with a dashed line.

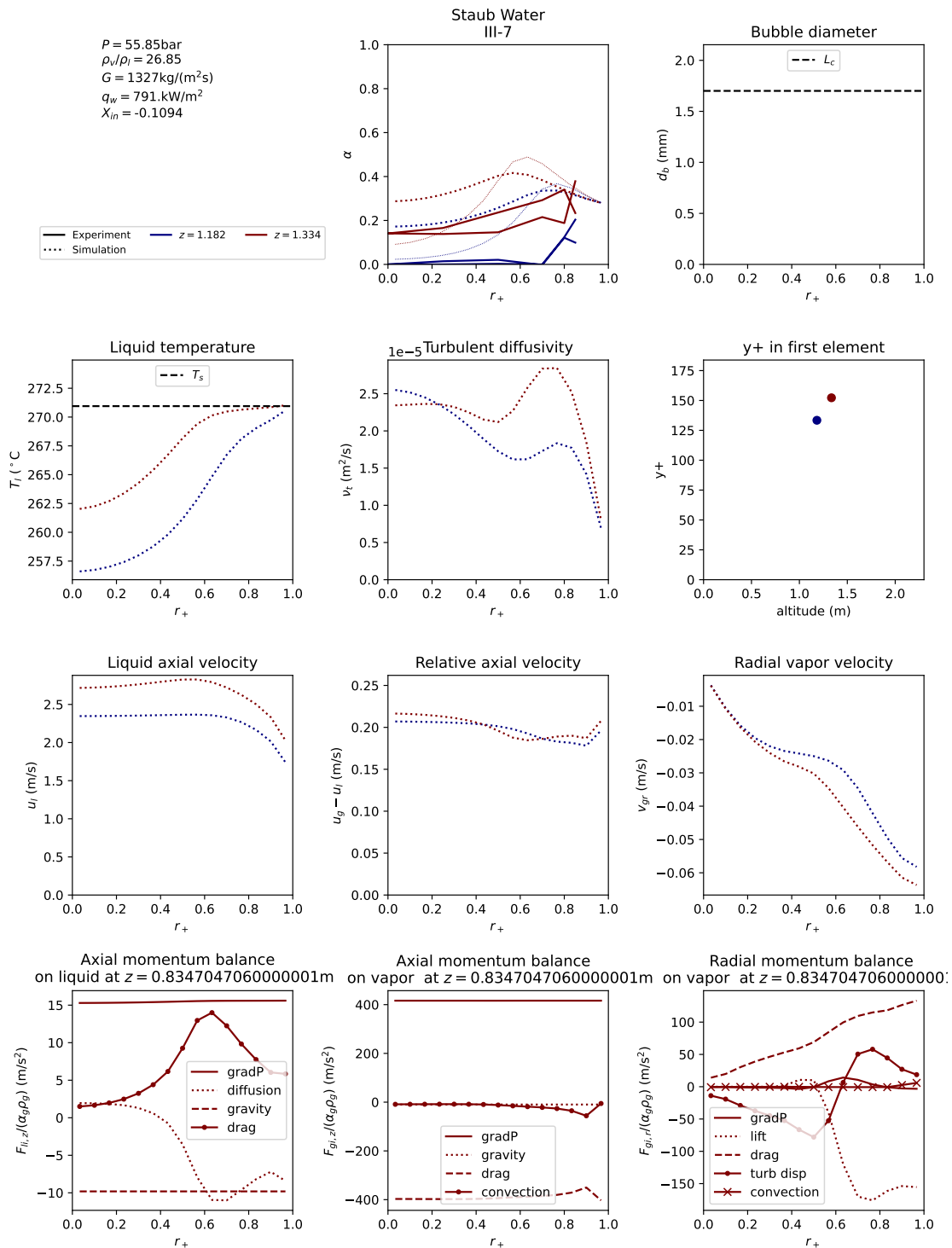


Figure F.52: Simulation results for test tube III-7 of Staub et al. 1969. Experimental results are represented with a full line and simulations with a dashed line.

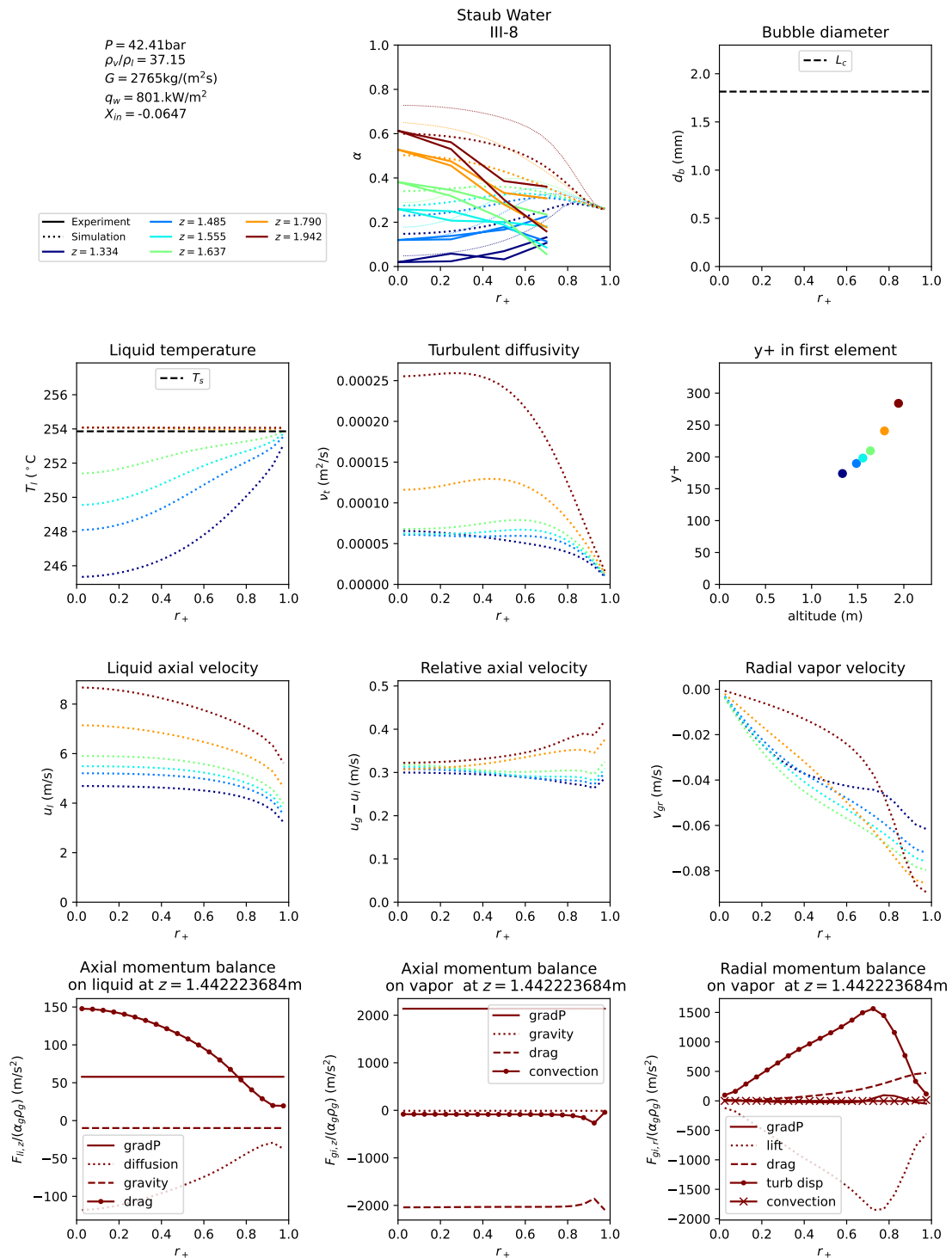


Figure F.53: Simulation results for test tube III-8 of Staub et al. 1969. Experimental results are represented with a full line and simulations with a dashed line.

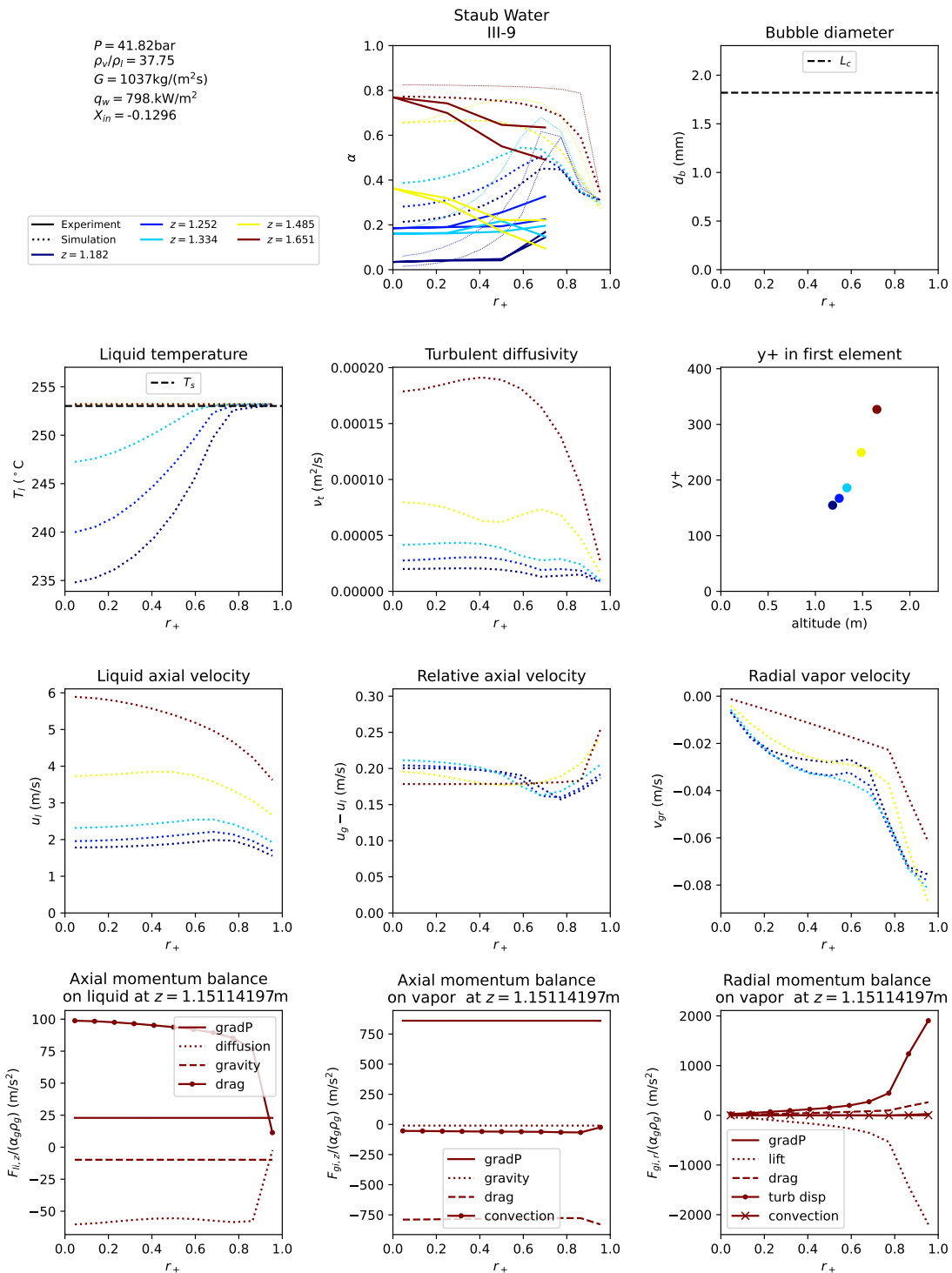


Figure F.54: Simulation results for test tube III-9 of Staub et al. 1969. Experimental results are represented with a full line and simulations with a dashed line.

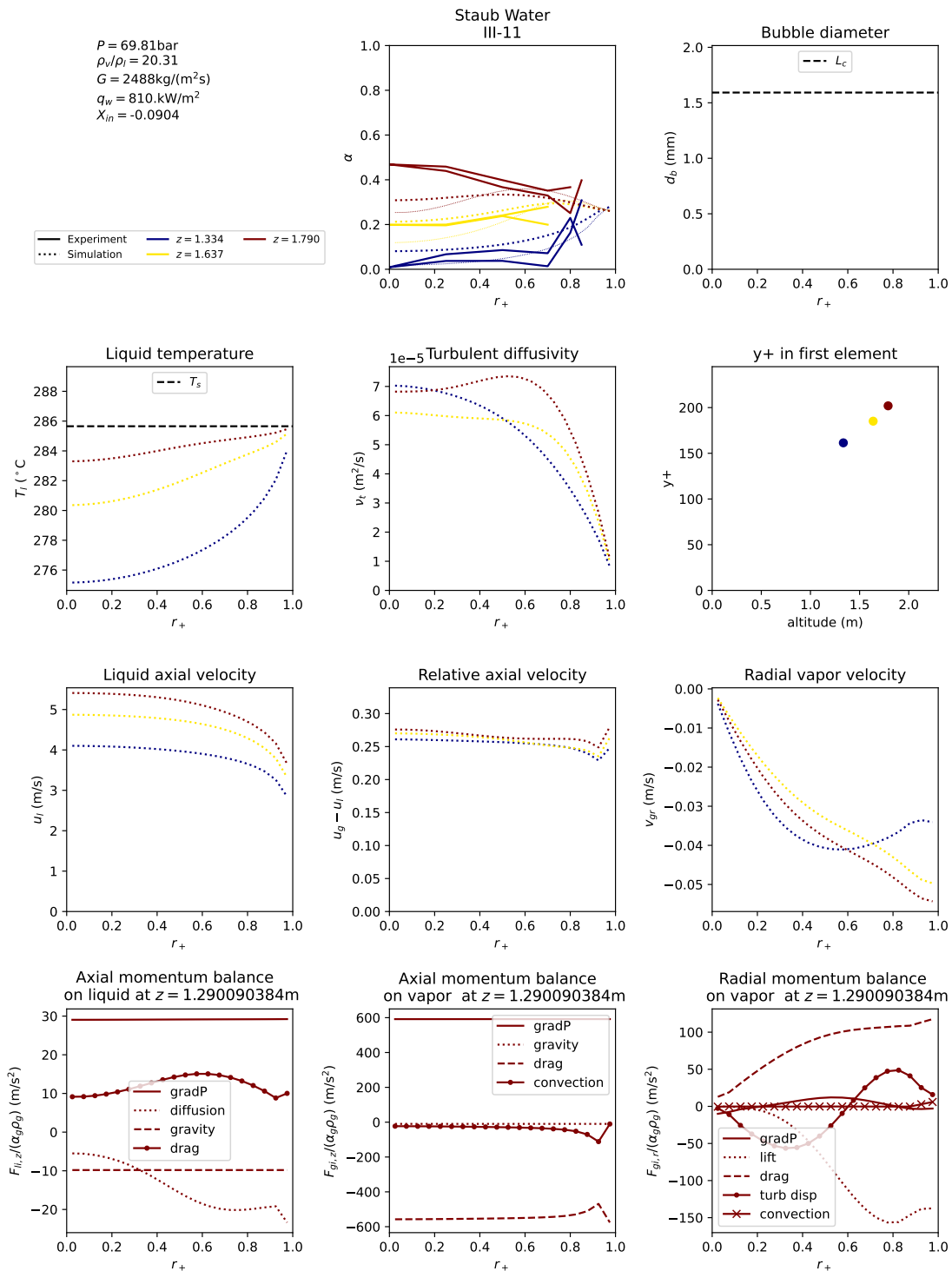


Figure F.55: Simulation results for test tube III-11 of Staub et al. 1969. Experimental results are represented with a full line and simulations with a dashed line.

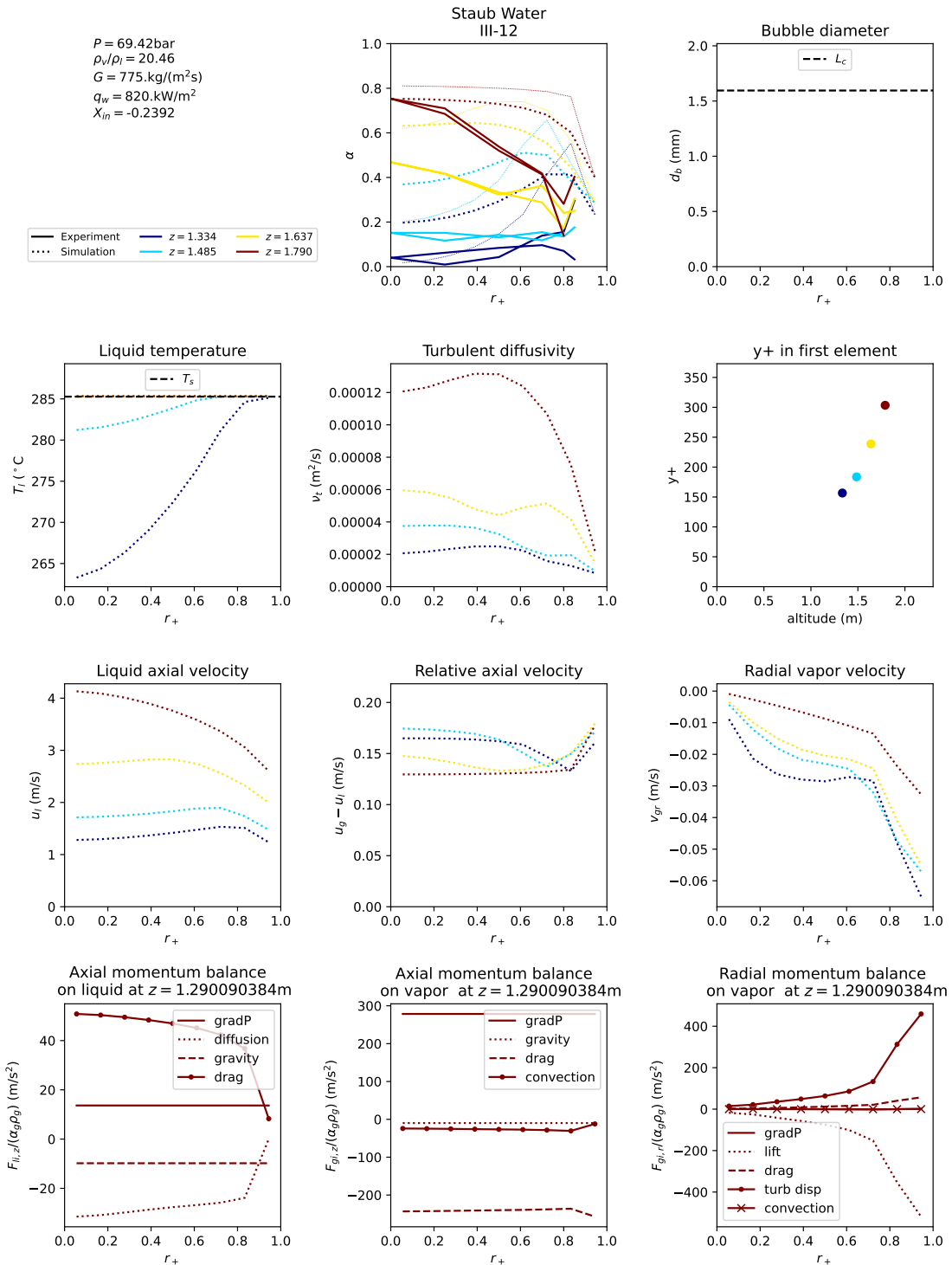


Figure F.56: Simulation results for test tube III-12 of Staub et al. 1969. Experimental results are represented with a full line and simulations with a dashed line.

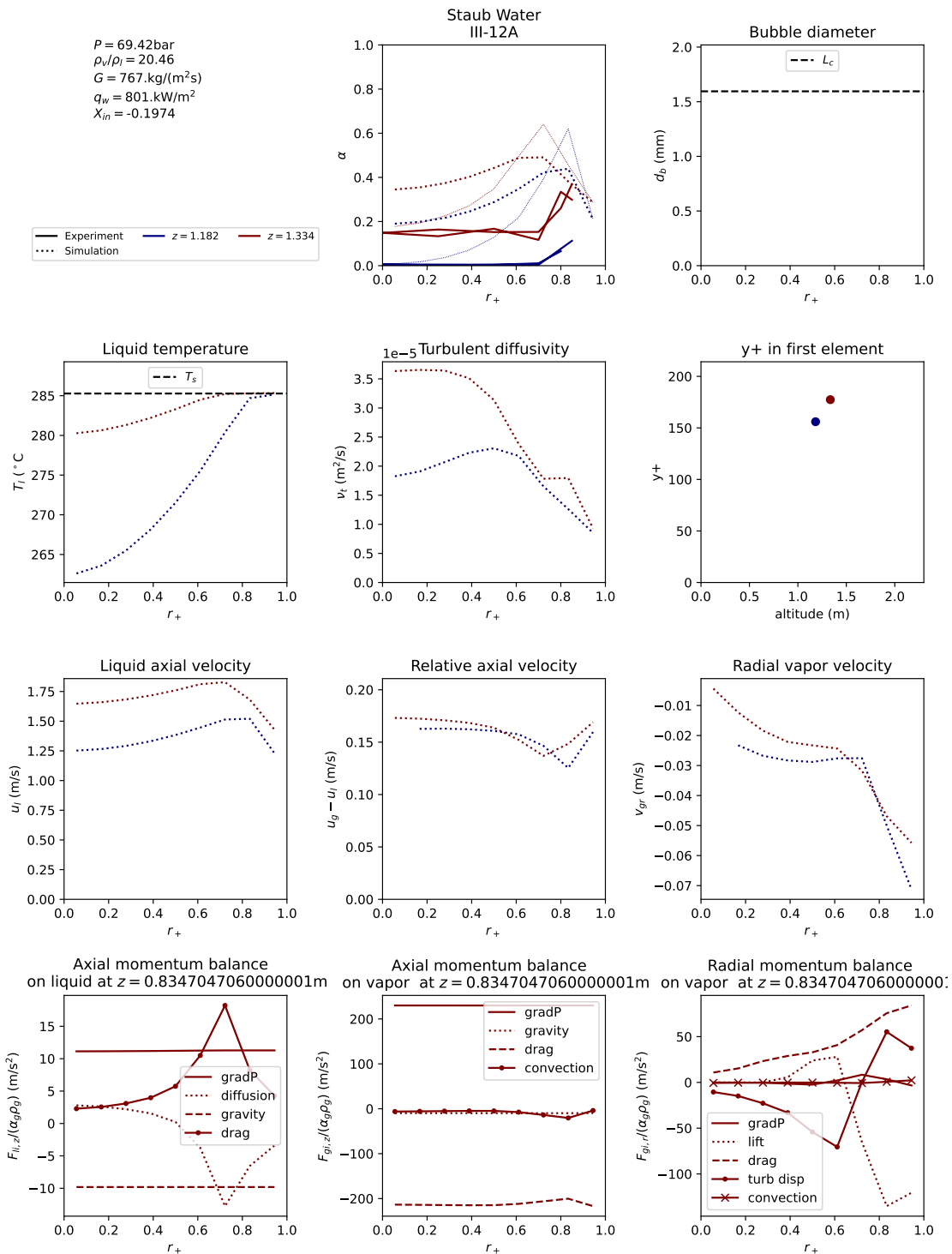


Figure F.57: Simulation results for test tube III-12A of Staub et al. 1969. Experimental results are represented with a full line and simulations with a dashed line.

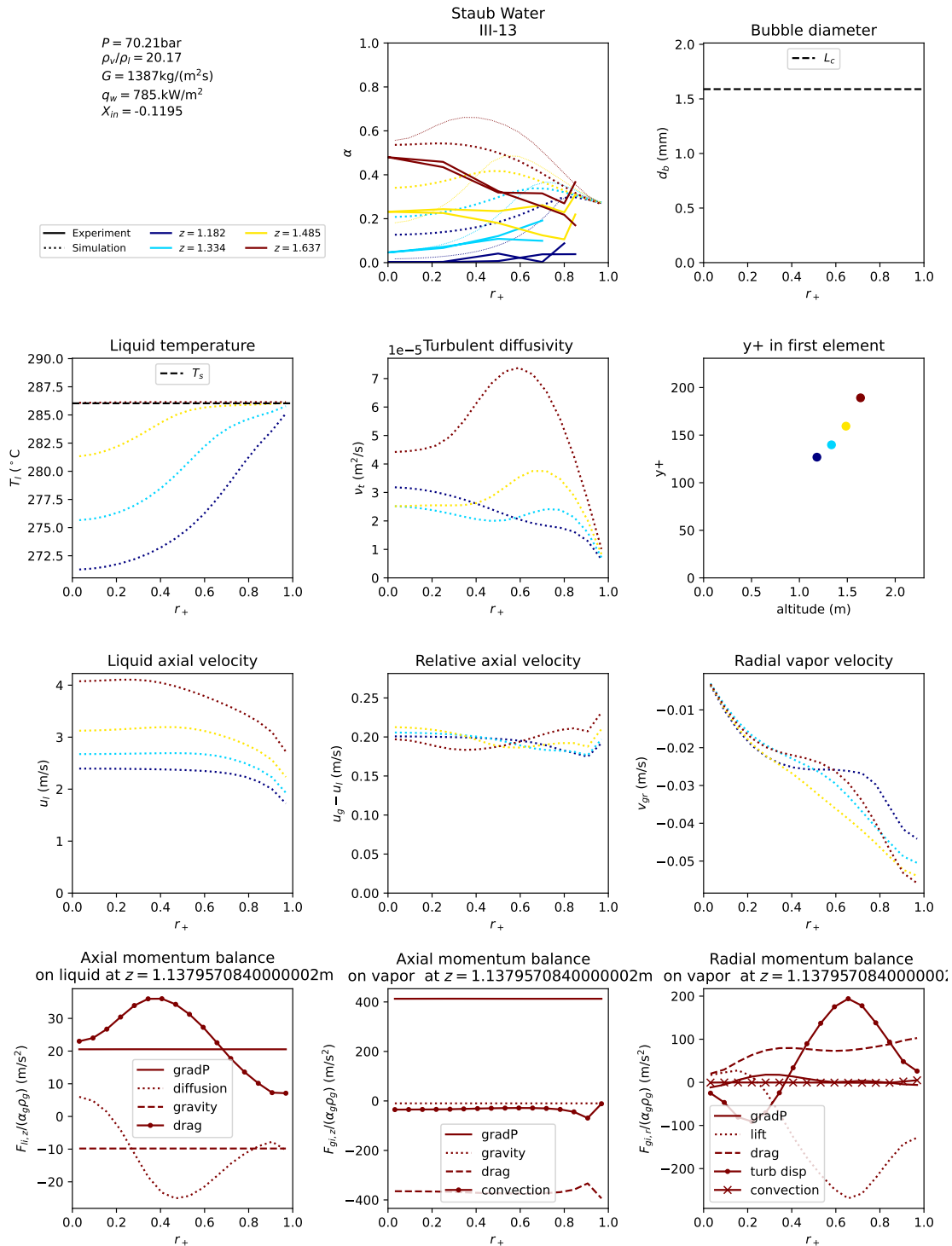


Figure F.58: Simulation results for test tube III-13 of Staub et al. 1969. Experimental results are represented with a full line and simulations with a dashed line.

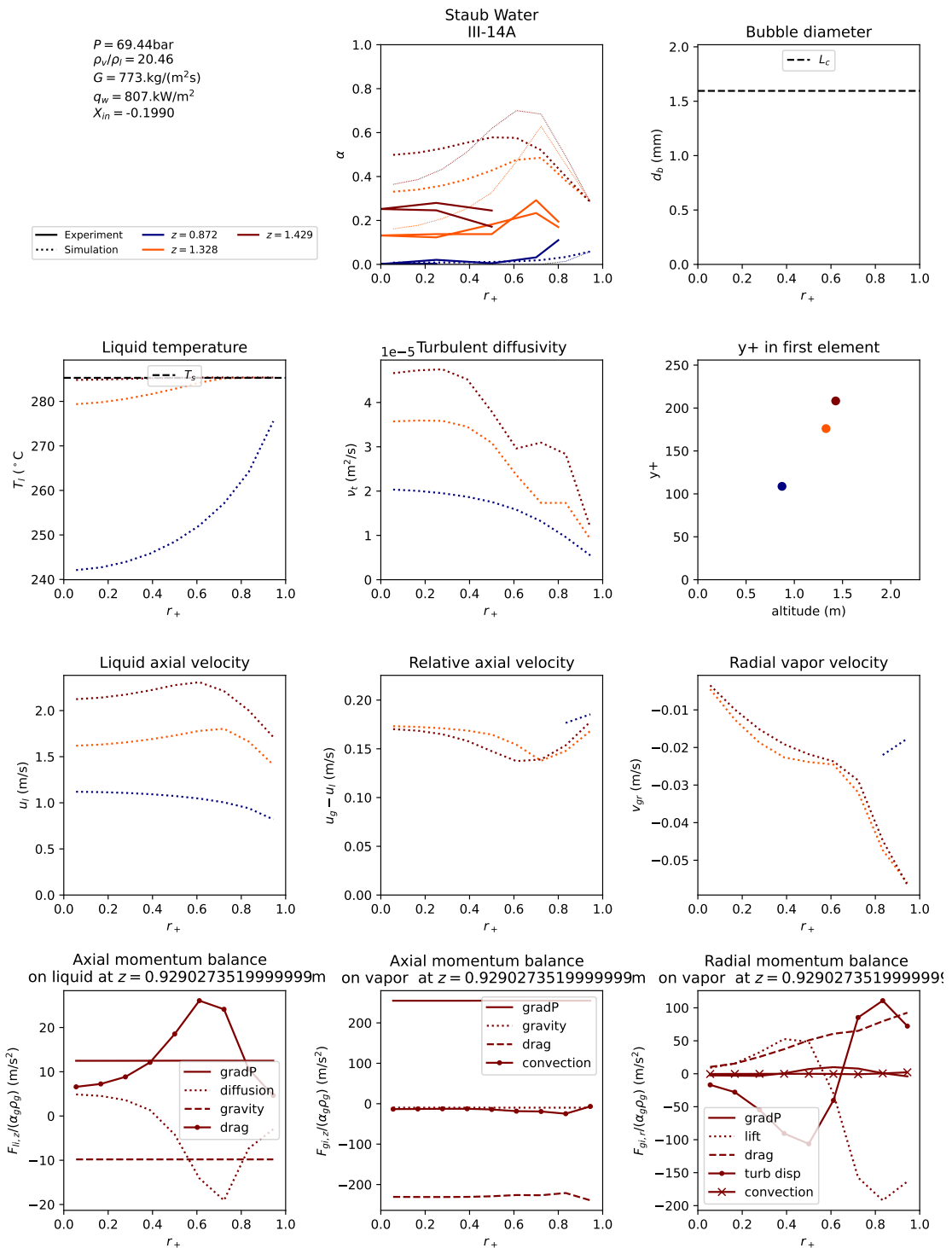


Figure F.59: Simulation results for test tube III-14A of Staub et al. 1969. Experimental results are represented with a full line and simulations with a dashed line.

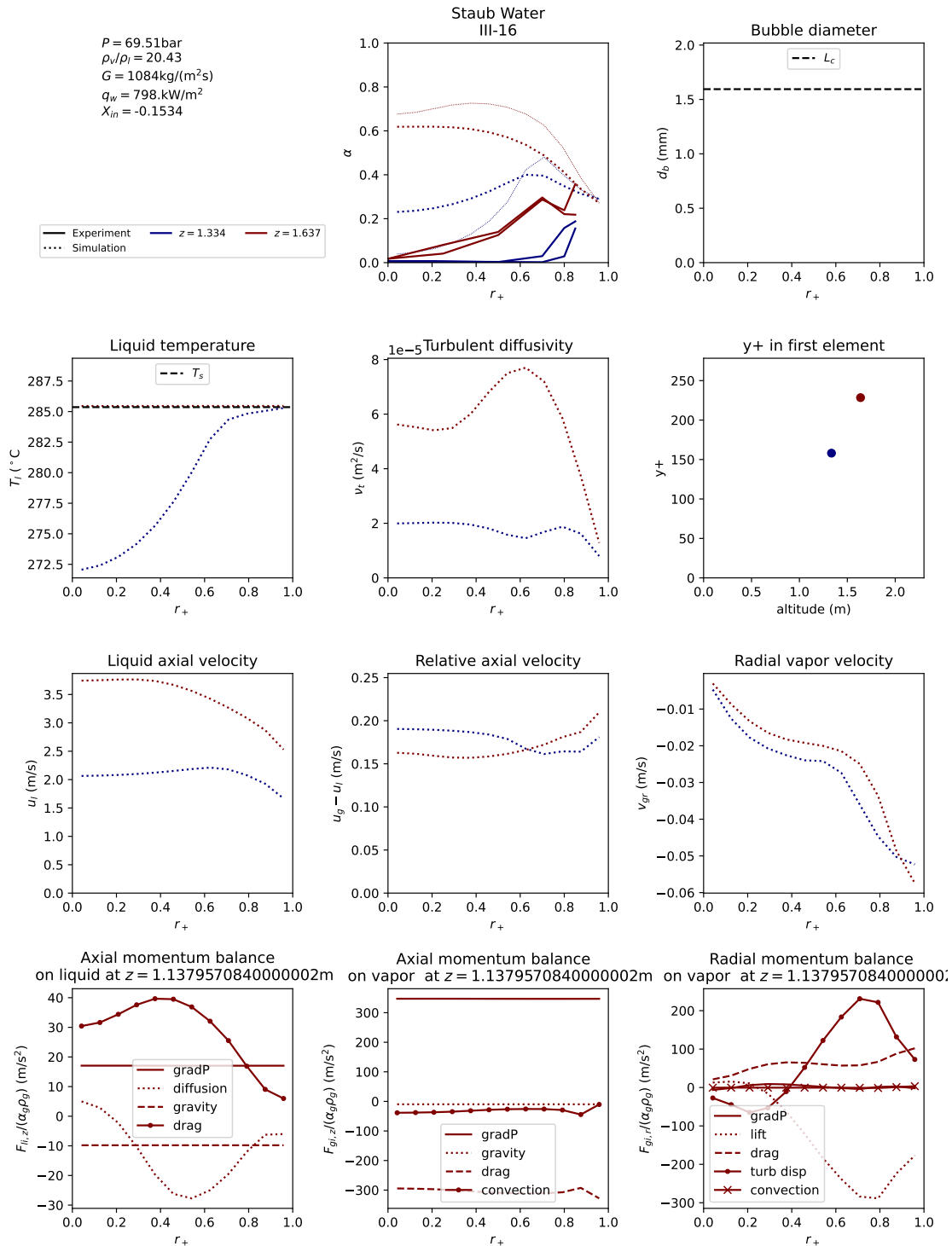


Figure F.60: Simulation results for test tube III-16 of Staub et al. 1969. Experimental results are represented with a full line and simulations with a dashed line.

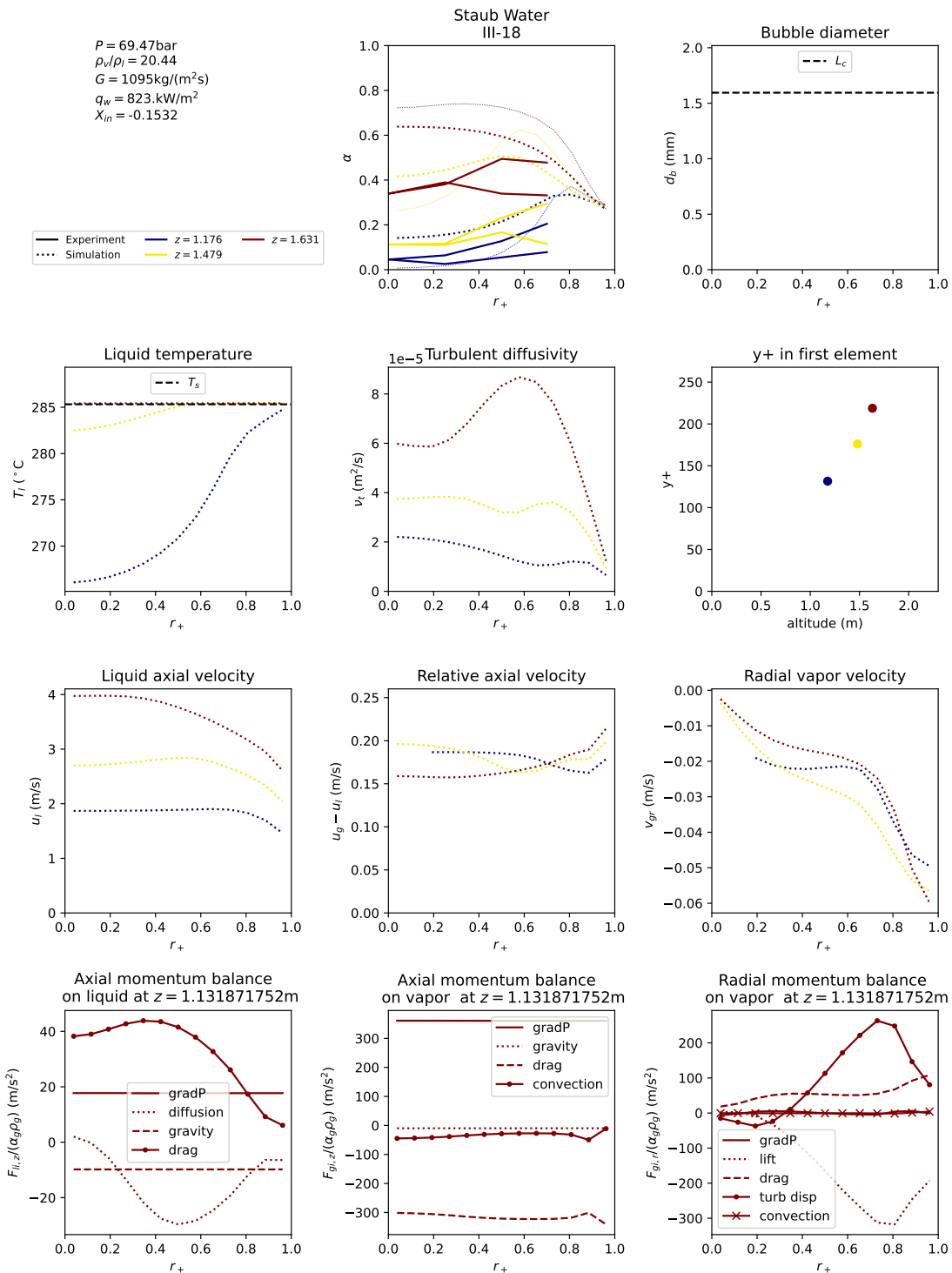


Figure F.61: Simulation results for test tube III-18 of Staub et al. 1969. Experimental results are represented with a full line and simulations with a dashed line.

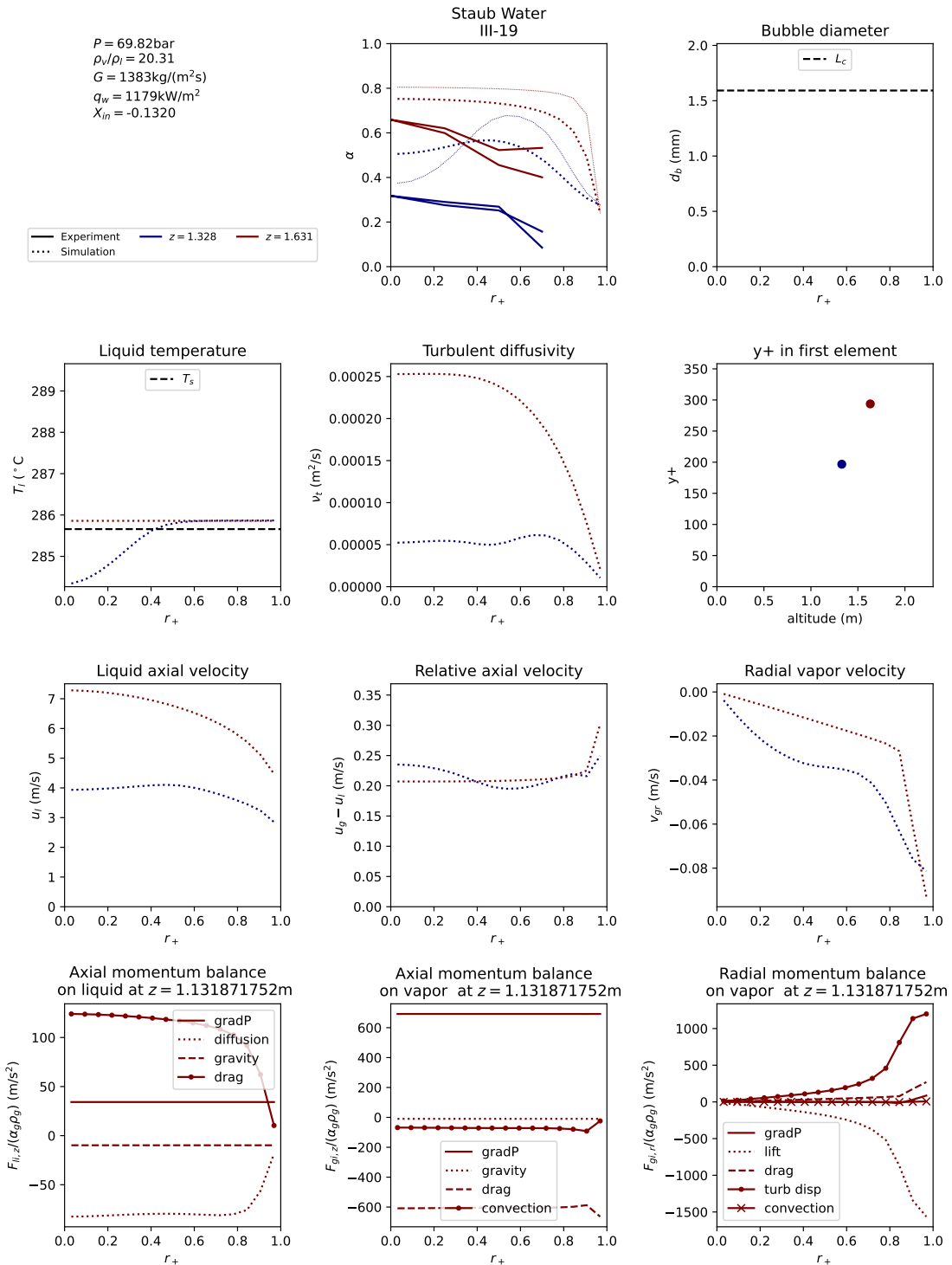


Figure F.62: Simulation results for test tube III-19 of Staub et al. 1969. Experimental results are represented with a full line and simulations with a dashed line.

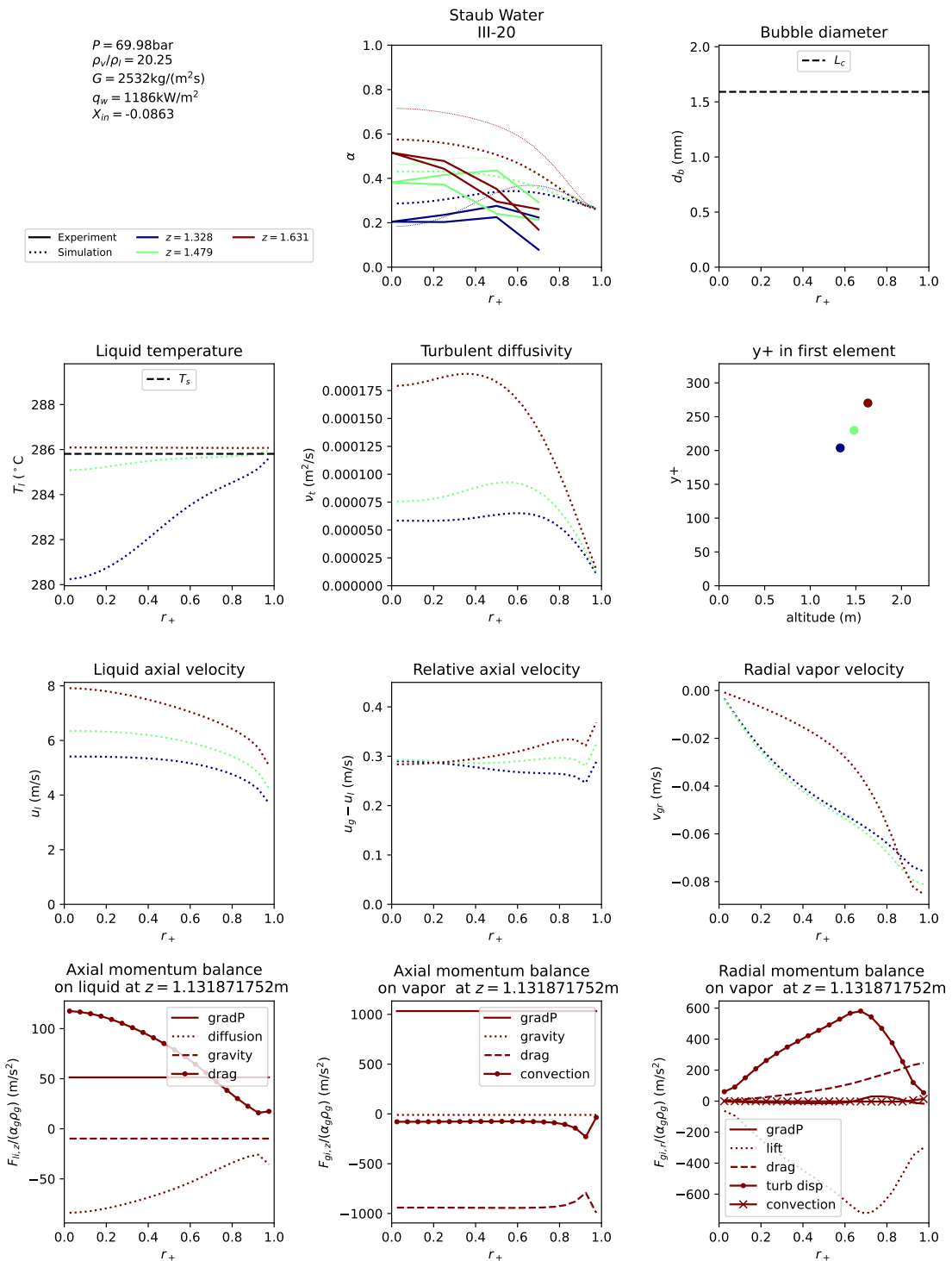


Figure F.63: Simulation results for test tube III-20 of Staub et al. 1969. Experimental results are represented with a full line and simulations with a dashed line.

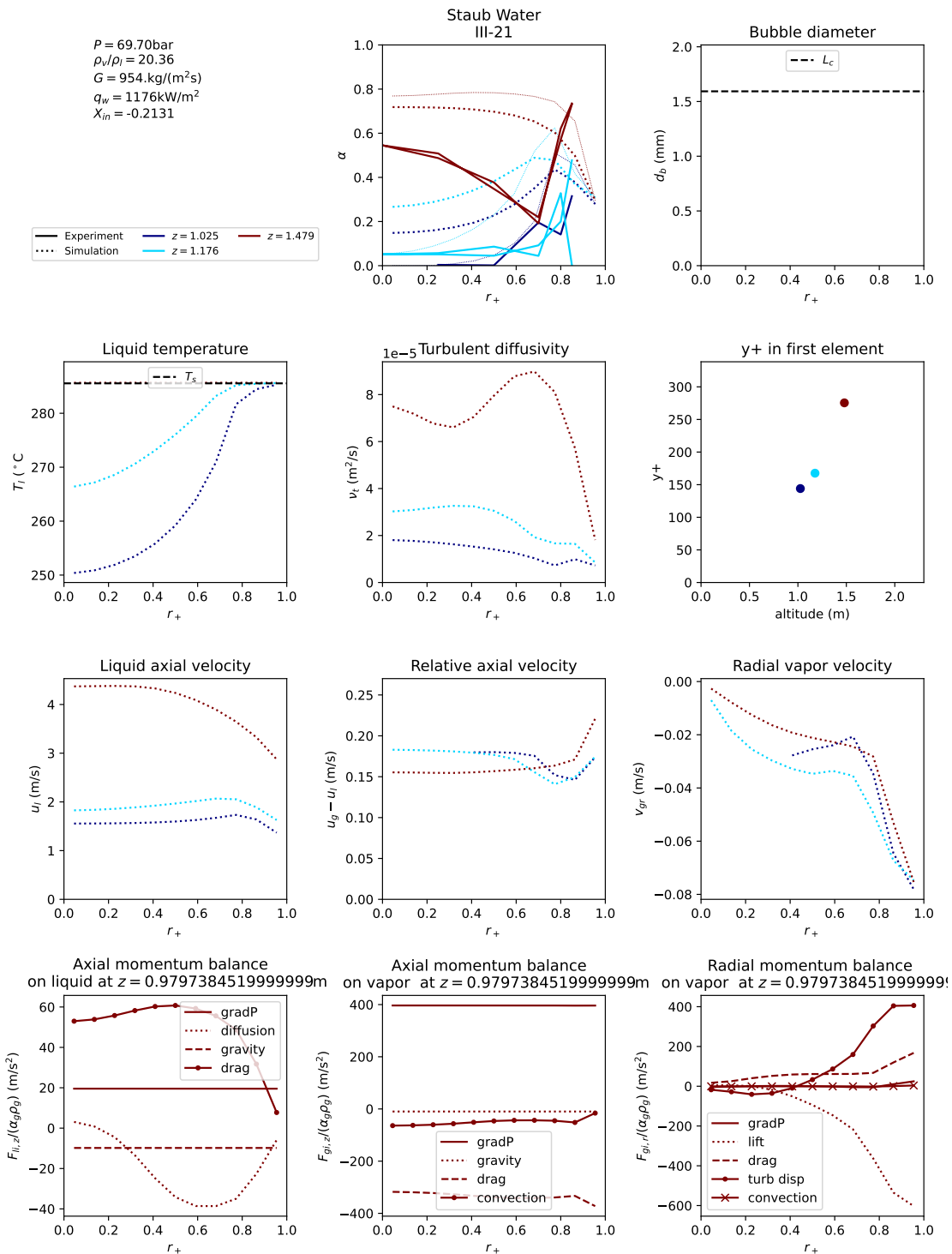


Figure F.64: Simulation results for test tube III-21 of Staub et al. 1969. Experimental results are represented with a full line and simulations with a dashed line.

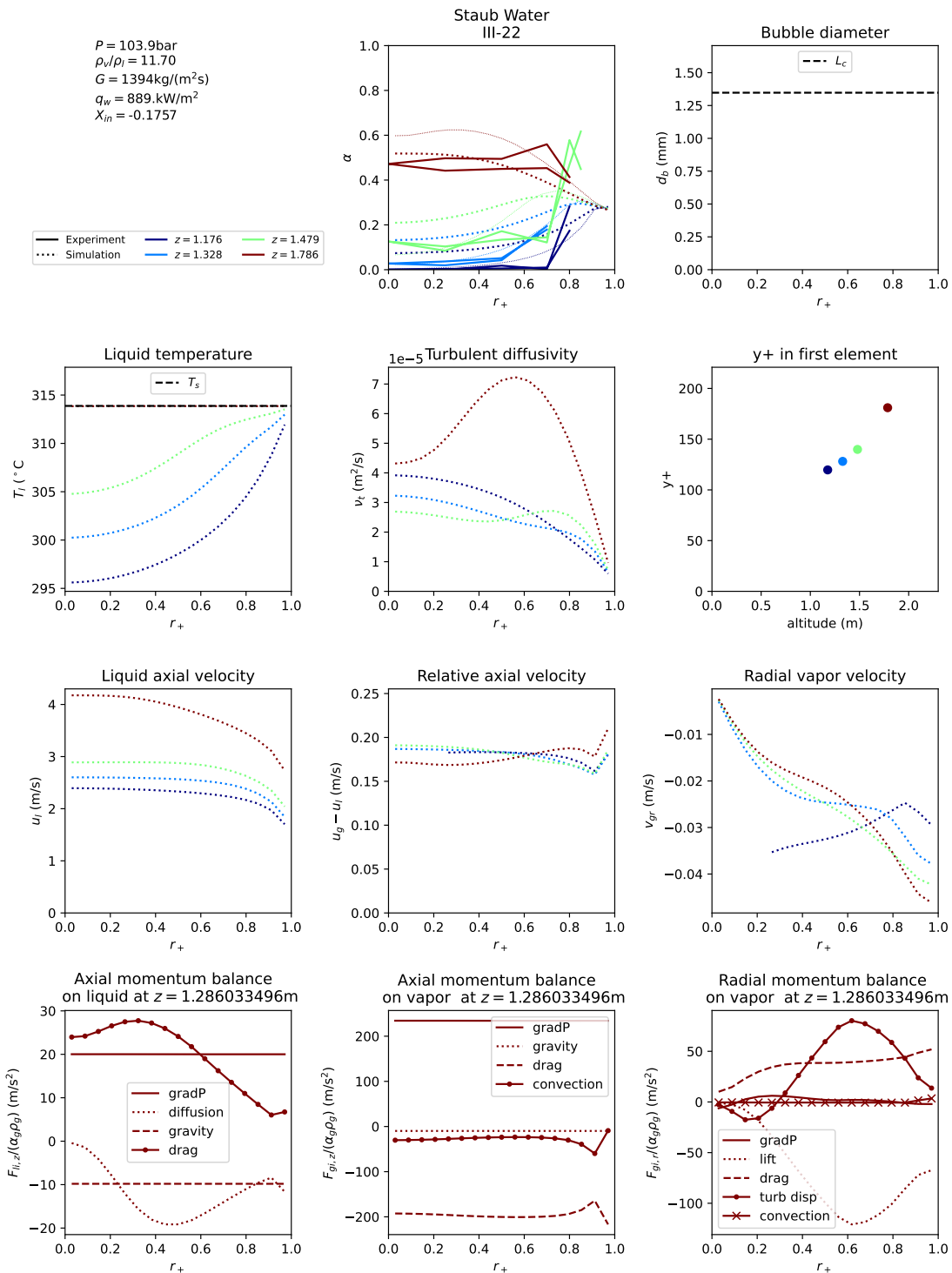


Figure F.65: Simulation results for test tube III-22 of Staub et al. 1969. Experimental results are represented with a full line and simulations with a dashed line.

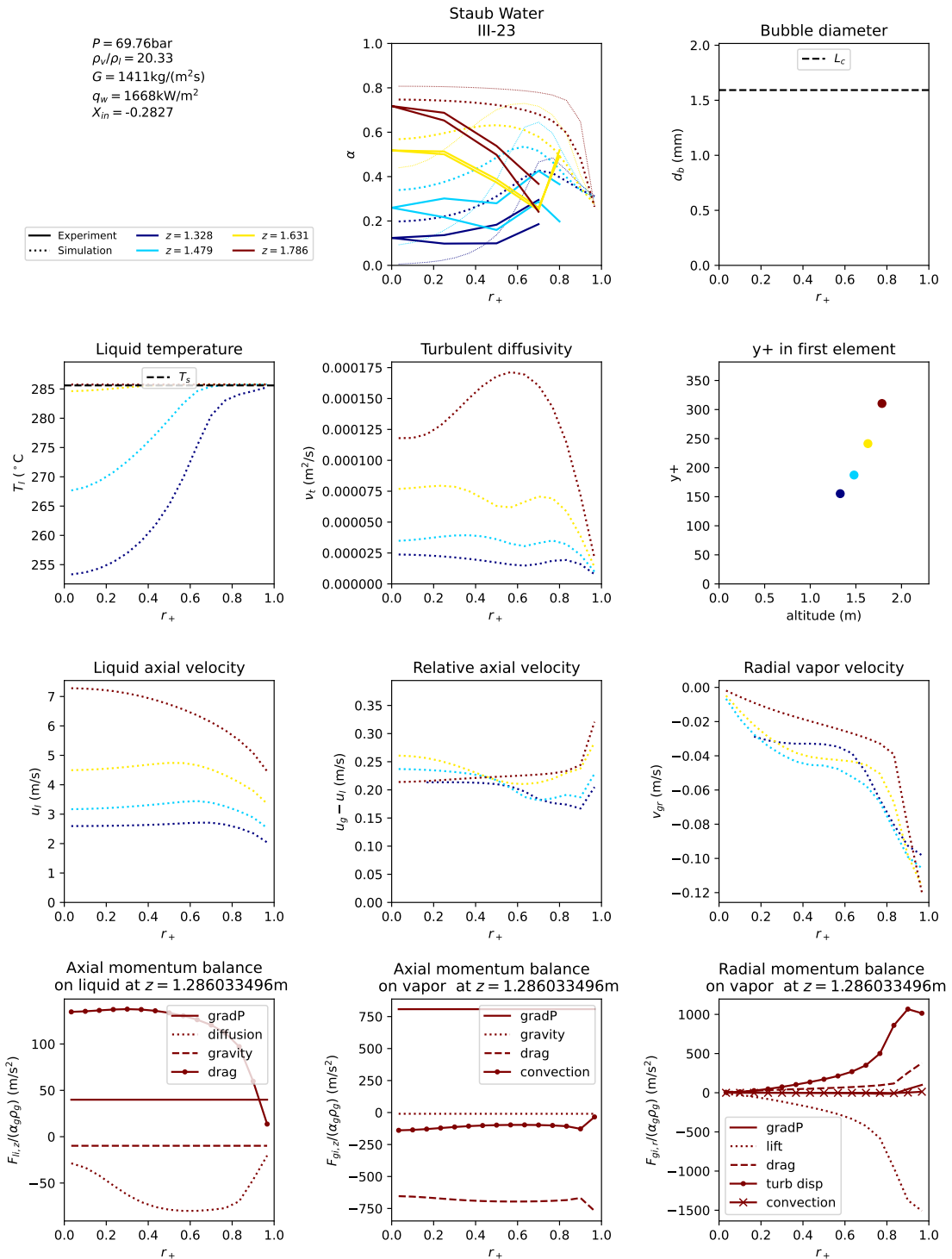


Figure F.66: Simulation results for test tube III-23 of Staub et al. 1969. Experimental results are represented with a full line and simulations with a dashed line.

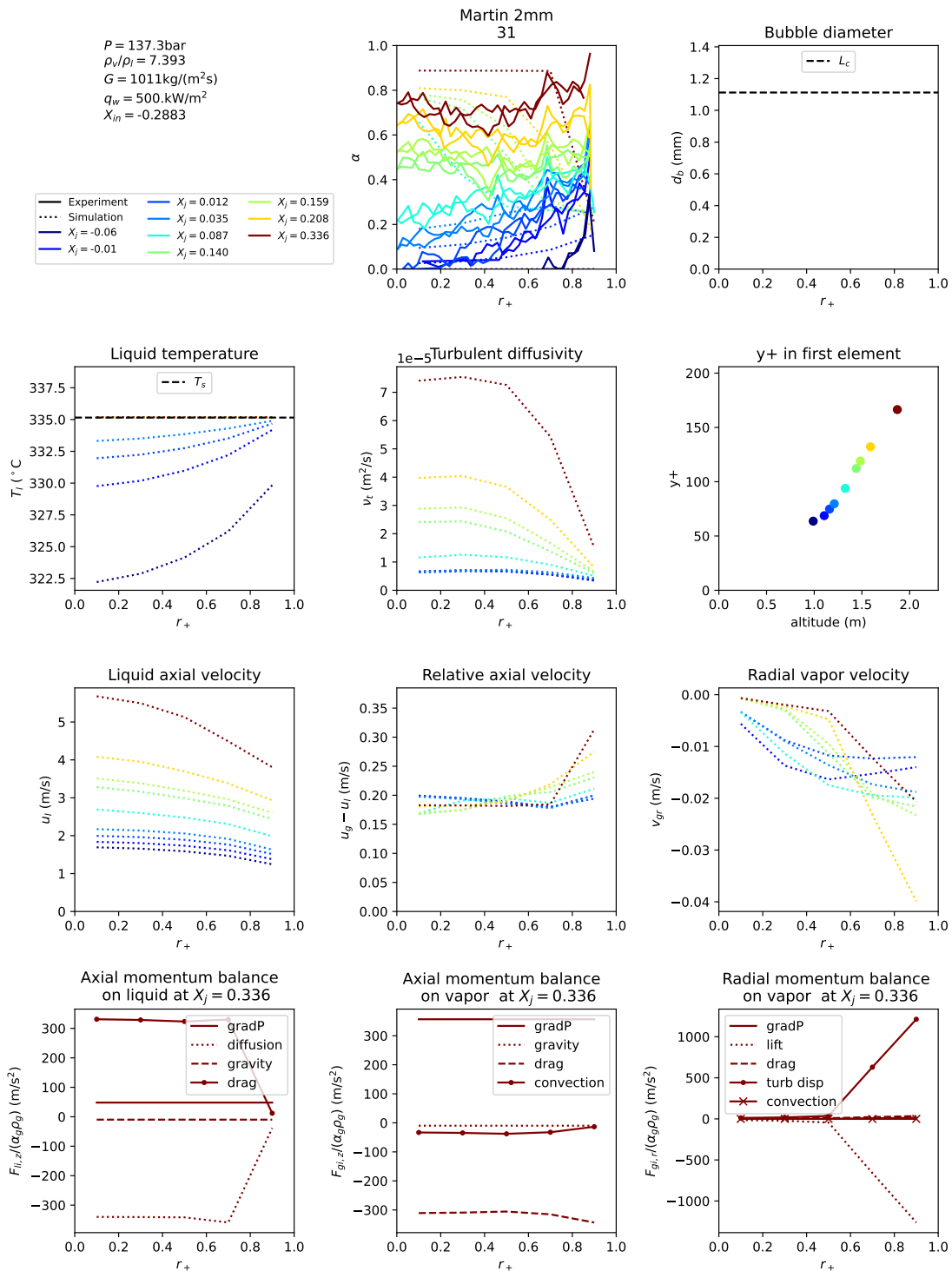


Figure F.67: Simulation results for test tube 31 of Martin 1969. Experimental results are represented with a full line and simulations with a dashed line.

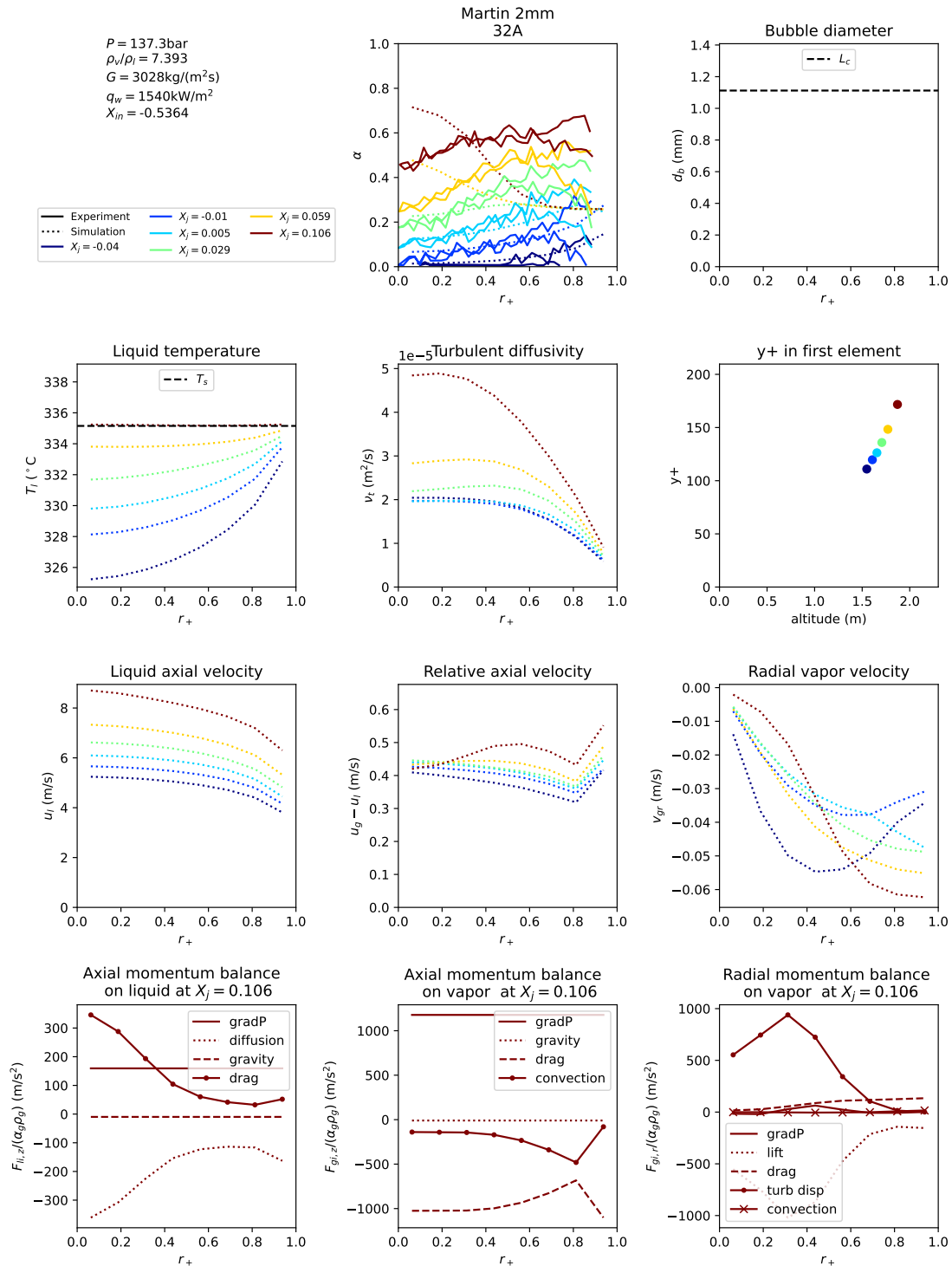


Figure F.68: Simulation results for test tube 32A of Martin 1969. Experimental results are represented with a full line and simulations with a dashed line.

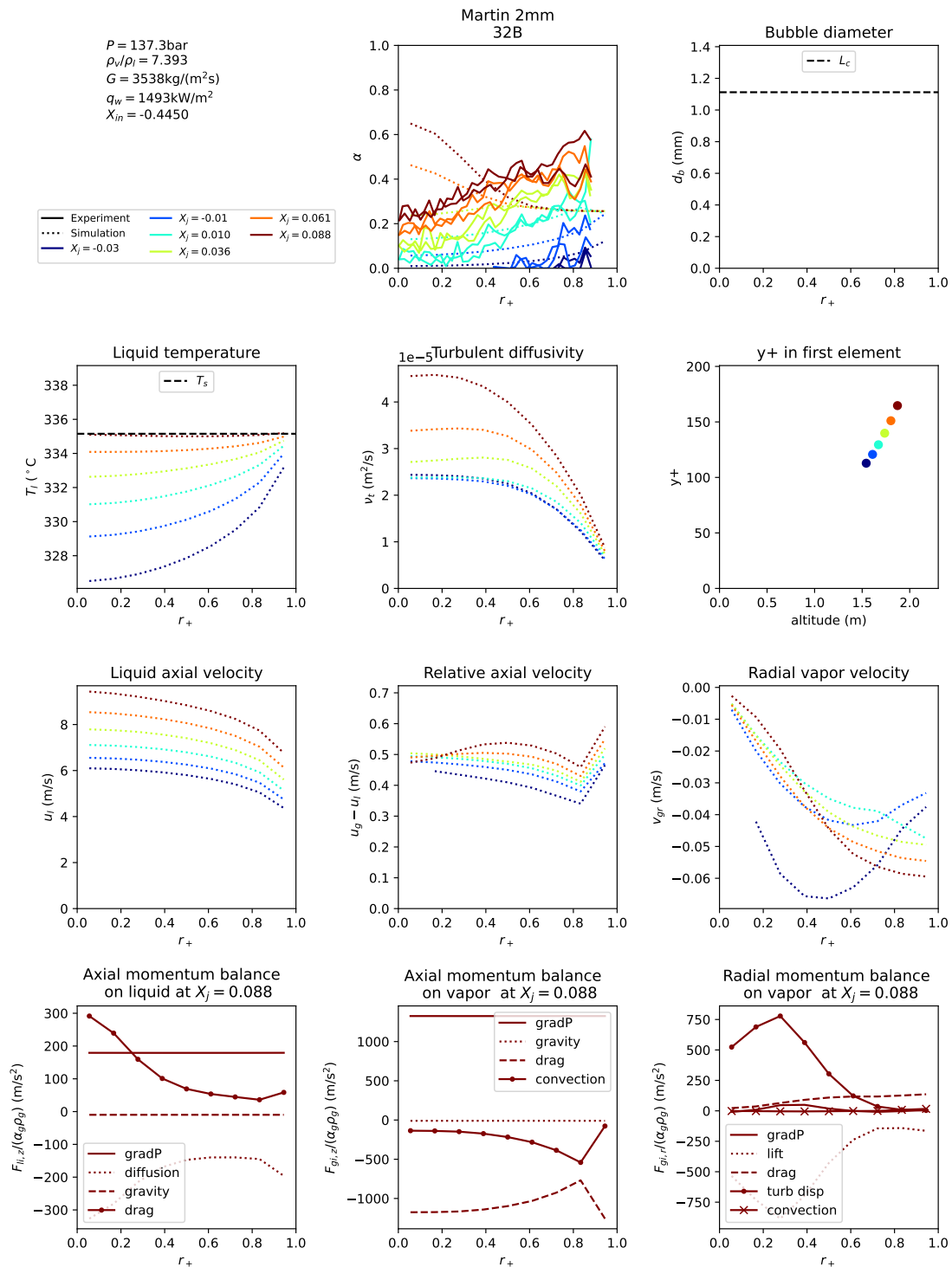


Figure F.69: Simulation results for test tube 32B of Martin 1969. Experimental results are represented with a full line and simulations with a dashed line.

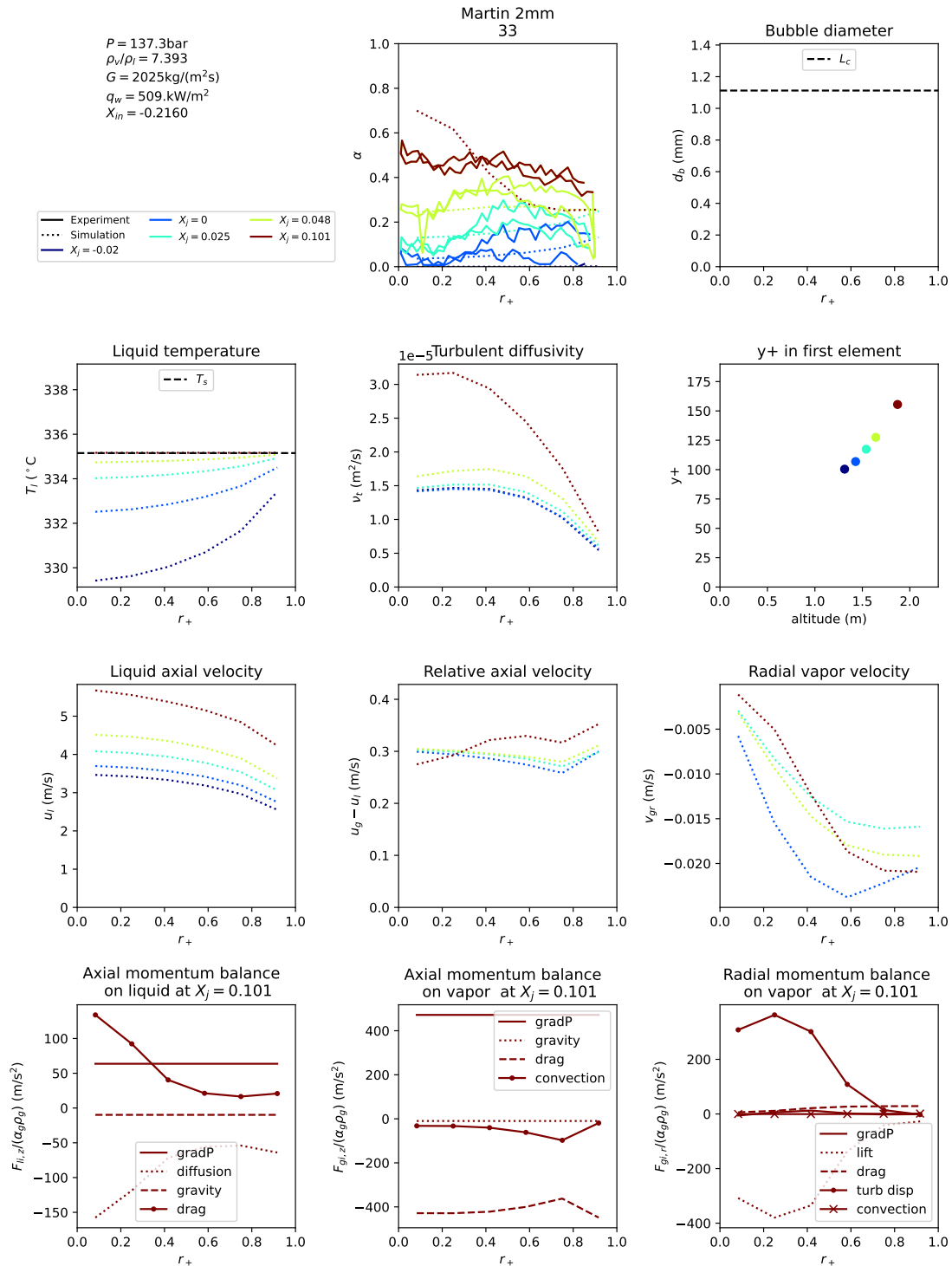


Figure F.70: Simulation results for test tube 33 of Martin 1969. Experimental results are represented with a full line and simulations with a dashed line.

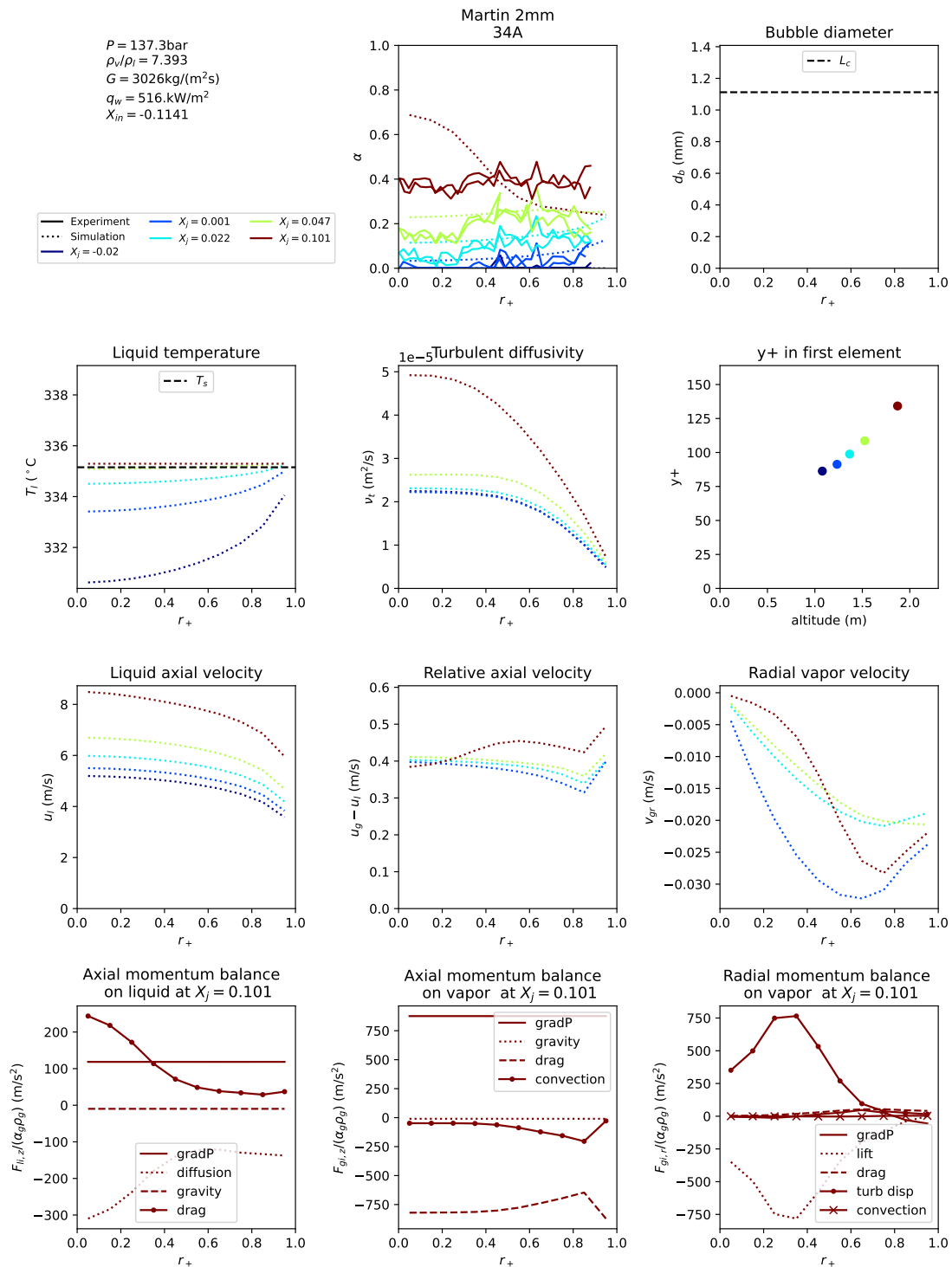


Figure F.71: Simulation results for test tube 34A of Martin 1969. Experimental results are represented with a full line and simulations with a dashed line.

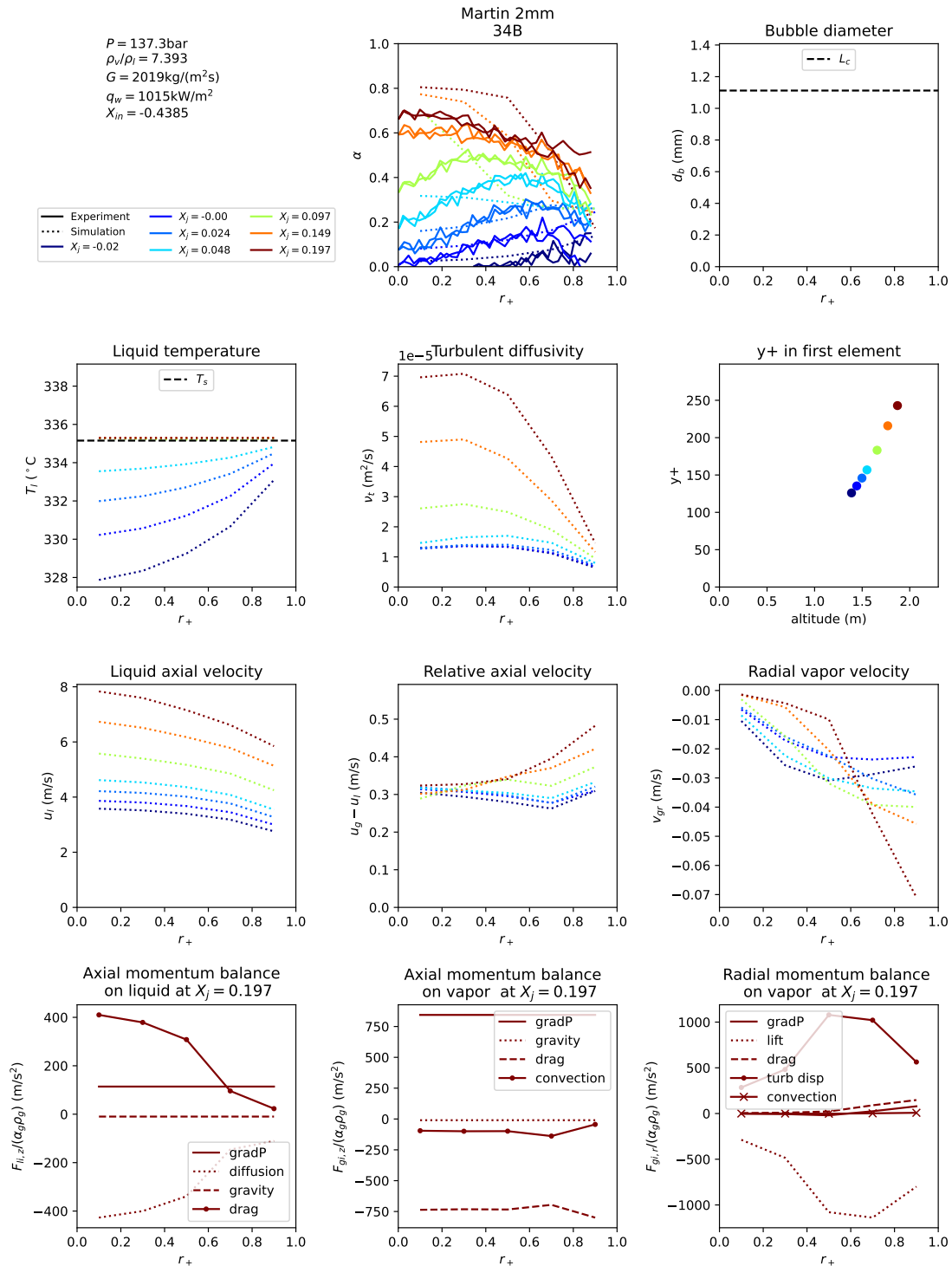


Figure F.72: Simulation results for test tube 34B of Martin 1969. Experimental results are represented with a full line and simulations with a dashed line.

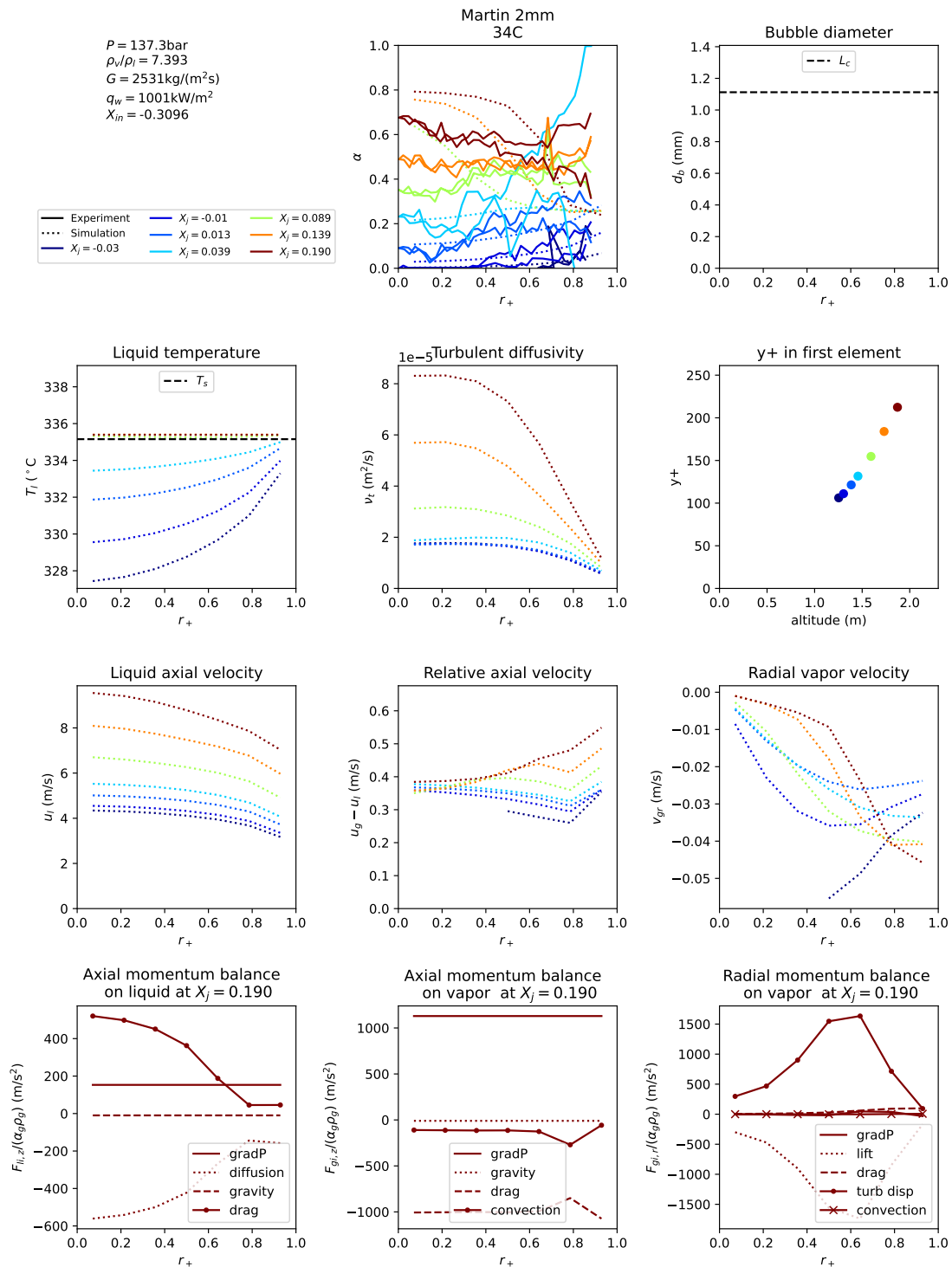


Figure F.73: Simulation results for test tube 34C of Martin 1969. Experimental results are represented with a full line and simulations with a dashed line.

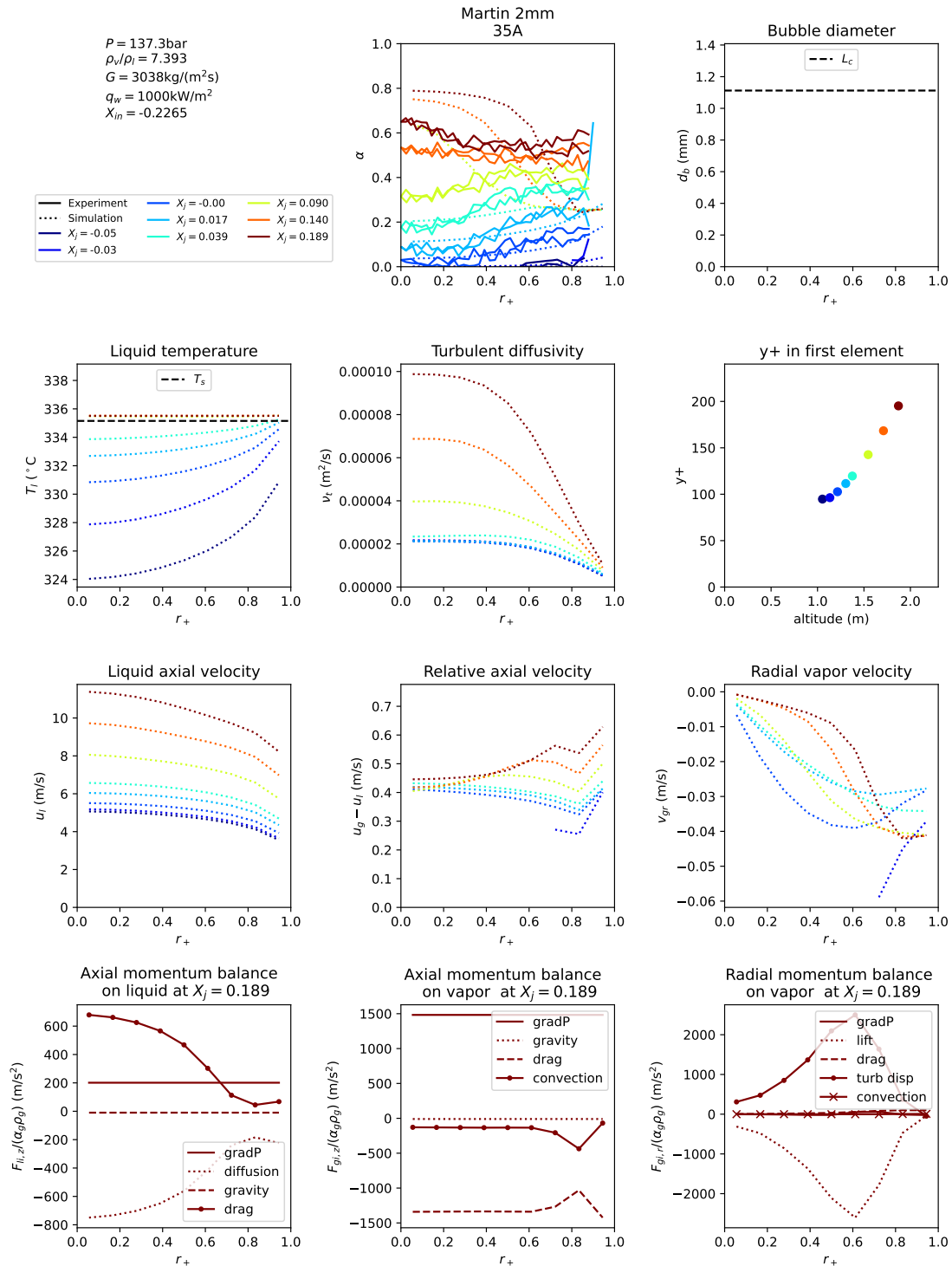


Figure F.74: Simulation results for test tube 35A of Martin 1969. Experimental results are represented with a full line and simulations with a dashed line.

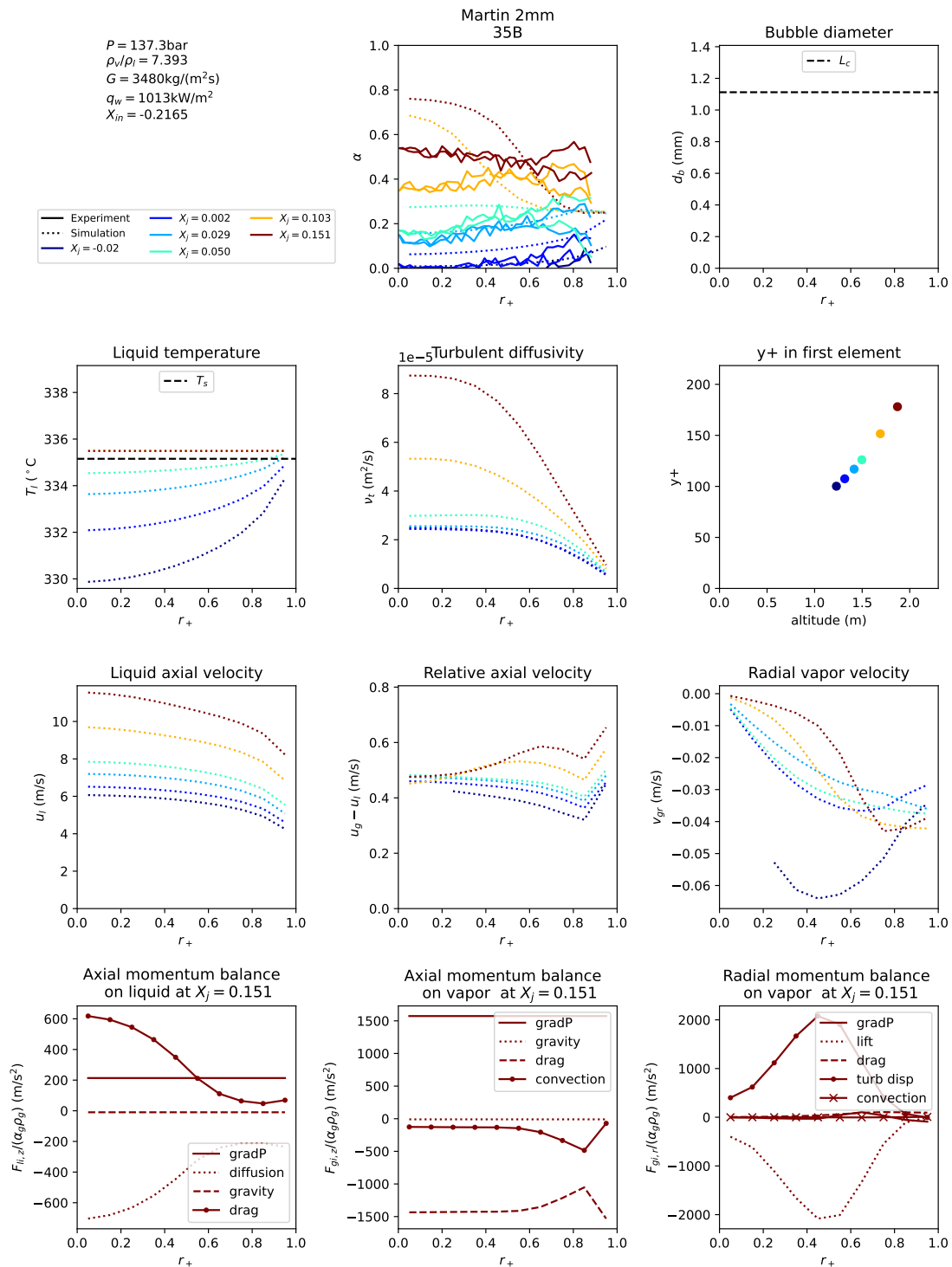


Figure F.75: Simulation results for test tube 35B of Martin 1969. Experimental results are represented with a full line and simulations with a dashed line.

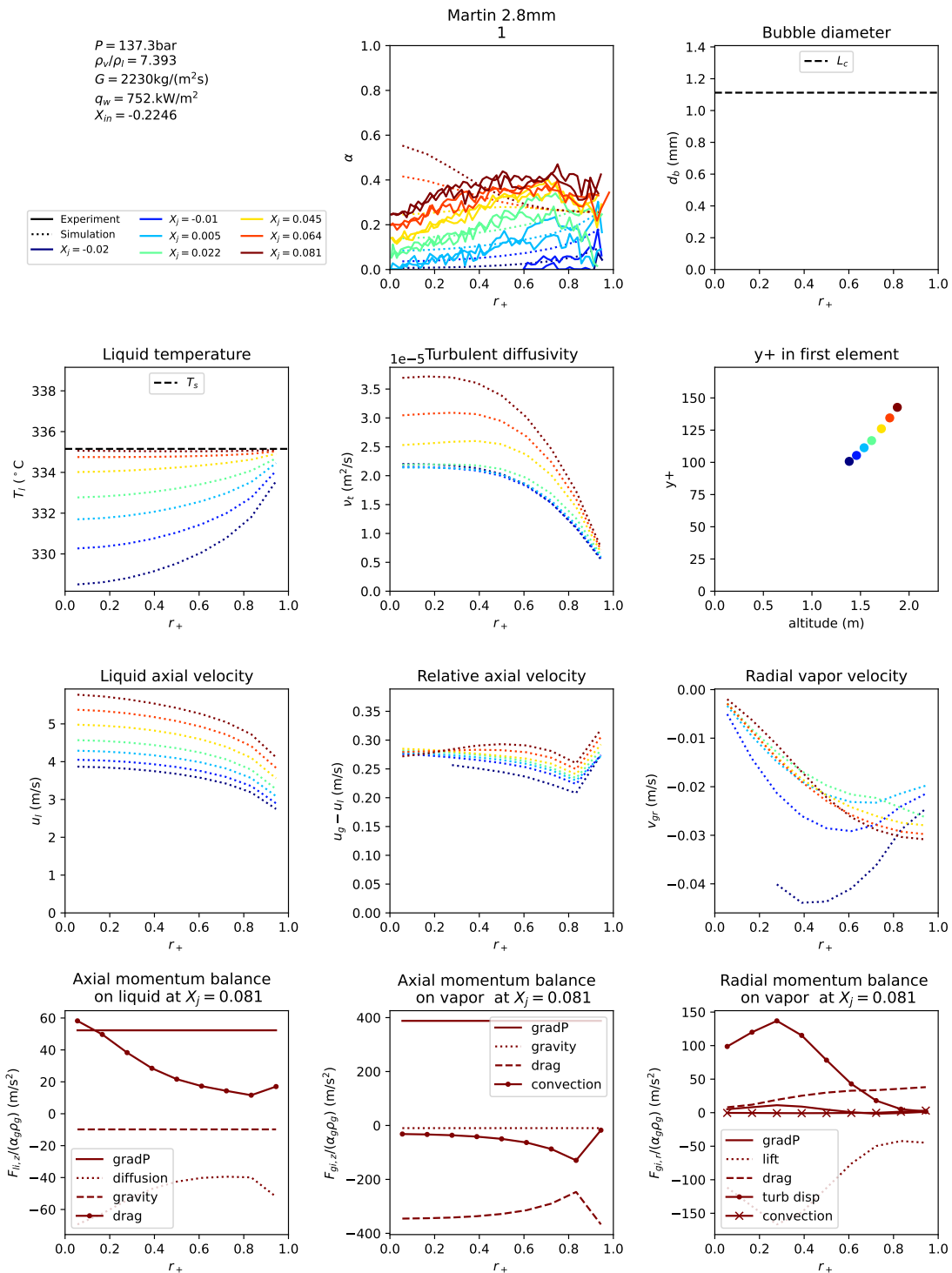


Figure F.76: Simulation results for test tube 1 of Martin 1969. Experimental results are represented with a full line and simulations with a dashed line.

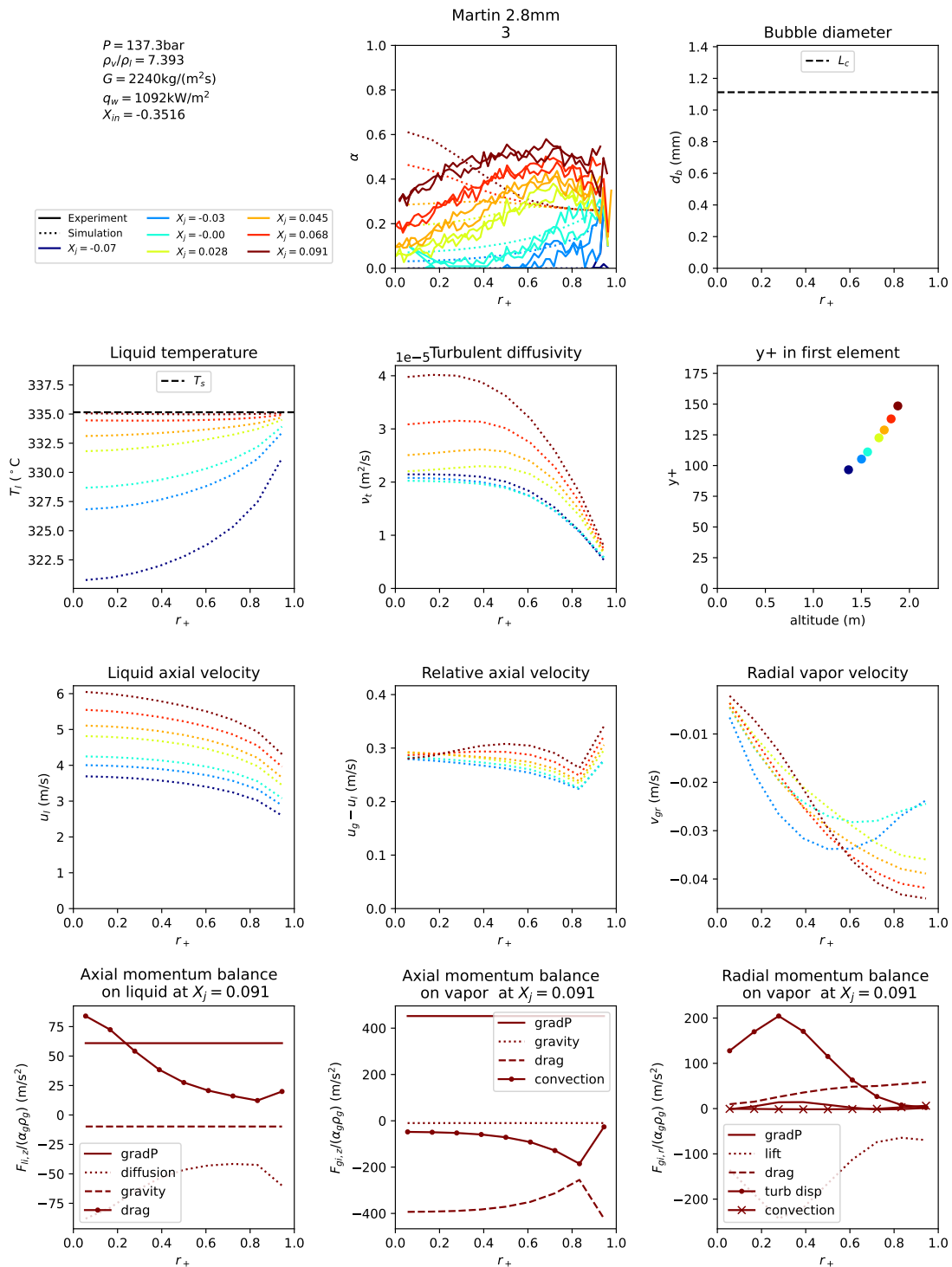


Figure F.77: Simulation results for test tube 3 of Martin 1969. Experimental results are represented with a full line and simulations with a dashed line.

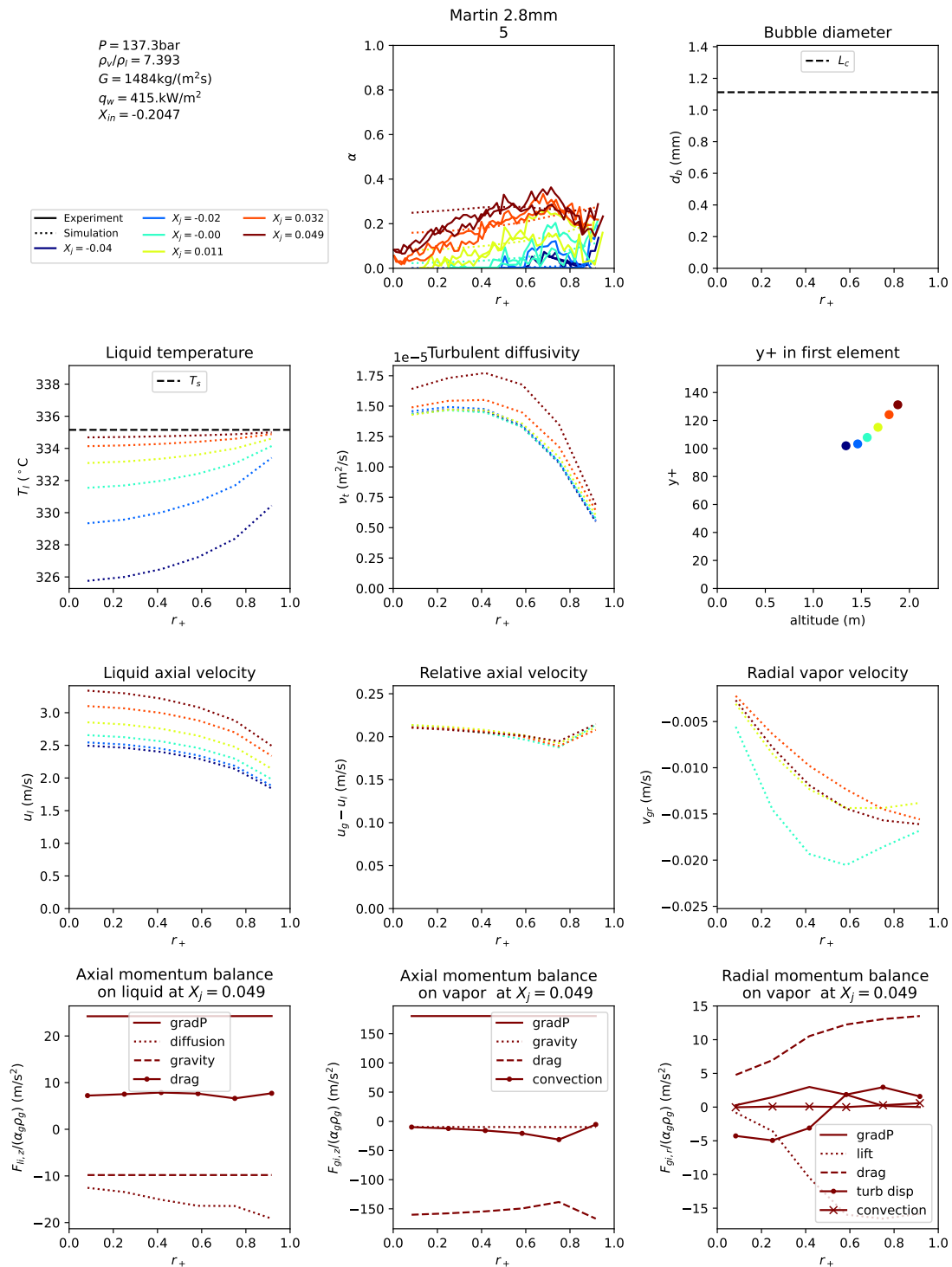


Figure F.78: Simulation results for test tube 5 of Martin 1969. Experimental results are represented with a full line and simulations with a dashed line.

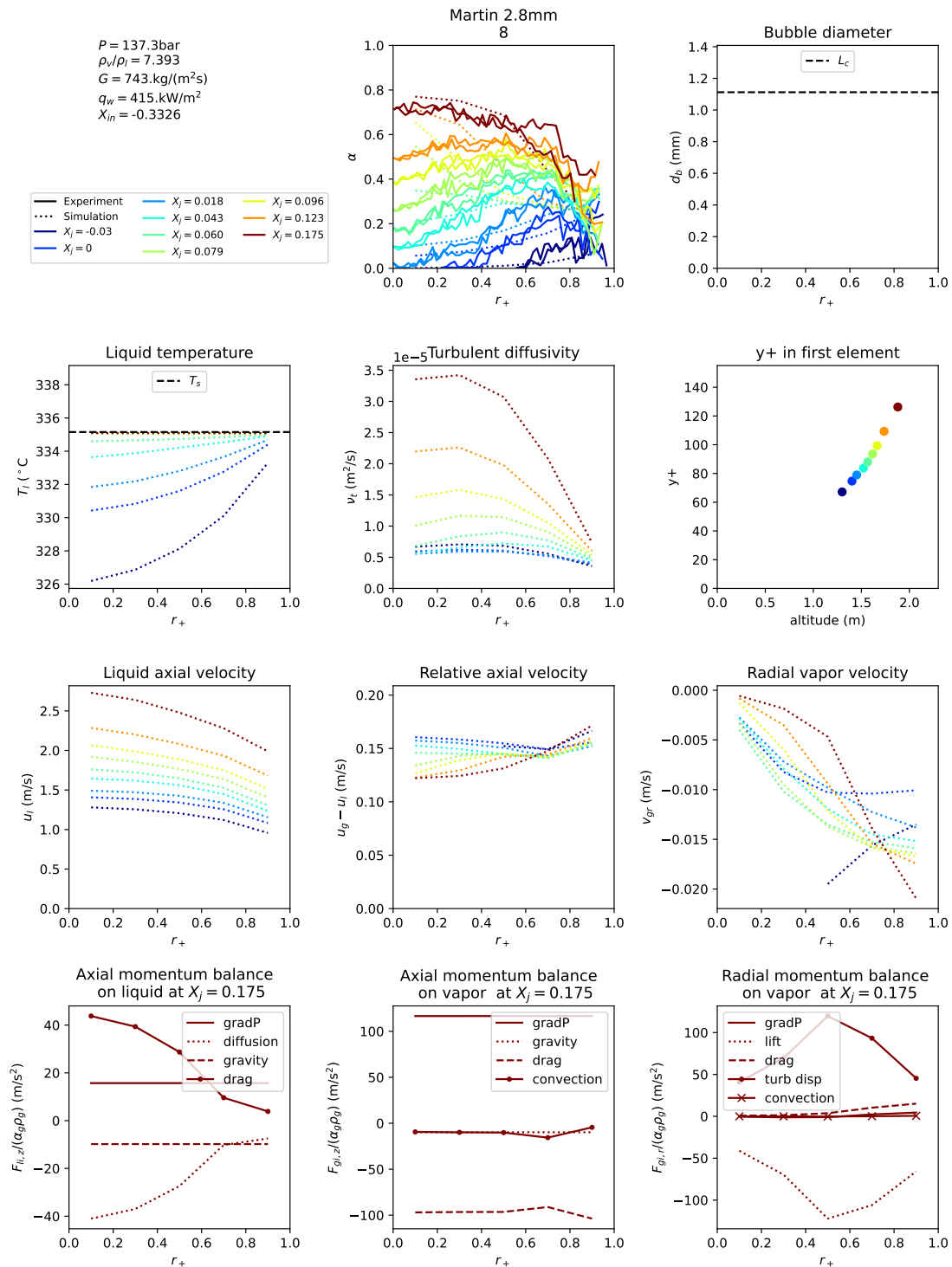


Figure F.79: Simulation results for test tube 8 of Martin 1969. Experimental results are represented with a full line and simulations with a dashed line.

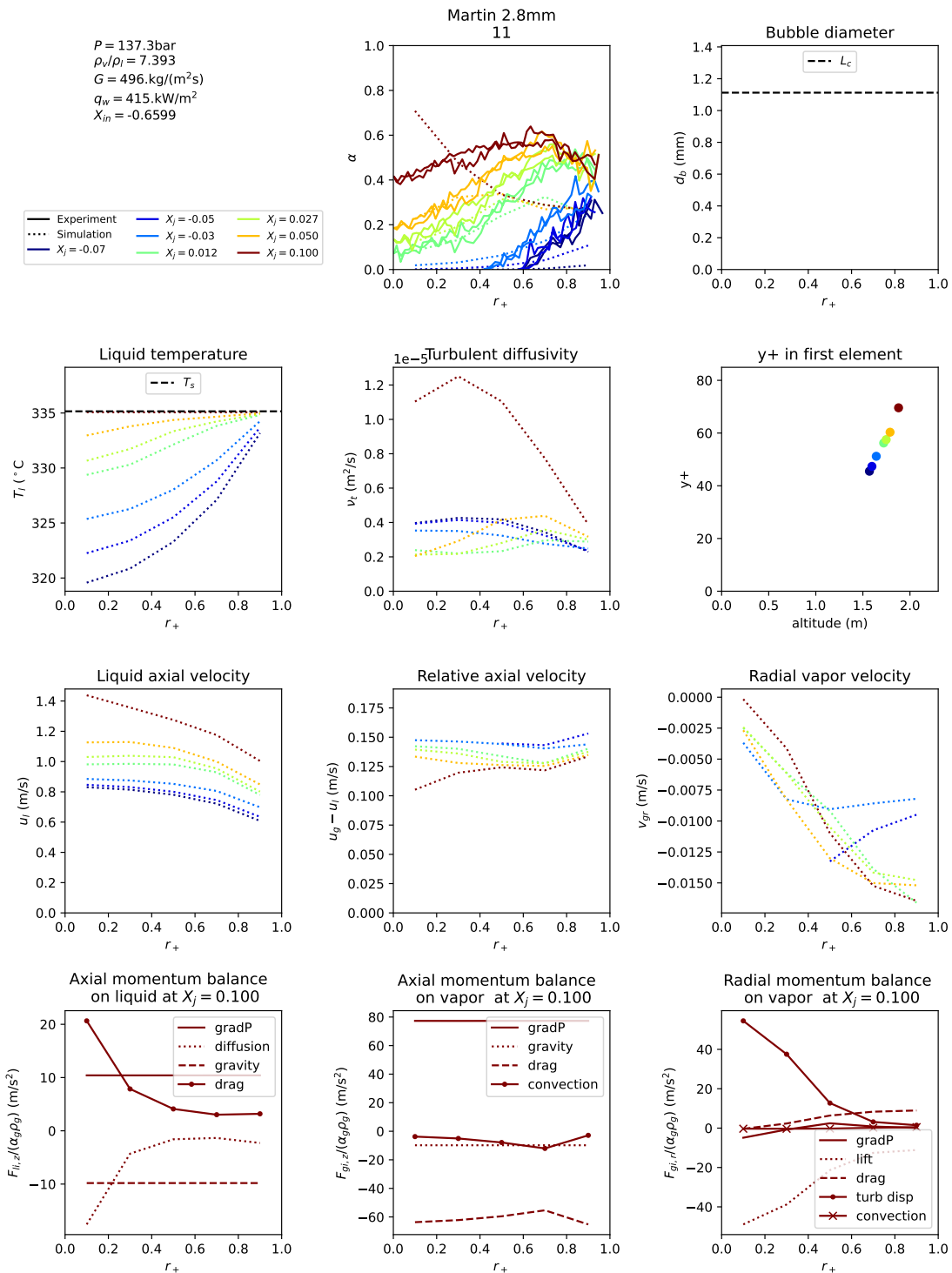


Figure F.80: Simulation results for test tube 11 of Martin 1969. Experimental results are represented with a full line and simulations with a dashed line.

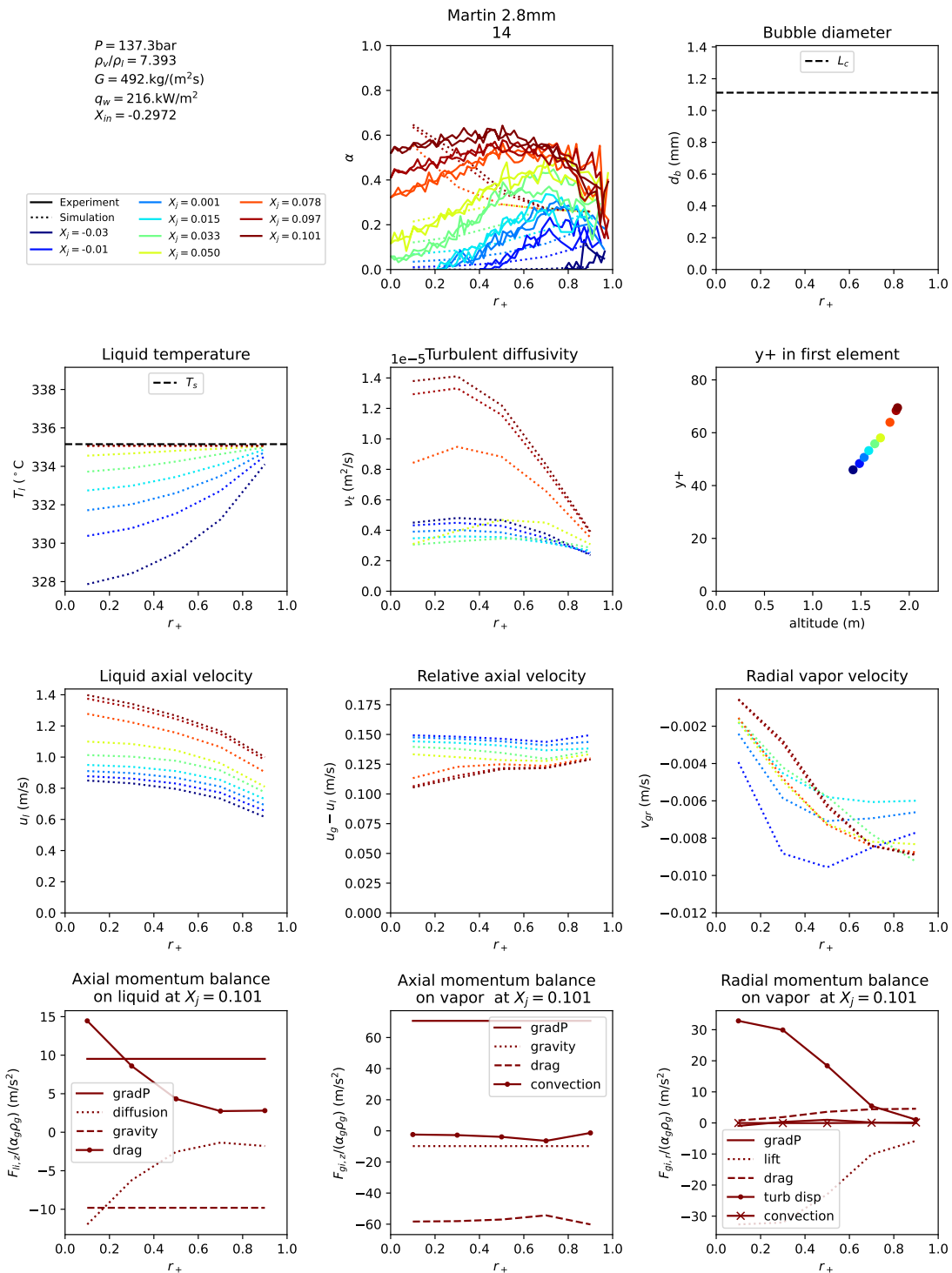


Figure F.81: Simulation results for test tube 14 of Martin 1969. Experimental results are represented with a full line and simulations with a dashed line.

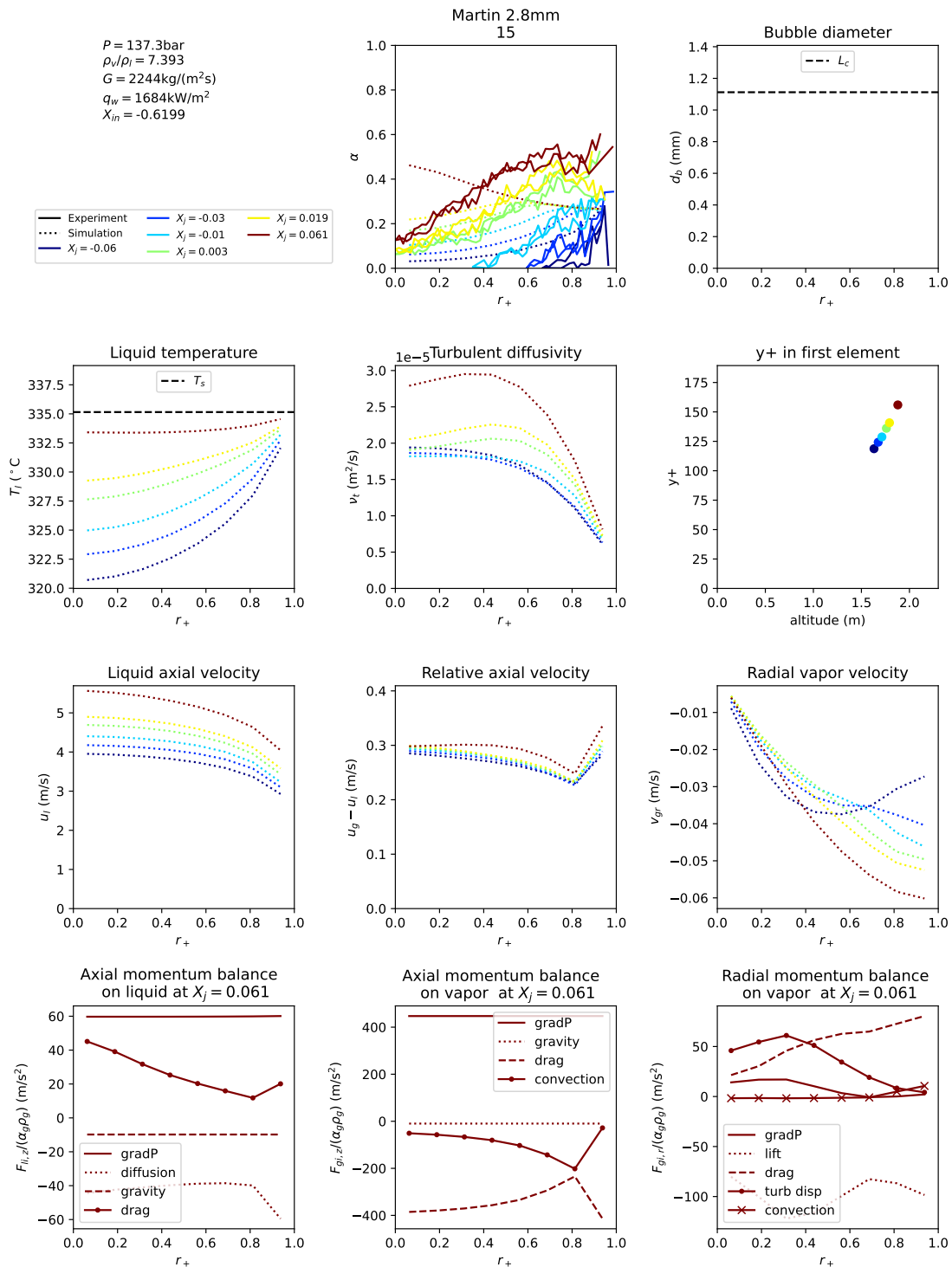


Figure F.82: Simulation results for test tube 15 of Martin 1969. Experimental results are represented with a full line and simulations with a dashed line.

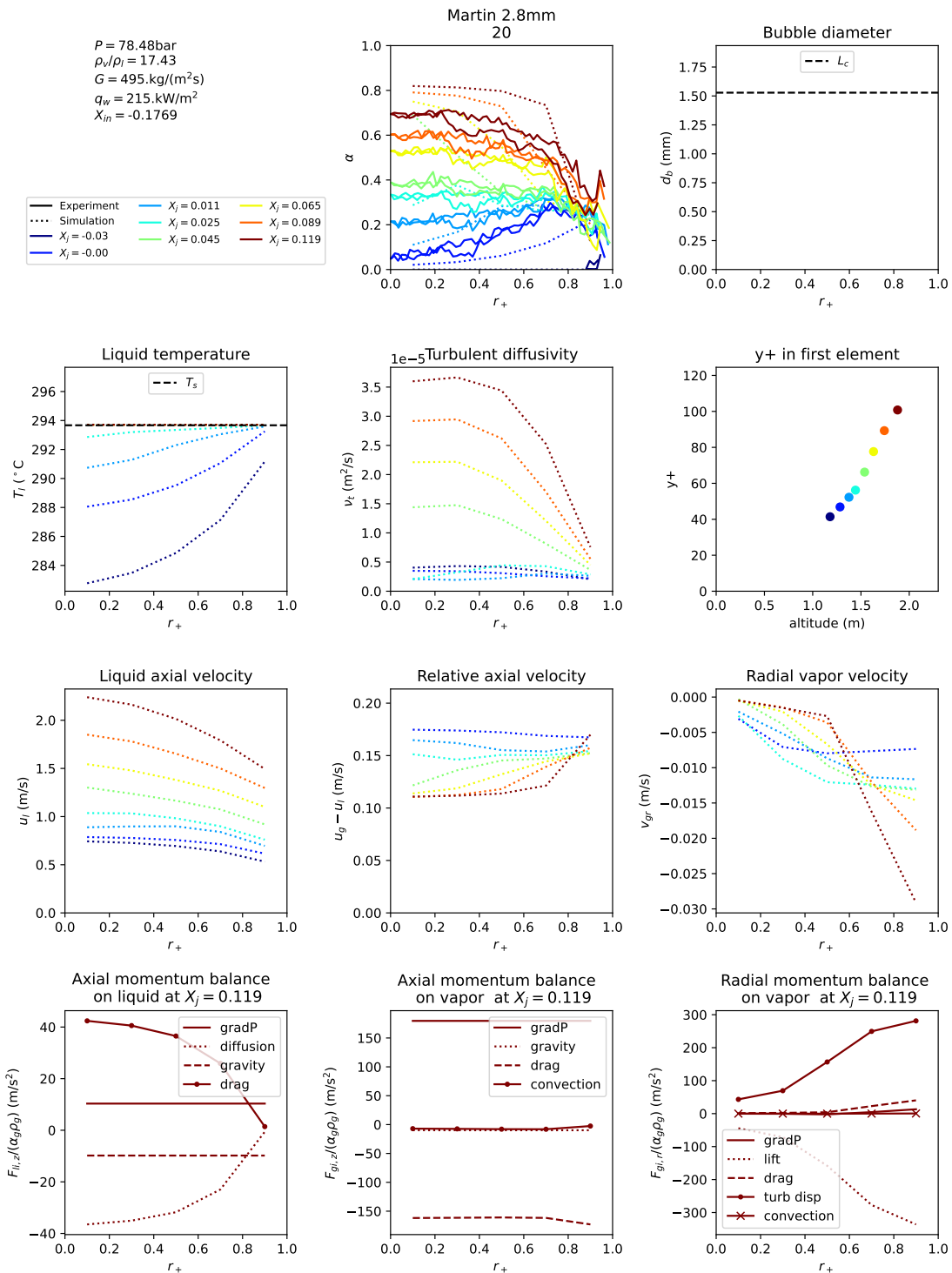


Figure F.83: Simulation results for test tube 20 of Martin 1969. Experimental results are represented with a full line and simulations with a dashed line.

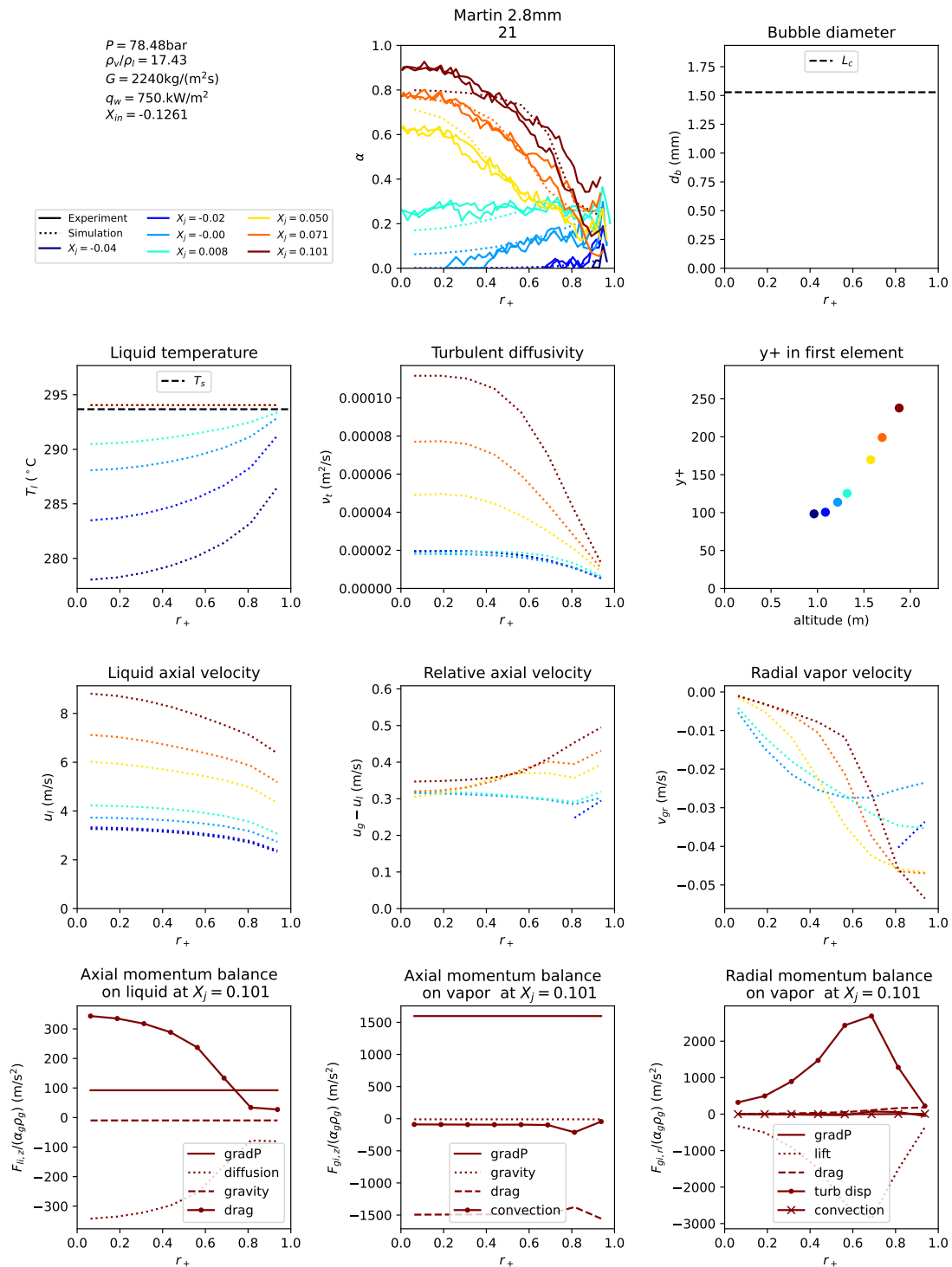


Figure F.84: Simulation results for test tube 21 of Martin 1969. Experimental results are represented with a full line and simulations with a dashed line.

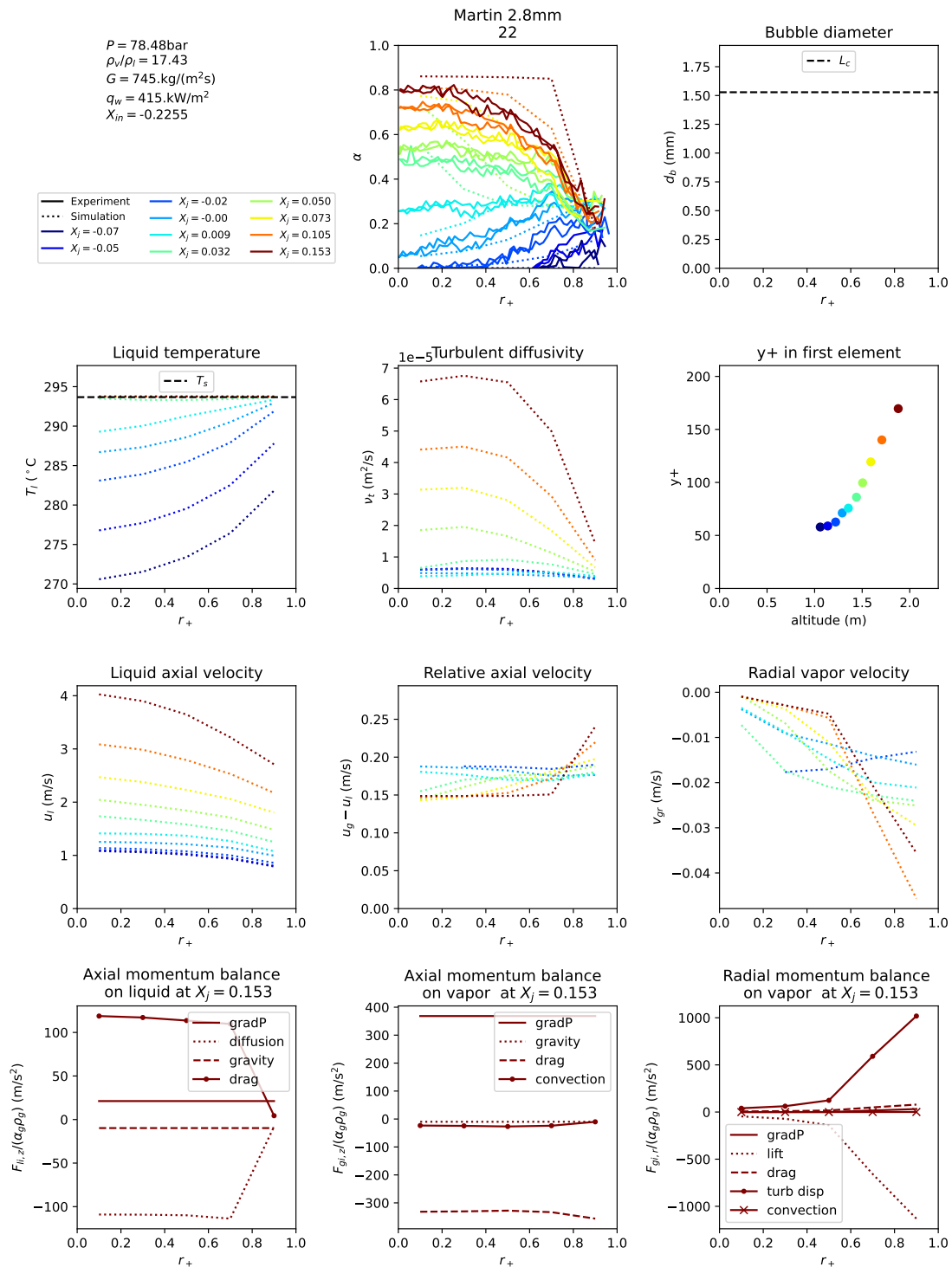


Figure F.85: Simulation results for test tube 22 of Martin 1969. Experimental results are represented with a full line and simulations with a dashed line.

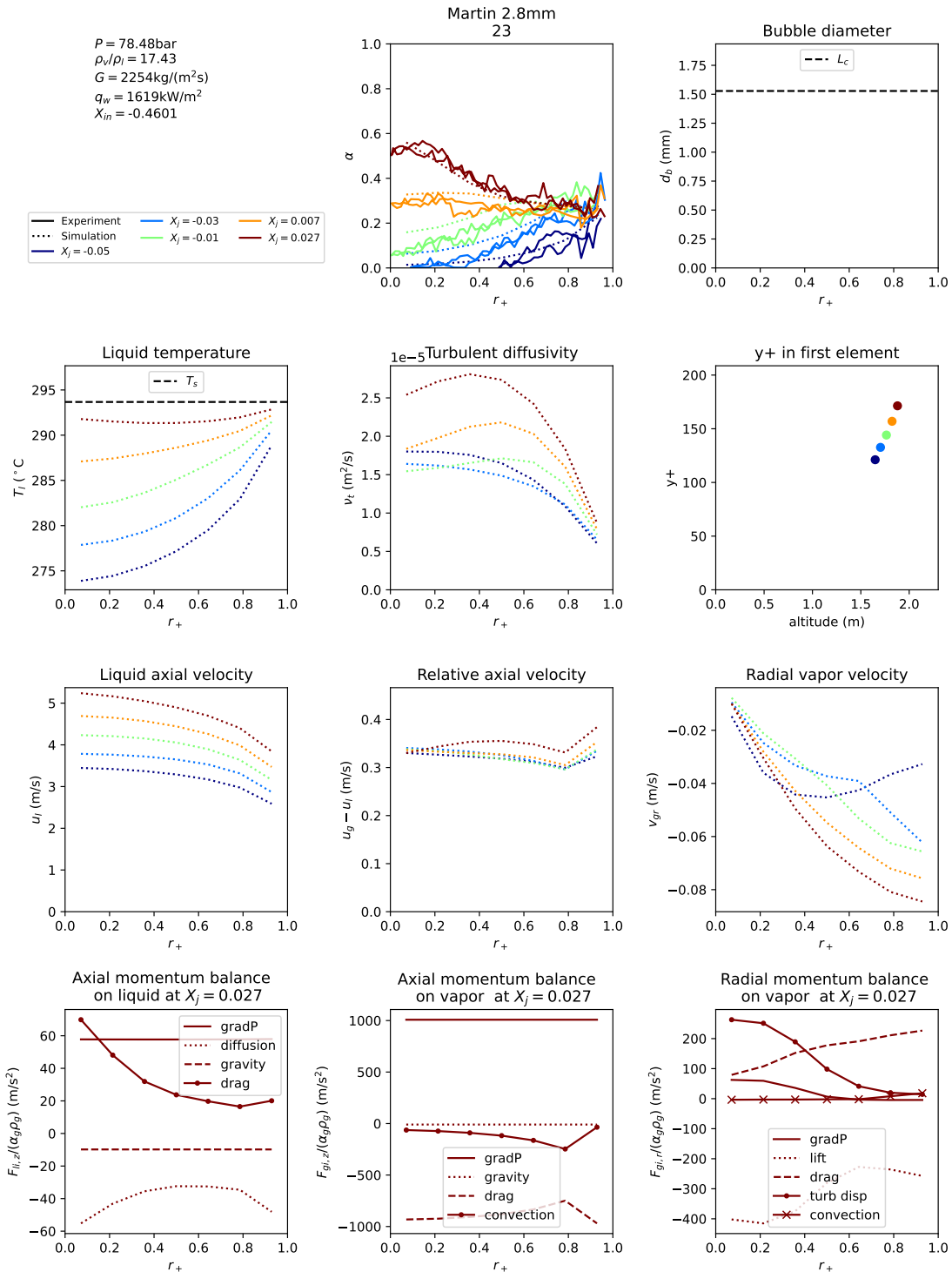


Figure F.86: Simulation results for test tube 23 of Martin 1969. Experimental results are represented with a full line and simulations with a dashed line.

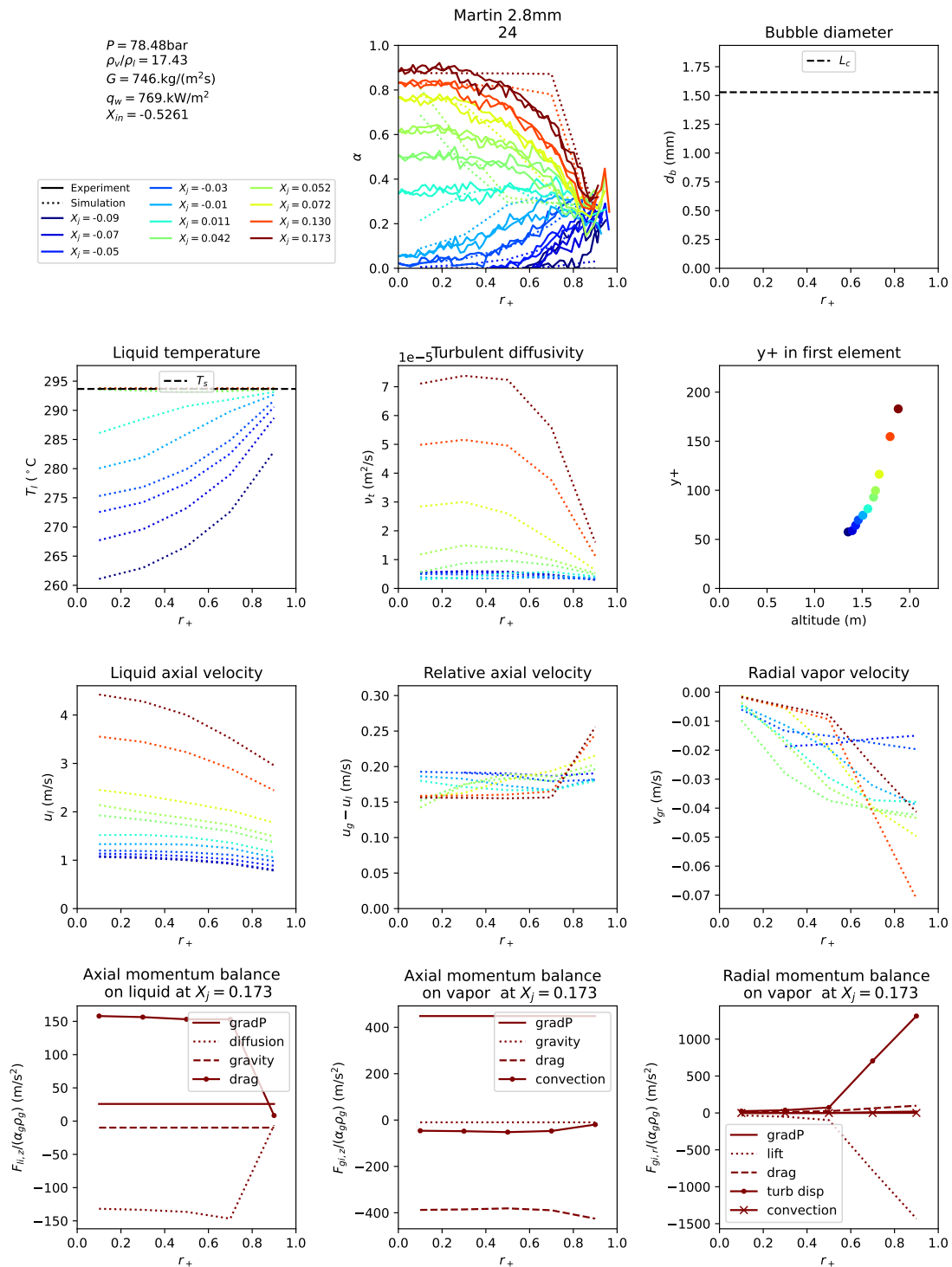


Figure F.87: Simulation results for test tube 24 of Martin 1969. Experimental results are represented with a full line and simulations with a dashed line.

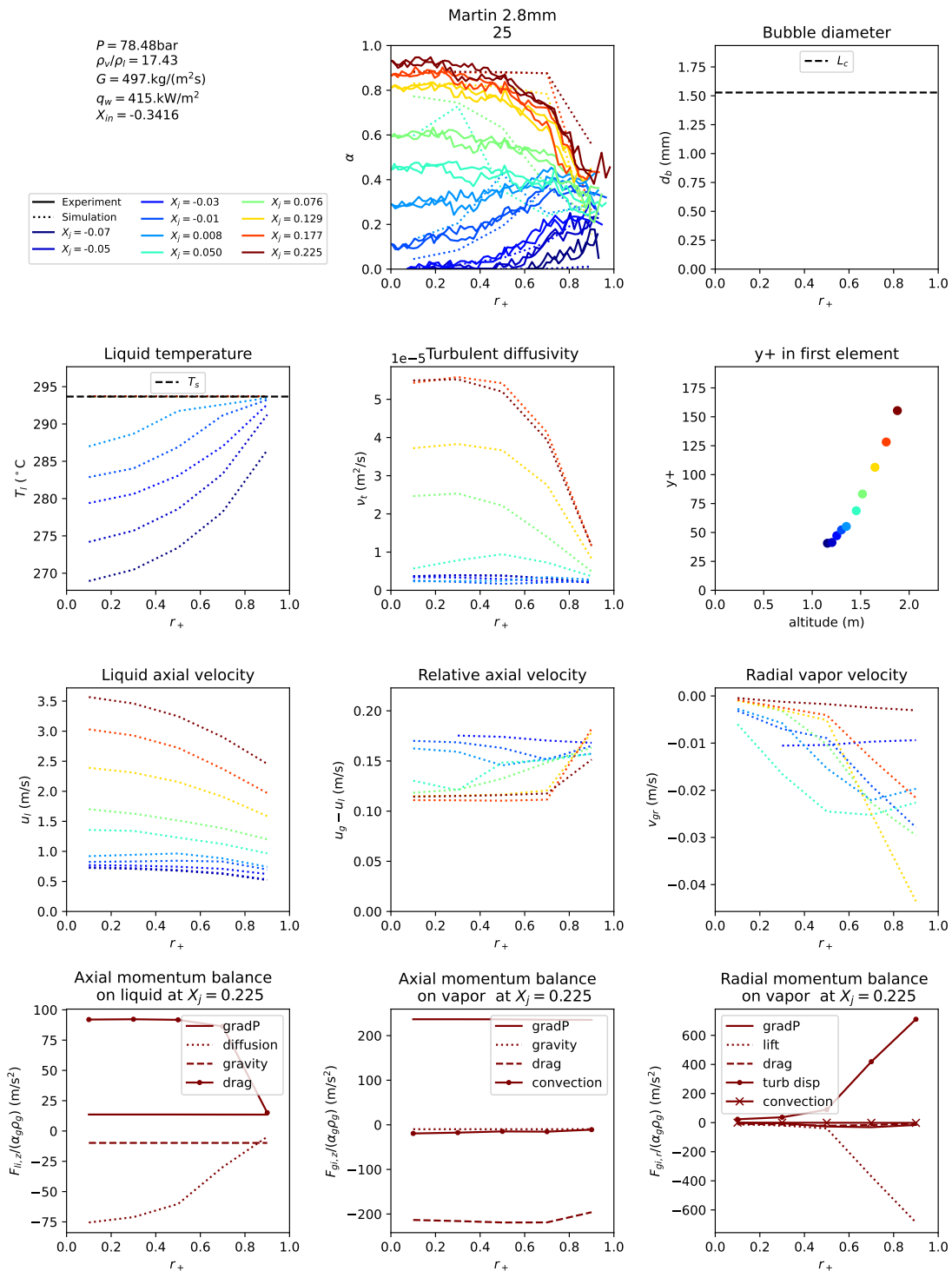


Figure F.88: Simulation results for test tube 25 of Martin 1969. Experimental results are represented with a full line and simulations with a dashed line.

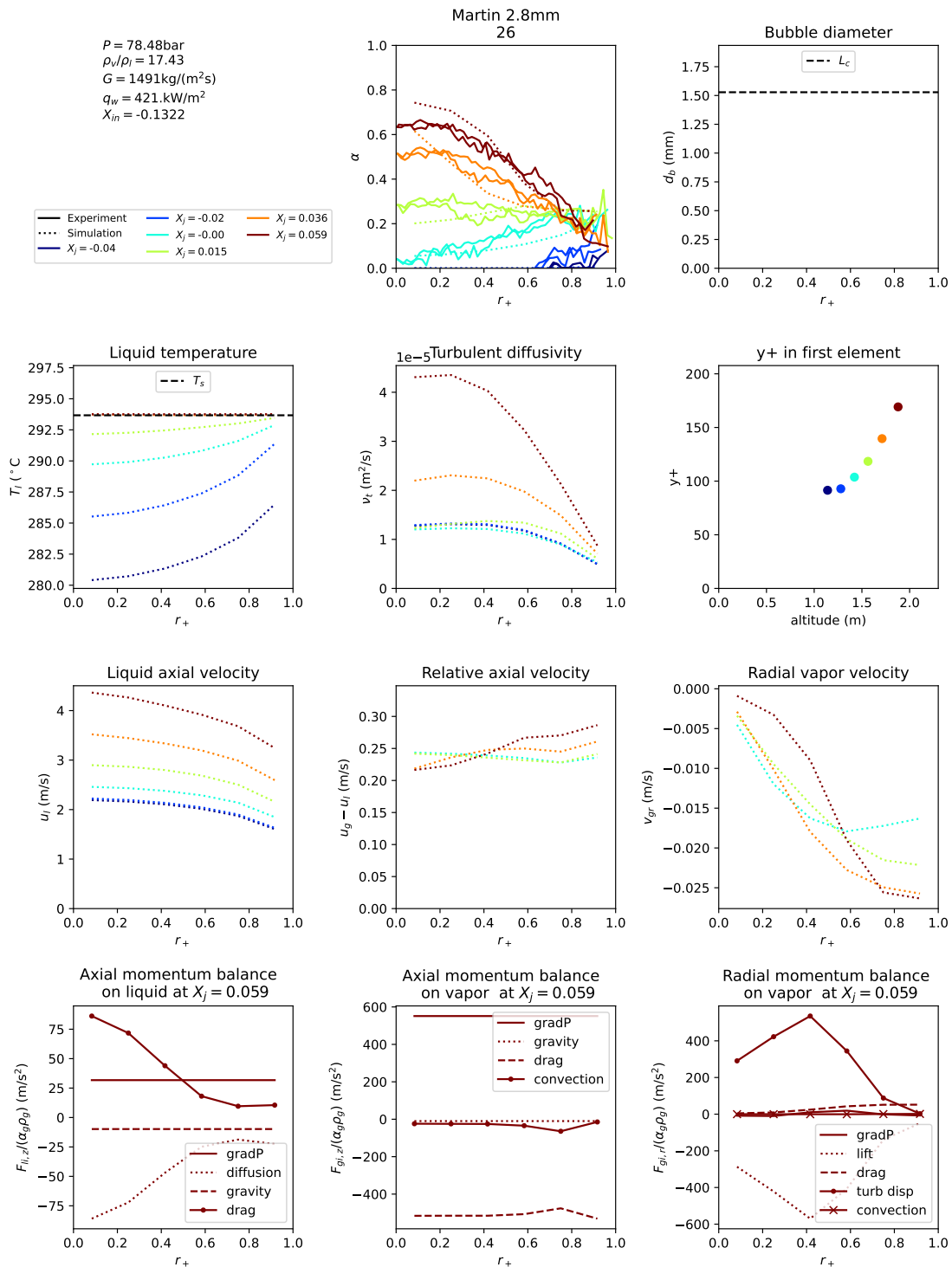


Figure F.89: Simulation results for test tube 26 of Martin 1969. Experimental results are represented with a full line and simulations with a dashed line.

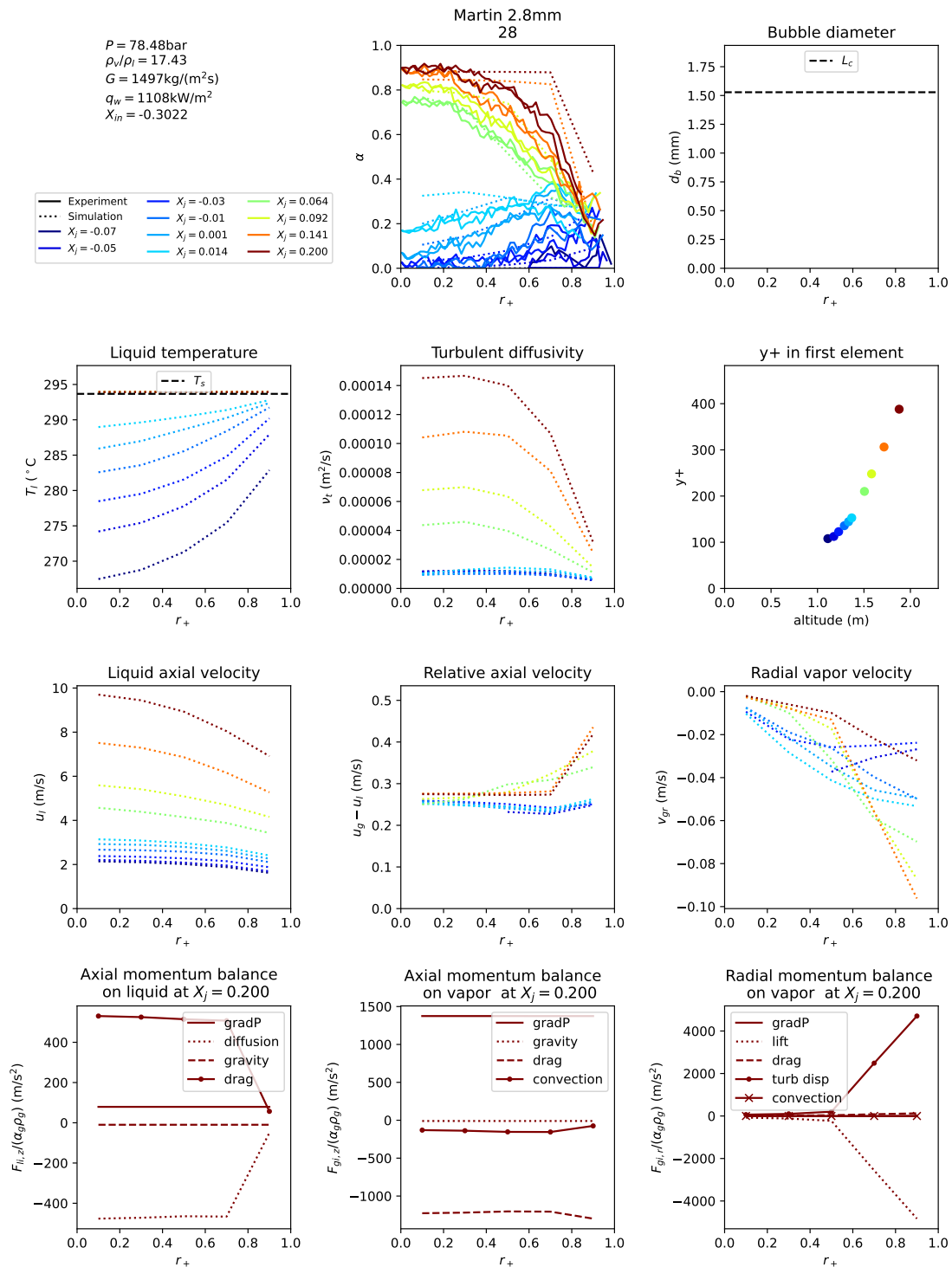


Figure F.90: Simulation results for test tube 28 of Martin 1969. Experimental results are represented with a full line and simulations with a dashed line.

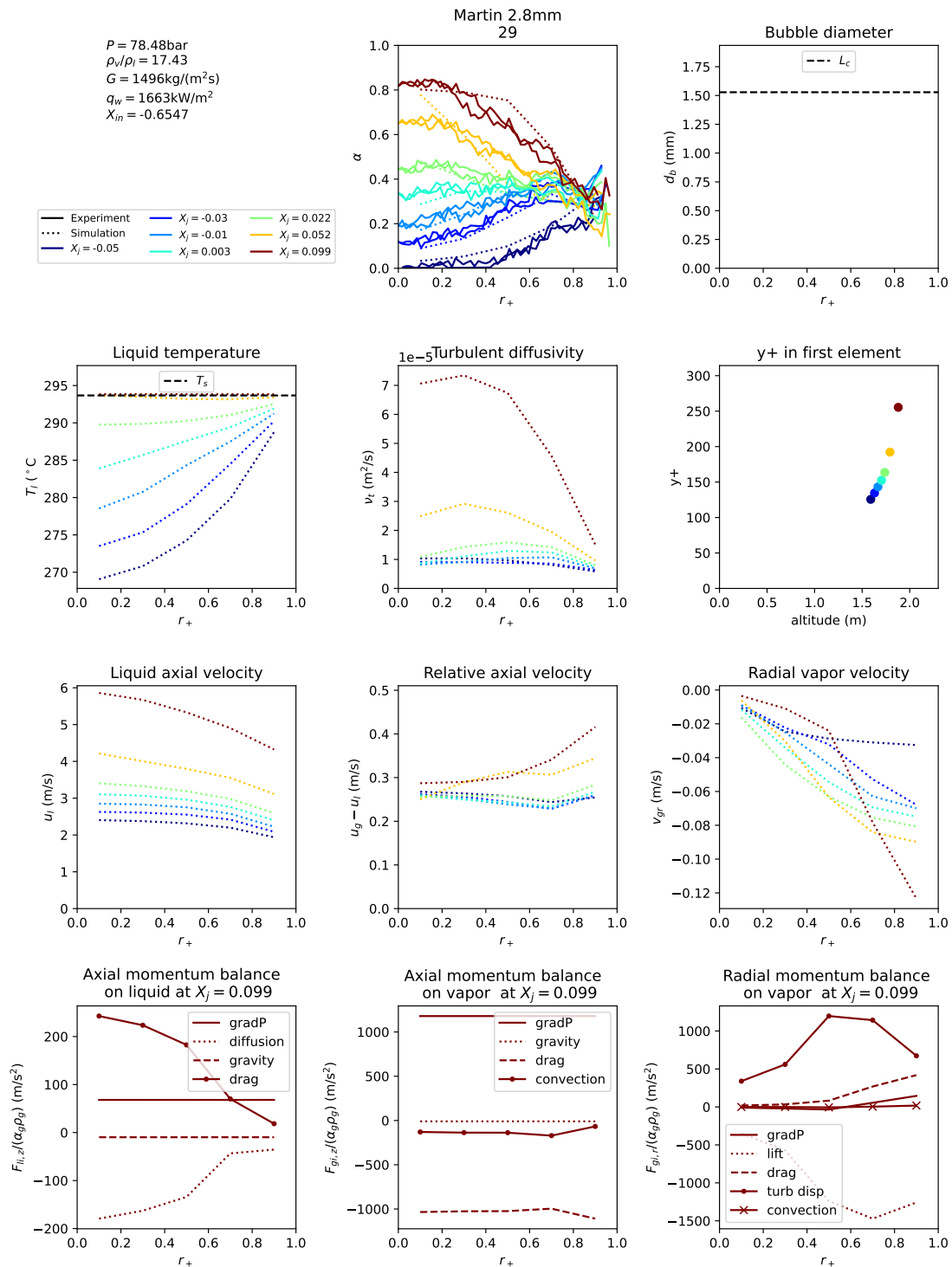


Figure F.91: Simulation results for test tube 29 of Martin 1969. Experimental results are represented with a full line and simulations with a dashed line.

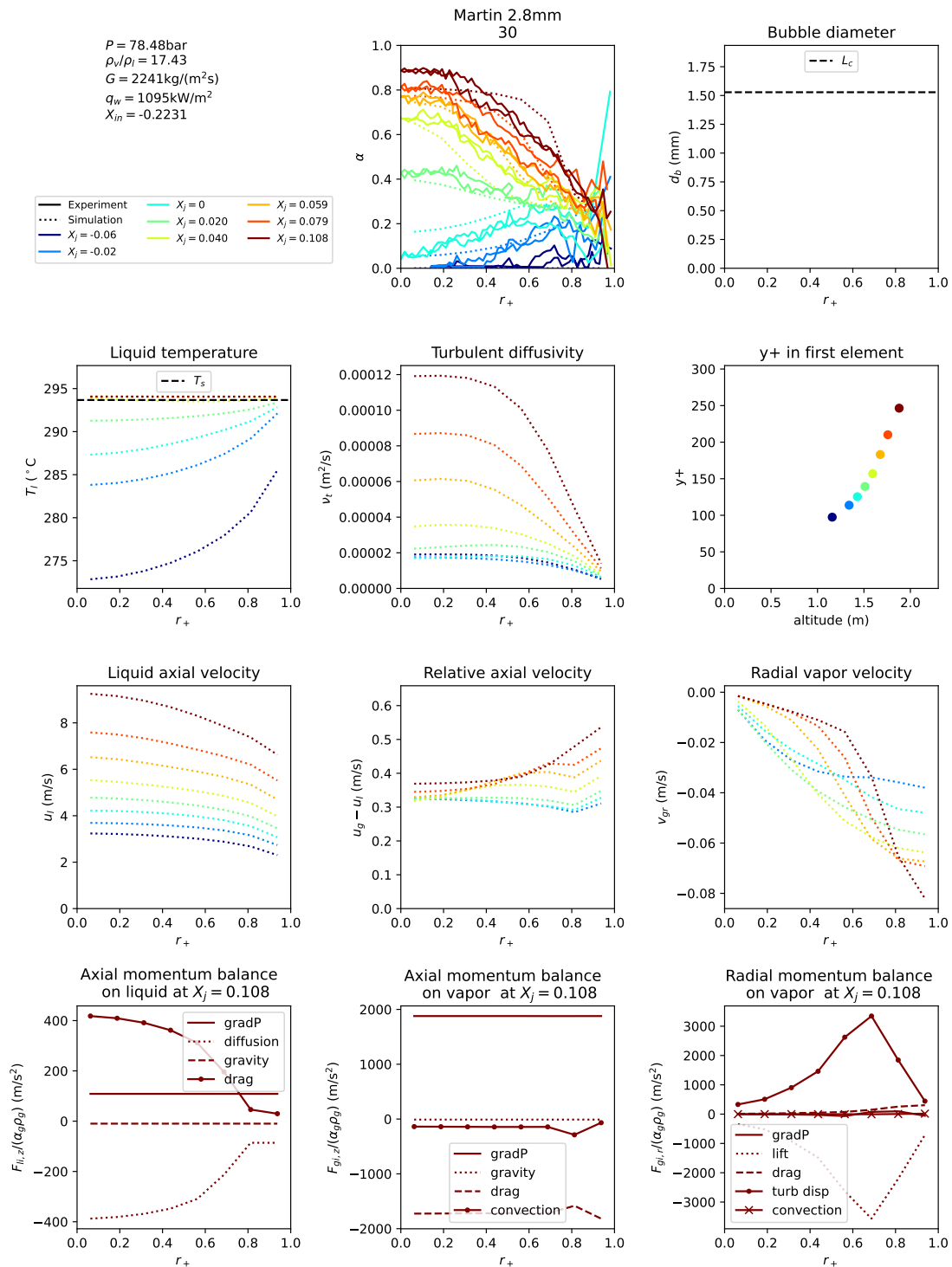


Figure F.92: Simulation results for test tube 30 of Martin 1969. Experimental results are represented with a full line and simulations with a dashed line.

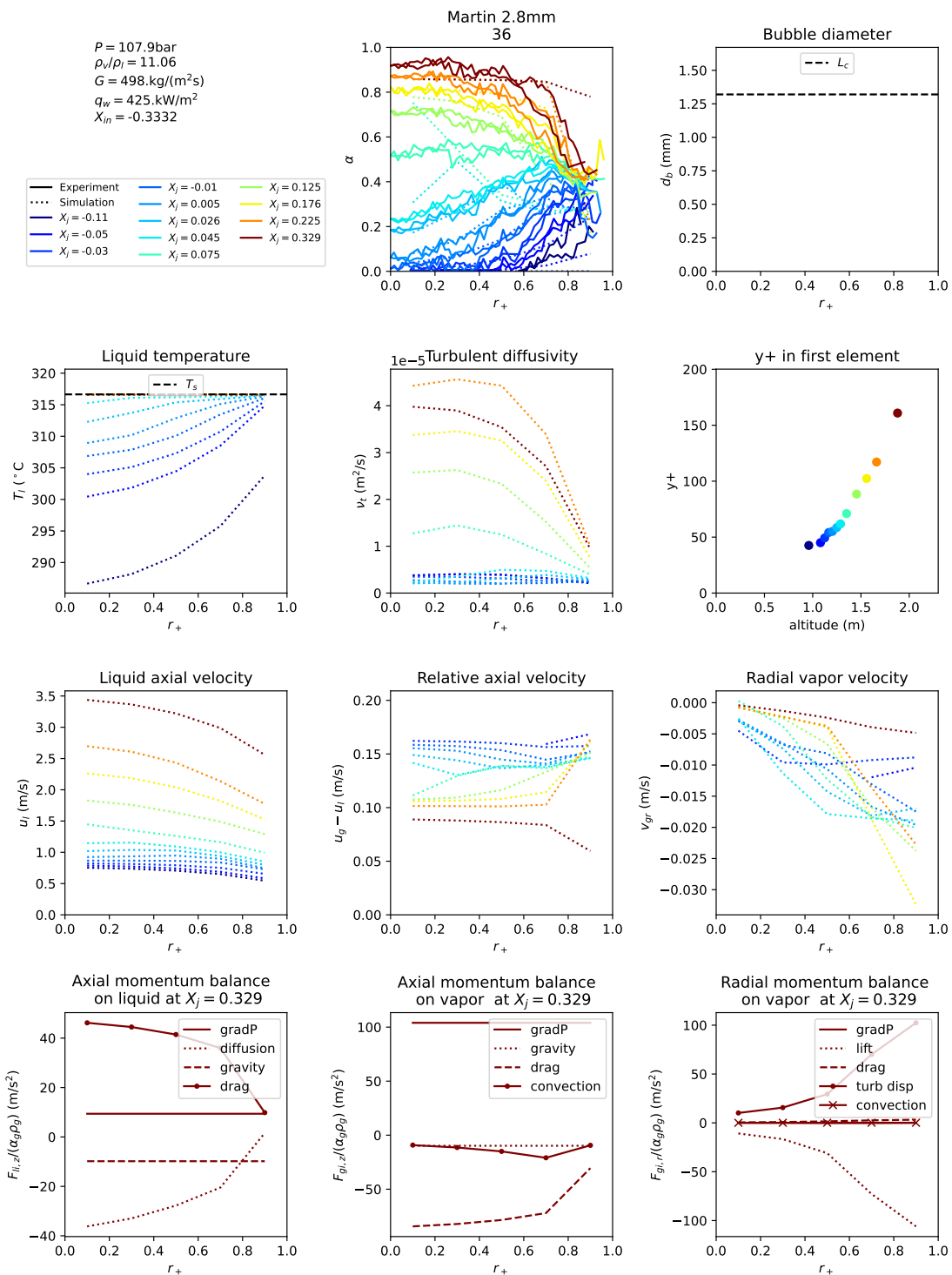
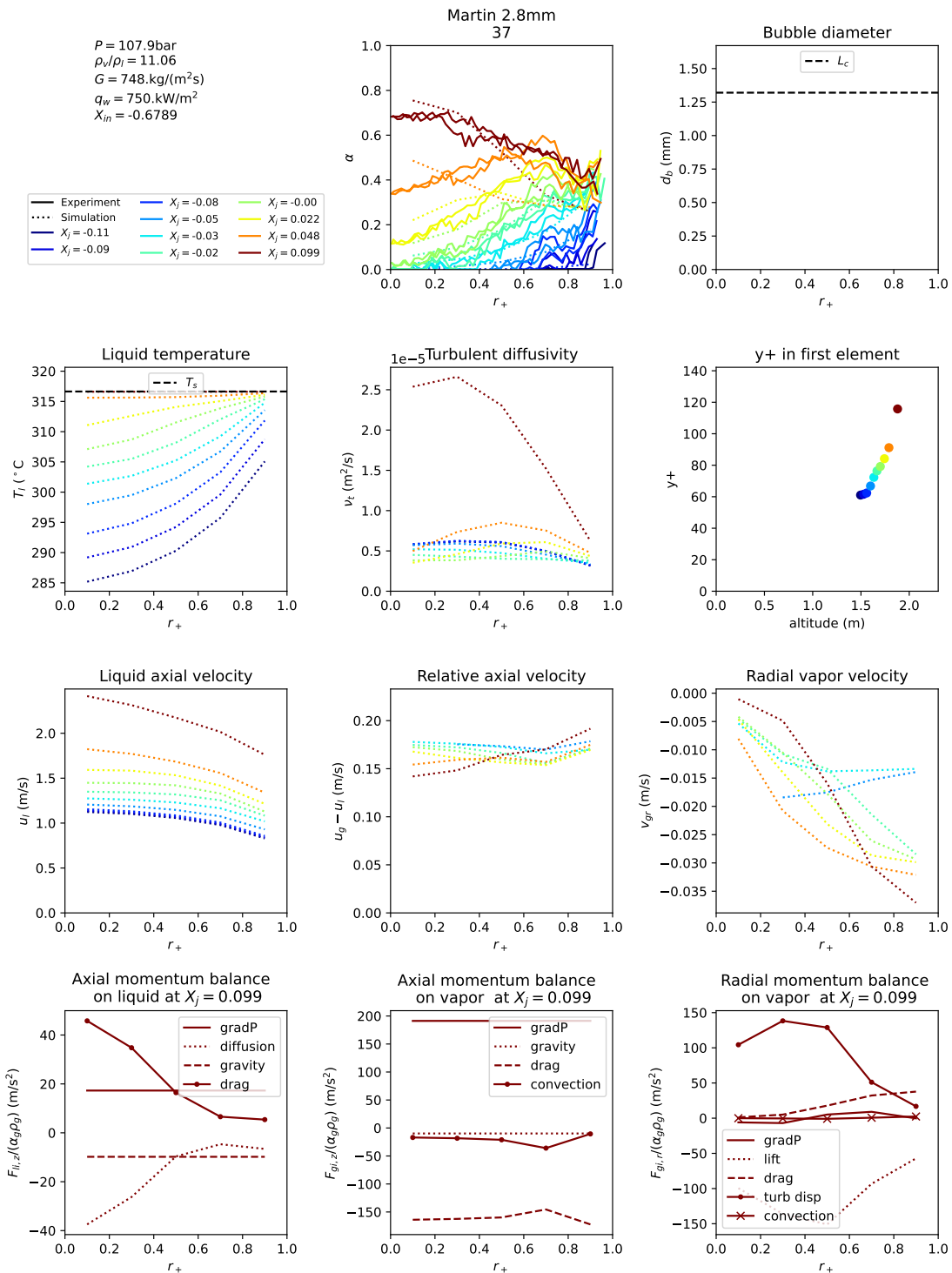


Figure F.93: Simulation results for test tube 36 of Martin 1969. Experimental results are represented with a full line and simulations with a dashed line.



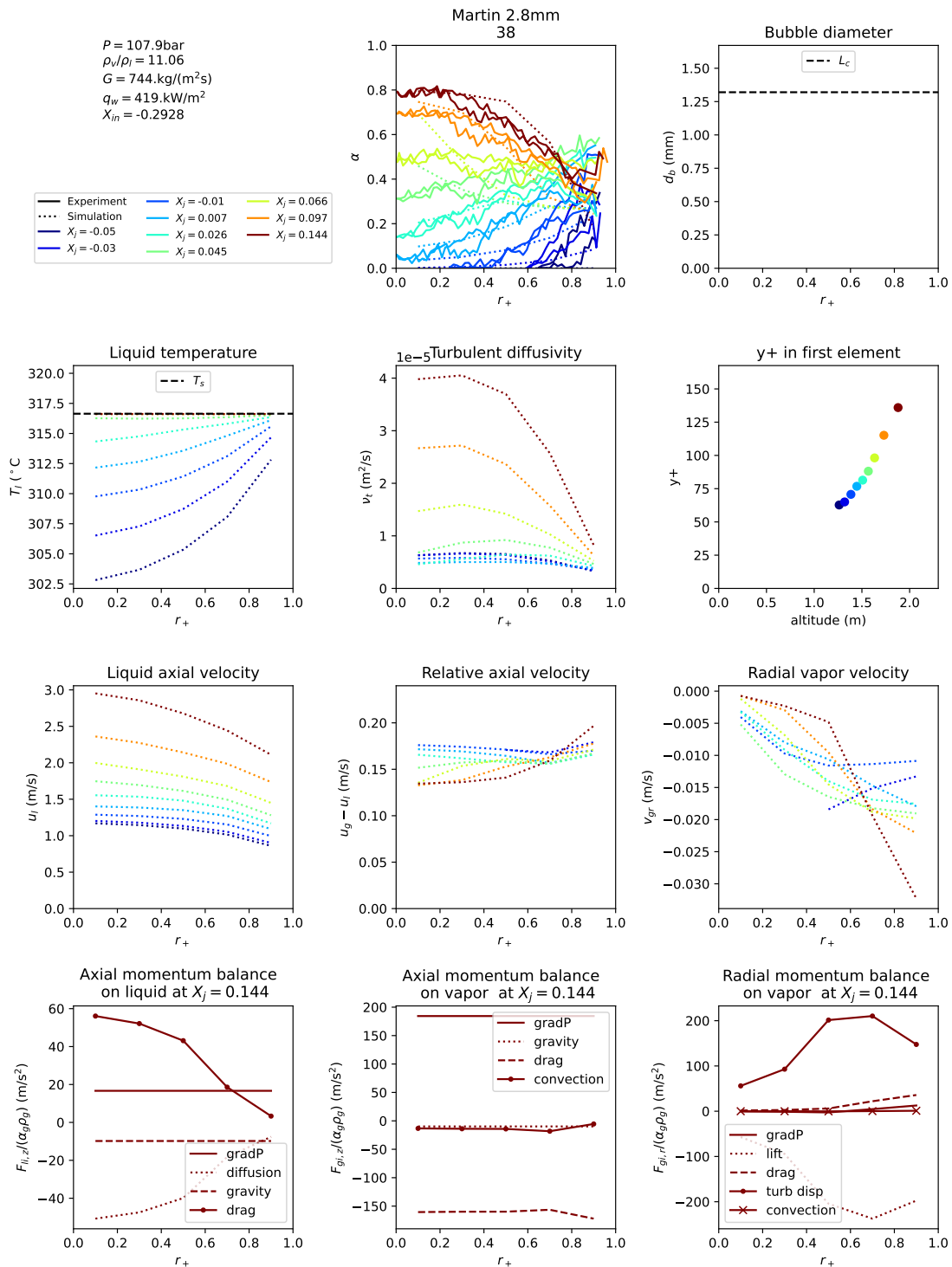


Figure F.95: Simulation results for test tube 38 of Martin 1969. Experimental results are represented with a full line and simulations with a dashed line.

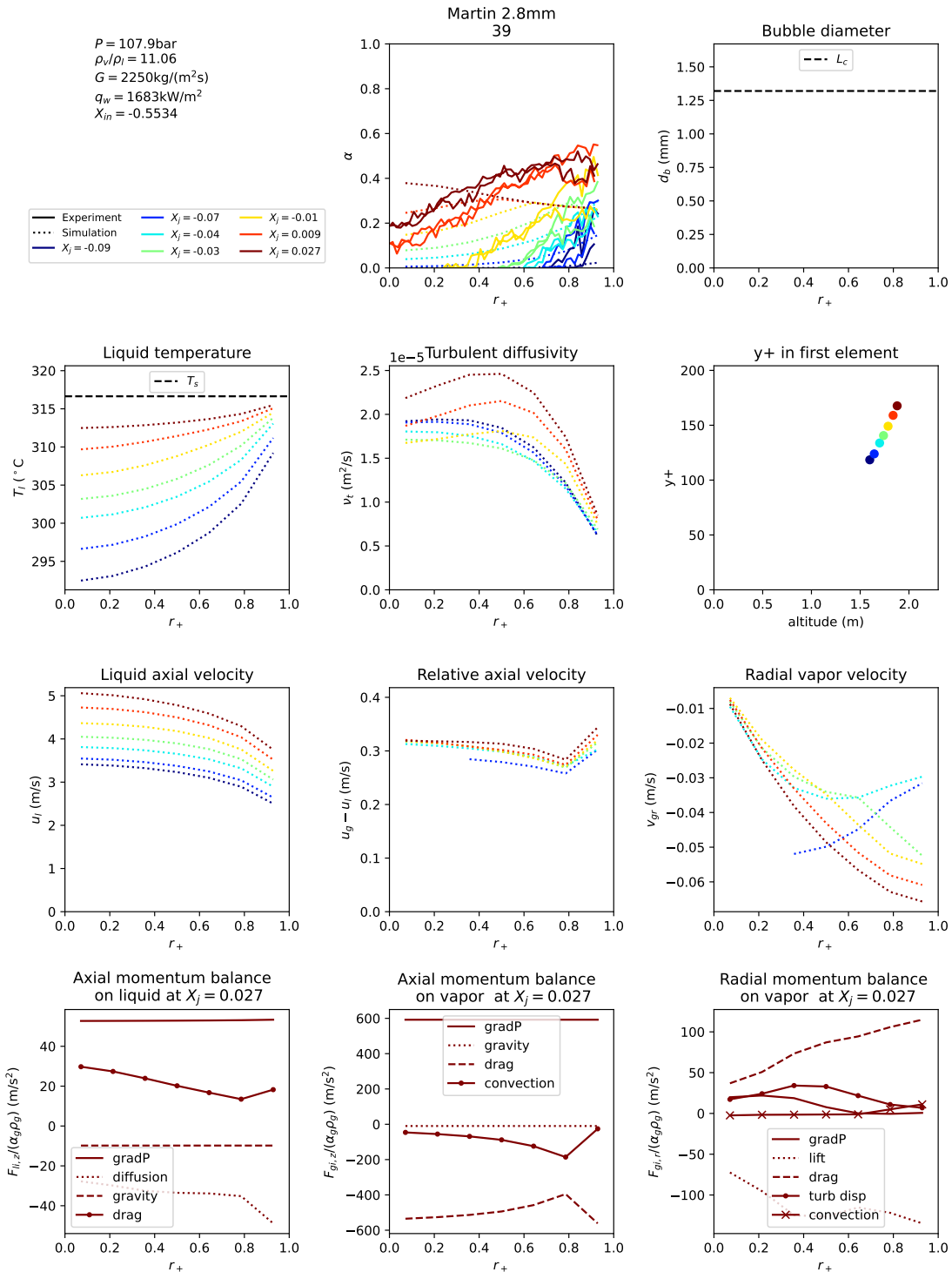


Figure F.96: Simulation results for test tube 39 of Martin 1969. Experimental results are represented with a full line and simulations with a dashed line.

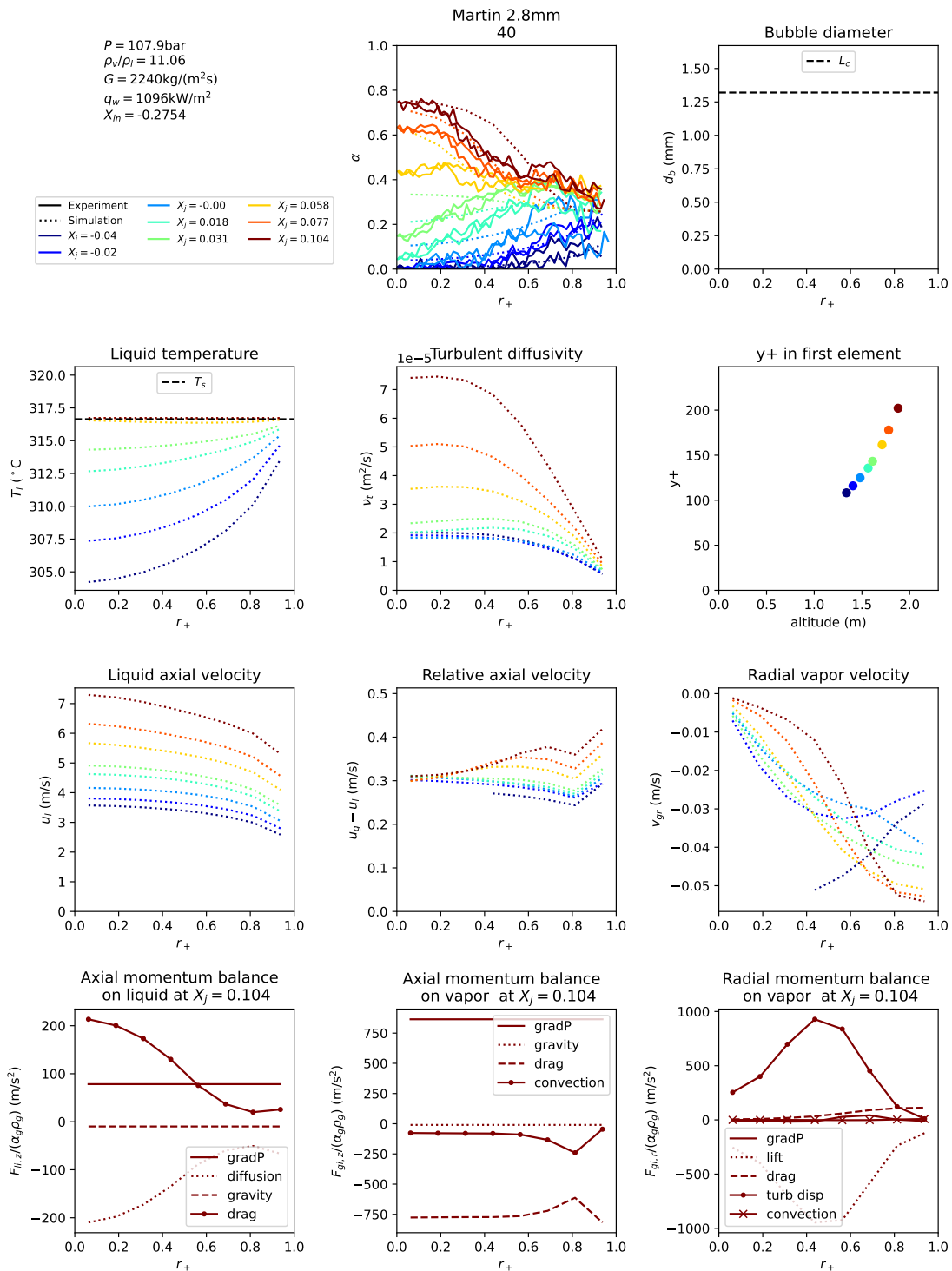
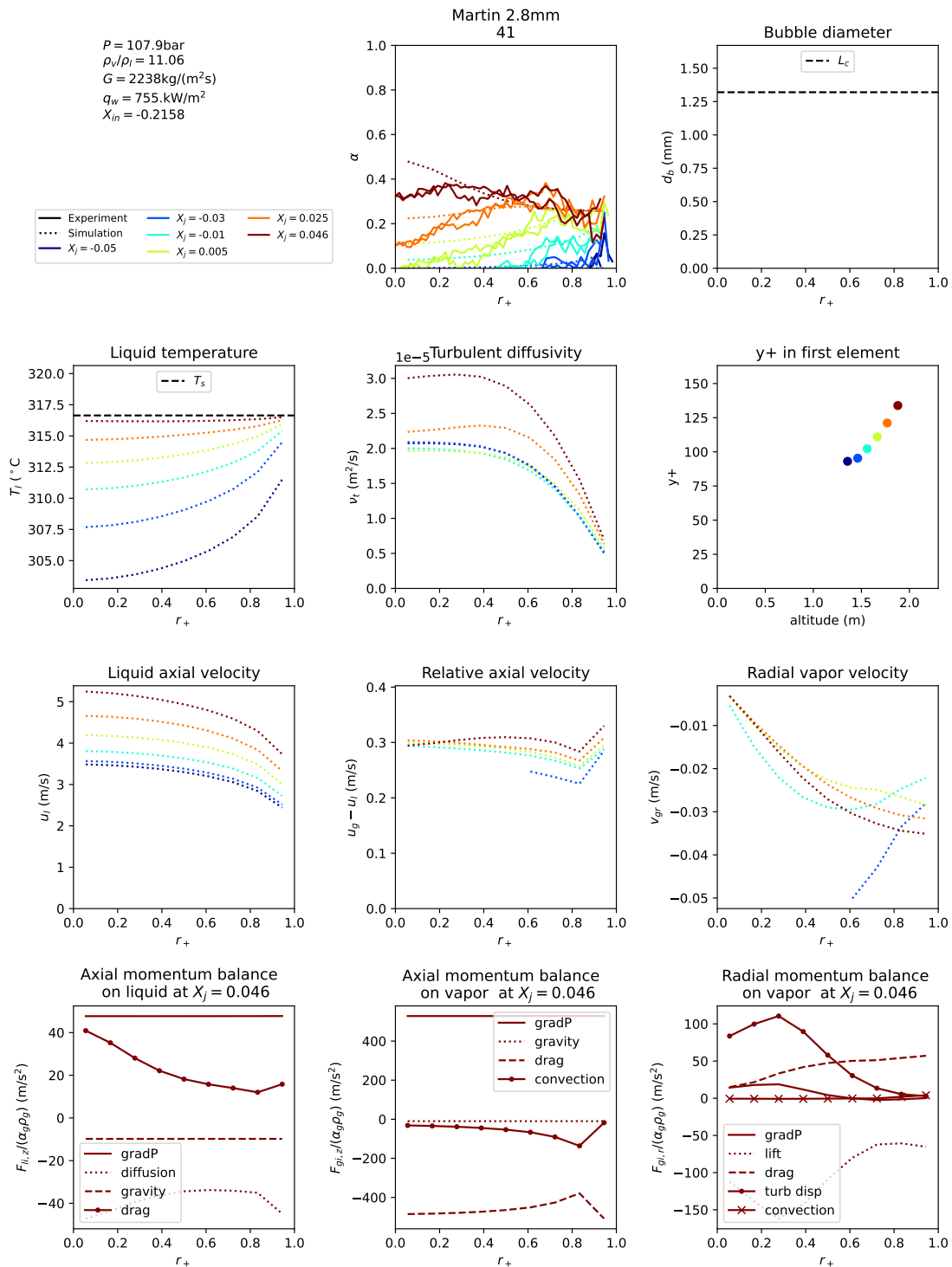


Figure F.97: Simulation results for test tube 40 of Martin 1969. Experimental results are represented with a full line and simulations with a dashed line.



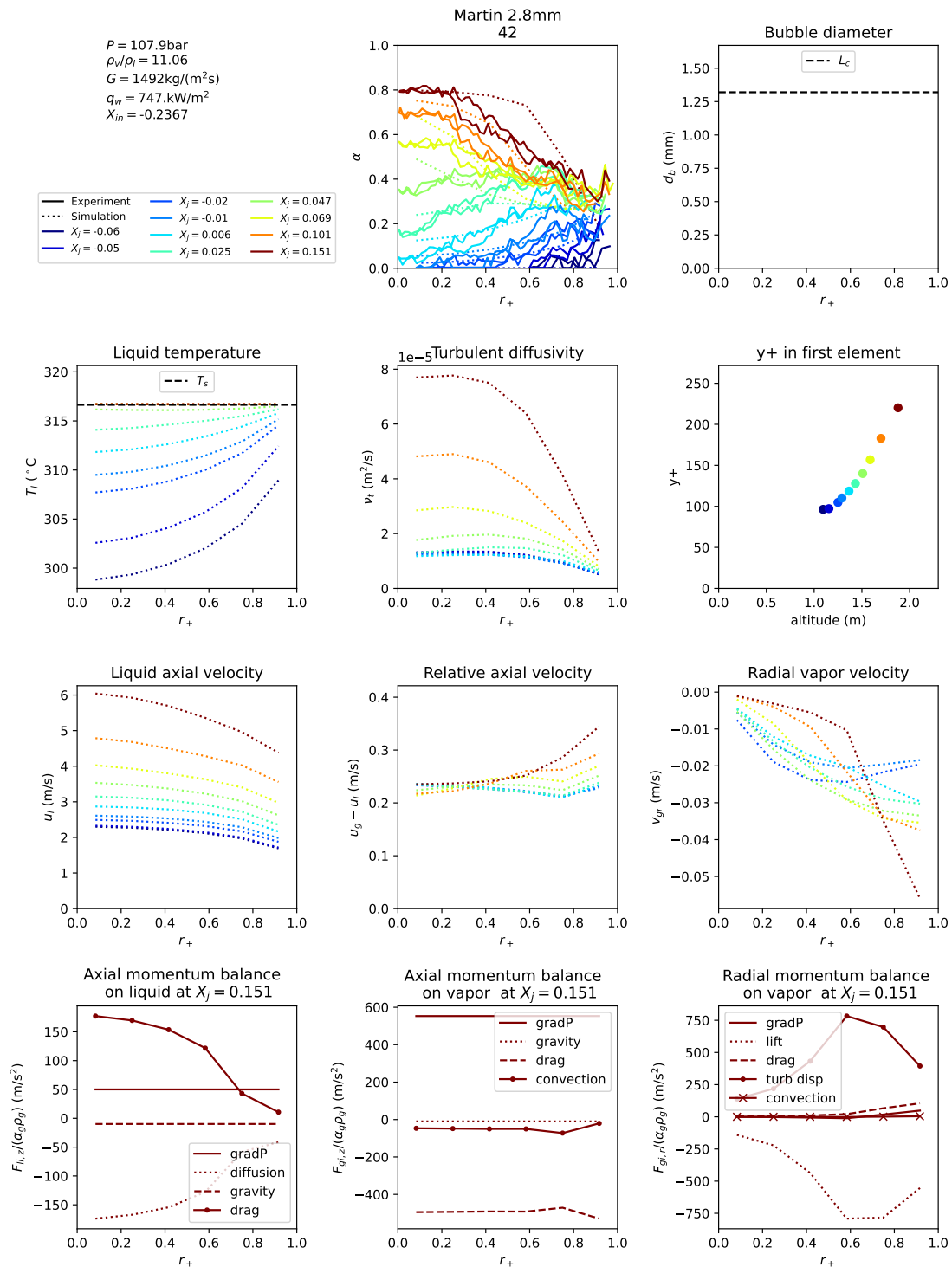


Figure F.99: Simulation results for test tube 42 of Martin 1969. Experimental results are represented with a full line and simulations with a dashed line.

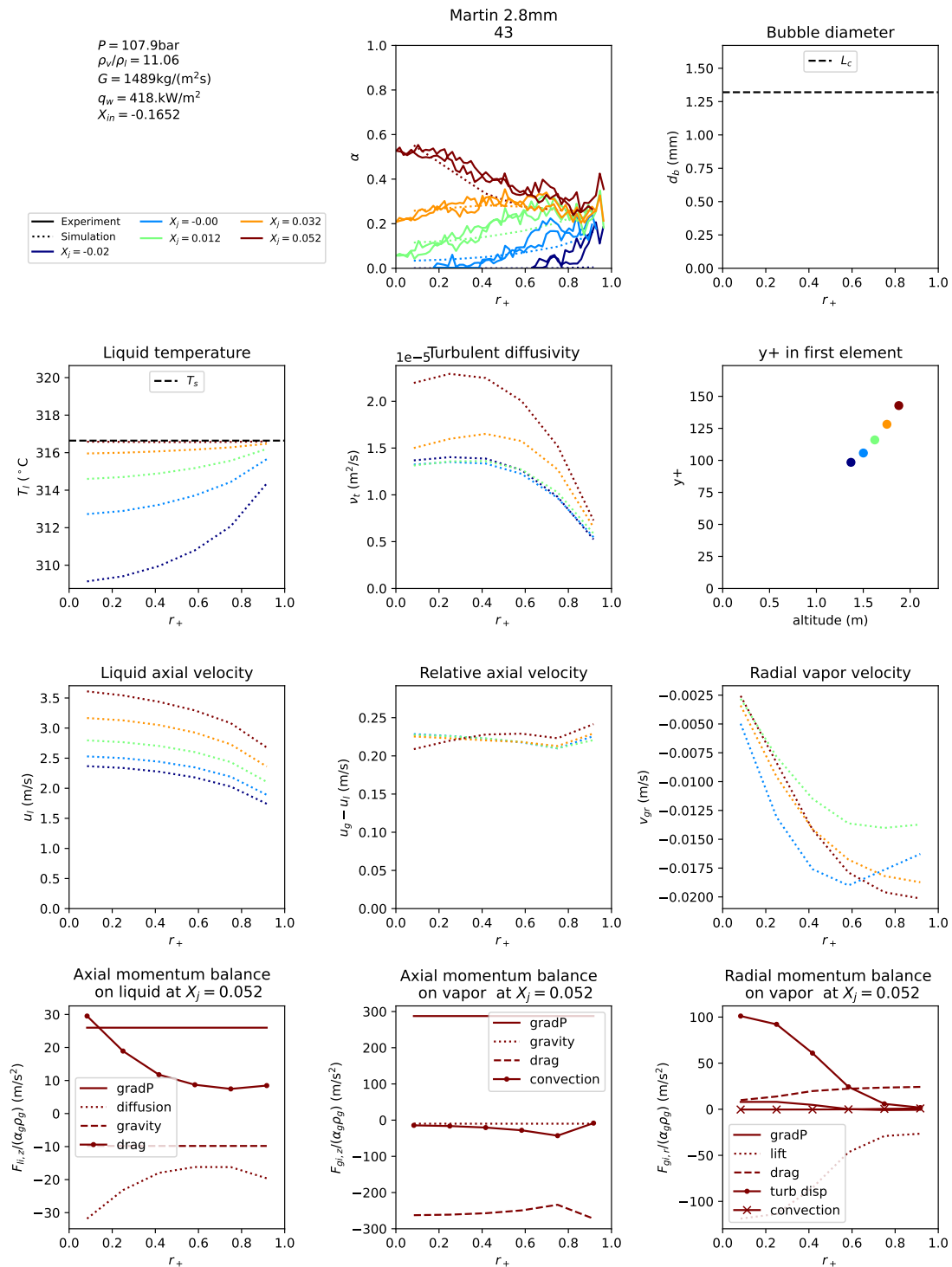


Figure F.100: Simulation results for test tube 43 of Martin 1969. Experimental results are represented with a full line and simulations with a dashed line.

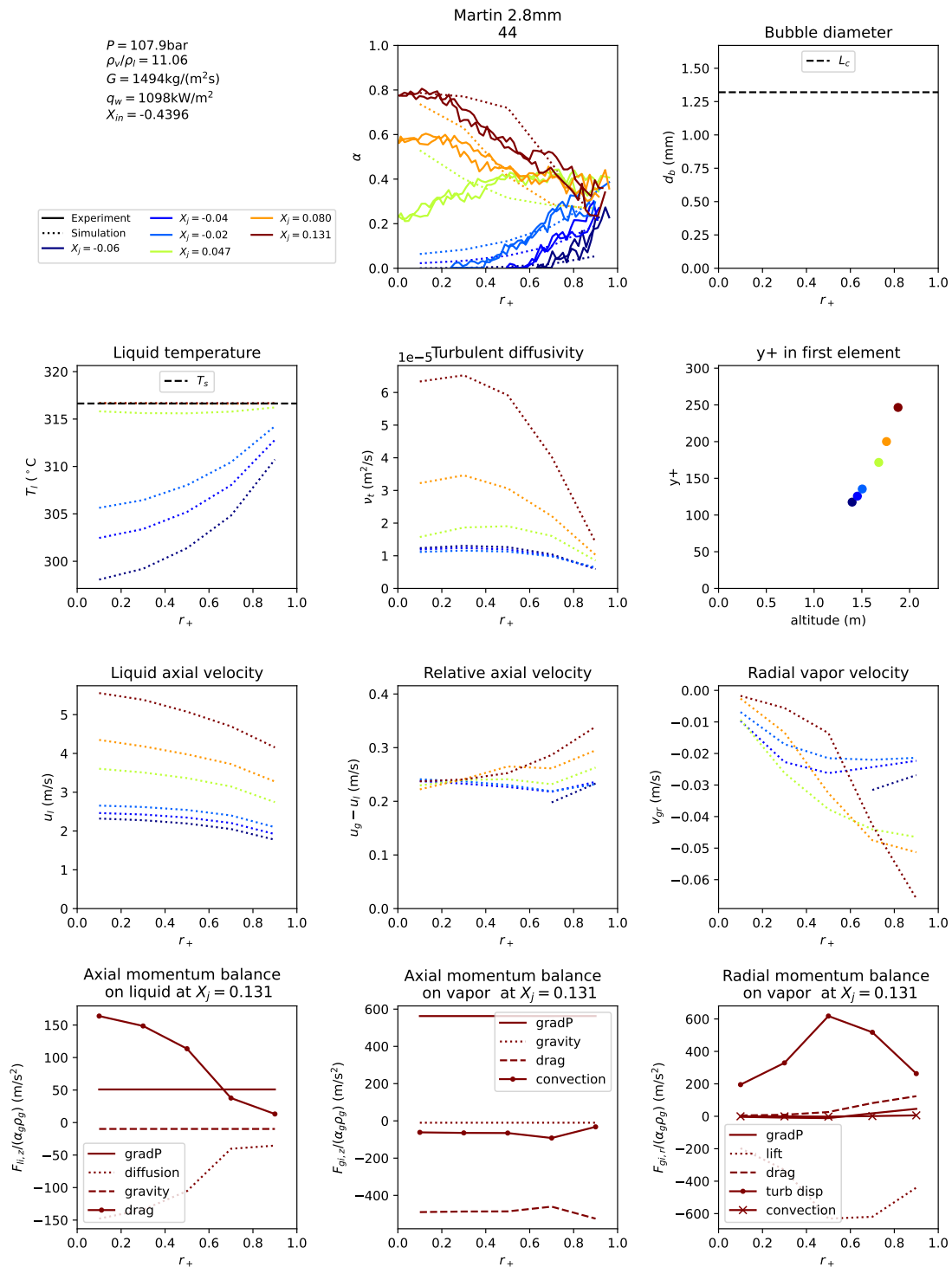
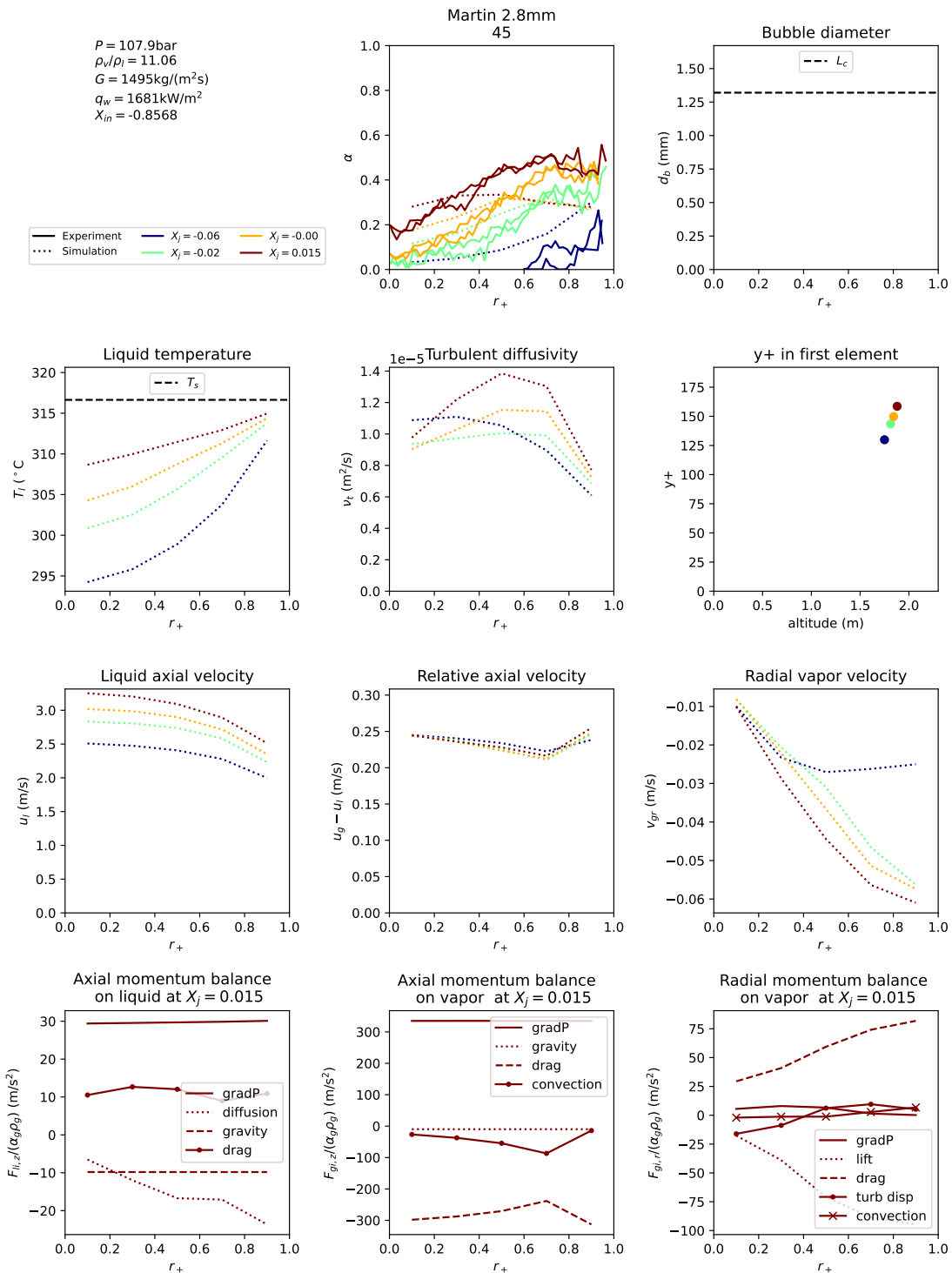


Figure F.101: Simulation results for test tube 44 of Martin 1969. Experimental results are represented with a full line and simulations with a dashed line.



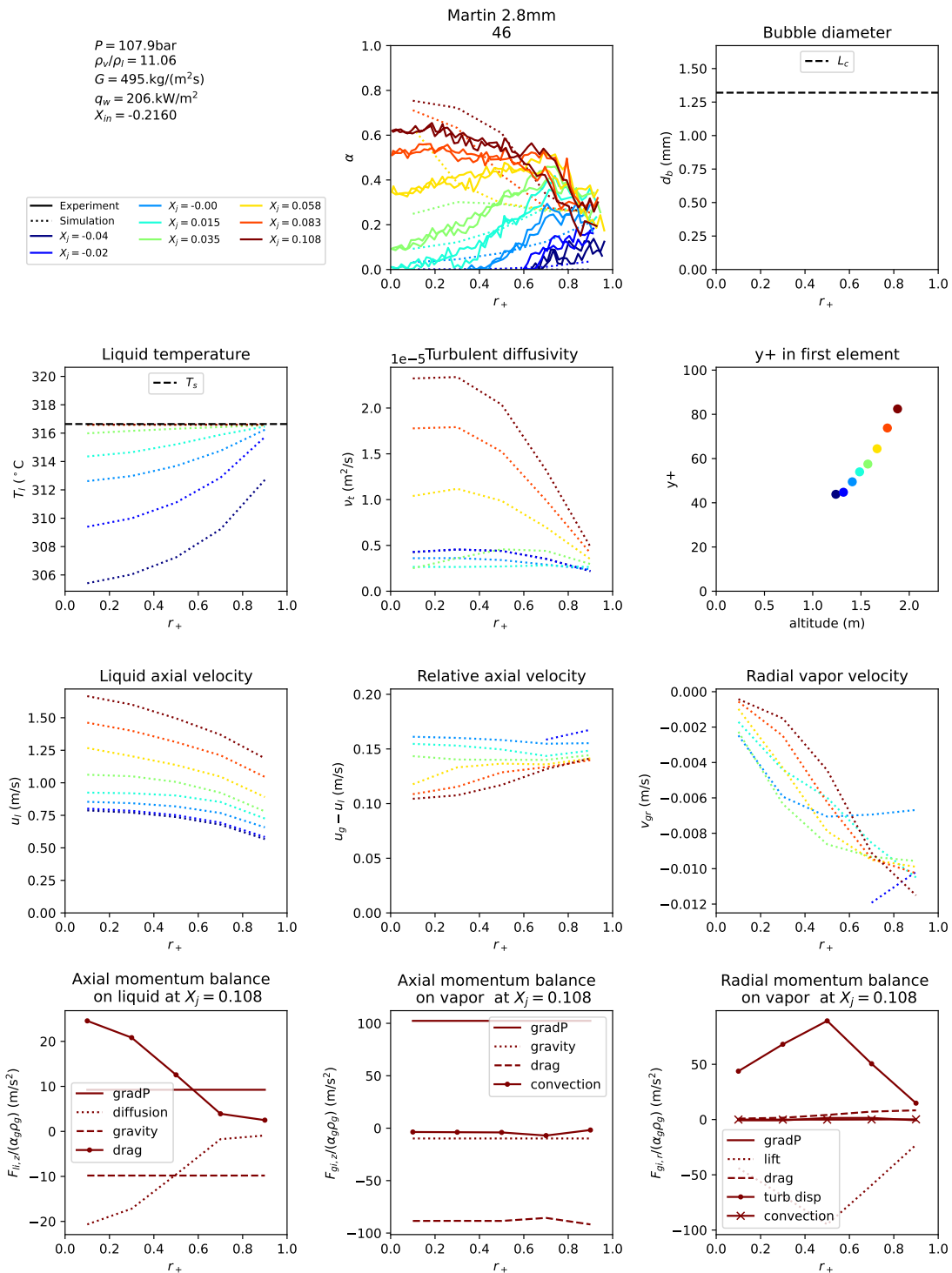


Figure F.103: Simulation results for test tube 46 of Martin 1969. Experimental results are represented with a full line and simulations with a dashed line.

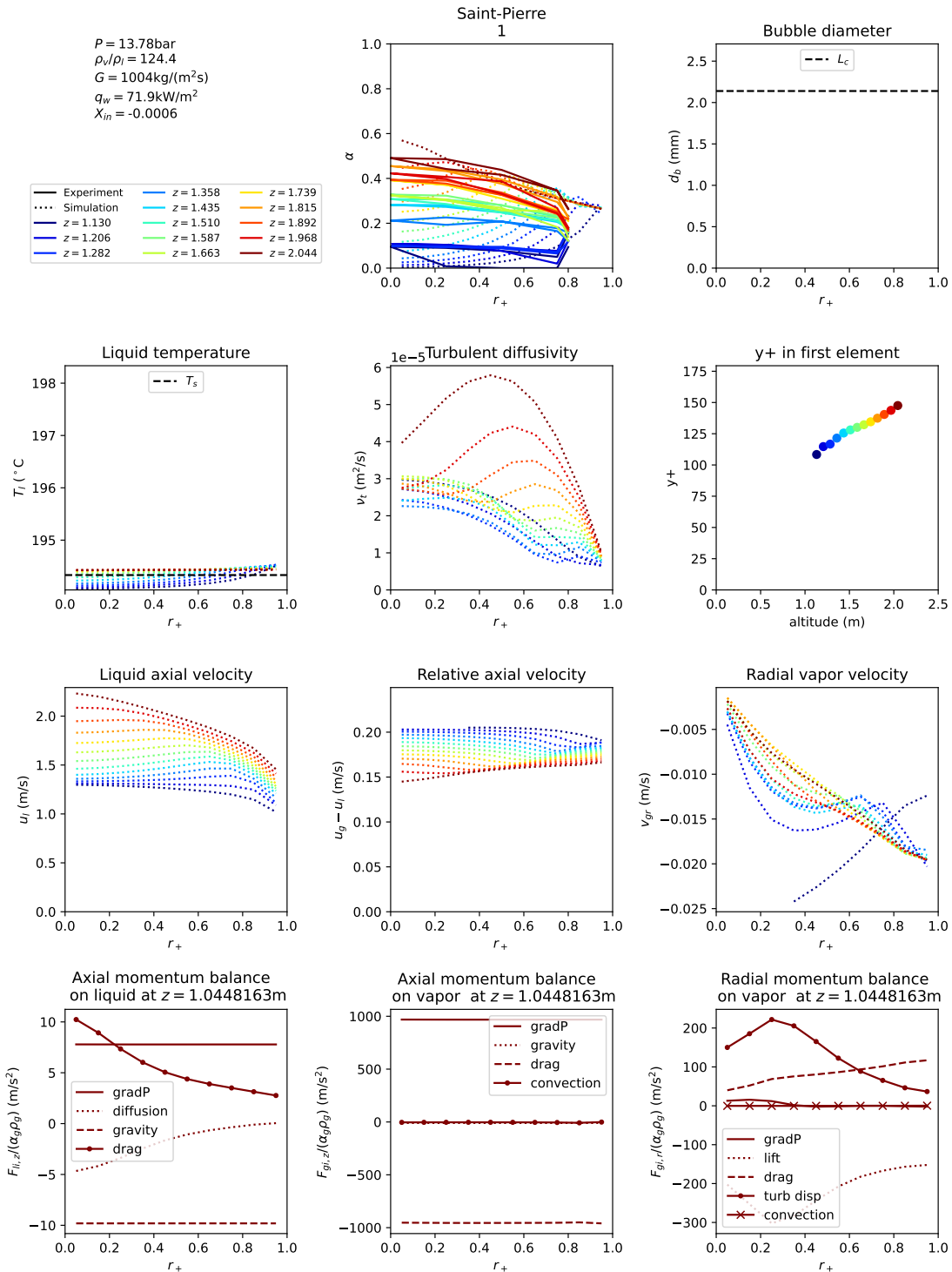


Figure F.104: Simulation results for test tube 1 of St.-Pierre 1965. Experimental results are represented with a full line and simulations with a dashed line.

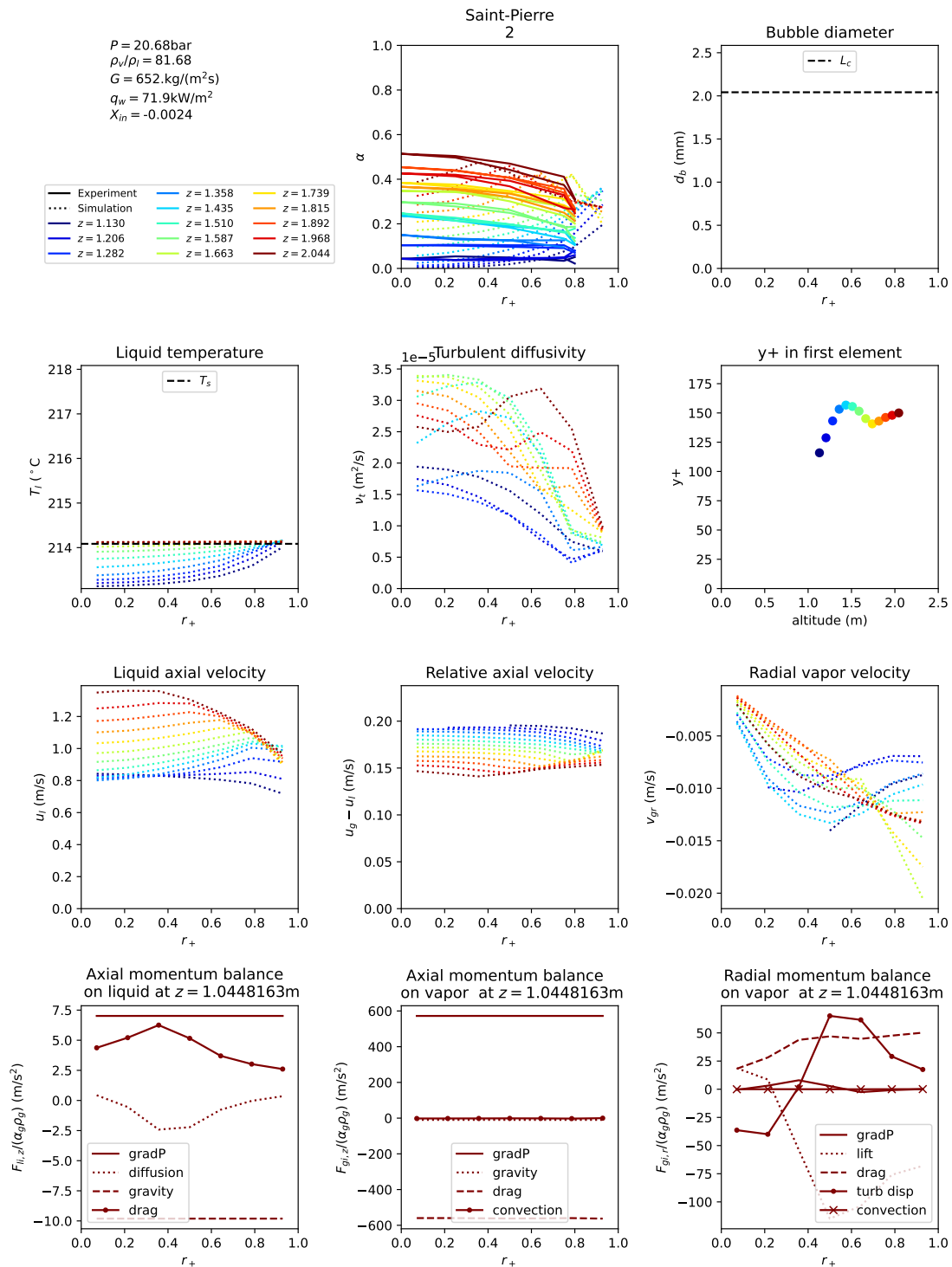


Figure F.105: Simulation results for test tube 2 of St.-Pierre 1965. Experimental results are represented with a full line and simulations with a dashed line.

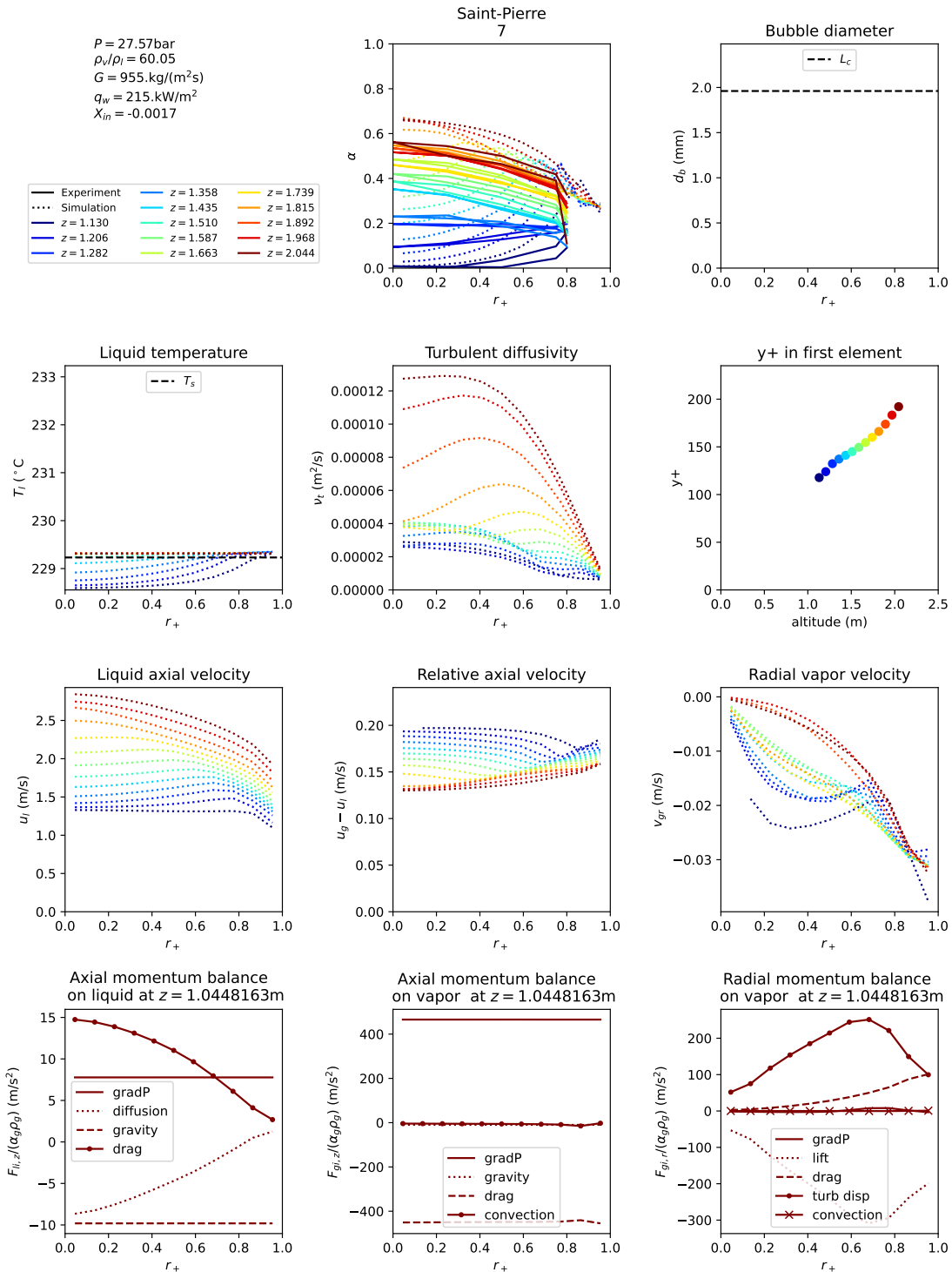


Figure F.106: Simulation results for test tube 7 of St.-Pierre 1965. Experimental results are represented with a full line and simulations with a dashed line.

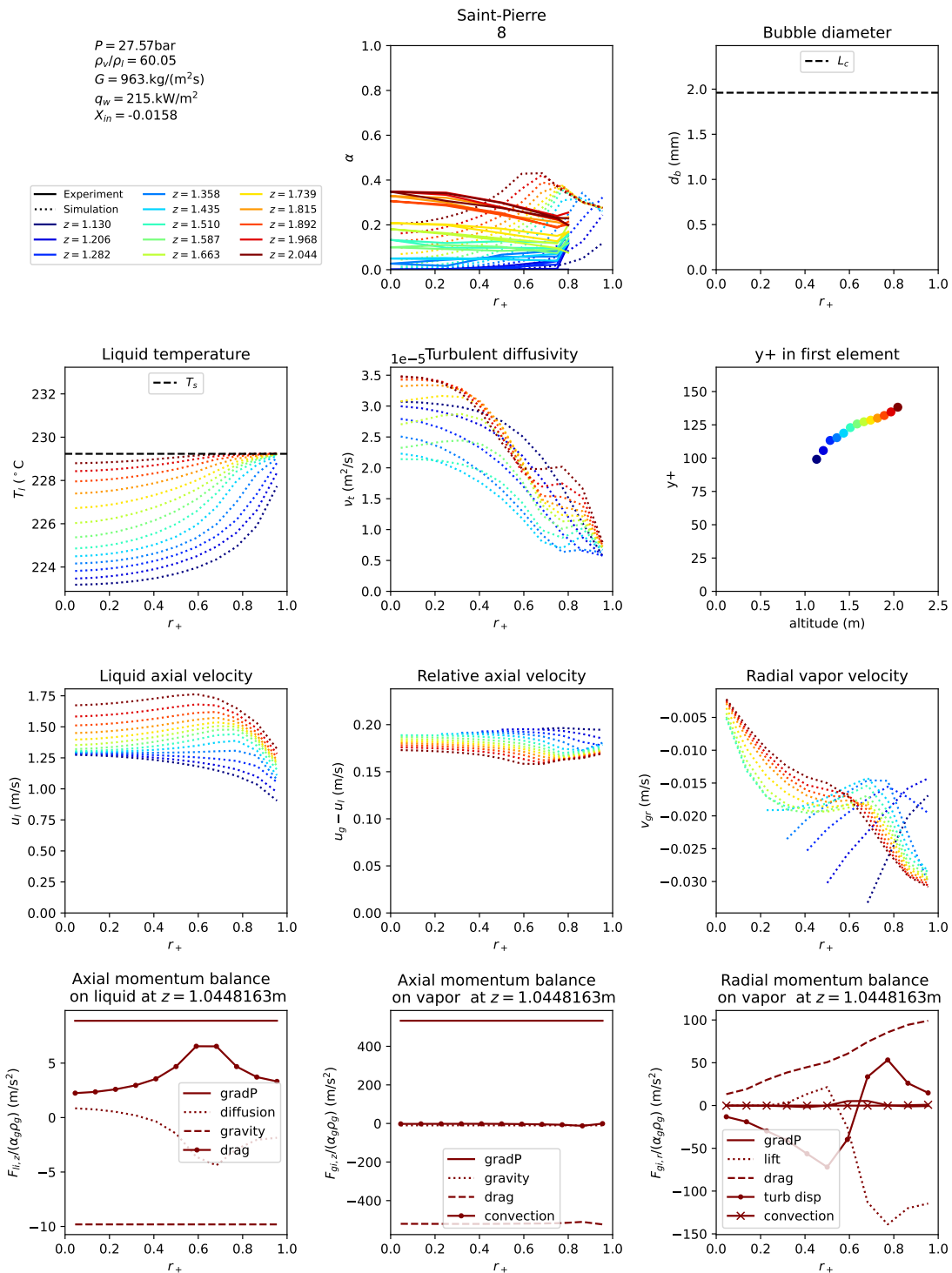


Figure F.107: Simulation results for test tube 8 of St.-Pierre 1965. Experimental results are represented with a full line and simulations with a dashed line.

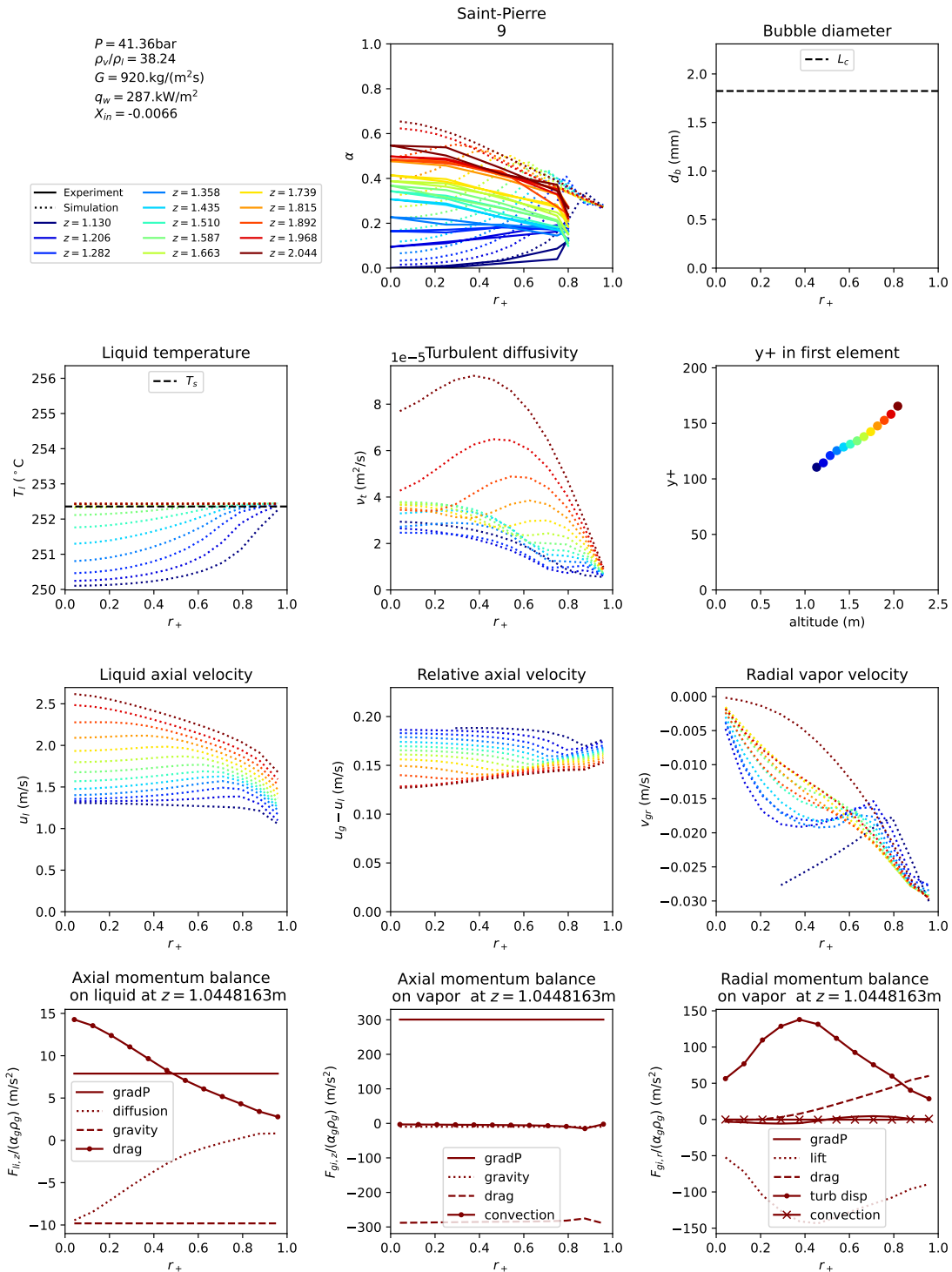


Figure F.108: Simulation results for test tube 9 of St.-Pierre 1965. Experimental results are represented with a full line and simulations with a dashed line.

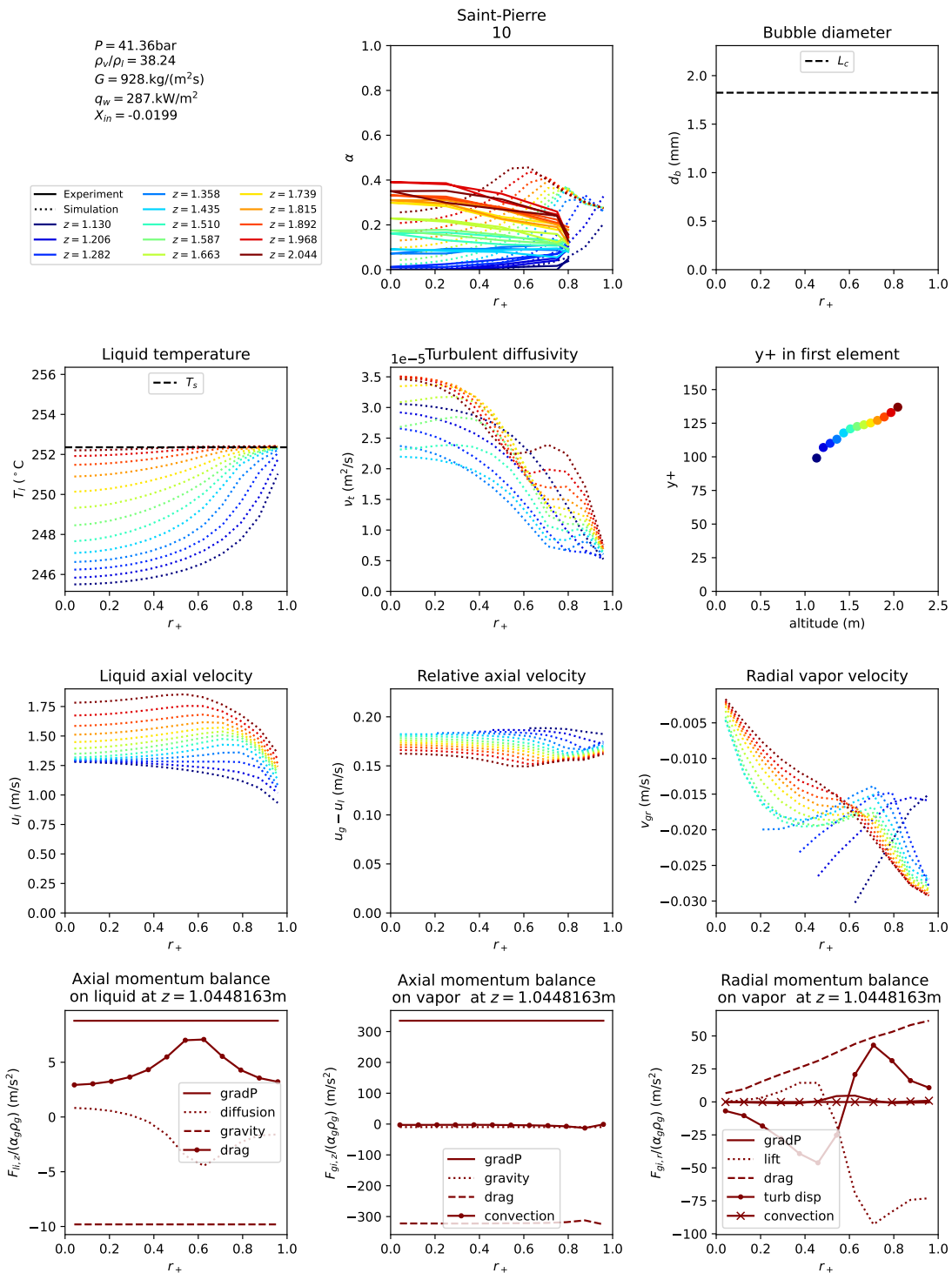


Figure F.109: Simulation results for test tube 10 of St.-Pierre 1965. Experimental results are represented with a full line and simulations with a dashed line.

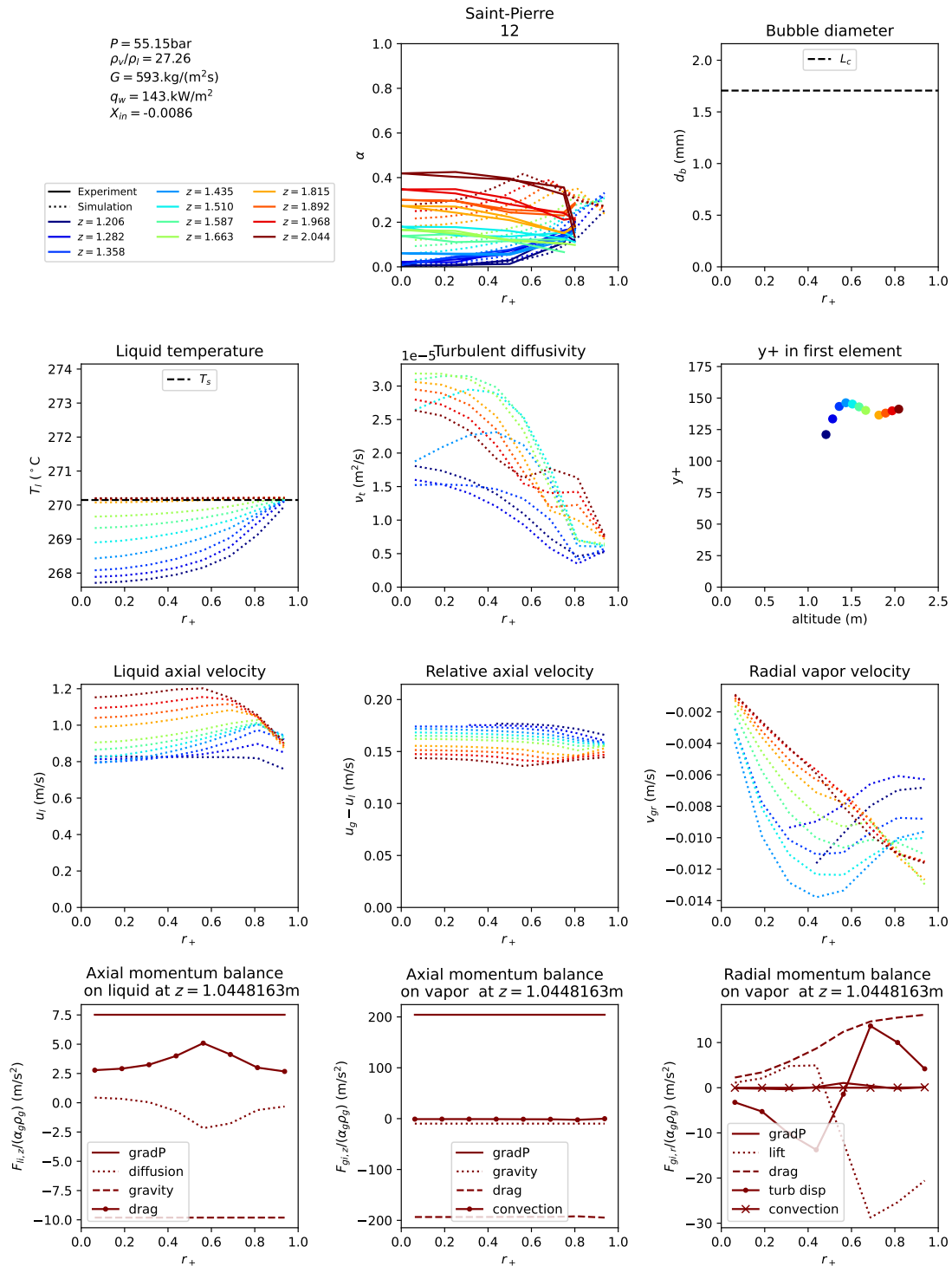


Figure F.110: Simulation results for test tube 12 of St.-Pierre 1965. Experimental results are represented with a full line and simulations with a dashed line.

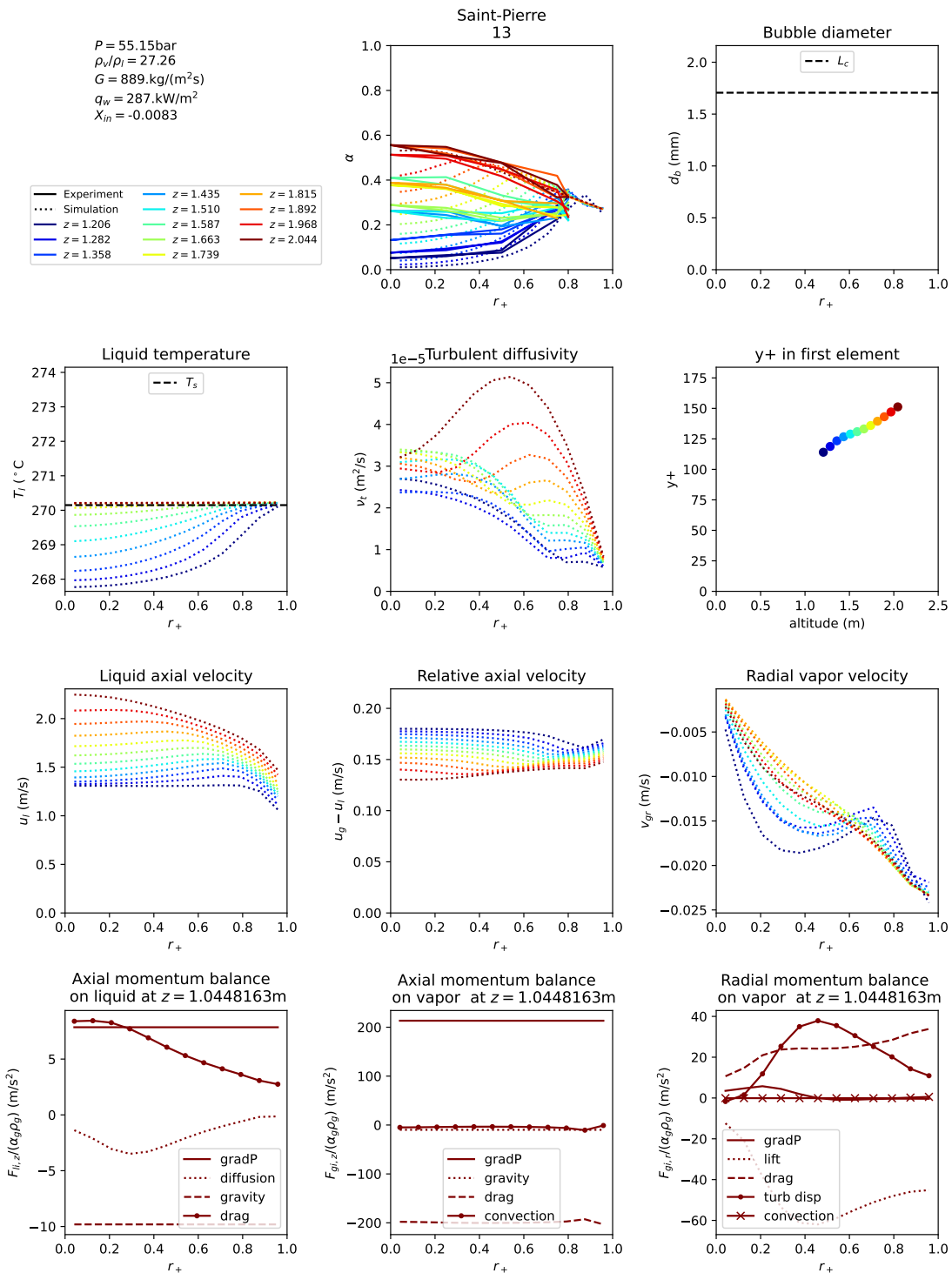


Figure F.111: Simulation results for test tube 13 of St.-Pierre 1965. Experimental results are represented with a full line and simulations with a dashed line.

Titre : Modélisation des écoulements bouillants en réacteur nucléaire par CFD : application à la prédiction du flux critique

Mots clés : CFD, Ecoulement diphasique, Flux Critique, Mécanismes de transfert de chaleur

Résumé : Sous des conditions incidentelles dans les réacteurs à eau pressurisée, l'eau utilisée pour refroidir le combustible nucléaire peut entrer en ébullition. Pour garantir la sûreté des réacteurs, il est indispensable de prédire la dynamique de ces écoulements multiphasiques. Les méthodes actuellement utilisées dans l'industrie s'intéressent aux caractéristiques à grande échelle des écoulements et nécessitent des expériences spécifiques pour chaque géométrie et configuration. L'objectif de cette thèse est de construire un outil numérique et un ensemble de modèles physiques pour prédire les caractéristiques des écoulements en ébullition dans des conditions de réacteur nucléaire à une échelle locale, dans le cadre des outils de CFD (computational fluid dynamics). Cela nous permettra à l'avenir de simuler des configurations pour lesquelles aucune expérience n'est disponible. Nous avons développé un module multiphasique dans le code TrioCFD du CEA. Il utilise un modèle RANS (Reynolds averaged Navier-Stokes) bi-fluide avec une équation de conservation de la masse, de la quantité de mouvement et de l'énergie pour un nombre de fluides quelconques, ou un modèle de dérive. Deux schémas numériques peuvent être utilisés pour résoudre ces équations : un qui permet des calculs rapides sur maillages cartésiens et axisymétriques et un permet des simulations sur maillages polyédriques quelconques. Des fermetures standards de forces de traînée, portance, dispersion turbulente et répulsion en paroi sont intégrées. L'outil de calcul est ensuite validé sur des écoulements à bulles eau-air à pression atmosphérique. Pour modéliser des écoulements bouillants, un terme de condensation et une partition de flux pariétale sont implémentés. La base de données DEBORA, un tube rempli de réfrigérant dans des conditions de similitude vis-à-vis des réacteurs nucléaires, est utilisée comme référence. Le diamètre expérimental est imposé dans le code pour simuler les expériences, ce qui nous permet de lancer des simulations sans les incertitudes liées à l'utilisation d'équations de transport d'aire interfaciale. Les taux de vide prédits par le code sont loin des résultats expérimentaux, et sont trop grands dans la zone en proche paroi. Ceci nous a poussé à regarder de près l'OSV (onset of significant void) dans les codes de CFD. Nous avons construit une base de données sur ce phénomène. En utilisant la structure de la température du liquide dans les écoulements bouillants, nous montrons que l'OSV en écoulement stationnaire développé a lieu lorsque la couche limite turbulente atteint la température de saturation. Ce critère est utilisé pour construire une partition de flux pariétale. Nous avons ensuite cherché à améliorer les fermetures dans le cœur de l'écoulement en réacteur nucléaire, soit dans des conditions de haute pression, flux thermique, débit massique et taux de vide. Nous montrons que dans cette situation les bulles de vapeur sont toujours déformées, i.e. non sphériques. Ceci nous permet de construire des fermetures de portance et de condensation, que nous combinons avec des formulations de traînée et de dispersion turbulente de la littérature. Ce jeu de fermetures est indépendant du diamètre de bulle. Les comparaisons avec l'expérience DEBORA donnent des bons résultats. Pour étendre la validation, nous avons construit une base de données haute pression (>40bar) en eau ou en similitude basée sur des expériences de la littérature qui incluent des sections annulaires, circulaires et rectangulaires. Les résultats obtenus sur les 114 conditions d'essai et 7 campagnes expérimentales sont satisfaisants. Pour finir, nous avons simulé des expériences de flux critique pour obtenir les conditions en proche paroi lors de la crise d'ébullition. L'analyse de ces résultats nous permet de construire un critère simple de flux critique en écoulement stationnaire où le liquide est sous-refroidi en proche paroi.

Title: Modeling flow boiling in nuclear reactor conditions using computational fluid dynamics: application to critical heat flux prediction

Key words: CFD, Two-phase flow, Critical heat flux, Heat transfer mechanisms

Abstract: Under incidental conditions in pressurized water reactors, the water used to cool the nuclear fuel can start to boil. It is essential to predict the dynamics of such multi-phase flows to guarantee reactor safety. The methods currently used in the industry today are focused on the large-scale characteristics of the flows and require specific experiments for every geometry and flow configuration. The aim of the present work is to build a numerical tool and a set of physical models to predict the characteristics of boiling flows in nuclear reactor conditions at a local scale, in a framework called computational fluid dynamics (CFD). In the future, this will enable us to simulate configurations where no experiment is available. We develop a multiphase module in CEA's TrioCFD open-source CFD code. A Reynolds averaged Navier-Stokes two-fluid framework that can solve a mass, momentum and energy equation for an arbitrary number of phases is implemented in two different numerical schemes: one that enables good performance on Cartesian and axisymmetric grids and one that can handle arbitrary polynomial meshes. For multiphase flows, standard drag, lift, turbulent dispersion and wall repulsion forces are coded. The software is validated on standard atmospheric-pressure adiabatic databases where the simulations agree with experimental data. A condensation term and a heat flux partition are added to this set of closures to simulate boiling flows. We first use the DEBORA database, a Freon-filled tube, to evaluate the performance of our set of closures. The experimental bubble diameter is enforced in the code along the whole length of the test section, enabling simulations without the uncertainty of interfacial area transport equations. The predicted void fraction profiles are far from the experimental results, often too high in the near-wall region. This prompts us to investigate the onset of significant void (OSV) in CFD codes. Using experimental data from a dozen different sources, we construct an OSV database. Combining this database with experimental liquid temperature measurements in boiling flows, we show that the OSV in a stationary developed flow occurs when the turbulent boundary layer reaches saturation temperature. This criterion is used to develop a simple heat flux partition that improves results on the DEBORA database compared with the closures from the literature. We then work on improving the bulk closure terms adapted to high-pressure, heat flux, mass flux and void fraction conditions of nuclear reactors. We show that in this situation, bubbles are deformable, i.e. non-spherical. We use this to construct our own lift coefficient and condensation term, and combine them with references from the literature for drag and turbulent dispersion. Innovatively, no interfacial area equation or population balance is required. This set of closures provides good agreement with the DEBORA experiment. To extend the validation, we built a database that includes recent and ancient high-pressure (>40bar) local void fraction measures in pipes, annulus and channels. The results obtained in 114 test conditions are close to experimental data. We then simulate critical heat flux (CHF) experiments to obtain physical quantities in the near-wall region at the boiling crisis. By analyzing these results, we build an empirical CHF criterion for stationary flows where the liquid remains subcooled in the near-wall region. It predicts the CHF with ~10% precision.